MICHAEL METH

QUANTUM SIMULATION WITH TRAPPED-ION QUDITS



QUANTUM SIMULATION WITH TRAPPED-ION QUDITS



Doctoral thesis submitted to the faculty for

MATHEMATICS, COMPUTER SCIENCE AND PHYSICS

In partial fulfillment of the requirements for the degree of

DOCTOR OF PHILOSOPHY (PH.D)

Carried out at the Institute for Experimental Physics under supervision of o.Univ.-Prof. Dr. Rainer Blatt

MICHAEL METH

2025

Michael Meth
Quantum simulation with trapped-ion qudits,
© 2025

ABSTRACT

Simulations enable the systematic study of complex phenomena in a safe and controlled environment. They cover a wide range of applications, from the natural sciences, industrial engineering and material science to tasks in our daily lives. For example, the aerodynamic properties of vehicles are studied in wind tunnels before entering the production phase. Likewise, the behavior of buildings under tension and compression forces are investigated using small scale models before laying the foundation. Moreover, the materials used in construction are tested beyond their point of failure, thereby enhancing safety and increasing longevity. These simulations are analog: a problem is physically realized on a small scale and tested extensively. With the rapid progress in computer science, many simulations are nowadays digital. Here, complex processes are described by mathematical models and algorithms, thereby mimicking nature as best as possible. The capabilities of digital simulators far exceed their analog counterparts and allow accessing regimes, which otherwise remain difficult to study by conventional methods.

A digital computer processes information as sequences of numbers encoded in binary format, which are manipulated by programmable electronic circuits. The smallest unit of information is the *binary digit (bit)*, which can be in either of the states zero or one. Complex calculations are decomposed into sets of few fundamental logic operations, which serve as the building blocks of more sophisticated algorithms. A digital simulation is realized using a mathematical model of a target problem. Using a set of instructions, the computer is instructed to compute the model for a certain set of input parameters. These simulations have proven very successful in many applications. However, certain problems in areas such as high-energy and quantum physics remain challenging even for the most advanced supercomputers. One fundamental issue is the rapid increase in the number of degrees of freedom, making large-scale computation significantly more difficult if not downright intractable. Quantum computers are promising candidates to overcome some of the limitations of classical systems, utilizing the phenomena of superposition and entanglement to enhance the computation. Many concepts of classical information science have been carried over to the field of quantum computing, among others the binary encoding of data in *quantum bits (qubits)*. However, most quantum systems are naturally high-dimensional, thereby offering the possibility of encoding data in more than just two discrete states. These *quantum digits (qudits)* hold great potential, with applications in the study of many-body systems, high-energy physics and fault tolerant quantum computation.

In this thesis we present a qudit quantum processor based on an existing trapped ion system. We show how qudits are encoded in the level structure of calcium ions and how they are manipulated using coherent laser pulses. An extension to the existing set of operations, called *quantum gates* is presented, which enables the manipulation of a target qudit conditioned on the state of a second control qudit. This *controlled rotation gate* is a natural extension of the *controlled-NOT gate* proposed by Cirac and Zoller to higher-dimensional systems.

A variant of this gate is used to study the ground states of the *Su-Schrieffer-Heeger* model, which describes a dimerized spin chain. We employ a hybrid algorithm to prepare approximations of the true ground state by variational optimization. A classical computer proposes sets of trial parameters, thereby tuning a sequence of quantum gates executed on the quantum processor. The energy of the quantum state is computed from a set of measurement outcomes and serves as the cost function of the algorithm, which is supposed to be minimized. Once a minimum has been found, the associated quantum state is a good approximation of the true ground state. Using this method, we simulate a *topological quantum phase transition* and observe the emergence of a *symmetry broken phase*.

In a second experiment we simulate phenomena in *quantum-electrodynamics (QED)*. QED is a gauge theory, which describes the interplay of charged matter with electromagnetic fields. We demonstrate the minimal instance: a single plaquette described by four sites which are populated by particles and antiparticles. The gauge fields are represented by qudits, which reside on the links between pairs of sites, thereby controlling the dynamics. This system enables the study of true 2D phenomena, namely the emergence of magnetic fields. Moreover, we investigate the effects of gauge field discretizations and observe an increase in accuracy with higher dimensional representations of the gauge fields.

ZUSAMMENFASSUNG

Simulationen ermöglichen die Untersuchung komplexer Phänomene in einer sicheren und kontrollierten Umgebung. Dabei wird ein breites Spektrum an Anwendungen abgedeckt, das sich weit über die Naturwissenschaften hinaus bis in das alltägliche Leben erstreckt. So werden beispielsweise die aerodynamischen Eigenschaften von Fahrzeugen in Windkanälen studiert, bevor eine Serienproduktion in Auftrag gegeben wird. Scher- und Kompressionsbelastungen von Bauwerken werden anhand von Modellen im kleinen Maßstab untersucht und die verwendeten Materialien auf bis über ihre Belastungsgrenze hinaus ausgiebig getestet. Diese Art von Simulationen ist analog: eine Problemstellung wird physisch im kleinen Maßstab nachgebildet und das Testsystem direkt beobachtet. Mit fortschreitender Entwicklung der Computertechnik wurden Simulationen zunehmend digitalisiert. Hierbei werden komplexe Abläufe in der Natur durch mathematische Modellierung und Algorithmen so gut wie möglich abgebildet. Die Fähigkeiten dieser Systeme überschreiten jene analoger Simulatoren und ermöglichen den Zugang zu Regimen, die andernfalls nur unter enormem Aufwand studiert werden können.

In einem digitalen Computer wird Information als Sequenz von Zahlen im Binärsystem dargestellt. Die kleinste Informationseinheit bildet das *Bit*, welches einen der zwei Zustände Null oder Eins annehmen kann. Mithilfe programmierbarer Schaltkreise wird eine kleine Anzahl von wenigen fundamentalen logischen Operationen realisiert, welche die Grundbausteine für komplexere Algorithmen darstellen. Eine digitale Simulation implementiert ein mathematisches Modell und leitet den Computer an, dieses für gewisse Parameter auszuwerten. Das Ergebnis dieser Berechnungen ist eine gute Näherung an das reale Verhalten eines physikalischen Systems. In vielen Bereichen sind diese Simulationen mehr als ausreichend um ein Fragestellung zufriedenstellend zu beantworten. Doch gerade in der Hochenergie- und Quantenphysik stößt ein klassischer digitaler Prozessor schnell an seine Grenzen. Einer der Gründe ist die rasch anwachsende Zahl an Freiheitsgraden, welche die Berechnungen verkomplizieren oder gar unmöglich machen. Abhilfe versprechen hier Quantencomputer, die durch Superposition und Verschränkung einige Limitierungen klassischer Computer auf natürliche Weise überwinden. Viele Konzepte der klassischen Informationstheorie wurden auf Quantencomputer übertragen, darunter auch die binäre Kodierung von Information in *Quanten-Bits (Qubits)*. Quantensysteme sind jedoch von Natur aus hochdimensional und bieten daher die Möglichkeit, Information in mehr als nur zwei Zuständen zu codieren. Diese *Quanten-Digits (Qudits)* bieten ein enormes Potential mit Anwendungen im Bereich der Simulation von Vielteilchensystemen, Hochenergiephysik und der Entwicklung von fehlertoleranter Quanteninformationsverarbeitung.

In der vorliegenden Arbeit wird ein digitaler Qudit-Quantenprozessor vorgestellt, welcher auf einem bereits bestehenden Ionenfallen-Quantencomputer aufbaut. In diesem System werden Qudits in den elektronischen Zuständen gefangener Kalzium-Ionen codiert und mit präzisen, kohärenten Laserpulsen kontrolliert. Die so realisierten Operationen, auch Quantengatter genannt, ermöglichen die Implementierung komplexer Algorithmen. Es wird eine Erweiterung des vorhandenen Gattersatzes präsentiert, welche die Manipulation eines Qudits unter einer Bedingung, die an den Zustand eines weiteren Qudits geknüpft ist,

erlaubt. Die Grundlage für dieses *controlled-rotation* Gatters bildet das von Cirac und Zoller vorgestellte *controlled-NOT* Gatter, das sich auf höherdimensionale Systeme fortsetzen lässt.

Eine reduzierte Variante dieses neuen Gatters wird in der Quantensimulation eines Vielteilchensystems angewandt. Hierbei werden die Grundzustände des *Su-Schrieffer-Heeger* Modells, das eine dimerisierte Spin-Kette beschreibt, mit einem hybriden Algorithmus erzeugt. Der Quantenprozessor wird mit einem klassischen Computer gekoppelt, welcher die Energie des erzeugten Zustandes misst. Auf Basis des Ergebnisses werden die Parameter der Quantengatter angepasst und die Energie erneut gemessen. Dieser Prozess wird wiederholt bis ein energetisches Minimum erreicht wird. Der damit verbundene Zustand stellt eine gute Annäherung an den tatsächlichen Grundzustand des Modells dar. Mithilfe dieser Methode wird ein *topologischer Phasenübergang* untersucht und ein *Symmetriebruch* beobachtet.

In einem weiteren Experiment werden Phänomene der *Quantenelektrodynamik (QED)* bei verschiedenen Kopplungsstärken simuliert. QED ist eine Gittereichtheorie, welche die Wechselwirkung zwischen geladenen massiven Teilchen und Feldern beschreibt. Die Eichfelder sind dabei von Natur aus hochdimensional und lassen sich daher ideal durch Qudits darstellen. In dieser Arbeit wird die Kopplung zwischen einem Eichfeld und dynamischer Materie simuliert. Hierbei wird eine viereckige Plakette betrachtet, welche von Teilchen und Antiteilchen besetzt wird, die durch Qubits abgebildet werden. Das Feld ist an den Kanten der Plakette ausgebildet und beeinflusst die Dynamik des Systems maßgeblich. Hier wird erstmalig der Aufbau eines Magnetfeldes simuliert, sowie eine Verbesserung der Genauigkeit mit zunehmender Dimension des Eichfeldes beobachtet.

ACKNOWLEDGMENTS

Although the title *"Doctor of Philosophy"* is awarded to a single person, progress – whether it is scientific, industrial or cultural – is rarely made by a lone individual. During my PhD programme I was given the opportunity to meet outstanding people, learn from and collaborate with experts, and also grow as an individual. I am eternally grateful for each and every one who accompanied me on my journey and their continuous support over the past few years.

I would like to thank my supervisors, first and foremost Professor Dr. Rainer Blatt, who initially sparked my interest in quantum physics while I was still completing my undergraduate studies. His enthusiasm for this field of research continues to inspire me, and his insightful comments have contributed to shape my perspective on science and its methods. I am equally grateful for Dr. Thomas Monz, whose expertise in securing funding allowed my colleagues and me to sleep soundly, never having to worry about our finances. Even during stressful times, he always maintained his sense of humor and was never hesitant to offer valuable advice. I would like to thank Dr. Philipp Schindler, who taught me to think outside the box and not to shy away from exploring alternative, less obvious methods. Besides physics, I benefited substantially from his knowledge in electronics and computer science – both essential fields in my everyday work in the laboratory. And finally, I want to thank Dr. Martin Ringbauer, whose calm and level-headed nature encouraged me to keep going during times when I doubted my work.

Over the past years, I have witnessed many people leave the group, either by graduating from their programme or by pursuing new positions in academia and industry. I am now the "last man standing" of the original team working on and maintaining the *Linear Trap* experiment, since my colleagues Dr. Alexander Erhard, Dr. Roman Stricker and Dr. Lukas Postler have already successfully completed their PhD. I had the pleasure not only of sharing an office with them, but also of experiencing the ups and downs of life as a PhD student together. All of them have contributed substantially to the current state of the *Linear Trap*, and without their hard work, novel ideas and continuous support, my research would not have been possible. A few years into my graduate studies Dr. Claire Edmunds joined the team as a postdoctoral fellow. Although supervising students was not part of her official duties, she never hesitated to assist me in my work and shared valuable advice, for which I am truly grateful.

I would also like to acknowledge the people with whom I had the pleasure of collaborating on several exciting research projects. The extensive work of Dr. Viacheslav Kuzmin and now Professor Dr. Pietro Silvi ultimately led to my first publication. I sincerely thank them for their hard work and dedication, their insightful discussions and – most notably – their patience, whenever progress in the laboratory stagnated. Later I had the pleasure to work with the team of Professor Dr. Christine Muschik, notably Dr. Jan Haase, Dr. Jinglei Zhang and Professor Dr. Luca Dellantonio. I am grateful for their continuous support — especially for the efforts of Dr. Zhang and Professor Dellantonio, with whom I am still in contact. I look forward to future collaborations, exciting new projects and interesting physics to be

investigated as a team.

With Dr. Martin Ringbauer now having established his own research group, new motivated graduate students have taken over the *Linear Trap*. Peter Tirler and Manuel John joined the group early on, followed by Keshav Pareek and Tim Gollerthan shortly thereafter after. I had the pleasure to work and assist them in their projects and will continue to do so after my graduation. I truly hope to live up to my own expectation of offering support that is as valuable as the guidance I received from my own supervisors.

I would like to thank my colleagues and friends both from the university – most notably my office mates Dr. Bassem Badawi, Dr. Lukas Gerster, Alex Steiner, Lorenz Panzl and Marco Valentini, who kept me company and lifted my spirits, even when times get tough. I am especially grateful for Dr. Christian Marciniak, who offered both scientific and interpersonal advice whenever I doubted some of my life choices. To all my colleagues from other research groups and institutes – too many to address them individually – I would like to express my gratitude for your support and the friendships we built along this journey.

Lastly, my heart goes out to my friends and family – especially to my mother Anita and my father Robert, who recently passed away after a short but fatal illness. Their love and support kept me going through both good times and hardships. I am thankful for and proud of my two sisters, Dr. Christina Meth and Chiara Schätzer, for their continuous reassurance and for keeping me on the right path.

I will be eternally grateful for what you – all of you – have done for me, and sincerely hope that I can return the favor and stand by your side whenever you need me.

We're all in this together.

"Non est ad astra mollis e terris via."
– Lucius Annaeus Seneca

CONTENTS

1 DIGITAL QUANTUM SIMULATION BEYOND THE BINARY 1
1.1 Representing data by sequences of numbers . . . 1
1.2 Classical and quantum information . . . 3
1.2.1 A binary formulation of quantum computing . . . 4
1.2.2 Manipulation of quantum states . . . 6
1.2.3 Quantum circuit model . . . 9
1.2.4 Measurements on quantum systems . . . 10
1.3 Beyond the binary – a case for higher dimensional systems . . . 11
1.3.1 Binary encoding . . . 11
1.3.2 "One-hot" encoding . . . 12

2 A QUANTUM PROCESSOR WITH TRAPPED IONS 15
2.1 Confining ions in space . . . 16
2.1.1 Trapping a single ion . . . 17
2.1.2 A linear chain of ions . . . 19
2.2 Trapped ions interacting with coherent light fields . . . 20
2.3 Cooling trapped ions with lasers . . . 26
2.3.1 Doppler cooling . . . 28
2.3.2 Sisyphus cooling . . . 30
2.3.3 Sideband cooling . . . 32
2.4 Optical pumping to selected ground states . . . 33
2.5 Readout of quantum states by fluorescence detection . . . 34

3 EXPERIMENTAL SETUP 37
3.1 Ion trap and vacuum chamber . . . 38
3.2 Laser light for quantum information processing . . . 41
3.2.1 Manipulating light with acousto-optic modulators . . . 41
3.2.2 Addressing subsets of ions in large registers . . . 43
3.2.3 Diode laser systems for laser cooling and readout . . . 44
3.2.4 Narrow-band laser for qudit manipulation . . . 46
3.3 Classical control of quantum algorithms . . . 48
3.3.1 Programmable pulse generator . . . 48
3.3.2 Pulse sequences for quantum information experiments . . . 50

4 REALIZING QUANTUM GATES IN TRAPPED ION QUDITS 53
4.1 Quantum gates on a single qudit . . . 53
4.1.1 Local rotations on a subspace . . . 54
4.1.2 Measurement protocols for trapped ion qudits . . . 55
4.1.3 QR decomposition of qudit spin operators . . . 56
4.2 Creating entanglement with bichromatic light fields . . . 58
4.2.1 Entangled states with arbitrary probability amplitudes . . . 61
4.2.2 AC Stark shifts, power imbalancing and spectator phases . . . 62
4.2.3 Off-resonant couplings and pulse amplitude shaping . . . 63
4.3 Mediating entanglement by controlled excitation of the collective motion . . . 64

4.3.1 Compensation of AC Stark shifts . . . 65
4.3.2 Native Cirac-Zoller type quantum gates in qudits . . . 68
4.3.3 Implementing scalable multi-qudit gates with controlled rotations . 70
4.4 Readout of qudits by sequential fluorescence detection . . . 73

5 STUDYING MANY-BODY PHYSICS ON QUANTUM SIMULATORS 75
5.1 Introduction to matrix product states . . . 75
5.1.1 Singular value decomposition and Schmidt coefficients . . . 76
5.1.2 Construction of matrix product states by sequential bipartition . . . 77
5.1.3 Valence bond picture . . . 81
5.1.4 Matrix product operators . . . 82
5.1.5 Expectation values . . . 84
5.1.6 Correlations and correlation length . . . 86
5.2 Hamiltonians and ground states of many-body systems . . . 87
5.2.1 Spectral gaps lead to exponentially decaying correlations . . . 88
5.2.2 Approximating ground states with variational algorithms . . . 92
5.3 Physical properties of many-body systems . . . 94
5.3.1 The Su-Schrieffer-Heeger model . . . 94
5.3.2 Topological quantum phases and phase transitions . . . 97
5.3.3 Mapping the SSH model onto qubits . . . 100

6 EXPERIMENTAL OBSERVATION OF A TOPOLOGICAL QUANTUM PHASE TRANSITION 103
6.1 Variational circuit with a global quantum data bus . . . 103
6.2 Implementation on a trapped ion system . . . 105
6.2.1 Initialization and qubit encoding . . . 105
6.2.2 Demonstration on a toy system . . . 107
6.2.3 Energy measurement and variational optimization . . . 108
6.3 Observing a quantum phase transition . . . 111
6.3.1 Trivial and topological regime in the standard SSH model . . . 111
6.3.2 Symmetry breaking in the extended SSH model . . . 112
6.4 Imperfections and error modelling . . . 113
6.4.1 Finite temperature and motional heating . . . 114
6.4.2 Depolarization and weighted Pauli errors . . . 115

7 QUANTUM FIELDS AND LATTICE GAUGE THEORIES 117
7.1 Preliminaries . . . 118
7.1.1 Lorentz transformations . . . 118
7.1.2 Relativistic notation . . . 120
7.1.3 Covariant formulation of classical electrodynamics . . . 121
7.2 Lagrangian field theory . . . 124
7.2.1 Principle of least action . . . 124
7.2.2 Classical fields and the Klein-Gordon equation . . . 125
7.3 Quantum fields . . . 127
7.3.1 Canonical quantization of the Klein-Gordon field . . . 128
7.3.2 The Dirac field . . . 131
7.3.3 Symmetry transformations and gauge fields . . . 135
7.4 Quantum electrodynamics . . . 139
7.4.1 Gauge fixing . . . 139

7.4.2 Quantization of the radiation field . . . 140
7.4.3 Propagators . . . 143
7.4.4 Feynman diagrams . . . 145
7.4.5 Renormalization and running coupling . . . 147
7.5 Hamiltonian formulation of gauge theories on a lattice . . . 150
7.5.1 Wilson lines and loops . . . 151
7.5.2 Fermions on the lattice . . . 153
7.5.3 Kogut-Susskind Hamiltonian . . . 157

8 SIMULATION OF A (2 + 1)D LATTICE GAUGE THEORY ON A QUDIT QUANTUM SIMULATOR 161
8.1 A gauge field interacting with dynamical matter . . . 161
8.1.1 Variational circuit and ground state approximation . . . 164
8.1.2 Experimental imperfections and noise modeling . . . 167
8.1.3 Observation of the dynamics between gauge field and matter . . . 168
8.1.4 Real-time evolution . . . 170
8.1.5 Alternative lattice model . . . 171
8.2 Interactions between pure gauge fields on a square lattice . . . 173
8.2.1 Variational circuits in two representations . . . 174
8.2.2 Encoding rotators in trapped-ion qudits . . . 175
8.2.3 Approximating the ground state of the pure-gauge Hamiltonian . . . 177
8.2.4 Refining the gauge field discretization . . . 179

9 SUMMARY AND OUTLOOK 183

A APPENDIX 187
A.1 Forced symmetry breaking in the SSH model by introduction of a magnetic bias field . . . 187
A.2 Design of the variational circuits in the pure-gauge case . . . 188
A.3 Approximating the ground states of the pure-gauge theory . . . 192

B LIST OF PUBLICATIONS 195

BIBLIOGRAPHY 197

LIST OF FIGURES

Figure 1.1 Optimal base to represent a number $n \in \mathbb{N}$ in a positional numeral system. . . . 2
Figure 1.2 Realization of a classical bit . . . 3
Figure 1.3 Representation of the quantum state of a qubit in 3D space . . . 8
Figure 1.4 Classical and quantum logic circuit implementing the Toffoli gate . 10
Figure 1.5 Binary-style encoding of a boson in two qubits . . . 12
Figure 1.6 One-hot encoding of a spin-S boson in $2S + 1$ qubits . . . 12
Figure 1.7 Spin-1 boson encoded in a physical qudit . . . 14
Figure 2.1 Quadrupole mass filter and linear Paul trap . . . 17
Figure 2.2 Approximation of an ion by a set of two or three energy levels . . . 21
Figure 2.3 Rabi oscillations . . . 24
Figure 2.4 Visualization of the quantum state on the Bloch sphere . . . 24
Figure 2.5 Two-level approximation including the motion of the ions . . . 26
Figure 2.6 Doppler cooling of a trapped ion . . . 29
Figure 2.7 Laser cooling techniques: Sisyphus cooling . . . 30
Figure 2.8 Laser cooling techniques: Polarization gradient cooling . . . 31
Figure 2.9 Laser cooling techniques: Sideband cooling . . . 33
Figure 2.10 Optical pumping . . . 34
Figure 2.11 Fluorescence detection . . . 35
Figure 3.1 Reduced level scheme of Calcium-40 . . . 37
Figure 3.2 Vacuum vessel and linear Paul trap . . . 39
Figure 3.3 Acousto-optic modulators – principle of operation and setups . . . 42
Figure 3.4 Ion addressing with acousto-optic deflectors . . . 44
Figure 3.5 Dipole lasers – setup, control and distribution . . . 45
Figure 3.6 Narrow-band qudit laser – setup, control and distribution . . . 47
Figure 3.7 M-ACTION pulse generator hardware – simplified circuit diagram 49
Figure 3.8 Pulse sequencing . . . 51
Figure 4.1 Rabi oscillations on a single ion in a larger register. . . . 54
Figure 4.2 W-encoding scheme for efficient QR decompositions . . . 58
Figure 4.3 Mølmer-Sørensen scheme: entangling two trapped ions via bichromatic light fields . . . 59
Figure 4.4 Time evolution of a state under the Mølmer-Sørensen interaction . 60
Figure 4.5 Scheme enabling full control over the Mølmer-Sørensen interaction by tuning of the laser intensity . . . 61
Figure 4.6 Compensation of AC Stark shifts by power imbalancing . . . 62
Figure 4.7 Pulse shaping . . . 63
Figure 4.8 Illustration of the blue sideband interaction . . . 65
Figure 4.9 Active compensation technique for AC Stark shifts on the blue sideband . . . 66
Figure 4.10 Measurement and compensation of AC Stark shifts on spectator levels in a qudit . . . 67
Figure 4.11 Controlled rotation gates . . . 69
Figure 4.12 n-bit controlled rotation gate . . . 71

Figure 4.13 Experimentally verified truth tables for the Toffoli gate 73
Figure 4.14 Readout of qudit states by fluorescence detection 74
Figure 5.1 Linear chain of spins 75
Figure 5.2 Schmidt decomposition of a quantum state 77
Figure 5.3 Decomposition of a quantum state (II) 78
Figure 5.4 Valence-bond picture for MPS 81
Figure 5.5 Graphical representation of matrix product unitaries 83
Figure 5.6 Norm of an MPS 84
Figure 5.7 Partitioning of the approximate ground state projector 88
Figure 5.8 Propagation of perturbations in 1D spin chain 90
Figure 5.9 Decay of correlations in a 1D spin chain 90
Figure 5.10 Workflow in a variational quantum eigensolver 93
Figure 5.11 Configurations of atoms in a 1D lattice 94
Figure 5.12 Energy bands in a dimerized 1D lattice 96
Figure 5.13 Lattice configuration in the insulating regimes: edge states 97
Figure 5.14 Band Hamiltonian and winding number 98
Figure 5.15 Many-body topological invariants 99
Figure 5.16 Energy spectrum and topological invariants in the SSH model . . . 101
Figure 5.17 Quantum phase transition in the extended SSH model 101
Figure 6.1 Variational quantum circuit preparing approximate ground states of the SSH model 104
Figure 6.2 Variational circuit in MPU form 105
Figure 6.3 Qubit encoding and spectral decoupling scheme in the SSH model 106
Figure 6.4 Quantum state at $T = -1$ simulated and implemented on $N = 4$ ions 107
Figure 6.5 Approximation of the ground state of the SSH model by variational optimization 109
Figure 6.6 Energy of the approximate ground states generated by variational optimization for different coupling strengths 110
Figure 6.7 Experimental observation of a quantum phase transition in the SSH model 112
Figure 6.8 Experimental observation of the phase transition in the *extended* SSH model 113
Figure 6.9 Impact of finite temperature and motional heating on the many-body topological invariants. 114
Figure 6.10 Depolarizing errors along the z axis impacting the many-body topological invariants 116
Figure 7.1 Illustration of Galilei and Lorentz transformations in 1D 119
Figure 7.2 Co- and contravariant components of a vector 121
Figure 7.3 Examples of Feynman diagrams for common processes in QED. . . 146
Figure 7.4 Feynman diagram for a fourth-order process 148
Figure 7.5 Discretization of spacetime by a regular lattice 150
Figure 7.6 Gauge fields on the lattice - Wilson lines and loops 152
Figure 7.7 Fermions on the lattice 155
Figure 7.8 Electric fields on the lattice 158
Figure 8.1 Quantum electrodynamics on a 2D square lattice 162
Figure 8.2 Variational quantum circuit preparing the ground state of a gauge field with four matter sites 165
Figure 8.3 Ground state approximation using a Bayesian optimizer coupled with a database 167

Figure 8.4 Quantum simulation of QED in 2D including gauge field and matter 169
Figure 8.5 Trotterized real-time evolution of the system under the Kogut-Susskind Hamiltonian . . . 171
Figure 8.6 Quantum simulation of the alternative lattice model . . . 172
Figure 8.7 Quantum simulation of a pure gauge theory with periodic boundary conditions . . . 174
Figure 8.8 Loops on the torus in the pure-gauge theory with periodic boundary conditions . . . 174
Figure 8.9 Variational circuits approximating the ground states of the pure-gauge Hamiltonian in two bases . . . 176
Figure 8.10 Approximating the ground state of the pure-gauge Hamiltonian in two qudit dimensions . . . 178
Figure 8.11 Plaquette operator of the pure gauge theory for different gauge field truncations . . . 180
Figure 8.12 Population of the qudit states in the pure-gauge theory . . . 181
Figure A.1 Forced symmetry breaking by magnetic bias fields . . . 187
Figure A.2 Decomposition of $\hat{H}_{loc.}$ into quantum gates . . . 191
Figure A.3 Energies in the pure gauge theory (qutrits) . . . 193
Figure A.4 Energies in the pure gauge theory (ququints) . . . 194

LIST OF TABLES

Table 4.1 Encoding of the quantum states in the 3-bit Toffoli scheme . . . 72
Table 6.1 Optimal solution for $T = 0$ in the SSH model obtained from numerical simulation of the reduced circuit . . . 107
Table 6.2 Residual sum of squares (RSS) for error models including finite temperature and motional heating . . . 115
Table 6.3 Residual sum of squares (RSS) for depolarizing errors along the quantization axis of the qubits . . . 116
Table 8.1 Encoding of particles and gauge fields in the simulation of QED in 2D with open boundary conditions . . . 163
Table 8.2 Mapping of the rotators onto the electronic states of trapped ions . 177

ACRONYMS

AOD *acousto-optic deflector*
AOM *acousto-optic modulator*
BCH *Baker-Campbell-Hausdorff*
BSB *blue sideband*
CCD *charge-coupled device*
COM *center-of-mass*
DDS *direct-digital synthesizers*
DP *double-pass*
EMCCD *electron-multiplied CCD*
FPGA *field-programmable gate array*
FSU *frequency stabilization unit*
GHZ *Greenberger-Horne-Zeilinger*
GKP *Gottesman-Kitaev-Preskill*
ITE *Imaginary Time Evolution*
LGT *lattice gauge theory*
MBTI *many-body topological invariant*
MPDO *matrix product density operator*
MPO *matrix product operators*
MPU *matrix product unitaries*
MPS *matrix product state*
MS *Mølmer-Sørensen*
NMR *nuclear magnetic resonance*
OBC *open boundary condtion*
PBC *periodic boundary condition*
PBS *polarizing beam splitter*
PGC *polarization-gradient cooling*
PI *photo-ionization*
PMT *photomultiplier tube*
QCD *quantum chromodynamics*
QDB *quantum data bus*
QEC *quantum error correction*
QED *quantum electrodynamics*
RF *radio-frequency*
RSB *red sideband*

SHG *second harmonic generation*

SSH *Su-Schrieffer-Heeger*

eSSH *extended Su-Schrieffer-Heeger*

SP *single-pass*

SVD *singular value decomposition*

TI *topological invariant*

VQE *variational quantum eigensolver*

PREAMBLE

In his keynote speech in 1981, the renowned physicist Richard Feynman suggested a new approach to studying complex physical systems via *exact* simulations [1]:

> *"There is, of course, a kind of approximate simulation, in which you [...] get an approximate view of what physics ought to do. [...] I want to talk about the possibility that there is to be an exact simulation, that the computer will do exactly the same as nature."*

We can think of some applications, where exact simulations already exist, such as *wind tunnels*, where the aerodynamics of vehicles and airfoils are studied to optimize their shape for maximum efficiency. This, however, is not what Feynman had in mind: he was concerned with the simulation of phenomena in quantum and particle physics. He envisioned a *universal quantum computer*, which harnesses the laws of quantum mechanics to *"do exactly the same as nature"* would [1, 2].

Quantum simulators are distinguished by their fundamental principle of operation [3–5]. In *analog* simulators, interactions are introduced directly e.g. in the form of electric and magnetic fields. The control parameters are typically continuous and can be precisely adjusted to implement the desired dynamics. This approach is contrasted by *digital* simulators, where the interactions are realized in a discrete manner by means of an appropriate *quantum circuit*. Such a simulator can be *programmed* using a small set of operations, which are analogous to the instructions used to write a program on a classical computer. Essentially, digital quantum simulators are *quantum computers*, enabling the systematic study of arbitrary target problems using suitable *programmable* Hamiltonians. Many quantum simulations were – and still are – realized in an analog way [6–8]. However, the tremendous progress in the field of quantum computing has paved the way to go fully digital, thereby enabling groundbreaking research in a wide variety of disciplines.

While the concepts of classical coding and information theory can be readily generalized to quantum computers, some of the fundamental paradigms appear to be unnecessarily restrictive. Notably, the binary representation of data prevents us from harnessing the full potential of quantum computers. Already in the early 2000s, numerous algorithms exploring alternative encodings have been proposed [9–11]. These algorithms are formulated in the framework of *quantum digits* or *qudits*: d-dimensional quantum systems that allow for a more efficient representation of information. Recently, these ideas have gained renewed interest in the community, since experimental advances have enabled the realization of qudit-based quantum processors [12–14].

This work presents a trapped-ion qudit quantum simulator and its experimental applications in many-body physics and quantum field theories. Notably, we investigate a *topological quantum phase transition* in a one-dimensional spin chain [15, 16], and demonstrate the simulation of quantum electrodynamics in $(2 + 1)$ dimension [17–19].

This thesis is organized as follows: Chapter 1 serves as a general introduction to the topic of quantum computing with qudits. The fundamentals of quantum information processing are presented in a hardware-agnostic manner. Starting from the binary formulation, the concepts are then generalized to multi-level systems.

In Chapter 2 we investigate the interaction of ions with electromagnetic fields, which is the fundamental principle enabling the realization of trapped-ion quantum computers. In particular, we discuss how coherent light fields are used to control the electronic state of an ion, thereby enabling processes such as laser cooling and the readout of quantum states.

Chapter 3 provides a detailed overview of our apparatus. Here we explain how classical electronics are used to manipulate laser light, which is then directed onto the ions to implement a quantum gate operation. The set of gate operations native to our hardware is thoroughly introduced in Chapter 4. Particular attention is given to the controlled-rotation gate, a generalization of the controlled-NOT gate proposed by Cirac and Zoller to qudits [20]. The fundamental interaction used to implement this operation is crucial to both experiments that have been carried out in this work.

The theoretical background for the quantum simulation of many-body systems is developed in Chapter 5. Here we discuss how a quantum state of a many-body system can be efficiently represented as a product of compact matrices. The concept of *topological quantum phases* is explained using the *Su-Schrieffer-Heeger* model as a prime example exhibiting topological properties. This model describing an interacting one-dimensional spin chain is then experimentally studied in Chapter 6. We employ a *variational quantum eigensolver*, a hybrid quantum-classical algorithm to approximate the ground state in different coupling regimes. By measuring *many-body topological invariants* we observe a *quantum phase transition* between two configurations of the spin chain.

Chapter 7 is a primer on quantum field theory. We first explain the concept of a classical field using the Klein-Gordon theory, before performing the quantization to obtain a quantum field. By combining the Dirac field with the free radiation field we introduce the Lagrangian of *quantum electrodynamics*, the theory of interacting fermions and electromagnetic fields. The Hamiltonian is computed and then discretized on a spatial lattice, enabling the systematic study of particle pair-creation processes and field dynamics. We experimentally investigate these phenomena in Chapter 8, using our quantum simulator to prepare ground states of the theory on a 2D lattice. As a first demonstration we simulate a single plaquette of four lattice sites, observing pair creation, the emergence of a magnetic flux and the time dynamics of the system. In a second experiment a grid of four plaquettes in the absence of particles is simulated. Here we study truncation effects by increasing the dimension of the qudits, which is a first step towards the investigation of a *running coupling*, an extensively studied topic in high-energy physics.

Finally, we conclude with a summary and potential avenues and future prospects for quantum simulation with trapped-ion qudits in Chapter 9.

1

DIGITAL QUANTUM SIMULATION BEYOND THE BINARY

This chapter is supposed to introduce the reader to the topic of quantum information processing. In Sec. 1.1 we first discuss how data is encoded in a computer. Here we show that certain encodings prove to be better suited than others, even when they represent the same data. The concepts of quantum states, gate operations, and circuits are explained in Sec. 1.2 without focusing on a specific hardware platform. We conclude with Sec. 1.3 by arguing why higher-dimensional quantum systems may be beneficial in the context of quantum simulation.

1.1 REPRESENTING DATA BY SEQUENCES OF NUMBERS

Mathematics is often considered a *universal language*: its laws do not vary, even as we move from earth to a distant star. However, we can find various ways to represent or *encode* numbers. Counting with our fingers[1] was likely the origin of the *decimal system*, which dates back 1600 BC [21, 22]. A more elaborate numeral system existed even earlier: around 2000 BC, Sumerians and Babylonians used the *sexagesimal system* based on the numbers 0 to 59 [23]. Records show, that this system already supported fractions and was used to compute approximations for the square root of two, namely $\sqrt{2} \approx 1 + 24/60 + 51/60^2 + 10/60^3 = 1.414212296\ldots$ [24].

These numeral systems are *positional*: multiples of their *base* are represented by shifting the position of the number to the left. In this notation, any number $n \in \mathbb{N}$ can be decomposed int440 an ordered sum of N terms

$$n = \sum_{i=1}^{N} d_i b^{i-1} = d_N b^{N-1} + d_{N-1} b^{N-2} + \ldots d_1 b^0 \qquad [1.1]$$

where i indicates the position of the *digits* $0 \leq d_i < b$ in the sequence. Each d_i is multiplied by powers of the *base* b. We call Eq. [1.1] the *representation* of n in base b of *width* N.

We can think of many bases to represent a number, however, some might be more convenient than others. This begs the question, if there exists an *optimal base* b_{opt} for positional numeral systems. Given N and b, the largest number we can write is $n_{max.} = b^N$. Keeping $n_{max.}$ constant, we compute the *capacity* $c = N \cdot b$ as a function of the base in Fig. 1.1(a) and find $b_{opt} = 2.71821\ldots = e$ (dashed) as the *economically optimal base* [25].

1 Interestingly, this varies between cultures: elementary school children in China learn to count from 0 to 10 on a single hand, allowing them to compute in the range from 0 to 100 using both hands.

The complexity of representing a number n is illustrated in Fig. 1.1(b) for $b = \{2, 3, 4, 5\}$. It is evident, that the optimal base e is well approximated by a *ternary* system with $b = 3$, which is reflected by the staircases slowly diverging from the dashed line [25].

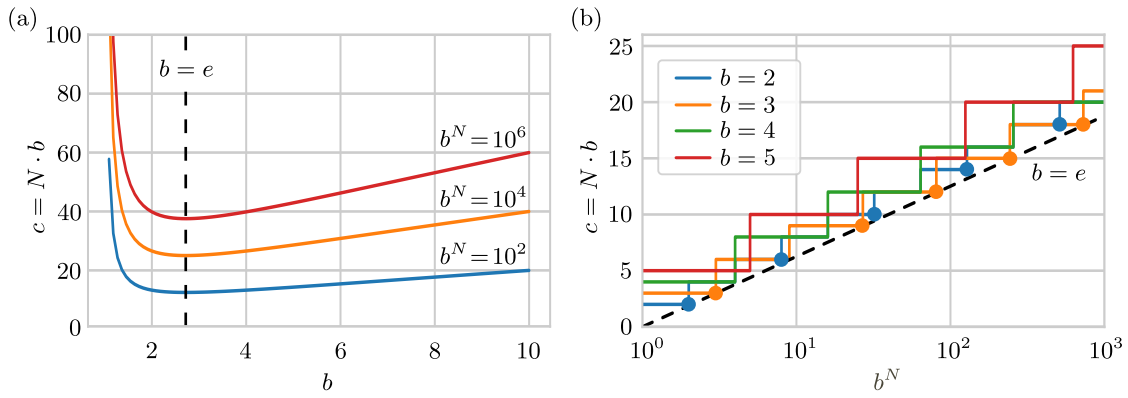


Figure 1.1: Representing numbers in a positional numeral system in different bases b: (a) for a constant number b^N represented by N digits, the capacity $c = N \cdot b$ has a minimum for $b = 2.71821\ldots = e$. (b) for $b \neq e$, the capacity diverges from the optimum (dashed) as b^N increases; the best approximation is achieved for $b = 3$.

In the early 17th century, Leibniz formally introduced the *binary system* where $b = 2$, which was already used a century prior by Harriot in his experiments weighing different substances between 1601 and 1605 [26]. This system is well suited to represent positive integers as combinations of the digits $d_i \in \{0, 1\}$ and positive floating point numbers can be approximated to arbitrary precision if we include M negative powers of b:

$$n = \sum_{i=1}^{N} d_i 2^{i-1} + \sum_{j=1}^{M} d_j b^{-j}. \qquad [1.2]$$

Modern computers encode numbers according to Eq. [1.2] with typical widths of $N + M = 32$ for *single-precision* and $N + M = 64$ for *double precision* floating point values. However, we still have not treated *negative* numbers: we encode the sign in the *leading digit* s, thereby reducing the width to $N + M - 1$:

$$s: \begin{cases} + \mapsto 0 \\ - \mapsto 1 \end{cases} \qquad n = s \cdot \left[\sum_{i=1}^{N-1} d_i 2^{i-1} + \sum_{j=1}^{M} d_j b^{-j} \right]$$

The binary system has prevailed due to its simplicity: we only have to store two values for each digit, namely 0 and 1. We can do so simply by monitoring the presence or absence of objects or physical quantities. However, carrying out meaningful calculations can be cumbersome and consumes $N + M$ resources for each number.

In 1950 Shannon proposed a *symmetrical notation* using odd numbers as bases [27]. With $b = 3$, a *balanced ternary* representation with digits $d_i \in \{-1, 0, +1\}$ is more compatible with the economically best base e and simplifies arithmetic on signed values. Such systems were realized in the Soviet Union: the *Setun machine* was a ternary computer, which was used for scientific purposes in the agricultural and nuclear sciences [25, 28]. Unfortunately, these systems did not pass the test of time due to larger costs and fundamental issues in their fabrication.

The simplicity of the binary system ultimately led to its dominance in the technical industry. However, arithmetic might be easier to implement in ternary systems and computing differential equations would be significantly simplified using base e [27]. This begs the question, if certain problems in quantum computing could also benefit from going beyond the binary to higher-dimensional systems.

1.2 CLASSICAL AND QUANTUM INFORMATION

Nowadays, computers almost exclusively operate in binary: data is represented as a sequence or *string* of binary numbers, where the *position* i of each number indicates the power of the base b^{i-1}. The smallest unit of data is a single binary digit – a *bit* – which can take the mutually exclusive values 0 and 1; a classical bit cannot be in 0 and 1 at the same time. Calculations are carried out following the laws of boolean algebra using *logic gates*. For example, the NOT gate negates the value a at its input to $\bar{a}$, while the OR gate contracts two inputs a and b to a single output $c = a \vee b$. In the late 19th century, Peirce showed the *universality* of the NOR – the contraction of NOT and OR – in his work *"A Boolean Algebra with One Constant"*[2] [29, 30]:

> *"Of course, it is not maintained that this notation is convenient; but only that it shows for the first time the possibility of writing both universal and particular propositions with but one copula [...]"*

A *universal set of gates* allows for the construction of *any* desired operation by sequences of the few gates contained in this set.

The binary paradigm of computing is merely a consequence of simplicity: the values of a bit can be represented by the presence or absence of charge, which can be stored in a capacitor. Fig. 1.2 illustrates a variant of the bit, where charge is allowed to flow to & from the capacitor via the *bit line* (BL), which is controlled by the *transistor* via a voltage applied to the *control line* (CL).

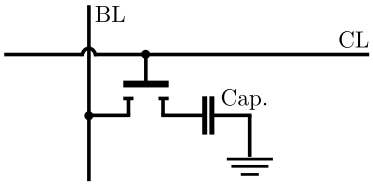


Figure 1.2: Realization of a classical bit: the *bit line* (BL) allows a current to flow towards / from a capacitor, which stores one bit of information by the presence or absence of charge. A *transistor* acts as an electronic switch, which connects / disconnects the capacitor from the BL depending on a voltage applied to the *control line* (CL).

The transistor is the fundamental control element of the modern microprocessor: its invention in 1948 lead to the development of today's electronics, from simple calculators to large high-performance computing architectures [31, 32].

While modern computers are powerful devices, however, many problems in quantum physics remain infeasible if not *intractable* with classical methods. This can be either due to

2 His work was considered *"to be discarded"* by the Harvard University Press up until 1926. It was finally published in 1933.

time constraints or the required amount of physical resources, which grow exponentially with the size of the system we want to study. However, this exponential scaling is native to quantum systems. Consequently, quantum computers are promising candidates to venture into regimes which are otherwise inaccessible.

We carry the paradigm of classical computing over to the quantum world and harness the laws of quantum mechanics to enhance our computation. The smallest unit of information is the *quantum digit* or *qudit*, which shares some of its properties with its classical analogue, but allows for *superposition* and *interference*. We will now discuss these concepts first in a binary context in Sec. 1.2.1 and then introduce the concept of quantum gates in Sec. 1.2.2, before we advance to the measurement of quantum states in Sec. 1.2.4.

1.2.1 *A binary formulation of quantum computing*

The quantum mechanical analogue of a classical bit is the *quantum bit* or *qubit*, which is constructed from two *basis states* labeled $|0\rangle$ and $|1\rangle$. These states form the basis of a Hilbert space[3] $\mathcal{H} = \mathbb{C}^2$ and can be written as column vectors

$$|0\rangle = \begin{pmatrix} 1 \\ 0 \end{pmatrix} \quad \text{and} \quad |1\rangle = \begin{pmatrix} 0 \\ 1 \end{pmatrix}. \tag{1.3}$$

We call Eq. [1.3] the *computational basis* of $\mathcal{H}$; other common bases are $|\pm\rangle = (|0\rangle \pm |1\rangle)/\sqrt{2}$ and $|\pm i\rangle = (|0\rangle \pm i\,|1\rangle)/\sqrt{2}$. Both basis vectors are mutually exclusive or *orthogonal*, such that the *scalar product* $\langle 0|1\rangle = 0$. Here, $\langle 0|$ represents the *hermitian conjugate* of $|0\rangle$, which we obtain by transposition and complex conjugation.

In contrast to a classical bit, the most general quantum state or *state vector* $|\psi\rangle$ of a qubit is described by

$$|\psi\rangle = \alpha\,|0\rangle + \beta\,|1\rangle \tag{1.4}$$

for $\alpha, \beta \in \mathbb{C}$, obeying the *normalization condition* $|\alpha|^2 + |\beta|^2 = 1$. We call $|\psi\rangle$ the *superposition* of $|0\rangle$ and $|1\rangle$ with associated *probability amplitudes* α and β. If we project the state onto any of the basis vectors – e.g. $|0\rangle$ – for N preparations of $|\psi\rangle$, we will obtain $|0\rangle$ a total of $n = N \cdot |\alpha|^2$ times. Therefore, $|\alpha|^2$ and $|\beta|^2$ are the *probabilities* $\mathcal{P}$ of finding the state $|0\rangle$ or $|1\rangle$ for each projection.

Note, that we require N *preparations* of the quantum state $|\psi\rangle$ to deduce $|\alpha|^2$ and $|\beta|^2$. This is due to the fact that after each *projective measurement*, the state $|\psi\rangle$ will always be classical. Depending on the measurement outcome, the quantum state is projected onto *either* $|0\rangle$ *or* $|1\rangle$, and therefore any subsequent projection yields the same result. Consequently, we have to prepare the same state N times to acquire enough statistics to determine the probabilities $|\alpha|^2$ and $|\beta|^2$.

Like its classical counterpart, a single qubit on its own has only limited application: depending on its physical realization, it can be used as a sensor, but not for any meaningful computation. We therefore add another qubit to our system with its state labeled $|\phi\rangle \in \mathcal{H}$. The joint quantum system is then described by the direct product

$$|\Psi\rangle = |\psi\rangle \otimes |\phi\rangle \in \mathcal{H}_1 \otimes \mathcal{H}_2, \tag{1.5}$$

3 A Hilbert space is a complete vector space with a metric introduced by the scalar product $\langle\cdot|\cdot\rangle$.

where the indices label the Hilbert space $\mathcal{H}_i$ of the respective qubit i; this concept is readily generalized for larger systems of N qubits.

These so-called *product states* or *separable states*, however, only cover a small fraction of the larger Hilbert space $\mathcal{H} = \mathcal{H}_1 \otimes \mathcal{H}_2$ [33]. A large portion of $\mathcal{H}$ is occupied by *entangled states*, which cannot be written as a product akin to Eq. [1.5]. Entangled states exhibit strong correlations between qubits, which are best illustrated by the prime example of the *Greenberger-Horne-Zeilinger* (GHZ)-like state [34, 35]

$$|\Phi\rangle = \alpha\,|00\rangle + \beta\,|11\rangle\,. \tag{1.6}$$

If we make a projective measurement on the state of one qubit and obtain the outcome $|1\rangle$, the second qubit will – with absolute certainty – also occupy the state $|1\rangle$.

We have thus far only covered *pure states*: a particular class of quantum states, for which we can write the state vector in terms of products of the basis states of the individual qubits. A more complete picture are *mixed states*, which are described by *density matrices* ϱ. For a pure state $|\Psi\rangle$, its associated density matrix is given by

$$\varrho = |\Psi\rangle\langle\Psi| \tag{1.7}$$

with entries $\varrho_{ij} \in \mathbb{C}$. For a single qubit in the general pure state defined in Eq. [1.4], its density matrix is given by

$$\varrho = (\alpha\,|0\rangle + \beta\,|1\rangle)\,(\alpha^*\,\langle 0| + \beta^*\,\langle 1|) = \begin{pmatrix} |\alpha|^2 & \alpha^*\beta \\ \alpha\beta^* & |\beta|^2 \end{pmatrix}, \tag{1.8}$$

where α^* and β^* are the complex conjugate of α and β, respectively. We deduce the following properties [36]:

- A density matrix ϱ is self-adjoint or *hermitian*: $\varrho^\dagger = \varrho$, where the dagger-symbol $\dagger$ indicates complex conjugation and transposition.
- It is positive semi-definite: its diagonal elements are the probabilities $|\alpha|^2$ and $|\beta|^2$, which are always positive and in the range $[0, 1]$
- The *trace* – the sum of its diagonal elements – is one: this is a direct consequence of the normalization condition $|\alpha|^2 + |\beta|^2 = 1$. The probability of finding the qubit in *any* state must be unity[4].

These properties apply regardless of whether the state is pure or mixed. As an example contrasting the pure state in Eq. [1.8], we consider the *maximally mixed state* of a single qubit

$$\rho = \frac{1}{2}\begin{pmatrix} 1 & 0 \\ 0 & 1 \end{pmatrix}$$

which cannot be written as a product and is obtained as a *probabilistic mixture* of quantum states. In fact, any density matrix ϱ can be imagined as a mixture of N pure states $\{|\phi_i\rangle\}_{i=1\ldots N}$, each contributing with an amplitude λ_i, such that

$$\varrho = \sum_i \lambda_i\,|\phi_i\rangle\langle\phi_i|\,. \tag{1.9}$$

4 There are some exceptions to this fundamental rule, which arise in the field of *quantum error correction*: a qubit can be *"lost"* entirely, and its state can be recovered from projective measurements on the remaining system, cf. *"Deterministic correction of qubit loss"* by Stricker et al. [37].

Note that the resulting state ϱ still has to adhere to the normalization condition $\mathrm{Tr}[\varrho] = 1$. The amount of mixture can be quantified by the *purity* [38, 39]

$$\mathrm{Pur}[\varrho] = \mathrm{Tr}[\varrho^2] \leq 1, \qquad [1.10]$$

which yields $\mathrm{Pur}[\varrho] = 1$ if and only if ϱ is pure.

Purity can also be used as a measure to quantify entanglement. We illustrate this concept using two-party GHZ-like state defined by Eq. [1.6] as an example. While the joint state $\varrho = |\Phi\rangle\langle\Phi|$ is pure, the density matrix σ of each individual qubit yields

$$\mathrm{Pur}[\sigma] = \frac{1}{2}$$

which corresponds to the *maximally mixed* state. When generalized to N qubits, we call a pure state ϱ *maximally entangled* if the purity of the reduced state σ of any bipartition satisfies[5] [40]

$$\mathrm{Pur}[\sigma] = \frac{1}{2}.$$

We conclude this paragraph by examining the *"similarity"* of two quantum states ϱ and σ by computing the *fidelity* [41]

$$\mathcal{F}(\varrho, \sigma) = \mathrm{Tr}\left[\sqrt{\sqrt{\sigma}\varrho\sqrt{\sigma}}\right]^2, \qquad [1.11]$$

which is a generalization of the overlap of matrices to positive semi-definite hermitian operators. We will use this metric throughout this thesis to quantify our results in comparison with theoretical predictions.

1.2.2 *Manipulation of quantum states*

We have introduced the concept of quantum states in the context of qubits as a more or less natural extension of the binary nature of computing into the quantum world. In this section, we discuss how to manipulate states using *quantum gates*, an analogue of the electronic logic gates in classical computers. Here, we only show the mathematical framework, while the physical mechanisms and their implementation is presented later in Ch. 2 and Ch. 4.

Let us consider the general state $|\psi\rangle$ of a single qubit given by Eq. [1.4]. When we manipulate the state, we still need to preserve the overall probability $|\alpha|^2 + |\beta|^2 = 1$, i.e. the length of $|\psi\rangle$ must remain unity. Any such operation can be described by the linear map

$$U\colon \mathcal{H} \mapsto \mathcal{H},\ |\psi\rangle \in \mathcal{H} \mapsto U(|\psi\rangle) \in \mathcal{H} \ \Big|\ \langle\psi|\psi\rangle = \langle U(|\psi\rangle)^\dagger | U(|\psi\rangle)\rangle = 1. \qquad [1.12]$$

The condition $\langle U(|\psi\rangle)^\dagger | U(|\psi\rangle)\rangle = 1$ is satisfied if $U^\dagger$ is the *inverse* of U. We say, that the map U acting on a qubit is a *unitary transformation* or an element of the *unitary group* $U(2)$. Moreover, $U^\dagger = U^{-1}$ implies that the determinant[6] $\det U \overset{!}{=} \pm 1$.

5 The *Greenberger-Horne-Zeilinger*-like state in Eq. [1.6] is a prime example of a maximally entangled state. In contrast, the three-qubit W-state $|W\rangle = \frac{|1,0,0\rangle + |0,1,0\rangle + |0,0,1\rangle}{\sqrt{3}}$ is entangled, but not maximally entangled.

6 As a consequence of U being invertible, it must have non-zero determinant. Simultaneously, it must conserve the norm of the state vector, which only holds for determinant ± 1.

Consequently, each U is either a reflection or a rotation. As any reflection can be realized by appropriate rotations, we assume $\det U = +1$ and conclude:

> *A quantum state $|\psi\rangle$ of a qubit is manipulated by unitary transformations $U\colon\ |\psi\rangle \mapsto U|\psi\rangle$, which are elements of the special unitary group $SU(2)$.*

A *group* is defined by a set G with elements $g \in G$ and an associated operation $\star$, which satisfies the following axioms [42, 43]

- There exists a unique *identity* element $e \in G$, such that $e \star g = g \star e = g \;\forall g \in G$.
- For each $g \in G$ there exists an *inverse* $g^{-1} \in G$, which satisfies $g \star g^{-1} = g^{-1} \star g = e$.
- For any elements $g_1, g_2 \in G$ there exists $g_3 = g_1 \star g_2 \in G$.

The group operation in $SU(2)$ is the matrix multiplication, which we write as $\cdot$ or drop entirely without sacrificing readability. Note, that $SU(2)$ is *non-abelian*: for any two unitaries U_i and U_j, the products $U_i \cdot U_j$ and $U_j \cdot U_i$ are generally not equal.

Each continuous group can be generated from a finite set of elements, which we call the *generators* of G [43]. Up to the complex factor i, the *Pauli matrices*

$$\sigma_x = \begin{pmatrix} 0 & 1 \\ 1 & 0 \end{pmatrix} \qquad \sigma_y = \begin{pmatrix} 0 & -i \\ i & 0 \end{pmatrix} \qquad \sigma_z = \begin{pmatrix} 1 & 0 \\ 0 & -1 \end{pmatrix} \tag{1.13}$$

are the *infinitesimal generators* of $SU(2)$. Each $i\sigma_j$ is an element of the *Lie algebra* $\mathfrak{s}(2)$ which generates $SU(2)$ via the *exponential map*

$$\exp\colon \mathfrak{s}(2) \mapsto SU(2) \Longrightarrow U(\vec{n}, \theta) = \exp\left(-\frac{i\theta\vec{n}\vec{\sigma}}{2}\right) = e^{-i\theta\vec{n}\vec{\sigma}/2}, \tag{1.14}$$

for a unit vector $\vec{n} = (n_x, n_y, n_z) \in \mathbb{R}^3$ and $\vec{\sigma} = (\sigma_x, \sigma_y, \sigma_z)$ [43, 44].

Closer inspection of Eq. [1.14] hints on a connection to euclidean geometry: $\vec{n}$ and $\vec{\sigma}$ are vectors with three elements. Indeed, there exists a connection between $SU(2)$ and the *special orthogonal group* $SO(3)$, which is the continuous group of *rotations* in real 3D-space; more technically, $SU(2)$ is the *double cover* of $SO(3)$ [42, 43].

The double cover of $SO(3)$ by $SU(2)$ enables a beautiful mapping of the quantum state of a single qubit onto a sphere with radius $r = 1$, which reflects the unit length of the state. We illustrate this mapping in Fig. 1.3: the computational basis states $|0\rangle$ and $|1\rangle$ are on the northern and southern pole of the sphere. A state vector $|\psi\rangle$ points from the origin to the surface and can be parametrized by a tuple of angles (θ, ϕ).

Note, that the orthogonality of $|0\rangle$ and $|1\rangle$ in $\mathcal{H} = \mathbb{C}^2$ translates to the states being anti-parallel – both states are on opposing poles of the Bloch sphere. This is a consequence of the double cover of $SO(3)$ by $SU(2)$: the unitary transformation U in Eq. [1.14] are defined using the *half angle* $\theta/2$, while the *full angle* is used in euclidean space.

Rotations of the state vector around the major axes of the coordinate system in $\mathbb{R}^3$ are defined with respect to $SU(2)$ by

$$\hat{X}(\theta) = e^{-i\theta\hat{\sigma}_x/2} \qquad \hat{Y}(\theta) = e^{-i\theta\hat{\sigma}_y/2} \qquad \hat{Z}(\theta) = e^{-i\theta\hat{\sigma}_z/2}, \tag{1.15}$$

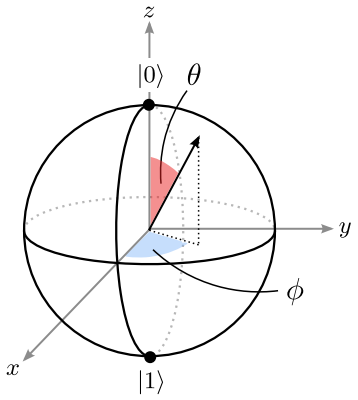


Figure 1.3: Representation of the quantum state of a qubit on the *Bloch sphere*: the state vector $|\psi\rangle$ points from the origin to the surface of the sphere. Two angles θ and ϕ define its orientation in 3D space. The computational basis states $|0\rangle$ and $|1\rangle$ are on opposing poles along the z axis.

where we have added a *hat* to indicate that these unitaries perform an action on the vector. This also applies to the Pauli matrices, which – up to a global phase factor – act as e.g. $\hat{\sigma}_x = \hat{X}(\pi)$. Together with the identity $\mathbb{1}$, the set $\{\mathbb{1}, \sigma_x, \sigma_y, \sigma_z\}$ forms a basis of the space of complex 2×2 operators [43].

We define a general rotation associated with the angles (θ, ϕ) on the Bloch sphere by

$$\hat{R}(\theta, \phi) = e^{-i\frac{\theta}{2}\left(\cos(\phi)\hat{\sigma}_x + \sin(\phi)\hat{\sigma}_y\right)}, \tag{1.16}$$

which we generalize to a larger system by taking the direct product. The rotation $\hat{R}^{(i)}(\theta, \phi)$ acting on the i-th qubit out of N is analogous to Eq. [1.16] after we have applied the map

$$\sigma_j \Longrightarrow \mathbb{1}^{(1)} \otimes \ldots \otimes \mathbb{1}^{(i-1)} \otimes \sigma_j^{(i)} \otimes \mathbb{1}^{(i+1)} \otimes \ldots \otimes \mathbb{1}^{(N)}. \tag{1.17}$$

For $\theta = \pi$ we call the unitary transformations in Eq. [1.15] the *Pauli gates*. Other examples are the *Hadamard gate* $\mathbb{H} = (\hat{\sigma}_x + \hat{\sigma}_z)/\sqrt{2}$ and the *phase gate*

$$\hat{P}(\phi) = \begin{pmatrix} 1 & 0 \\ 0 & e^{i\phi} \end{pmatrix}. \tag{1.18}$$

These gates act *locally* on a single qubit and therefore cannot lead to *correlations* in larger systems. However, we must be able to entangle two or more qubits to realize a meaningful quantum computation. A gate capable of creating entanglement between two subsystems is the controlled NOT or $C\hat{X}$ gate [20]

$$C\hat{X} = \begin{pmatrix} 1 & 0 & 0 & 0 \\ 0 & 1 & 0 & 0 \\ 0 & 0 & 0 & 1 \\ 0 & 0 & 1 & 0 \end{pmatrix}, \tag{1.19}$$

which we will thoroughly discuss in Sec. 4.3.2. Together with the arbitrary rotations $\hat{R}^{(i)}(\theta, \phi)$ and the local phase gate $\hat{P}^{(i)}(\phi)$, the $C\hat{X}$ gate is used to form a *universal gate set*. Any possible operation on a quantum processor can be reduced to combinations of gate operations drawn from this set.

We now briefly come back to the general case of density matrices and use Eq. [1.9] to derive the transformation properties of ϱ. The pure states $|\phi_i\rangle$ transform under a unitary operator $\hat{U}$ as $|\phi_i\rangle \mapsto \hat{U}|\phi_i\rangle$, and its conjugate obeys $(\hat{U}|\psi\rangle)^\dagger = \langle\psi|\hat{U}^\dagger$. Consequently, the density matrix undergoes a *double-sided transformation*

$$\varrho \mapsto \hat{U}\varrho\hat{U}^\dagger. \tag{1.20}$$

We call sequences of quantum gates, which implement a meaningful computation, a *quantum algorithm*. Even before the realization of the first proper quantum computer, these algorithms were extensively studied. In 1985, Deutsch formulated a problem regarding binary functions [45]: given a function $f : \{0,1\} \mapsto \{0,1\}$, can we deduce if the function is balanced $f(0) \neq f(1)$ or constant $f(0) = f(1)$ just from a single measurement? While a classical computer must evaluate the function *twice*, a quantum computer would obtain the correct outcome from just one measurement. The algorithm was later extended to n bits by Deutsch and Josza in 1992 [46]. Realizations came later using *nuclear magnetic resonance* (NMR) and trapped ions [47, 48]. Other prominent algorithms were proposed by Shor and Gover in the context of factorization and unstructured search problems [49–51].

A quantum algorithm of *depth* N preparing the final state $|\psi\rangle$ from an input state $|\phi\rangle$ is given by

$$|\phi\rangle = \prod_{i=1}^{N} \hat{U}_i |\phi\rangle = \hat{U}_N \hat{U}_{N-1} \dots \hat{U}_1 |\psi\rangle\,, \tag{1.21}$$

where each $\hat{U}_i$ corresponds to a quantum gate in our universal set, either acting on a single qubit or on multiple qubits at once [39]. A more intuitive *graphical* representation of the algorithm is provided by the *quantum circuit model*, which we introduce in the next section.

1.2.3 *Quantum circuit model*

Another analogy to classical computing is the graphical representation of sequences of quantum gates as a *circuit*. In contrast to electronics, where we use a set of logic gates that can contract two or more inputs into a single output, the number of lines entering and leaving a quantum gate must be equal. We illustrate a classical circuit and its analogue as a quantum gate in Fig. 1.4(a). Both gates describe the same action: if both *control (qu)bits* a and b are set, the state of the *target (qu)bit* y is negated on the output y'. We call this operation a *controlled controlled-NOT gate* or *(quantum) Toffoli gate*, an extension of the aforementioned controlled-NOT gate [39, 52].

While the classical circuit contracts all inputs to a single output y', the quantum version of the gate has three input qubits, which are carried through the operation as indicated by the horizontal lines. Moreover, all quantum gates are *reversible*, which does not work in classical electronics, even if we route the inputs to the output side (dashed lines). It is important to keep these fundamental differences in mind whenever we draw a graphical representation of a circuit.

The quantum Toffoli gate is illustrated by three horizontal lines, which are vertically interconnected: the qubits a and b *control* the state of the *target*, which is indicated by the cross-hair on the line. To date, there is no *"direct"* implementation of this gate via a single interaction. Fig. 1.4(b) shows a *decomposition* into gates taken from our universal set, where

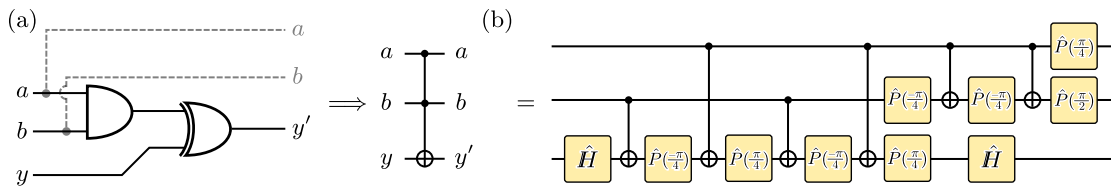


Figure 1.4: Circuit implementing the same operation using classical and quantum logic gates: (a) realization of the circuit using an AND gate and a XOR gate. The quantum analogue is represented by three lines, each resembling a qubit. The *control* qubits a and b act on the *target* y indicated by the cross-hair. (b) Decomposition of the gate using the Hadamard gate $\hat{\mathbb{H}}$, the phase gate $\hat{P}$ and controlled NOT gates, which are depicted similar to the Toffoli gate with a single control input [39].

we have contracted the rotations $\hat{X}(\pi)\hat{Y}(\pi/2)$ to form the Hadamard gate $\hat{\mathbb{H}}$ [39]. We entangle the target with its control qubits using the controlled NOT gate, which we draw similar to the Toffoli gate with a single control input.

We emphasize that the decomposition of a quantum circuit is not necessarily unique and strongly depends on the universal set of gates *native* to the quantum hardware. While a particular gate might be trivial to realize on one specific hardware platform, it might be highly inefficient or infeasible to do so natively on a different quantum device. Using compilation tools such as IBM's *Qiskit* transpiler can therefore generate overly complicated decompositions [53, 54]. While still being correct, thorough post-processing can significantly improve the overall performance of a computation when it is implemented on the actual hardware.

1.2.4 *Measurements on quantum systems*

We have already used the notion of a *measurement* in the context of projections. Formally, a *measurement* is described by a complete set of operators $\{\hat{M}_i\}$ satisfying $\sum_i \hat{M}_i^\dagger \hat{M}_i = \mathbb{1}$ [39]. The index i is associated with the measurement outcome, which we expect to measure with a probability [55]

$$\mathcal{P}_i = \langle\psi|\hat{M}_i^\dagger \hat{M}_i|\psi\rangle \qquad [1.22]$$

for a state $|\psi\rangle$. Fundamentally, we perform sequences of projective measurements $\hat{P}_i$ and seek to reconstruct physically meaningful outcomes from the probabilities $\mathcal{P}_i$. Each physical quantity is an *observable* $\hat{O}$, which satisfies $\hat{O}^\dagger = \hat{O}$. We decompose $\hat{O}$ into

$$\hat{O} = \sum_i \lambda_i \hat{P}_i \qquad [1.23]$$

where the $\hat{P}_i$ are projectors onto the eigenbasis of $\hat{O}$. This *spectrum* of $\hat{O}$ is essentially the collection of the eigenvalues E_i, which we measure with probability $\mathcal{P}_i$. Consequently, the *expectation value* is given by the sum

$$\langle O\rangle = \sum_i E_i \mathcal{P}_i. \qquad [1.24]$$

In the case of $\langle O\rangle$ being diagonal with respect to the computational basis, we obtain the full spectrum by performing just one projective measurement. However, both bases rarely

coincide and we have to employ a circuit of unitary transformations $\prod_j \hat{U}_j$ to rotate our quantum state *before* we project in the computational basis e.g. on the state $|1\rangle$:

$$\hat{P}_i = \hat{P}_{|1\rangle} \prod_j \hat{U}_j \qquad [1.25]$$

This formalism is readily extended to the general case of density matrices following the formalism introduced in Eq. [1.20].

1.3 BEYOND THE BINARY – A CASE FOR HIGHER DIMENSIONAL SYSTEMS

The argument raised by Shannon in favor of symmetrical notations can be applied to quantum systems, although in a different context. While we are also concerned about the computational complexity of an algorithm, we arrive at Shannon's conclusion from a physical point of view by asking the question

How can we efficiently encode bosons on a digital quantum simulator?

Having an integer spin $S \in \mathbb{N}_{>0}$, the general *pure* state $|\psi\rangle$ of a boson is described by the superposition of $2S+1$ basis states

$$|\psi\rangle = c_{-S}\,|-S\rangle + c_{-S+1}\,|-S+1\rangle + \ldots + c_0\,|0\rangle + \ldots c_{S-1}\,|S-1\rangle + c_S\,|S\rangle\,, \qquad [1.26]$$

where the $c_{i=-S,\ldots,S} \in \mathbb{C}$ are the respective probability amplitudes. Being a quantum state, $|\psi\rangle$ must be normalized, imposing the condition $\sum_{i=-S}^{S} |c_i|^2 = 1$ on the c_i. Note, that the description is completely analogous to the qubit case in Eq. [1.8], we only need to consider more states.

Similar to classical computers, where we encode larger numbers in multiple bits, boson can be distributed over two or more qubits. In the following paragraphs we will introduce two possible encoding schemes and discuss an application for the case of a spin-1 particle.

1.3.1 *Binary encoding*

We first look at Fig. 1.5(a), which we call the *binary-style* encoding. The boson B is represented as a *diamond*, where the facets represent the computational basis states labeled $|0\rangle_b$, $|-1\rangle_b$ and $|+1\rangle_b$ [18]. A colored facet indicates the probability $\mathcal{P}_i$, which increases in contrast as $\mathcal{P}_i$ approaches unity. Colors show phase factors on a *color wheel*, where we have mapped the color blue to $\phi = 0$ while $\phi = \pi$ would be colored in red.

The boson is encoded using the states of two qubits labeled Q_1 and Q_2 according to the truth table in Fig. 1.5(a). Note, that B is not mapped to the state $|11\rangle$, which we therefore discard as being *non-physical*. However, if we were to populate this state, either due to imperfections in our gate operations, fundamental mistakes in our algorithm or decoherence processes, we would *lose information*. We can mitigate this effect by *post-selection*: after we have measured our quantum state, we remove datasets containing non-physical outcomes at the cost of an increase in sampling overhead.

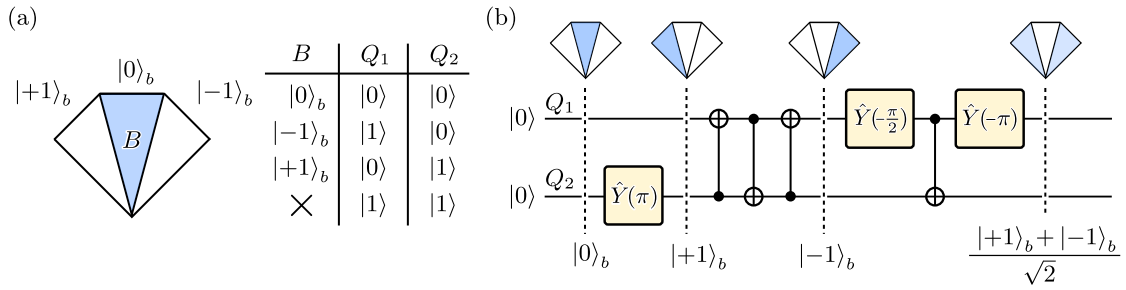
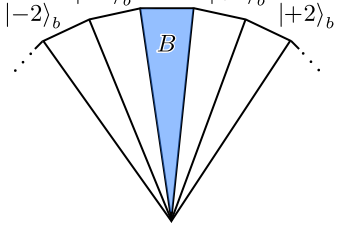


Figure 1.5: Binary-style encoding of a spin-1 boson B in two qubits Q_1 and Q_2: (a) the boson is represented as a diamond with 3 facets. Colored facets show the populated states, contrast and color indicate probability and phase. The three basis states $|0\rangle_b$, $|-1\rangle_b$ and $|+1\rangle_b$ are encoded in Q_1 and Q_2 according to the truth table; the non-physical state $|11\rangle$ is discarded. (b) Quantum circuits, which act locally on the boson translate into entangling circuits on the qubit system.

An example of a quantum circuit manipulating the state of a binary-style encoded boson is presented in Fig. 1.5(b). While this algorithm does not perform a meaningful computation, it highlights another drawback: local rotations on bosons translate into entangling gates on qubits. In current state-of-the-art quantum hardware, the performance of entangling gates can be up to a factor of 10 lower compared to gates acting on single qubits. Consequently, the fidelity of the outcome will decrease as the depth of the quantum circuit increases. This will become even more critical when encoding systems of larger spin $S > 1$, which are distributed over $N = \lceil \log_2(2S+1) \rceil$ qubits.

1.3.2 *"One-hot" encoding*

A different approach is shown in the truth table in Fig. 1.6(a), which we refer to as the *one-hot encoding*. Each basis state $|i\rangle_b$ of B has its designated qubit i, which encodes the population $\mathcal{P}(|i\rangle_b)$ in the state $|1\rangle$.



B	⋯	Q_{-2}	Q_{-1}	Q_0	Q_{+1}	Q_{+2}	⋯
×	$\|0\rangle$	$\|0\rangle$	$\|0\rangle$	$\|0\rangle$	$\|0\rangle$	$\|0\rangle$	$\|0\rangle$
⋮	⋮	⋮	⋮	⋮	⋮	⋮	⋮
$\|-2\rangle_b$	$\|0\rangle$	$\|1\rangle$	$\|0\rangle$	$\|0\rangle$	$\|0\rangle$	$\|0\rangle$	$\|0\rangle$
$\|-1\rangle_b$	$\|0\rangle$	$\|0\rangle$	$\|1\rangle$	$\|0\rangle$	$\|0\rangle$	$\|0\rangle$	$\|0\rangle$
$\|0\rangle_b$	$\|0\rangle$	$\|0\rangle$	$\|0\rangle$	$\|1\rangle$	$\|0\rangle$	$\|0\rangle$	$\|0\rangle$
$\|+1\rangle_b$	$\|0\rangle$	$\|0\rangle$	$\|0\rangle$	$\|0\rangle$	$\|1\rangle$	$\|0\rangle$	$\|0\rangle$
$\|+2\rangle_b$	$\|0\rangle$	$\|0\rangle$	$\|0\rangle$	$\|0\rangle$	$\|0\rangle$	$\|1\rangle$	$\|0\rangle$
⋮	⋮	⋮	⋮	⋮	⋮	⋮	⋮

Figure 1.6: One-hot encoding of a spin-S boson in qubits. The population of each basis state $|i\rangle_b$ of the boson is encoded in the probability of $|1\rangle_i$ on the qubit i. As each $|i\rangle_b$ is mapped onto one qubit, the system size grows as the product $N \cdot (2S+1)$ for N bosons.

While this encoding scheme appears to be a more natural way to realize the boson, its unfavorable scaling renders the simulation of large bosonic systems unfeasible. Each boson

is encoded in $N = \lceil \log_2(2S+1) \rceil$ qubits, leading to a growth of the system size both in N with every added boson as well as $2S$ for incrementing spin. Modern state-of-the-art devices are limited from a few tens of qubits in trapped ion systems up to 1121 qubits in superconducting systems, simulations of many-body dynamics in integer-spin systems or gauge theories still remains challenging on qubit-based devices [56–58].

However, most quantum computers encode qubits in higher-dimensional systems; their the additional degrees of freedom remain unused, just waiting to be exploited. The polarization and spatial modes in photons can be exploited to encode spin-1 particles, with recent works realizing multi-mode bosons up tp $M = 12$ [59–61]. In superconducting devices, the weak anharmonicity in transmissions allows the encoding of spin-1 bosons [62]. Progress in trapped ion systems enabled the first *universal qudit quantum processor* up to $M = 3$ in Calcium ions, with partial control up to $M = 6$ in Barium [14, 63]. In analogy to classical digits, we call these systems *quantum digits* or *qudits* and denote their dimension with d.

Our mathematical foundation introduced in the previous sections can be readily extended to qudits. We have already shown the general pure state of a $2M+1$-dimensional qudits in Eq. [1.26], which is just an expansion of the qubit case to include more basis states. This also applies to concepts like density matrices and unitary operations, which are now elements of $SU(d)$.

The $d^2 - 1$ infinitesimal generators of $SU(d)$ are the *generalized Gell-Mann matrices* $\{\Lambda\}$, which were first introduced in the context of $SU(3)$ to describe symmetries in Baryons and Mesons [64]. Each Λ is essentially a 2×2 Pauli matrix $\sigma_{x,y,z}$ embedded in a $d \times d$ matrix [65]. The symmetric x and anti-symmetric y matrices are

$$\Lambda_x^{(j,k)} = |j\rangle\langle k| + |k\rangle\langle j| \qquad \text{and} \qquad \Lambda_y^{(j,k)} = i\,|k\rangle\langle j| - i\,|j\rangle\langle k| \tag{1.27}$$

for *tuples* (j,k) satisfying $1 \leq j < k \leq d$. Moreover, we have $d-1$ diagonal matrices

$$\Lambda_z^k = \sqrt{\frac{2}{k(k+1)}} \left(\sum_{j=1}^{k} |j\rangle\langle j| - k\,|k+1\rangle\langle k+1| \right) \tag{1.28}$$

with $1 \leq k \leq d-1$. We point out, that the set of Pauli matrices is recovered for $d = 2$.

Encoding N spin-M bosons in *natural qudits* of dimension $d = 2M+1$ greatly simplifies our quantum algorithms. First, the size of our system grows linearly with N as opposed to $N = \lceil 2M+1 \rceil$ in the binary-style encoding, or even $N \cdot (2M+1)$ in the one-hot scheme. This opens up the path to quantum simulation of larger spin-M systems. Second, local operations on bosons *remain* local in qudits. However, the visual representation of the state vector as a point on a sphere no longer applies; we cannot comprehend how such a high-dimensional object would look like.

We conclude this section by introducing an extension to the quantum circuit model. With d basis states, we can no longer draw the qudit as a single line. Therefore, we propose to expand the line into multiple ones, which we stack vertically to indicate each basis state $|i\rangle_b$. This concept is illustrated in Fig. 1.7(a) and applied to the quantum circuit in Fig. 1.7(b). Since Fig. 1.5(b) implements the same operations, we directly compare both strategies. Here, local rotations on the boson represented by the boxes connecting two basis states $|i\rangle_b$ and $|j\rangle_b$ *remain* local on a qudit. Our encoding significantly reduces the circuit depth with respect to the number of entangling gates needed to implement the same operation.

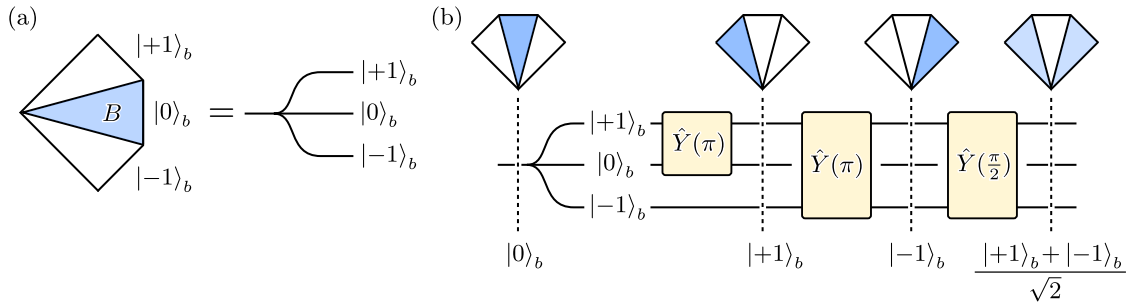


Figure 1.7: Spin-1 boson encoded in a physical qudit: (a) we draw the qudit as an expanding set of lines, each corresponding to one of its basis states $|i\rangle_b$. (b) Local rotations on the boson remain local on the qudit. Each operation is implemented without the need for entangling gates.

When used appropriately, qudits can significantly enhance the performance of a quantum processor. Especially in the context of quantum simulations, where integer-spin systems emerge naturally, a qudit-based algorithm will reduce the register size and can be implemented with fewer entangling gates. Consequently, simulations that previously seemed too challenging on state-of-the-art qubit platforms become realistic with qudits.

In the upcoming chapters, we introduce our *universal trapped-ion qudit quantum processor*, and discuss the fundamental interactions and their implementation on the hardware level. We then show its capabilities by employing novel quantum algorithms to study a *topological quantum phase transition* and realize – for the first time – a quantum simulation of a lattice gauge theory including gauge fields and matter in two spatial dimensions [14, 16, 19].

2

A QUANTUM PROCESSOR WITH TRAPPED IONS

The fundamental task of a processor is the controlled manipulation of data based on a predefined list of commands, which we call a *program*. Data is provided in a predefined format to a programmable logic unit, which then modifies it using a set of basic Boolean operations. This set is designed in such a way that any arbitrary program can be implemented through clever concatenation. The result of a computation is then either stored in a memory cell or directly presented to the user in a readable form. While technological capabilities have continuously evolved since the birth of the first processors, these basic requirements have remained almost unchanged.

In this chapter, we discuss a similar formulation that applies to quantum processors and show how these requirements are addressed in trapped-ion systems. Proposed by DiVincenzo in 1995/96, the following criteria must be satisfied to realize a quantum processor [66–68]:

> *The degrees of freedom required to hold data and perform computation should be available as dimensions of the Hilbert space of a quantum system. This quantum system should be more-or-less isolated from its environment. [...] the Hilbert space must be precisely delineated. [...] a multi-particle system is necessary [...]*

In a quantum processor, data is represented as the quantum state of a scalable system of well characterized quantum digits, which we encode in the electronic states of atoms. The atoms are ionized and confined by electromagnetic fields in an ion trap, which we will introduce in Sec. 2.1 with emphasis on the *linear Paul trap* implemented in the experimental apparatus presented in Ch. 3.

> *Another requirement of quantum computation is that it must be possible to place the quantum system in a fiducial starting quantum state [...]*

The interaction of ions with coherent monochromatic light is discussed in Sec. 2.2. This allows us to control and manipulate the electronic and motional state of registers of trapped ions, engineering well defined fiducial states prior to every computation by laser cooling and optical pumping, see Sec. 2.3 and Sec. 2.4.

> *[...] the precision required in quantum computation: if the state of the computer at some instant is ideally supposed to be the state Ψ, then the actual state after one clock cycle, ϱ (a density matrix), should differ from Ψ by only a small amount [...]*

Quantum systems are incredibly susceptible to external perturbations, which can lead to the loss of information. While imperfections are inevitable, we must ensure that phase relations remain *coherent* over long periods. A fundamental limit to the coherence time is imposed by the spontaneous decay of the internal state of the ion, which can be mitigated by careful

choice of atomic species and qubit encoding; further details on technical limitations are given in Ch. 3.

> *The next requirement is at the heart of quantum computation: It must be possible to subject the quantum system to a controlled sequence of unitary transformations. All of our quantum algorithms are expressed in terms of such sequences. [...]*

We manipulate the quantum state of trapped ions through controlled interactions with pulsed laser light. The fundamentals of the interaction between light and matter are discussed in Sec. 2.2 and more details are provided in Ch. 4, where we introduce the native *quantum gate operations* available on our platform.

> *Last, but not least, it is necessary that it be possible to subject the quantum system to a "strong" form of measurement. [...]*

The quantum state of trapped ions is interrogated by detecting photons: the ground state of the ion is coupled to a short-lived metastable state, which decays by emitting a photon. These fluorescence cycles occur repeatedly as the ion interacts with the light field, allowing a large number of photons to be collected by photosensitive devices. More details on this process are presented in Sec. 2.5.

2.1 CONFINING IONS IN SPACE

Ions are charged atoms or molecules carrying a non-vanishing net charge Ze, where e is the elementary charge and $Z \in \mathbb{Z}$ labels the degree of ionization, i.e. how many electrons have been added to or removed from the otherwise neutral atom or molecule. An ion located at a position $\vec{r}$ will interact with an electric field $\vec{E}(\vec{r})$, which exerts a force $\vec{F}(\vec{r}) = -Ze\vec{E}(\vec{r})$. If we are able to engineer a field, which vanishes at a certain point in space $\vec{r}_0$ while providing a restoring force growing linearly with the displacement $|\vec{r} - \vec{r}_0|$, the ion is confined in a small region around $\vec{r}_0$; in the remainder of our discussion we let $\vec{r}_0 = 0$ and $Z = +1$.

The electric field is given by the gradient of a scalar potential $\Phi(\vec{r})$, which – in the simplest case – must be harmonic for the force to be linear in $|\vec{r}|$. In vacuum under the absence of sources and sinks, a generic harmonic potential of the form

$$\Phi(\vec{r}) = \frac{\Phi_0}{|\vec{r}|^2}\left(\alpha r_x^2 + \beta r_y^2 + \gamma r_z^2\right)$$

must obey the *Laplace equation* $\nabla^2\Phi(\vec{r}) = 0$ by proper choice of $\alpha, \beta, \gamma \in \mathbb{R}$. Consequently, *at least* one of the parameters must be negative, such that the force $\vec{F}(\vec{r})$ must be repulsive in these directions, which would prevent us from ever trapping an ion. However, when allowing the potential to *oscillate* in time we can engineer a harmonic *pseudopotential* in two dimensions. Experimentally, this is realized by applying two sinusoidal voltages offset by a phase $\Delta\phi = \pi$ to opposing pairs of rod electrodes separated by a distance $2R$ as shown in Fig. 2.1(a) [69].

This configuration was first introduced in the context of mass spectrometry by Wolfgang Paul and Helmut Steinwedel in 1953 [70, 71] as a *quadrupole mass filter*. Ions moving along the z axis in Fig. 2.1(a) will interact with the electric field and exhibit different trajectories depending on their mass and charge, allowing them to be distinguished upon impact on a detector by their time of flight. Later in 1958 Paul trapped Krypton ions in a

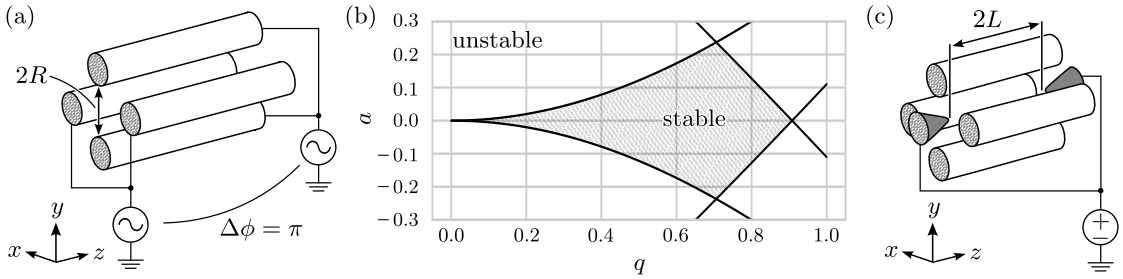


Figure 2.1: (a) a quadrupole mass filter realized by two opposing pairs of rod electrodes, to which an oscillating voltage is applied. (b) choosing the *geometric factors* a and q to fall in the shaded region of the *stability diagram* will cause the ions to move on stable trajectories in the $x-y$ plane. (c) two additional electrodes added to the quadrupole mass filter realize a linear Paul trap, allowing the confinement of ions in all three dimensions.

device he called an *ion cage* by adding a static potential along the third axis[72]. Nowadays, these ion cages are called *Paul traps* and are realized in a variety of geometries and form factors, down to the size of microchips.

2.1.1 *Trapping a single ion*

We first discuss the motion of a single ion in the geometry shown in Fig. 2.1(a) and let the electrodes extend to infinity along the z axis. Applying a voltage $V(t) = V_0 + V_1\cos(\Omega_{rf}t)$ with offset V_0, ampltiude V_1 oscillating with frequency Ω to pairs of opposing electrodes, we generate the potential of the form

$$\Phi(x,y,t) = (V_0 + V_1\cos(\Omega t))\,\frac{x^2-y^2}{2R^2}. \tag{2.1}$$

From $\vec{F}(\vec{r}) = m\frac{d^2}{dt^2}\vec{r} = -e\nabla\Phi(\vec{r},t)$ with m the mass of the chosen ion species we obtain the equations of motion in the x and y direction

$$\begin{aligned}\frac{d^2}{dt^2}x(t) + \frac{e}{2mR^2}(V_0 + V_1\cos(\Omega t))x(t) = 0\\ \frac{d^2}{dt^2}y(t) - \frac{e}{2mR^2}(V_0 + V_1\cos(\Omega t))y(t) = 0.\end{aligned}$$

With $2\tau = \Omega t$ the time derivative transforms into $\frac{d^2}{dt^2} = \frac{\Omega^2}{4}\frac{d^2}{d\tau^2}$, which we substitute to obtain the homogeneous *Mathieu equations*

$$\begin{aligned}\frac{d^2}{d\tau^2}x + \left(\frac{4eV_0}{m\Omega^2R^2} + \frac{4eV_1}{m\Omega^2R^2}\cos(2\tau)\right)x = \frac{d^2}{d\tau^2}x + (a + 2q\cos(2\tau))x = 0\\ \frac{d^2}{d\tau^2}y - (a + 2q\cos(2\tau))y = 0\end{aligned} \tag{2.2}$$

with *geometric factors* $a = \frac{4eV_0}{m\Omega^2R^2}$ and $q = \frac{2eV_1}{m\Omega^2R^2}$ [69, 73]. By tuning the voltages $V_0 \propto a$ and $V_1 \propto q$ we force the ion onto stable trajectories, which exist for a and q in the shaded region of the *stability diagram* in Fig. 2.1(b).

Using Floquet's theorem, the stable solutions to the Mathieu equations can be expressed as a Fourier series [74–76]

$$u(t) = Ae^{i\beta t}\sum_n C_{2n}(a,q)e^{in\Omega t} + Be^{-i\beta t}\sum_n C_{2n}(a,q)e^{-in\Omega t}, \tag{2.3}$$

where $u(t) = x(t), y(t)$ and $\beta = \sqrt{a + q^2/2}$. The coefficients $C_{2n}(a, q)$ depend on powers of the parameters a, q and satisfy the recursion relation [75]

$$C_{2n+2}(a,q) - \frac{a - (2n+\beta)^2}{q} C_{2n}(a,q) + C_{2n-2}(a,q) = 0.$$

In the limit $|a|, |q| \ll 1$ only a few $C_{2n}(a, q)$ contribute significantly to Eq. [2.3]. Consequently, the function $u(t)$ can be well approximated by

$$u(t) = u_0 \left(1 + \frac{q}{2}\cos(\Omega t)\right) \cos(\omega_u t) \qquad [2.4]$$

for an initial position u_0, where the two contributions oscillate at different frequencies. The ion is bound onto a circular trajectory or *orbit* governed by a slow *secular motion* with $\omega_u = \frac{\beta\Omega}{2} \ll \Omega$, which is perturbed by the fast *micromotion* following the frequency Ω of the voltage source.

Thus far we have considered a potential in the $x - y$ plane generated by infinitely long electrodes, neglecting any dynamics along the z axis. While this is a good approximation to describe a mass filter, we seek to trap an ion in a small volume in space. Adding a static voltage V_{DC} to an extra pair of needle-shaped electrodes separated by a distance $2L$ as shown in Fig. 2.1(c) allows us to properly confine an ion. Modifying Eq. [2.1] to account for the finite length of the trap, we obtain the total potential

$$\begin{aligned} \Phi(x,y,z,t) &= \Phi_{rad.}(x,y,z,t) + \Phi_{ax.}(x,y,z) = \\ &= (V_0 + V_1\cos(\Omega t)) \left(\frac{x^2 - y^2}{2R^2} + \frac{\alpha z^2}{L^2}\right) + \frac{V_{DC}}{2L^2}(2z^2 - x^2 - y^2) \end{aligned} \qquad [2.5]$$

with $\Phi_{ax.}$ the *axial* and $\Phi_{rad.}$ the *radial* potential for $\alpha \in \mathbb{R}$. The now *inhomogeneous* Mathieu equations yield results analogous to Eq. [2.4], albeit with different secular frequencies ω_u along the individual axes [75].

For small displacements from the origin the contribution of the micromotion can be neglected. Along each axis $u = x, y, z$ the equations of motion then read

$$m\frac{d^2}{dt^2}u = -\frac{d}{du}\bar{\Phi}_u = -m\omega_u^2 u$$

where $\bar{\Phi}_u$ is the harmonic *pseudopotential*

$$\bar{\Phi}_u = \frac{1}{2}m\omega_u^2 u^2 \qquad [2.6]$$

with $\omega_u = \frac{\beta\Omega}{2}$ the frequency of the secular motion in Eq. [2.4]. The ion will escape this potential if its orbit extends beyond the physical boundaries of the trap. On such trajectories, the energy of the ion exceeds the *trap depth*

$$\bar{\Phi}_u = \frac{1}{2}m\omega_u^2 u^2 \approx \frac{eV_1^2}{4m\Omega^2 D_u^2} \qquad [2.7]$$

with $D_u = R, L$ depending on the axis $u = x, y, z$ [73].

2.1.2 *A linear chain of ions*

Trapping a single ion is rarely enough to investigate interesting phenomena. The geometry introduced in Fig. 2.1(c) is a simplification of a *linear Paul trap*, which allows us to trap multiple ions arranged in a *linear chain*[1] along the z axis. The potential Eq. [2.6] must then also consider the Coulomb repulsion between the N ions, such that

$$\bar{\Phi}_z(t) = \frac{1}{2}\sum_{i=1}^{N} m\omega_z^2 z_i^2(t) + \frac{e^2}{8\pi\epsilon_0}\sum_{i,j=1|i\neq j}^{N}\frac{1}{|z_i(t)-z_j(t)|}, \tag{2.8}$$

where $z_i(t)$ is the position of the $i-$th ion and ϵ_0 the *permittivity* of the vacuum [77]. Assuming only small displacements $q_i(t)$, we approximate $z_i(t) = z_i^{(0)} + q_i(t)$ where $z_i^{(0)}$ are the equilibrium positions determined by

$$\frac{d}{dz}\Phi_z(t)\big|_{z_i=z_i^{(0)}} = 0. \tag{2.9}$$

The Coulomb interaction couples the motion of the individual ions. Following the derivation by James in Ref. [77], the motion is approximated by the *Lagrangian*

$$L = \frac{m}{2}\left[\sum_{i=1}^{N}\left(\frac{d}{dt}q_i(t)\right)^2 - \omega_z^2\sum_{i,j=1}^{N}A_{i,j}q_i(t)q_j(t)\right], \tag{2.10}$$

where $A_{i,j}$ is a matrix containing the partial derivatives $\frac{\partial^2}{\partial q_i \partial q_j}\bar{\Phi}_z$ evaluated at the equilibrium positions, where $q_i = q_j = 0$.

The eigenvalues μ_p and eigenvectors $\vec{b}^{(p)}$ of $A_{i,j}$ allow us to gain some knowledge about the nature of the dynamics in the ion chain: the entries $b_i^{(p)}$ of $\vec{b}^{(p)}$ define the *direction* and *relative amplitude* of the oscillation about the equilibrium for each ion with a frequency $\omega_p = \sqrt{\mu_p}\omega_z$. Associated with the smallest eigenvalue $\mu_p = 1$ is the vector $\vec{b}^{(1)} = \frac{1}{\sqrt{N}}(1,1,\ldots,1)$ describing the *center-of-mass* (COM) motion, where all ions oscillate collectively with ω_z [77].

With respect to the $\vec{b}^{(p)}$ we define p-th *normal mode* as

$$Q_p(t) = \sum_i \vec{b}_i^{(p)} q_i(t)$$

and rewrite the Lagrangian in Eq. [2.10], such that

$$L = \frac{m}{2}\sum_p\left[\left(\frac{d}{dt}Q_p(t)\right)^2 - \omega_p^2 Q_p(t)^2\right]. \tag{2.11}$$

From classical mechanics, we know that the Lagrangian is defined as the *difference* of the kinetic energy T and the potential energy U; in contrast, the *Hamiltonian* H is just the *sum* of these two terms. We identify the kinetic energy as

$$T(t) = \frac{m}{2}\sum_p\left(\frac{d}{dt}Q_p(t)\right)^2 = \frac{1}{2m}\sum_p\left(m\frac{d}{dt}Q_p(t)\right)^2 = \frac{1}{2m}\sum_p P_p^2$$

1 In the remainder of this thesis we use the terms *ion chain*, *ion crystal*, *ion string* and *ion register* interchangeably.

and define the *momentum* $P_p = m\frac{d}{dt}Q_p(t)$; the potential energy is given by

$$U(t) = \frac{m}{2}\sum_p \omega_p^2 Q_p^2(t).$$

We arrive at the Hamiltonian of the harmonic oscillator [36]

$$H = T(t) + U(t) = \frac{1}{2m}\sum_p P_p^2(t) + \frac{m}{2}\sum_p \omega_p^2 Q_p^2(t) = \hbar\omega_z \sum_p \sqrt{\mu_p}\left[\hat{a}_p^\dagger \hat{a}_p + \frac{1}{2}\right], \qquad [2.12]$$

where we have introduced the *creation and annihilation operators* $\hat{a}_p^\dagger$ and $\hat{a}_p$ following. Common eigenstates to these operators are *number states* $|n\rangle_p$, satisfying

$$\hat{a}_p^\dagger |n\rangle_p = \sqrt{n+1}\,|n+1\rangle_p \qquad \text{and} \qquad \hat{a}_p |n\rangle_p = \sqrt{n}\,|n-1\rangle_p .$$

At this point, the motion of the particles is *quantized*: excitations are discrete and associated with the creation or destruction of *phonons*. For each mode p, the most general state is given by the superposition

$$|\phi\rangle_p = \sum_n c_{n,p}|n\rangle_p = \sum_n c_{n,p}\frac{\hat{a}_p^\dagger}{\sqrt{n_p}}|0\rangle_p \qquad [2.13]$$

with coefficients $c_{n,p}$, where $|0\rangle_p$ describes the *motional ground state*.

The concepts introduced in this section allow us to fulfill the first of DiVincenzo's criteria: the carriers of quantum information – the ions – are well-defined, and the size of the system can be adjusted more or less at will by trapping different numbers of ions. Moreover, motion plays a crucial role in mediating *entanglement*, which will become apparent in later chapters. Without control over the motional states of a trapped-ion system, the capabilities of the quantum processor would be severely limited.

2.2 TRAPPED IONS INTERACTING WITH COHERENT LIGHT FIELDS

In this section, we discuss the interaction between trapped ions and electromagnetic radiation, which is a fundamental building block of the quantum processor. All relevant processes – from state preparation and the manipulation of quantum information to the detection of the quantum state – are implemented using precisely tuned light pulses with frequencies in different regions of the electromagnetic spectrum. In the following, we consider light as a monochromatic wave with a fixed frequency ω_L generated by a laser system. The light interacts with a *hydrogen-like* ion with one un-paired electron in its outer shell, thus having a net charge $+e$.

In a first step, we ignore the contribution of motion in the ion trap derived in Sec. 2.1 and write the *minimal coupling Hamiltonian* [78]

$$\begin{aligned} H(t) &= \frac{1}{2m}\left(\vec{p} - e\vec{A}(\vec{r},t)\right)^2 + V(\vec{r}) - \frac{e}{m}\vec{S}\vec{B}(\vec{r},t) \\ &= \frac{1}{2m}\vec{p} + V(\vec{r}) - \frac{e}{m}\vec{p}\vec{A}(\vec{r},t) + \frac{e^2}{2m}\vec{A}^2(\vec{r},t) - \frac{e}{m}\vec{S}\vec{B}(\vec{r},t) \\ &= H_0 + H_1(t) \end{aligned} \qquad [2.14]$$

where $V(\vec{r})$ is the potential binding the electron to the nucleus and $\frac{e}{m}\vec{S}\vec{B}(\vec{r},t)$ is the interaction of its spin with the magnetic field. Using Maxwell's equations in Coulomb

gauge we compare the individual terms in the time-dependent interaction Hamiltonian $H_1(t)$ [79, 80]. For a vector potential given by $\vec{A}(\vec{r},t) = A_0\vec{\epsilon}\cdot e^{i(\vec{k}\vec{r}-\omega_L t)} + c.c.$ with wave vector $\vec{k}_L$ and polarization $\vec{\epsilon}$ we express the amplitude A_0 in terms of the electric field

$$\vec{E}(\vec{r},t) = -\frac{d}{dt}\vec{A}(\vec{r},t) \Longrightarrow E_0\vec{\epsilon}\cdot e^{i(\vec{k}\vec{r}-\omega_L t)} + c.c. = -i\omega_L A_0\vec{\epsilon}\cdot e^{i(\vec{k}\vec{r}-\omega_L t)} + c.c. \longrightarrow A_0 = \frac{iE_0}{\omega_L}.$$

Hence, the term $\frac{e^2}{2m}\vec{A}(\vec{r},t)^2$ is smaller than $\frac{e}{m}\vec{p}\vec{A}(\vec{r},t)$ by a factor $1/\omega_L$ and can therefore be neglected; a similar argument applies to the spin-interaction term. The Hamiltonian then simplifies to

$$H(t) = \hat{H}_0 - \frac{e}{m}\vec{p}\vec{A}(\vec{r},t) = H_0 + H_1(t) \qquad [2.15]$$

When interacting with the electromagnetic wave, the electron can be excited from a state $|g\rangle$ to another state $|e\rangle$, which are simultaneous eigenstates to H_0 with energies $\hbar\omega_g$ and $\hbar\omega_e$, respectively. This process occurs whenever the frequency of the light field ω_L is close to $\omega_{eg} = \omega_e - \omega_g$. In the following paragraphs we assume $\omega_L \approx \omega_{eg}$ and let $|\omega_{kk'} - \omega_L| \gg 1$ for any other pair of states $|k\rangle, |k'\rangle \neq |e\rangle, |g\rangle$, such that we can safely ignore all other energy levels $\{k\}_i$. The ion is then modeled as a two-level system as shown in Fig. 2.2 with *ground state* $|g\rangle$ and *excited state* $|e\rangle$ which satisfy $\hbar\omega_e > \hbar\omega_g = 0$.

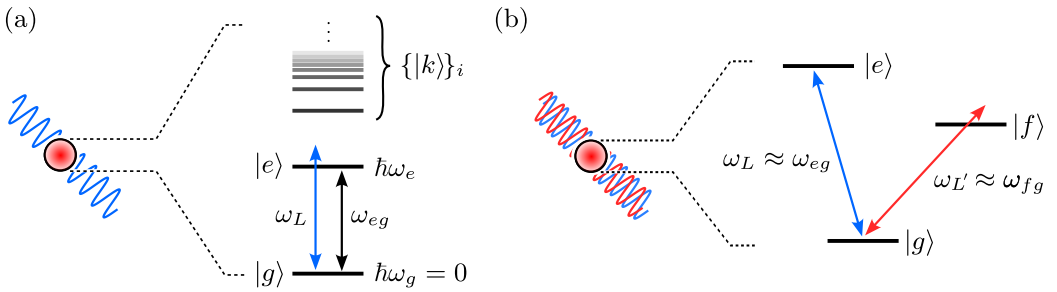


Figure 2.2: (a) Approximation of the ion as a system of two states $|e\rangle$ and $|g\rangle$: only these states are coupled by the monochromatic light field with $\omega_L \approx \omega_{eg}$; all other states can be ignored. (b) A three-level ion featuring two transitions to two excited states $|e\rangle$ and $|f\rangle$ from a common ground state $|g\rangle$. This is a more realistic model for an ion to be used in quantum information processing experiments.

The probability amplitude $\mathcal{P}_{|g\rangle\to|e\rangle}$ for the ion to be excited after having interacted with the light field for a small interaction time t is given by

$$\mathcal{P}_{|g\rangle\to|e\rangle} = \int_0^t \langle e|U(t)|g\rangle\, dt = \int_0^t \langle e|\exp\left(-\frac{iH(t)t}{\hbar}\right)|g\rangle \approx -\int_0^t \frac{e}{m}\langle e|\vec{p}\vec{A}(\vec{r},t)|g\rangle\, dt.$$

The vector potential is now approximated in the limit of *long wavelengths*: λ is large compared to other relevant length scales in the Hamiltonian, which are on the order of a few Bohr radii a_0. The spatial component of the vector potential is given by the series

$$\begin{aligned}\vec{A}(\vec{r},t) = A_0\vec{\epsilon}\left(e^{i\vec{k}\vec{r}}e^{-i\omega_L t} + e^{-i\vec{k}\vec{r}}e^{i\omega_L t}\right) &\approx A_0\vec{\epsilon}\left(1 + i\vec{k}\vec{r} + \ldots\right)e^{-i\omega_L t} + c.c. \\ &\approx \vec{A}(0,t) - i\vec{k}\vec{r}\cdot A_0\vec{\epsilon}\cdot\left(e^{i\omega_L t} - e^{-i\omega_L t}\right) + \ldots,\end{aligned} \qquad [2.16]$$

for which we keep only terms up to second order in the exponent, such that[2]

$$\mathcal{P}_{|g\rangle\to|e\rangle} \approx -\int \frac{e}{m}\langle e|\vec{p}\vec{A}(0,t)|g\rangle\, dt - \int \frac{ie}{m}A_0\left(e^{i\omega_L t} - e^{-i\omega_L t}\right)\langle e|\vec{k}\vec{r}\cdot\vec{\epsilon}\vec{p}|g\rangle\, dt. \qquad [2.17]$$

2 Note, that the momentum and the vector potential commute in the Coulomb gauge. Here we have implicitly used $\vec{p}\vec{A}(\vec{r},t) = \vec{A}(\vec{r},t)\vec{p}$ before expanding $\vec{A}(\vec{r},t)$.

We now substitute the classical variables for position and momentum with the operators $\vec{r} \to \hat{X}, \vec{p} \to \hat{P} = -i\hbar\nabla$ and use the commutation relation

$$\left[\hat{H}_0, \hat{X}\right] = \frac{i\hbar}{m}\hat{P} \longrightarrow \hat{P} = -i\frac{m}{\hbar}\left[\hat{H}_0, \hat{X}\right] \tag{2.18}$$

to simplify the first term in Eq. [2.17]

$$\begin{aligned} -\frac{e}{m}\langle e|\hat{\vec{P}}\vec{A}(0,t)|g\rangle &= -\frac{e}{m}A_0\vec{\epsilon}\cdot\left(e^{i\omega_L t}+e^{-i\omega_L t}\right)\langle e|\hat{P}|g\rangle \\ &= i\frac{e}{\hbar}A_0\vec{\epsilon}\cdot\left(e^{i\omega_L t}+e^{-i\omega_L t}\right)\langle e|\left[\hat{H}_0,\hat{X}\right]|g\rangle \\ &= i\frac{e}{\hbar}A_0\vec{\epsilon}\cdot\left(e^{i\omega_L t}+e^{-i\omega_L t}\right)\hbar\omega_{eg}\langle e|\hat{X}|g\rangle \\ &\approx i\omega_L A_0\vec{\epsilon}\cdot\left(e^{i\omega_L t}+e^{-i\omega_L t}\right)\hat{d}_{eg} = i\omega_L\hat{d}_{eg}\vec{A}(0,t) \end{aligned} \tag{2.19}$$

where $\hat{d}_{eg} = e\langle e|\hat{X}|g\rangle$ is the *electric dipole moment* for the transition $|g\rangle \leftrightarrow |e\rangle$ [77].

The second term is notably more difficult: we use the identity[3]

$$(\vec{k}\vec{r})(\vec{\epsilon}\vec{p}) = (\vec{k}\times\vec{\epsilon})(\vec{r}\times\vec{p}) + (\vec{k}\vec{p})(\vec{\epsilon}\vec{r}) = |k|\vec{\epsilon}_\perp\vec{L} + (\vec{k}\vec{p})(\vec{\epsilon}\vec{r})$$

and identify the outer products as the *angular momentum* $\vec{L} = \vec{r}\times\vec{p}$ and the polarization of the magnetic field $\vec{\epsilon}$. With $|k| = \omega_L/c$ we obtain

$$\begin{aligned} &-i\frac{e}{m}A_0\left(e^{i\omega_L t}-e^{-i\omega_L t}\right)\cdot\langle e|(\vec{k}\vec{r})(\vec{\epsilon}\vec{p})|g\rangle \\ &\qquad = -i\frac{e\omega_L}{mc}A_0\vec{\epsilon}_\perp\left(e^{i\omega_L t}-e^{-i\omega_L t}\right)\langle e|\vec{L}|g\rangle - i\frac{e}{m}A_0\left(e^{i\omega_L t}-e^{-i\omega_L t}\right)\langle e|(\vec{k}\vec{p})(\vec{\epsilon}\vec{r})|g\rangle \end{aligned}$$

and using the definition of $\vec{A}(\vec{r},t)$ in Eq. [2.16] we identify

$$i\omega_L A_0\vec{\epsilon}\left(e^{i\omega_L t}-e^{-i\omega_L t}\right) = \frac{\partial}{\partial t}\vec{A}(\vec{r}=0,t)$$

and thus

$$\begin{aligned} &-i\frac{e}{m}A_0\left(e^{i\omega_L t}-e^{-i\omega_L t}\right)\cdot\langle e|(\vec{k}\vec{r})(\vec{\epsilon}\vec{p})|g\rangle \\ &\qquad = \frac{e}{m\omega_L}\langle e|\vec{L}|g\rangle\,\vec{k}\times\frac{\partial}{\partial t}\vec{A}(0,t) - \frac{e}{m\omega_L}\vec{k}\,\langle e|\vec{p}\vec{r}|g\rangle\,\frac{\partial}{\partial t}\vec{A}(0,t). \end{aligned}$$

Promoting the classical variables to operators, the probability $\mathcal{P}_{|g\rangle\to|e\rangle}$ given by Eq. [2.17] then reads

$$\mathcal{P}_{|g\rangle\to|e\rangle} \approx \int \underbrace{i\omega_L\hat{d}_{eg}\vec{A}(0,t)}_{\text{el. dipole}}\,dt + \frac{e}{m\omega_L}\int \underbrace{\left[\langle e|\vec{L}|g\rangle\,\vec{k}\times\frac{\partial}{\partial t}\vec{A}(0,t)\right.}_{\text{mag. dipole}} \underbrace{\left. - \vec{k}\,\langle e|\hat{P}\hat{X}|g\rangle\,\frac{\partial}{\partial t}\vec{A}(0,t)\right]}_{\text{el. quadrupole}}\,dt. \tag{2.20}$$

When the electron of an ion is excited by an electromagnetic wave, its quantum numbers n, l and m change by an integer Δn, Δl and Δm, respectively. Depending on the quantity of Δn, Δl and Δm we speak of *electric* or *magnetic dipole* or *electric quadrupole transitions*. As a consequence of conservation of energy and momentum, not any arbitrary combination of these numbers is physically possible; this is reflected by the *selection rules* [80, 81]. As the

3 For vectors $\vec{a},\vec{b},\vec{c}$ and $\vec{d}$ it holds $(\vec{a}\times\vec{b})(\vec{c}\times\vec{d}) = (\vec{a}\vec{c})(\vec{b}\vec{d}) - (\vec{a}\vec{d})(\vec{b}\vec{c})$.

quantum numbers for $|e\rangle$ and $|g\rangle$ have not been specified, Eq. [2.20] is general and contains contributions of the electric and magnetic dipole as well as the electric quadrupole[4].

In the remainder of this thesis we focus exclusively on electric dipole and electric quadrupole transitions. We therefore model the ion as a three-level system with a common ground state $|g\rangle$ and two excited states $|e\rangle$ and $|f\rangle$ as illustrated in Fig. 2.2(b). The transition $|g\rangle \leftrightarrow |e\rangle$ is treated as a dipole, while $|g\rangle \leftrightarrow |f\rangle$ is associated with a quadrupole transition. We further assume that these transitions are well separated in frequency, such that tuning ω_L will excite *either* the quadrupole *or* the dipole transition, but not both simultaneously. Such a model is a realistic approximation of an ion used in a trapped-ion quantum processor. A real ion offers a rich set of different states and transitions, which are used to realize various processes, such as laser cooling and the encoding of quantum information.

Using Eq. [2.20] we finally write down the Hamiltonian, yet in the *absence* of motion

$$\hat{H} = \hat{H}_0 + \sum_{i=e,f} \frac{\hbar\Omega_{ig}}{2} \left(|i\rangle\langle g| + |g\rangle\langle i|\right)\left(e^{i\omega_L t} + e^{-i\omega_L t}\right), \qquad [2.21]$$

where Ω_{ig} is the *Rabi frequency* associated with the transition between $|g\rangle$ and the respective state $|i\rangle = |e\rangle, |f\rangle$. For an electric field with amplitude $E_0 = \omega_L A_0$, which is in resonance with the ion, we obtain on the dipole transition [77]

$$\Omega_{eg} = \frac{2\omega_L}{\hbar}\left|\vec{d}_{eg}\vec{A}(0,t)\right| = \frac{2E_0}{\hbar}\left|\vec{\epsilon}\vec{d}_{eg}\right| = \Omega_{\text{dip.}}$$

and on the quadrupole transition [77, 82]

$$\Omega_{fg} = \left|\frac{eE_0}{\hbar}\langle f|(\vec{\epsilon}\vec{r})(\vec{k}\vec{p})|g\rangle\right| = \left|\frac{eE_0}{\hbar}\vec{\epsilon}\vec{q}_{fg}\right| = \Omega_{\text{quad.}}.$$

Solving the Schrödinger equation for a generic Ansatz wave function

$$|\psi\rangle(t) = c_g(t)|g\rangle + c_e(t)|e\rangle$$

in the interaction picture, we obtain a coupled pair of differential equations for the complex amplitudes $c_g(t), c_e(t)$ [80]

$$i\frac{d}{dt}c_g(t) = \frac{\Omega}{2}c_e(t) \qquad i\frac{d}{dt}c_e(t) = \frac{\Omega}{2}c_g(t) + \Delta c_e(t)$$

The probability to end up in the excited state at a time t is given by [80, 81]

$$\mathcal{P}_e(t) = |c_e(t)|^2 = \frac{\Omega^2}{\Omega^2 + \Delta^2}\sin^2\left(\sqrt{\Omega^2 + \Delta^2}\, t/2\right) \qquad [2.22]$$

with $\Delta = \omega_{eg} - \omega_L$ the *detuning* of the electromagnetic wave from the bare frequency ω_{eg} of the two-level system. An ion interacting with a light field close to resonance oscillates between the states $|e\rangle$ and $|g\rangle$ according to Eq. [2.22]. These *Rabi oscillations* are shown in Fig. 2.3 for different detunings; detuning the laser from resonance increases the effective Rabi frequency while preventing the ion from being fully excited [80].

4 Note, that higher orders in the expansion of $\vec{A}(\vec{r},t)$ would lead to *octupoles*.

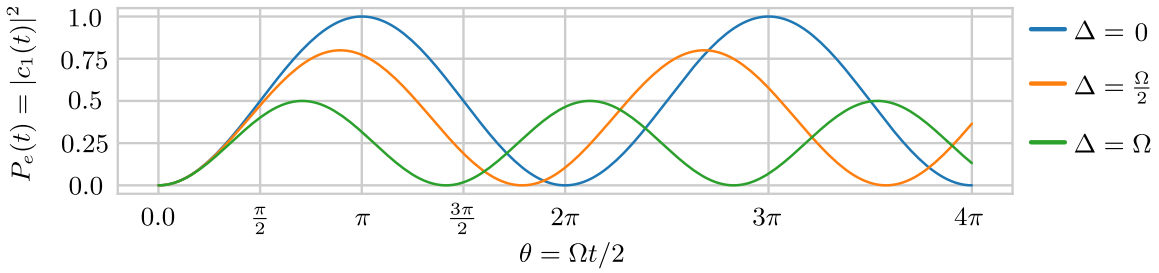


Figure 2.3: A two-level ion interacting with an electromagnetic wave detuned by a frequency Δ from the frequency of the bare ion undergoes *Rabi oscillations*. The ion is periodically excited from the ground state $|g\rangle$ to the excited state $|e\rangle$ with effective Rabi frequency $\Omega' = \sqrt{\Omega^2 + \Delta^2}$. Increasing Δ_L will decrease the probability to excite the ion while simultaneously increasing the frequency of the oscillations.

For any given Ω we can create arbitrary superpositions of $|g\rangle$ and $|e\rangle$ by tuning the interaction time t. The coefficients $c_g(t)$ and $c_e(t)$ must obey the *normalization condition* $|c_g(t)|^2 + |c_e(t)|^2 = 1$, which is always satisfied for the parametrization

$$|\psi\rangle = \cos(\theta/2)\,|g\rangle + \sin(\theta/2)e^{i\phi}\,|e\rangle \qquad [2.23]$$

for any pair of angles (θ, ϕ). In this notation, $|\psi\rangle$ can be visualized as a vector pointing, from the origin to surface of the *Bloch sphere* illustrated in Fig. 2.4, which we have already introduced in Sec. 1.2.2.

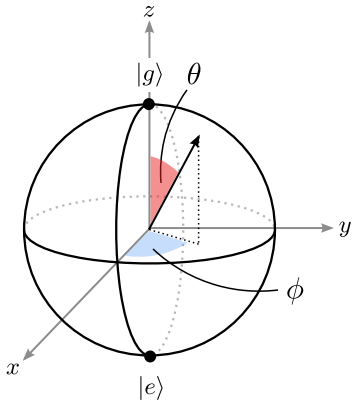


Figure 2.4: Visualization of the state $|\psi\rangle = \cos(\theta/2)\,|g\rangle + \sin(\theta/2)e^{i\phi}\,|e\rangle$ on the *Bloch sphere*. $|\psi\rangle$ is parametrized by the two angles θ and ϕ, which are closely related to the properties of the light field and its interaction time with the ion.

By comparing Eq. [2.23] with the result for $|c_e(t)|^2$ in Eq. [2.22] we derive a closed-form expression for the angle θ. For $\Delta = 0$, we obtain $\theta = \Omega t$, which corresponds to the *area* of a light pulse interacting with the ion. In the context of quantum algorithms, a pulse implementing an angle equal to a fraction of π is referred to as a π/n-pulse, where $n \in \mathbb{N}_{>0}$. The second angle ϕ is directly controlled by a *phase* imprinted onto the light field. Details on the implementation of these pulses are provided in Ch. 3.

We will now add motion according to Eq. [2.12] and consider the axial motion of a string of ions along the z direction of the trap, cf. Fig. 2.1(c). Without long-wave approximation, the Hamiltonian of the joint system of ion and trap reads

$$\begin{aligned}\hat{H} &= \hbar\omega_{eg}\left|e\right\rangle\left\langle e\right| + \hbar\omega_z \sum_{p=1}^{N}\sqrt{\mu_p}\left(\hat{a}_p^\dagger\hat{a}_p + \frac{1}{2}\right) \\ &\quad + \frac{\hbar\Omega}{2}\left(\left|e\right\rangle\left\langle g\right| + \left|g\right\rangle\left\langle e\right|\right)\left(e^{i(k_z z-\omega_L t)} + e^{-i(k_z z-\omega_L t)}\right) \\ &= \hat{H}_0 + \hat{H}_{\text{mech.}} + \hat{H}_I(t),\end{aligned} \tag{2.24}$$

with k_z the projection of $\vec{k}$ along the z axis. For simplicity we consider a single ion and consequently only a single mode of motion exists. A generic Ansatz for the wavefunction is [75, 82]

$$\left|\psi\right\rangle = \sum_n \sum_{i\in\{e,g\}} c_{i,n}(t)\left|i,n\right\rangle$$

with $\left|i,n\right\rangle = \left|i\right\rangle \otimes \left|n\right\rangle$ the eigenstates of $H_0 + H_{\text{mech.}}$. We write the position in z using the operator $\hat{Z} = z_0\left(\hat{a}^\dagger + \hat{a}\right)$ and introduce the *Lamb-Dicke parameter*

$$\eta_z = k_z z_0 = \sqrt{\frac{\hbar k_z^2}{2m\omega_z}} = \frac{2\pi}{\lambda}\Delta z \tag{2.25}$$

with Δ_z the extent of the ground state wave packet and λ the wavelength of the light. In the interaction picture, the time-dependent part $\hat{H}_I(t)$ of the Hamiltonian in Eq. [2.24] is given by

$$\begin{aligned}\hat{H}_I(t) &\approx \frac{\hbar\Omega}{2}\Big[\left|e\right\rangle\left\langle g\right|\exp\left(i\eta\hat{a}e^{-i\omega_z t} + i\eta\hat{a}e^{i\omega_z t} - i\Delta t\right) \\ &\qquad + \left|g\right\rangle\left\langle e\right|\exp\left(-i\eta\hat{a}e^{-i\omega_z t} - i\eta\hat{a}e^{i\omega_z t} + i\Delta t\right)\Big] \\ &\approx \frac{\hbar\Omega}{2}\Big[\left|e\right\rangle\left\langle g\right|\left(1 + i\eta(\hat{a}e^{-i\omega_z t} + \hat{a}^\dagger e^{i\omega_z t})\right)e^{-i\Delta t} \\ &\qquad + \left|g\right\rangle\left\langle e\right|\left(1 - i\eta(\hat{a}e^{-i\omega_z t} + \hat{a}^\dagger e^{i\omega_z t})\right)e^{i\Delta t}\Big] \\ &= \hat{H}_{\text{carrier}}(t) + \hat{H}_{\text{RSB}}(t) + \hat{H}_{\text{BSB}}(t)\end{aligned} \tag{2.26}$$

where the fast oscillating terms with frequency $\omega_{eg} + \omega_L$ have been neglected and the exponential has been expanded in the limit of $\lambda \gg z_0$. This is known as the *Lamb-Dicke regime*, in which the characteristic inequality $\eta^2(2n+1) \ll 1$ must be satisfied [75, 77].

We identify three terms in Eq. [2.26], which introduce the dynamics illustrated in Fig. 2.5(a):

- $\hat{H}_{\text{carrier}}(t) = \frac{\hbar\Omega}{2}\left(\left|e\right\rangle\left\langle g\right|e^{-i\Delta t} + \left|g\right\rangle\left\langle e\right|e^{i\Delta t}\right)$ – interactions which do *not* change the motional state of the ion excite the ion via the *carrier transition* $\left|e\right\rangle \leftrightarrow \left|g\right\rangle$ for $\Delta = 0$.
- $\hat{H}_{\text{RSB}}(t) = \frac{i\eta\hbar\Omega}{2}\left(\left|e\right\rangle\left\langle g\right|\hat{a}e^{i(\Delta+\omega_z)t} - \left|g\right\rangle\left\langle e\right|\hat{a}^\dagger e^{-i(\Delta+\omega_z)t}\right)$ – tuning the light field to $\Delta = -\omega_z$ couples the electronic states *and* simultaneously changes the motional quantum state, such that $\left|g,n\right\rangle \leftrightarrow \left|e,n-1\right\rangle$
- $\hat{H}_{\text{BSB}}(t) = \frac{i\eta\hbar\Omega}{2}\left(\left|e\right\rangle\left\langle g\right|\hat{a}^\dagger e^{i(\Delta-\omega_z)t} - \left|g\right\rangle\left\langle e\right|\hat{a}e^{-i(\Delta-\omega_z)t}\right)$ – conversely to $\hat{H}_{\text{RSB}}(t)$, for $\Delta = +\omega_z$ the motional state changes to $\left|n\right\rangle \leftrightarrow \left|n+1\right\rangle$

Detuning the light field to $\Delta = \pm\omega_z$ couples the states $|g\rangle \leftrightarrow |e\rangle$ while simultaneously changing the motion of the ion. For a single ion two resonances appear symmetric around the carrier transition at frequencies $\Delta = \pm\omega_z$ as shown in Fig. 2.5(b). Depending on the wavelength $\lambda_L = 2\pi c/\omega_L$ of the light with respect to the carrier transition, we associate these *sidebands* with a color: since long wavelengths correspond to the red side of the optical spectrum, we call $\Delta = -\omega_z$ (larger λ_L) the *red sideband* (RSB) and conversely, $\Delta = +\omega$ (smaller λ_L) is called the *blue sideband* (BSB).

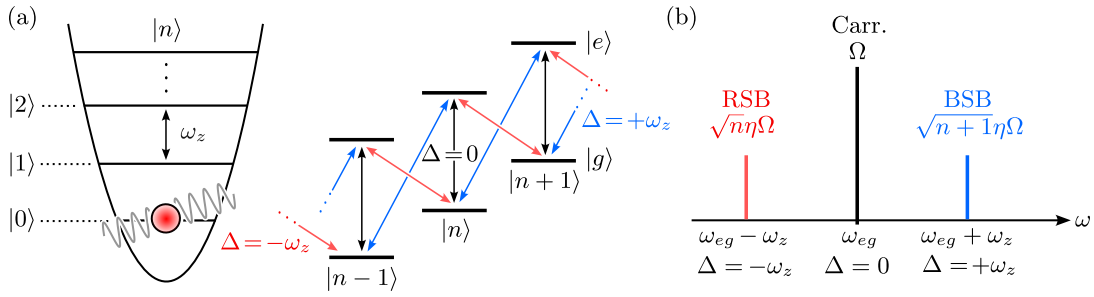


Figure 2.5: Two-level ion in a harmonic trap: (a) the joint system of ion and trap can be imagined as a ladder, where each step corresponds to an integer number of phonons $|n\rangle$. Exciting the electronic state $|e\rangle$ on the respective *sideband*, we simultaneously "climb up / down the ladder" by exciting / de-exciting the motion $|n\rangle \rightarrow |n \pm 1\rangle$. On the *carrier*, the motion will remain unaffected. (b) in the spectrum, the sidebands appear as resonances symmetric around the carrier transition at a detuning $\Delta_L = \pm\omega_z$. Their coupling with respect to the carrier is suppressed by the Lamb-Dicke parameter $\eta \ll 1$ and depends on the motional state.

Compared to the Rabi frequency Ω on the carrier transition the effective Rabi frequencies on the sidebands $\Omega' = \sqrt{n}\eta\Omega$ are suppressed by the Lamb-Dicke factor η and depend on the excitation of the motion. Consequently, the laser intensity $I_0 \propto \Omega^2$ must be increased significantly to drive oscillations on the sideband with a period similar to the carrier.

2.3 COOLING TRAPPED IONS WITH LASERS

The energy of an ion being excited by an electromagnetic wave with wave vector $\vec{k}_L$ increases by a discrete amount $\hbar\omega_{eg}$. This gain is associated with the *absorption* of a *photon* with momentum $\hbar\vec{k}_L$. Due to the conservation of energy and momentum, an ion moving with velocity $\vec{v}$ experiences a recoil, changing its $\vec{v}$ by a small amount

$$\Delta\vec{v}_r = \frac{\hbar\vec{k}_L}{m}. \qquad [2.27]$$

The excited state $|e\rangle$ decays to ground state $|g\rangle$ after an average time T_1 by *spontaneous emission* of another photon in a process called *fluorescence*. While the momentum transfer during absorption is directional, spontaneous emission is considered to be isotropic and thus does not change $\vec{v}$ when averaged over many events. After N cycles of continuous absorption and emission in a time interval Δt, the velocity will have changed by $\Delta\vec{v} = N\vec{v}_r$ due to a mean force [83]

$$\vec{F}_r = m\frac{\Delta\vec{v}}{\Delta t} = \frac{N}{\Delta t}m\vec{v}_r \approx \hbar\vec{k}_L\Gamma \qquad [2.28]$$

exerted on the ion by the light field. The number of fluorescence cycles per second is proportional to the *natural line width* $\Gamma = 1/T_1$ and thus characteristic for the respective

transition $|g\rangle \leftrightarrow |e\rangle$. For an ion moving towards the light field, the vectors $\vec{k}_L$ and $\vec{v}$ are anti-parallel and $\vec{F}_r$ is negative, slowing it down in a process called *laser cooling*.

The ion must undergo many fluorescence cycles in a short period of time for $\vec{F}_r$ to have significant impact. Transitions with small T_1 on the order of a few nanoseconds are associated with dipole transitions, cf. Sec. 2.2. In the following discussion, we follow the arguments made in Ref. [83] for a free particle, which leads to results that are comparable with the more thorough analysis including the trap as presented in Refs. [84, 85]. The interaction Hamiltonian is given by

$$\hat{H}_I(\vec{r},\vec{t}) = -\hat{d}_{eg}\vec{E}(\vec{r},t) = \frac{\hbar\Omega_{dip.}(\vec{r})}{2}\left(e^{i\vec{k}_L\vec{r}-\omega_L t}\,|e\rangle\langle g| + \text{h.c.}\right), \tag{2.29}$$

where h.c. denotes the hermitian conjugate. In the Heisenberg picture, the force operator $\hat{F}$ is defined by

$$\hat{F} = \frac{\partial\hat{P}}{\partial t} = -\frac{i}{\hbar}[\hat{P},\hat{H}] = -\nabla\hat{H}_I,$$

where $\hat{P} = -i\hbar\nabla$ is the momentum operator; using Eq. [2.29] we obtain

$$\begin{aligned}\vec{F} = -\nabla\hat{H}_I &= -\frac{\hbar\Omega_{dip.}}{2}\vec{k}_L\left(e^{i\vec{k}\vec{r}-\omega_L t}\,|e\rangle\langle g| + \text{h.c.}\right) - \frac{\hbar\nabla\Omega_{dip.}(\vec{r})}{2}\left(e^{i\vec{k}_L\vec{r}-\omega_L t}\,|e\rangle\langle g| + \text{h.c.}\right) = \\ &= \hat{F}_{diss.} + \hat{F}_{react.}\end{aligned} \tag{2.30}$$

and identify two different contributions to the total force: a *dissipative* force $\hat{F}_{diss.}$ proportional to the intensity of the light field and a *reactive dipole force* $\hat{F}_{react.}$, which depends on the field's gradient [83, 86].

We will first consider the dissipative force by letting the ion interact with a single plane wave. Since the size of the wave packet given by $\lambda_M = h/m|\vec{v}|$ for a thermal velocity $|\vec{v}| \approx 100$ m/s is small compared to the wavelength λ_L of the light, we can neglect the spatial variation with $\vec{r}$ and approximate $\vec{k}_L\vec{r} \approx$ const.. For simplicity, we set $\vec{r} = 0$ and compute the mean force

$$\vec{F} = \langle\hat{F}_{diss.}\rangle = -\text{Tr}[\varrho\nabla\hat{H}_I] \tag{2.31}$$

with the density matrix ϱ describing the internal state of the ion in terms of $|g\rangle$ and $|e\rangle$. The dynamics of ϱ, including spontaneous emission, are given by the master equation in Lindblad form [75, 87]

$$\frac{d\varrho}{dt} = -\frac{i}{\hbar}\left[\hat{H},\varrho\right] - \frac{\Gamma}{2}\left[\sigma_+\sigma_-\varrho + \varrho\sigma_+\sigma_- - 2\sigma_-\varrho\sigma_+\right],$$

where $\sigma_+ = |e\rangle\langle g|$ and $\sigma_- = |g\rangle\langle e|$. This equation then leads to the familiar *optical Bloch equations*, which have a *steady-state* solution labeled ϱ_S [80]. Eq. [2.31] then reads [82, 83]

$$\vec{F} = -\text{Tr}[\varrho_S\nabla\hat{H}_I] = \hbar\vec{k}_L\frac{\Gamma}{4}\cdot\frac{\Omega_{dip.}^2}{\Delta_L^2 + \frac{\Gamma^2}{4} + \frac{\Omega_{dip.}^2}{2}} = \hbar\vec{k}_K\Gamma\varrho_{S,ee} \tag{2.32}$$

with detuning $\Delta_L = \omega_{eg} - \omega_L$ and $\varrho_{S,ee}$ the population of the excited state. This result is in agreement with Eq. [2.28], since $\Gamma\varrho_{S,ee}$ describes the mean number of fluorescence cycles the ion undergoes every second.

2.3.1 *Doppler cooling*

This cooling technique is called *Doppler cooling* due to the Doppler shift of the wavelength caused by the motion of the ion: as the ion moves within the light field, the wavelength λ_L appears to be shifted by

$$\Delta\lambda_L = \frac{|\vec{v}|\cos(\theta)}{c}\lambda_L,$$

where θ is the angle enclosed by $\vec{k}_L$ and $\vec{v}$. Consequently, λ_L must be deliberately detuned for the light to remain resonant with the dipole transition. With $\Delta_L = \omega_{eg} - \omega_L + \vec{k}_L\vec{v}$ the mean force Eq. [2.32] now depends on $\vec{v}$ and can be approximated in the limit of small velocities by

$$\vec{F} \approx \vec{F}_0 + \alpha\vec{v} \approx \hbar\vec{k}_L\frac{\Gamma S_0}{2} + \alpha\vec{v}, \qquad [2.33]$$

where α is the *friction coefficient* [83]

$$\alpha = \hbar|\vec{k}_L|^2\frac{S_0}{(1+S_0)^2}\cdot\frac{4\Delta\Gamma}{4\Delta^2+\Gamma^2}$$

and S_0 denotes the *saturation parameter*

$$S_0 = \frac{2\Omega_{dip.}^2}{4\Delta_L^2+\Gamma^2}. \qquad [2.34]$$

Note that S_0 must be well below unity to not saturate the transition $|g\rangle \leftrightarrow |e\rangle$, which would render cooling ineffective. Substituting $k_L = |\vec{k}_L|$ and $\vec{k}_L\vec{v} = k_L v\cdot\cos(\theta)$ in Eq. [2.33] yields

$$\begin{aligned}\vec{F} \approx \vec{F}_0 + \alpha\vec{v} &= \hbar\vec{k}_L\frac{\Gamma S_0}{2} + \hbar k_L^2\frac{S_0}{(1+S_0)^2}\cdot\frac{4\Delta\Gamma}{4\Delta^2+\Gamma^2}\cdot\vec{v} \\ &= \hbar\vec{k}_L\frac{\Gamma S_0}{2}\left(1 + \frac{1}{(1+S_0)^2}\frac{8\Delta_L}{\Gamma^2+4\Delta_L^2}\cdot\vec{k}_L\vec{v}\right) \qquad [2.35] \\ S_0 \ll 1 : (1+S_0)^2 \approx 1 \longrightarrow &= \frac{\hbar\vec{k}_L\Gamma}{2}S_0\left(1 + \frac{8\Delta_L}{\Gamma^2+4\Delta_L^2}\cdot k_L v\right),\end{aligned}$$

which for $\Delta < 0$ acts as a viscous that slows the ion down [82, 83].

Consider an ion trapped in a harmonic potential Φ of the form given in Eq. [2.6]. For simplicity we restrict the discussion to one spatial dimension and assume that the ion is oscillating with a frequency ω_z along the z axis of the trap, cf. Fig. 2.1(c). As the ion moves back and forth in the potential $\Phi(z)$ its velocity varies in time [84]

$$\vec{v}(t) = v_0\vec{e}_z\cos(\omega_z t)$$

with $\vec{e}_z$ the unit vector pointing in the z direction.

Suppose that a light field with frequency $\omega_L = \omega_{eg} + \Delta$ and wave vector $\vec{k}_L = -k_L\vec{e}_z$ illuminates the ion as illustrated in Fig. 2.6. Since $\vec{k}_L$ and $\vec{e}_z$ are anti-parallel, the change in velocity $\Delta\vec{v}_r$ in Eq. [2.27] caused by a photon exciting the ion is negative, i.e. along the $-z$ axis. Consequently, cooling can only occur in the half-period of oscillation in which the ion moves towards the light field. For a detuning of $\Delta \approx -k_L v_0$ the probability to excite the ion is large, while it becomes negligible as the ion moves in the opposite direction[5].

5 Heating is observed for $\Delta = +k_L v_0$, where the converse statements about the excitation probabilities apply.

We require that $\omega_z < \Gamma$, meaning that the ion undergoes many fluorescence cycles during one oscillation in the trap [83, 88]. In this so-called *weak confinement* regime, the velocity change due to the trapping potential is small, and thus the ion can be treated as a free particle [82, 83]. This treatment is consistent with the rigorous quantum-mechanical calculations carried out by Wineland and Itano in Ref. [85].

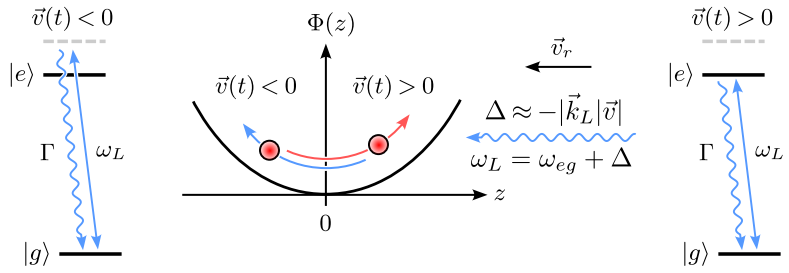


Figure 2.6: Doppler cooling of an ion trapped by a harmonic pseudopotential $\Phi(z)$. The ion is in the ground state $|g\rangle$ and oscillates along the z axis while it is illuminated by a light field with frequency $\omega_L = \omega_{eg} + \Delta$ and wave vector $\vec{k}_L$ which propagates in the $-z$ direction. For a detuning $\Delta = -\vec{k}_L\vec{v}(t)$, the light becomes resonant as the ion moves towards the light source with velocity $\vec{v}(t) > 0$. Then, photons excite the state $|e\rangle$ and transfer momentum $-\hbar|\vec{k}_L|$. Since spontaneous emission is isotropic, the velocity of the ion decreases. Conversely, the probability to excite the ion is small when $\vec{v}(t) < 0$.

.

Doppler cooling is fundamentally limited by spontaneous emission. Following Ref. [82], the *cooling rate* is given by

$$\dot{E}_{cool} = \langle \vec{F}\vec{v} \rangle = \left| \frac{dF}{dv} \right|_{v=0} \langle v^2 \rangle = \hbar k_L \Gamma \frac{8\Delta\Omega_{dip.}^2}{(\Gamma^2 + 4\Delta^2)^2} \langle v^2 \rangle ,$$

which at the very end of the process is balanced by the *heating rate*

$$\dot{E}_{heat} = \frac{\hbar^2 k_L^2}{2m} \Gamma \varrho_{S,ee} = \frac{\hbar^2 k_L^2}{2m} \frac{\Gamma\Omega_{dip.}^2}{\Gamma^2 + 4\Delta^2} = E_r \frac{\Gamma\Omega_{dip.}^2}{\Gamma^2 + 4\Delta^2} \qquad [2.36]$$

with *recoil energy* E_r. From $\dot{E}_{cool} = -\dot{E}_{heat}$ we compute the kinetic energy

$$m \langle v^2 \rangle = \frac{\hbar\Gamma}{2} \left(\frac{\Gamma}{-2\Delta} - \frac{2\Delta}{\Gamma} \right) = k_B T,$$

which is minimized for $\Delta = -\Gamma/2$. With this detuning, the ion is cooled to its characteristic *Doppler temperature* [82, 89]

$$T_D = \frac{\hbar\Gamma}{4k_B}(1 + \beta), \qquad [2.37]$$

where the parameter β has been introduced to account for anisotropies in realistic spontaneous emission processes.

Laser cooling was first demonstrated in trapped ions by Neuhauser et al. and Wineland et al. in 1978 [90, 91]. Ten years later, temperatures below T_D close to the recoil limit $T_r = E_r/k_B$ have been observed and verified by independent measurements [92, 93]. While initially lacking an explanation it was speculated, that these observations were attributed to spatial variations in the intensity and polarization of two counter-propagating laser beams. This technique is now known as *Sisyphus cooling*, which we will touch upon in the next paragraphs following the semi-classical treatment in [83, 86, 94].

2.3.2 *Sisyphus cooling*

We now add another level $|g'\rangle$ to our description of the ion as shown in Fig. 2.7(a) and tune the frequency ω_L of the light *above* the resonance of the transition $|g\rangle \leftrightarrow |e\rangle$, such that $\Delta_L = \omega_L - \omega_{eg} > 0$. Spontaneous decay of the excited state $|e\rangle$ can occur to both $|g'\rangle$ and $|g\rangle$ with a *branching ratio* $0 \leq \beta \leq 1$, such that the effective decay rates are given by $\beta\Gamma$ and $(1-\beta)\Gamma$, respectively; we also allow the state $|g'\rangle$ to decay to $|g\rangle$ at a rate Γ'.

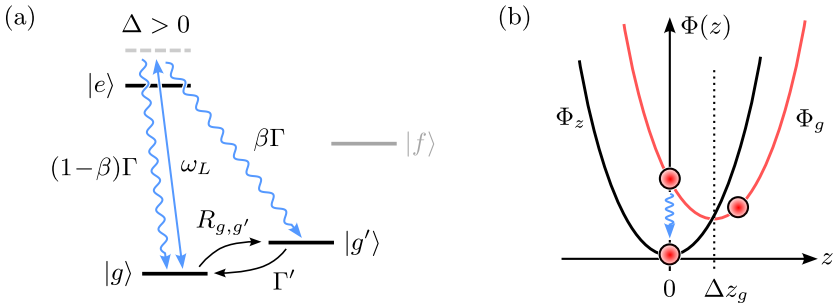


Figure 2.7: Sisyphus cooling technique: (a) the ion is described by the three levels $|g\rangle$, $|g'\rangle$ and $|e\rangle$. A standing wave with frequency ω_L couples the ion in the ground state $|g\rangle$ to the excited state $|e\rangle$, which decays to either $|g\rangle$ or $|g'\rangle$ with a branching ratio β. (b) the light field induces a shift, which leads to a displacement of the trapping potential by Δz_g. As the ion moves in the shifted potential well, it will decay from $|g\rangle$ to $|g'\rangle$ associated with Φ_z, reducing its energy.

Following Ref. [94] we compute the time evolution of the populations considering the contributions of the individual decay channels

$$\begin{aligned} \frac{d\varrho_{gg}}{dt} &= -\frac{\Gamma S_0}{2}\cos^2(\vec{k}_L\vec{r})(\varrho_{gg}-\varrho_{ee}) + \Gamma'\varrho_{g'g'} + \Gamma(1-\beta)\varrho_{ee} \\ \frac{d\varrho_{ee}}{dt} &= \frac{\Gamma S_0}{2}\cos^2(\vec{k}_L\vec{r})(\varrho_{gg}+\varrho_{ee}) - \Gamma\varrho_{ee} \\ \frac{d\varrho_{g'g'}}{dt} &= -\Gamma'\varrho_{g'g'} + \Gamma\beta\varrho_{ee}. \end{aligned} \qquad [2.38]$$

where S_0 is the saturation parameter previously defined in Eq. [2.34]. In the regime $S_0 \ll 1$ the excited state is on average not populated. Then the steady-state solutions for the population of $|g\rangle$ and $|g'\rangle$ are

$$\varrho_{S,gg} = \frac{\Gamma'}{\langle R_{g,g'}\rangle + \Gamma'} \quad \text{and} \quad \varrho_{S,g'g'} = \frac{\langle R_{g,g'}\rangle}{\langle R_{g,g'}\rangle + \Gamma'}, \qquad [2.39]$$

where $\langle R_{g,g'}\rangle$ is the average rate for a transition from $|g\rangle$ to $|g'\rangle$ via $|e\rangle$ to occur.

We now let the trapped ion interact with a standing wave [83, 94]

$$\vec{E}(\vec{r},t) = E_0\vec{\epsilon}\cos(\vec{k}_L\vec{r})\cos(\omega_L t)$$

created by two (perfectly) counter-propagating light fields. Again, we assume for simplicity that the ion moves along the z axis and let $\vec{k}_L$ be parallel to z, cf. Fig. 2.1(c). Cooling is then governed by the dipole force $\vec{F}_{react.}$ along the z axis, which according to Eq. [2.30] given by

$$F_{react.}(z) = -\frac{\hbar\nabla\Omega_{dip.}(z)}{2}\cos(\omega_L t),$$

where $\nabla\Omega_{dip.}(z)$ is the gradient of the Rabi frequency in the z direction. This restoring force is associated with a potential of the form [94]

$$\Phi_L(z) = \frac{\hbar}{2}\sqrt{\Omega_{dip.}(z)^2 + \Delta_L^2} - \frac{\hbar\Delta_L}{2} \approx \frac{\hbar}{2}\left(\Delta_L + \frac{\Omega_{dip.}(z)^2}{2\Delta_L}\right) - \frac{\hbar\Delta_L}{2} = \frac{\hbar}{4\Delta_L}\Omega_{dip}(z)^2, \quad [2.40]$$

where the root is approximated by a Taylor series for $\Omega_{dip.}(z) \ll \Delta_L$. As the Rabi frequency is proportional to the electric field we obtain the largest dipole force at $k_L z = \pm\pi/4$ and we expand Eq. [2.40]

$$\Phi_L(z) \approx \frac{\hbar\Omega_0^2}{4\Delta_L}\left(\frac{1}{2} - k_L z + \frac{\pi}{4}\right),$$

where Ω_0 is the amplitude of $\Omega_{dip.}(z)$. The effective trapping potential with respect to the ground state is then

$$\Phi_g(z) = \frac{1}{2}m\omega_z^2 z^2 + \Phi_L(z)$$

with motional frequency ω_z, which has a minimum at the position

$$\Delta z_g \approx \frac{\hbar k_L \Omega_0^2}{4\Delta_L m\omega_z^2}. \quad [2.41]$$

Assuming the trapping potential Φ_z is centered around $z = 0$, Φ_g is shifted by a small amount Δz_g as shown in Fig. 2.7(b). This shift allows us to cool the ions in a process akin to the punishment bestowed upon the ancient greek king Sisyphus, who was damned to eternally push a heavy boulder up a steep slope just for it to roll back down to the foot of the mountain. The cooling process is described as follows: when the ion is in $|g\rangle$, the induced AC Stark shift can be seen as a perturbation of the trapping potential, which can be seen as a spatial displacement of the minimum by Δz_g. As it is excited, it can decay to $|g'\rangle$ with a rate $\beta\Gamma$ and in doing so, falls into the unperturbed well Φ_z, thereby losing energy $\Delta E = \Phi_g - \Phi_z$. After an average time $1/\Gamma'$ the ion decays back to $|g\rangle$ and the process begins anew.

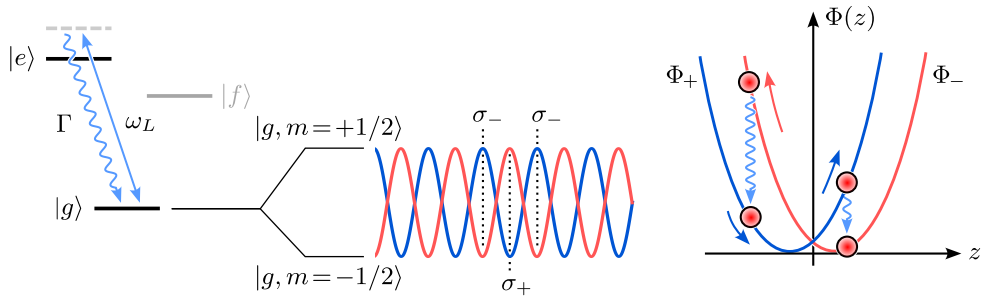


Figure 2.8: Laser cooling with polarization gradients: a constant magnetic bias field is applied to lift the degeneracy of the ground state, leading to two states $|g\rangle$ and $|g'\rangle$ with different magnetic quantum numbers $m = \pm 1/2$. Both states experience AC Stark shifts of equal magnitude and opposite sign, depending on the local polarization. Two state-dependent, spatially shifted harmonic potentials $\Phi_\pm$ emerge for the two ground states. As the ion moves through the potential landscape, the periodic exchange of population between $|g\rangle$ and $|g'\rangle$ causes the ion to lose kinetic energy, thereby slowing it down.

The Sisyphus scheme is experimentally realized using *polarization gradients* [86, 95, 96]: the states $|g\rangle$ and $|g'\rangle$ are both ground states of the ion with different magnetic quantum numbers $m = \pm 1/2$, which become non-degenerate in the presence of a constant magnetic

bias field $\vec{B}$. Two counter-propagating lights field induce a spatially modulated AC Stark shift that depends on the local polarization. While *magnitude* of the shift is equal, its *sign* is opposite for $|g, m = -1/2\rangle$ and $|g', m = +1/2\rangle$ as shown in Fig. 2.8.

A periodic redistribution of the ground state populations between two shifted potential wells labeled $\Phi_\pm$ as a function of the local polarization of the light field results in a cooling effect [94–96]: if the polarization with respect to the quantization axis defined by $\vec{B}$ is σ^+ (right-circular), the well associated with $|g, m = -1/2\rangle$ has a higher energy compared to $|g, m = +1/2\rangle$. Consequently, the ion loses energy as it transitions from Φ_- to Φ_+. This process is analogous for σ^- (left-circular) polarization, but in this case, the transition is from Φ_+ to Φ_-.

The cooling rate is given by [94]

$$\dot{E}_{cool} = -\varrho_{S,gg} \langle R_{g,g'} \Phi_g(z) - \Phi_z \rangle + \varrho_{S,g'g'} \Gamma' \langle \Phi_g(z) - \Phi_z \rangle$$

which competes with recoil heating at a rate $\dot{E}_{heat}$ analogous to Eq. [2.36]. *Doppler heating* due to the positive detuning of the light field can be neglected as long as the branching ratio does not strongly favor a decay into one of the ground states. In optimal conditions, the theoretical limit of Sisyphus cooling techniques is given by [94]

$$T_S = \frac{\hbar \omega_z}{k_B} \sqrt{\beta}, \qquad [2.42]$$

with the parameter β accounting for any anisotropies. This temperature is well below the Doppler limit T_D, cf. Eq. [2.37]. In realistic experimental environments, the ratio

$$\frac{T_S}{T_D} = \frac{4\sqrt{\beta}\omega_z}{\Gamma(1+\beta)} < 1$$

is smaller than unity, since $\omega_z \approx 2\pi \cdot 1$ MHz while the natural linewidth is on the order of $\Gamma \approx 100$ MHz. Assuming $\beta \approx 1$, these numbers yield an estimate of

$$T_S < 0.1 \cdot T_D.$$

2.3.3 *Sideband cooling*

Both Doppler and polarization gradient cooling are unable to bring the ion to its absolute motional ground state $|n = 0\rangle$. If we were able to selectively excite the red sidebands individually, we could selectively remove phonons in an iterative process called *sideband cooling*. However, the large natural linewidth $\Gamma_{dip.}$ of the dipole transition $|g\rangle \leftrightarrow |e\rangle$ relative to ω_z prevents the motional sidebands from being spectrally resolved. A narrow quadrupole transition on the other hand satisfies the *strong coupling* condition [82, 83]

$$\Gamma_{quad.} \ll \omega_z \qquad [2.43]$$

and tuning $\Delta_L = -\omega_z$ couples $|g\rangle$ and $|f\rangle$ on the red sideband; see Fig. 2.9(a). The cooling scheme is illustrated in Fig. 2.9(b): an ion initially in the motional state $|n\rangle$ is excited on the red sideband, annihilating a single phonon in the process, such that $|n\rangle \longrightarrow |n-1\rangle$. In the Lamb-Dicke regime, spontaneous emission predominantly occurs on channels that preserve the motional state [84]. After many cycles, the ion will therefore reach its electronic and motional ground state $|g\rangle \otimes |n = 0\rangle$, thereby ending the cooling process.

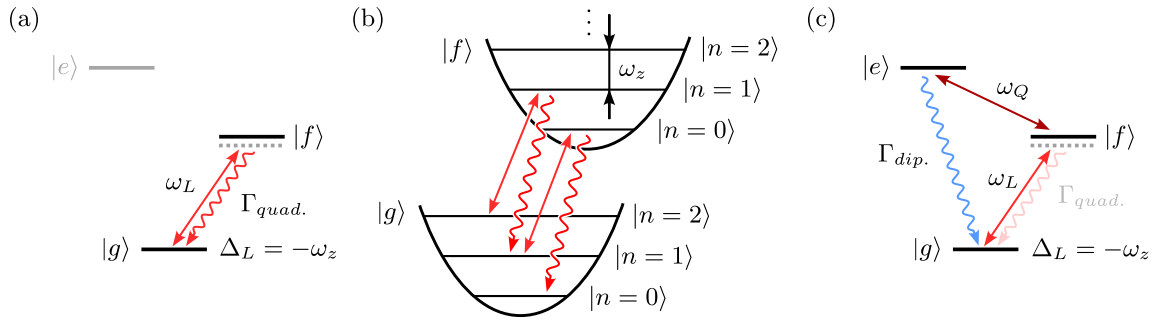


Figure 2.9: Sideband cooling to the motional ground state: (a) a quadrupole transition has a sufficiently narrow natural linewidth $\Gamma_{quad.} \ll \omega_z$, allowing us to resolve the motional sideband. (b) for a negative detuning $\Delta_L = -\omega_z$ the transition $|g\rangle \leftrightarrow |f\rangle$ is excited on the red sideband, where a single phonon is annihilated. As $|f\rangle$ decays, the motional state of the ion is preserved; each cycle of absorption and spontaneous emission controllably de-excites the motion until the ion ends up in its electronic and motional ground state. (c) the long lifetime $T_1 = \Gamma_{quad}^{-1}$ of $|f\rangle$ leads to a low cooling rate. This can be overcome by coupling $|f\rangle$ to the state $|e\rangle$ by a second light field with frequency ω_Q, using the fast decay with rate $\Gamma_{dip.}$ to speed up the cooling process.

The natural lifetime T_1 of a transition satisfying Eq. [2.43] is on the order of a few seconds. This significantly slows down the cooling process, as, on average, the ion undergoes only a single fluorescence cycle within T_1. Coupling $|f\rangle$ and $|e\rangle$ with a second laser field of frequency ω_Q realizes a *closed cycle transition* shown in Fig. 2.9(c), allowing us to benefit from the broad linewidth of the dipole transition $\Gamma_{dip.} \gg \Gamma_{quad.}$, while still resolving the motional sidebands on the quadrupole transition. An estimate for the effective linewidth is given by [97]

$$\Gamma_{dip.} \geq \Gamma_{\text{eff.}} = \frac{\Omega_Q^2}{(\Gamma_Q + \Gamma_{quad.})^2 + 4\Delta_Q^2} \gg \Gamma_{quad.},$$

where Ω_Q is the Rabi frequency of the transition $|f\rangle \leftrightarrow |e\rangle$, which has a linewidth Γ_Q. The parameter Δ_Q describes the detuning of the light field with frequency ω_Q from ω_{ef}.

Fig. 2.9(c) is a good approximation to the level structure of an ion suitable to be used in a trapped-ion quantum processor. These types of level schemes are found in the alkaline-earth metals, in transition metals such as mercury, and the lanthanides Ytterbium and Lutetium [98, 99].

2.4 OPTICAL PUMPING TO SELECTED GROUND STATES

In the context of Sisyphus cooling in Sec. 2.3.2 we have briefly discussed that the degeneracy of the ground states $|g, m = -1/2\rangle$ and $|g, m = +1/2\rangle$ is lifted in the presence of a magnetic bias field. After a sequence of Doppler, polarization-gradient, and sideband cooling, these states will be populated with approximately equal probability. On the narrow quadrupole transition, both states are spectrally resolved and can be selectively coupled to the metastable state $|f\rangle$. In the following discussion we target $|g, m = +1/2\rangle$ as illustrated in Fig. 2.10. Using the technique already employed for sideband cooling, a rapid decay to the ground state is achieved by coupling $|f\rangle$ with $|e\rangle$ using an optical dipole transition, cf. Sec. 2.3.3. The spontaneous emission from $|e\rangle$ to $|g, m = \pm 1/2\rangle$ does not favor either of the ground states: assuming a branching ratio $\beta = 0.5$, state $|g, m = -1/2\rangle$ will be populated

with a probability of 99.9% after 10 cycles.

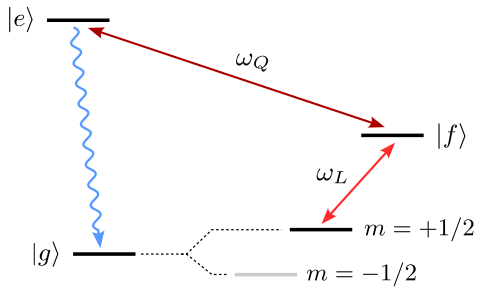


Figure 2.10: Preparation of the ground state $|g, m = -1/2\rangle$ by optical pumping: the non-degenerate ground states $|g, m = \pm 1/2\rangle$ are initially populated with equal probability. The state $|g, m = +1/2\rangle$ is excited to $|f\rangle$ via the quadrupole transition and $|f\rangle$ is coupled to $|e\rangle$. Spontaneous decay from $|e\rangle$ occurs to either of the ground states $|g, m = \pm 1/2\rangle$, however, since only $|g, m = +1/2\rangle$ is coupled with $|f\rangle$, population will be transferred from $|g, m = +1/2\rangle$ to $|g, m = -1/2\rangle$ after a few cycles.

While laser cooling allows us to bring the ion to its motional ground state, this *optical pumping* technique prepares a definite electronic ground state, here $|g, m = -1/2\rangle$. This is the last ingredient to fulfill DiVincenzo's second criterion: we have prepared our system in a well defined fiducial state.

2.5 READOUT OF QUANTUM STATES BY FLUORESCENCE DETECTION

The last of DiVincenzo's criteria concerns the detection of the quantum state at the end of each computation. An ion offering a level structure analogous to Fig. 2.10 allows one to optically distinguish the population of the state $|f\rangle$ from that in $|g\rangle$ by recording the fluorescence on the dipole transition $|g\rangle \leftrightarrow |e\rangle$ with the light field tuned to resonance $\Delta_L = 0$. Fluorescence occurs only if the ion is initially in the ground state; if the state $|f\rangle$ is populated, no signal will be observed.

A simplified setup is illustrated in Fig. 2.11: a photosensitive detector with surface area A is illuminated by light collected by an objective, shown here by a lens at a working distance d from the position of the ion. Assuming isotropic emission, the detector will receive

$$\langle N \rangle = \Gamma_{dip.} \cdot \frac{A}{4\pi \cdot d^2} \cdot \tau \qquad [2.44]$$

photons per time interval τ, which are then converted into an electric signal. However, not every photon will trigger a response from the detector. This effect is accounted for by *quantum efficiency* $\eta_{QE} \leq 1$ of the device.

A rather simple detector is the *photomultiplier tube* (PMT): electrons released from a photosensitive surface upon photon impact are multiplied as they pass through a series of dynodes due to the principle of secondary emission [100]. In the limit of low intensities, as is the case when recording fluorescence due to spontaneous emission, PMTs register the impact of individual photons with a quantum efficiency $\eta_{QE} \leq 0.4$. The resulting signal is converted into a histogram, enabling the discrimination of the state $|g\rangle$ from $|f\rangle$ as shown in Fig. 2.11. However, these devices cannot distinguish light from different sources, preventing individual ions from being spatially resolved.

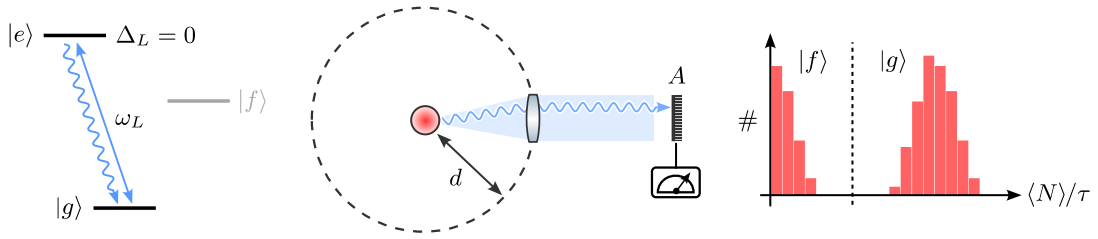


Figure 2.11: Simplified setup for the recording of fluorescence light emitted by spontaneous decay on the $|g\rangle \leftrightarrow |e\rangle$ transition. The light is focused on a photosensitive detector with surfacea are A by an objective at working distance d, indicated here by a single lens. Photons reaching the detector are converted into an electric signal, which indicates if the ion has been in the ground state. No signal will be observed if the ion is in the state $|f\rangle$. The number of photons arriving on the detector per time interval is recorded and converted into a histogram, allowing for proper discrimination of $|g\rangle$ and $|f\rangle$.

Charge-coupled devices (CCDs) used in digital camera systems offer a high spatial resolution with a quantum efficiency of up to $\eta_{QE} \approx 0.95$ [101, 102]. CCDs require a more sophisticated optical setup, as the ions must be properly focused onto the chip to prevent coma and spherical aberrations [103]. Each ion illuminates only a small number of pixels, allowing us to obtain a histogram for each ion, which enables proper state discrimination even for large ion chains.

3

EXPERIMENTAL SETUP

The experiments presented in this thesis are performed on strings of up to eight Calcium ions, specifically of the isotope $^{40}Ca^{+}$. Calcium is a common choice in many state-of-the-art quantum processors today, as its relevant atomic transitions are in the optical and near-infrared regimes, where reliable and well-tested laser systems are commercially available.

Fig. 3.1(a) illustrates the relevant energy levels and transitions. An optical dipole transition at 397nm couples the $4^2S_{1/2}$ ground state with the $4^2P_{1/2}$ state, which has a short lifetime of $T_1[P_{1/2}] = 7.10(2)$ns [104], allowing for efficient implementation of Doppler cooling, polarization gradient cooling and quantum state readout by fluorescence detection. Spontaneous decay from the $4^2P_{1/2}$ to the metastable $3^2D_{3/2}$ state, which has a lifetime of $T_1[3^2D_{3/2}] = 1.20(1)$s [105], is suppressed by continuous re-pumping with a laser at 866 nm. Sideband cooling and optical pumping are realized on the quadrupole transition coupling the ground state with the $3^2D_{5/2}$ state at 729nm, forming a closed cycle with another dipole transition at 854 nm to the $4^2P_{3/2}$ state.

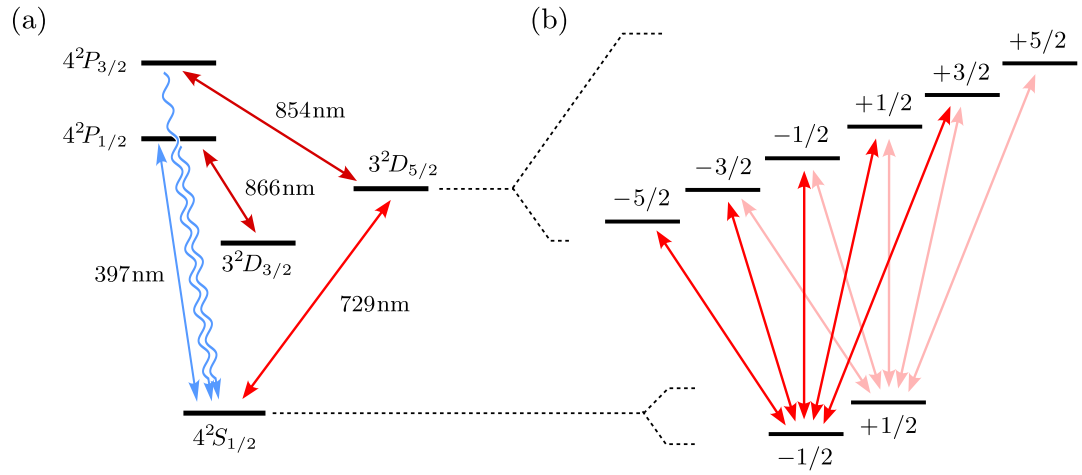


Figure 3.1: Reduced level scheme of $^{40}Ca^{+}$: (a) the $4^2S_{1/2}$ state is coupled to a short-lived $4^2P_{1/2}$ state via a dipole transition, allowing for laser cooling and readout. Re-pumping prevents the $3^2D_{3/2}$ state from being populated due to spontaneous decay of the $4^2P_{1/2}$ state. Quantum information is encoded in the ground state and the metastable $3^2D_{5/2}$ state and manipulated via a narrow quadrupole transition at 729 nm. (b) A static magnetic field exposes the multiplet in the $4^2D_{5/2}$ state, which together with the two $4^2S_{1/2}$ states allow for the encoding of quantum digits up to dimension $d = 7$.

With an experimentally measured lifetime of $T_1[3^2D_{5/2}] = 1.168(7)$s the $3^2D_{5/2}$ state is well suited to encode and store quantum information [105]. The narrow linewidth of the $4^2S_{1/2} \leftrightarrow 3^2D_{5/2}$ transition allows for efficient manipulation of the quantum state. In the

presence of a static magnetic field $\vec{B}$, the anomalous Zeeman effect leads to a splitting of the states into uniformly spaced multiplets [81]. Of particular interest are the six states in the $3^2D_{5/2}$ manifold with magnetic quantum numbers $m = \pm 5/2, \pm 3/2, \pm 1/2$ as well as the two ground states with $m = \pm 1/2$ shown in Fig. 3.1(b), allowing for the encoding of *qudits* up to dimension $d = 7$. This limit is imposed by the indistinguishability of the two ground states in the fluorescence signal.

In the following sections we give a detailed overview of our setup. The vacuum vessel and the ion trap are presented in Sec. 3.1, where we provide characteristic values for all relevant quantities in our setup. Sec. 3.2 shows the optical components, including a thorough description of the devices used to control the properties of light and direct it onto selected ions. These devices are controlled by electronic signals, which are provided by the control hardware discussed in Sec. 3.3.

3.1 ION TRAP AND VACUUM CHAMBER

The apparatus is centered around the macroscopic linear Paul trap designed by S. Gulde as part of his doctoral research [106]. A rendering of the trap is shown in Fig. 3.2(a): an amplified *radio-frequency* (RF) signal[1] at $\Omega_{RF} = 2\pi \cdot 23.492$ MHz is applied to pairs of blade-shaped electrodes, which create an oscillating potential for the radial confinement of the ions. Axial confinement is achieved using a pair of tip electrodes connected to a stable high-voltage source[2]. For a given voltage V_{DC}, the axial trap frequency ω_z is well approximated by

$$\omega_z \approx 2\pi \sqrt{\frac{V_{DC}}{500\ \mathrm{V}}} \cdot 859.6\ \mathrm{kHz}$$

where $\omega_z = 2\pi \cdot 859.6$ kHz was measured at $V_{DC} = 500\ V$. Radially, we measure frequencies $\omega_{x,y} \approx 2\pi \cdot 3.6$ MHz [107], for which we observe a small degeneracy of $\Delta\omega \approx 20$ kHz with respect to x and y. Furthermore, $\omega_{x,y}$ drift within a range of ≈ 50 kHz over the course of several minutes, which can be attributed to thermal effects affecting the electric circuitry of the trap. However, these drifts do not impact the performance of our quantum processor, as we neither actively cool nor drive the radial sidebands during our computations.

We compute the trap depth $\bar{\Phi}_{x/y,z}$ according to Eq. [2.7] in Sec. 2.1.1. Using the dimensions provided in Fig. 3.2, we obtain a (radial) depth of

$$\bar{\Phi}_{x/y} = \frac{m}{2}\omega_{x,y}^2 r^2 = \frac{m}{8}\omega_{x,y}^2 d^2 = 67.85\ \mathrm{eV}$$

where the radius $r = d/2$ is readily obtained from the vertical separation $d = 1.6$ mm of the blade electrodes. For the axial confinement, we take our measurement $\omega_z = 2\pi \cdot 859.6$ kHz at 500 V and compute $\bar{\Phi}_z$ using the length $L = 5$ mm between the two tip electrodes to arrive at

$$\bar{\Phi}_z = \frac{m}{8}\omega_z^2 L^2 = 37.73\ \mathrm{eV}.$$

At these depths, the system does not require any cryogenic cooling: the entire apparatus can be operated at room temperature.

1 RF source: Rohde & Schwarz SMB-100-A; wideband amplifier: Mini-Circuits ZHL-42W+
2 ISEG ECH244 crate with CC24 main controller with EBS-C0-30 3 kV 8-channel bipolar module

The trap is located at the center of a vacuum chamber designed by H.C. Nägerl [108], providing optical access through various viewports. A top-down view of the apparatus is illustrated in Fig. 3.2(b). We refer to each viewport by its orientation on a compass, with the flange on the top of the image facing north (N). This flange connects a titanium sublimation pump together and an ion-getter pump[3] to the chamber, creating an ultra-high vacuum with a pressure[4] of $\approx 5 \cdot 10^{-11}$ mBar. The trap is aligned at an angle of 22.5° relative to the N-S axis, allowing all laser beams to overlap with the ion string.

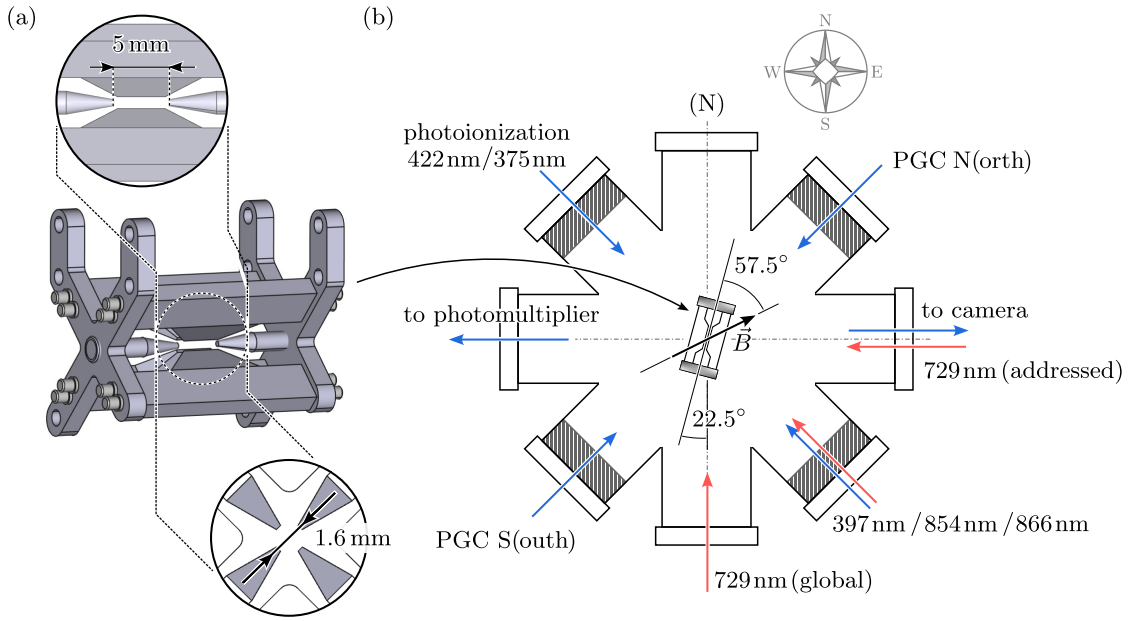


Figure 3.2: Top view of the vacuum chamber (a) with the macroscopic linear Paul trap (a) at its center. Vacuum pumps attached to the northern flange (N), reducing the pressure in the chamber down to $\approx 5 \cdot 10^{-11}$ mBar. Light enters and leaves the chamber through the remaining viewports: photoionization is achieved by two beams from the NW, while laser cooling is realized by beams entering from SE and along the NE-SW axis. Qudit manipulation is implemented along two perpendicular axes: global control is achieved from S, while subsets of ions can be addressed via E. A photomultiplier (W) and a sensitive EMCCD camera (E) allow fluorescence light to be detected. Rings of permanent magnets (hatched) mounted on the NE/NW and SE/SW flanges create a constant magnetic bias field oriented at an angle of 57.5° with respect to the trap axis.

The ions are loaded from an *"oven"* positioned directly below the trap: ^{40}Ca is deposited on a metal surface, which is heated by an electric current, releasing a stream of neutral atoms. *Photo-ionization* (PI) is realized by two laser beams[5] entering from NW in a two-step process: the electron is excited by the 422 nm laser and removed from the atom by the second beam at a wavelength of 375 nm [109]. Laser cooling and state detection are implemented using three laser beams with wavelengths of 397 nm, 854 nm and 866 nm. The light enters the chamber via the SE port counter-propagating to the PI beams, illuminating all ions collectively; the position of the beams can be adjusted remotely by piezoelectric actuators[6]. On the perpendicular axis, *polarization-gradient cooling* (PGC) is realized by two beams with orthogonal linear polarization entering through the NE and SW port [107].

3 VacIon Plus 20, Varian MiniVac controller
4 Continuous pressure monitoring via pump controller
5 Two Toptica DL 100 diode laser modules, including gratings for coarse tuning of the output wavelength.
6 4x Newport Picomotor Piezo Linear Actuators model 8303, Newport 4 channel motion controller model 8742

The quantum state of the ions can be manipulated via either of two laser beams at 729 nm propagating along orthogonal axes: collective control is achieved by the *global* beam coming from the south, while subsets of ions can be addressed via the beam(s) entering the chamber from the east. In this configurations, both beams have a finite spatial overlap with the trap axis, allowing for the implementation of axial entangling gates, see Ch. 4. We calculate the *Lamb-Dicke parameter* η by measuring the Rabi frequencies Ω on the carrier transition and $\Omega' = \eta\Omega$ on the first BSB of the axial COM; taking the ratio, we obtain $\eta_{\text{global}} = 0.103(2)$ and $\eta_{\text{addressed}} = 0.034(2)$ for the respective beam axes. The optical paths guiding both beams to the vacuum chamber are independent. Local variations in the path length due to mechanical and thermal stress on the individual components lead to fluctuations in the relative phase of both light fields. Consequently, both paths are considered to be *incoherent* with respect to each other and therefore cannot be used simultaneously to implement quantum gates in an algorithm: once a beam has been chosen, all gate operations must be carried out with respect to that axis[7].

An objective[8] with an $NA \approx 0.29$ and a working distance of 66 mm is mounted on a six-axis translation stage[9] close to the eastern viewport [107], focusing the laser beams onto the ions while simultaneously imaging the fluorescence light onto a sensitive *electron-multiplied CCD* (EMCCD) camera[10]. On the opposite (western) flange, a second objective[11] with an $NA \approx 0.2$ and working distance of $D = 65$ mm enables the collective detection of the light emitted by all ions on a *photomultiplier tube* (PMT)[12] [110]. Using the definition in Eq. [2.44] we estimate the number of photons per ion arriving at the objective within exposure interval of $\tau = 1$ ms and obtain

$$\langle N \rangle = \Gamma_{dip.} \frac{A}{4\pi D^2} \tau \approx \Gamma_{dip.} \frac{NA^2}{4} \tau \approx 1500. \qquad [3.1]$$

With an active area of ≈ 1 cm^2 of the PMT and assuming a quantum efficiency $\eta_{QE} \approx 0.3$ typical for such devices, we can expect ≈ 80 detection events per millisecond. This number agrees well with our observations of $60 - 70$ events per ion in the ground state, while we measure $\approx 5 - 10$ when the ion is hidden in any of the $D_{5/2}$ states. We therefore deduce, that a *detection window* of $\tau = 1$ ms is sufficient to faithfully distinguish the states via their fluorescence signal [14]. A similar argument holds for the camera, where we observe ≈ 200 events per millisecond due to the notably higher quantum efficiency of $\eta_{QE} = 90\%$ [111].

The magnetic bias field is generated by two pairs of rings of small permanent magnets mounted onto the flanges of the vacuum vessel as indicated by the hatched surfaces in Fig. 3.2(b). These magnets create a field $\vec{B}$ with a strength of ≈ 0.42 mT pointing along an axis tilted at an angle of 57.5° with respect to the trap axis [107], see Fig. 3.2 (b). This configuration enables the coupling of the states with $\Delta m = \pm 0, \pm 1$ and $\Delta m = \pm 2$ via the quadrupole transition [82].

7 An exception to this rule are laser pulses with the sole purpose of introducing Stark shifts, cf. Ch. 4.
8 Silloptics S6ASS2241
9 Assembled with Newport components, 2x Newport motion controller model 8742 (linked)
10 Oxford instruments / Andor Technology iXon X3
11 Nikon MNH-23150-ED Plan 1.5x
12 Electron-Tubes Inc. P25

3.2 LASER LIGHT FOR QUANTUM INFORMATION PROCESSING

Encoding and manipulating quantum information in trapped ion systems requires precise control over the properties of light. The light is continuously emitted by a laser and shaped into a stream of pulses using *acousto-optic* elements [112]. We first discuss how the acousto-optic effect can be used to control intensity, frequency ω_L and phase ϕ_L of the light in Sec. 3.2.1 and present a method to address single ions in Sec. 3.2.2. These are the prerequisites for the upcoming sections, where we look at the light sources: the three lasers driving the dipole transitions are introduced in Sec. 3.2.3 followed by the more elaborate narrow-band laser system for qudit manipulation in Sec. 3.2.4. Our discussion of the optical setup will be important in Ch. 4 in the context of quantum gates, especially those generating entanglement.

3.2.1 *Manipulating light with acousto-optic modulators*

We control the properties of light using *acousto-optic modulators* (AOMs). Such a device is illustrated in Fig. 3.3(a): an electric signal with frequency f, phase p and amplitude a is applied to a piezoelectric transducer, which is bonded to one facet of a transparent crystal [112]. This transducer converts the signal into a sound wave traveling through the crystal with wave vector $\vec{K}$ and wavelength Λ, resulting in a spatial modulation of the refractive index of the medium, thereby creating a tunable grating. Light described by the wave vector $\vec{k}$ and wavelength $\lambda \ll \Lambda$ incident at an angle α is diffracted by the grating according to *Bragg's law*

$$\sin(\alpha) = n\frac{\lambda}{2\Lambda} \qquad [3.2]$$

where $n \in \mathbb{Z}$ specifies the order of diffraction. In many practical applications we are only interested in $n = \pm 1$ and the unperturbed beam, which we call the 0^{th} *order*. Due to the conservation of energy and momentum, the frequency ω_L' of the diffracted beam is shifted depending on the overlap of $\vec{k}$ and $\vec{K}$. If the z-component of $\vec{k}$ and $\vec{K}$ are anti-parallel, the frequency is *up-shifted* to $\omega_L' = \omega_L + 2\pi f$, see Fig. 3.3(a). In contrast, for parallel z components energy is deposited in the vibration of the crystal, which creates a *down-shift* of the frequency to $\omega_L' = \omega_L - 2\pi f$. As no new photons are created, the intensity of the incoming beam is distributed among the 0^{th} order and the diffracted beam(s) depending on the amplitude a of electric signal applied to the AOM.

AOMs are designed for a given optical wavelength and operate within a frequency band of $\Delta f \approx 10 - 50$ MHz around a specified *center frequency* f_C in the VHF band[13], which can be customized during fabrication [114]. Under optimal conditions, diffraction efficiencies of up to 90% can be achieved over the entire bandwidth. Laser pulses are created by modulating the parameters of the electric signal, thereby altering the properties of the sound wave. Changes to any of the parameters are not instantaneous but rather take effect after a characteristic *rise time* $t_r \approx 10 - 100$ ns, which is the time it takes for the sound wave to propagate from the transducer through the *active aperture* $A \approx 0.1 - 5$ mm, where light and sound wave interact[14].

13 According to IEEE STD 521, letters are assigned to radiofrequency signals ranging from 3 MHz to 100 GHz, with VHF identifying the band from 30 MHz to 300 MHz.

14 The active aperture A is given by the width of the crystal facet exposed to the incident beam. Its height only affects the shape of the diffracted beams and is often ignored.

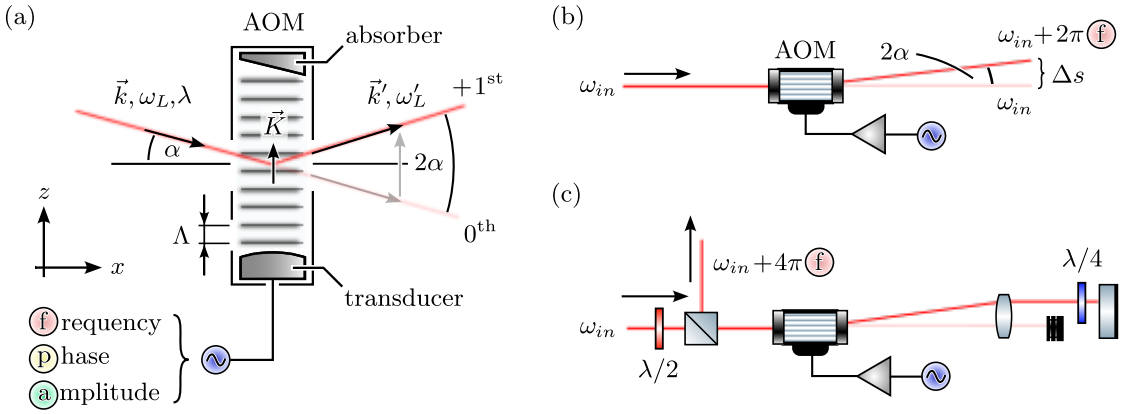


Figure 3.3: (a) operation principle of an *acousto-optic modulator* (AOM): an electric signal (blue circle) is sent to a transducer, which generates a sound wave in a crystal. The sound wave modulates the refractive index of the medium, acting as a diffraction grating for an incoming laser beam. Due to the conservation of energy and momentum, the frequency of the diffracted beam is shifted by $2\pi f$. (b) *single-pass* (SP) configuration: the incoming beam is displaced and shifted in frequency depending on the parameters of the electric signal. (c) *double-pass* (DP) configuration: the beam passes the AOM twice, leading to a shift of $4\pi f$; in contrast to the SP setup, the beam always points in the same direction and is not displaced as the frequency of the sound wave is adjusted. Two wave retarders (blue and red disks) rotate the polarization to distinguish the incoming from the twice diffracted beam using a *polarizing beam splitter* (PBS) cube [113].

We distinguish between two optical setups:

- *Single-pass* (SP) configuration:

  In this configuration illustrated in Fig. 3.3(b), light passes the device *once*, shifting frequency and phase of the diffracted beam by $\Delta\omega = \pm 2\pi f$ and $\Delta\phi = p$, respectively. The deflection angle is approximated following Eq. [3.2] in the limit of $\lambda \ll \Lambda$ by

  $$2\alpha \approx \frac{\lambda}{\Lambda},$$

  which is on the order of a few mrad/MHz. Any change in f causes a displacement $\Delta s \approx 2\alpha \cdot d$ of the diffracted beam, which increases with the distance d from the AOMs. Consequently, the SP configuration is limited to those applications where either the frequency is kept constant or spatial displacements do not affect the performance of the larger optical setup. An exception are *fiber-coupled* AOMs, where the diffracted beam is coupled into an optical fiber positioned close to the crystal, thereby maintaining a constant coupling efficiency even for large deflection angles.

- *Double-pass* (DP) configuration:

  Spatial displacements can be entirely eliminated by allowing the light to pass through the same device *twice* as shown in Fig. 3.3(c) [115]. The AOM is positioned at the focal point of a convex lens with focal distance F, directing the diffracted beam onto a path parallel to its optical axis; the 0-th order is blocked. A planar mirror then reflects the light back along the same path through the AOM, where it is diffracted again. Consequently, the total frequency shift is given by $\Delta\omega = 4\pi f$ and the phase

accumulates to $\Delta\phi = 2\pi$. The second diffraction occurs with the same angle 2α but in the opposite direction, such that incident and diffracted beam coincide. Both beams can be separated by their polarization on a *polarizing beam splitter* (PBS) cube using two wave retarder plates: the $\lambda/2$ plate (red) aligns the polarization of the incident beam with respect to the PBS, while the diffracted beam passes through the $\lambda/4$ plate (blue) twice, introducing an effective shift of $\lambda/2$ and causing a reflection on the beam cube.

The DP configuration effectively doubles the frequency tuning range of the SP, which comes at the cost of a lower total diffraction efficiency of $< 80\%$. This disadvantage however is outweighed by a significant improvement in the switching characteristics of the AOM, especially at the falling edge of a laser pulse. Moreover, DPs are resilient to temperature drifts, which are detrimental to SP units: changing the amplitude of the electric signal changes the thermal load on the transducer of the AOM, which causes instabilities in the position of the diffracted beam. In a DP configuration, this *beam pointing* is mitigated by design as any displacement from the first pass is cancelled in the second pass. Consequently, we use DP units to *create* the laser pulses and resort to SP for additional *modulation* and *ion addressing*.

3.2.2 *Addressing subsets of ions in large registers*

The ability to selectively interact with individual ions within a larger register is crucial for any quantum processor. Without it, all quantum gate operations would affect the whole ion string collectively, rendering the system impractical for most digital quantum algorithms. Various methods have been developed to enable the addressing of individual ions and larger subsets [106, 116, 117]. In the present setup, we use *acousto-optic deflectors* (AODs) – a type of AOM with active aperture $A > 5 - 10$ mm optimized for large deflection angles – to address up to two ions simultaneously [118][15].

An AOD in SP configuration allows us to precisely control the position of the diffracted beam by tuning the frequency f of the sound wave. The frequency of the light field reaching the ion is then given by $\omega_L \pm 2\pi f$ and depends on the position: as the beam moves, ω_L must be continuously adjusted by an upstream DP unit to remain resonant with each ion. Simultaneously applying a second signal with frequency f' to the AOD would also allow us to address a second ion, however, the light on one ion will always be detuned by $\Delta_L = \pm 2\pi|f' - f|$. This issue is mitigated by the design shown in Fig. 3.4(a), where two AODs labelled A and B are used in tandem [119, 120]. The AODs are rotated at an angle of 45° with respect to the plane of the ions and are perpendicular to each other, such that the $\vec{K}$ vectors of the sound wave are orthogonal.

The displacement of the individual diffracted beams in the x/z plane is illustrated at the bottom of Fig. 3.4(a). We assume the first AOD A driven at frequency f uses the -1^{st} diffraction order, deflecting the diffracted beam labelled -1^{st}_A in the $-x/+z$ direction. The position of this beam is outside of the ion plane and the light is detuned by $-2\pi f$. As it enters the second AOD B, the beam is deflected towards the ions in $+x/+z$ direction and shifted back into resonance, cancelling the detuning of the light field.

15 Adding more signal sources would allow for the simultaneous addressing of larger sub-registers. However, since the intensity of the incident beam is finite, less light will be focused onto each individual ion

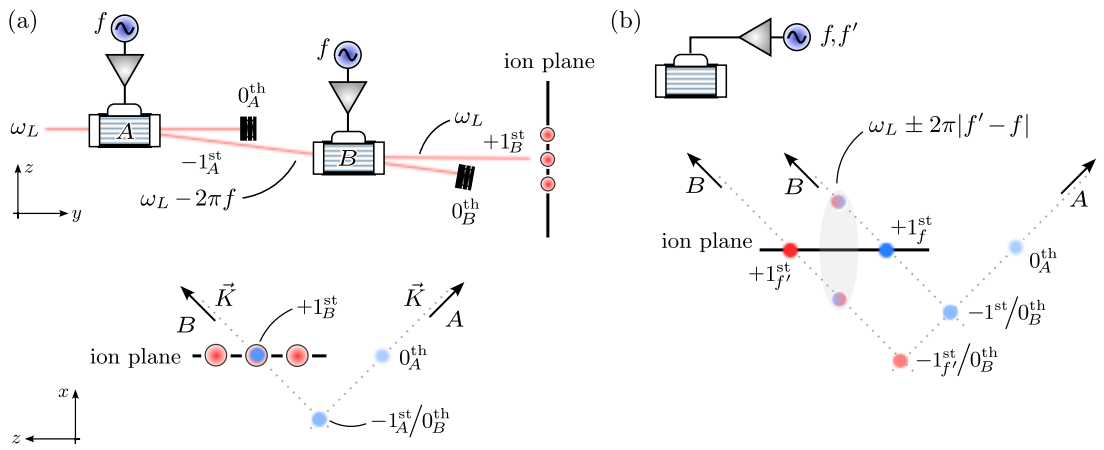


Figure 3.4: Ion addressing setup: (a) the incident beam passes through two *acousto-optic deflectors* (AODs), which are orthogonal to each other and rotated at an angle of 45° with respect to the plane of the ion string. An electric signal with frequency f is applied to both devices, which operate on opposite diffraction orders, thereby canceling the frequency shifts introduced by the AODs. Tuning f allows moving the beam along the ion string, addressing only one ion at a time. (b) Applying two frequencies f and f' simultaneously allows one to address a pair of ions. Additional spots appear above and below the ion plane, which are detuned by $\pm 2\pi|f' - f|$ [113].

Applying two frequencies f and f' simultaneously to both AODs allows us to selectively address *two* ions in the register. The position of the two spots of the diffracted beams illustrated in Fig. 3.4(b) can be independently adjusted: changing f' will cause the red spot to move, while the blue beam is controlled by f. Next to those beams, two *off-axis spots* appear above and below the ion plane, which are detuned by $\pm 2\pi|f' - f|$ with respect to ω_L. The intensity of the light in each beam can be adjusted via the amplitudes of the electric signals supplying the AODs.

3.2.3 *Diode laser systems for laser cooling and readout*

The dipole transitions in Fig. 3.1 are driven by three commercially available diode laser systems, which are distributed among six endpoints in a shared laboratory [121]. These lasers provide light at wavelengths of 397 nm, 854 nm and 866 nm for laser cooling, readout and reset of the qudit prior to each computation. A fraction of the light from each laser is sent to a compact *frequency stabilization unit* (FSU)[16], which features a medium-finesse reference cavity enabling simultaneous locking of multiple lasers at different wavelengths using the Pound-Drever-Hall scheme [122]. With this setup we achieve linewidths of less than 100kHz with daily fluctuations in the range of 2 MHz [121].

Recently, significant efforts have been made to reduce floor space: the optical table measuring 200 × 125 cm, which hosted the two near-infrared lasers together with optics, FSU and control electronics has been replaced by a compact rack-based solution with a 19″ form factor [121]. On a footprint of 80 × 80 cm two fiber coupled diode lasers[17] operating at wavelengths of 854 nm and 866 nm, each provide an optical power of ≈ 1.1 W. The light is distributed by optical fibers, simultaneously supplying up to six apparatuses with 100 mW

16 Alpine Quantum Computing (AQT) *"Beech"*
17 Toptica MTA pro, modular amplified tunable single-mode lasers for 19″ rack integration

at both wavelengths. Compact AOM units operating in DP configuration are used to shape the light into laser pulses. These units are 19″-compatible and operate at a center frequency of approximately 200 MHz.

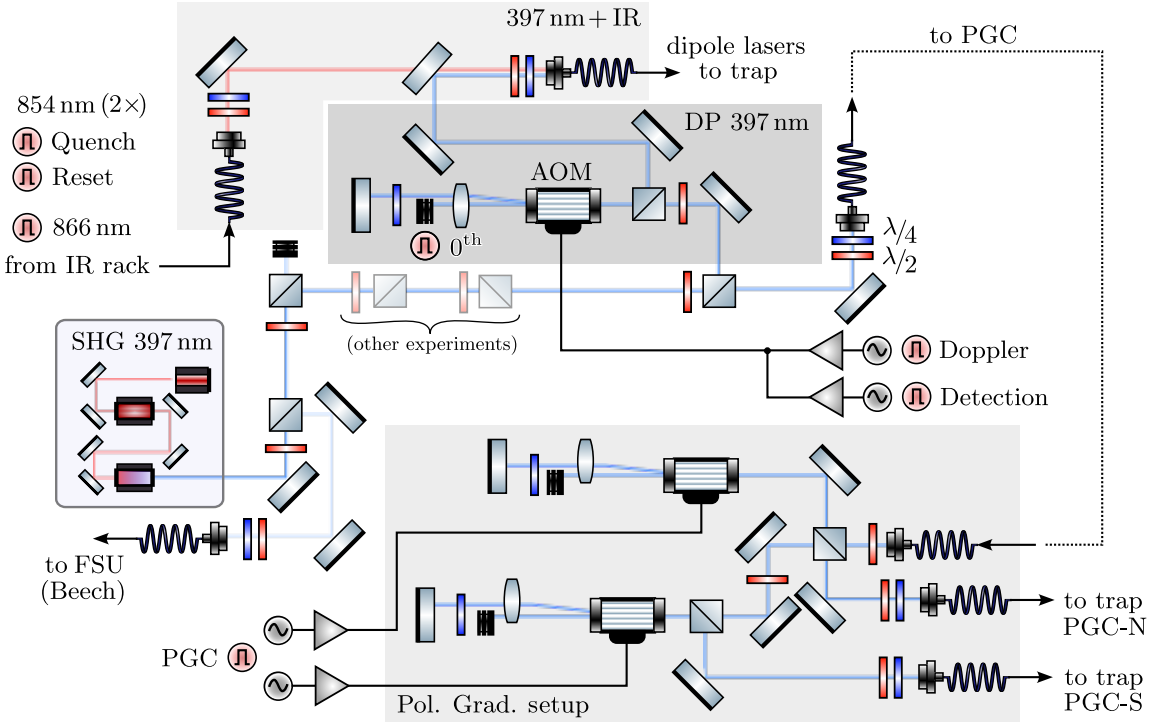


Figure 3.5: Schematic of the setup creating the 397 nm light used for laser cooling and readout. Two optical paths are relevant to our apparatus: in the first path, a single AOM in DP configuration creates the laser pulses for Doppler cooling and readout. The light is combined with the two laser beams at 854 nm and 866 nm and sent through a shared fiber to the ion trap. Both near-infrared lasers are provided by a compact rack-integrated laser system. In the second path, a single fiber is connected to a small breadboard, where two DP units create the pulses used during polarization gradient cooling. Note that two wave retarder plates (red and blue) are used to match the polarization of the light with the fiber, stabilizing the intensity at the output [113].

We couple the light of the near-infrared lasers into a common fiber connecting the rack system with the setup illustrated in Fig. 3.5. Here the light of a diode laser operating at a wavelength of of 793 nm is amplified and converted to 397 nm by *second harmonic generation*[18] (SHG) from an amplified diode laser. This system provides an output power of ≈ 150 mW at th 397 nm, of which a small fraction is coupled to a fiber connected to the FSU for stabilization. The remaining ≈ 140 mW pass through multiple $\lambda/2$ retarder plates and *polarizing beam splitter* (PBS), distributing the light among different paths. At the end of the distribution chain, the 397 nm light is shared between two paths. In the first path, an AOM[19] operating in DP configuration close to 130 MHz creates the laser pulses for Doppler cooling and state detection. The light is then combined with the two near-infrared laser beams and coupled to a single fiber, which is ultimately connected to our ion trap. A pair of $\lambda/2$ (red) and $\lambda/4$ wave retarder plates are used to align the polarization to the orientation of the fiber, reducing intensity fluctuations at the output.

18 Toptica TA-SHG pro, high-power tunable frequency-doubled diode laser
19 Gooch & Housego 3100 – 125

The second path connects the setup to a small optical breadboard, where two DP units[20] operating at 230 MHz generate the pulses used during polarization gradient cooling.

The electric signals driving the AOM units are generated by seven static RF signal generators[21], which are represented in Fig. 3.5 by the gray circles depicting a sine wave. Two generators are connected to the DP unit creating the 397 nm pulses applied during state detection and readout, while another pair controls the PGC setup. The three remaining sources supply compact DP-AOM units in the IR rack, which generate laser pulses at 866 nm and 854 nm, respectively. All RF signals are amplified and connected to fast RF switches, which are controlled by sets of binary logic signals depicted by the red circles. If a logic signal is set, the corresponding RF is routed to its designated endpoint. We will discuss these signals and the order in which they are applied later in Sec. 3.3.1 in more detail.

3.2.4 *Narrow-band laser for qudit manipulation*

We recall the introduction to Ch. 2: the third criterion introduced by DiVincenzo concerns perturbations that negatively impact the quantum state. When encoding the quantum state of a qudit in the Zeeman manifold of $^{40}Ca^{+}$, these perturbations are primarily attributed to *fluctuations* of the bias magnetic field and the laser driving the narrow $4^2S_{1/2} \leftrightarrow 3^2D_{5/2}$ quadrupole transition. The timescale T_2 over which these fluctuations occur sets an upper bound on the duration or length of a quantum algorithm. We refer to T_2 as the system's *coherence time*: the larger T_2, the more quantum gates we can implement before information is drowned by noise. Leaving fluctuations in the magnetic field aside, the coherence time is either limited by the linewidth $\Delta\nu$ of the laser or the natural lifetime of the $3^2D_{5/2}$ state, which sets a strict upper bound. Assuming a duration of 20 μs for each resonant gate and estimating 200 μs for entangling operations, a quantum algorithm of 500 single-qudit and 200 two-qudit gates is expected to take ≈ 50 ms; these are reasonable numbers for most current applications. Consequently, the linewidth of our laser system must be on the order of $\Delta\nu \lesssim 10$ Hz.

At present, our apparatus can be connected to two different laser systems with comparable performance:

- a diode-pumped *titanium sapphire* (Ti:Sa) solid-state laser[22] setup built by R. Stricker [123], which is locked to a reference cavity with a finesse of $\mathcal{F} = 479500(1600)$ built and characterized by A. Erhard [124]. With this system, we measure $T_2 = 0.21(4)$ s via Ramsey spectroscopy with Hahn echo [107].
- a compact *diode laser*[23] (DL) locked to a cavity with a finesse of $\mathcal{F} \approx 200000$ [121, 125]. The light is distributed between various apparatuses and therefore requires amplification using using multiple *tapered amplifiers*[24] (TA). Using the same technique as we did for the Ti:Sa, the coherence time measurements yield $T_2 = 0.28(3)$ s.

20 2x Gooch & Housego 3200 – 125
21 Analog Devices AD9854 direct digital synthesizers
22 Pump laser: Lighthouse Photonics Sprout Series G or Coherent Verdi with up to 18 W optical power at 532 nm. Titanium-Sapphire system: MSquared Lasers Ltd SolsTIS-PSX with ≈ 4 W at 729 nm.
23 Toptica DL Pro customized for 729 nm
24 Toptica BoosTA and Toptica BoosTA Pro

The optical setup is illustrated in Fig. 3.6: the light from both lasers arrives via optical fibers at the setup close to our apparatus. We receive ≈ 20 mW from the diode laser system, which is amplified by a TA and up-shifted by an AOM in SP configuration operating at a frequency of 80 MHz. After coupling the light into a short fiber we measure ≈ 120 mW at the output. Note, that the Ti:Sa already provides sufficient power and does neither require amplification nor additional frequency shifting [123]. We switch between both lasers by connecting the respective fiber to the coupler (C), see Fig. 3.6.

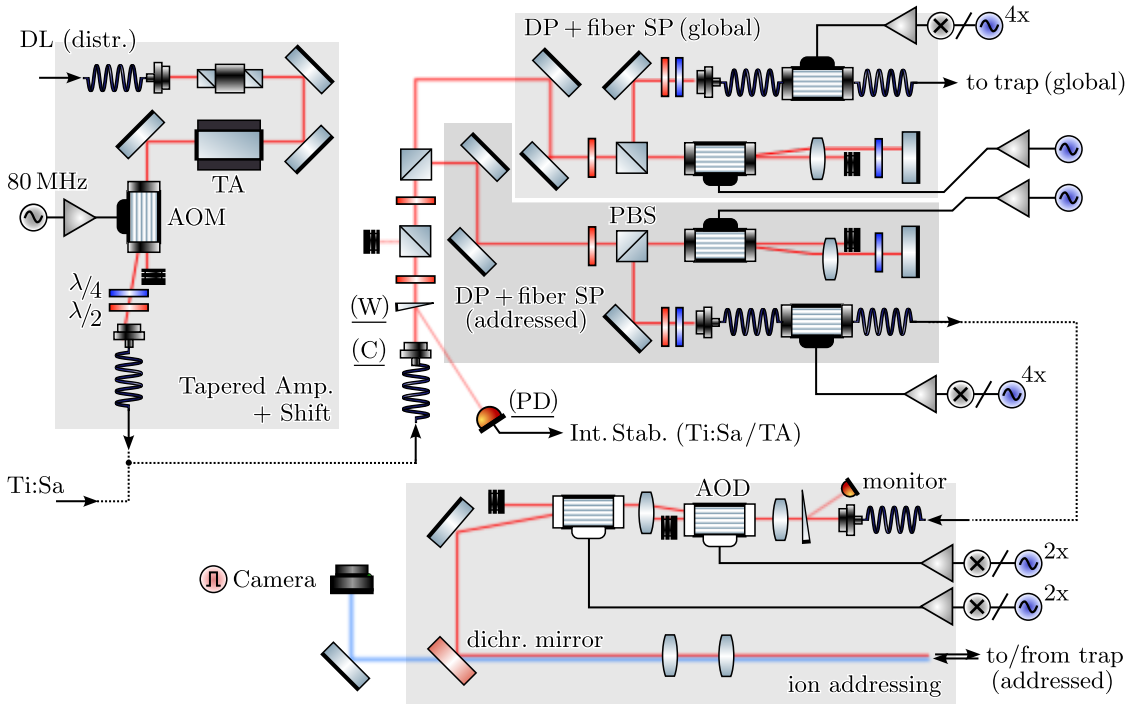


Figure 3.6: Optical setup creating the light pulses used to manipulate the quantum state of qudits. We can switch between a Titanium-Sapphire (Ti:Sa) solid-state laser and an amplified diode laser by connecting the respective fiber to the coupler (C). A fraction of the light is reflected by the a wedge (W) and directed onto a photodiode (PD), which generates a reference signal for an intensity stabilization unit. The light is distributed between two nearly identical paths: an AOM in DP configuration generates the laser pulses, which are then sent through a fiber coupled AOM operating in SP. Both SP are driven by four frequency generators controlled by a programmable pulse generator, enabling multi-chromatic operation, cf. Ch. 4. The light carried by the output fibers is then either sent directly to the trap (global beam) or connected to the ion addressing unit, cf. Sec. 3.2.2. The light then enters the vacuum chamber via the same viewport used to image the ions onto the camera during readout [113].

A small fraction of the light arriving at (C) is picked off by a *wedge* (W) and guided onto a photodiode (PD). The (PD) is connected to a PID controller[25], which generates a signal that attenuates either the TA (DL setup) or the drive signal of a *fiber noise cancellation* (FNC) unit (Ti:Sa setup), thereby stabilizing the intensity of the light at (C) [123]. After (W) the light is distributed between two paths, where two DP AOM[26] units operating around 230 MHz generate the laser pulses realizing the quantum gates, which are then coupled to their respective fiber-coupled SP AOMs[27]. Each SP is connected to four signal generators

25 Stanford Research Systems (SRS) SIM Series 960 analog PID
26 IntraAction / Gooch and Housego ATM 235
27 Gooch and Housego Fiber-Q customized for 729 nm

shared by both devices, providing frequencies around a center frequency of 145.24 MHz, enabling additional modulation capabilities required for entangling gate operations, see Ch. 4.

The light carried by output fibers of the SP AOMs is either directly sent to the ions (global beam) or passes through the addressing unit[28] (addressed beam), which allows for the addressing of subsets of ions in large ion strings. Both AODs operate close to 50 MHz and offer sufficient range to individually address up to 16 ions in our trap. A dichroic mirror deflects the 729 nm beams from the addressing unit through the adjustable objective with an $NA = 0.29$ onto the ion, while simultaneously allowing fluorescence light to pass and being imaged onto the chip of the camera.

Each AOM in Fig. 3.6 receives its signal from a programmable pulse generator; an exception is the AOM after the TA, which is operated at a constant frequency of 80 MHz. This pulse generator controls our experimental apparatus in real-time and enables the implementation of quantum algorithms. Its functionality will be examined in the upcoming section in more detail.

3.3 CLASSICAL CONTROL OF QUANTUM ALGORITHMS

Realizing quantum algorithms on a trapped-ion quantum processor can fundamentally be described as *applying electronic signals to acousto-optic modulators with specific parameters at the right time*. While this sounds trivial, the requirements on the classical hardware generating these signals are rather challenging. First, a common notion of *time* must be established, which is measured by a global *clock* that starts ticking as soon as the first quantum gate is applied. This clock serves as an absolute reference, synchronizing all electric signals. Second, the relative phase between two laser pulses must be precisely controlled, requiring all signals to be *phase coherent* over the duration of the quantum algorithm.

3.3.1 *Programmable pulse generator*

We employ the programmable signal generator *M-ACTION*[29] developed by V. Negnevitsky as part of his doctoral research and maintained by M. Stadler at the ETH Zürich [126, 127], which has been extensively adapted to interface with the existing experimental apparatus [128, 129]. A simplified circuit diagram is shown in Fig. 3.7. At the core of the system is the AMD Xilinx Zynq XC7Z020 *system-on-chip* (SOC), which combines computing power of an ARM Cortex-A9 *microprocessor* (µP) with the real-time capabilities of an AMD Xilinx Artix 7 *field-programmable gate array* (FPGA) on a single microchip [130][30]. Prior to every computation, the µP of the SOC receives a quantum algorithm from a desktop computer via a network connection. This algorithm is already decomposed into a set of pre-programmed operations, which are then converted into a stream of parameters to be processed further by the FPGA.

28 2x AA Acousto-Optics DTSKY-400-730-020
29 *Modular Advanced Control of Trapped IONs*
30 While the XC7Z020 features two independent Cortex-A9 cores, only one of them is actively used.

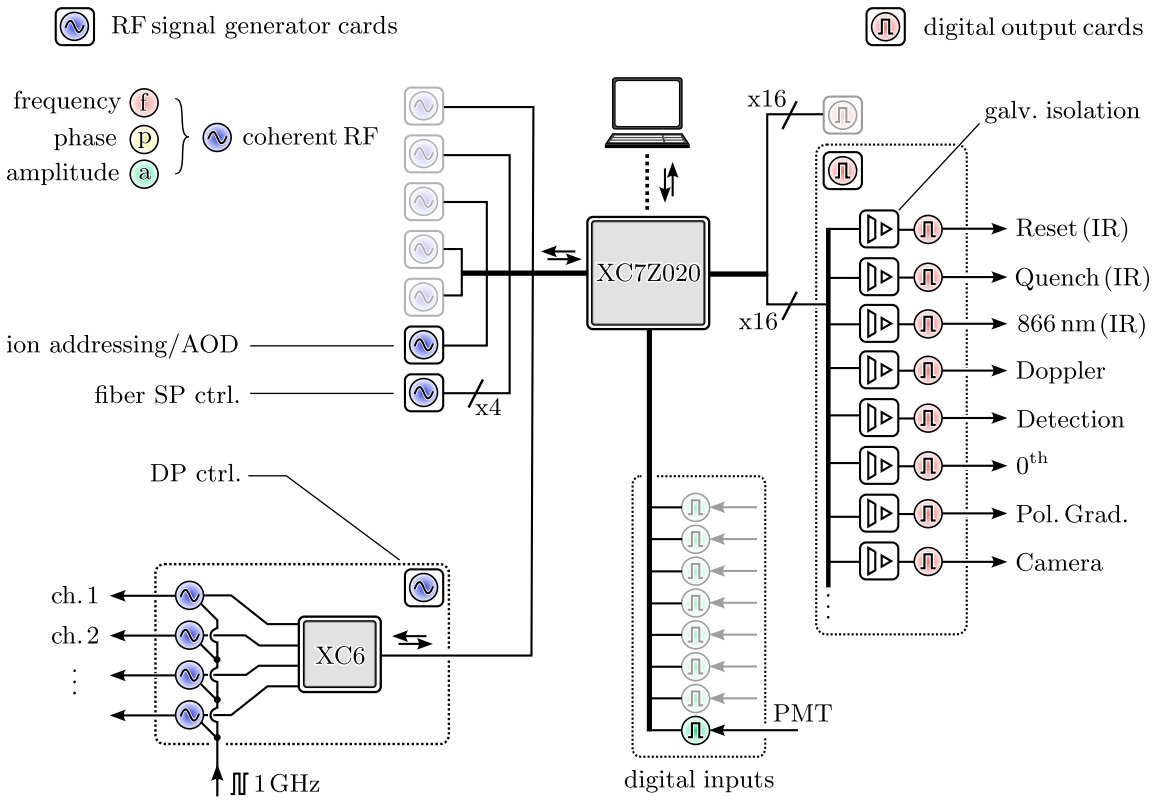


Figure 3.7: Simplified circuit diagram of the *M-ACTION* pulse generator hardware [126, 128]: a desktop computer sends a compiled quantum algorithm to a Xilinx XC7Z020 SoC, which converts the instructions into streams of electric signals. The system is capable of controlling up to 32 single channel frequency synthesizers and 32 digital output channels in real time with a timing resolution of 8 ns. Eight digital input channels collect data from the experiment, enabling in-sequence feed-forward. In our setup, we use 10 signal generators to control the AOMs, which generate laser pulses for quantum state manipulation, see Fig. 3.6. Cooling and state detection are controlled digitally by triggering external (incoherent) signal generators, cf. Fig. 3.5. A single input channel is connected to a PMT, which counts photons emitted by the ions.

The FPGA holds two logic cores:

- a high speed interface enables communication with up to eight AMD Xilinx Spartan XC6 FPGAs connected to the XC7Z020 via a common backplane[31]. Each XC6 programs and triggers up to four Analog Devices AD9910 *direct-digital synthesizers* (DDS) on a shared circuit board[32] [131]. When clocked at 1 GHz, each DDS generates analog signals with frequencies up to 400 MHz at a resolution of 233 mHz; the phase can be adjusted with a step size of 96 mrad. All DDS channels are synchronized via the shared 1 GHz clock source, establishing a common time base. A 125 MHz signal derived from one DDS on each circuit board supplies the XC6, limiting the system's timing resolution to 8 ns. At this speed, the program counter of the XC6 would allow for 2^{36} clock cycles or 9.16 minutes of phase coherent operation [126], far exceeding the coherence time of the ion. The analog output is provided by a 14 bit *digital-analog*

31 Enterpoint Milldown Backplane 1
32 Enterpoint DDS1 Channel Card 1.2b and Enclustra

converter (DAC) and a *variable gain amplifier* (VGA, enabling complex pulse shapes, which will be discussed further in Ch. 4.

- a pulse controller executes the compiled quantum algorithm in real time with respect to an internally generated 166 MHz clock signal. Each instruction from the µP is processed by a digital input/output (I/O) controller and increments the program counter of the XC6 via the backplane, thereby triggering a signal on the respective DDS. The I/O controller drives up to 32 single-ended output channels adhering to the *LV-TTL* standard [132], which are individually galvanically isolated to protect the sensitive XC7Z020 from voltage spikes and stray currents. Eight digital input channels serve as counter registers, enabling fluorescence detection when connected to a PMT or avalanche photodiode detector. The counters are monitored by the µP, which can re-program the pulse controller, altering the pulse sequence based on measurement outcomes. These *feed-forward* capabilities have been demonstrated experimentally by correcting information loss in a logical qubit [37].

Our apparatus is controlled by the ten frequency synthesizers and eight digital outputs shown in Fig. 3.7. Each channel is connected to a device in the optical setups illustrated in Fig. 3.5 and Fig. 3.6. The DDS channels exclusively control the AOMs of the 729 nm laser as well as the AODs of the ion addressing unit, while TTL signals trigger static sources for the near-infrared and 397 nm lasers. A single PMT is used for fluorescence detection, while the actual readout is performed asynchronously by the *Andor* EMCCD camera.

3.3.2 *Pulse sequences for quantum information experiments*

When writing a quantum algorithm, we implicitly assume that the system is already prepared in a well-defined initial state; processes such as laser cooling, ground state pumping and the readout of the quantum state are not considered. These tasks are included in a *generic pulse sequence*, which is "wrapped" around the actual algorithm and repeated automatically. Fig. 3.8(a) shows the sequence in its entirety, with symbols and labels corresponding to M-ACTIONs circuitry in Fig. 3.7.

Each evaluation or *shot* of an algorithm starts with a *reset pulse* on the 854 nm transition, preventing population trapping in the $3^2D_{5/2}$ manifold from prior computations. Then, *Doppler cooling* is performed by triggering the static signal sources of the 866 nm and 397 nm lasers, cf. Fig. 3.5 in Sec. 3.2.3. Simultaneously, we record the fluorescence of the ions using the PMT to detect *heating* of the ion crystals, which causes an automatic *recrystallization* event: the axial and radial confinement of the trap is lowered, re-capturing the ions before the computation is attempted again. After an optional step of *polarization gradient cooling*, M-ACTION triggers the near-infrared lasers and emits the necessary signals to create laser pulses using the 729 nm laser, driving the quadrupole transition for *sideband cooling* and *optical pumping* to the $4^2S_{1/2}(m = -1/2)$ ground state.

Creating a laser pulse on the quadrupole transition involves multiple signals, each driving the AOMs in Fig. 3.6 described in Sec. 3.2.4. The sections of the sequence presented in Fig. 3.8(b) differ only by the number of signals and channels. Each "pulse" starts at t_0 (t_1, t_2) by configuring the ion addressing unit (two signals per AOD) and the fiber-coupled SP AOMs (four signals applied to both AOMs), where we only change the parameters of the signals while keeping the output power constant; this ensures thermal stability of the devices [128]. A delay of 10 μs is added, allowing the AODs of the addressing unit to

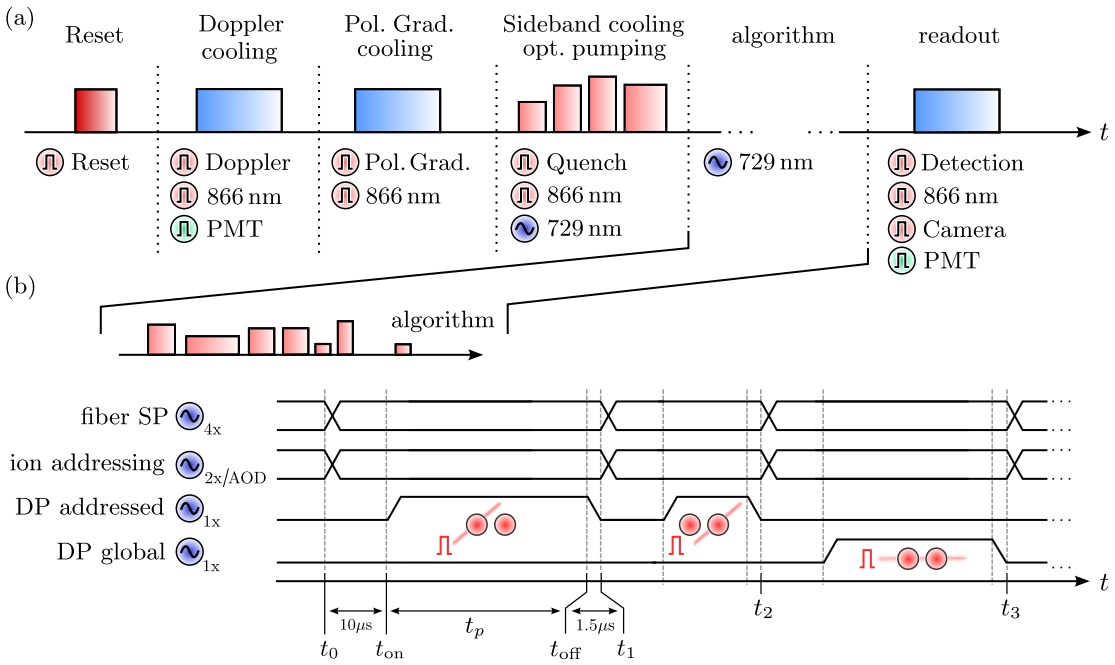


Figure 3.8: Pulse sequencing: (a) qudit state reset, laser cooling and readout are usually not part of a quantum algorithm, which assumes that these processes occur by default before and after each computation. The algorithm itself is just a section of a larger, *generic pulse sequence*, which includes these processes. Signals involved in creating the laser pulses are shown by the respective symbols and labels, which correspond to the labels in Fig. 3.5 and Fig. 3.6 describing the optical setup and the control hardware M-ACTION. (b) The parameters of a laser pulse on the quadrupole transition are controlled by 10 of M-ACTIONs frequency synthesizers, which are switched in a specific order. Addressing unit and fiber AOMs are configured first, before the DP units create the actual pulses driving the quadrupole transition.

stabilize, before the respective DP unit is enabled, addressing either all ions collectively (DP global) or small subsets (DP addressed). The *duration* t_p of the pulse is measured from the start of the rising edge to the end of the plateau: this mitigates the finite rise time of the AOMs and allows us to effectively describe a *square pulse*. Note, that *multichromatic pulses* have a different pulse shape, which we will discuss in Ch. 4 in the context of *entangling gates*. Each pulse ends with an additional delay of 1.5 μs, which is induced by M-AQTION as the minimal time between two successive commands[33].

Each shot ends with the readout of the quantum state after the quantum algorithm has been executed. Compared to Doppler cooling, we trigger a different signal generator, creating a resonant pulse on the 397 nm dipole transition. Next to the PMT, we simultaneously trigger the *Andor* EMCCD camera to distinguish the fluorescence of the individual ions. The readout of a d-dimensional qudit is a bit more elaborate and cannot be represented by a single pulse: the 397 nm pulse is repeated $d-1$ times with additional *shelving pulses* on the quadrupole transition and *in-sequence re-cooling* in between. We will further discuss the qudit detection scheme in the upcoming Ch. 4.

33 The actual minimum is calculated from the clock speed of the FPGA and is close to 1.3 μs, where we then added 200 ns as an additional margin.

4

REALIZING QUANTUM GATES IN TRAPPED ION QUDITS

This chapter is concerned with the realization of DiVincenzo's sixth criterion: we must be able to control the state of the quantum system by sequences of unitary transformations. In our trapped ion quantum processor, which we have thoroughly introduced in the previous chapters, the quantum state is encoded in the electronic states of $^{40}Ca^{+}$. Coherent light generated by a laser couples the $4^2S_{1/2}$ ground states with the $3^2D_{5/2}$ states via a narrow quadrupole transition. A sophisticated setup of optics and real-time control electronics shapes the light into pulses, which realize unitary transformations called *quantum gate operations* – or *quantum gates* for short – the quantum analogue of the boolean logic operations in classical electronics.

We now discuss how quantum gates are physically realized and will refer back to the dedicated sections in Ch. 3 whenever we describe the implementation on the hardware level. First, we introduce resonant single-qudit interactions in Sec. 4.1 and describe how qudit operators can be decomposed to be compatible with our trapped-ion platform. We then continue with the discussion of entangling gates. In Sec. 4.2, we revisit the well-established Mølmer-Sørensen gate and develop a method to realize GHZ-like states $\alpha\,|00\rangle + \beta\,|11\rangle$ with controllable probability amplitudes. We then introduce an extension to the controlled-NOT scheme in Sec. 4.3, which proves to be exceptionally well suited to mediate entanglement in qudits. Finally, we discuss the readout of the quantum state by sequential fluorescence detection and electron shelving in Sec. 4.4.

4.1 QUANTUM GATES ON A SINGLE QUDIT

We first introduce a fundamental set of quantum gates employed to manipulate the state of a single qudit up to dimension $d = 7$ (*qusept*). Each gate is realized by sequences of laser pulses, each acting on a small subspace spanned by two states $|g\rangle$ and $|e\rangle$, where $|g\rangle$ is encoded in either of the $4^2S_{1/2}$ ground states and $|e\rangle$ represents one of the metastable $3^2D_{5/2}$ states. Since both of these states are coupled directly by a narrow quadrupole transition $|g\rangle \leftrightarrow |e\rangle$, a quantum gate acting on the subspace $\{|g\rangle, |e\rangle\}$ can be implemented by a single laser pulse. However, if we choose to encode two states $|i\rangle$ and $|j\rangle$ exclusively in the $3^2D_{5/2}$ manifold, a transition $|i\rangle \leftrightarrow |j\rangle$ is realized by temporarily populating one of the ground states, which acts as an auxiliary state. As such, a quantum gate acting on the subspace $\{|i\rangle, |j\rangle\}$ is composed of multiple laser pulses. This approach generalizes to higher dimensions and more advanced quantum gates, see e.g. Sec. 4.1.3.

We refer to the available couplings offered by the level structure of the ions as the *coupling map*. Together with the characteristic properties of our quantum processor, e.g. the orientation of the magnetic field, the spectrum of the motional modes, we choose a suitable

encoding, which is tailored to the quantum algorithm we seek to implement. The encoding may vary among the individual ions in the same register to further enhance the fidelity of the computation.

4.1.1 *Local rotations on a subspace*

The restrictive coupling reduces each interaction to a small subspace spanned by two states $\{|g\rangle, |e\rangle\}$. Therefore, we employ rotations analogous to those previously discussed in the context of qubits in Sec. 1.2.2. The definition in Eq. [1.16] readily generalizes to qudits: a rotation acting on the qudit labeled by the index i is given by

$$\hat{R}^{(i)}(\theta, \phi) = e^{-i\frac{\theta}{2}\left(\cos(\phi)\sigma_x^{(i)} + \sin(\phi)\sigma_y^{(i)}\right)}, \qquad [4.1]$$

where the Pauli matrices σ_x and σ_y are defined with respect to the subspace $\{|g\rangle, |e\rangle\}$. Such a rotation can be implemented by a single laser pulse tuned to be in resonance with the $|g\rangle \leftrightarrow |e\rangle$ transition by a suitable RF signal, which is applied for a duration $t \propto \theta$ with phase ϕ to the DP AOM units in our setup, see Fig. 3.6.

We introduce Rabi oscillations on a single ion in the center of a register of three ions by successively increasing the duration of the laser pulse t via the RF signal applied to the DP AOMs, while keeping the amplitude a constant. From the data presented in Fig. 4.1 we calculate a Rabi frequency $\Omega = 2\pi \cdot 13.84(7)$ kHz.

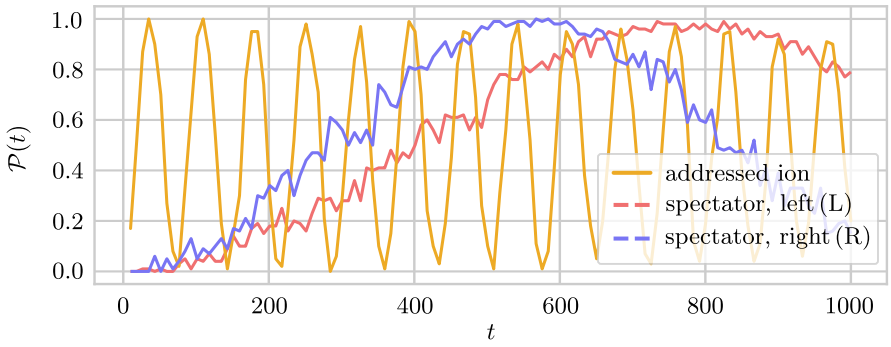


Figure 4.1: Rabi oscillations on the $4^2S_{1/2}(m = -1/2) \leftrightarrow 3^2D_{5/2}(m = -1/2)$ transition when addressing the central ion in register of three ions. The population $\mathcal{P}(t)$ of the $3^2D_{5/2}(m = -1/2)$ state of the addressed ion oscillates in time with a frequency $\Omega = 2\pi \cdot 13.84(7)$ kHz. We observe unwanted coupling with the neighboring spectator ions, which yields to slow oscillations in the populations with frequencies $\Omega_L = 2\pi \cdot 0.33$ kHz and $\Omega_R = 2\pi \cdot 0.52$ kHz on the left (L) and right (R) spectator, respectively. This *cross-talk* is a consequence of a small residual overlap of the light field addressing the central ion with both its spectators.

Notably, we observe slow oscillations with frequencies of $\Omega_L = 2\pi \cdot 0.33(1)$ kHz and $\Omega_R = 2\pi \cdot 0.52(5)$ kHz on the left (L) and right (R) *spectator* ions, which are the immediate neighbors of the addressed ion in the register. These unwanted excitations are attributed to *cross-talk*: the intensity profile of a laser beam is not a perfect Gaussian, but is rather described by an *Airy disk* [103, 133]. The circular aperture of the imaging objective focusing the light onto the ions leads to concentric fringes, which carry a small fraction of the total intensity of the laser beam. These fringes may overlap with the neighboring spectators, thereby causing residual excitations. We compute the average ratio of the Rabi frequencies

between both spectators and the addressed ion and obtain $\sum_{L,R} \Omega_i / 2\Omega = 3.1(2)\%$. The asymmetry $\Omega_L < \Omega_R$ can be tuned by proper alignment of both the addressing unit and the objective, which can be electronically adjusted by piezoelectric actuators.

Moreover, our ion trap is not perpendicular with respect to the objective, see Fig. 3.2. Therefore, the beam will be marginally de-focused as it is moved over the register, thereby changing its width. This effect can already be observed when imaging the ions onto the EMCCD camera: in large crystals, the outermost ions will appear larger. However, the separation of the ions is not uniform and will grow as we move from the center to the edges of a register [77]. In our setup, the impact of these de-focusing effects is negligible in chains of up to 16 ions, which are the longest chains we can reliably control.

We mitigate residual cross-talk through proper alignment of the optics and appropriate inter-ion spacing, which can be adjusted by the voltage applied to the tip electrodes of the trap, see Sec. 2.1. Furthermore, we employ *composite rotations*, which are implemented by the sequence [134]

$$\hat{R}_3^{(i)}(\theta, \phi, \lambda) = \hat{Z}^{(i)}(\phi)\hat{X}^{(i)}(\pi/2)\hat{Z}^{(i)}(\theta)\hat{X}^{(i)}(-\pi/2)\hat{Z}^{(i)}(\lambda), \tag{4.2}$$

where the operation $\hat{Z}^{(i)}(\theta)$ corresponds to a rotation of the state vector around the z-axis of the Bloch sphere, see Sec. Eq. [1.16] and Ref. [134] for an illustration of the sequence on the Bloch sphere. These gates are realized by *AC Stark shifts* induced by a laser beam detuned by approximately $\Delta_{AC} \approx 2\pi \cdot 10$ MHz from the $4^2S_{1/2}(m = -1/2) \leftrightarrow 3^2D_{5/2}(m = -5/2)$ transition [134, 135]. Note that since the effective Rabi frequency scales as

$$\Omega_{AC} = \Omega^2 / 2\Delta_{AC}, \tag{4.3}$$

each $\hat{Z}^{(i)}(\theta)$ requires substantially higher intensities than resonant gates to achieve reasonably fast rotations on timescales of approximately $2\pi \cdot 10 - 100$ kHz.

The performance of the resonant single-qudit quantum gates is characterized via *randomized benchmarking* measurements [14, 123, 136][1]. We measure an *infidelity* below $1 - \mathcal{F} = 10^{-4}$ on the subspace $\{|g\rangle = 4^2S_{1/2}(m = -1/2), |e\rangle = 3^2D_{5/2}(m = -1/2)\}$ [123]. Note that instabilities in the magnetic field have a stronger impact on states with larger magnetic quantum number m. However, on the time scales relevant for most quantum algorithms, these fluctuations can be safely neglected in our apparatus. We therefore assume a gate fidelity close to $\mathcal{F} = 99.99\%$ for all of our single-qudit gates.

4.1.2 *Measurement protocols for trapped ion qudits*

Measuring the expectation value $\langle \hat{O} \rangle$ of an observable $\hat{O}$ on a quantum state $|\psi\rangle$ is a highly non-trivial task. Projective measurements allow us to directly obtain results only for diagonal observables, such that we need to find a circuit $\hat{C} = \prod_j \hat{U}_j$ that diagonalizes $\hat{O}$ before measuring $\hat{C}|\psi\rangle$. Finding $\hat{C}$ requires knowledge of the eigensystem of $\hat{O}$, which is generally not accessible. However, one can reconstruct $\langle \hat{O} \rangle$ from a linear combination of other observables called *Pauli strings* $\hat{P}_i$, which are easily diagonalizable, such that

$$\langle \hat{O} \rangle = \sum_i c_i \langle P_i \rangle \tag{4.4}$$

1 *Gate set tomography* measurements have also been performed back in 2017 by Stricker [123, 137].

for $c_i \in \mathbb{R}$. A proper algorithm for computing the decompositions of $\hat{O}$ has been developed by Shlosberg et al. in the context of qubits [138], and was recently generalized to higher dimensions by Simon et al. [139].

The Pauli strings $\hat{P}_i$ are tensor products of the *clock* and *shift* matrices

$$\hat{Z}_d = \sum_{k=0}^{d-1} \omega^k |k\rangle \langle k| \qquad \text{and} \qquad \hat{X}_d = \sum_{k=0}^{d-2} |k+1\rangle \langle k| + |0\rangle \langle d-1|, \tag{4.5}$$

respectively, with $\omega = \exp(2\pi i/d)$. These operators are generalizations of the Pauli matrices to d dimensions [140]; note that we recover $X_2 = \sigma_x$ and $Z_2 = \sigma_z$ for $d = 2$. In terms of $\hat{Z}_d$ and $\hat{X}_d$, each $\hat{P}_i$ can be expressed as [139]

$$\hat{P}_i = \bigotimes_{j=1}^{N} \hat{X}_{d_j}^{r_j} \hat{Z}_{d_j}^{s_j}, \tag{4.6}$$

where $r_j, s_j \in \{0, \ldots, d_j - 1\}$ with j labeling the respective qudit an N qudit register.

Given a decomposition of $\hat{O}$, we measure the Pauli strings and take the sum of the measurement outcomes weighted by the coefficients c_i in Eq. 4.4 to reconstruct an estimate for the expectation value $\langle \hat{O} \rangle$. Each coefficient is computed by

$$c_i = \frac{\mathrm{Tr}[\hat{P}_i^\dagger \hat{O}]}{D}, \tag{4.7}$$

where $D = \prod_{j=1}^{N} d_j$ is the dimension of the joint Hilbert space of the qudits with local dimensions d_j.

Using the clock and shift matrices in Eq. [4.5] we introduce the spin operators acting locally on a qudit j [139]

$$\hat{S}_\alpha^{(j)} = \sum_{r_j, s_j} C_\alpha^{r_j, s_j} \hat{X}_{d_j}^{r_j} \hat{Z}_{d_j}^{r_j}, \tag{4.8}$$

with coefficients $C_\alpha^{r_j, s_j} \in \mathbb{C}$ and $\alpha \in \{x, y, z\}$. These operators provide a more efficient formalism to express the Pauli strings and can be readily translated into operations, which are natively available on our quantum processor by employing *QR decomposition* using *Givens rotations* $\hat{G}_j$ [141–143].

4.1.3 *QR decomposition of qudit spin operators*

The spin operators $\hat{S}_\alpha^{(j)}$ acting on a qudit j with local dimension d are represented by a square matrix, which can be decomposed into a unitary $\hat{Q} = \prod_i \hat{G}_i^{(k,l)_j}(\theta_i, \phi_i)$ and an (upper) triangular matrix $\hat{R}$, such that

$$\hat{S}_\alpha^{(j)} = \hat{Q}\hat{R} = \prod_i \hat{G}_i^{(k,l)_j}(\theta_i, \phi_i)\hat{R}. \tag{4.9}$$

A Givens rotation $\hat{G}_i^{(k,l)_j}(\theta_i, \phi_i)$ acting on the subspace $\{|k\rangle, |l\rangle\}_j$ spanned by the states $|k\rangle$ and $|l\rangle$ satisfying $k < l \leq d$ is given by [143]

$$\hat{G}_i^{(k,l)_j}(\theta_i, \phi_i) = \sum_{m \neq k,l} |m\rangle \langle m| + \cos(\theta_i)\left[|k\rangle \langle k| + |l\rangle \langle l|\right] + \sin(\theta_i)\left[e^{i\phi_i} |k\rangle \langle l| - e^{-i\phi_i} |l\rangle \langle k|\right], \tag{4.10}$$

with angles θ_i and ϕ_i parametrizing the rotation. Applying its hermitian conjugate $\left(\hat{G}_i^{(k,l)_j}(\theta_i,\phi_i)\right)^\dagger$ to $\hat{S}_\alpha^{(j)}$ we obtain the matrix

$$M_i = \left(\hat{G}_i^{(k,l)_j}(\theta_i,\phi_i)\right)^\dagger \hat{S}_\alpha^{(j)},$$

which allows us to compute both angles by zeroing a specific matrix element of M_i.

We illustrate the decomposition using the example shown in Eq. [4.11]. Starting with the last element of the first column, we compute the angles θ_1 and ϕ_1 for the rotation $\left(\hat{G}_1^{(d-1,d)_j}(\theta_1,\phi_1)\right)^\dagger$ for a local spin operator $\hat{S}_\alpha^{(j)}$ with components $S^{(k,l)} \in \mathbb{C}$. The relevant entries of the matrices are highlighted in red. From the product

$$M_1 = \underbrace{\begin{pmatrix} 1 & 0 & \cdots & & \\ 0 & \ddots & & & \\ \vdots & & & \cos(\theta_1) & -\sin(\theta_1)e^{i\phi_1} \\ & & & \mathbf{\sin(\theta_1)e^{-i\phi_1}} & \mathbf{\cos(\theta_1)} \end{pmatrix}}_{\hat{G}_1^{(d-1,d)\dagger}(\theta_1,\phi_1)} \underbrace{\begin{pmatrix} S^{(0,0)} & \cdots & S^{(0,d)} \\ \vdots & & \vdots \\ \mathbf{S^{(0,d-1)}} & & \\ \mathbf{S^{(0,d)}} & \cdots & S^{(d,d)} \end{pmatrix}}_{\hat{S}_\alpha^{(i)}} \overset{!}{=} \begin{pmatrix} & \cdots & \\ \vdots & \ddots & \vdots \\ \mathbf{0} & \cdots & \end{pmatrix} \tag{4.11}$$

we obtain the characteristic equation

$$M_1^{(0,d)} = \sin(\theta_1)e^{-i\phi_1}S^{(0,d-1)} + \cos(\theta_1)S^{(0,d)} = 0,$$

which we solve for the angles θ_1 and ϕ_1. Writing the complex values $S^{(k,l)}$ in their *polar form* with angles $\varphi^{(k,l)}$ we identify

$$\tan(\theta_1) = \frac{|S^{(0,d)}|}{|S^{(0,d-1)}|} \exp\left[i\left(\phi_1 + \pi + \varphi^{(0,d-1)} - \varphi^{(0,d)}\right)\right], \tag{4.12}$$

which fixes $\phi_1 = \varphi^{(0,d)} - \varphi^{(0,d-1)} - \pi$, since the right-hand side of the equation must be real. Solving for θ_1 completes the first step of the QR decomposition algorithm, and we continue with the next matrix

$$M_2 = \left(\hat{G}_i^{(d-2,d-1)_j}(\theta_2,\phi_2)\right)^\dagger M_1$$

to compute θ_2 and ϕ_2 from the matrix element $M_2^{(0,d-2)}$ following Eq. [4.12]. With each step we iterate over all columns until we arrive at the triangular matrix

$$\hat{R} = \prod_i \left(\hat{G}_i^{(k,l)_j}(\theta_i,\phi_i)\right)^\dagger \hat{S}_\alpha^{(j)}.$$

Instead of measuring $\hat{S}_\alpha^{(i)}$ directly, we apply a sequence of Givens rotations to a quantum state before performing a single projective measurement from which we extract $\langle \hat{S}_\alpha^{(i)} \rangle$.

Each $\hat{G}_i^{(k,l)_j}(\theta_i,\phi_i)$ can be implemented on our quantum processor by sequences of single-qudit gates of the form Eq. [4.1] acting on the designated subspace. Since not every pair of states $(|i\rangle, |j\rangle)$ can be coupled directly by a single operation, the complexity of the sequence depends on the chosen encoding scheme. For qudits realized in ^{40}Ca ions it is favorable to establish the *W-encoding* illustrated in Fig. 4.2(a) prior to applying any of the

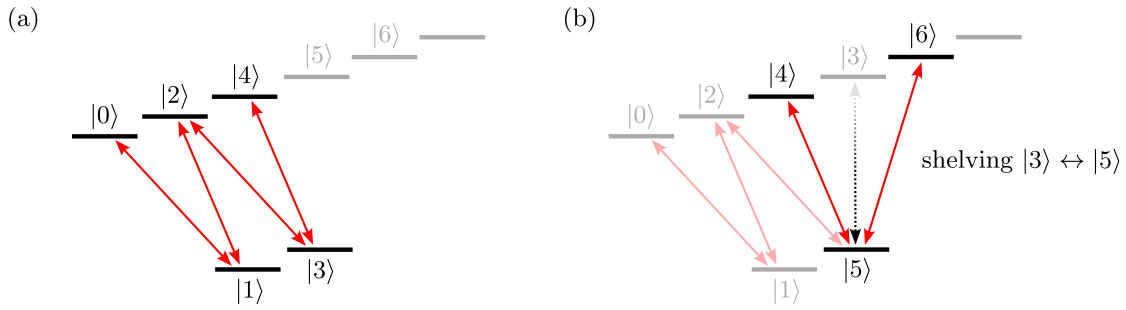


Figure 4.2: W-encoding scheme employed in trapped ion qudits for efficient QR decompositon of a local spin operator $\hat{S}_\alpha^{(i)}$ by Givens rotations. (a) The computational basis states of the qudits couple in pairs $(|i\rangle, |i+1\rangle)$ up to dimension $d = 5$. (b) For $d = 7$ an additional shelving pulse exchanges the population in $|5\rangle$ with $|3\rangle$ in the ground state manifold, thereby enabling a pair-wise coupling in the subspaces $\{|4\rangle, |5\rangle\}$ and $\{|5\rangle, |6\rangle\}$, respectively.

Givens rotations, which can then be implemented by a single laser pulse. Note that for qudits beyond dimension $d = 5$ additional shelving pulses must be introduced to establish the required couplings as shown in Fig. 4.2(b).

We acknowledge recent work by Mato et al., approaching efficient qudit operator decomposition from a computer science perspective [144, 145]. Using decision diagrams, an optimal encoding can be tailored to qudit-based quantum algorithms realized in any hardware platform. With the coupling map in mind, an efficient decomposition of a quantum algorithm is constructed, which can significantly reduce the number of local gate operations, thereby enhancing the performance of the quantum processor.

4.2 CREATING ENTANGLEMENT WITH BICHROMATIC LIGHT FIELDS

We now introduce a mechanism enabling the entanglement of trapped-ion qudits in a genuine two-body interaction. The scheme was first introduced by Mølmer and Sørensen in 1999 as an extension to an earlier proposal by Milburn [146–148]. Using excitations of their collective motion, the ions become entangled via interaction with a light field illuminating both ions at the same time. Acting on two qudits labelled i and j in the subspace $\{|g\rangle, |e\rangle\}$ shown in Fig. 4.3(a), the Hamiltonian is given by

$$\begin{aligned}\hat{H}_{MS}^{(i,j)}(t) = 2\Omega\hat{S}_y^{(i,j)}\cos(\Delta t) - \sqrt{2}\eta\Omega\hat{S}_x^{(i,j)}\big[\hat{X}\left(\cos((\omega_z-\Delta)t)+\cos((\omega_z+\Delta)t)\right)\\ +\hat{P}\left(\sin((\omega_z-\Delta)t)+\sin((\omega_z+\Delta)t)\right)\big]\end{aligned} \quad [4.13]$$

with Rabi frequency Ω on the carrier transition and detuning Δ for an interaction time t. The two-qudit spin operators $\hat{S}_x^{(i,j)}$ and $\hat{S}_y^{(i,j)}$ are defined as

$$\hat{S}_\alpha^{(i,j)} = \frac{1}{2}\left(\hat{\mathbb{1}}^{(i)}\otimes\sigma_\alpha^{(j)} + \sigma_\alpha^{(i)}\otimes\hat{\mathbb{1}}^{(j)}\right) \quad [4.14]$$

with $\alpha \in \{x, y\}$, where $\hat{\mathbb{1}}^{(k)}$ is the identity operation acting on the respective qudit. Note, that the matrices σ_α act on the subspace $\{|g\rangle, |e\rangle\}$, which is embedded in a larger space. Coupling with the motional states in Eq. [4.13] is introduced by the position and momentum operators $\hat{X} = (\hat{a} + \hat{a}^\dagger)/\sqrt{2}$ and $\hat{P} = i(\hat{a} - \hat{a}^\dagger)/\sqrt{2}$ [36].

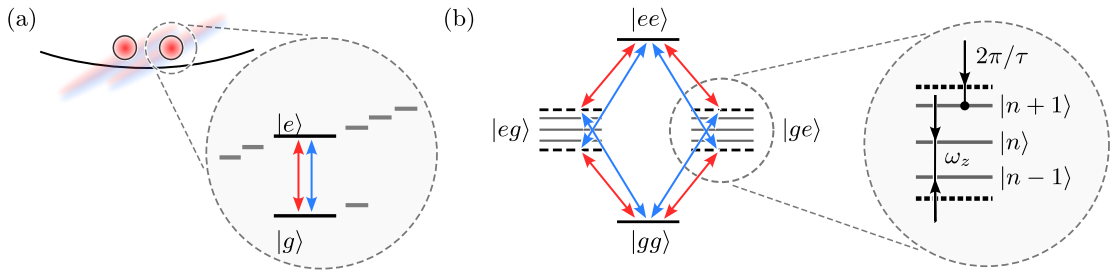


Figure 4.3: Scheme envisioned by Mølmer and Sørensen employed to entangle two trapped ions via their collective motion: (a) we consider the subspace $\{|g\rangle, |e\rangle\}$ and simultaneously address two ions with two laser beams detuned by $2\pi/\tau$ from the red and blue motional sideband of the COM mode. (b) Coupling of the respective states by the bichromatic light field. Note, $|eg\rangle$ and $|ge\rangle$ involve the motional states $|n \pm 1\rangle$.

The Hamiltonian in Eq. [4.13] is realized by a *bichromatic* light field, which can be imagined as a superposition of two laser pulses with duration t, each tuned to a different frequencies. Implementing the scheme as proposed by Mølmer and Sørensen requires a *symmetric* detuning Δ of the laser beams close to the red and blue motional sidebands of a chosen motional mode. The diagram in Fig. 4.3(b) illustrates the interactions of the respective quantum states introduced by each component of the laser pulse [109, 149].

We choose the COM mode due to the favourable coupling, which is nearly homogeneous for all ions in the register [77]. Given $\Delta \approx \omega_z$ and assuming $\omega_z \approx 2\pi \cdot 1\,\text{MHz} \gg \Omega$, the first term in Eq. [4.13] describing the interaction with the carrier transition $|g\rangle \leftrightarrow |e\rangle$ can be neglected. Further neglecting the fast oscillating terms with frequency $\omega_z + \Delta \approx 2\omega_z$ simplifies the Hamiltonian to

$$\hat{H}_{MS}^{(i,j)}(t) = -\sqrt{2}\eta\Omega\hat{S}_x^{(i,j)}\left(\hat{X}\cos((\omega_z - \Delta)t) + \hat{P}\sin((\omega_z - \Delta)t)\right). \qquad [4.15]$$

The time dynamics of the ions with respect to Eq. [4.15] in phase space is described by a circular trajectory with amplitude $\sqrt{2}\eta\Omega$ and frequency $\omega_z - \Delta$ as illustrated in Fig. 4.4(a) [147]. One revolution – a *loop* – is completed after a characteristic interaction time τ

$$\tau = \frac{2\pi}{\omega_z - \Delta}, \qquad [4.16]$$

which we call the *gate time*. If the area $A(\tau) = 2\eta^2\Omega^2$ of the circle is equal to $\pi/2$, we obtain the entangled state

$$|\psi\rangle = \frac{1}{\sqrt{2}}\left(|gg\rangle + |ee\rangle\right), \qquad [4.17]$$

and the ions are disentangled from the motion; the *unwanted* or *odd-parity* states $|eg\rangle$ and $|ge\rangle$ are not occupied. Note, that Eq. [4.16] diverges if the detuning would exactly match the frequency of the sidebands. We can achieve a desired gate time by adjusting the residual detuning $\delta = \omega_z - \Delta$, such that $\delta = 2\pi/\tau$ as indicated in Fig. 4.3(b).

The evolution of the population $\mathcal{P}(t)$ of the electronic states with increasing interaction time t up to 4τ is shown in Fig. 4.4(b). At each multiple of τ, the trajectory in phase space undergoes one full loop. Here, the odd-parity states $|eg\rangle$ and $|ge\rangle$ are not populated and we obtain either the maximally entangled state in Eq. [4.17] (odd multiples of τ) or

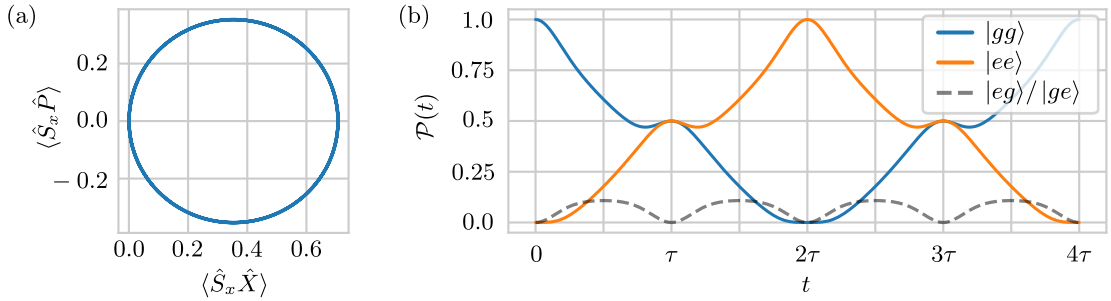


Figure 4.4: Time evolution of a state under the Mølmer-Sørensen interaction: (a) the trajectory in phase space describes a circle with area A. For a characteristic interaction time $t = \tau$ this loop is closed at the origin, which marks the point where the electronic states of the ions are disentangled from the motion. Both qudits are in the entangled state $(|gg\rangle + |ee\rangle)/\sqrt{2}$ and the two unwanted states $|ge\rangle, |eg\rangle$ are not populated. (b) Evolution of the state populations $\mathcal{P}(\theta)$ with the angle θ, which is proportional to the duration t of the bichromatic laser pulse.

recover the product states $|gg\rangle$ and $|ee\rangle$ (even multiples of τ).

We discuss the implementation of the interaction on a hardware level and refer to the optical setup presented in Fig. 3.6 of the previous chapter. The laser pulse is created using the AOMs in DP configuration, where we apply an RF signal with amplitude $a_{DP} \propto \sqrt{\Omega}$ and frequency tuned to resonance with the respective quadrupole transition coupling the states $|g\rangle \leftrightarrow |e\rangle$. Two RF signals with frequencies $f_\pm = 145.24\ \text{MHz} \pm (\omega_z/2\pi + 1/\tau)$ and amplitudes $a_\pm$ are combined[2] to supply the fiber-coupled SP AOMs, thereby realizing the bichromatic light field. Both amplitudes are normalized to a constant value $a_{sat.}$ below the saturation threshold of the AOM. The light is then guided onto the ions via the addressing unit, illuminating only the selected pair (i, j).

Analogous to the single-qudit gates, we define the *Mølmer-Sørensen* (MS) *gate* acting on the ions i and j by

$$\hat{MS}^{(i,j)}(\theta, \phi) = e^{-i\theta\left(\hat{S}_x^{(i,j)} \cos(\phi) + \hat{S}_y^{(i,j)} \sin(\phi)\right)^2}, \qquad [4.18]$$

bichromatic light field couples the states where we can control the axis of the rotation by the phase ϕ of the laser pulse of duration $t \propto \theta$. The state $|g\rangle$ and $|e\rangle$ are encoded in the $4^2S_{1/2}$ and $3^2D_{5/2}$ manifolds, respectively, and are coupled by the bichromatic light field via the optical quadrupole transition. This is reflected in our definition of the two-qudit spin operators, where we have introduced the matrices $\sigma_\alpha^{(k)}$ as a convenient reduction of the respective generalized Gell-Mann matrices to the subspace $\{|g\rangle, |e\rangle\}$.

In contrast to our single-qudit gates, the rotation angle θ cannot be controlled by the interaction time t. With the duration τ of the gate being fundamentally linked to the detuning δ with respect to the motional sidebands, changing t would lead to residual entanglement of the electronic states with the motional modes and thereby population of the odd-parity states. However, since $\theta \propto \Omega$ it must be proportional to the *area* of the laser pulse, which can be controlled by the amplitude a_{DP} on the DP AOMs; this scheme is introduced in the upcoming section.

2 Mini-Circuits ZFSC-2-1-S+ or comparable

4.2.1 *Entangled states with arbitrary probability amplitudes*

The rotation angle θ of a single-qudit gate is adjusted by changing the duration t of the laser pulse. Creating entangled states of the form

$$|\psi(\theta,\phi)\rangle = \cos(\theta)\,|gg\rangle + e^{i\phi}\sin(\theta)\,|ee\rangle \qquad [4.19]$$

via the MS interaction is significantly more complex, as the pulse length t is intrinsically linked to the phase space trajectory, which closes at the origin at a characteristic time τ. Consequently, any $t \neq \tau$ will prevent the loop in Fig. 4.4(a) from closing, resulting in the population of the unwanted states $|ge\rangle$ and $|eg\rangle$.

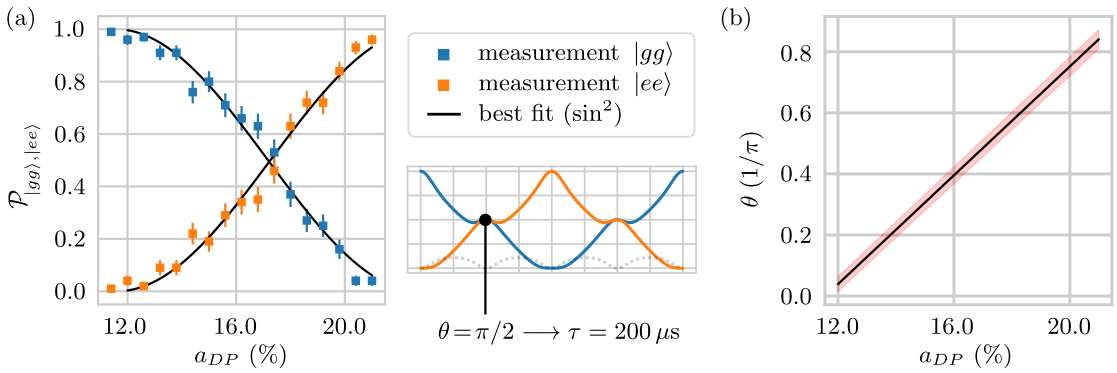


Figure 4.5: MS gate creating GHZ states of two qubits with arbitrary weights: (a) the duration of the laser pulse is kept constant at $t = \tau = 200\ \mu$s, where the loop in phase space is always closed. Tuning the amplitude a_{DP} of the DP AOM implements the state $\cos(\theta)\,|gg\rangle + \sin(\theta)\,|ee\rangle$, while the unwanted states $|ge\rangle$ and $|eg\rangle$ remain unpopulated. Error bars in the data indicate quantum projection noise. (b) By fitting a $\sin^2$ function to the data we compute the rotation angle θ as a function of a_{DP}. The shaded area corresponds to one standard deviation of statistical uncertainty which is calculated from the fit parameters.

The state in Eq. [4.19] can be implemented for arbitrary rotation angles θ by varying the intensity of the light field while keeping interaction time $t = \tau$ constant. This is achieved by tuning the amplitude a_{DP} of the RF signal controlling the DP AOM, cf. Fig. 3.6). For a characteristic time $\tau = 200\ \mu$s we measure the populations $\mathcal{P}_{|gg\rangle}$ and $\mathcal{P}_{|ee\rangle}$ of the states $|gg\rangle$ and $|ee\rangle$ as a function of a_{DP}, obtaining the data shown in Fig. 4.5(a). For amplitudes well below the saturation threshold $a_{sat.} \approx 60\%$ of the DP AOM, the populations oscillate periodically as a_{DP} is increased. Our data is well approximated by the function

$$\mathcal{P}(a_{DP}) = \sin^2(2\pi \cdot a_{DP}/T + \varphi)$$

with period T phase offset φ. Using Eq. [4.19], this fit allows us to compute the rotation angle θ as a function of a_{DP} shown in Fig. 4.5(b).

Tuning of the signal amplitude on the DP AOM enables the implementation of MS gates with angles within the range $\theta \in [0, \pi]$. For larger ion registers a_{DP} increases significantly, eventually approaching the threshold $a_{sat.}$. In this regime we experimentally observe strong non-linearities for $\theta > 0.7\pi$. To mitigate these effects we employ the following strategy: rotations with $\theta > 0.7\pi$ is decomposed into n MS gates with constant angle $\theta = \pi/2$, while the residual angle $\theta' = \theta - n\pi/2$ is implemented by tuning a_{DP}.

4.2.2 *AC Stark shifts, power imbalancing and spectator phases*

Coupling the ions to their collective motion is an inefficient process. The effective Rabi frequency $\Omega' = \eta\Omega$ scales with the Lamb-Dicke parameter, which is well below unity. Compared to gates on resonance with the carrier transition $|g\rangle \leftrightarrow |e\rangle$, creating a maximally entangled state within a reasonable interaction time $\tau = 200\ \mu$s requires substantially higher intensities of the light field at the position of the ions. This is accompanied by AC Stark shifts Δ_{AC}, introducing a detuning as shown in Fig. 4.6(a). The maximally entangled state in Eq. [4.17] is recovered if we further detune the laser by $\Delta\omega = \Delta_{AC} = 2\pi \cdot 1.05$ kHz.

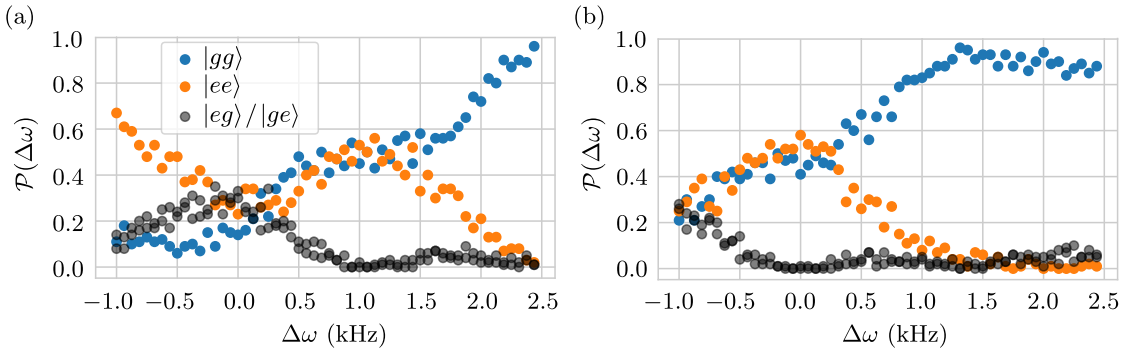


Figure 4.6: Compensation of AC Stark shifts by power imbalancing: (a) the larger intensity of the bichromatic light field driving the MS gate introduces AC Stark shifts, leading to a detuning $\Delta_{AC} = 2\pi \cdot 1.05$ kHz. (b) this shift is compensated by adjusting the amplitudes $a_\pm$ of the RF signals applied to the DP AOMs. For a gate duration $\tau = 200\ \mu$s we measure a ratio $a_+/a_- = 0.857$.

A more convenient method is realized by adjusting the ratio of the amplitudes $a_\pm$ of the RF signals on the SP AOM units enabling the bichromatic field. In a technique we call *power imbalancing*, we keep a_- constant while increasing a_+ until the residual detuning vanishes. This scheme is verified by our data presented in Fig. 4.6(b), where the initial shift $\Delta_{AC} = 2\pi \cdot 1.05$ kHz observed in Fig. 4.6(a) is cancelled for the ratio $a_+/a_- = 0.857$. Note, that while we change the values of the individual signal amplitudes, we keep the amplitude of the combined signal constant close to the saturation threshold $a_{sat.}$.

Here we also acknowledge the additional phases picked up by the spectator states $\{|i\rangle\}_{i\neq e,g}$, which are only partially attributed to AC Stark shifts labelled $\Delta_{|i\rangle}$. Our definition of the spin operators in Eq. [4.14] via the matrices $\sigma_\alpha^{(k)}$ acting on the subspace $\{|g\rangle, |e\rangle\}$ introduces a global phase factor, which manifests as a local phase shift ϕ_0 on each spectator state $|i\rangle$. Experimentally, we measure the *combined* shift $\phi_{|i\rangle}(t) = \phi_0 + \Delta_{|i\rangle} t$ acquired during an interaction of duration t by Ramsey spectroscopy [107]. With $\phi_{|i\rangle}(t)$ known, we then add this factor to each gate involving the respective spectator, thereby compensating the shift for gates of arbitrary t. A similar technique is applied to a different kind of entangling gate, which we thoroughly discuss in Sec. 4.3.

4.2.3 *Off-resonant couplings and pulse amplitude shaping*

Exciting the ions with a high intensity laser pulse with a square-shaped envelope introduces a wide range of frequencies ω in the spectrum. Its Fourier transform is spread out with non-vanishing amplitudes even far away from the frequency ω_L of the pulse up to infinity. These frequencies manifest as perturbations in the trajectory of the ions in phase space, preventing the loop in Fig. 4.4(a) from closing at the origin [149]. Consequently, the ions remain weakly entangled with the motional states, and the electronic states $|eg\rangle, |ge\rangle$ are populated. Additionally, coupling to other modes in the spectrum further impacts the gate performance.

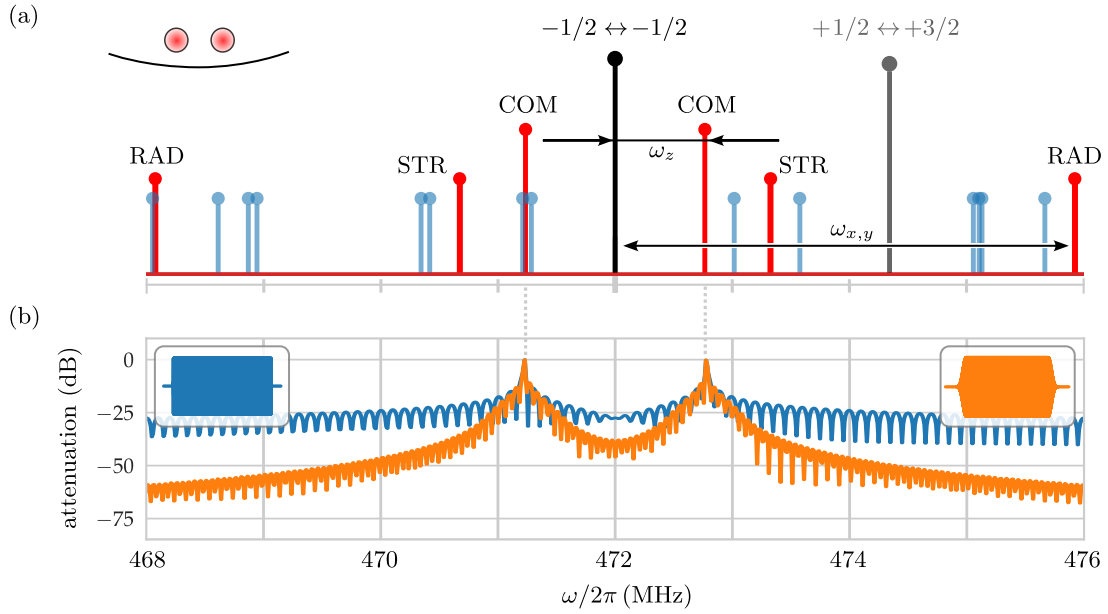


Figure 4.7: Pulse shaping: (a) spectrum of the joint system of two trapped ions at a bias field $|\vec{B}| = 0.42$ mT centered around the $4^2S_{1/2}(m = -1/2) \leftrightarrow 3^2D_{5/2}(m = -1/2)$ carrier transition. We show the two *axial* sidebands at $\omega_z = 2\pi \cdot 860$ MHz (COM) and $\sqrt{3}\omega_z$ (STR), and the radial modes $\omega_{x,y} = 2\pi \cdot 4$ MHz (RAD) with respect to this carrier in red, while the blue lines are associated with other carrier transitions. (b) A bichromatic square pulse (blue) leads to unwanted frequency components, which are attenuated to ≈ -25 dB. In contrast *shaping* of the rising and falling edges of the pulse (orange) results in a significantly larger attenuation.

A simulation of the spectrum of two trapped ions is illustrated in Fig. 4.7(a). Using the experimentally measured frequencies (black) on the quadrupole transition at a bias field strength of $|\vec{B}| = 0.42$ mT, we obtain a good approximation to the real quantum processor. We implement the MS gate on the COM mode with the red and blue sideband at frequencies $\pm\omega_z = \pm 2\pi \cdot 0.86$ MHz around the $4^2S_{1/2}(m = -1/2) \leftrightarrow 3^2D_{5/2}(m = -1/2)$ carrier transition with $\omega_L \approx 2\pi \cdot 472$ MHz and assume a gate time $\tau = 200$ μs. The *stretch mode* (STR) is shown at $\pm(\omega_L + \sqrt{3}\omega_z)$ and two *radial modes* (RAD), which are $\approx 2\pi \cdot 4$ MHz detuned from ω_L and separated by only a few kHz. To distinguish the sidebands of the chosen transition from its neighbours, e.g. those around the $S_{1/2}(m = +1/2) \leftrightarrow D_{5/2}(m = +3/2)$ transition to the right, we choose a different color scheme (red) and larger amplitudes. Note, that these do not encode the respective coupling strengths and are merely a visual guide to the reader.

In reality, the spectrum is significantly more complex compared to the simplified picture, where we consider just a single transition and its accompanying sidebands. This *mode crowding* can lead to various pitfalls, most notably when axial modes of different carriers start to overlap, which can be detected by simulations of the spectrum. While the ratio between the axial trap frequencies is fixed, their values can be adjusted via the DC voltage applied to the endcap electrodes, resulting in a clean spectrum without overlapping modes.

We show the spectra of two bichromatic laser pulses with principal frequencies $\omega = \omega_L \pm (\omega_z + 2\pi/\tau)$ realizing a MS gate with characteristic gate time $\tau = 200\ \mu$s in Fig. 4.7(b). The Fourier transform of the pulse with a square envelope (blue) yields the sinc function in frequency space, with a nearly homogeneous attenuation of -25 dB for all signal components away from ω. Due to the high intensity of the light field, these frequencies weakly couple with other modes and neighbouring carrier transitions. We mitigate these effects by modulation of the pulse amplitudes akin to Roos et. al. [149]. The edges of the pulse follow the shape of the *Nuttall window function* [126, 150]

$$w(\mathcal{T}) = 0.3558 - 0.4874 \cdot \cos(\pi\mathcal{T}) + 0.1442 \cdot \cos(2\pi\mathcal{T}) - 0.0126 \cdot \cos(3\pi\mathcal{T}) \qquad [4.20]$$

with *normalized shape time* $\mathcal{T} \in [0,1]$. For $\mathcal{T}$ corresponding to 5 μs on each slope we obtain the pulse (orange) shown in Fig. 4.7(b), which offers a significantly better suppression of the unwanted frequency components down to ≈ -50 dB at the neighboring $4^2S_{1/2}(m = +1/2) \leftrightarrow 3^2D_{5/2}(m = +3/2)$ carrier transition.

We employ this technique for all pulses exciting the motional sideband, where the small Lamb-Dicke factor $\eta \approx 0.034(2)$ requires a significant increase in the intensity of the light field to achieve experimentally feasible interaction times. As each pulse must complete the full modulation cycle of $2\mathcal{T} \approx 10\ \mu$s, the minimal pulse duration is limited.

4.3 MEDIATING ENTANGLEMENT BY CONTROLLED EXCITATION OF THE COLLECTIVE MOTION

A different approach to creating entanglement in trapped ion systems was introduced by Cirac and Zoller in 1995, pre-dating the scheme of Mølmer and Sørensen [20]. In their seminal work, they propose to actively entangle ions with the collective motion using *single ion operations* on the *blue sideband* (BSB). This fundamental interaction illustrated in Fig. 4.8 acting on the ion labeled by k is described by the *Anti-Jaynes-Cummings* (AJC) Hamiltonian

$$\hat{H}^{(k)}_{\mathrm{AJC}} = \frac{i\hbar}{2}\eta\Omega\left(\hat{a}^\dagger\sigma_+^{(k)}e^{i(\Delta-\omega_z)t-i\phi} - \hat{a}\sigma_-^{(k)}e^{-i(\Delta-\omega_z)t+i\phi}\right), \qquad [4.21]$$

where $\sigma_+^{(k)} = |e\rangle\langle g|$ is the raising operator on the subspace $\{|g\rangle, |e\rangle\}$ of the qudit, while $\hat{a}^\dagger$ simultaneously creates a photon $|n\rangle \to |n \pm 1\rangle$; the operators $\sigma_-^{(k)} = |g\rangle\langle e|$ and $\hat{a}$ have the opposite effect. The quantum states are encoded, such that $|g\rangle$ is one of the two $4^2S_{1/2}$ ground states and $|e\rangle$ is any of the excited states in the $3^2D_{5/2}$ manifold. The light field is detuned from the quadrupole transition $|g\rangle \leftrightarrow |e\rangle$ by $\Delta = \omega_z$ and has the phase ϕ.

For an interaction time t proportional to the angle θ, the Hamiltonian in Eq. [4.21] realizes the local *blue sideband gate*, which we write as

$$\hat{B}^{(k)}(\theta,\phi) = e^{i\theta\hat{H}^{(k)}_{\mathrm{AJC}}/2\hbar}. \qquad [4.22]$$

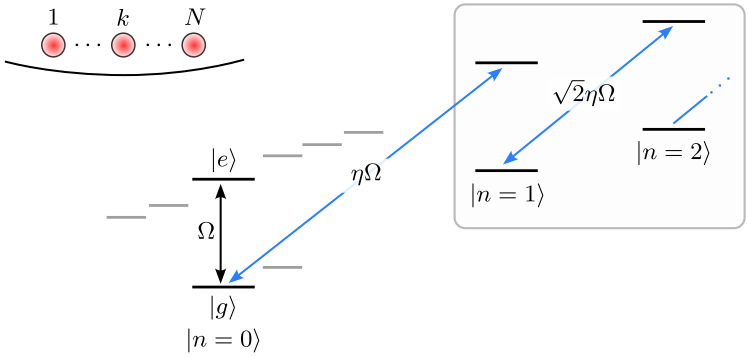


Figure 4.8: Illustration of the blue sideband interaction: the k-th ion is addressed by a laser pulse, exciting the ion from the state $|g\rangle$ to $|e\rangle$ while simultaneously creating a phonon $|n\rangle \rightarrow |n+1\rangle$. Conversely, an excited ion in $|e\rangle$ is de-excited to $|g\rangle$ while a phonon is annihilated, such that $|n\rangle \rightarrow |n-1\rangle$.

Note, that this gate depends on both the state of the ion *and* its motion: the motion is excited *if and only if* the ion is in $|g\rangle$. Conversely, the electronic state of the ion can only be de-excited if and only if the system is not in its motional ground state $|n \neq 0\rangle$. This allows for *conditioned* operations, which inherently require the treatment of the ion as qudit rather than a mere qubit. In the remainder of this section we will discuss the implementation of $\hat{B}(\theta, \phi)$ in more detail and show their applications in the context of qudits.

4.3.1 *Compensation of AC Stark shifts*

Similar to the MS gate, the effective interaction strength $\Omega' = \eta\Omega$ with $\eta \ll 1$ is significantly suppressed compared to the carrier transition $|g\rangle \leftrightarrow |e\rangle$ with Rabi frequency Ω. Consequently, the intensity of the light field exciting the ion via the motional sideband must be increased substantially, thereby introducing AC Stark shifts. These shifts affect the gate operation and have an impact on the spectator states $|i\rangle$ in the qudit.

We employ two schemes to compensate these shifts. On the subspace $\{|g\rangle, |e\rangle\}$ we use a technique similar to Häffner et al. [135], where a second, far detuned laser beam is applied simultaneously to the pulse exciting the sideband. This second beam introduces a second shift of equal magnitude, but in opposite direction, thereby restoring the resonance condition. For the spectator states, we first measure the shift $\Delta(\theta)$ introduced by the $\hat{B}^{(k)}(\theta, \phi)$ via Ramsey spectroscopy [107]. Second, we compute the acquired phase $\phi(\theta)$ for each sideband pulse, which is then added in software to the subsequent laser pulses coupling the spectators. We now discuss both schemes in more detail.

Active compensation scheme with a detuned laser beam

Here we refer to the optical setup introduced in Sec. 3.2.4 and describe the implementation of laser pulses driving the blue sideband on the level of RF signals applied to the individual AOMs. The pulse is primarily controlled by the DP units, which are detuned by $\Delta_{RF} = \omega_z/2$ from the frequency matching the carrier transition; as the light has to pass the device twice, we achieve the desired detuning of $\Delta = \omega_z$.

Analogous to the MS gate, we employ pulse shaping using the window function in Eq. [4.20] with a slope time of 5 μs, limiting the minimum pulse length to ≈ 12.5 μs, when including additional delays in the control hardware. The light is then up-shifted by the fiber-coupled SP AOMs by 145.24 MHz and sent to the ion via the ion addressing unit. Such a laser pulse introduces AC Stark shifts which depend on the effective Rabi frequency Ω'. For $\Omega' = 2\pi \cdot 8$ kHz on the blue sideband of the $4^2S_{1/2}(m = -1/2) \leftrightarrow 3^2D_{5/2}(m = -1/2)$ quadrupole transition, we measure the bare shift $\Delta_{AC} = -7.66$ kHz as shown in Fig. 4.9(a).

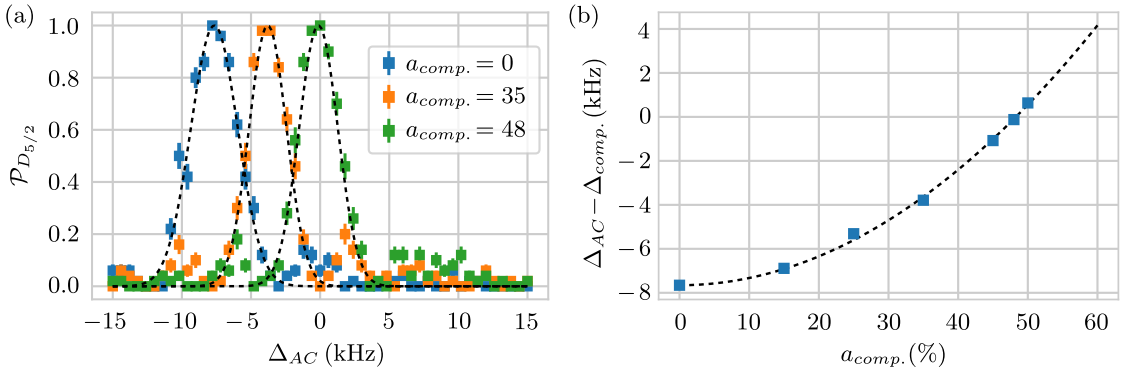


Figure 4.9: Active compensation of AC Stark shifts using a second, off-resonant laser beam: (a) the shift Δ_{AC} is canceled by increasing the amplitude $a_{comp.}$ of a second radiofrequency signal applied to the single-pass AOMs in our setup. This results in a second laser beam that induces an opposite shift $\Delta_{comp.}$. We measure Δ_{AC} for different compensation amplitudes: for $a_{comp.} = 0$ (blue) we observe the bare shift $\Delta_{AC} = -7.66$ kHz, which is compensated by applying a signal with amplitude $a_{comp.} = 48\%$ (green) to the AOMs; the error bars indicate quantum projection noise. (b) The residual shift $\Delta_{AC} - \Delta_{comp.}$ follows the square law $\Delta_{AC} - \Delta_{comp.} = c \cdot a_{comp.}^2 + \Delta_{AC}$ with $c = 0.00328(4)$ obtained by fitting of a quadratic model; statistical uncertainties are on the order of a few Hz and are hidden by the data markers.

We now apply a second RF signal to the SP AOMs at a frequency of 143.9 MHz, introducing an additional off-resonant component in the light field detuned by -1.34 MHz from the COM mode. Increasing the amplitude $a_{comp.}$ of the RF signal we induce an opposite shift $\Delta_{comp.}$. We illustrate the residual shift $\Delta_{AC} - \Delta_{comp.}$ for two values of $a_{comp.}$ in Fig. 4.9(a), where we achieve a nearly perfect cancellation for $a_{comp.} = 48\%$ of the maximum output voltage of the frequency synthesizers. The residual shift is measured for increasing values of $a_{comp.}$ and we fit a quadratic model to the data shown in Fig. 4.9(b). This model is justified since the intensity of the light field is proportional to the square of the signal amplitude. We obtain a square law $\Delta_{AC} - \Delta_{comp.} = c \cdot a_{comp}^2 + \Delta_{AC}$ with $c = 0.00328(4)$, i.e. $\Delta_{comp.} = c \cdot a_{comp.}^2$.

Our technique has one major caveat: as the amplitude of the combined RF signal increases, saturation effects in the SP AOMs reduce their efficiency and consequently the intensity of the output beam decreases. We therefore normalize the total amplitude to a constant value where we measure the maximum in the optical power. Due to this normalization, any increase in $a_{comp.}$ reduces the optical power in the beam driving the blue sideband and Ω' decreases. We account for this effect by increasing the RF amplitude on the DP AOM, which does not impact the compensation on the SP AOMs, since the ratio of the signals remains constant.

Passive compensation in software

The *active* compensation technique presented in the previous paragraph is well suited to cancel the AC Stark shifts introduced on the subspace $\{|g\rangle, |e\rangle\}$, where the gate $\hat{B}^{(k)}(\theta, \phi)$ is implemented. Moreover, a combined effect of both light fields realizing the compensated gate leads to additional shifts $\Delta_{|i\rangle}$ on the spectator states $\{|i\rangle\}$ of our qudit. While these could, in principle, also be compensated by additional laser fields, the required intensities are beyond the capabilities of the system. Instead, we follow a simpler approach account for these shifts by computing the phase $\boldsymbol{\phi(\theta)}$ acquired during the interaction time $t \propto \theta$, which is then added in software to every subsequent gate operation involving the state $|i\rangle$.

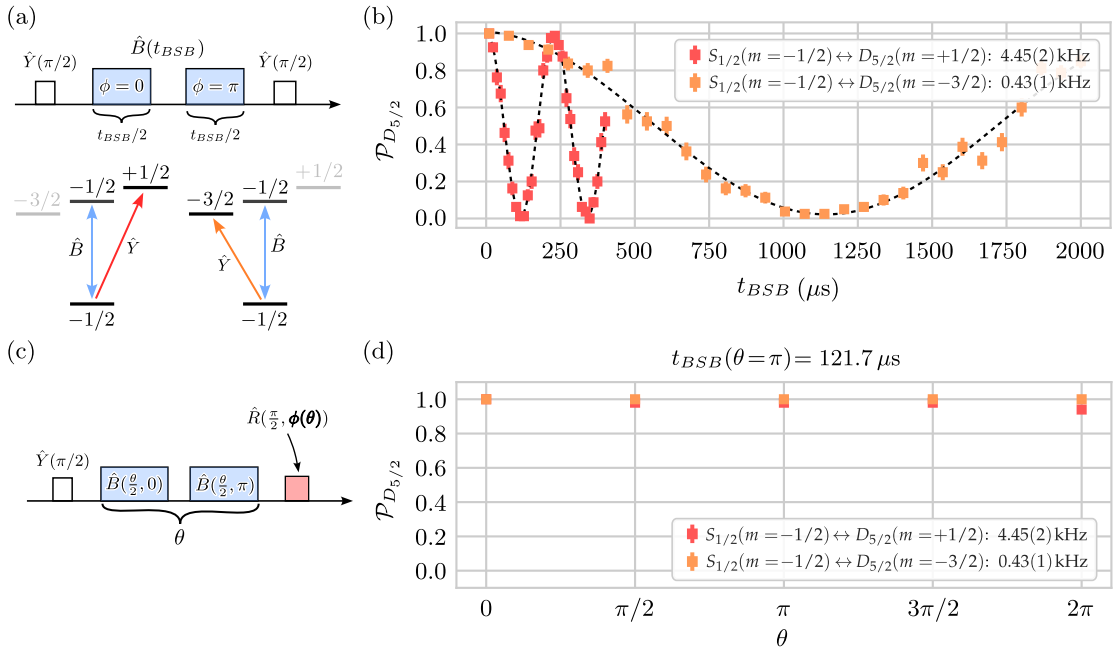


Figure 4.10: Measurement and compensation of AC Stark shifts on spectator levels in a qudit with local dimension $d = 4$ (*ququart*): (a) we implement a sequence performing Ramsey spectroscopy on the spectator transitions and introduce the blue sideband gates $\hat{B}^{(k)}$ on the $4^2S_{1/2}(m = -1/2) \leftrightarrow 3^2D_{5/2}(m = -1/2)$ transition as a perturbation, leading to AC Stark shifts Δ_{AC}. (b) Scanning the duration t_{BSB} of $\hat{B}^{(k)}$ causes the populations of the spectator states to oscillate. The frequency of this oscillation is used to compute $\Delta_{AC} = 4.45(2)$ kHz on the $4^2S_{1/2}(m = -1/2) \leftrightarrow 3^2D_{5/2}(m = +1/2)$ transition (red) and $\Delta_{AC} = 0.43(1)$ kHz on the $4^2S_{1/2}(m = -1/2) \leftrightarrow 3^2D_{5/2}(m = -3/2)$ transition (orange); the error bars represent quantum projection noise. (c) For a given rotation angle $\theta \propto t_{BSB}$ of the $\hat{B}^{(k)}$ the AC Stark shift induces a phase $\boldsymbol{\phi(\theta)}$. This phase is added to the second pulse of the Ramsey sequence, thereby compensating the shift as shown in (d) for selected values of $\theta \in [0, 2\pi]$.

Coupling two states $|i\rangle$ and $|j\rangle$ in the qudit will always involve one of the ground states. We measure the shift on the transition $|g\rangle \leftrightarrow |e\rangle$ via Ramsey spectroscopy as illustrated in Fig. 4.10(a). Here we realize a qudit with dimension $d = 4$ – a *ququart* – encoded in the $4^2S_{1/2}(m = -1/2)$ ground state and three states in the $3^2D_{5/2}(m)$ manifold, notably those with magnetic quantum numbers $m \in \{-3/2, -1/2, +1/2\}$. The $\hat{B}^{(k)}(\theta, \phi)$ are implemented on the transition coupling the $4^2S_{1/2}(m = -1/2)$ with the $3^2D_{5/2}(m = -1/2)$ state, while the other states act as spectators. A $\hat{Y}(\pi/2)$ gate creates a superposition of the respective spectator with the ground state. We then apply two $\hat{B}^{(k)}$ with opposite phase, each for a duration $t_{BSB}/2$, thereby effectively realizing a perturbation of length t_{BSB} while

also returning to the ground state after the operation. A second $\hat{Y}(\pi/2)$ pulse completes the sequence. If $\Delta_{|i\rangle} = 0$, the spectator state is then populated with probability $\mathcal{P}_{D_{5/2}} = 1$.

Scanning the effective duration t_{BSB} of the $\hat{B}^{(k)}$ we obtain oscillations in the population $\mathcal{P}_{5/2}$ of the respective excited state. As shown in Fig. 4.10(b), the AC Stark shifts $\Delta_{|i\rangle}$ induced on the two spectators varies significantly. On the transition coupling the ground state with $3^2D_{5/2}(m = +1/2)$, which is detuned by $\delta \approx -2\pi \cdot 5$ MHz with respect to the frequency of the gate, we obtain a shift of $\Delta_{|m=+1/2\rangle} = 4.45(2)$ kHz. In contrast, the shift induced on the $4^2S_{1/2}(m = -1/2) \leftrightarrow 3^2D_{5/2}(m = -3/2)$ transition with $\delta \approx -2\pi \cdot 7$ kHz is by a factor of 10 smaller – we measure $\Delta_{|m=-3/2\rangle} = 0.43(1)$ kHz.

From the data we compute the phase $\phi(t) = \Delta_{|i\rangle} \cdot t$ acquired on the spectator states during the gate $\hat{B}^{(k)}(\theta \propto t)$. This phase is then added to the second $\pi/2$ pulse in our sequence as sketched in Fig. 4.10(c). With this scheme, we successfully account for the AC Stark shifts as shown by our data in Fig. 4.10(d), where the effective duration t matches the pulse lengths associated with a $\theta = n\pi/2$ rotation for $n = 0, 1, \ldots 4$; we expect the population to remain constant at $\mathcal{P}_{D_{5/2}} = 1$. Note, that we cannot measure the *sign* of $\Delta_{|i\rangle}$ from the data in Fig. 4.10(b) alone. Picking the wrong sign yields to oscillations in the data in Fig. 4.10(d) – we then simply map $\Delta_{|i\rangle} \to -\Delta_{|i\rangle}$ and repeat the measurement to ensure proper cancellation.

As both schemes are employed simultaneously, the calibration of our apparatus prior to executing a meaningful quantum algorithm can be quite extensive. However, we only measure the shifts for those states that are actually populated. A clever choice of encoding can further simplify the calibration, as some spectator states might not experience a shift from a $\hat{B}^{(k)}$ implemented on a far detuned transition.

4.3.2 *Native Cirac-Zoller type quantum gates in qudits*

The proposal by Cirac and Zoller to mediate entanglement via the collective motion of trapped ions marked a fundamental milestone in establishing the field of quantum information processing [20]. A first implementation of their CNOT gate, which is mathematically described by

$$|i, j\rangle \mapsto |i, i \oplus j\rangle \qquad [4.23]$$

with $\oplus$ the addition modulo 2, was first realized in $^{40}Ca^+$ by Schmidt-Kaler et al. in 2003 [110, 151]. Their experiment deviated from the original proposal by using a Ramsey sequence enclosing a *composite phase gate* rather than an auxiliary level as suggested in the original proposal [48]. With this approach an average gate fidelity of 71(3)% was measured, which, considering the technical limitations at that time, was a remarkable achievement.

We now follow the original proposal more closely and harness the qudit capabilities of our apparatus to realize a *controlled rotation gate* $C\hat{R}(\theta, \phi)$. Let us consider two ions, each encoding a single qubit as illustrated in Fig. 4.11(a). Depending on the state of the *control* qubit (c, left), we excite the motion by injecting a single phonon, which enables the rotation $\hat{R}(\theta, \phi)$ on the *target* (t, right). The target is realized as a *qutrit* with dimension $d = 3$ and encodes a qubit in the $3^2D_{5/2}$ manifold, which is manipulated by sequentially coupling the states $|0\rangle$ and $|1\rangle$ with an auxiliary ground state $|g\rangle$.

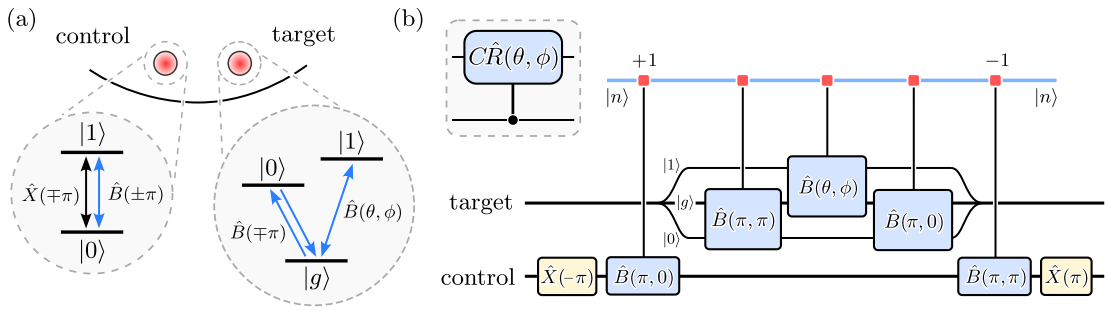


Figure 4.11: Controlled rotation gates $C\hat{R}(\theta,\phi)$: (a) the *control* qubit (left) is defined by the states $|0\rangle$ (ground state) and $|1\rangle$ (excited state), while the *target* qubit is encoded in two excited states, which are coupled via an auxiliary ground state $|g\rangle$. (b) a single $C\hat{R}(\theta,\phi)$ is realized by a sequence of single ion blue sideband gates $\hat{B}(\theta,\phi)$ and two resonant $\hat{X}(\pi)$ pulses with opposite phase on the control qubit. Depending on the state of the control qudit, the collective motion (blue line) is excited, which conditions the operation on the target.

Let the operation be conditioned by the state $|1\rangle$ of the control qubit and follow the pulse sequence in Fig. 4.11(b). The system is prepared in the motional ground state $|n=0\rangle$. We first exchange the population of $|0\rangle$ and $|1\rangle$ on the control by applying the operation $\hat{X}^{(c)}(-\pi)$. The state $|1\rangle$ is now mapped to the ground state and we inject a phonon by $\hat{B}^{(c)}(\pi,0)$, changing the motional state to $|n=1\rangle$. If the control is in $|0\rangle$, which is now mapped to $3^2D_{5/2}$, the operation has no effect and we remain in motional ground state.

The rotation on the target is realized by three sideband pulses $\hat{B}^{(t)}$, which bring population from $|0\rangle$ or $|1\rangle$ to $|g\rangle$ *iff* $|n=1\rangle$. Let us first consider the target being in $|0\rangle$: the pulse $\hat{B}^{(t)}(\pi,\pi)$ maps $|0\rangle$ to $|1\rangle$ while simultaneously *removing* the phonon, bringing the system back to the motional ground state. We then inject another phonon by the second pulse $\hat{B}^{(t)}(\theta,\phi)$, exciting the motion and populating $|1\rangle$. The operation on the target is finalized by $\hat{B}^{(t)}(\pi,0)$, mapping $|0\rangle$ back to the $3^2D_{5/2}$ manifold. If the ion is in $|1\rangle$, the first pulse does not change its motional state. $\hat{B}(\theta,\phi)$ brings the population to $|g\rangle$, before being mapped to $|0\rangle$ by the last $\hat{B}^{(t)}(\pi,0)$. After the sequence has ended, the motional state prior to the manipulation of the target will be restored.

Finally, we invert the phonon injection on the control by executing the sequence in reverse: we bring $|1\rangle\otimes|n=1\rangle$ to both the electronic and the motional ground state (-1), while the population of $|0\rangle$ hidden in the excited state associated with $|n=0\rangle$ remains preserved. A $\hat{X}(\pi,0)$ pulse restores the original encoding and ends the operation.

Our scheme can be readily extended to support high-dimensional control and target qudits. Applying the QR decomposition introduced in Sec. 4.1.3, we can thus decompose any operator $\hat{O}$ into a sequence of blue sideband pulses, thereby realizing *controlled operators* $C\hat{O}$. The dimension of the target is limited only by the number of excited states offered by the ion species, as the ground states are exclusively used as auxiliaries. However, due to the level structure of $^{40}Ca^{+}$ the dimension of our target qudits is limited to at most $d=6$ (*qusext*).

We can also manipulate $m \in \mathbb{N}$ target qudits and realize a $C\hat{R}^m(\theta,\phi)$ gate simply by concatenation of blue sideband pulses. The pulse sequence is then given by

$$\hat{X}^{(c)}(\pi)\hat{B}^{(c)}(\pi,\pi)\left(\prod_{t=1}^{m}\hat{B}^{(t)}_{|g\rangle,|0\rangle}(\pi,0)\hat{B}^{(t)}_{|g\rangle,|1\rangle}(\theta,\phi)\hat{B}^{(t)}_{|0\rangle,|g\rangle}(\pi,\pi)\right)\hat{B}^{(c)}(\pi,0)\hat{X}^{(c)}(-\pi), \quad [4.24]$$

where the subscripts indicate the states coupled by the respective $\hat{B}^{(t)}$. This gate is later implemented in Ch. 8 to change the quantum state of two gauge fields encoded in qudits up to dimension $d = 5$ depending on the state of a common control.

Controlled rotation gates and all variations thereof are well suited to be employed in variational quantum algorithms, where the rotation angles θ must be tuned over a wide range. This property is inherited by the fundamental resource operation, the blue sideband gates $\hat{B}^{(k)}(\theta,\phi)$, where θ is controlled by the duration of the laser pulse. In contrast, the *tuning range* of the MS gates is fairly narrow, limited by the maximum amplitude $a_{sat.}$ of the RF signal saturating the DP AOMs and non-linearities for large amplitudes, see our discussion in Sec. 4.2.1.

4.3.3 *Implementing scalable multi-qudit gates with controlled rotations*

Interactions between qudits are typically realized by concatenation of single-qudit and two-qudit quantum gates. Direct implementation would greatly simplify quantum circuits, reducing the circuit depth and potentially increase the fidelity of the prepared target state. A prominent example of a genuine multi-qudit gate is the n-bit controlled-NOT gate called *Toffoli* gate [52]. To our knowledge, the earliest demonstration of this gate has been shown via liquid state *nuclear magnetic resonance* (NMR) by Cory et al. in 1998 [152]. In 2007, a proposal by Ralph showed an efficient decomposition using qudits encoded in photons, which was later realized by Lanyon et al. in 2008 [59, 60]. In trapped ion systems, Monz et al. implemented the 2-bit Toffoli gate, using the collective motion of the ions to effectively encode a *qutrit* [153]. Work on superconducting transmon qudits by Reed et al. with application to quantum error correction followed in 2012 [154].

Here we present a natural extension of our controlled rotation gate and realize the n-bit controlled rotation gate $C^n\hat{R}(\theta,\phi)$ using sequences of local blue sideband pulses $\hat{B}^{(k)}$. Compared to the implementation by Monz et al., our scheme changes the motional state at most by a single phonon [153]. Here we also acknowledge a recent preprint by Fang et al., which demonstrates Toffoli gates in $^{171}Yb^+$ qudits up to dimension $d = 5$ by excitation of higher-order radial modes on the *red sideband* [155].

Our n-bit controlled rotation gate is described mathematically by

$$C^n\hat{R}(\theta,\phi)\,|c_1,\ldots,c_n,\psi\rangle = \begin{cases} |c_1,\ldots,c_n\rangle \otimes \hat{R}^{(t)}(\theta,\phi)\,|\psi\rangle & \text{if } c_i = 1\ \forall i = 1\ldots n \\ |c_1,\ldots,c_n\rangle \otimes \hat{\mathbb{1}}^{(t)}\,|\psi\rangle & \text{else} \end{cases} \quad [4.25]$$

where $\hat{\mathbb{1}}^{(t)}$ acts as the identity on the target state $|\psi\rangle$. We encode the qubits as shown in Fig. 4.12, where we distinuish between the *primary* control and the *secondary* control qubits. Their choice is not specific to any particular ion in the register, the only difference is that the state $|0\rangle$ of the secondary controls is hidden in one of the $3^2D_{5/2}$ states, allowing the ground state $|g\rangle$ in the $4^2S_{1/2}$ manifold to be used as an auxiliary. The target is encoded in

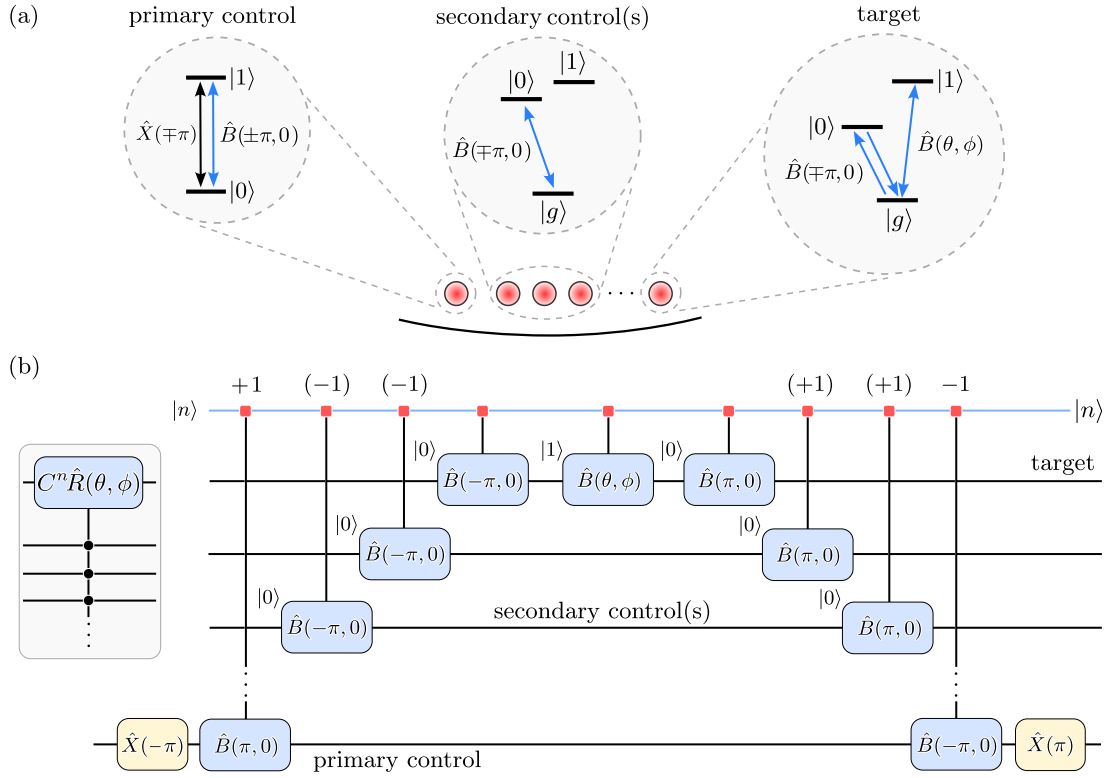


Figure 4.12: n-bit controlled rotation gate $C^n\hat{R}(\theta,\phi)$: (a) the operation is conditioned on the joint state of n control qubits. One of the controls is encoded as an ordinary qubit, while the others are embedded in a *qutrit* similar to the target. (b) Gate sequence implementing the n-bit Toffoli-type gate $C^n\hat{R}(\theta,\phi)$: the *primary* control qubit injects / removes a phonon, while the *secondary* qubits, which are encoded in a *qutrit*, remove the phonon *iff* their state does not match the control state. A sequence of three sideband gates $\hat{B}^{(k)}$ manipulates the target, implementing a rotation $\hat{R}(\theta,\phi)$. The operations on the controls are then executed in reverse to recover the initial state. Note, that we indicate the state coupling with the auxiliary ground state $|g\rangle$ by the ket vector next to each $\hat{B}^{(k)}$ instead of expanding the *qutrit* into multiple lines.

a *qutrit* analogous to the $C\hat{R}(\theta,\phi)$ gate introduced in Sec. 4.3.2.

In its first steps, the pulse sequence shown in Fig. 4.12(b) is analogous to the controlled rotation gate. The primary control excites the motion from the ground state $|n=0\rangle$ to $|n=1\rangle$ if its electronic state is $|1\rangle$ – if this condition is not met, no phonon will be injected and the pulse sequence effectively implements the identity. The secondary controls then *test* the opposite condition $|c_i\rangle = |0\rangle$: as soon as one of the control qubits is in $|0\rangle$, the phonon is removed from the COM mode and the system is in its motional ground state $|n=0\rangle$. Consequently, all subsequent operations have no effect. However, if all controls are in $|1\rangle$, the rotation $\hat{R}(\theta,\phi)$ is applied to the target. The sequence on the controls is then reversed, thereby restoring their initial electronic state and the motional ground state, if it has ever been excited in the first place.

Our scheme is verified by realizing a 3-bit quantum Toffoli gate $C^3\hat{X}$ on a string of 4 ions. The operation is defined as

$$|c_1,\ldots c_n,t\rangle \mapsto |c_1,\ldots c_n,t\oplus c_1\cdot\ldots c_n\rangle$$

for $c_i, t \in \{0,1\}$ and $\oplus$ the addition modulus 2, which we implement via a single 3-bit controlled rotation $C^n\hat{R}(\pi,0)$.

We aim for an effective Rabi frequency $\Omega' \approx 2\pi \cdot 8$ kHz on the blue sideband. Experimentally, we observe only minimal variations of a few Hz between individual ions, which can be attributed to the alignment of the addressing setup and its associated optics described in Sec. 3.2. The encoding is chosen to minimize AC Stark shifts on the spectator states. We measure a shift of $\Delta_{AC} \approx 400$ Hz for the $\hat{B}^{(k)}(\theta,\phi)$ implemented on the blue sideband of the $4^2S_{1/2}(m=-1/2) \leftrightarrow 3^2D_{5/2}(m=-1/2)$ transition; see Fig. 4.10(b) for details on the measurement protocol. Conversely a $\hat{B}^{(k)}$ of the $4^2S_{1/2}(m=-1/2) \leftrightarrow 3^2D_{5/2}(m=-3/2)$ transition has only a small impact on the $3^2D_{5/2}(m=-1/2)$ state. We therefore mitigate errors not only by employing the compensation schemes introduced in Sec. 4.3.1, but also by clever choice of qudit encoding, which is summarized in Tab. 4.1.

(ion)	$\|g\rangle$	$\|0\rangle$	$\|1\rangle$
primary (1)	-	$4^2S_{1/2}(m=-1/2)$	$3^2D_{5/2}(m=-1/2)$
secondary (2 & 3)	$4^2S_{1/2}(m=-1/2)$	$3^2D_{5/2}(m=-1/2)$	$3^2D_{5/2}(m=-3/2)$
target (4)	$4^2S_{1/2}(m=-1/2)$	$3^2D_{5/2}(m=-3/2)$	$3^2D_{5/2}(m=-1/2)$

Table 4.1: Chosen encoding for the 3-bit Toffoli gate, where the secondary qubit and the target are embedded in *qutrits*. We minimize AC Stark shifts on the spectator states by choosing the two levels with magnetic quantum numbers $m=-1/2$ and $m=-3/2$ in the $3^2D_{5/2}$ manifold, which are not significantly shifted by laser pulses on the blue sideband, coupling either of the states with the ground state.

We implement the operation for all input states and obtain the *truth table* shown in Fig. 4.13(a), where we have already mapped all *qutrits* back to their qubit subspace. Comparing our result with the ideal operation in Eq. [4.25] we compute an overlap of 95.2(2)%. This result is a merely a crude estimate of the gate performance. A thorough characterization, e.g. by *quantum process tomography* [156, 157] has not yet been performed[3]. Our results can be seen as a proof of concept and verify that our pulse sequence can indeed reproduce the functionality of n-bit Toffoli gate.

Our scheme is inherently scalable: adding another secondary control qubits extends the sequence by just two π-pulses on the blue sideband. We verify the scalability argument by realizing the 4-bit Toffoli gate, for which we measure the truth table in Fig. 4.13(b) and compute an overlap of 95.1(2)%, which is comparable to the 3-bit version. While this result might be surprising at first, we emphasise that the operation is dominated by the performance of the identity operation. With good control over the AC Stark shifts, errors in the gate can be attributed to imperfect rotations of each $\hat{B}^{(k)}$ that actually changes the motional state. If the control condition is satisfied, five $\hat{B}^{(k)}$ inject/remove phonons to/from the COM mode, which marks the "worst case"; only four $\hat{B}^{(k)}$ affect the motion if one control qubit violates the condition.

3 Quantum process tomography on a system of $N=4$ qubits would require $4^N \cdot 3^N = 20736$ measurements to fully characterize the gate. Depending on the length of the algorithm, our quantum processor acquires data at a rate of one outcome per second, which would translate to approximately 6 hours of continuous operation. Accounting for automatic continuous recalibration of the setup, we expect the tomography can be performed in 8 hours, followed by numerical reconstruction of the process matrix. We consider this to be beyond the scope of a proof of concept measurement, especially for the implementation of the 4-bit Toffoli, which would last 3 days (248832 measurements).

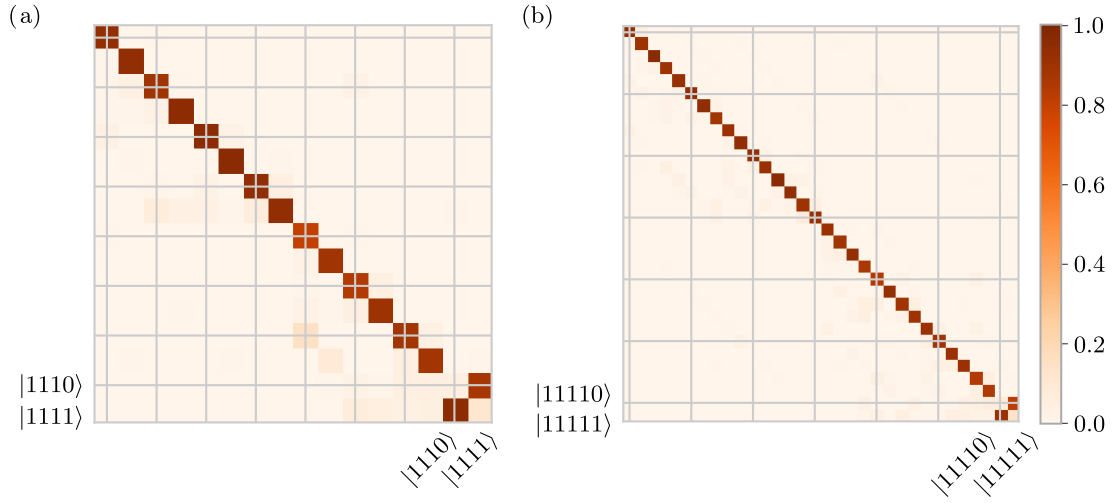


Figure 4.13: Experimentally verified truth tables: (a) the 3-bit Toffoli gate is implemented on 4 ions. Comparing the result with the ideal outcome we compute an overlap of 95.2(2)%. Our implementation is inherently scalable, enabling the realization of the 4-bit Toffoli gate in (b) by concatenation of secondary control qubits; we compute an overlap of 95.1(2)%.

Extending our arguments in the closing remarks of Sec. 4.3.1, our scheme does also support multiple targets. By concatenations of the sequence similar to Eq. [4.24], we can realize n-bit controlled rotations on m targets, which we label $C^n\hat{R}^m(\theta,\phi)$. In contrast to the $C\hat{R}^m(\theta,\phi)$, we have not yet implemented these gates in a quantum algorithm.

4.4 READOUT OF QUDITS BY SEQUENTIAL FLUORESCENCE DETECTION

The computational basis states of the qudits are read out by sequential detection of the state-dependent fluorescence light emitted by the ions [14]. Using a laser at a wavelength of 397 nm, we couple the $4^2S_{1/2}$ ground states to the short-lived $4^2P_{1/2}$ state and convert the scattered photons into an electronic signal via a PMT as discussed in Sec. 2.5; see Fig. 3.5 and Sec. 3.3.2 for details on the implementation.

Consider a qudit of dimension $d = 7$ in the W-encoding scheme illustrated in Fig. 4.14(a), where we have made a small alteration to Fig. 4.2 by mapping $|6\rangle$ to the $3^2D_{5/2}(m = +5/2)$ state for efficiency. The readout is then performed by *shelving* of the populations to the ground state manifold using single-qudit π-pulses on the respective quadrupole transition. Note, that the states $|1\rangle$ and $|3\rangle$ encoded in the $4^2S_{1/2}$ ground state cannot be distinguished by their fluorescence. We therefore start each readout sequence by an initial shelving pulse, bringing $|3\rangle$ to the $3^2D_{5/2}(m = +3/2)$ state.

The readout sequence for a single qudit is shown in Fig. 4.14(b). After the initial shelving pulse (green) mapping $|3\rangle$ to $|6\rangle$ we bring $|0\rangle$ to the ground state and observe the fluorescence signal. If photons have been collected, the qudit was in the state $|0\rangle$ and the remaining sequence is obsolete. This process is repeated iteratively until we have mapped out the states up to $|5\rangle$; $|6\rangle$ does not need to be detected, as we can deduce the outcome from the previous five measurements.

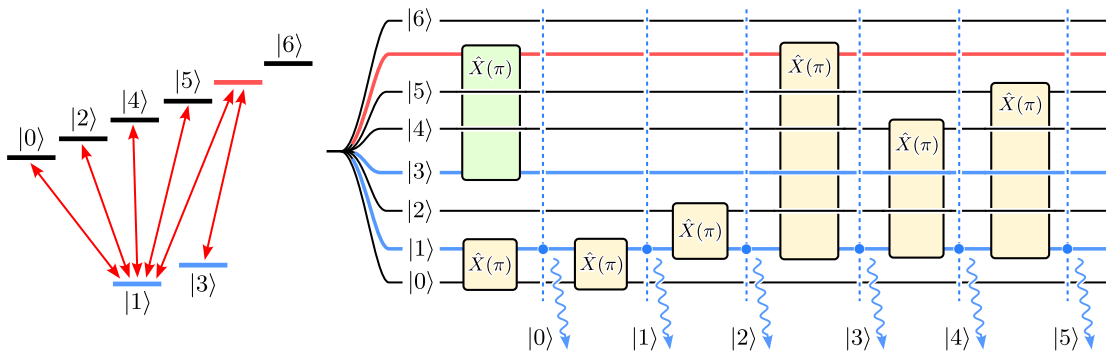


Figure 4.14: Readout of the computational basis states of a qudit with dimension $d = 7$ by fluorescence detection. The states $\{|i\rangle\}_{i=0,\dots,6}$ are encoded in the $4S_{1/2}$ ground state and $3^2D_{5/2}$ excited state manifold. Population of the ground states cannot be distinguished by the fluorescence signal, requiring an additional *unpopulated* excited state for intermediate *shelving*. The readout is then performed as a sequence of local resonant π rotations followed by laser pulses on the short-lived 397 nm dipole transition, cf. Sec. 2.5.

This scheme can be applied to larger systems of N ions, which are read either simultaneously or sequentially. The outcomes are then combined into a single number using the positional notation in Eq. [1.1] with base d introduced in Ch. 1. In our apparatus we employ a sensitive EMCCD camera to detect the fluorescence light emitted from different ions in parallel. Each fluorescence cycle will change the motional state of the entire register, thereby reducing the performance of the shelving pulses. Therefore, we perform additional cycles of Doppler and polarization gradient cooling after each detection pulse[4]. In our experiment, reading out the system of d-dimensional qudits requires $d-1$ fluorescence pulses and includes $d-2$ re-cooling steps. With a detection window $t_{det.} = 1$ ms and $t_{cool} = 2.5$ ms for each cooling cycle obtain an estimate for the readout time

$$T = (d-1)t_{det.} + (d-2)t_{cool} + d \cdot t_X$$

where t_X is the duration of each of the d shelving pulses – in most cases, $d \cdot t_X$ can be neglected. As we can read out all qudits in parallel, T does not grow with the register size and only depends on the local dimension d. The readout of a qudit system is comparable with reading out the qubit base, introducing an insignificant overhead in the runtime of the algorithm.

4 In theory, we could directly use the photons scattered during Doppler and polarization gradient cooling to detect the state, albeit with a lower yield. This would require minor changes on the hardware level and has thus far neither been tested not implemented.

5

STUDYING MANY-BODY PHYSICS ON QUANTUM SIMULATORS

The study of phenomena emerging in systems of many particles via classical methods is limited to small "toy systems". Since the required computational resources grow rapidly as the number of particles N increases, the capabilities of even the most powerful supercomputers are quickly exhausted. As the Hilbert space $\mathcal{H}$ grows exponentially with N, the number of probability amplitudes required to describe a general superposition of just ≈ 300 spins would already exceed the estimated number of particles in the observable universe. However, many phenomena require us to consider significantly more spins. In this section we develop methods allowing us to study many-body systems in one dimension by efficiently representing *large* quantum states as sequences of *small* matrices. We then discuss the properties of ground states of *local* Hamiltonians and study a simple model describing a linear chain of interacting particles, which exhibits many interesting properties such as *topological quantum phases*. These phenomena can be investigated on current state-of-the-art quantum processors.

5.1 INTRODUCTION TO MATRIX PRODUCT STATES

Let us consider the case of a chain of N sites in one spatial dimension as shown in Fig. 5.1. At each site $i \in \{0 \dots N-1\}$, an associated Hilbert space $\mathcal{H}_i = \mathbb{C}^d$ spanned by a set of orthonormal basis vectors $\{|s_i\rangle\}$ hosts a d-dimensional spin.

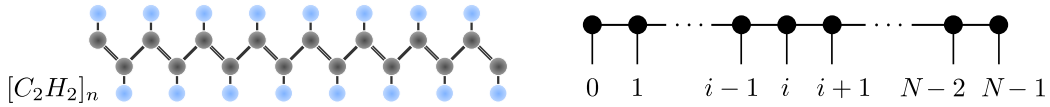


Figure 5.1: The organic polymer *polyacetlyene* $[C_2H_2]_n$ can be described by a *matrix product state* (MPS) of N sites, each hosting a d-dimensional spin [16, 158].

The most general pure quantum state describing a one-dimensional many-body system is given by

$$|\Psi\rangle = \bigotimes_k |\psi_k\rangle = \sum_{s_0,\dots,s_{N-1}} c_{s_0,s_1,\dots,s_{N-1}} |s_0,\dots,s_{N-1}\rangle\,, \qquad [5.1]$$

where the indices s_i run over the whole d local basis states on each site, covering all d^N combinations. Associated with each local product state $|s_0,\dots s_{N-1}\rangle = |s_0\rangle \otimes \dots \otimes |s_{N-1}\rangle$ are the probability amplitudes $c_{s_0,\dots s_{N-1}} \in \mathbb{C}$, which form a tensor C of rank N, fully characterizing $|\Psi\rangle$.

The tensor C however is an inefficient representation of $|\Psi\rangle$. Fortunately, for most phenomena realized in nature C is *sparse*, i.e. a large number of coefficients are zero. Aiming to reduce the number of computational resources, it is thus unreasonable to consider these

coefficients in our representation of $|\Psi\rangle$. This observation is fundamental to many-body physics: *physically meaningful* quantum states of many-body systems are contained in a small subspace of the Hilbert space $\mathcal{H} = \mathbb{C}^N$ [159]. We can arrive at this conclusion from another angle: when studying systems present in *nature*, we often look at the *low energy spectrum* of the Hamiltonian describing a certain target problem. Here, interactions are *localized*, often restricted to *next* or *next-to-next* neighbors. In one spatial dimension, quantum states of interest can then be efficiently written as *matrix product states* MPSs [160, 161], where the *large* tensor C is decomposed into sets of *small*, more manageable tensors $\{M\}_k$. A formal recipe for this decomposition closely following the works by G. Vidal [162] and R. Gawatz [163] is discussed in the upcoming sections.

5.1.1 *Singular value decomposition and Schmidt coefficients*

We are interested in investigating the quantum state $|\Psi\rangle$ of a many-body problem by looking at its associated tensor of probability amplitudes labeled C. This tensor exhibits a certain structure, which captures the entanglement present in the system described by $|\Psi\rangle$. When breaking up C into tensors of smaller rank by *singular value decomposition* (SVD), this structure remains preserved [43]. Let us consider a Hilbert space $\mathcal{H}$ and create an arbitrary bipartition $\mathcal{H}_U \bigotimes \mathcal{H}_V = \mathcal{H}$. We then perform an SVD and decompose C into *three* smaller tensors, namely [43]

$$C = U\Lambda V^T = \begin{pmatrix} | & | & \\ u_0 & u_1 & \cdots \\ | & | & \end{pmatrix} \cdot \begin{pmatrix} \lambda_0 & 0 & \cdots \\ 0 & \lambda_1 & \\ \vdots & & \ddots \end{pmatrix} \cdot \begin{pmatrix} — & v_0 & — \\ — & v_1 & — \\ & \vdots & \end{pmatrix}. \tag{5.2}$$

Here, $U \in \mathcal{H}_U$ is a matrix formed by the left-hand eigenvectors $|u_k\rangle \in \mathcal{H}_U$, while $V \in \mathcal{H}_V$ contains the right-hand eigenvectors $|v_k\rangle \in \mathcal{H}_V$. These vectors are *pairwise orthogonal*, i.e. satisfy $\langle u_k|u_l\rangle = \langle v_k|v_l\rangle = 0$ for all $k \neq l$. The matrix Λ is diagonal and contains the real-valued *Schmidt coefficients* $\lambda_k \geq 0$, which are the square root of the eigenvalues of $C^\dagger C$ satisfying $\sum_k \lambda_k^2 = 1$ since the corresponding state $|\Psi\rangle$ must be normalized.

Since Λ is diagonal, we write Eq. [5.2] as the sum

$$C = \sum_k \lambda_k |u_k\rangle \langle v_k|$$

and sort the Schmidt coefficients in *descending* order, i.e. $\lambda_0 > \lambda_1 > \ldots > 0$. Moreover, a closer inspection of Λ shows that a significant number of λ_k will often go to zero. Therefore, only a small number of eigenvectors are required to faithfully represent C, which is a consequence of the statement made previously about the sparsity of C. Discarding all $\lambda_k = 0$ and its associated vectors, we write the quantum state as

$$|\Psi\rangle = \sum_k^\chi \lambda_k |u_k\rangle \otimes |v_k\rangle, \tag{5.3}$$

which is known as the Schmidt decomposition of $|\Psi\rangle$ with *Schmidt rank* $\chi \geq 1$. We can already make some statements about the quantum state $|\Psi\rangle$ merely by looking at its Schmidt rank: the larger χ, the larger is the amount of entanglement in the system [164].

The Schmidt decomposition allows us to write the sum in Eq. [5.1] over *all* complex probability amplitudes $c_{s_0,\ldots,s_{N-1}} \in \mathbb{C}$ as a compact sum over the strictly positive $\lambda_k > 0$. Moreover, imposing a lower bound ϵ on the Schmidt coefficients allows us to efficiently *approximate* any quantum state we wish to decompose.

5.1.2 *Construction of matrix product states by sequential bipartition*

We now construct an MPS starting from Eq. [5.1] and sequentially apply Schmidt decompositions and local basis transformations [162, 163]. In each step, the Hilbert space $\mathcal{H}$ is partitioned into $\mathcal{H}_U$ and $\mathcal{H}_V$, with $\mathcal{H}_U$ covering just a single site as depicted in Fig. 5.2(a) [165]. We decompose $|\Psi\rangle$ according to Eq. [5.3] and obtain

$$|\Psi\rangle = \sum_{k_0}^{D_0} \lambda_{k_0}[0]\, |u_{k_0}[0]\rangle \otimes |v_{k_0}[1\ldots N-1]\rangle\,, \tag{5.4}$$

where $[0]$ labels the first site and $[1\ldots N-1]$ denotes the remaining $N-1$ sites. The sum over the *bond index* k_0 accounts for the D_0 coefficients $\lambda_{k_0}[0] \in \Lambda[0]$. D_0 is called the *bond dimension* satisfying $1 \leq D_0 \leq \chi$ for a decomposition with Schmidt rank χ. In essence, the bond dimension quantifies the amount of entanglement present between the two subspaces $\mathcal{H}_U$ and $\mathcal{H}_V$.

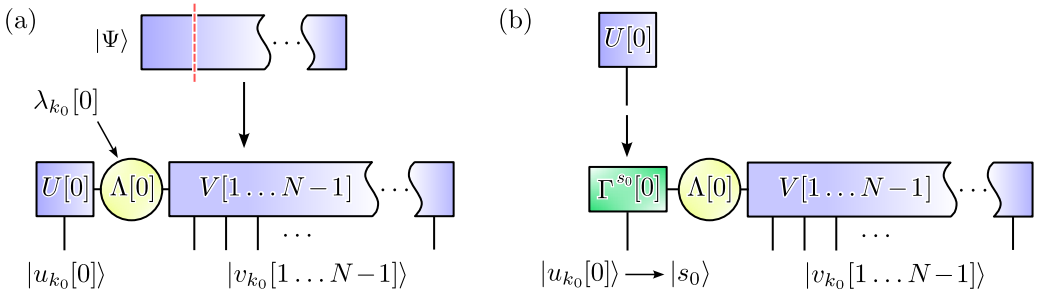


Figure 5.2: Schmidt decomposition of a quantum state $|\Psi\rangle$: (a) Graphical representation of Eq. [5.4]. The decomposition partitions the Hilbert space into the left and right subspaces $\mathcal{H}_U$ and $\mathcal{H}_V$, see Eq. [5.2]. $\mathcal{H}_U$ contains a single site denoted by $[0]$, while $[1\ldots N-1]$ labels the sites forming $\mathcal{H}_V$. The vectors $|u_{k_0}[0]\rangle \in \mathcal{H}_U$ and $|v_{k_0}[1\ldots N-1]\rangle \in \mathcal{H}_V$ correspond to the columns of the tensors $U[0]$ and $V[1\ldots N-1]$, respectively, and are illustrated as *downward-facing legs*. $\Lambda[0]$ is a diagonal matrix containing the Schmidt coefficients $\lambda_{k_0}[0]$. (b) A transformation $\Gamma^{s_0}[0]$ is applied to map the $|u_{k_0}[0]\rangle$ to the local spin basis $|s_0\rangle$.

We then apply a basis transformation [162, 163]

$$|u_{k_0}[0]\rangle = \sum_{s_0} \Gamma^{s_0}_{k_0}[0]\, |s_0\rangle\,, \tag{5.5}$$

which maps the left eigenvectors $|u_{k_0}[0]\rangle$ to the local spin basis $\{|s_0\rangle\}$ as illustrated in Fig. 5.2(b). The right eigenvectors $|v_{k_0}[1\ldots N-1]\rangle$ in Eq. [5.4] are decomposed further following Eq. [5.3], such that

$$|v_{k_0}[1\ldots N-1]\rangle = \sum_{k_1}^{D_1} \lambda_{k_1}[1]\, |u_{k_0,k_1}[1]\rangle \otimes |v_{k_1}[2\ldots N-1]\rangle\,. \tag{5.6}$$

Note that since $|v_{k_0}[1\ldots N-1]\rangle$ depends on the *first* bipartition, the $|u_{k_0,k_1}[1]\rangle$ of the *second* decomposition must retain the bond index k_0.

Combining Eq. [5.4] and Eq. [5.6] yields

$$\begin{aligned}|\Psi\rangle &= \sum_{k_0}^{D_0}\sum_{s_0}\lambda_{k_0}[0]\Gamma^{s_0}_{k_0}[0]\,|s_0\rangle \otimes \sum_{k_1}^{D_1}\lambda_{k_1}[1]\,|u_{k_0,k_1}[1]\rangle \otimes |v_{k_1}[2\dots N-1]\rangle \\ &= \sum_{k_0}^{D_0}\sum_{k_1}^{D_1}\sum_{s_0}\sum_{s_1}\lambda_{k_0}[0]\Gamma^{s_0}_{k_0}[0]\lambda_{k_1}[1]\Gamma^{s_1}_{k_0,k_1}[1]\,|s_0\rangle \otimes |s_1\rangle \otimes |v_{k_1}[2\dots N-1]\rangle\,,\end{aligned} \tag{5.7}$$

where we have applied another basis transformation $\Gamma^{s_1}[1]$ with coefficients $\Gamma^{s_1}_{k_0,k_1}[1]$ to bring the left eigenvectors $|u_{k_0,k_1}[1]\rangle$ into the basis $\{|s_1\rangle\}$, see Fig. 5.3(a).

This iterative decomposition ultimately leads to an expression of the form [162]

$$\begin{aligned}|\Psi\rangle = &\sum_{k_0}^{D_0}\dots\sum_{k_{N-2}}^{D_{N-2}}\sum_{s_0}\dots\sum_{s_{N-2}}\lambda_{k_0}[0]\Gamma^{s_0}_{k_0}[0]\lambda_{k_1}[1]\Gamma^{s_1}_{k_0,k_1}[1]\dots \\ &\dots\lambda_{k_{N-2}}[N-2]\Gamma^{s_{N-2}}_{k_{N-3},k_{N-2}}[N-2]\,|s_0,s_1,\dots s_{N-2}\rangle \otimes \underbrace{|v_{k_{N-2}}[N-1]\rangle}_{\sum_{s_{N-1}}\Gamma^{s_{N-1}}_{k_{N-2}}[N-1]|s_{N-1}\rangle} \\ = &\sum_{\{k_i\}}\sum_{\{|s_i\rangle\}}\lambda_{k_0}[0]\Gamma^{s_0}_{k_0}[0]\lambda_{k_1}[1]\Gamma^{s_1}_{k_0,k_1}[1]\dots|s_0,s_1,\dots,s_{N-1}\rangle\,,\end{aligned} \tag{5.8}$$

where the final basis transformation $\Gamma^{s_{N-1}}[N-1]$ acts on the right eigenvector $|v_{k_{N-2}}[N-1]\rangle$.

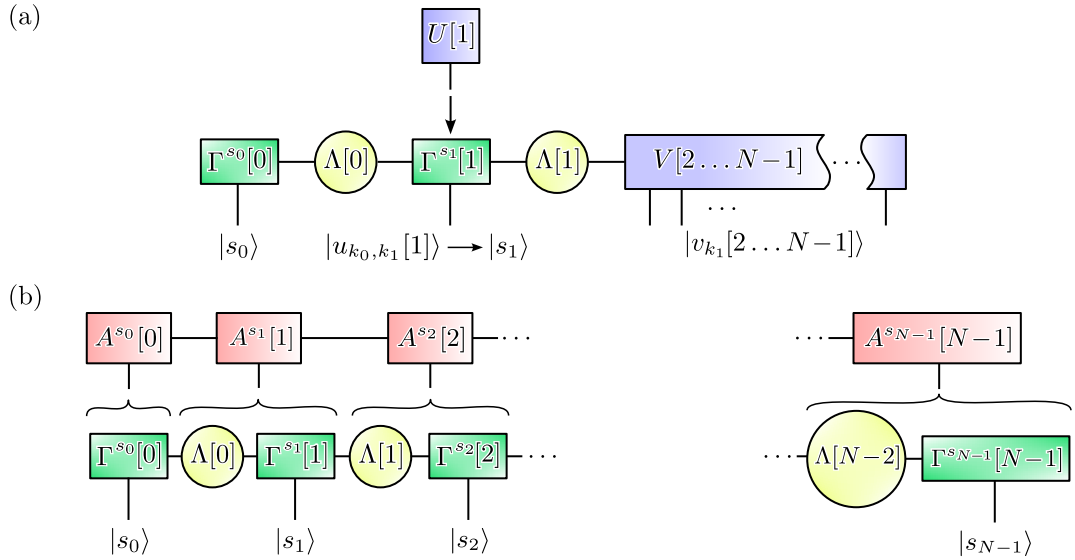


Figure 5.3: Decomposition of a quantum state: (a) Graphical representation of the second decomposition step in Eq. [5.7]. (b) The state is fully defined by $N-1$ diagonal matrices $\Lambda[i]$ and N basis transformations $\Gamma^{s_i}[i]$. The products $\Lambda[i-1]\Gamma^{s_i}[i]$ are contracted to form the tensors $A^{s_i}[i]$.

We inspect Eq. [5.8] more closely and define [162, 163]

$$\lambda_{k_{i-1}}[i-1]\cdot\Gamma^{s_i}_{k_{i-1},k_i}[i] = A^{s_i}_{k_{i-1},k_i}[i],$$

which are the elements of the matrices $A^{s_i}[i]$ illustrated in Fig. 5.3(b) fully characterizing the quantum state $|\Psi\rangle$. The shape of $A^{s_i}[i]$ is given by the bond dimensions connecting the

sites $i-1$ and i, i.e. $D_{i-1} \times D_i$. Thus, the $A^{s_i}[i]$ for $i \neq 0, N-1$ are matrices, while $A^{s_0}[0]$ and $A^{s_{N-1}}[N-1]$ must be vectors, since they only carry a single bond index k_0 and k_{N-2}, respectively.

The state $|\Psi\rangle$ can therefore be written as a product of these tensors, namely

$$\begin{aligned} |\Psi\rangle &= \sum_{\{s_i\}} \sum_{\{k_i\}}^{\{D_i\}} A^{s_0}_{k_0}[0] A^{s_1}_{k_0,k_1}[1] A^{s_2}_{k_1,k_2}[2] \dots A^{s_{N-1}}_{k_{N-2}}[N-1] \, |s_0, s_1, s_2, \dots s_{N-1}\rangle \,, \\ &= \sum_{\{s_i\}} A^{s_0}[0] A^{s_1}[1] \dots A^{s_{N-1}}[N-1] \, |s_0, s_1 \dots s_{N-1}\rangle \,. \end{aligned} \tag{5.9}$$

This representation of $|\Psi\rangle$ is known as an MPS. By comparison with Eq. [5.1], we identify the probability amplitudes

$$c_{s_0,s_1\dots,s_{N-1}} = A^{s_0}[0] \cdot A^{s_1}[1] \dots A^{s_{N-1}}[N-1] = \prod_{i=0}^{N-1} A^{s_i}[i] \in \mathbb{C}.$$

Note that this further underpins our previous claim about the dimension of the tensors on the edges of the spin chain: since $c_{s_0,s_1\dots,s_{N-1}}$ are complex scalars, the tensor $A^{s_0}[0]$ must be a row vector, while $A^{s_{N-1}}[N-1]$ must be a column vector.

We briefly acknowledge a formulation often found in the treatment of infinitely large systems and periodic structures [166, 167]. Here, one often employs *periodic boundary conditions* (PBCs): the first and last site of the spin chain become directly connected. Consequently, $A^{s_0}[0]$ and $A^{s_{N-1}}[N-1]$ also become matrices and $|\Psi\rangle$ is described by [160, 161]

$$|\Psi\rangle = \sum_{\{s_i\}} \mathrm{Tr}[A^{s_0}[0] A^{s_1}[1] \dots A^{s_{N-1}}[N-1]] \, |s_0, s_1, \dots s_{N-1}\rangle \,. \tag{5.10}$$

Example - the W state as an MPS

This recipe for the construction of an MPS is best described exemplified by considering a small system of three spins at sites $(0, 1, 2)$ in a W state, i.e.

$$|\Psi\rangle = \frac{1}{\sqrt{3}} \left(|100\rangle + |010\rangle + |001\rangle\right) = \frac{1}{\sqrt{3}} |0\rangle \otimes \left(|01\rangle + |10\rangle\right) + \frac{1}{\sqrt{3}} |1\rangle \otimes |00\rangle \,. \tag{5.11}$$

Following the recipe, we construct a matrix C of coefficients[1], mapping the local basis states $\{|s_0\rangle\} = \{|0\rangle, |1\rangle\}$ on site $i = 0$ to the joint system $\{|00\rangle, |01\rangle, |10\rangle, |11\rangle\}$.

$$C = \frac{1}{\sqrt{3}} \begin{array}{c} \begin{matrix} |00\rangle & |01\rangle & |10\rangle & |11\rangle \end{matrix} \\ \begin{pmatrix} 0 & 1 & 1 & 0 \\ 1 & 0 & 0 & 0 \end{pmatrix} \end{array} \begin{matrix} |0\rangle \\ |1\rangle \end{matrix} \tag{5.12}$$

Decomposing this matrix according to Eq. [5.2], we obtain the matrices U, Λ and V, highlighting the non-zero Schmidt coefficients in Λ in red; these are the coefficients we consider in the later steps.

$$U = \begin{pmatrix} 1 & 0 \\ 0 & 1 \end{pmatrix} = \left(|u_0[0]\rangle, |u_1[0]\rangle\right) \quad \Lambda = \begin{pmatrix} \sqrt{2}/\sqrt{3} & 0 & 0 & 0 \\ 0 & 1/\sqrt{3} & 0 & 0 \end{pmatrix} \quad V = \frac{1}{\sqrt{2}} \begin{pmatrix} 0 & \sqrt{2} & 0 & 0 \\ 1 & 0 & -1 & 0 \\ 1 & 0 & 1 & 0 \\ 0 & 0 & 0 & 1 \end{pmatrix}$$

1 We can identify the coefficients of C by explicitly writing the tensor product in Eq. [5.11] for the first site $i = 0$.

Since the columns of the matrix U are the eigenvectors $|u_0[0]\rangle = |0\rangle$ and $|u_1[0]\rangle = |1\rangle$, which are already in the local spin basis, the transformations $\Gamma_i^{s_0}[0]$ must be the identity. These are the *trivial* tensors

$$A^0[0] = \langle u_0[0]| = \langle 0| \qquad \text{and} \qquad A^1[0] = \langle u_1[0]| = \langle 1|$$

acting on the left edge of the spin chain; note that these must be row vectors, since they will be applied from the left.

With Λ having two non-zero coefficients, we only have to keep the first column vectors in V and consequently

$$V^T = \frac{1}{\sqrt{2}} \begin{array}{c} \begin{matrix} |00\rangle & |01\rangle & |10\rangle & |11\rangle \end{matrix} \\ \begin{pmatrix} 0 & 1 & 1 & 0 \\ \sqrt{2} & 0 & 0 & 0 \end{pmatrix} \end{array} = \begin{pmatrix} |v_0[1,2]\rangle \\ |v_1[1,2]\rangle\,, \end{pmatrix}$$

where the rows of V^T are the right eigenvectors $|v_i[1,2]\rangle$. This completes the first singular value decomposition, which explicitly reads

$$C = U\Lambda V^T = \Big(u_0[0],\ u_1[0]\Big) \cdot \frac{1}{\sqrt{3}} \begin{pmatrix} \sqrt{2} & 0 \\ 0 & 1 \end{pmatrix} \cdot \begin{pmatrix} v_0[1,2] \\ v_1[1,2] \end{pmatrix}.$$

We then continue with the first eigenvector $|v_0[1,2]\rangle$

$$|v_0[1,2]\rangle = \frac{1}{\sqrt{2}} \begin{array}{c} \begin{matrix} |00\rangle & |01\rangle & |10\rangle & |11\rangle \end{matrix} \\ \begin{pmatrix} 0 & 1 & 1 & 0 \end{pmatrix} \end{array} = \frac{1}{\sqrt{2}} \left(|01\rangle + |10\rangle\right)$$

and analogous to Eq. [5.12] write

$$C_0' = \frac{1}{\sqrt{2}} \begin{array}{c} \begin{matrix} |0\rangle & |1\rangle \end{matrix} \\ \begin{pmatrix} 0 & 1 \\ 1 & 0 \end{pmatrix} \end{array} \begin{matrix} |0\rangle \\ |1\rangle \end{matrix}$$

Upon multiplication with the associated Schmidt coefficient $\lambda_0 = \sqrt{\frac{2}{3}}$ we directly identify the tensor

$$A^0[1] = \frac{1}{\sqrt{3}} \begin{pmatrix} 0 & 1 \\ 1 & 0 \end{pmatrix}.$$

For the second eigenvector $|v_1[1,2]\rangle$ we obtain

$$C_1' = \begin{array}{c} \begin{matrix} |0\rangle & |1\rangle \end{matrix} \\ \begin{pmatrix} 1 & 0 \\ 0 & 0 \end{pmatrix} \end{array} \begin{matrix} |0\rangle \\ |1\rangle \end{matrix}$$

and with $\lambda_1 = \frac{1}{\sqrt{3}}$ we arrive at

$$A^1[1] = \frac{1}{\sqrt{3}} \begin{pmatrix} 1 & 0 \\ 0 & 0 \end{pmatrix}.$$

We are left to compute the $A^{s_2}[2]$ on the right edge of the spin chain, which must be column vectors such that the products $A^{s_0}[0]A^{s_1}[1]A^{s_2}[2]$ are scalars. Using the C_i' we identify

$$A^0[2] = |0\rangle \qquad \text{and} \qquad A^1[2] = |1\rangle$$

which are just the adjoints of $A^{s_0}[0]$. With these results the W-state in Eq. [5.11] can be represented as the MPS

$$\begin{aligned}|\Psi\rangle &= \sum_{s_i=\{0,1\}} A^{s_0}[0]A^{s_1}[1]A^{s_2}[2]\,|s_0,s_1,s_2\rangle \\ &= A^1[0]A^0[1]A^0[2]\,|100\rangle + A^0[0]A^1[1]A^0[2]\,|010\rangle + A^0[0]A^0[1]A^1[2]\,|001\rangle \\ &= \frac{1}{\sqrt{3}}\left(|100\rangle + |010\rangle + |001\rangle\right)\end{aligned}$$

5.1.3 *Valence bond picture*

An alternative approach to constructing an MPS is the *valence bond picture*, where each physical spin of dimension d is replaced by an *ancilla* with dimension $D > d$, i.e. virtual spins of higher dimension [160, 168]. Consider a spin at site i is connected to M neighboring sites as shown in Fig. 5.4(a) for $M = 2$. We place two ancillae on each site – one for each end of a *link* $(i, i \pm 1)$ – and prepare a maximally entangled state [160]

$$|\phi_{i,i\pm1}\rangle = \frac{1}{\sqrt{D}}\sum_{j=0}^{D-1}|j[i]\rangle \otimes |j[i\pm1]\rangle = \frac{1}{\sqrt{D}}\left(|00\rangle + \ldots |D-1, D-1\rangle\right), \qquad [5.13]$$

which establishes the so-called *valence bond* between the sites i and $i \pm 1$. Note that the local dimension of the ancillae at the end of one link must be identical $D[i] = D[i \pm 1] = D$.

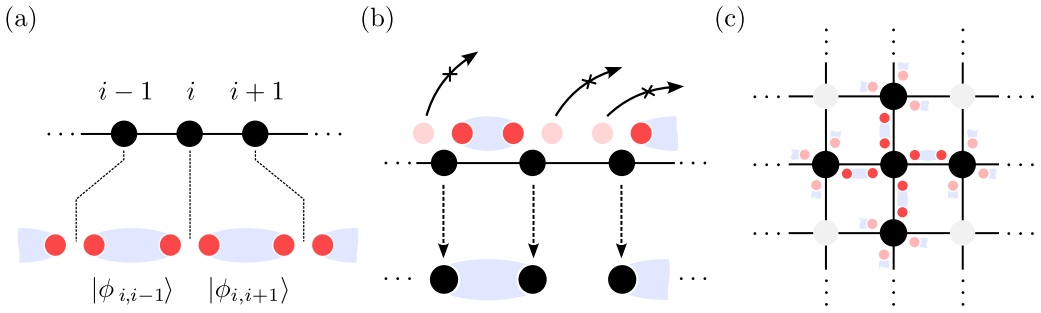


Figure 5.4: Construction of an MPS in the *valence bond picture*: (a) the physical d-dimensional spin on each site is replaced virtual spins or *ancillae* of higher dimension D, which are maximally entangled with the neighboring sites, forming a *valence bond* (blue) between connected sites. (b) the MPS is then obtained by *projection* into the local spin basis, hence MPS are *projected entangled pair states* (PEPS) in 1D. (c) this approach is intuitively scalable to higher spatial dimensions as shown here for a regular lattice in 2D.

The quantum state $|\Phi\rangle$ of the virtual system is then the tensor product over all *entangled pairs* of the ancillae Eq. [5.13]

$$|\Phi\rangle = \bigotimes_{i=1}^{N}|\phi_{i-1,i}\rangle\,,$$

and by successively applying local projection operators $\hat{P}_i$ of the form given in Eq. [5.14] we recover the physical state $|\Psi\rangle$ [160]. The local projections are shown schematically in

Fig.5.4(b), where the projection is chosen such that the sites $(i-1,i)$ and $(i+1,i+2)$ are entangled:

$$P[i] = \frac{1}{\sqrt{D}} \sum_{s_i} \sum_{\{|\phi_{i-1,i}\rangle\}} A^{s_i}_{i-1,i}[i] \, |s_i\rangle \langle \phi_{i,i-1}| \longrightarrow |\Psi\rangle = \left[\bigotimes_{i=1}^{N} P[i] \right] |\Phi\rangle \,. \tag{5.14}$$

From Eq. [5.14] we recover the MPS as readily defined in Eq. [5.1]. As we've constructed the state by local projections on entangled pairs of virtual spins, MPS are a subclass of *projected entangled pair states* (PEPS), which are their analogue in two spatial dimensions. The construction of PEPS is identical to the method discussed in this section, albeit with more ancillae on each site, see Fig. 5.4(c).

5.1.4 *Matrix product operators*

Up until this point we have only discussed MPS describing pure quantum states. In this section, we generalize the framework to mixed states, which are described by *matrix product density operators* (MPDOs) [160, 169]. We consider the MPS as defined by Eq. [5.9] and calculate

$$\begin{aligned} |\Psi\rangle \langle \Psi| &= \sum_{\{s_i\}} \sum_{\{s_i'\}} \cdot \sum_{\{k_i\}}^{D_i} \sum_{\{k_i'\}}^{D_i'} A^{s_0}_{k_0}[0] \dots A^{s_{N-1}}_{k_{N-2}}[N-1] A^{\dagger\, s'_{N-1}}_{k_{N-2}}[N-1] \dots A^{\dagger\, s'_0}_{k_0'}[0] \\ &\qquad \cdot |s_0, \dots, s_{N-1}\rangle \langle s_0', \dots, s_{N-1}'| \\ &= \sum_{\{s_i\}} \sum_{\{s_i'\}} M^{s_0,s_0'}[0] \dots M^{s_{N-1}s'_{N-1}}[N-1] \, |s_0, \dots, s_{N-1}\rangle \langle s_0', \dots, s_{N-1}'| = \varrho \end{aligned} \tag{5.15}$$

which is the MPDO of a pure state ϱ. The matrices $M^{s_i,s_i'}[i]$ are defined by the tensor product

$$M^{s_i,s_i'}[i] = \sum_{k_i}^{D_i} \sum_{k_{i+1}}^{D_{i+1}} A^{s_i}_{k_i,k_{i+1}}[i] \otimes A^{\dagger\, s_i'}_{k_i,k_{i+1}}[i] \tag{5.16}$$

and are specific to the local spin state $|s_i\rangle$ at the respective site i. Note that if we are given the $M^{s_i,s_i'}[i]$, we can recover the $A^{s_i}_{k_i,k_{i+1}}[i]$ by singular value decomposition [169]. The density matrix ϱ in Eq. [5.15] is necessarily positive-semidefinite since $|\Psi\rangle$ is pure. Note that by choosing the bond dimensions D_i and D_{i+1} sufficiently large, we can describe any density matrix [170].

We also seek to construct MPDOs representing mixed states, for which Eq. [5.15] is not *directly* applicable. However, we can always transform any mixed state into a pure MPS by virtually increasing the local dimension of the spins by adding a *local* ancilla $|a_i\rangle$, such that [171]

$$|\tilde{\Psi}\rangle = \sum_{\{s_i\}} \sum_{\{a_i\}} \prod_{i=0}^{N-1} A^{s_i,a_i}[i] \, |s_0 a_0, \dots, s_{N-1} a_{N-1}\rangle \tag{5.17}$$

with $|s_i a_i\rangle = |s_i\rangle \otimes |a_i\rangle$. It is important to emphasize that the MPDO $\tilde{\varrho} = |\tilde{\Psi}\rangle \langle \tilde{\Psi}|$ is defined on a larger Hilbert space; it *does not* describe the *physical* mixed state. However, we recover the MPDO ϱ describing our mixed state by tracing over the virtual ancillas

$$\varrho = \mathrm{Tr}_{\{a_i\}} \left[\tilde{\varrho} \right] .$$

By appropriate choice of the $M^{s_i,s_i'}[i]$ in Eq. [5.16] we can represent any general operator as a product of matrices [169]; such operators are hence called *matrix product operators* (MPOs). Moreover, if the MPOs are unitary, we speak of *matrix product unitaries* (MPU), which allow for an efficient representation of MPS algorithms analogous to the quantum circuit model discussed in Sec. 1.2.3.

A graphical representation of an MPU U_i is shown in Fig. 5.5(a): the unitary is illustrated as a square box, with a set of incoming and outgoing lines representing the spins. Let U_i be the i-th unitary in a larger MPU circuit $\prod_i U_i$, with U_{i-1} and U_{i+1} labeling the preceding and subsequent MPU, respectively. A set of spins $\{|s_i\rangle\}$ which have not been manipulated by U_{i-1} enter from the top, while those carried over from U_{i-1} enter from the left. After U_i has been applied, the pins partaking in U_{i+1} leave the box U_i to the right, and a set $\{|s_j'\rangle\}$ exits via the bottom edge, indicating that they will not be acted upon by U_{i+1} [160].

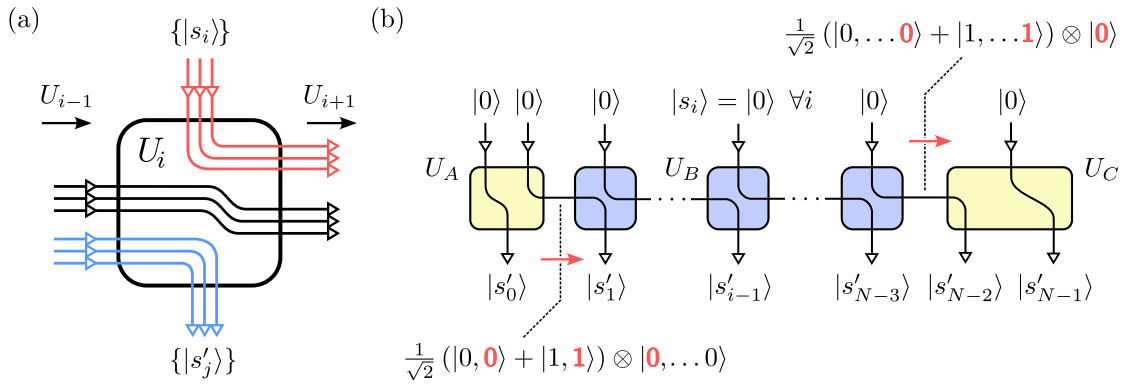


Figure 5.5: Graphical representation of *matrix product unitaries* (MPUs). (a) An MPU U_i is represented by a square box acting on a subset of spins illustrated by a set of lines. Spins $\{|s_i\rangle\}$ that have not been manipulated by the preceding MPU U_{i-1} enter from the top (red), while spins carried over from U_{i-1} enter from the left (black / blue). After U_i has been applied, spins partaking in the subsequent MPU U_{i+1} leave the box to the right (black / red), while spins $\{|s_j'\rangle\}$ not acted upon by U_{i+1} exit via the bottom (blue). (b) Example of an MPU algorithm preparing an N-spin GHZ state. All spins are initially prepared in the product state $|0,\ldots 0\rangle$. The MPU U_A is applied to the first spin pair, creating the GHZ state $1/\sqrt{2}(|00\rangle + |11\rangle)$ without acting on the remaining spins. The second spin is carried over to U_B, where it becomes entangled with the third spin, which is still in the state $|0\rangle$; both spins are highlighted in the expression below. U_B is then sequentially applied until the final two spins are entangled by U_C.

An example of an MPU algorithm is illustrated in Fig. 5.5(b): three unitaries $U_{A,B,C}$ are applied to a chain of N spins prepared in the state $|0,\ldots 0\rangle$ to implement a GHZ state, see Eq. [1.6]. U_A acts on the first two spins in the chain, creating the entangled state

$$U_A\,|0,\ldots 0\rangle = \frac{1}{\sqrt{2}}\,(|0,0\rangle + |1,1\rangle) \otimes |0,\ldots 0\rangle\,.$$

Only the second spin is carried over to the next MPU U_B, while the first spin labeled $|s_0'\rangle$ leaves the circuit, since it is not acted upon by the subsequent MPUs. After the final MPU U_C has been applied, the system is in the state

$$U_C U_B \ldots U_B U_A\,|0,\ldots 0\rangle = \frac{1}{\sqrt{2}}\,(|0,\ldots 0\rangle + |1,\ldots 1\rangle)\,.$$

The circuit diagram already gives some insight into the properties of the state: U_A and U_C only act on the first and the last spin, which we call the *edges* of the spin chain, while U_B acts on the *bulk*, i.e. the spins located in the center. Since U_B is applied sequentially on pairs of bulk spins, the state exhibits *translational invariance* – if we were to displace a spin deep inside the bulk by one site, the physical properties of the state would remain unchanged [169].

While certain properties of the MPS can be inferred from the MPU circuit diagram, we are interested in computing and later actually measuring physical quantities and correlation functions, which we will discuss in the following sections of this chapter.

5.1.5 *Expectation values*

Systems described by MPS are studied by computing *expectation values* $\langle \hat{O}[i] \rangle$ of *local* operators acting on a site i. A crucial ingredient in these calculations are *transfer matrices* [163, 172], which we will introduce in this section by looking at a practical example, namely the norm of an MPS $|\Psi\rangle$ illustrated by the diagram in Fig. 5.6(a).

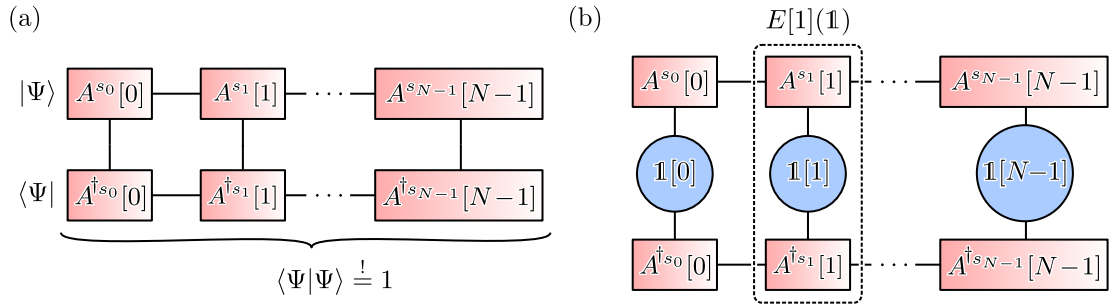


Figure 5.6: Graphical representation of the norm $\langle\Psi|\Psi\rangle = 1$ of an MPS: (a) The quantum state $|\Psi\rangle$ is shown in its MPS form, cf. Eq. [5.9]. Downward facing legs indicate a column vector, while the legs of its Hermitian conjugate – the row vector $\langle\Psi|$ – point upwards; the complex-valued matrices corresponding to $\langle\Psi|$ are also conjugated. (b) The norm is equivalent to the expectation value of the identity operator $\langle\Psi|\mathbb{1}|\Psi\rangle = 1$. Inserting local identity operators $\mathbb{1}[i]$ leads to the definition of the *transfer matrix* $E[i](\mathbb{1})$.

Since the state must obey $\langle\Psi|\Psi\rangle = 1$, this normalization condition is equivalent to the expectation value of the identity operator

$$\langle\Psi|\mathbb{1}|\Psi\rangle = \langle\Psi|\mathbb{1}[0]\cdot\mathbb{1}[1]\cdot\ldots\mathbb{1}[N-1]|\Psi\rangle \stackrel{!}{=} 1,$$

which must also hold for any site i on which a *local* identity operator $\mathbb{1}[i]$ acts on. Using the definition in Eq. [5.9] we compute

$$\langle\Psi|\Psi\rangle = \sum_{\{k_i\}}^{D_i}\sum_{\{k_i'\}}^{D_i'}\sum_{\{s_i\}}\sum_{\{s_i'\}} \langle\{s_i'\}|\, A^{\dagger\, s_{N-1}'}_{k_{N-2}}[N-1]\ldots A^{\dagger\, s_0'}_{k_0'}[0] A^{s_0}_{k_0}[0]\ldots A^{s_{N-1}}_{k_{N-2}}[N-1]\,|\{s_i\}\rangle\,, \tag{5.18}$$

where we have introduced the abbreviation $|\{s_i\}\rangle = |s_0,\ldots,s_{N-1}\rangle$. We then expand the sums over the N spins into the product

$$\sum_{\{s_i\}}|s_0,\ldots,s_{N-1}\rangle = \sum_{s_0}|s_0\rangle\otimes\sum_{s_1}|s_1\rangle\otimes\ldots\sum_{s_{N-1}}|s_{N-1}\rangle$$

and reorder Eq. [5.18]:

$$\langle\Psi|\Psi\rangle = \sum_{\{k_i\}}^{D_i}\sum_{\{k_i'\}}^{D_i'}\sum_{s_{N-1}'} A^{\dagger\, s_{N-1}'}_{k_{N-2}} \langle s_{N-1}'| \otimes \dots \\ \dots \sum_{s_0'} A^{\dagger\, s_0'}_{k_0'}[0]\, \langle s_0'| \sum_{s_0} A^{s_0}_{k_0}[0]\, |s_0\rangle \otimes \dots \\ \dots \sum_{s_{N-1}} A^{s_{N-1}}_{k_{N-2}}[N-1]\, |s_{N-1}\rangle\,. \tag{5.19}$$

Due to the orthonormality of the spin states $\langle s_i'|s_i\rangle = \delta_{s_i',s_i}$ Eq. [5.19] further simplifies to

$$\langle\Psi|\Psi\rangle = \sum_{\{k_i\}}^{D_i}\sum_{\{k_i'\}}^{D_i'}\sum_{s_{N-1}} A^{\dagger\, s_{N-1}}_{k_{N-2}}[N-1]\left(\dots\left(\sum_{s_0} A^{\dagger\, s_0}_{k_0'}[0]A^{s_0}_{k_0}[0]\right)\dots\right)A^{s_{N-1}}_{k_{N-2}}[N-1] \tag{5.20}$$

and we identify expressions of the form [163, 172]

$$\sum_{s_i} A^{\dagger\, s_i}_{k_{i-1}',k_i'}[i]A^{s_i}_{k_{i-1},k_i}[i] = E_{k_{i-1}',k_i',k_{i-1},k_i}[i](\mathbb{1}). \tag{5.21}$$

These are coefficients of the *transfer matrix* $E[i](\mathbb{1})$ associated with the identity operator, which is defined as the tensor product

$$E[i](\mathbb{1}) = \sum_{s_i} A^{\dagger\, s_i}[i] \otimes A^{s_i}[i]. \tag{5.22}$$

We then order Eq. [5.20] incrementally with respect to the sites and obtain

$$\langle\Psi|\Psi\rangle = \sum_{\{k_i\}}^{D_i}\sum_{\{k_i'\}}^{D_i'} E_{k_0',k_0}[0](\mathbb{1})E_{k_0',k_1',k_0,k_1}[1](\mathbb{1})E_{k_1',k_2',k_1,k_2}[2](\mathbb{1})\dots E_{k_{N-2}',k_{N-2}}[N-1](\mathbb{1}) \overset{!}{=} 1 \tag{5.23}$$

which must be equal to unity since the quantum state $|\Psi\rangle$ must be normalized.

Any pair of coefficients associated with transfer matrices supported on neighboring sites i and $i+1$ shares two bond indices k_i and k_i'. Summing over these indices yields a *contraction* of the form

$$\sum_{k_i'}\sum_{k_i} E_{k_{i-1}',\mathbf{k_i'},k_{i-1},\mathbf{k_i}}[i]E_{\mathbf{k_i'},k_{i+1}',\mathbf{k_i},k_{i+1}}[i+1] = E'_{k_{i-1}',k_{i+1}',k_{i-1},k_{i+1}}.$$

By sequentially contracting the tensors in Eq. [5.23] the norm of the quantum state can be written as the trace over the product of transfer matrices [163]

$$\langle\Psi|\Psi\rangle = \mathrm{Tr}[E[0](\mathbb{1})E[1](\mathbb{1})\dots E[N-1](\mathbb{1})] = 1. \tag{5.24}$$

This concept can be generalized to any local operator $\hat{O}[j]$. Computing its expectation value $\langle\hat{O}[j]\rangle = \langle\Psi|\hat{O}[j]|\Psi\rangle$ yields an expression analogous to Eq. [5.19] – however, at site j we obtain

$$\sum_{s_j'}\sum_{s_j}\langle s_j'|\hat{O}[j]|s_j\rangle\, A^{\dagger\, s_j'}_{k_{j-1}',k_j',k_{j-1},k_j}A^{s_j}_{k_{j-1}',k_j',k_{j-1},k_j} = E_{k_{j-1}',k_j',k_{j-1},k_j}[j](\hat{O}).$$

These coefficients define the transfer matrix associated with the operator $\hat{O}[i]$ as [163, 173]

$$E[j](\hat{O}) = \sum_{s_j'}\sum_{s_j}\langle s_j'|\hat{O}[j]|s_j\rangle\, A^{\dagger\, s_j'}[j] \otimes A^{s_j}[j]. \tag{5.25}$$

Analogous to Eq. [5.24] the expectation value is then given by [163]

$$\langle\hat{O}[j]\rangle = \mathrm{Tr}[E[0](\mathbb{1})\dots E[j](\hat{O})\dots E[N-1](\mathbb{1})] = \mathrm{Tr}[E[j](\hat{O})]. \tag{5.26}$$

5.1.6 *Correlations and correlation length*

Of particular interest are the expectation values of *products* of local operators $\hat{O}[i]$ and $\hat{O}[j]$ acting on two sites separated by a distance $c = |i - j|$. Such quantities are relevant when investigating *correlations* in quantum many-body systems. We first look at

$$\begin{aligned}\langle \hat{O}[i]\hat{O}[j]\rangle &= \langle \Psi|\hat{O}[i]\hat{O}[j]|\Psi\rangle \\ &= \mathrm{Tr}\left[E[0]\dots E[i-1]E[i](\hat{O})E[i+1]\dots \right. \\ &\qquad \left. \dots E[j-1]E[j](\hat{O})E[j+1]\dots E[N-1]\right]\end{aligned} \tag{5.27}$$

and assume, for simplicity, that the quantum state $|\Psi\rangle$ is translationally invariant, such that all identity transfer matrices are identical

$$E[i](\mathbb{1}) = E(\mathbb{1})$$

for any site i. Since the trace operation is cyclic [43], Eq. [5.27] simplifies to

$$\begin{aligned}\langle \hat{O}[i]\hat{O}[j]\rangle &= \mathrm{Tr}[E[i](\hat{O})\underbrace{E(\mathbb{1})\dots E(\mathbb{1})}_{c-1 \text{ times}}E[j](\hat{O})\underbrace{E(\mathbb{1})\dots E(\mathbb{1})}_{N-c-1 \text{ times}}] \\ &= \mathrm{Tr}\left[E[i](\hat{O})E(\mathbb{1})^{c-1}E[j](\hat{O})E(\mathbb{1})^{N-c-1}\right]\end{aligned} \tag{5.28}$$

and we are left with computing $E^{c-1}(\mathbb{1})$ and $E^{N-c-1}(\mathbb{1})$. We use the spectral decomposition

$$E(\mathbb{1}) = \sum_k \lambda_k |u_k\rangle \langle v_k|$$

and compute the product of $n \in \mathbb{N}$ transfer matrices [163]

$$\underbrace{E(\mathbb{1})\dots E(\mathbb{1})}_{n \text{ times}} = E^n(\mathbb{1}) = \prod_{i=1}^{n}\sum_{k_i}\lambda_{k_i}|u_{k_i}\rangle\langle v_{k_i}| = \sum_k \lambda_k^n |u_k\rangle\langle v_k|\,, \tag{5.29}$$

where we have used the pair-wise orthonormality of the left and right eigenvectors $|u_k\rangle$ and $|v_k\rangle$, respectively, see Sec. 5.1.1. Sorting the eigenvalues such that $\lambda_0 \geq \lambda_1 \geq \dots$, we write Eq. [5.29] as

$$E^n(\mathbb{1}) = \lambda_0^n |u_0\rangle\langle v_0| + \lambda_0^n \sum_{k>0}\left(\frac{\lambda_k}{\lambda_0}\right)^n |u_k\rangle\langle v_k|\,. \tag{5.30}$$

Since for any $k > 0$ the fraction λ_k/λ_0 is smaller than unity, only a few terms in Eq. [5.30] are significant, even more so in the limit of large n.

We return to Eq. [5.28] and note that the distance c between the sites is small compared to N. It is therefore appropriate to approximate

$$E^{N-c-1}(\mathbb{1}) \approx \lambda_0^{N-c-1}|u_0\rangle\langle v_0|$$

while we also consider the first eigenvalue $\lambda_1 < \lambda_0$ for $E^{c-1}(\mathbb{1})$, such that

$$E^{c-1}(\mathbb{1}) \approx \lambda_0^{c-1}\left(|u_0\rangle\langle v_0| + \left(\frac{\lambda_1}{\lambda_0}\right)^{c-1}|u_1\rangle\langle v_1|\right).$$

Inserting these approximations into Eq. [5.28] we obtain

$$\begin{aligned}\langle \hat{O}[i]\hat{O}[j]\rangle &= \mathrm{Tr}\left[E[i](\hat{O})E(\mathbb{1})^{c-1}E[j](\hat{O})E(\mathbb{1})^{N-c-1}\right] \\ &= \lambda_0^N \,\mathrm{Tr}\left[E[i](\hat{O})\,|u_0\rangle\langle v_0|\,E[j](\hat{O})\,|u_0\rangle\langle v_0|\right] \\ &\quad + \lambda_0^N \left(\frac{\lambda_1}{\lambda_0}\right)^{c-1} \mathrm{Tr}\left[E[i](\hat{O})\,|u_1\rangle\langle v_1|\,E[j](\hat{O})\,|u_0\rangle\langle v_0|\right].\end{aligned} \tag{5.31}$$

Using the definition in Eq. [5.24] we conclude that if we only keep the dominant eigenvalue λ_0 in the spectral decomposition of the product $E^n(\mathbb{1})$, the norm must satisfy

$$\langle\Psi|\Psi\rangle = \mathrm{Tr}\left[E^N(\mathbb{1})\right] = \lambda_0^N \mathrm{Tr}\left[|u_0\rangle\langle v_0|\right] \overset{!}{=} 1$$

and therefore, λ_0 must be equal to unity for the quantum state to be normalized[2]. Eq. [5.31] then simplifies to [163]

$$\langle \hat{O}[i]\hat{O}[j]\rangle = \langle \hat{O}[i]\rangle\langle \hat{O}[j]\rangle + \left(\frac{\lambda_1}{\lambda_0}\right)^{c-1} \mathrm{Tr}\left[E[i](\hat{O})\,|u_1\rangle\langle v_1|\,E[j](\hat{O})\,|u_0\rangle\langle v_0|\right],$$

where the second term decays with the distance $c = |i-j|$ since $\lambda_0 > \lambda_1$. In fact, the correlations

$$C(\hat{O}[i],\hat{O}[j]) = \langle \hat{O}[i]\hat{O}[j]\rangle - \langle \hat{O}[i]\rangle\langle \hat{O}[j]\rangle$$

decay *exponentially* with characteristic *correlation length* [160, 163]

$$\xi = -\frac{1}{\log(\lambda_1)}. \tag{5.32}$$

This result is one of the fundamental properties of an MPS: correlations are *short-ranged* and *decay exponentially* with correlation length ξ. One may therefore assume, that phenomena in one-dimensional spin chains are localized. However, we will see later in this chapter, that *global properties* can emerge from local interactions and short-ranged correlations.

5.2 HAMILTONIANS AND GROUND STATES OF MANY-BODY SYSTEMS

When studying many-body systems in the limit of low energies, their spins often interact only with a few select neighbors. Hamiltonians describing such systems are said to be *k-local* and can be written as

$$\hat{H} = \sum_i \hat{H}_i,$$

where each $\hat{H}_i$ acts on $k \in \mathbb{N}$ spins [160, 174]. Prime examples include the Heisenberg model and its generalizations [175, 176].

In k-local systems it might therefore be sufficient to consider just a small number of spins and perform sets of *local* measurements to study *global* properties. In this section we will argue that the ground states of any k-local Hamiltonian, whose spectrum exhibits a finite *energy gap* ΔE above the ground state, can be efficiently described by an MPS.

2 Note that $\mathrm{Tr}[|u_0\rangle\langle v_0|] = \langle v_0|u_0\rangle \overset{!}{=} 1$ since the left and right eigenvectors are pair-wise orthonormal, see Eq. [5.30] and Sec. 5.1.1.

5.2.1 *Spectral gaps lead to exponentially decaying correlations*

Let us consider a k-local Hamiltonian $\hat{H} = \sum_i \hat{H}_i$ and its non-degenerate ground state $|\Psi_0\rangle$, satisfying $\hat{H}|\Psi_0\rangle = E_0|\Psi_0\rangle$. We assume that the spectrum of $\hat{H}$ exhibits a finite gap $\Delta E = E_1 - E_0$, separating the first excited state $|\Psi_1\rangle$ with energy E_1 from the ground state. Moreover, we assume that the Hamiltonian is *frustration-free*, meaning that $|\Psi_0\rangle$ is the simultaneous ground state of all local $\hat{H}_i$ with energy $E_{0,i}$.

Following the arguments made by Aharonov et al. in Ref. [177] and Ref. [178] one can show that correlations in the ground state of a gapped k-local Hamiltonian decay exponentially. Without loss of generality, we shift the energy scale such that

$$E_0 = E_{0,i} = 0$$

and assume that the $\hat{H}_i$ are projectors satisfying

$$\forall i: \ \hat{H}_i|\Psi_0\rangle = 0 \longrightarrow \hat{H}|\Psi_0\rangle = \sum_i \hat{H}_i|\Psi_0\rangle = 0.$$

We then define the operator [177]

$$\hat{\Pi} = \prod_i (\mathbb{1} - \hat{H}_i) = \prod_i \hat{P}_i, \tag{5.33}$$

which approximates the ground state projector $|\Psi_0\rangle\langle\Psi_0|$. Since two $\hat{H}_i$ supported on the same sites do not necessarily commute, Eq. [5.33] depends on the chosen ordering of the individual terms. It is thus convenient to partition the system into *layers* [178]

$$L = \{i \mid \forall j \in L : [\hat{P}_i, \hat{P}_j] = 0\},$$

for which any pair of projectors $\hat{P}_i$ and $\hat{P}_j$ commute. We then write Eq. [5.33] as the ordered product

$$\hat{\Pi} = \prod_k \hat{\Pi}_{L_k} = \prod_k \prod_{i \in L_k} \hat{P}_i, \tag{5.34}$$

where each $\hat{\Pi}_{L_k}$ is associated with its respective layer L_k. An example for a 2-local Hamiltonian is illustrated in Fig. 5.7 [178].

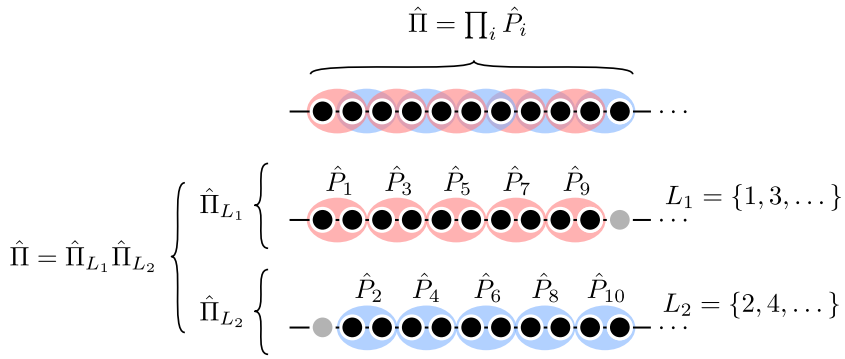


Figure 5.7: Partitioning of the approximate ground state projector $\hat{\Pi}$ of a 2-local Hamiltonian into two layers L_1 and L_2, which are chosen such that any pair of projectors $\hat{P}_i$ and $\hat{P}_j$ within the same layer commute. The projectors $\hat{\Pi}_1$ and $\hat{\Pi}_2$ are defined as the products of the $\hat{P}_i$ belonging to layers L_1 (red) and L_2 (blue), respectively.

We now consider any state $|\Phi\rangle$ that is *not* a ground state of at least one of the local terms $\hat{H}_j$, i.e. there exists a j for which $\hat{H}_j |\Phi\rangle \neq 0$. It then follows that[3]

$$\|\hat{P}_j |\Phi\rangle\|^2 = \langle\Phi|\hat{P}_j^2|\Phi\rangle = \langle\Phi|\hat{P}_j|\Phi\rangle = 1 - \langle\Phi|\hat{H}_j|\Phi\rangle < 1,$$

since $\langle\Phi|\hat{H}_j|\Phi\rangle > 0$ and consequently

$$\|\hat{\Pi} |\Phi\rangle\|^2 = \langle\Phi|\hat{\Pi}|\Phi\rangle < 1. \tag{5.35}$$

The projectors $\hat{P}_j$ therefore penalize any state other than the exact ground state $|\Psi_0\rangle$ of $\hat{H}$ by reducing its norm, while leaving $|\Psi_0\rangle$ invariant. It has been shown that the upper bound on the norm in Eq. [5.35] is given by [177, 178]

$$\|\Pi |\Phi\rangle\| \leq \frac{1}{(1 + \Delta E/\Omega(k))^{1/3}} < 1, \tag{5.36}$$

where ΔE is the aforementioned spectral gap and $\Omega(k)$ is a function that depends on the k-locality of the Hamiltonian; this inequality is known as the *detectability lemma*.

Now let $|\Phi\rangle$ be orthogonal to $|\Psi_0\rangle$ and consider the state

$$|\Psi\rangle = a |\Psi_0\rangle + b |\Phi\rangle \qquad \text{with} \qquad a, b \in \mathbb{C} : \ |a|^2 + |b|^2 = 1. \tag{5.37}$$

After applying the approximate ground state projector $\hat{\Pi}$ in Eq. [5.33] the state

$$\hat{\Pi} |\Psi\rangle = a |\Psi_0\rangle + b \cdot \hat{\Pi} |\Phi\rangle$$

is not normalized, since according to Eq. [5.35] its norm is less than unity:

$$\|\hat{\Pi} |\Psi\rangle\|^2 = \langle\Psi|\hat{\Pi}|\Psi\rangle = a \langle\Psi|\Psi_0\rangle + b \langle\Psi|\hat{\Pi}|\Phi\rangle = |a|^2 + |b|^2 \cdot \|\hat{\Pi} |\Phi\rangle\|^2 < 1.$$

We thus must normalize $\hat{\Pi} |\Psi\rangle$ to obtain a valid quantum state $|\Psi'\rangle$

$$|\Psi'\rangle = \frac{\hat{\Pi} |\Psi\rangle}{\|\hat{\Pi} |\Psi\rangle\|} = \frac{a}{\|\hat{\Pi} |\Psi\rangle\|} |\Psi_0\rangle + \frac{b}{\|\hat{\Pi} |\Psi\rangle\|} \hat{\Pi} |\Phi\rangle .$$

By inspection of the probability amplitudes, we observe that $|\Psi'\rangle$ now has a *larger* overlap with the exact ground state $|\Psi_0\rangle$ than $|\Psi\rangle$

$$\frac{|a|}{\|\hat{\Pi} |\Psi\rangle\|} > |a| \qquad \text{since} \qquad \|\hat{\Pi} |\Psi\rangle\|^2 < 1$$

and simultaneously, the contribution of $|\Phi\rangle$ in $|\Psi'\rangle$ becomes *smaller*. Therefore, applying Eq. [5.33] m times yields an increasingly better approximation of the exact ground state projector $|\Psi_0\rangle \langle\Psi_0|$ [177, 178]

$$\underbrace{\hat{\Pi}\hat{\Pi}\hat{\Pi}\ldots}_{m \text{ times}} = \hat{\Pi}^m \approx |\Psi_0\rangle \langle\Psi_0| + \epsilon(m) \tag{5.38}$$

up to an error $\epsilon(m)$, which depends on the spectral gap as the change in magnitude of the probability amplitudes with each projection is bounded by Eq. [5.36].

3 Since the $\hat{P}_j$ are projectors, they must satisfy $\hat{P}_j^\dagger \hat{P}_j = \hat{P}_j^2 = \hat{P}_j$ for any j.

This approximation of the ground state projector in Eq. [5.38] is used to show the exponential decay of correlations in systems that are described by a k-local Hamiltonian $\hat{H}$ [178]. Let $\hat{O}[i]$ be an operator acting on the i-th spin in a 1D chain. Since $\hat{O}[i]$ is local, it commutes with all but k local terms $\hat{H}_j$ of $\hat{H}$, and consequently with all but k projectors $\hat{P}_l$ in $\hat{\Pi}$, see Eq. [5.33]. By partitioning $\hat{\Pi}$ into layers according to Eq. [5.34] one can illustrate how a perturbation introduced by $\hat{O}[i]$ will propagate through the spin chain: each successive application of $\hat{\Pi}$ causes the perturbation to spread further, forming a *causality cone* as depicted in Fig. 5.8 [178, 179].

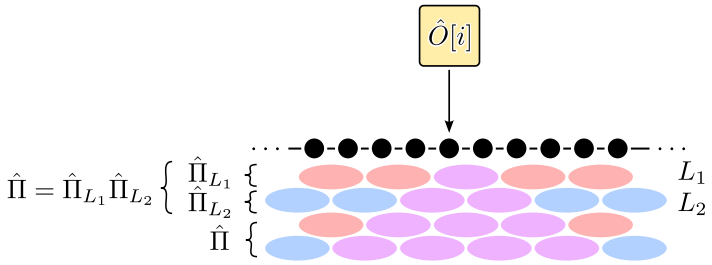


Figure 5.8: Propagation of perturbations in a 1D spin chain: consider a 2-local Hamiltonian and the approximate ground state projector $\hat{\Pi}$, which is partitioned into two layers L_1 (red) and L_2 (blue) with projectors $\hat{\Pi}_{L_1}$ and $\hat{\Pi}_{L_2}$, respectively, cf. Fig. 5.7. The local operator $\hat{O}[i]$ introduces a perturbation that propagates further outwards each time $\hat{\Pi}$ is applied, forming a *causality cone* (magenta).

Upon closer inspection of $\hat{\Pi}$ we note that any projector $\hat{P}_l$, which is not supported on the site i, readily commutes with $\hat{O}[i]$. Moreover, since in a frustration-free Hamiltonian $|\Phi_0\rangle$ is the simultaneous ground state to all local terms $\hat{H}_i$, $\hat{P}_l$ satisfies

$$\hat{P}_l\hat{O}[i]\,|\Psi_0\rangle = \hat{O}[i]\hat{P}_l\,|\Psi_0\rangle = |\Psi_0\rangle\,. \tag{5.39}$$

We then introduce a second operator $\hat{O}[j]$ acting on the spin j, which is separated from the site i by a distance $c = |i - j|$. As illustrated in Fig. 5.9, a perturbation caused by $O[i]$ has propagated to site j once $\hat{\Pi}$ – partitioned according to Eq. [5.34] – has been applied m times. Evidently, the number of projections necessary to cover the distance c is proportional to m [178]: the further both sites i and j are apart, the more projections must be applied.

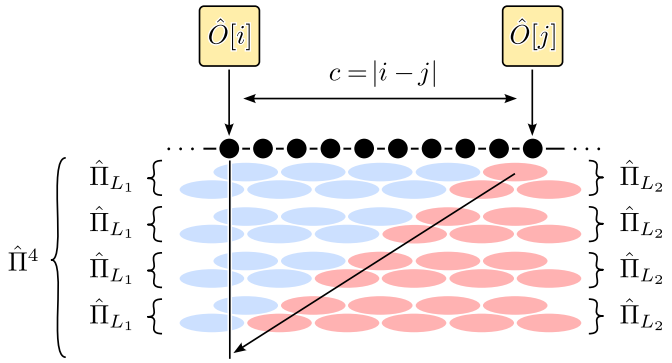


Figure 5.9: Decay of correlations in a 1D spin chain subject to a 2-local Hamiltonian. The operators $\hat{O}[i]$ and $\hat{O}[j]$, each acting on the spins i and j, respectively, introduce perturbations in the system; both spins are separated by a distance $c = |i - j|$. The perturbation caused by $\hat{O}[j]$ has spread to the site i after the operator $\hat{\Pi}$ has been applied $m = 4$ times.

Suppose we partition $\hat{\Pi}$ similarly to Eq. [5.34] into two layers L_1 and L_2, such that [178]

$$L_1 = \{i \mid \forall k \in L\colon \left[\hat{P}_k, \hat{O}[j]\right] = 0\} \quad \text{and} \quad L_2 = \{i \mid \forall k \in L\colon \left[\hat{P}_k, \hat{O}[i]\right] \neq 0\},$$

see Fig. 5.9. With this partition $\hat{\Pi} = \hat{\Pi}_{L_2}\hat{\Pi}_{L_1}$ satisfies

$$\hat{\Pi}_{L_2}\hat{\Pi}_{L_1}\hat{O}[j]\,|\Psi_0\rangle = \hat{\Pi}_{L_2}\hat{O}[j]\hat{\Pi}_{L_1}\,|\Psi_0\rangle = \hat{\Pi}_{L_2}\hat{O}[j]\,|\Psi_0\rangle\,,$$

since $\hat{\Pi}_{L_1}$ must by definition commute with $\hat{O}[j]$; the operator $\hat{\Pi}_{L_1}$ is *outside* of the causality cone of $O[j]$. In contrast, $\hat{\Pi}_{L_2}$ commutes with $\hat{O}[i]$, and thus

$$\langle\Psi_0|\hat{O}[i]\hat{\Pi}\hat{O}[j]|\Psi_0\rangle = \langle\Psi_0|\hat{O}[i]\hat{\Pi}_2\hat{\Pi}_1\hat{O}[j]|\Psi_0\rangle = \langle\Psi_0|\hat{O}[i]\hat{O}[j]|\Psi_0\rangle\,.$$

Such a partitioning is applied to the projector $\hat{\Pi}^m$ in Eq. [5.38]. We arrange the layers exactly as illustrated in Fig. 5.9 and compute the expectation value of $\hat{O}[i]\hat{O}[j]$ with respect to the ground state $|\Psi_0\rangle$ [178]

$$\begin{aligned}\langle\Psi_0|\hat{O}[i]\hat{O}[j]|\Psi_0\rangle &= \langle\Psi_0|\hat{O}[i]\hat{\Pi}^m\hat{O}[j]|\Psi_0\rangle \\ &\approx \langle\Psi_0|\hat{O}[i]\left\{|\Psi_0\rangle\langle\Psi_0| + \epsilon(m)\right\}\hat{O}[j]|\Psi_0\rangle \\ &= \langle\Psi_0|\hat{O}[i]|\Psi_0\rangle\langle\Psi_0|\hat{O}[j]|\Psi_0\rangle + f(\epsilon(m))\end{aligned} \qquad [5.40]$$

$$\langle\hat{O}[i]\hat{O}[j]\rangle_0 \approx \langle\hat{O}[i]\rangle_0\langle O[j]\rangle_0 + f(\epsilon(m)),$$

where $f(\epsilon(m))$ is a function that depends on the error $\epsilon(m)$ introduced by the approximation of the ground state projector.

It has been shown by Aharonov et al. in Ref. [178] that $f(\epsilon(m))$ is given by

$$f(\epsilon(m)) = \|\hat{O}[i]\|\cdot\|\hat{O}[j]\|e^{-g(m)}$$

for a function $g(m)$. Since the number of projections m one has to apply until a perturbation introduced by $\hat{O}[j]$ has propagated to the site i depends on the separation of the sites $c = |i - j|$ we conclude that $m \propto c$ and let $g(m) = h(c)$. Using Eq. [5.40] we compute the correlation function

$$C(\hat{O}[i], \hat{O}[j])_0 = \langle\hat{O}[i]\hat{O}[j]\rangle_0 - \approx \langle\hat{O}[i]\rangle_0\langle O[j]\rangle_0 \approx \|\hat{O}[i]\|\cdot\|\hat{O}[j]\|e^{-h(c)}, \qquad [5.41]$$

which decays exponentially with a function $h(c)$.

Following the arguments in Ref. [178] we have shown that correlations in the ground state indeed decay exponentially. The exponential dependence can be naively explained by noting that the each time the projector is applied, the fraction of $|\Phi\rangle$ in Eq. [5.37] shrinks by a constant factor k. Thus the probability amplitude $b(m)$ depends on the number of projections m and satisfies

$$\frac{\mathrm{d}}{\mathrm{d}m}b(m) = -kb(m)$$

which is the familiar differential equation for an exponential decay; for a rigorous argument see Ref. [178]. Associated with this decay is a characteristic decay constant labeled ξ – the so-called *correlation length* – that depends on the inverse of the energy gap [178]

$$\xi = \mathcal{O}\left(\frac{1}{\Delta E}\right)$$

as a consequence of the detectability lemma Eq. [5.36]. Note that in the beginning of this section we have assumed that our Hamiltonian $\hat{H}$ is frustration-free, which imposes a strong restriction on the system. However, it has been shown by Hastings and Koma in Ref. [179] and by Nachtergaele and Sims in Ref. [180] that Eq. [5.41] also holds in frustrated systems.

We emphasize the importance of this result: exponentially decaying correlations in the ground state are a characteristic property of a k-local Hamiltonian, whose spectrum exhibits a gap[4] – i.e. the ground state manifold is separated by a finite energy gap from the first excited states [179]. Such a gap is a prominent fingerprint of *topological quantum phases*[5] [181, 182], a concept that we will discuss later in Sec. 5.3.2 of this chapter. Moreover, k-local Hamiltonians are naturally compatible with the MPS formalism, which provides an efficient framework to study its properties [179, 183]. In particular, for any MPS we can construct a frustration-free *parent Hamiltonian* [160, 168]. The energy gap also allows us to employ a certain class of quantum algorithms [184], which allow us to approximate the exact ground state of $\hat{H}$ on a quantum simulator. These algorithms are discussed in the upcoming section and are later implemented on our hardware to experimentally study quantum phase transitions in Ch. 6 and lattice gauge theories in Ch. 8.

5.2.2 *Approximating ground states with variational algorithms*

It has been shown, that the problem of finding the ground state to k-local Hamiltonians is computationally hard [185, 186]. Good approximations can be obtained by variational algorithms [187, 188], however convergence cannot be guaranteed to be achieved with practically available resources; at worst, an algorithm converges in exponential time. However, we might be able to distribute the workload onto systems, which are by design better suited to carry out the individual parts of the computation: the quantum state is evaluated on a *quantum device*, while the optimization procedure is carried out classically based on the measurement outcomes obtained from the quantum system. Such strategies are covered under the umbrella of *variational quantum algorithms* (VQA) [184], which we will briefly introduce in this section.

VQAs are tailored to solve a specific problem encoded in an *ansatz*, which is motivated by the symmetries and the structure of the entanglement. The ansatz yields a *parametrized* unitary $U(\boldsymbol{\theta})$ for a set of parameters $\boldsymbol{\theta} = \{\theta_i\}$, which can be decomposed into a circuit of quantum gates $U_j(\boldsymbol{\theta}_j)$ [184]

$$U(\boldsymbol{\theta}) = \prod_j U_j(\boldsymbol{\theta}_j). \qquad [5.42]$$

Each U_j is itself tuned by a subset of parameters $\boldsymbol{\theta}_j = \{\theta_j\} \subset \boldsymbol{\theta}$. In a digital quantum qudit processor, the $\boldsymbol{\theta}$ are rotation angles controlling sequences of single qudit and entangling gates.

Studying the ground states of k-local Hamiltonians $\hat{H} = \sum_k \hat{H}_k$, the goal of a VQA is to approximate the eigenstate of $\hat{H}$ with the lowest energy E_0; these algorithms are hence known as *variational quantum eigensolvers* (VQEs) [184]. The unitaries in Eq. [5.42] given by

4 The converse is also true: correlations in the ground state of a k-local gapped Hamiltonian decay exponentially.
5 Note that topological properties do not necessarily require that the Hamiltonian is gapped, see for example the gapless topological superconductor studied in Ref. [181].

$U_j(\boldsymbol{\theta}_j) = \prod_k e^{-i\theta_{j,k}\hat{H}_k}$ and are consequently themselves k-local. On a system of N spins, the circuit generates a parametrized quantum state

$$|\Psi(\boldsymbol{\theta})\rangle = U_0(\boldsymbol{\theta}_0)U_1(\boldsymbol{\theta}_1)\dots U_m(\boldsymbol{\theta}_m)\,|s_0,\dots s_{N-1}\rangle \qquad [5.43]$$

from a generic initial state $|s_0,\dots s_{N-1}\rangle$. Comparing the two equations Eq. [5.43] and Eq. [5.9] in Sec. 5.1.2 it becomes apparent, that $|\Psi\rangle$ is a MPS, where the unitaries $U_j(\boldsymbol{\theta})$ are closely related to the $A^{s_i}[i]$, see Eq. [5.9].

Finding the ground state is an iterative process in which the energy $E(\boldsymbol{\theta}) = \langle\Psi(\boldsymbol{\theta})|\hat{H}|\Psi(\boldsymbol{\theta})\rangle$ is supposed to be minimized by adjusting the input parameters $\boldsymbol{\theta}$. We compute the energy from a set of measurement outcomes $\{\langle O_j\rangle_j\}$ and relay the result $E(\boldsymbol{\theta}) = E(\{\langle O_j\rangle\}_j)$ – a real-valued number – to a classical optimization algorithm. The energy serves as a *cost function*: the algorithm seeks to minimize $E(\boldsymbol{\theta})$ by proposing new sets of input parameters $\boldsymbol{\theta}' = \{\theta_i'\}$ to the circuit, exploring the *energy landscape* in the process. A continuous feedback between the classical computer and the quantum processor illustrated in Fig. 5.10 allows the VQE to converge towards an optimal solution for a parameter set $\boldsymbol{\theta}_{opt.}$. The corresponding quantum state $|\Psi(\boldsymbol{\theta}_{opt.})\rangle$ is a good approximation of the ground state $|\Psi\rangle$.

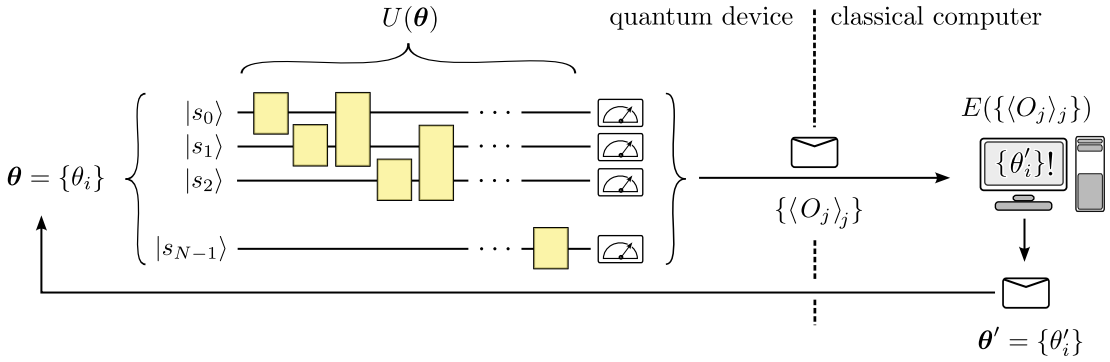


Figure 5.10: Workflow in a VQE: the complex task of computing the quantum state for a given set of input parameters $\boldsymbol{\theta}$ to a parametrized circuit $U(\boldsymbol{\theta})$ (yellow) is carried out on a quantum device, while the measurement outcomes $\{\langle O_j\rangle_j\}$ are evaluated on a classical computer; the target problem is encoded in the quantum circuit. In the context of many-body physics, the VQE aims to approximate the ground state of a complex Hamiltonian. The energy $E(\{\langle O_j\rangle_j\})$ of the generated state is reconstructed from the measurement outcomes and serves as a cost function to a classical optimization algorithm, which proposes new sets of trial parameters $\boldsymbol{\theta}'$ until the energy is minimized.

Choosing the most effective classical optimization algorithm requires intricate knowledge about the target problem, which is often lacking for quantum many-body systems. If the cost function was analytically known, computing the ground state would be a trivial task. Advances in machine learning and data science have led to a variety of protocols [189]: while gradient based methods achieve faster convergence, *derivative-free* strategies do not require any local analytical representation of the energy landscape, making them easy to implement and problem agnostic. However, these algorithms require many iterations until they converge to a solution, making the optimization process rather slow. Fortunately, the number of iterations in itself does not pose an issue to current state-of-the-art quantum processors, which can operate mostly unsupervised, constantly monitoring and automatically optimizing the fidelities of the quantum gate operations.

5.3 PHYSICAL PROPERTIES OF MANY-BODY SYSTEMS

Studying the ground state manifold is sufficient to deduce most of the equilibrium physics of a many-body system [160, 172]. We have argued in the previous sections, that these states can be efficiently represented by a MPS with its properties encoded in a set of tensors $\{A^{s_i}[i]\}$. Many structures in nature are *periodic* and yield to *translational invariant* MPS, reducing the cardinality of $\{A^{s_i}[i]\}$ to just a few elements – in some instances, even a single tensor will be able to fully describe the quantum state. A thorough analysis of the matrices $A^{s_i}[i]$ in Eq. [5.9] then allows us to learn about the physical properties of an N-body system without having to deal with a vast number of parameters [190].

Interesting properties of many-body systems are its *symmetries*, *topology* and the emergence of *quantum phase transitions*. We will introduce these concepts by exploring a set of N atoms on a 1D lattice with lattice constant a. This system undergoes a *Peierls transition* [191, 192], where *dimers* form as a stable configuration of the lattice shown in Fig. 5.11(a). These dimers are the *unit cells* of a larger *superlattice* and equally spaced with constant $2a$. Each particle is allowed to a) exchange the position *within* the dimer with amplitude J and b) *hop* to the neighboring unit cell with amplitude J'.

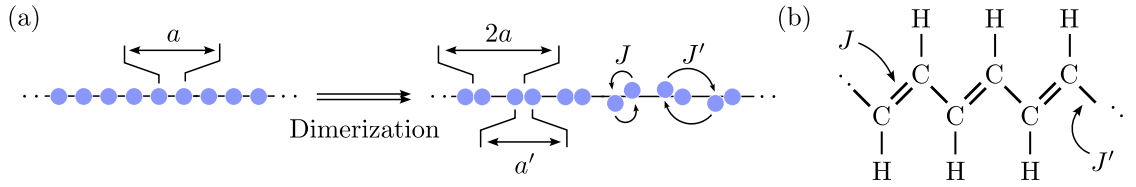


Figure 5.11: Configuration of a 1D chain of atoms: (a) an equidistant lattice, where all atoms are separated by a distance a, is stabilized by the formation of *dimers* [191, 192]. The lattice constant changes to $a' < a$ for each dimer, which is the *unit cell* of the lattice. Particles are allowed to exchange their position within the unit cell with amplitude J as well as *hop* between cells with J'. (b) The structure of *(trans-)polyacetylene* $[C_2H_2]_n$ is a well studied example of an organic polymer exhibiting dimerization and interactions between nearest neighbors.

This model was first introduced by Wu-Pei Su, John Robert Schrieffer and Alan Jay Heeger in 1979 when studying the conductive properties of *(trans-)polyacetylene* $[C_2H_2]_n$ [158, 193]. This organic polymer illustrated in Fig. 5.11(b) is a prime example of a *topological insulator*, which can be doped with e.g. Bromine or Iodine to become a good conductor. For this discovery, Su, Schrieffer and Heeger were awarded with the Nobel price in chemistry in 2000 [194, 195].

In this section we discuss the ground states of the *Su-Schrieffer-Heeger* (SSH) model and introduce the concept of *topological quantum phases*. We further show how to map the model onto a chain of spins, which can then be realized on a quantum hardware platform. By introducing an extension to the Hamiltonian, we show how we can ultimately observe *symmetry breaking* on a small system with just a handful of particles.

5.3.1 *The Su-Schrieffer-Heeger model*

Consider the lattice structure shown in Fig. 5.11(a) with its dimers being the unit cells of the superlattice with constant $2a$. The N particles are allowed to hop both within and between

the cells with amplitudes J and J', respectively, while only being allowed to interact with their immediate neighbors. We write the Hamiltonian

$$\begin{aligned}\hat{H} &= \begin{pmatrix} 0 & J & 0 & 0 & \dots \\ J & 0 & J' & 0 & \dots \\ 0 & J' & 0 & J & \dots \\ 0 & 0 & J & 0 & \dots \\ \vdots & \vdots & \vdots & \vdots & \ddots \end{pmatrix} \\ &= J \sum_{i=0}^{N/2-1} \left[|2i\rangle \langle 2i+1| + |2i+1\rangle \langle 2i| \right] + J' \sum_{i=0}^{N/2-2} \left[|2i+1\rangle \langle 2i+2| + |2i+2\rangle \langle 2i+2| \right] \\ &= J \sum_n \left[|a,n\rangle \langle b,n| + |b,n\rangle \langle a,n| \right] + J' \sum_n \left[|b,n\rangle \langle a,n+1| + |a,n+1\rangle \langle b,n| \right],\end{aligned} \tag{5.44}$$

where we break down the lattice with sites i into the ordered pair of indices (a,b) for each unit cell, which are labelled by n. With respect to the superlattice, we obtain

$$\begin{aligned}\hat{H} &= \begin{pmatrix} \boldsymbol{J} & \boldsymbol{J'} & 0 & 0 & \dots \\ \boldsymbol{J'}^T & \boldsymbol{J} & \boldsymbol{J'} & 0 & \dots \\ 0 & \boldsymbol{J'}^T & \boldsymbol{J} & \boldsymbol{J'} & \dots \\ \vdots & \vdots & \vdots & \vdots & \ddots \end{pmatrix} = \boldsymbol{J} \sum_n |n\rangle \langle n| + \boldsymbol{J'} \sum_n |n\rangle \langle n+1| + \boldsymbol{J'}^T \sum_n |n+1\rangle \langle n| \\ &= \hat{H}_J + \hat{H}_{J'},\end{aligned} \tag{5.45}$$

with the matrices $\boldsymbol{J} = \begin{pmatrix} 0 & J \\ J & 0 \end{pmatrix}$ and $\boldsymbol{J'} = \begin{pmatrix} 0 & 0 \\ J' & 0 \end{pmatrix}$, and $\boldsymbol{J'}^T$ being the transpose of $\boldsymbol{J'}$. Note that the shape of $\boldsymbol{J'}$ restricts the hopping *between* dimers to neighboring sites $(i, i+1)$ of the superlattice.

The *inter-cell* Hamiltonian $\hat{H}_{J'}$ in Eq. [5.45] describes the hopping of particles in a discrete periodic potential $V(n) = V(n+2a)$ introduced by the structure of the superlattice with lattice constant $2a$. We introduce the *translation operator* $T = \sum_i |i\rangle \langle i+1|$ and its eigenstates $|k\rangle = \sum_n e^{2ika \cdot n} |n\rangle$ to diagonalize $\hat{H}_{J'}$ [196], such that

$$\begin{aligned}H_{J'} &= \boldsymbol{J'} T + \boldsymbol{J'}^T T^\dagger = \boldsymbol{J'} e^{-2ika} \sum_n |n\rangle \langle n| + \boldsymbol{J'}^T e^{2ika} \sum_n |n\rangle \langle n| \\ &= \begin{pmatrix} 0 & J' e^{2ika} \\ J' e^{-2ika} & 0 \end{pmatrix} \sum_n |n\rangle \langle n|.\end{aligned} \tag{5.46}$$

The eigenstates $|k\rangle$ are superpostions of *Bloch waves* [182, 197], which are the solution to the Schrödinger equation for a particle in a periodic potential. Its *momentum* or *wave number* k is continuous within the *Brillouin zone* defined by the interval $k \in [-\pi/2a, \pi/2a]$.

Inserting Eq. [5.46] into Eq. [5.45] we get the *band Hamiltonian* $\hat{H}_B(k)$

$$\begin{aligned}\hat{H} &= \left[\begin{pmatrix} 0 & J \\ J & 0 \end{pmatrix} + \begin{pmatrix} 0 & J'e^{2ika} \\ J'e^{-2ika} & 0 \end{pmatrix}\right] \sum_n |n\rangle \langle n| \\ &= \begin{pmatrix} 0 & J + J'e^{2ika} \\ J + J'e^{-2ika} & 0 \end{pmatrix} \sum_n |n\rangle \langle n| \\ &= \hat{H}_B(k)\, \mathbb{1}_k \end{aligned} \tag{5.47}$$

and compute the *energy bands* from the characteristic polynomial

$$E(k) = \pm\sqrt{J^2 + J'^2 + 2JJ'\cos(2ka)}. \tag{5.48}$$

The problem is now descibed in the Hilbert space of the dimers. We obtain the *band structure* $E(k)$, which is continuous in k and periodic with period $\kappa = \pm m\pi/2a$ for $m \in \mathbb{N}$. Fig. 5.12 shows the energy bands in the Brillouin zone for different values of J and J' with E_F indicating the *Fermi energy*. E_F is defined as the energy in the limit of low energies, where the lattice starts to *freeze* and hopping is suppressed. It is characteristic for the respective structure and defines its conductive properties [197]: if the Fermi energy lies in an energy band, the material is a *conductor* – see Fig. 5.12 for $J = J'$ at the boundaries of the Brillouin zone $k = \pm\pi/2a$, where the energies become degenerate. In contrast, if E_F is within a *band gap*, the structure is an *insulator*.

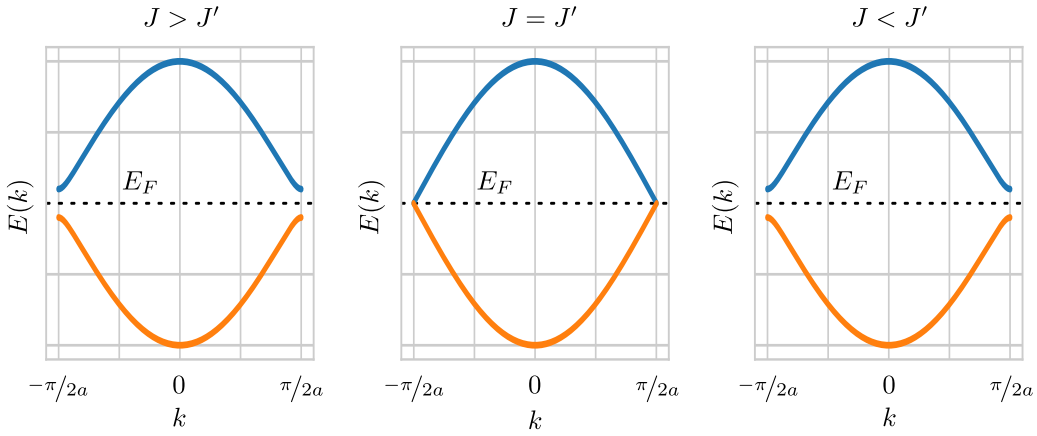


Figure 5.12: Energy bands in a dimerized lattice in 1D: an energy gap emerges when tuning the hopping amplitudes J and J' are not equal. Here, the structure is an *insulator*, as the Fermi energy E_F lies within the gap. For $J = J'$, the energies is degenerate for $k = \pm\pi/2a$ and coincide with E_F; the system becomes a *conductor*.

Although the band gap is symmetric in J and J' about the conducting phase it is intuitively clear, the configuration of the particles on the lattice must be different in the respective regime. This becomes immediately apparent when looking at the finite system shown in Fig. 5.13(a). For $J \gg J'$ we observe the regular or *trivial* case, where the particles form pairs of tightly bound dimers. These dimers begin to break apart when we increase J' until in the limit $J \ll J'$ we end up with strong coupling between unit cells, with two quasi unbound particles remaining at the left and right edge of the lattice. Two distinct *edge modes* emerge, which are characterized by their vanishing energy and their strong localization of the wave function $|\psi_e^{\pm}\rangle$ at the boundaries of the system [182].

We simulate a lattice of $N = 20$ sites and plot the energy spectrum as a function of J' for fixed $J = 1$ in Fig. 5.13(b). At $J' = 2$ the amplitudes of the two zero energy modes $|\psi_e^{\pm}\rangle$ in Fig. 5.13(d) given by the height of the bars are already fairly localized to the first and last lattice site with negligible contributions from the bulk sites. This localization becomes more pronounced as J' is increased further; for comparison, we show the delocalized *bulk mode* associated with the largest energy in Fig. 5.13(c).

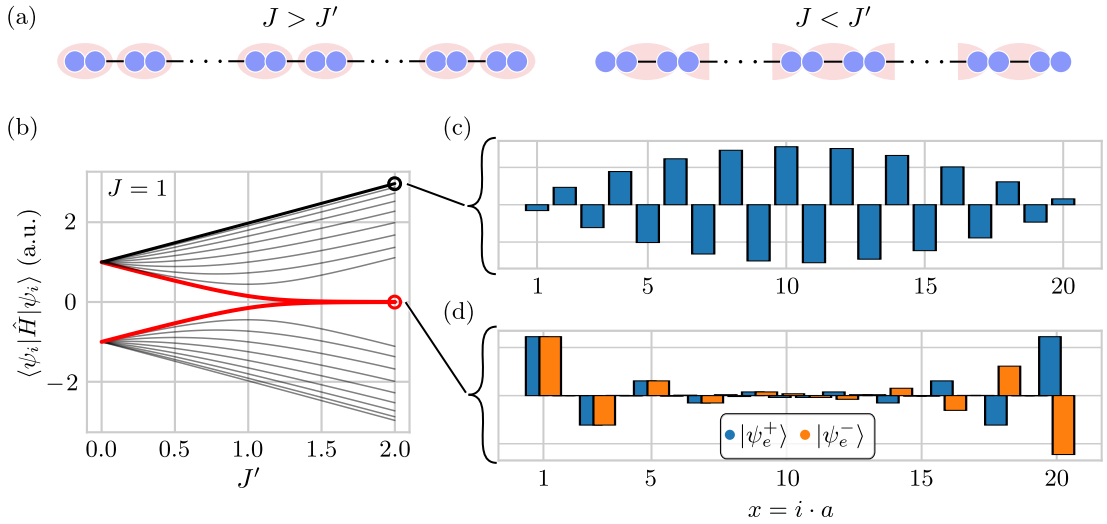


Figure 5.13: Lattice configuration in the insulating regimes and edge states: (a) a large difference in the hopping amplitudes J and J' leads to different arrangements of the particles on the lattice. For $J \gg J'$ the system forms tightly bound dimers, while $J \ll J'$ favors strong coupling between neighboring unit cells. Both states are insulators, as particles cannot *hop* along the lattice. (b) Simulation results of a finite lattice of $N = 20$ sites with constant $J = 1$: (d) two zero energy states $|\psi_e^{\pm}\rangle$ emerge, which are located at the left and right boundary of the structure; these *edge modes* become more prominent with increasing J'. The amplitude of the wave function reflects the localization compared to one of many *bulk states*, such as the one shown here for the eigenstate with the largest energy in (d).

The properties of the edge states of the system can be deduced by merely looking at the bulk; conversely, behavior of the bulk states can be computed at the boundaries [182, 198]. This *bulk-boundary correspondence* is crucial for the classification of quantum many-body systems and closely linked to the subject of *topological quantum phases*, which we will discuss in the next paragraphs.

5.3.2 *Topological quantum phases and phase transitions*

Topology is a fundamental topic in *complex analysis* concerned with the properties of structures under local transformations. Two systems are said to be *topologically equivalent*, if they can be transformed into each other by deformations without the creation or merging of *holes* [199, 200]. This concept can be extended to physical systems: for example, the characteristic zero energy edge modes in the SSH model in the regime $J \ll J'$ are preserved under local deformations – we speak of a *topological quantum phase* [182, 198]. The correspondence between boundary and bulk allows us to identify topological quantum phases by looking at *topological invariants* (TIs), which can be obtained merely from the bulk and

capture the symmetries of the system. These symmetries induce strong correlations that *protect* quantum states against local perturbations. Consequently states associated with a *symmetry protected topological phase* are promising candidates to encode robust qubits [201].

We discuss the topological properties of the SSH model by looking at the band Hamiltonian in Eq. [5.47], which we express in terms of the Pauli matrices σ_x and σ_y, such that

$$\hat{H}_B(k) = J\sigma_x + J'\sigma_x \cos(2ka) - J' \sin(2ka)\sigma_y = \vec{H}_B(k)\vec{\sigma}. \qquad [5.49]$$

The terms $\hat{H}_B^x(k) = J + J'\cos(2ka)$ and $\hat{H}_B^y(k) = -J'\sin(2ka)$ can be understood as the entries of a vector $\vec{H}_B(k)$, which describes the evolution of $\hat{H}_B$ with k as trajectory in phase space [182]. J introduces a displacement in the x direction, while J' corresponds to the radius of a circle drawn over the Brillouin zone $k \in [-\pi/2a, \pi/2a]$ as shown in Fig. 5.14. We associate a *winding number* ν with each trajectory, counting the revolutions of a continuous curve around the origin[6].

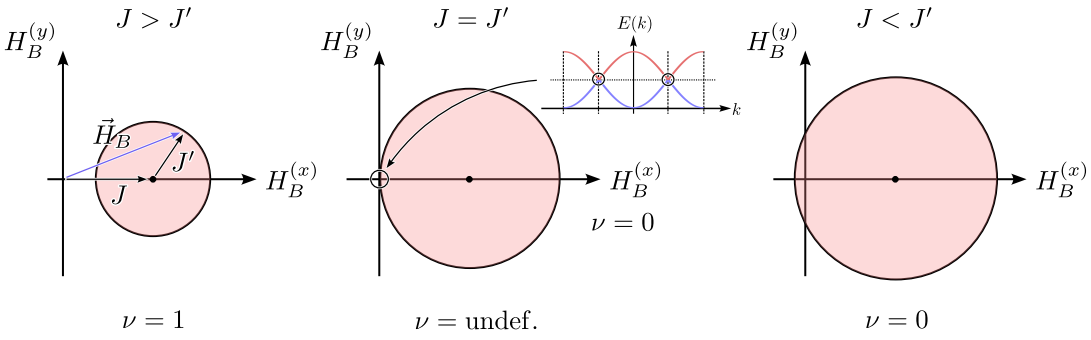


Figure 5.14: Band Hamiltonian and winding number: varying the hopping amplitudes leads to different trajectories of the band Hamiltonian $\hat{H}_B(k)$. The two insulating regimes $J > J'$ and $J < J'$ differ in their *winding number* ν, which classifies different topological structures by counting the number of revolutions of the trajectory around the origin. Note that ν is undefined in the conducting phase $J = J'$, when the circle passes exactly through the origin.

We obtain different winding numbers $\nu = 0$ and $\nu = 1$ in the insulating regimes, where either inter- or intra-cell interactions dominate. For a constant J, tuning of the coupling J' does not change ν until we approach the *critical point* $J = J'$, where the trajectory $\vec{H}_B(k)$ passes through the origin and ν is undefined. Hence, the winding number is a TI: it remains constant under deformations introduced by J' as long as we stay in the same topological regime. At the critical point the system undergoes a *topological phase transition*, where symmetries of the Hamiltonian break, indicated by a rapid change in the TI [202].

To experimentally observe a topological phase transition we need to find appropriate *many-body topological invariants* (MBTIs), which can be reconstructed from the outcomes of a few sets of local measurements. For example, one might be tempted to measure the purity $\mathrm{Tr}[\varrho_{i,i+1}]$ of the quantum state for a pair of neighboring sites $(i, i+1)$ somewhere in the bulk. From Fig. 5.13(a) we can immediately see, that the purity in the center of the lattice yields different values in the respective regimes: for $J \ll J'$, we obtain $\mathrm{Tr}[\varrho_{N/2,N/2+1}] = 1$ and $J \gg J'$ yields $\mathrm{Tr}[\varrho_{N/2,N/2+1}] = 0.25$. However, a lower purity can also be obtained if

6 We do not care about the sign of ν, which would indicate the clockwise or counter-clockwise evolution of a point on the trajectory. Here, we are only interested in the fact that ν is different in both insulating regimes.

the probed state is *not* close to the exact ground state, making the purity a less ideal choice of MBTI. Finding a suitable MBTI is key when aiming to faithfully resolve a quantum phase transition.

Here we look at two MBTIs corresponding to a spatial reflection and time reversal symmetry [203, 204]. We consider the subsystem of four sites labelled $I = (i, j, k, l)$ in the center of a finite lattice and measure its quantum state $\varrho_{i,j,k,l} = \varrho_I$, e.g. by quantum state tomography; the states of the left and right partition of I are $\varrho_l = \mathrm{Tr}[\varrho_I]_{(i,j)}$ and $\varrho_r = \mathrm{Tr}[\varrho_I]_{(k,l)}$. The MBTI associated with the reflection symmetry is defined by

$$Z_R = \frac{\mathrm{Tr}[\varrho_I \hat{R}]}{\sqrt{(\mathrm{Tr}[\varrho_l^2] + \mathrm{Tr}[\varrho_r^2])/2}}, \qquad [5.50]$$

where the operator $\hat{R}$ introduces a *spatial reflection* $\hat{R}\,|i, j, k, l\rangle = |l, k, j, i\rangle$ about the center of I as shown in Fig. 5.15(a). Z_R effectively measures the nature of the bonds between the particles: in the trivial case, the state of subsystem I is described by two disjoint dimers disconnected from the larger lattice and we measure $Z_R = 1$. In contrast, the topological phase is strongly coupled to particles *outside* of I, resulting in $Z_R = -1$. We plot Z_R as a function of J' with constant $J = 1$ for systems of $N = 8$ and $N = 12$ particles in the top panel of Fig. 5.15(b). The MBTI allows us to observe the phase transition between the trivial and the topological phase, which becomes more pronounced when increasing the number of particles.

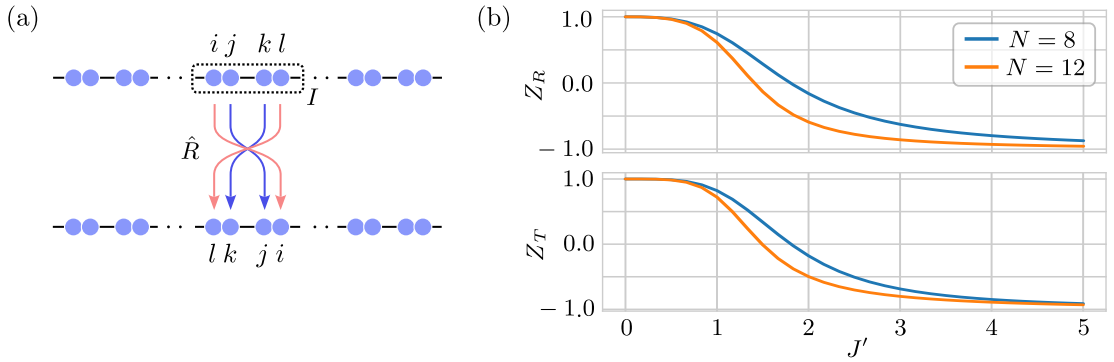


Figure 5.15: Many-body topological invariant associated with spatial reflection symmetry: (a) the operator $\hat{R}$ swaps the sites of the subsystem (i, j, k, l) indicated by the dashed box, such that $(i, j, k, l) \longrightarrow (l, k, j, i)$. (b) The MBTIs Z_R and Z_T for a system of $N = 8$ and $N = 12$ particles at constant $J = 1$, showing a phase transition between a trivial phase ($Z_{R/T} = 1,\ J \gg J'$) and a topological phase ($Z_{R/T} = -1,\ J \ll J'$).

The second MBTI is related to a time reversal symmetry [204]. Studying such a symmetry generally requires the preparation of two quantum states $\varrho_\pm$, each evolving in opposite directions in time. Here we show the MBTI Z_T, which approximates the time reversal by reflecting the quantum state ϱ_l of the left partition of I [205]. We define

$$Z_T = \frac{\mathrm{Tr}[\varrho_I \hat{U}_T \varrho_l^{T_l} \hat{U}_T^\dagger]}{\left[(\mathrm{Tr}[\varrho_l^2] + \mathrm{Tr}[\varrho_r^2])/2\right]^{3/2}}, \qquad [5.51]$$

with T_l denoting the partial transpose operation on the left partition and $\hat{U}_T = \sigma_i^y \sigma_j^y$ the product of Pauli operators σ^y on the sites (i, j). The plot of the quantum phase transition is shown in the bottom panel of Fig. 5.15(b).

5.3.3 *Mapping the SSH model onto qubits*

We conclude this chapter by mapping the Hamiltonian in Eq. [5.44] onto a system of spins by introducing the operators $\hat{c}_i^\dagger$ and $\hat{c}_i$, which create and annihilate a particle at a site i. The expression $\hat{c}_i^\dagger \hat{c}_{i+}$ describes the hopping from site i to site $i+1$ and its hermitian conjugate does the opposite. For a finite system of size N, the hopping amplitude J (J') couples the pairs of sites $(i, i+1)$ for i odd (even); we write

$$\begin{aligned}\hat{H} &= J \sum_{i=0}^{N/2-1} \left[|2i\rangle\langle 2i+1| + |2i+1\rangle\langle 2i|\right] + J' \sum_{i=0}^{N/2-2} \left[|2i+1\rangle\langle 2i+2| + |2i+2\rangle\langle 2i+2|\right] \\ &= J \sum_{i\ \text{odd}}^{N} \left(\hat{c}_i^\dagger \hat{c}_{i+1} + \hat{c}_i \hat{c}_{i+1}^\dagger\right) + J' \sum_{i\ \text{even}}^{N} \left(\hat{c}_i^\dagger \hat{c}_{i+1} + \hat{c}_i \hat{c}_{i+1}^\dagger\right)\end{aligned}$$

With only one particle at each lattice site, we can write $\hat{c}_i^\dagger = \hat{\sigma}_i^+$ and $\hat{c}_i = \hat{\sigma}_i^-$ which are closely connected to the Pauli matrices $\hat{\sigma}_i^x$ and $\hat{\sigma}_i^y$. By introducing a single parameter T to control the hopping between neighboring sites we obtain

$$\begin{aligned}\hat{H} &= J \sum_{i\ \text{odd}}^{N} \left(\hat{\sigma}_i^+ \hat{\sigma}_{i+1}^- + \hat{\sigma}_i^- \hat{\sigma}_{i+1}^+\right) + J' \sum_{i\ \text{even}}^{N} \left(\hat{\sigma}_i^+ \hat{\sigma}_{i+1}^- + \hat{\sigma}_i^- \hat{\sigma}_{i+1}^+\right) \\ &= J \sum_{i\ \text{odd}}^{N} \left(\hat{\sigma}_i^x \hat{\sigma}_{i+1}^x + \hat{\sigma}_i^y \hat{\sigma}_{i+1}^y\right) + J' \sum_{i\ \text{even}}^{N} \left(\hat{\sigma}_i^x \hat{\sigma}_{i+1}^x + \hat{\sigma}_i^y \hat{\sigma}_{i+1}^y\right) \\ &= \sum_{i=1}^{N-1} \left(\frac{J+J'}{2} + (-1)^{i-1}\frac{J-J'}{2}\right) \left(\hat{\sigma}_i^x \hat{\sigma}_{i+1}^x + \hat{\sigma}_i^y \hat{\sigma}_{i+1}^y\right) \\ &= \sum_{i=1}^{N-1} \left(1 + (-1)^{i-1} T\right) \left(\hat{\sigma}_i^x \hat{\sigma}_{i+1}^x + \hat{\sigma}_i^y \hat{\sigma}_{i+1}^y\right).\end{aligned} \tag{5.52}$$

We show the spectrum of this Hamiltonian for a finite system of $N = 8$ particles in Fig. 5.16(a) in the limit of low energies with the ground state highlighted in red. Four degenerate states emerge in the topological phase as $T \to -1$, which are distinguished by the states of the unpaired edge qubits. In the trivial regime $T > 0$, the ground state is unique and well separated from the first excited states. The quantum phase transition is observed via the MBTIs Z_R and Z_T shown in Fig. 5.16(b) for the ground state $|\psi_0\rangle$ and low-energy eigenstates $|\psi_{i>0}\rangle$.

Compared to the energy, the MBTIs are better suited to distinguish the exact ground state $|\psi_0\rangle$ from the other low-energy eigenstates near the point of degeneracy. In this regime, a quantum state $|\phi\rangle$ prepared by the variational algorithm may have a residual overlap with these eigenstates, in turn broadening the phase transition in Z_R. However, the feature may vanish entirely in Z_T if the second excited state $|\psi_2\rangle$ contributes significantly to $|\phi\rangle$, see Fig. 5.16(b).

Modifying Eq. [5.52] by adding the term $\delta\sigma_i^z\sigma_{i+1}^z$ with $\delta \geq 0$ yields the *extended Su-Schrieffer-Heeger* (ESSH) model [158, 204]

$$\hat{H} = \sum_{i=1}^{N-1} \left(1 + (-1)^{i-1} T\right) \left(\hat{\sigma}_i^x \hat{\sigma}_{i+1}^x + \hat{\sigma}_i^y \hat{\sigma}_{i+1}^y + \delta\sigma_i^z\sigma_{i+1}^z\right), \tag{5.53}$$

which allows us to resolve the symmetry breaking occurring during the quantum phase transition. Tuning both δ and T, we plot the phase diagram for Z_R in a system of $N = 8$

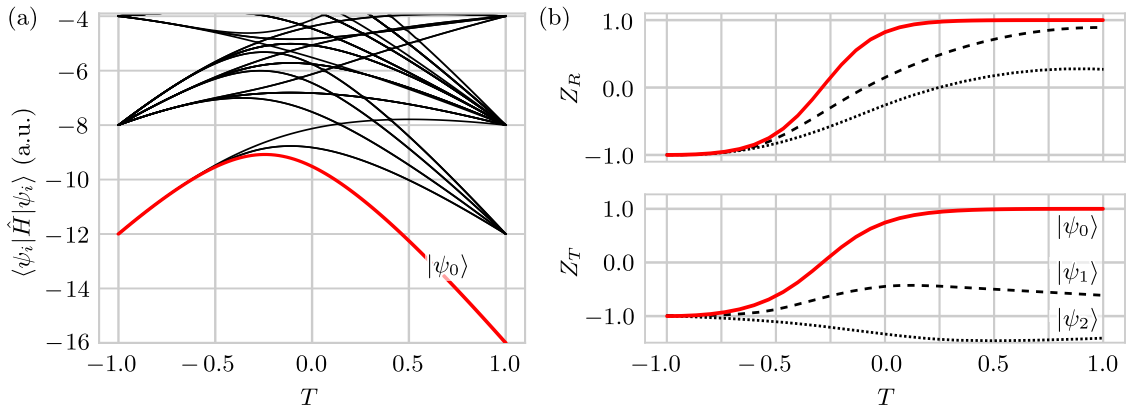


Figure 5.16: Energy spectrum and topological invariants of the ground state $|\psi_0\rangle$ (red) and low-energy eigenstates $|\psi_{i>0}\rangle$ (black): (a) the model hosts a 4-fold degenerate ground state manifold in the topological phase for $T = -1$, while the ground state is unique with a large energy gap in the trivial regime $T > 0$. (b) Topological invariants Z_R and Z_T computed for the exact ground state (red) and the first (dashed) and second (dotted) excited states labeled $|\psi_1\rangle$ and $|\psi_2\rangle$, respectively.

particles in Fig. 5.17. The broken symmetry manifests as a "plateau" with $Z_R = Z_T = 0$, which becomes increasingly wide for large δ.

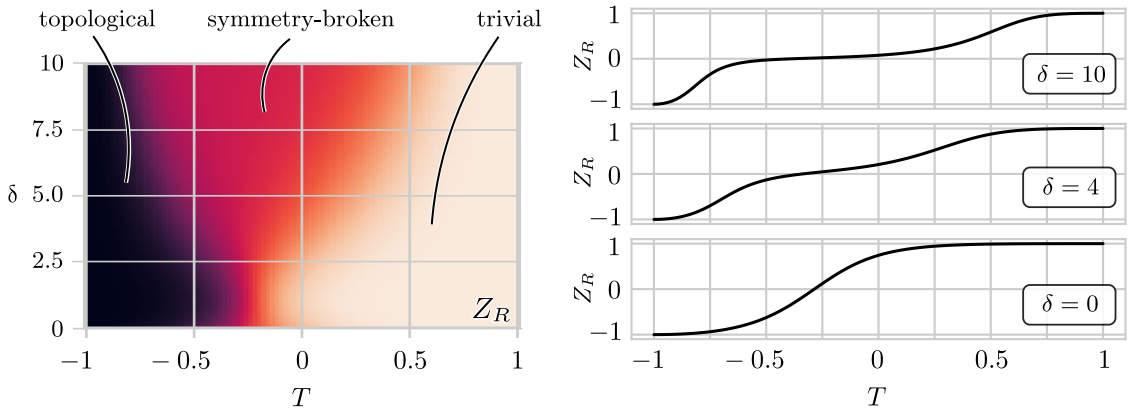


Figure 5.17: Quantum phase transition in the *extended Su-Schrieffer-Heeger* (ESSH) model: an extra term $\delta\sigma_i^z\sigma_{i+1}^z$ allows to observe a third, symmetry broken phase in the model. This phase manifests as a plateau in the topological invariant, here shown for Z_R, which becomes wider as δ increases.

We ultimately seek to implement the ESSH model on a digital quantum simulator, approximate the ground states for $\delta = 0$ and $\delta = 4$ and experimentally verify the quantum phase transition, which we will show in the next chapter.

6

EXPERIMENTAL OBSERVATION OF A TOPOLOGICAL QUANTUM PHASE TRANSITION

In this chapter we show the quantum simulation of the eSSH model introduced in Sec. 5.3.3 on a trapped ion quantum processor. On a system of $N = 8$ trapped Calcium ions, we prepare approximations to the ground state of the Hamiltonian given in Eq. [5.53] by employing a variational quantum eigensolver protocol [16]. A classical optimization algorithm computes the energy of a quantum state generated by a parametrized quantum circuit from a set of local measurements. With the aim to minimize the energy, the algorithm proposes sets of input parameters to the quantum circuit until it converges to an optimal solution. This solution implements a good approximation of the ground state, for which we then reconstruct the *many-body topological invariant*s (MBTIs) described in Sec. 5.3.2 from state tomography measurements [206].

6.1 VARIATIONAL CIRCUIT WITH A GLOBAL QUANTUM DATA BUS

We follow the protocol proposed by Kuzmin and Silvi [15], where a global *quantum data bus* (QDB) is used to mediate entanglement between the particles. Each particle labeled by k can access the QDB individually by means of a local interaction $\hat{h}^{(k)}$, natively available on the quantum hardware. A variational quantum circuit parametrized by a set of parameters $\boldsymbol{\theta} = \{\theta_i\}_i$ is constructed with $h^{(k)}$ as its fundamental resource. The circuit $U(\boldsymbol{\theta})$ is a sequence of operations

$$U(\boldsymbol{\theta}) = \prod_i U^{(\{k\}_i)}(\theta_i), \tag{6.1}$$

where each $U^{(\{k\}_i)}(\theta_i)$ acts on a set of particles $\{k\}_i$; in our implementation, $\{k\}_i$ is just a single site k. The $U^{(k)}(\theta_i)$ are defined by

$$U^{(\{k\})}(\theta_i) = U^{(k)}(\theta_i) = \exp\left(-i\theta_i \hat{h}^{(k)}\right), \tag{6.2}$$

where θ_i is continuous in the interval $[-2\pi, 2\pi]$. Fig. 6.1 shows the proposed circuit for a string of 8 particles, each encoding a qubit with states $|\uparrow\rangle$ and $|\downarrow\rangle$. The system is initialized in a *Neel* or *staggered* state $|\downarrow\uparrow\downarrow\ldots\rangle$ with the QDB in the "empty" state $|0\rangle_{QDB}$.

Each $U^{(k)}(\theta_i)$ is a single operation entangling the k-th qubit with the QDB, which carries information accessible to all other qubits in the register. Our circuit is parametrized by the set $\boldsymbol{\theta} = \{\theta_1, \ldots, \theta_{14}\}$, with (disjoint) subsets $\boldsymbol{\theta}_{A,\ldots,D}$ characteristic for one of four unique *chunks* illustrated in Fig. 6.1. While $\boldsymbol{\theta}_A = \{\theta_1, \theta_2\}$ and $\boldsymbol{\theta}_D = \{\theta_{13}, \theta_{14}\}$ are executed once, affecting the qubit pairs on the left and right edge of the register, the chunks $\boldsymbol{\theta}_B$ and $\boldsymbol{\theta}_C$ are repeatedly applied as the circuit progresses. This structure of the circuit is *independent* of the system size [15]: we can effectively prepare states for arbitrarily large systems without increasing the number of variational parameters.

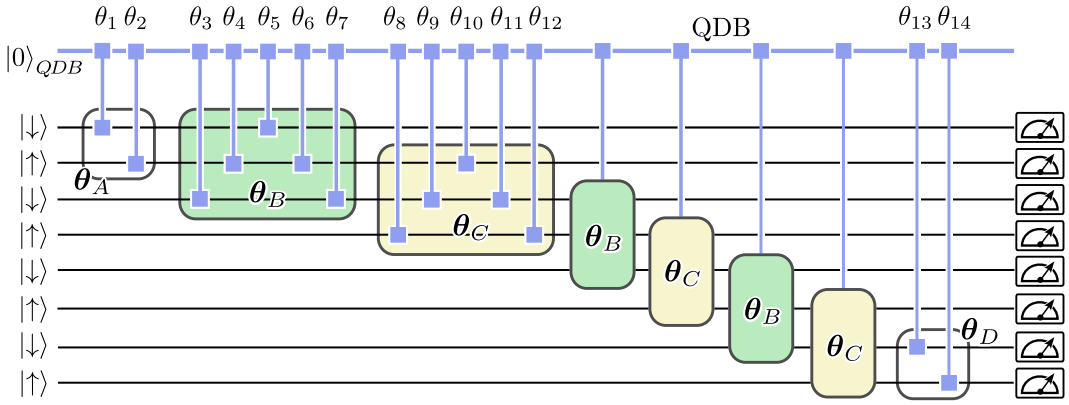


Figure 6.1: Variational quantum circuit employed to prepare approximate ground states of the eSSH model: the circuit is shown for a system of 8 qubits, which are initially prepared in the state $|\downarrow\uparrow\downarrow\ldots\rangle$; the QDB is prepared in the state $|0\rangle_{QDB}$. Each vertical blue line represents a parameterized operation $U^{(k)}(\theta_i)$, entangling the k-th qubit with the QDB. The circuit is split into *chunks* characterized by their sets of parameters $\boldsymbol{\theta}_{A,\ldots,D}$. Chunks with parameters $\boldsymbol{\theta}_B$ and $\boldsymbol{\theta}_C$ are repeatedly applied, each time shifting the set of participating qubits by one. This strategy allows the preparation of even larger quantum states without increasing the number of parameters.

The target Hamiltonian of our model defined in Eq. [5.53] is k-local, including only interactions between nearest neighbors ($k = 2$), and has a spectral gap. Following the arguments made in Sec. 5.2, the ground state can be efficiently represented by a MPS. The structure of the MPSis encoded in the variational circuit in Fig. 6.1, where each chunk forms one the following *matrix product unitaries* (MPUs)

$$\begin{aligned} A[1] &= U^{(2)}(\theta_2)U^{(1)}(\theta_1) = A[1](\boldsymbol{\theta}_A) \\ A[i]_{even} &= U^{(i+1)}(\theta_7)U^{(i)}(\theta_6)U^{(i-1)}(\theta_5)U^{(i)}(\theta_4)U^{(i+1)}(\theta_3) = A[i]_{even}(\boldsymbol{\theta}_B) \\ A[i]_{odd} &= U^{(i+1)}(\theta_{12})U^{(i)}(\theta_{11})U^{(i-1)}(\theta_{10})U^{(i)}(\theta_9)U^{(i+1)}(\theta_8) = A[i]_{odd}(\boldsymbol{\theta}_C) \\ A[N] &= U^{(N)}(\theta_{14})U^{(N-1)}(\theta_{13}) = A[N](\boldsymbol{\theta}_D) \end{aligned} \qquad [6.3]$$

Note, that the $A[i]_{even}$ ($A[i]_{odd}$) are only applied to even (odd) site indices for $i = 2, \ldots, N-1$; the edges of the register are treated separately by $A[1]$ and $A[N]$. In terms of these MPUs the circuit can be graphically represented by the network shown in Fig. 6.2. With the exception of $A[1]$ and $A[N]$, a single qubit at site $(i+1)$ enters the circuit in either of the classical states $|\uparrow\rangle$ or $|\downarrow\rangle$ and is manipulated by $A[i]$, $A[i+1]$ and $A[i+2]$ before it does no longer partake and can be measured. Since $A[i]$ and $A[i+2]$ are identical, the MPS exhibits two-site translational invariance, which is also evident from the Hamiltonian in Eq. [5.53], see Sec. 5.2.

Assuming our variational eigensolver has found an optimal solution $\boldsymbol{\theta}^*$, the approximated ground state can be written as MPS of the form

$$|\Psi(\boldsymbol{\theta}^*)\rangle = \sum_{\{s_i\}} A^{s_1}[1]\ldots A^{s_N}[N]\,|s_1,\ldots,s_N\rangle = A[1]\ldots A[N]\,|\downarrow\uparrow\ldots\uparrow\rangle\,,$$

where all $A^{s_i}[i]$ are zero *except* those given in Eq. [6.3], when the input state is the *Neel* state $|s_1,\ldots s_N\rangle = |\downarrow\uparrow\ldots\uparrow\rangle$.

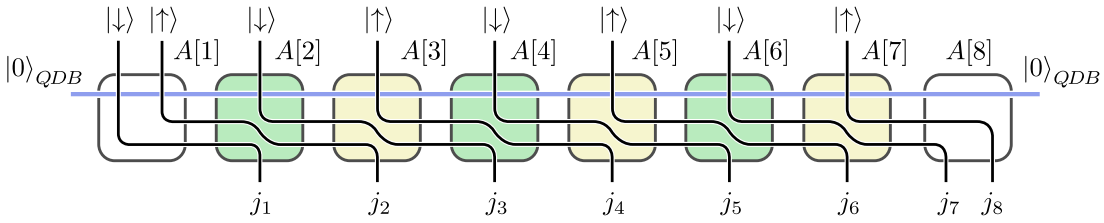


Figure 6.2: Variational circuit as a network of MPUs: the circuit is constructed from four different MPUs, where the green and yellow MPUs are repeatedly applied. The qubits enter from the top in a pure state, either $|\uparrow\rangle$ or $|\downarrow\rangle$ and are affected by at most three MPUs. We obtain a two-site translational invariant MPS which approximates the ground states of the SSH model.

6.2 IMPLEMENTATION ON A TRAPPED ION SYSTEM

A trapped ion quantum processor natively offers a QDB: information can be exchanged between any pair of ions by controlled excitations of the collective motion. An ideal candidate is the axial COM mode with frequency ω_z, which is well separated from other modes in the spectrum and has an approximately homogeneous coupling to all ions in the register. We excite the COM mode by implementing the Anti-Jaynes-Cummings (AJC) interaction as described in Sec. 4.3: a single laser pulse detuned by $+\omega_z$ from the carrier transition with duration t_p illuminates a single ion at a time, effectively realizing the rotation $\hat{B}(\theta, \phi)$, where $\theta \propto t_p$ and ϕ given by the phase of the light field.

6.2.1 *Initialization and qubit encoding*

Here, we briefly discribe how the proposed quantum circuit in Fig. 6.1 is implemented on our quantum processor. After a sequence of laser cooling and optical pumping, the ions are prepared in the electronic state $4S_{1/2}(m = -1/2)$ and in their motional ground state. We measure a residual mean phonon number of $\bar{n} < 0.05$, which is a good approximation to an empty QDB. We then excite all ions with *even* indices to the $3D_{5/2}$ manifold, thereby preparing the *Néel* state $|\downarrow, \uparrow, \ldots, \uparrow\rangle$ as the input state to our circuit.

The entire circuit is realized by controllably coupling one ion at a time with the QDB via the AJC interaction. The effective Rabi frequency scales with the Lamb-Dicke parameter η. With $\eta = 0.034(2)$, exciting the motion requires substantially more optical power in the laser beam illuminating each ion. We work at an axial COM frequency of $\omega_z = 2\pi \cdot 0.94$ MHz, where the separation of the individual ions is on the order of a few micrometers. Consequently, the finite size of the laser beam at the position of the ion introduces cross-talk between nearest neighbors, cf. Sec. 4.1.

These unwanted couplings are mitigated by employing the *qudit-enhanced encoding* shown in Fig. 6.3, where the qubits are encoded in different manifolds of the ions. Notably, we encode all qubits that are initially in the state $|\downarrow\rangle$ of the Néel state in the Zeeman states with $m = -1/2$, while the others are encoded in $m = +1/2$. At a magnetic bias field of 0.42 mT, the corresponding optical transitions $4S_{1/2}(m = -1/2) \leftrightarrow 3D_{5/2}(m = -1/2)$ and $4S_{1/2}(m = 1/2) \leftrightarrow 3D_{5/2}(m = 1/2)$ are separated by a frequency of $2\pi \cdot 4.71$ MHz, *spectrally decoupling* the ions. Note that establishing this encoding requires additional laser pulses to transfer the ions to their respective manifold. These *transfer pulses* are still subject to

next-neighbor cross-talk, which we suppress by employing the local composite rotations $U_3(\theta, \phi)$ described in Sec. 4.1.1.

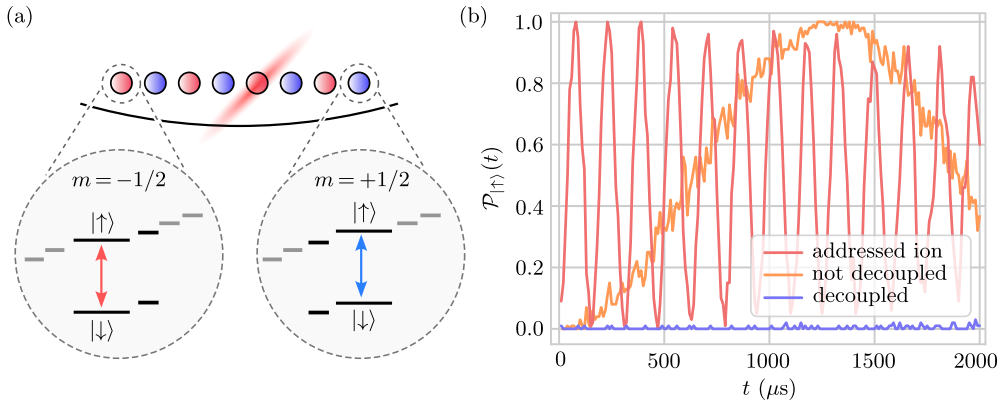


Figure 6.3: Qubit encoding and spectral decoupling: (a) the qubit is encoded in the Zeeman states $|\downarrow\rangle = |4S_{1/2}(m = \pm 1/2)\rangle$ and $|\uparrow\rangle = |3D_{5/2}(m = \pm 1/2)\rangle$ with alternating sign on neighboring ions. The corresponding optical transitions are separated by $\approx 2\pi \cdot 4.7$ MHz, such that the ions are pair-wise decoupled. (b) Rabi oscillations driven on a single ion with two neighboring spectators encoding the qubits in different manifolds $m = \pm 1/2$. The laser pulse of duration t leads to oscillations with frequency $\Omega = 2\pi \cdot 6.23(3)$ kHz (red) on the addressed ion, while resonant cross-talk affects the spectator in the $4^2S_{1/2}(m = -1/2)$ ground state (orange); the Rabi frequency is measured to be $\Omega_{spect.} = 2\pi \cdot 0.231(2)$ kHz. In contrast, the decoupled ion does not leave its ground state $4^2S_{1/2}(m = +1/2)$, with negligible excitation after $t > 2000$ μs.

To highlight the effectiveness of this encoding scheme, we induce Rabi oscillations on a single ion and observe the population of the excited state $\mathcal{P}_{|\uparrow\rangle}(t)$ as a function of the laser pulse duration t. The data in Fig. 6.3(b) shows the evolution of the addressed ion encoded in the $m = -1/2$ manifold with frequency $\Omega = 2\pi \cdot 6.32(3)$ kHz. Simultaneously, we observe slow, yet pronounced excitation of the spectator ion with a frequency $\Omega_{spect.} = 2\pi \cdot 0.231(2)$ kHz, where the qubit is encoded in the same manifold. In contrast, the right neighbor with $m = +1/2$ never leaves its ground state $|\downarrow\rangle = 4^2S_{1/2}(m = +1/2)$ with negligible contributions at t far exceeding 10 Rabi cycles of the addressed ion.

Following the preparation of the initial Néel state, the full circuit is implemented by the quantum gates $\hat{B}(\theta, \phi)$ resonant with the blue sideband of the collective motion, see Sec. 4.3. Therefore, Eq. [6.1] can be written as

$$U(\boldsymbol{\theta}) = \prod_{i,k} \hat{B}^{(k)}(\theta_i, \phi = 0) \qquad [6.4]$$

with gates $\hat{B}^{(k)}(\theta, \phi = 0) = \hat{B}^{(k)}(\theta)$ where the index k labels the addressed ion as specified by the circuit in Fig. 6.1. By appropriate choice of laser intensity, we aim for an effective Rabi frequency of $\eta\Omega \approx 2\pi \cdot 8$ kHz. Faster oscillations lead to large AC Stark shifts exceeding 10 kHz, which prove difficult to compensate using the technique described in Sec. 4.3.1 [135]. Passive compensation of spectator levels (e.g. $3^2D_{5/2}(m = -3/2)$) does not need to be implemented, as these states will never be populated.

6.2.2 *Demonstration on a toy system*

We demonstrate the implementation on a reduced system of $N = 4$ ions. Here, the ground state $|\Psi\rangle_0$ is approximated by four MPUs

$$|\Psi\rangle_0 \approx A[1]A[2]_{even}A[3]_{odd}A[4]\,|{\downarrow}{\uparrow}{\downarrow}{\uparrow}\rangle\,,$$

requiring a total of 14 $\hat{B}(\theta)$ operations. We compute the optimal set of parameters $\boldsymbol{\theta}_{opt.}$ by numerically simulating the circuit $\prod_i \hat{B}^{(k)}(\theta_i)$ without noise. For a coupling $T = +1$ in the SSH Hamiltonian $\hat{H}$ given by Eq. [5.52], we simulate the state $|\psi\rangle_{sim.}(\boldsymbol{\theta})$ and minimize the energy $E(\boldsymbol{\theta}) = \langle\psi_{sim.}|\hat{H}|\psi_{sim.}\rangle$ using a simple gradient-free downhill-simplex optimization algorithm [207].

θ_1	θ_2	θ_3	θ_4	θ_5	θ_6	θ_7	θ_8	θ_9	θ_{10}	θ_{11}	θ_{12}	θ_{13}	θ_{14}
1.2	0.4	0.15	0.94	1.17	0.07	0.06	0.92	1.6	0.13	1.03	2.83	0.18	3.89

Table 6.1: Optimal solution for $T = +1$ obtained from numerical simulation of the reduced circuit. All angles are given in units of π and rounded to the second decimal.

We obtain an optimal solution for the angles listed in Tab. 6.1, implementing the state $\varrho_{sim.}$ shown in Fig. 6.4(a); the density matrix is real valued, hence $\varrho_{sim.} = \mathrm{Re}(\varrho_{sim.})$. The experimentally realized state $\varrho_{exp.}$ in Fig. 6.4(b) is reconstructed via quantum state tomography using maximum likelihood methods [206, 208, 209]. Imperfections, which we will discuss more thoroughly in Sec. 6.4, manifest as non-zero amplitudes in $\mathrm{Im}(\varrho_{exp.})$, reducing the fidelity of the state to $\mathcal{F} = 89.7(11)\%$. Neglecting state preparation and measurement errors, we estimate an average fidelity $\mathcal{F}(\hat{B}) = 99.23\%$ for each $\hat{B}(\theta)$ in our circuit. Here we assume $\mathcal{F} = \mathcal{F}(\hat{B})^n$ with $n = 14$ the number of gates required to construct the circuit. This approach does not consider the performance of the operation on the individual ions. A proper characterization of the gate would require different methods, such as randomized benchmarking or gate set tomography [136, 137].

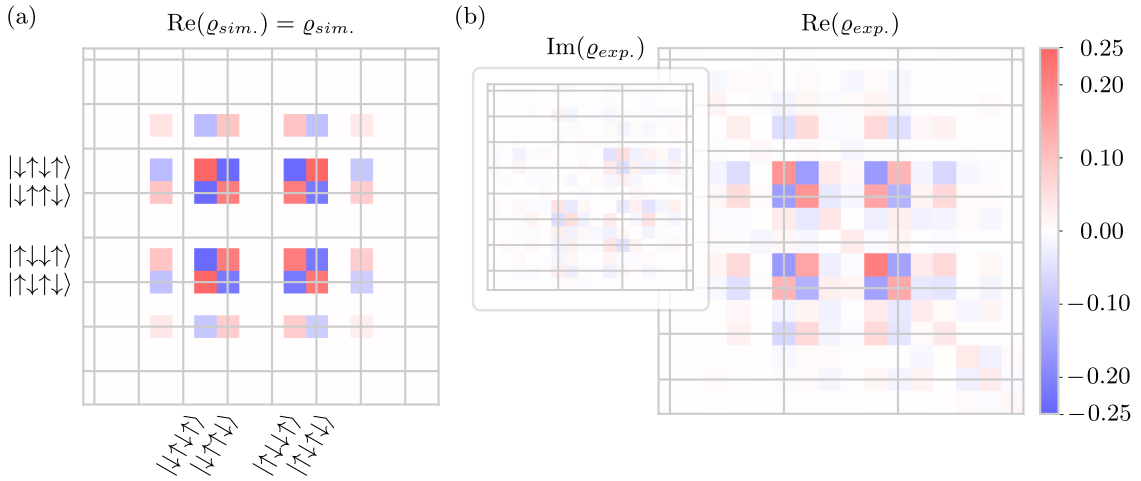


Figure 6.4: Simulated and experimentally verified quantum state implemented using the optimal set of parameters given in Tab. 6.1. The numerical solution of the density matrix is shown in (a), while the state realized on the quantum processor is depicted in (b); the state is reconstructed via state tomography and maximum likelihood estimation.

6.2.3 *Energy measurement and variational optimization*

The variational circuit in Eq. [6.1] is parametrized by a vector of 14 angles $\boldsymbol{\theta} = \{\theta_1, \ldots, \theta_{14}\}$, which are tuned by a hybrid quantum-classical algorithm. Variational quantum eigensolvers discussed in Sec. 5.2.2 approximate the ground states of a Hamiltonian by a repeated exchange of data between a classical computer and a quantum processor. Each iteration i of the algorithm generates a quantum state $\varrho(\boldsymbol{\theta}_i)$ for a set of trial parameters $\boldsymbol{\theta}_i$ proposed by a classical computer.

We measure $\varrho(\boldsymbol{\theta}_i)$ collectively in the X, Y, and Z bases and compute $\langle O_j O_{j+1} \rangle_{O=X,Y,Z}$ for each pair of qubits $(j, j+1)$ in the register. Recalling the Hamiltonian of the extended Su-Schrieffer-Heeger model

$$\hat{H} = \sum_{i=1}^{N-1} \left(1 + (-1)^{i-1} T\right) \left(\hat{\sigma}_i^x \hat{\sigma}_{i+1}^x + \hat{\sigma}_i^y \hat{\sigma}_{i+1}^y + \delta \sigma_i^z \sigma_{i+1}^z\right),$$

we take the weighted sum of the outcomes to compute the energy $E(\boldsymbol{\theta}_i) = \mathrm{Tr}[\hat{H}\varrho(\boldsymbol{\theta}_i)]$, which serves as the cost function to be minimized by a classical optimizer. Note, that residual information in the QDB does not enter in the cost function and is traced out upon measurement. With constantly improving guesses of the input parameters, the algorithm converges to the state $\varrho(\boldsymbol{\theta}^*)$, which is a good approximation to the ground state of the ESSH model.

We employ a pattern search algorithm, which samples the parameter space locally around a *candidate solution* $\boldsymbol{\theta}_{\text{cand.}}$ [210, 211]. In each sampling step a single parameter $\theta_i \in \boldsymbol{\theta}_{\text{cand.}}$ is varied, starting with the most significant direction of the vector $\theta_{\text{cand.}}$ based on previous evaluations of the cost function. Once all directions have been tested and a new minimum has been found, the optimizer updates $\boldsymbol{\theta}_{\text{cand.}} \mapsto \boldsymbol{\theta}_{\text{cand.}+1}$ and *decreases* the step size before performing another iteration. If no improvement has been made, the search region is *increased* and new samples are taken [210, 212]. Each evaluation of the cost function is based on noisy measurement outcomes, which can negatively impact the performance of the algorithm. By taking all the previous iterations into account we fit a Gaussian process model to the data, providing a better estimate for the energy [213, 214]. Employing optimal measurement budget allocation strategies, the algorithm can request additional samples, whenever the data is deemed to be too noisy to make a clear decision on the location of a new minimum [215].

The implementation of the optimizer is analogous to Fig. 5.10 in Sec. 5.2.2: quantum circuit compilation and measurement outcome evaluation are performed on two separate classical computers, which exchange information via a local area network. An example of a full variational optimization for the coupling parameters $T = \delta = 0$ is shown in Fig. 6.5, where the measurement data is presented with one standard deviation of statistical uncertainty. Starting with the initial guess $\boldsymbol{\theta}_0 = \{\theta_i = 0\}_{i=1\ldots14}$, the algorithm samples the parameter landscape before it performs its first *proper* optimization step, which brings the energy down from $E(\boldsymbol{\theta}) = \langle \hat{H} \rangle_0 \approx 0$ to $E(\boldsymbol{\theta}) = -4$. There, additional samples are taken to further reduce the energy with its current optimum indicated by the solid line. We allow the algorithm to explore other regions in the parameter space far away from its best guess whenever it discovers a plateau[1], preventing it from getting *stuck* at a local minimum.

1 The data close to the 340-th iteration in Fig. 6.5 shows such a *re-exploration* phase.

However, it quickly converges back to the optimal solution.

We achieve a *best value* $E(\boldsymbol{\theta}_{opt.}) = -7.9(7)$ compared to the exact minimum $\langle \hat{H} \rangle_{min} = -9.52$. Each data point in Fig. 6.5 is accompanied by a (noiseless) simulation (cyan) of the quantum circuit using the current guess $\boldsymbol{\theta}_i$ as input. This highlights the impact of noise present in the experiment, which cannot be accounted for by in-situ optimization of the circuit parameters by VQE.

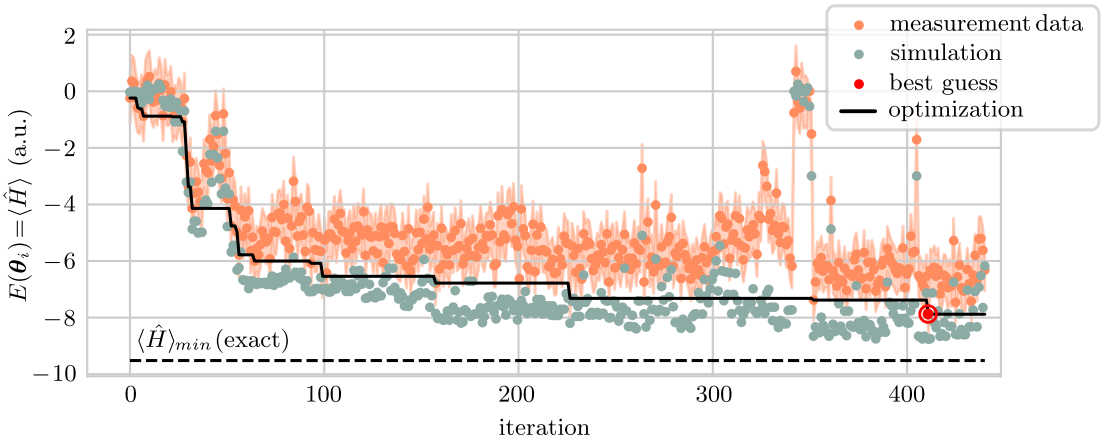


Figure 6.5: Approximation of the ground state of the SSH model for $T = \delta = 0$ by variational optimization. The energy $\langle \hat{H} \rangle$ associated with the prepared quantum state continuously decreases as the algorithm progresses (orange); the shaded region indicates one standard deviation statistic uncertainty. The solid line illustrates the current minimum. A *best guess* (red) for the optimal parameters $\boldsymbol{\theta}_{opt.}$ is found after 410 iterations. For each iteration we numerically simulate the quantum circuit and compute $\langle \hat{H} \rangle$ (cyan) to verify that the algorithm indeed approximates the ground state (dashed line).

Tuning the coupling parameters T and δ in the Hamiltonian, we reproduce the diagram shown in Fig. 5.16. For each $T \in [-1, 1]$ the variational optimization algorithm prepares approximations to the ground state with energies $E(\boldsymbol{\theta}_{opt.})$ for optimal solutions $\boldsymbol{\theta}_{opt.}$. We show the *best energies* in Fig. 6.6 with numerical simulations of the circuit $U(\boldsymbol{\theta}_{opt.})$ to better compare our outcomes with the exact ground state energy E_0. The energies $E_1, \ldots, E_4$ of the first few excited states $|\phi\rangle_i$ are included to further support the arguments we make in the following paragraphs.

The data in Fig. 6.6(a) shows the optimal energies in the standard SSH model $\delta = 0$ obtained from the optimization algorithm. Each data point is computed from 100 evaluations of the same circuit on the quantum processor, and reconstructed from three basis measurements per point. Far away from the critical point, i.e. $|T| \gg 0$, the ground state is well separated from the excited states. Four degenerate states with energy E_0 emerge at $T = -1$, which cannot be distinguished by our measurement protocol. Our experimental data is well above the theoretical minimum E_0, however, the numerical simulation of the circuit confirms that the parameters $\boldsymbol{\theta}_{opt.}$ indeed implement a state, which is a good approximation of the true ground state. We therefore conclude, that the higher energies observed in our measurements are dominated by the noise in our apparatus and not a fundamental problem of the quantum circuit and its implementations. A more detailed analysis of the noise processes is presented in Sec. 6.4.

As we approach the critical point $T \approx 0$ from below, the degeneracy is slowly lifted: the true ground state $|\Psi\rangle_0$ and the first excited states differ by a small amount ΔE. In the presence of noise, this energy gap is difficult to resolve. Consequently, the algorithm converges to a solution, which deviates from $|\Psi\rangle_0$, but has still significant overlap. As it will become evident in Sec 6.3, the many-body topological invariants are not impacted by weak mixture with the excited states and can still faithfully resolve the phase transition.

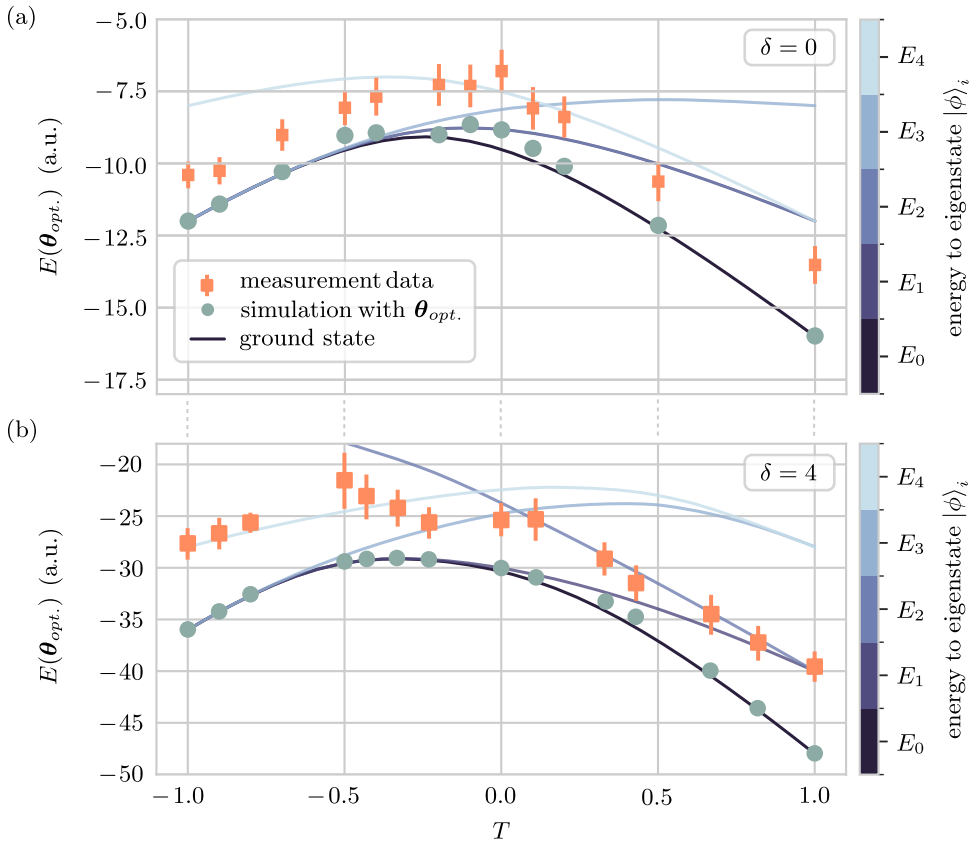


Figure 6.6: Energy of the approximate ground states generated by variational optimization for different coupling strengths. For selected values of the coupling strength T in the interval $T \in [-1, 1]$ we run the VQE and record the achieved optima. A simulation of the circuit (cyan) confirms the a good approximation of the ground state, which is otherwise not immediately evident from the noisy data; we show the ideal energies of the ground state (black) and the first few excited states (shades of blue) for direct comparison with our data. (a) best values obtained for the coupling strength $\delta = 0$ and (b) for $\delta = 4$ (extended model).

Similar arguments can be made for the states obtained from optimization in the *extended* SSH model, where we choose $\delta = 4$ to faithfully resolve the third, symmetry-broken regime in the phase diagram. From our data in Fig. 6.6(b) alone one might be tempted to conclude, that the prepared quantum states are far away from the true ground state. In comparison with the numerical simulation of the circuit, this argument can be dismissed: the simulated states agrees remarkably well with the $|\Psi\rangle_0$.

We stress once more, that the parameters $\boldsymbol{\theta}_{opt.}$ used in our numerical simulations are obtained from real experimental evaluations of the circuit on the quantum device. They are thus a good qualifier to gauge the performance of our circuit, which is impacted by various error mechanisms present in our setup; these will be discussed in Sec. 6.4. The

optimal parameters are recorded and used to map out the phase diagram by computing many-body topological invariants in Sec. 6.3.

6.3 OBSERVING A QUANTUM PHASE TRANSITION

We use the optimal parameters $\boldsymbol{\theta}_{opt.}$ obtained via the variational optimization discussed in Sec. 6.2.3 to prepare approximations of the true ground state $|\Psi\rangle_0$ of the (extended) SSH model. By measuring the quantum state $\varrho_{3,4,5,6}$ of the four-qubit subsystem at the center of the ion string – the *bulk* – we compute the MBTIs $\tilde{Z}_R$ and $\tilde{Z}_T$ introduced in Sec. 5.3.2. These MBTIs are associated with spatial reflection and time reversal symmetries, enabling us to resolve a quantum phase transition from the *trivial* to the *topological* regime.

6.3.1 *Trivial and topological regime in the standard SSH model*

The phase transition in the standard SSH model with coupling $\delta = 0$ is shown in Fig. 6.7. Each data point is computed from the four-qubit bulk states, which we reconstruct from state tomography on the subsystem[206, 209]. Our results agree well with the theoretical prediction for a system with $N = 8$ and bulk size $n = 4$, where the phase transition is smeared out over a large range of the coupling strength T. In the limit of large system sizes, the transition is more pronounced and localized around the critical point $T = 0$. We identify the *topological* regime for $T < 0$, while the *trivial* phase is recovered for $T > 0$.

Deviations from the predicted values are observed in the topological regime $T < 0$, which are also present in the results obtained by numerical simulation of the circuit with the respective $\boldsymbol{\theta}_{opt.}$. Interestingly, these values lie *below* the target curve. By comparison with theoretical values of the MBTIs for the first few excited states it becomes apparent, that the quantum states prepared by the variational algorithm in the topological regime are approximations of superpositions of the low-energy states. Such a behavior is expected due a four-fold degeneracy in this phase of the SSH model. Our argument is strengthened by the points at $T = -0.5$ and $T = -0.4$, where the simulated outcome for $\tilde{Z}_R$ is in between the two curves. These are exactly those points, where the degeneracy of the eigenstates is lifted just enough to observe a small energy gap ΔE, c.f. Fig. 6.6(a). However, the individual states cannot be faithfully distinguished by the optimizer in the presence of realistic noise.

We propose a simple solution to enhance the performance of the algorithm in future experiments: the ground state of the SSH model lies in a subsector of the Hamiltonian, where the *magnetization* $\langle M \rangle$ is zero. This observation allows engineering of a *penalty term*, which – when added to the cost function – already excludes two of the degenerate *ferromagnetic* states with $\langle M \rangle = \pm 2$.

The positive offset in our data is attributed to *decoherence* associated with the COM mode, which manifests in depolarization along the z axis of the qubits. These processes are detected in the topological phase, where both MBTIs are sensitive to phase errors. We present a more thorough analysis of the error mechanisms in the closing Sec. 6.4 of this chapter and continue our discussion with the symmetry breaking in the extended SSH model.

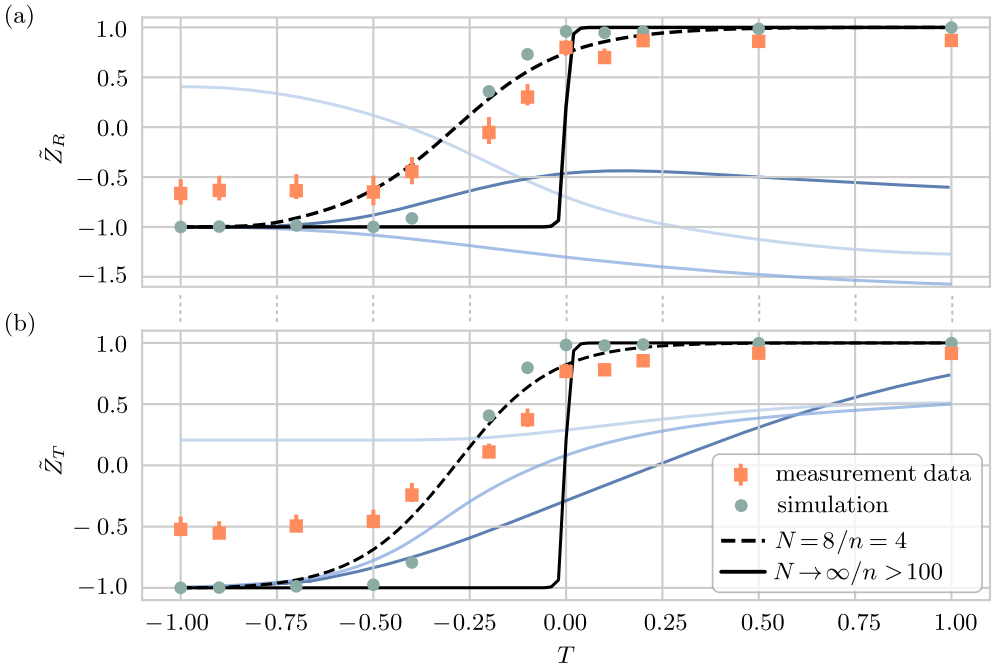


Figure 6.7: Quantum phase transition in the ordinary SSH model ($\delta = 0$). We show the MBTIs $\tilde{Z}_R$ in (a) and $\tilde{Z}_T$ in (b) obtained via quantum state tomography of the $n = 4$ bulk qubits in the center of the ion string. The data (orange) agrees with the theoretical prediction for a system of the same size (black dashed line). Note that in the limit of large system and bulk sizes, the transition would occur almost instantaneously as the critical point $T = 0$ is approached (black solid line). In the regime $T < 0$, the optimization algorithm approximates one of the degenerate eigenstates, which is evident from the numerical simulation (cyan) when compared to the theoretical results of the first few eigenstates (blue shaded lines). However, the different regimes in the SSH model can still be faithfully resolved.

6.3.2 *Symmetry breaking in the extended SSH model*

The additional $\delta\sigma_z^{(i)}\sigma_z^{(i+1)}$ interaction in the Hamiltonian gives rise to a *symmetry broken* phase between the topological and trivial regimes, where the ground state is *antiferromagnetic*. Here, both MBTIs approach a plateau and remain zero as the coupling T is close to the critical point at $T = 0$. Our results for $\delta = 4$ are summarized in Fig. 6.8. In direct comparison with the theoretical outcome all three regimes can be identified. However, the significant deviations in the topological and symmetry-broken phase merit further discussion.

We begin by examining the symmetry-broken phase, where the data exhibits a characteristic plateau. However, both measurement and numerical simulation results are in good agreement with the thermodynamic limit. This is attributed to the performance of the variational algorithm in the presence of noise and leads to a *polarization* into a less entangled state with spontaneous symmetry breaking, which is much closer to the state for $N \to \infty$. In theory, we can engineer this mechanism by forcefully lifting the degeneracy of the eigenstates by *pinning* the qubits on the edges of the string, such that

$$\hat{H} = \hat{H}_{eSSH}(T, \delta) + B(\sigma_z^{(1)} - \sigma_z^{(8)}) \qquad [6.5]$$

with sufficiently large magnetic field B. We find a good agreement with our experimental data for $B = 3$, see Appendix A.1.

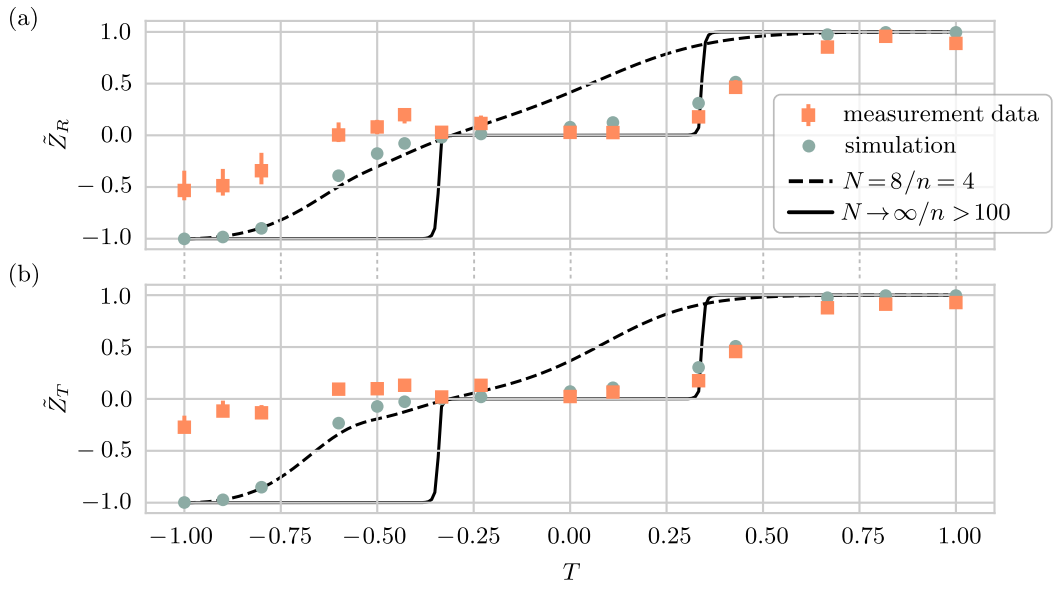


Figure 6.8: Quantum phase transition in the *extended* SSH model for $\delta = 4$. Next to the topological and the trivial regime, a third *symmetry broken* phase emerges as a plateau in the MBTIs as the coupling strength approaches the critical point $T = 0$. In this phase, the experimental data (orange) agrees with the thermodynamic limit (black, solid) rather than the prediction of the finite sized system (dashed). This feature is also present in simulation results (cyan), indicating that the algorithm prepares a different, yet physical ground state of the model. Deviations in the topological regime are attributed to depolarization, which the MBTIs $\tilde{Z}_R$ (a) and $\tilde{Z}_T$ (b) are sensitive to.

However, the polarization into the exact anti-ferromagnetic ground state cannot explain the deviations deep in the topological regime for $T < -0.75$, where the both MBTIs yield results that are well above -1. We again attribute the offset to depolarization: compared to the SSH mode, the additional term $\sigma_z^{(i)}\sigma_z^{(i+1)}$ in the ESSH Hamiltonian makes the quantum state less robust, further enhancing the sensitivity of the MBTIs. Note that for a fully depolarized state both MBTIs would approach zero in the topological phase.

Our protocol is well suited to preparing approximations of the ground states and low-energy eigenstates of the (extended) SSH model for different coupling strengths. We can faithfully resolve the phase transition between the individual regimes by measuring the two MBTIs $\tilde{Z}_R$ and $\tilde{Z}_T$. However, the topological regime proves to be challenging to access, as the quantum states are sensitive to experimental imperfections and noise.

6.4 IMPERFECTIONS AND ERROR MODELLING

We now investigate the impact of noise to explain the deviations between the experimental data an the theoretical prediction for the values of $\tilde{Z}_{R/T}$ in the topological regime. Our numerical simulation of the circuit in Fig. 6.1 is adapted to include an imperfect preparation of the QDB and heating of the COM mode. These effects manifest as phase errors on the qubits and lead to depolarization. For simplicity, we assume that each error occurs after

each blue sideband operation $\hat{B}^{(k)}(\theta_i)$ in Eq. [6.4] is applied. The performance of the model is quantified by computing the *residual sum of squares* (RSS) [216]

$$RSS = \sum_T \left(\tilde{Z}_{R,T}^{data}(T) - \tilde{Z}_{R,T}^{model}(T) \right)^2$$

for each value of T for the respective MBTI $\tilde{Z}_{R/T}$. We present our analysis using the extended SSH model at $\delta = 4$, where we further examine depolarizing effects along the individual spatial axes.

6.4.1 *Finite temperature and motional heating*

The motional state of the ion string is disturbed by electric field fluctuations, which introduce displacements of the ion string. As motion is associated with temperature, we call this process the *motional heating* of the ions. This mechanism is described by the channel

$$\varrho \mapsto \varrho' = (1-p) \cdot \varrho + p \cdot \hat{a}^\dagger \varrho \hat{a},$$

mapping the unperturbed state ϱ onto ϱ'. The probability $p = \Gamma_H \cdot t$ is given by the *heating rate* of the COM mode with $\Gamma_H = 27(1)$ phonons per second measured on our apparatus and the elapsed time t as the circuit progresses. This time is estimated using the target Rabi frequency $\Omega \approx 2\pi \cdot 8$ kHz on the blue sideband in our experiment, such that the rotation $\hat{B}^{(k)}(\pi)$ is associated with a duration $t_\pi = 125\ us$.

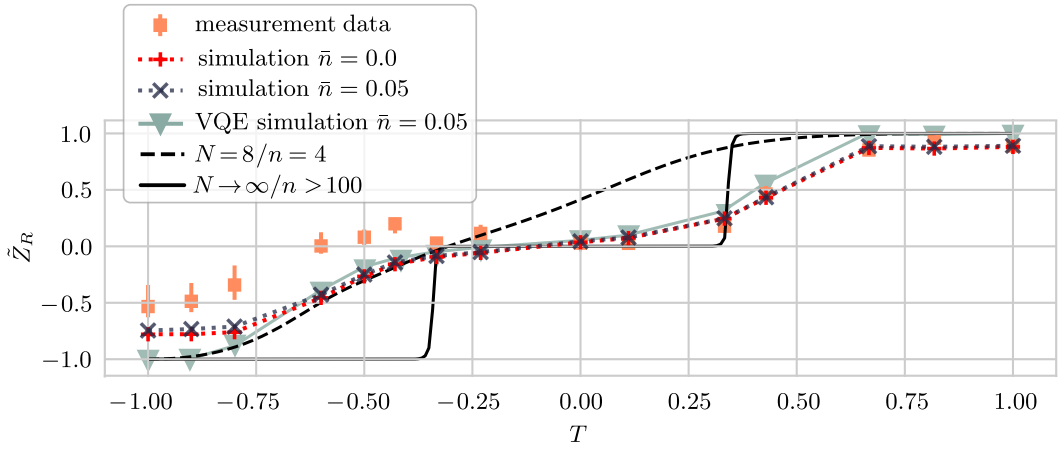


Figure 6.9: Impact of finite temperature and motional heating. We simulate the quantum circuit with the optimal parameters $\boldsymbol{\theta}_{opt.}$ and compute the MBTI $\tilde{Z}_R$ assuming a heating rate $\Gamma_H = 27(1)$ phonons per second and *initial* mean phonon numbers of $\bar{n} = 0.0$ (red) and $\bar{n} = 0.05$ (blue) for the COM mode. A simulation of the optimization algorithm at $\bar{n} = 0.05$ (cyan) *without* heating processes converges to a similar solution, which is in agreement with our data (orange) in the regime $T \approx 0$ near the critical point.

Fig. 6.9 shows our results for $\tilde{Z}_R$ assuming a perfectly cooled initial state with mean phonon number $\bar{n}(t=0) = 0.0$ (red) and an initial temperature of $\bar{n}(t=0) = 0.05$ (blue), which is a realistic value in our trapped ion processor. The circuit is simulated with the optimal parameters $\boldsymbol{\theta}_{opt.}$ obtained from our variational optimization measurements. Our results are in good agreement with the experimental outcomes (orange). In contrast with the ideal simulation in Fig. 6.8, the error model can in part reproduce the deviations observed in the topological regime, where the MBTIs are shifted to more positive values.

A comparison of the models by their respective RSS is given in Tab. 6.2.

However, the broadening of the plateau characteristic for the symmetry-broken phase is already present in our ideal simulation result. This is a strong indication, that the optimal parameters $\boldsymbol{\theta}_{opt.}$ implement a state which differs significantly from the true ground state. We therefore implement the VQE running the simulated circuit assuming an initial temperature $\bar{n}(t=0) = 0.05$. The algorithm converges to a solution (cyan) and reproduces the observed broadening.

model	$RSS\ \tilde{Z}_R$	$RSS\ \tilde{Z}_T$	RSS (averaged)
motional heating, $\bar{n}(t=0) = 0.0$	0.84(21)	0.45(11)	0.65(16)
motional heating, $\bar{n}(t=0) = 0.05$	0.71(18)	0.35(11)	0.65(16)
simulated VQE without heating, $\bar{n}(t=0) = 0.05$	1.11(96)	1.92(48)	1.52(22)

Table 6.2: Comparison of the residual sum of squares for different error models considering a finite initial temperature $\bar{n}(t=0)$ of the QDB and motional heating with heating rate $\Gamma_H = 27(1)$ phonons per second.

We conclude that finite temperature effects contribute to the broadening of the plateau in the symmetry-broken phase, while motional heating can explain some of the deviations observed in the topological regime.

6.4.2 *Depolarization and weighted Pauli errors*

The decoherence in the COM mode translates to local errors on the qubits as they are coupled to the QDB. These errors are modeled by a depolarizing channel [217]. On N qubits, this channel is given by

$$\varrho \mapsto \varrho' = \left(1 - \sum_{i=x,y,z} p_i\right)^N \cdot \varrho + \prod_j^N \sum_{i=x,y,z} p_i \hat{\sigma}_i^{(j)},$$

where the probabilities $p_{x,y,z}$ quantify the single-qubit Pauli errors $\sigma_{x,y,z}^{(n)}$ along the respective axis. Note, that $p_{x,y}$ are associated with imperfect rotation angles θ and therefore proportional to both intensity fluctuations of the light field and the duration of the laser pulse. These errors are expected to be *equal* along both axes and we therefore let $p_x = p_y$.

From the discussion of the capabilities of our apparatus, specifically the electronic control hardware in Sec. 3.3.1, we recall, that the pulse duration can be adjusted with a resolution of $\Delta t = 8$ ns. Fluctuations occuring on a similar scale have a negligible impact on the duration of a π pulse and can thus be ignored. Furthermore, the intensity of the laser pulses is actively stabilized, c.f. Sec. 3.2.4. We therefore conclude that the probabilities p_x and p_y are small and can be *neglected*. This argument is supported by our simulations, where we achieve the best approximations of the data for $p_x = p_y = 0$ and $p_z > 0$.

We show the numerical simulation of the circuit including depolarization along the z axis of the qubits for different probabilities p_z in Fig. 6.10 with the respective RSS in Tab. 6.3. While these errors have a small impact on the trivial phase, their impact in the topological regime results in a shift of the MBTI which is agreement with our data.

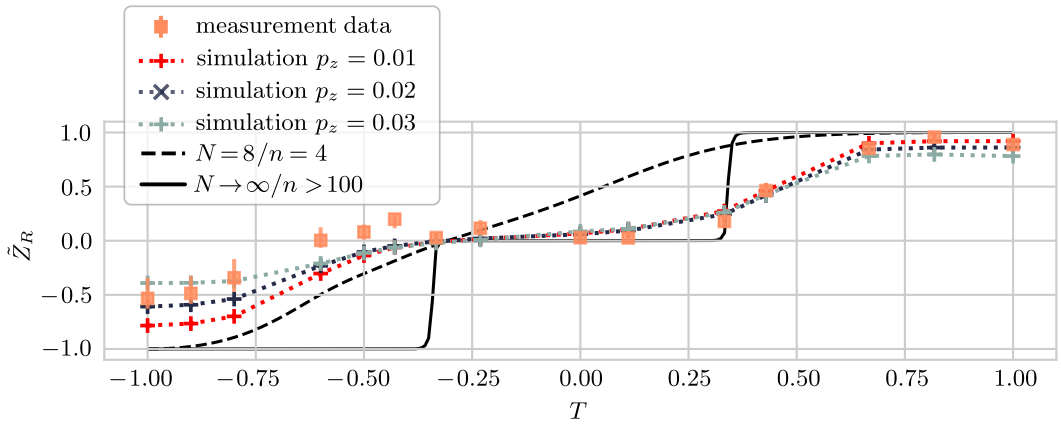


Figure 6.10: Numerical simulation of the quantum circuit including depolarization along the quantization axis (z axis) of the qubits. A significant impact is observed in the topological regime, where the value of the MBTI increases with p_z. A good approximation is achieved for $p_z = 0.03$, which yields an $RSS = 0.13(5)$ when averaged over both MBTIs.

By estimating the duration of our circuit $T_{circ.} \approx 34 \cdot t_\pi = 4.25$ ms we can exclude the laser as the dominant source of decoherence, as $T_2 \gg T_{circ.}$. However, when comparing our results to the observations made in Sec. 6.4.1, we argue that motional heating and finite temperatures of the initial state lead to decoherence of the COM mode, which effectively manifests in *phase* errors on the qubits. We find the best approximation for $p_z = 0.03$ with an averaged residual sum of squares of $RSS = 0.13(5)$.

probability	$RSS\ \tilde{Z}_R$	$RSS\ \tilde{Z}_T$	RSS (averaged)
$p_z = 0.01$	0.51(17)	0.64(14)	0.58(15)
$p_z = 0.02$	0.24(10)	0.19(7)	0.22(9)
$p_z = 0.03$	0.17(7)	0.098(4)	0.13(5)

Table 6.3: Comparison of the residual sum of squares for different probabilities of single-qubit Pauli errors in the z axis. A good agreement is found for $p_z = 0.03$ with an averaged $RSS = 0.13(5)$.

We conclude this chapter and briefly summarize our results: a variational quantum circuit preparing approximations of the ground states of the (extended) SSH model has been implemented on our trapped ion quantum processor. For different values of the coupling strengths T and δ a classical optimization algorithm has been employed to minimize the energy of quantum states prepared on the apparatus by tuning of the input parameters controlling the circuit. Once a minimum has been found, we fully reconstructed the state of the bulk by using quantum state tomography and maximum likelihood estimation. From these results, we computed the many-body topological invariants $\tilde{Z}_R$ and $\tilde{Z}_T$ to observe a quantum phase transition. Imperfections in our data can be attributed to decoherence of the QDB due to finite temperatures and motional heating, which translate into local Pauli errors on the qubits, leading to depolarization along the quantization axis.

7

QUANTUM FIELDS AND LATTICE GAUGE THEORIES

We perceive the world around us by interactions of our body with radiation: our eyes receive a constant stream of light, which is converted into electric signals to be interpreted by our brain. Similarly, our skin is sensitive to the heat irradiated from objects, which we can sense even at unimaginably large distances. Somehow, radiation must be able to propagate through space and time, even in the absence of a physical medium.

In 1852 Faraday extensively studied the attractive forces exerted on metals by permanent magnets. His observations lead to the speculation that forces are carried by *force lines*, which depend on the nature of the underlying force [218]. Inspired by these results, Maxwell further extended Faraday's picture to describe the interactions of static charges by *molecular vertices* [219]. Later in 1865 Maxwell formulated a consistent theory of electromagnetism and introduced the concept of an *electromagnetic field* [79].

> *"The theory I propose may therefore be called a theory of the Electromagnetic Field, because it has to do with the space in the neighbourhood of the electric or magnetic bodies and in may be called a Dynamical Theory, because it assumes that in that space there is matter in motion, [...] or we may endeavor to render it empty of all gross matter [...] There is always, however, enough of matter left to receive or transmit the undulations of light and heat, and [...] we are obliged to admit that the undulations are those of an aetheral substance [...]"*

At the time of Maxwell's studies it was still assumed that waves necessarily require a medium to propagate. Therefore, Maxwell suggested that electromagnetic radiation is carried by the so-called *luminiferous aether*, a hypothetical substance which permeates the universe. It was ultimately Einstein's theory of special relativity in 1905 which reformulated this concept [220]. Later in his work on general relativity, Einstein considered fields – in his context the *graviational field* – as a property of space itself [221, 222].

> *"Recapitulating, we may say that according to the general theory of relativity space is endowed with physical qualities; in this sense, therefore, there exists an ether. [...] But this ether may not be thought of as endowed with the quality characteristic of ponderable media, as consisting of parts which may be tracked through time."* [223]

We therefore imagine a field as a continuous function that permeates space and time. It reflects the properties of a physical quantity and obeys the laws of general relativity.

Up until the early 1920s electromagnetism was treated as a purely *classical* theory. However, after thoroughly studying the work of Einstein and Planck, de Broglie speculated in his doctoral thesis in 1924 that electrons are intimately coupled to *phase waves* with wavelengths characteristic to the electron's momentum [224].

> *It seems to us that the fundamental idea pertaining to quanta is the impossibility to consider an isolated quantity of energy without associating a particular frequency to it.*

De Broglies theory can be viewed as one of the foundations of modern quantum mechanics, directly inspiring Schrödinger to propose his non-relativistic wave equation describing the dynamics of particles, atoms and molecules in 1926 [225]. In the same year, the seminal work of Jordan, Born and Heisenberg laid the foundation for a quantum treatment of the free radiation field [226, 227]. It was Dirac's article on the emission and absorption of radiation which first provided a proper formulation of *quantum electrodynamics* (QED), a quantized theory of electromagnetic fields [228]. Together with his quantum theory of the electron published in 1928 [229], Dirac managed to unify quantum mechanics, classical fields and general relativity into a *relativistic quantum field theory*.

In this chapter, we discuss relativistic quantum fields with the focus on QED, which we will later study on a trapped-ion quantum processor in Ch. 8. We first revisit fundamental concepts of special relativity in Sec. 7.1, before introducing the general methods of classical field theory in Sec. 7.2, which also apply to quantum fields. Using the classical *Klein-Gordon field* as an example, we quantize the theory in Sec. 7.3 and follow Dirac's seminal work to derive the *Dirac field*, describing the dynamics of massive charged particles and *antiparticles* with half-integer spin. Demanding local invariance under symmetry transformations, we arrive at the concept of *gauge fields*, which are at the foundation of QED in Sec. 7.4, where we show some peculiarities of the theory. We conclude this chapter with a *Hamiltonian formulation* of QED on a lattice in Sec. 7.5, which provides a natural framework that can be efficiently investigated using current state-of-the-art quantum simulators.

Next to the original publications we closely follow the literature by Mandl & Shaw [78], Griffiths [230] and Weinberg [231], as well as the lecture series by Tong [232, 233]. Moreover, we employ the CGS system common in electrodynamics unless explicitly stated otherwise.

7.1 PRELIMINARIES

In this section we briefly revisit the concept of Lorentz transformations and introduce the index notation commonly used in general relativity. We then provide a *covariant* formulation of Maxwell's equations, which are essential in the study of classical and quantum electrodynamics.

7.1.1 *Lorentz transformations*

Suppose we want to describe photons of a light pulse as they propagate from a source S at the origin of our coordinate system to a detector D as illustrated in Fig. 7.1(a). Traveling at the speed of light c, a photon emitted by S will have traveled the distance $\overline{SD}$ in a time interval $t = \overline{SD}/c$, before it will be registered by D, e.g. as a "click". Consequently, [234, 235]

$$c^2t^2 = \overline{SD}^2 = x^2 \implies c^2t^2 - x^2 = 0 \tag{7.1}$$

and all vectors $\vec{v} = (t, x)$ satisfying this equation define the surface of the *light cone*[1].

1 Vectors $\vec{v}$ describing a point on the light cone are called *light-like*, in contrast to *space-like* vectors $|\vec{v}|^2 < 0$ and *time-like* vectors $|\vec{v}|^2 > 0$.

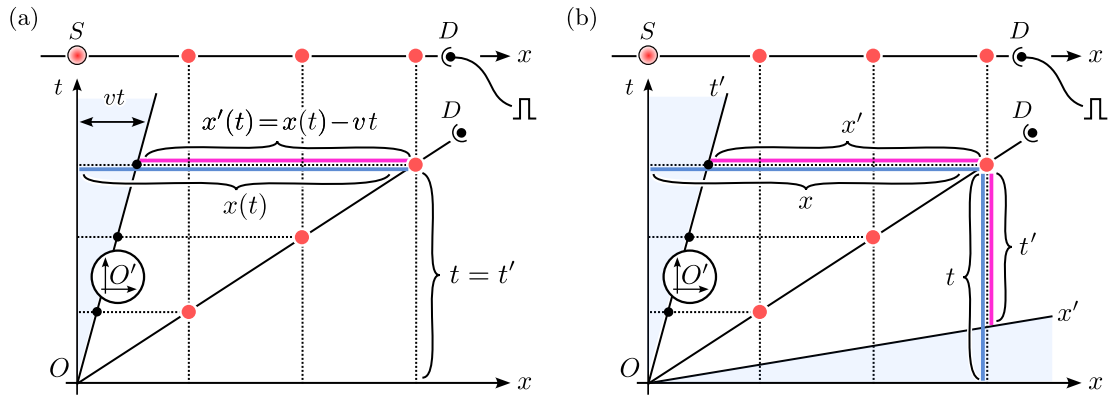


Figure 7.1: Illustration of Galilean and Lorentz transformations. A light source S emits photons at $t = 0$, which are registered by a detector D at a distance $\overline{SD}$ after some time t, obeying $c^2t^2 = \overline{SD}^2$. In a moving reference frame O' an observer equipped with a clock measuring time t' travels past the source with velocity v. (a) in the limit $v \ll c$, both clocks tick synchronously. The distance x' in O' (magneta) is related to x in O (blue) via the *Galilei transformation* $x' = c(1 - v/c)t$. (b) as v becomes comparable to the speed of light, the clock t in O (blue) appears to tick slower than t' in O' (magnenta). The appropriate *Lorentz transformation* Λ distorts both axes of the coordinate system with respect to the light cone, where the light pulse propagates.

Next to our frame of reference labeled O, we introduce a second frame O' associated with an observer moving with a constant velocity v along the y axis. As O' moves past O, the origins of both frames will briefly coincide, causing S to emit a photon as illustrated in Fig. 7.1(b). We observe its position as the time t progresses: in O, the photon has traveled $x(t) = ct$, while the distance $x'(t)$ in O' appears to be compressed [234].

Note that we deliberately did not attribute the *same* time to each reference frame. Although it is tempting to write $x'(t) = c(1 - v/c)t$, these *Galilean transformations* are only valid in the limit of $v \ll c$. As we move closer to relativistic velocities, time will differ significantly between O and O'. We therefore introduce a second "clock" for the observer in O', which measures the time t'. From O's perspective, t appears to be *dilated*, passing drastically slower as v approaches the speed of light. However, both frames still obey Eq. [7.1] [234], i.e.

$$c^2t^2 - x^2 = 0 = c^2t'^2 - x'^2 \Longleftarrow c(t^2 - t'^2) = x^2 - x'^2. \qquad [7.2]$$

From this *invariance of the quadratic form*, we deduce the properties of the *Lorentz transformations* Λ, which maps O onto O' and vice versa; for a derivation of Λ from physical principles the reader is directed to the work by J.-M. Levy in Ref. [236]. For a general vector in space and time, we obtain three classes of possible transformations [234]:

- *Rotations* $\Lambda_R \in SO(3)$ in 3D space, where $SO(3)$ is the *special orthogonal group* we have already introduced in the context of the Bloch sphere in Sec. 1.2.
- *Reflections* $\Lambda_S \in O(3)\backslash SO(3)$ in space. Here, $O(3)\backslash SO(3)$ is the *orthogonal group* without $SO(3)$, containing all transformations Λ_S satisfying $\det \Lambda_S = -1$
- *Boosts* with velocity v along an arbitrary direction $\vec{n}$. We typically decompose complex boosts into sequences of rotations and reflections, allowing us to perform a much simpler Λ_B along one of the axes of the coordinate systems.

While we are familiar with rotations and reflections, a *boost* e.g. along the x direction with velocity v takes the form [234, 235]

$$\Lambda_B = \begin{pmatrix} 1/\sqrt{1-v^2/c^2} & -v/c\sqrt{1-v^2/c^2} & 0 & 0 \\ -v/c\sqrt{1-v^2/c^2} & 1/\sqrt{1-v^2/c^2} & 0 & 0 \\ 0 & 0 & 1 & 0 \\ 0 & 0 & 0 & 1 \end{pmatrix} = \begin{pmatrix} \gamma & -\gamma\beta & 0 & 0 \\ -\gamma\beta & \gamma & 0 & 0 \\ 0 & 0 & 1 & 0 \\ 0 & 0 & 0 & 1 \end{pmatrix}, \quad [7.3]$$

where we have introduced the *Lorentz factor* $\gamma = 1/\sqrt{1-\beta^2}$ with $\beta = v/c$. The set of rotations, reflections and boosts together with the matrix multiplication form the *Lorentz group* $O(1,3)$, with the *special orthochronous group*[2] $SO(1,3)^+$ and the familiar $SO(3) = SO(1,3)$ as prominent subgroups.

The Lorentz group is of fundamental importance when discussing the concepts of *co- and contravariant* formulations: a covariant or *Lorentz-invariant* theory does not change under any Λ, and therefore has the same form regardless of the chosen frame of reference. Covariant theories can be written in a compact and elegant way using *four-vectors* which we introduce in the next chapter.

7.1.2 *Relativistic notation*

The Lorentz boost along the y direction in Eq. [7.3] is given by the 4×4 matrix Λ_B, establishing a mapping between vectors $\vec{X}$ and $\vec{X}'$, each having $(3+1)$ components. These vectors are objects in $(3+1)D$ *spacetime*, related by a Lorentz transformation Λ, such that

$$\vec{X}' = \begin{pmatrix} ct' \\ x' \\ y' \\ z' \end{pmatrix} = \Lambda \begin{pmatrix} ct \\ x \\ y \\ z \end{pmatrix} = \Lambda\vec{X}.$$

However, we rarely need to explicitly write down the entries of $\vec{X}$ and $\vec{X}'$. We introduce the notation used in general relativity [234]

$$\vec{X} = X^\nu \quad \text{with} \quad X^0 = ct, \;\; X^1 = x, \;\; X^2 = y, \;\; X^3 = z \quad [7.4]$$

and call X^ν a *contravariant four-vector* with components labeled $X^{\nu=0,\dots,3}$; these vectors are identified by a greek superscript. Geometry and causality of spacetime are captured by the *metric tensor* [234]

$$g_{\mu,\nu} = \delta_{0,0} - \sum_{i=1,2,3} \delta_{i,i}, \quad [7.5]$$

where $\delta_{i,j}$ is the familiar Kronecker delta. Note that depending on the literature, Eq. [7.5] can have the opposite sign. In this thesis, we consistently use the *signature* $(+,-,-,-)$, often abbreviated to $g(1,-3)$.

Applying $g_{\mu,\nu}$ to the contravariant vector X^ν, we obtain its *covariant* form

$$X_\mu = g_{\mu,\nu}X^\nu = (ct, -x, -y, -z), \quad [7.6]$$

2 The special orthochronous group $SO(1,3)^+$ maps time always onto the *forward light cone* with $t > 0$.

where we have used Einsteins summation convention to *contract* the greek sub- and superscripts ν [222]. Then, the square norm of X^μ is given by the scalar product of the co- and contravariant four-vectors [234]

$$X_\mu X^\mu = g_{\mu,\nu} X\nu X^\mu = c^2t^2 - x^2 - y^2 - z^2, \tag{7.7}$$

which is just the *invariant quadratic form* in Eq. [7.1].

The concept of co- and contravariance is illustrated in Fig. 7.2. We consider the vector $\vec{X}$ in a $2D$ subspace of spacetime with respect to the local basis $(\vec{e}_1, \vec{e}_2)$ in Fig. 7.2(a). The covariant components (X_1, X_2) of $\vec{X}$ are defined as the *orthogonal projections* of $\vec{X}$ onto the basis vectors [234]. Conversely, the contravariant components (X^1, X^2) are obtained from *parallel projections*. For a transformation Λ, which brings $\vec{e}_1$ and $\vec{e}_2$ closer towards $\vec{X}$ as shown in Fig. 7.2(b), the covariant components X_i follow its respective basis vector and are stretched. In contrast, the contravariant components X^i shrink as the transformation is applied.

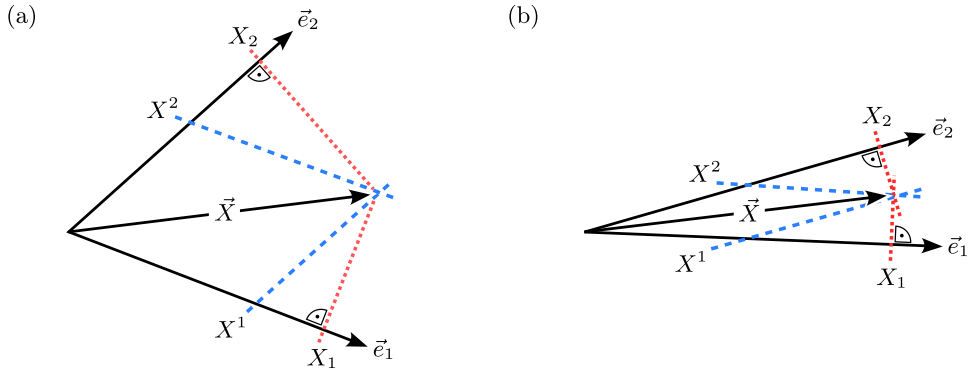


Figure 7.2: Illustration of the co- and contravariant components of a vector $\vec{X}$. The *orthogonal projection* of $\vec{X}$ onto the basis vectors $(\vec{e}_1, \vec{e}_2)$ define the covariant components (X_1, X_2), while *parallel projections* yield the contravariant components (X_1, X_2). Under a transformation Λ, which moves $\vec{e}_1$ and $\vec{e}_2$ closer towards $\vec{X}$, the covariant components X_i increase in magnitude , while the values of the contravariant entries X^i decrease.

Describing the dynamics of systems in $(3+1)D$ spacetime in terms of gradients and curls mandates the formulation of a *covariant derivative* ∂_μ, which is defined as [234]

$$\partial_\mu = \frac{\partial}{\partial X^\mu} = \left(\frac{1}{c}\frac{\partial}{\partial t}, \frac{\partial}{\partial x}, \frac{\partial}{\partial y}, \frac{\partial}{\partial z}\right) = \left(\frac{1}{c}\frac{\partial}{\partial t}, \nabla\right). \tag{7.8}$$

Its contravariant form is computed via the metric tensor, changing the sign with respect to the spatial derivatives, such that $\partial^\mu = g^{\mu,\nu}\partial_\nu = (1/c \cdot \partial/\partial t, -\nabla)$.

The concepts presented in this section will accompany us throughout this chapter, allowing for very compact notations of classical and quantum field theories. For instance, the covariant formulation of classical electrodynamics enables us to write all four Maxwell equations simultaneously in one expression, which we will introduce in the next section.

7.1.3 *Covariant formulation of classical electrodynamics*

We have introduced the mathematical framework to write classical electrodynamics – a not *strictly* covariant theory – in a form that is both elegant and, even more significantly, *Lorentz-*

invariant [235]. The fundamental set of equations in electrodynamics were formulated in 1865 by Maxwell [79]. In the presence of charges and currents, the dynamics of the electric field $\vec{E}$ and the magnetic field $\vec{B}$ are described by four equations [230]

$$\begin{aligned} &\text{(i):} \quad \nabla\vec{B} = 0 \qquad &&\text{(ii):} \quad \nabla\times\vec{E} + \tfrac{1}{c}\tfrac{\partial}{\partial t}\vec{B} = 0 \\ &\text{(iii):} \quad \nabla\vec{E} = 4\pi\varrho \qquad &&\text{(iv):} \quad \nabla\times\vec{B} - \tfrac{1}{c}\tfrac{\partial}{\partial t}\vec{E} = \tfrac{4\pi}{c}\vec{j} \end{aligned} \tag{7.9}$$

where ϱ and $\vec{j}$ are the charge and current densities arising from static and moving particles in space. Associated with $\vec{E}$ and $\vec{B}$ are the *electric scalar potential* ϕ and the *vector potential* $\vec{A}$, such that

$$\vec{B} = \nabla\times\vec{A} \qquad \text{and} \qquad \vec{E} = -\nabla\phi - \frac{1}{c}\frac{\partial}{\partial t}\vec{A}. \tag{7.10}$$

We now closely examine the spatial components of each field in non-relativistic euclidean coordinates: for example, consider the x-component of $\vec{B}$ and $\vec{E}$, which are given by [234]

$$B_x = \nabla\times\vec{A}\Big|_x = \partial_y A_z - \partial_z A_y \qquad \text{and} \qquad E_x = -\partial_x\phi + 1/c\cdot\partial_t A_x.$$

In the relativistic notation using four-vectors, the components are labeled by a Greek superscript μ, where $\mu = 0$ labels the time coordinate and $\mu = 1,\dots 3$ are assocated with the spatial coordinates, cf. Eq. [7.4]. We now naively replace the indices and obtain [234]

$$B_x = \partial^2 A^3 - \partial^3 A^2 \qquad \text{and} \qquad E_x = -\partial^1\phi - \partial^0 A^1,$$

which looks strikingly similar to contravariant derivatives ∂^ν applied to a *four-potential* $A^\mu = (\phi, \vec{A})$. However, the definition of ∂^ν will introduce a minus sign with respect to the spatial derivatives, which we have yet to account for.

Our example brings us to the *electromagnetic tensor* $F^{\mu,\nu}$, which is defined as[3] [78, 234]

$$F^{\mu,\nu} = \partial^\mu A^\nu - \partial^\nu A^\mu = \begin{pmatrix} 0 & -E_x/c & -E_y/c & -E_z/c \\ E_x/c & 0 & -B_z & B_y \\ E_y/c & B_z & 0 & -B_x \\ E_z/c & -B_y & B_x & 0 \end{pmatrix}. \tag{7.11}$$

This result already highlights the elegance of the relativistic notation: Eq. [7.10] reduces to one elegant expression, namely the tensor $F^{\mu,\nu}$.

Now consider the two inhomogeneous equations (iii) and (iv) in Eq. [7.9], which are known as *Gauss' law* and *Ampere's law*. With respect to $F^{\mu,\nu}$, Gauss' law is given by [234]

$$4\pi\varrho = \nabla\vec{E} = \partial_x E_x + \partial_y E_y + \partial_z E_z = \partial_1 F^{1,0} + \partial_1 F^{2,0} + \partial_2 F^{3,0} = \partial_\mu F^{\mu,0},$$

where we substitute ∇ by the covariant derivative ∂_μ in Eq. [7.8], and used Einstein's convention to contract the sum. Note that since $F^{\mu,\nu}$ is trace-less, the partial derivative $\partial_0 F^{0,0} = \frac{1}{c}\partial_t F^{0,0} = 0$.

Likewise, the x-component of the current density $\vec{j}$ in Ampere's law is given by [234]

$$\frac{4\pi}{c} j_x = \partial_y B_z - \partial_z B_y - \frac{1}{c}\partial_t E_x = \partial_2 F^{2,1} + \partial_3 F^{3,1} + \partial_0 F^{0,1} = \partial_\mu F^{\mu,1}.$$

3 Computing $F^{2,3} = \partial^2 A^3 - \partial^3 A^2 = -B_x$ and $F^{0,1} = \partial^1 A^0 - \partial^0 A^1 = -E_x/c$ now yields the correct signature for the components E_x and B_x of the electric and magnetic field.

We conclude that ϱ and $\vec{j}$ must be components of a *four-current* $J^\mu = (c\varrho, \vec{j})$, which allows us to express the inhomogeneous Maxwell equations in the covariant form

$$\partial_\mu F^{\mu,\nu} = \frac{4\pi}{c} J^\nu. \tag{7.12}$$

Applying the covariant derivative to J^ν yields the *continuity equation* [235]

$$\partial_\nu J^\nu = \frac{\partial}{\partial t}\varrho + \nabla J = 0, \tag{7.13}$$

which is a fundamental consequence of the antisymmetric nature of $F^{\mu,\nu} = -F^{\nu,\mu}$ and the *conservation of charge*.

In the first paragraph of this section, we have claimed that this formulation of classical electrodynamics will be Lorentz-invariant. Indeed, applying a Lorentz-transformation to the electromagnetic tensor yields

$$F^{\mu,\nu} = \Lambda^\mu_\alpha \Lambda^\nu_\beta F^{\alpha,\beta} = F^{\alpha,\beta}.$$

We illustrate this by example and use the Lorentz boost Λ_B defined in Eq. [7.3] to compute the component E'_y in the boosted frame O' [234, 235]:

$$\begin{aligned}
F^{2',0'} = E'_y &= \Lambda^{2'}_{B,\alpha}\Lambda^{0'}_{B,\beta}F^{\alpha,\beta} \\
&= \Lambda^{2'}_{B,\alpha}(\Lambda^{0'}_{B,0}F^{\alpha,0} + \Lambda^{0'}_{B,2}F^{\alpha,2}) \\
&= \Lambda^{2'}_{B,\alpha}(\gamma F^{\alpha,0} - \gamma\beta F^{\alpha,2}) \\
&= \Lambda^{2'}_{B,0}(\gamma F^{0,0} - \gamma\beta F^{0,2}) + \Lambda^{2'}_{B,2}(\gamma F^{2,0} - \gamma\beta F^{2,2}) \\
&= \gamma^2\beta^2\beta E_y - \gamma^2 E_y \\
&= \gamma^2 E_y(1-\beta^2) \\
&= E_y \\
\\
\longrightarrow E'_y &= E_y.
\end{aligned}$$

Since this result holds for any of the components of $F^{\mu,\nu}$, the entire electromagnetic tensor must be invariant under the boost Λ_B. Notably, $F^{\mu,\nu}$ is invariant under any general Lorentz transformation Λ [235].

Expressing Maxwell's equations in terms of the four-potential A^μ yields the wave equation $\Box A^\mu = 4\pi/cJ^\mu$, where $\Box = \partial_\mu\partial^\mu$ is the *d'Alembertian*. Solutions to $\Box A^\mu$ are waves, which upon quantization lead to QED and the emergence of the photon from symmetry arguments. We will discuss these topics in the remainder of this chapter.

7.2 LAGRANGIAN FIELD THEORY

In classical mechanics, we often describe the dynamics of a closed system in terms of forces $\vec{F}_i$, masses m_i, and accelerations $\vec{a}_i$. Introduced by Newton at the end of the 17th century, this formalism was well suited to describe most of the macroscopic phenomena that were studied at that time. However, with the advent of quantum mechanics and general relativity, it was soon discovered that Newton's framework is fundamentally incompatible with these theories. Alternative formulations of mechanics were introduced by Lagrange in 1788 and later by Hamilton in 1834, expressing the equations of motion in terms of energies [237].

For a single particle at position $\vec{r}$ traveling at a non-relativistic velocity $\vec{v} = \dot{\vec{r}}$, the *Lagrangian* is given by [43, 78]

$$L(\vec{r}, \dot{\vec{r}}) = T(\dot{\vec{r}}) - U(\vec{r}), \tag{7.14}$$

where $T(\dot{\vec{r}})$ and $U(\vec{r})$ are the kinetic and potential energies, respectively.

7.2.1 *Principle of least action*

Let our particle follow a parametrized trajectory $\vec{r}(t)$ between two points A and B in spacetime. We introduce the generalized coordinates $\vec{r}(t) \mapsto q(t)$ and $\dot{\vec{r}}(t) \mapsto \dot{q}(t) = \frac{d}{dt}q(t)$ and set $A = q(t = t_0)$ and $B = q(t = t_1)$. For each possible path $\overline{AB} = q(t)$ we compute the *action*, which is formally defined by [232, 237]

$$S[q(t)] = \int_{t_0}^{t_1} L(q(t), \dot{q}(t))\, dt. \tag{7.15}$$

Conceptually, $S[q(t)]$ is comparable to the work $W = \int_A^B \vec{F}\, ds$ in Newtonian mechanics: the action quantifies the *change in energy* as the particle moves along its path. It is a fundamental concept in quantum mechanics and field theories and at the heart of Feynman's path integral formalism, where a particle explores all possible trajectories connecting A and B *simultaneously*. In this framework, the time evolution of a system is described by the operator [238]

$$\hat{U}(t_0, t_1) = A(t) \sum_i e^{iS[q_i(t)]/\hbar},$$

where each path $q_i(t)$ contributes equally with amplitude $A(t)$. However, each $q_i(t)$ introduces a complex phase, which is proportional to the action $S[q_i(t)]$. The classical trajectory is recovered as the most probable path.

In nature, a system follows the trajectory that *extremizes* $S[q(t)]$, which is known as the *principle of least action*. Suppose the trajectory $q(t)$ satisfies this principle and we introduce a small perturbation $\epsilon \cdot \delta q(t)$ with $\epsilon \ll 1$, which vanishes at A and B. The Lagrangian can be approximated by the Taylor series

$$L\left(q + \epsilon \cdot \delta q, \dot{q} + \epsilon \cdot \frac{d}{dt}\delta q\right) = L(q, \dot{q}) + \epsilon \left[\delta q \frac{\partial}{\partial q} L + \frac{d}{dt}\delta q \frac{\partial}{\partial \dot{q}} L\right] + \mathcal{O}(\epsilon^2), \tag{7.16}$$

where $\mathcal{O}(\epsilon^2)$ labels all terms of higher orders in ϵ. Note that we did not explicitly write the time coordinate for the sake of brevity and readability. With this approximation, the action in Eq. [7.15] reads

$$\begin{aligned} S[q(t)+\epsilon\delta q(t)] &= S[q(t)] + \epsilon \int_{t_0}^{t_1} \left[\delta q(t)\frac{\partial}{\partial q}L + \frac{d}{dt}\delta q(t)\frac{\partial}{\partial \dot{q}}L\right] dt \\ &= S[q(t)] + \epsilon \cdot \delta S[q(t)]. \end{aligned} \tag{7.17}$$

By our assumption, the first term in Eq. [7.17] is extremized for our trajectory $q(t)$. We continue with the perturbation $\delta S[q(t)]$, which can be simplified via integration by parts of the second term to [232]

$$\begin{aligned} \delta S[q(t)] &= \int_{t_0}^{t_1} \left[\delta q(t)\frac{\partial}{\partial q}L + \frac{d}{dt}\delta q(t)\frac{\partial}{\partial \dot{q}}L\right] dt \\ &= \int_{t_0}^{t_1} \delta q(t) \left[\frac{\partial}{\partial q}L - \frac{d}{dt}\frac{\partial}{\partial \dot{q}}L\right] dt + \cancel{\delta q(t)\frac{\partial}{\partial \dot{q}}L\Big|_{t_0}^{t_1}}, \end{aligned} \tag{7.18}$$

where the last term cancels due to $\delta q(t)$ vanishing at the boundaries A and B. If $S[q(t)]$ is extremized, the remaining integral must vanish for arbitrary $\delta q(t)$. Consequently, the bracket in Eq. [7.18] must be zero and we obtain the *Euler-Lagrange equation* [78]

$$\delta S[q(t)] \stackrel{!}{=} 0 \Longrightarrow \frac{\partial}{\partial q}L(q,\dot{q}) - \frac{d}{dt}\frac{\partial}{\partial \dot{q}}L(q,\dot{q}) = 0, \tag{7.19}$$

which provides an alternative formulation of the equations of motion in classical mechanics.

7.2.2 *Classical fields and the Klein-Gordon equation*

We now extend our formalism and introduce the concept of *classical fields*. Essentially, a field is the generalization of a classical theory: massive bodies in Newtonian mechanics are replaced by gravitational fields $\vec{G}$, and the dynamics of charges in electrodynamics are described by the electric and magnetic field $\vec{E}$ and $\vec{B}$, respectively.

A field $\phi(r^\mu)$ with $x^\mu = (ct, \vec{r})$ is defined as a continuous quantity permeating $(3+1)D$ spacetime, mediating the interactions in the system we want to investigate. In contrast to classical theories, the dynamics of $\phi(r^\mu)$ are not described by a Lagrangian $L(\phi, \partial_\mu\phi)$, but rather a *Lagrangian density* $\mathcal{L}(\phi, \partial_\mu\phi)$, such that

$$L(\phi, \partial_\mu\phi) = \int_V \mathcal{L}(\phi, \partial_\mu\phi)\, d^3r \tag{7.20}$$

with ∂_μ denoting the covariant derivative introduced in Sec. 7.1. The classical action defined in Eq. [7.15] generalizes to

$$S[\phi] = \int_\Omega \mathcal{L}(\phi, \partial_\mu\phi)\, d^4r, \tag{7.21}$$

where we now have to integrate over a region Ω in spacetime [230]. Analogous to our discussion in the previous section, we introduce a small variation $\phi \mapsto \phi + \epsilon\delta\phi$ and repeat the derivation, ultimately arriving at the *Euler-Lagrange equation for fields*[4] [232]

$$\frac{\partial}{\partial\phi}\mathcal{L}(\phi, \partial_\mu\phi) - \partial_\mu \frac{\partial}{\partial(\partial_\mu\phi)}\mathcal{L}(\phi, \partial_\mu\phi) = 0. \tag{7.22}$$

We now consider the field theoretical analogue of the classical harmonic oscillator[5] and use the Lagrangian density [78]

$$\mathcal{L}(\phi, \partial_\mu\phi) = \frac{1}{2}\partial_\mu\phi\partial^\mu\phi - \frac{1}{2}M^2\phi^2 \tag{7.23}$$

to derive the dynamics of the field $\phi(x^\mu)$; the excitations of $\phi(x^\mu)$ correspond to physical particles with rest mass M. Following Eq. [7.22] we compute

$$\begin{aligned}
\frac{\partial}{\partial\phi}\mathcal{L}(\phi, \partial_\mu\phi) &= \frac{\partial}{\partial\phi}\left(\frac{1}{2}\partial_\mu\phi\partial^\mu\phi - \frac{1}{2}M^2\phi^2\right) = -M^2\phi \longrightarrow \\
&= \partial_\mu \frac{\partial}{\partial(\partial_\mu\phi)}\mathcal{L}(\phi, \partial_\mu\phi) \\
&= \partial_\mu \frac{\partial}{\partial(\partial_\mu\phi)}\left(\frac{1}{2}\partial_\mu\phi\partial^\mu\phi - \frac{1}{2}M^2\phi^2\right) \\
&= \frac{1}{2}\partial_\mu \frac{\partial}{\partial(\partial_\mu\phi)}\partial_\mu\phi \cdot g^{\mu,\nu}\partial_\nu\phi \\
&= \frac{1}{2}\partial_\mu\left[\left(\frac{\partial}{\partial(\partial_\mu\phi)}\partial_\mu\phi\right) \cdot g^{\mu,\nu}\partial_\nu\phi + \partial_\mu\phi \cdot g^{\mu,\nu}\left(\frac{\partial}{\partial(\partial_\mu\phi)}\partial_\nu\phi\right)\right] \\
&= \frac{1}{2}\partial_\mu\left[\partial^\mu\phi + \partial^\nu\phi\left(\frac{\partial}{\partial(\partial_\mu\phi)}\partial_\nu\phi\right)\right] \\
&= \frac{1}{2}\partial_\mu\left(\partial^\mu\phi + \partial^\nu\phi \cdot \delta^\mu_\nu\right) \\
\\
\longrightarrow -M^2\phi &= \partial_\mu\partial^\mu\phi
\end{aligned} \tag{7.24}$$

where δ^μ_ν is the Kronecker-Delta, since the partial derivative with respect to $\partial_\mu\phi$ for $\partial_\nu\phi$ only exists if $\mu = \nu$. Note that since ϕ and $\partial_\mu\phi$ in the Lagrangian are treated as independent variables, the partial derivative $\frac{1}{2}\frac{\partial}{\partial\phi}\left(\partial_\mu\phi\partial^\mu\phi\right)$ in the first line of Eq. [7.24] must vanish. Likewise, the term $\frac{1}{2}M^2\phi^2$ does not explicitly depend on $\partial_\mu\phi$ and thus $\frac{1}{2}M^2\frac{\partial}{\partial(\partial_\mu\phi)}\phi^2 = 0$. Using the *d'Alembertian* $\partial_\mu\partial^\mu = \frac{1}{c^2}\frac{\partial^2}{\partial t^2} - \nabla^2 = \Box$, we arrive at [78]

$$\partial_\mu\partial^\mu\phi + M^2\phi = \left(\Box + M^2\right)\phi = 0, \tag{7.25}$$

which is known as the *Klein-Gordon equation*, the relativistic generalization of the classical harmonic oscillator for a scalar field $\phi(r^\mu)$ [239, 240].

The Klein-Gordon equation is a relativistic *inhomogeneous wave equation*. A general solution is given by a superposition of plane waves

$$\phi(r^\mu) = \sum_{k_\mu} \psi(k_\mu)e^{-ik_\mu r^\mu} \tag{7.26}$$

4 Note that in the case of N fields, Eq. [7.22] must be satisfied for each ϕ_i with $i = 1, \ldots, N$.

5 The Lagrangian of a classical harmonic oscillator for a particle of mass M in one dimension is given by $L = \frac{1}{2}M(\partial_t x)^2 - \frac{1}{2}Mx^2$, which motivates the Lagrangian density in Eq. [7.23].

where $k^\mu = (k^0, k_x, k_y, k_z) = (k^0, \vec{k})$ are the *four-wave vectors* and $\psi(k_\mu)$ are the amplitudes associated with each wave contributing to $\phi(r^\mu)$. Solving Eq. [7.25] yields

$$\left(\Box + M^2\right)\phi(r^\mu) = \sum_{k_\mu} \psi(k_\mu)(\Box + M^2)e^{-ik_\mu r^\mu} = \sum_{k_\mu} \psi(k_\mu)(M^2 - k_\mu k^\mu)e^{-ik_\mu r^\mu} \stackrel{!}{=} 0, \quad [7.27]$$

which is *trivially* satisfied if all amplitudes $\psi(k_\mu)$ are zero. The *non-trivial* solution for arbitrary $\psi(k_\mu)$ imposes a restrictions on the k^μ, namely [78]

$$M^2 - k_\mu k^\mu = M^2 - \left((k^0)^2 - k_x^2 - k_y^2 - k_z^2\right) = M^2 - (k^0)^2 + \vec{k}^2 \stackrel{!}{=} 0.$$

Since the components of $\vec{k}$ describe the propagation of a wave $\psi(\vec{k})e^{i\vec{k}\vec{r}}$ in space, the condition $\vec{k} = \vec{0}$ implies $k^0 = 0$. For $\vec{k} \neq \vec{0}$, k^0 must satisfy $k^0 = \pm\sqrt{M^2 + \vec{k}^2}$. Using the relation by de Broglie we introduce the *four-momentum*

$$p^\mu = \hbar k^\mu = (E/c, \hbar\vec{k}) = (E/c, \vec{p}), \quad [7.28]$$

where E denotes the relativistic energy. Since $E/c = p^0 = \hbar k^0 = \hbar\sqrt{M^2 + \vec{k}^2}$, we obtain the relativistic *energy-momentum relation*[6] [78]

$$E^2 = \hbar^2 c^2 M^2 + \hbar^2 \vec{k}^2 = m^2 c^4 + \vec{p}^2 c^2 \quad [7.29]$$

and identify $M = mc/\hbar$, where m is the *rest mass* of a spinless particle. This is one of the familiar results in general relativity formulated by Einstein: the *equivalence of mass and energy* [221, 222].

7.3 QUANTUM FIELDS

We now seek to quantize the classical field to formulate a *quantum field theory* and consider the Klein-Gordon field as our first example. Since the field is essentially an infinite set of harmonic oscillators, we follow the familiar strategy of canonical quantization. In the quantum treatment of the harmonic oscillator we introduce the position and momentum operators $\hat{X}$ and $\hat{P}$, respectively, which satisfy *commutation relations* [36]

$$[\hat{X}, \hat{P}] = \hat{X}\hat{P} - \hat{P}\hat{X} = i\hbar.$$

Therefore, we call $\hat{P}$ the *conjugate variable* of $\hat{X}$ and vice versa. This formalism readily extends to fields: for a field $\phi(r^\mu)$, we introduce the *field conjugate* [78]

$$\pi(r^\mu) = \frac{\partial}{\partial(\partial_0\phi)}\mathcal{L}(\phi, \partial_\mu\phi) \quad [7.30]$$

which corresponds to the momentum operator $\hat{P}$. The field and its conjugate must also satisfy certain commutation relations as we will discover in this section. First, we will derive the quantum Klein-Gordon field and then continue with the *Dirac field*, which describes the relativistic dynamics of massive, charged particles. We then discuss the implications of symmetry transformations and introduce the concept of *gauge fields* as the foundation for the discussion of *quantum electrodynamics*.

6 A more compact notation of the energy-momentum relation is simply $p^\mu p_\mu = m^2c^2$.

7.3.1 *Canonical quantization of the Klein-Gordon field*

We now motivate the canonical quantization by comparing the relativistic, yet classical field $\phi(r^\mu)$ with the quantum harmonic oscillator. The classical solution in Eq. [7.26] is decomposed into two components $\phi^\pm(r^\mu)$ [78]

$$\phi(r^\mu) = \phi^+(r^\mu) + \phi^-(r^\mu) = \sum_{k_\mu} \left(\psi^+(k_\mu) e^{-ik_\mu r^\mu} + \psi^-(k_\mu) e^{ik_\mu r^\mu} \right), \tag{7.31}$$

each described by a Fourier series[7] associated with the positive and negative wave vectors, respectively. We then compute the field conjugate $\pi(r^\mu)$ as per Eq. [7.30] and obtain

$$\begin{aligned} \pi(r^\mu) &= \frac{\partial}{\partial(\partial_0\phi)} \mathcal{L}(\phi, \partial_\mu\phi) = \partial^0\phi(r^\mu) \\ &= -i \sum_{k_\mu} k_0 \left(\psi^+(k_\mu) e^{-ik_\mu r^\mu} - \psi^-(k_\mu) e^{ik_\mu r^\mu} \right) \\ &= \pi^+(r^\mu) + \pi^-(r^\mu) \end{aligned} \tag{7.32}$$

Computing the sum and difference of Eq. [7.31] and Eq. [7.32] allows for the computation of analytic expressions for the amplitudes $\psi^\pm(k_\mu)$. For simplicity, we assume a single k_μ and obtain

$$\psi^+(k_\mu) = e^{ik_\mu r^\mu} \left[k_0\phi(r^\mu) + i\pi(r^\mu) \right] \quad \text{and} \quad \psi^-(k_\mu) = e^{-ik_\mu r^\mu} \left[k_0\phi(r^\mu) - i\pi(r^\mu) \right]. \tag{7.33}$$

Evidently, the $\psi^\pm(k_\mu)$ are their mutual complex conjugates. Therefore, let $\psi^+(k_\mu) \mapsto \psi(k_\mu)$ and consequently $\psi^-(k_\mu) \mapsto \psi^*(k_\mu)$, where the superscript denotes complex conjugation. This substitution will be applied in the remainder of this section.

Since the classical Klein-Gordon equation is the relativistic generalization of the description of the harmonic oscillator, it is not surprising that $\psi(k_\mu)$ and $\psi^\star(k_\mu)$ are analogous to the familiar ladder operators $\hat{a}$ and $\hat{a}^\dagger$ in the quantum treatment [83]. We now compute the classical analogue of the commutator in quantum mechanics, which we will use extensively in later calculations. Given two functions $f(q, \dot{q})$ and $g(q, \dot{q})$, which depend on the conjugate variables q and $\dot{q}$, the *equal-time Poisson bracket* is given by [241]

$$\{f, g\} = \frac{\partial f}{\partial q}\frac{\partial g}{\partial \dot{q}} - \frac{\partial g}{\partial q}\frac{\partial g}{\partial \dot{q}}.$$

With $\phi(r^\mu)$ and $\pi(r^\mu) = \partial_\mu\phi(r^\mu)$ being canonical conjugates, we compute the bracket

$$\{\psi(k_\mu), \psi^\star(k_\mu)\} = \frac{\partial\psi(k_\mu)}{\partial\phi}\frac{\partial\psi^\star(k_\mu)}{\partial\pi} - \frac{\partial\psi^\star(k_\mu)}{\partial\phi}\frac{\partial\psi(k_\mu)}{\partial\pi} = -2ik_0, \tag{7.34}$$

which can be readily identified from Eq. [7.33]. Note that due to the symmetry of the bracket $\psi(k_\mu)$ also satisfies $\{\psi^\star(k_\mu), \psi(k_\mu)\} = 2ik_0$ and evidently

$$\{\psi(k_\mu), \psi(k_\mu)\} = \{\psi^\star(k_\mu), \psi^\star(k_\mu)\} = 0.$$

A field satisfying the Klein-Gordon equation obeys the relativistic energy-momentum relation in Eq. [7.29]. The energy and consequently k_0 are defined by the spatial component $\vec{k}$ of the four wave vector, which allows for the substitution [78]

$$k_0 = \frac{1}{\hbar}\frac{E(\vec{k})}{c}.$$

7 Note that a Fourier transform would be more appropriate to reflect the infinite number of variables in a continuous space. However, a series is more illustrative in the calculations presented in this section.

By the same line of reasoning, we replace k_μ in the argument by $\vec{k}$ and obtain for Eq. [7.34]

$$\{\psi(\vec{k}), \psi^\star(\vec{k})\} = -2ik_0 = \frac{1}{i\hbar}\frac{2E(\vec{k})}{c}.$$

We introduce $C(\vec{k}) = \sqrt{2E(\vec{k})/c}$ and normalize $\psi(\vec{k})$ by introducing

$$\psi(\vec{k}) = \frac{1}{C(\vec{k})}a(\vec{k}),$$

where $a(\vec{k})$ and its conjugate $a^\star(\vec{k})$ are time-independent functions reflecting the properties of $\psi(\vec{k})$. Ultimately, we obtain the Poisson brackets [78]

$$\{\psi(\vec{k}), \psi^\star(\vec{k})\} = \{a(\vec{k}), a^\star(\vec{k})\} = \frac{1}{i\hbar} \Longrightarrow \{\phi(r^\mu), \pi(r^\mu)\} = 1. \tag{7.35}$$

The field variables obey the classical analogue of the commutation relations of the position, momentum and ladder operators in the quantum treatment of the harmonic oscillator. This result is not surprising, since the Klein-Gordon equation is the field theoretical description of the same system in a relativistic, yet classical way. We now quantize the field by promoting the variables to operators [36, 242]

$$\phi(r^\mu) \mapsto \hat{\Phi}(r^\mu) \qquad \pi(r^\mu) \mapsto \hat{\Pi}(r^\mu) \qquad a(\vec{k}) = \hat{A}(\vec{k}) \tag{7.36}$$

and replace the complex conjugate with the hermitian conjugate, which we label by the dagger symbol in the superscript. Following the definition of the field $\phi^\dagger(r^\mu)$ in Eq. [7.31] the *field operator* $\hat{\Phi}(r^\mu)$ now reads

$$\hat{\Phi}(r^\mu) = \sum_{k_\mu}\left(\hat{A}^\dagger(\vec{k})e^{-ik_\mu r^\mu} + \hat{A}(\vec{k})e^{ik_\mu r^\mu}\right). \tag{7.37}$$

We use the relationship between the Poisson brackets and commutators

$$\{f, g\} = i\hbar\left[\hat{F}, \hat{G}\right],$$

where the functions (f, g) have become operators $(\hat{F}, \hat{G})$, to compute the bosonic commutation relations for the operators in Eq. [7.36] [78]

$$\begin{array}{ll} \left[\hat{\Phi}(x^\mu), \hat{\Pi}(y^\mu)\right] = i\hbar\delta(x^\mu - y^\mu) & \left[\hat{\Pi}(x^\mu), \hat{\Pi}(y^\mu)\right] = \left[\hat{\Phi}(x^\mu), \hat{\Phi}(y^\mu)\right] = 0 \\ \left[\hat{A}(\vec{k}), \hat{A}^\dagger(\vec{k}')\right] = \delta(\vec{k} - \vec{k}') & \left[\hat{A}(\vec{k}), \hat{A}(\vec{k}')\right] = \left[\hat{A}^\dagger(\vec{k}), \hat{A}^\dagger(\vec{k}')\right] = 0 \end{array} \tag{7.38}$$

where x^μ and y^μ are two coordinates in spacetime and $\vec{k}, \vec{k}'$ are the wave vectors in space. The common eigenstates of the ladder operators $\hat{A}(\vec{k})$ and $\hat{A}^\dagger(\vec{k})$ are number states labeled $|n\rangle_k$, which satisfy the relations

$$\hat{A}^\dagger(\vec{k})\,|n\rangle_k = \sqrt{n_k + 1}\,|n\rangle_k \qquad \text{and} \qquad \hat{A}(\vec{k})\,|n\rangle_k = \sqrt{n_k}\,|n-1\rangle_k. \tag{7.39}$$

These states represent particles manifesting as excitations of the field $\hat{\Phi}(r^\mu)$ from a unique *vacuum state* $|0\rangle_k$, which is characterized by $\hat{A}(\vec{k})\,|0\rangle_k = 0$. While $\hat{\Phi}(r^\mu)$ is a quantity which cannot be directly observed, we can measure the presence and absence of particles via the number operator [232]

$$\hat{N}(\vec{k}) = \hat{A}^\dagger(\vec{k})\hat{A}(\vec{k}) \qquad \text{with} \qquad \hat{N}(\vec{k})\,|n\rangle_k = n(\vec{k})\,|n\rangle_k.$$

We define the *Hamiltonian density* $\mathcal{H}$ of the field [78]

$$\mathcal{H}(\hat{\Phi}, \hat{\Pi}) = \hat{\Pi}(r^\mu)\partial_0\hat{\Phi}(r^\mu) - \mathcal{L}(\hat{\Phi}, \partial_\mu\hat{\Phi}) \tag{7.40}$$

and introduce the Hamilton operator $\hat{H}$ by integrating $\mathcal{H}$ over a finite volume V in space. Using Eq. [7.30] we compute the field conjugate and obtain

$$\hat{H} = \int_V \mathcal{H}(\hat{\Phi}, \hat{\Pi})\ d^3r = \frac{1}{2}\int_V \left(m^2\hat{\Phi}^2 + \hat{\Pi}^2 - (\nabla\hat{\Phi})^2\right)\ d^3r,$$

which simplifies using the operators $\hat{A}^\dagger(\vec{k})$ and $\hat{A}(\vec{k})$ to

$$\hat{H} = \sum_{\vec{k}} E(\vec{k})\left(\hat{A}^\dagger(\vec{k})\hat{A}(\vec{k}) + \frac{1}{2}\right) = \sum_{\vec{k}} E(\vec{k})\left(\hat{N}(\vec{k}) + \frac{1}{2}\right). \tag{7.41}$$

Moreover, we introduce the momentum

$$\hat{P} = \int_V \Pi\nabla\Phi\ d^3r = \sum_{\vec{k}} \hbar\vec{k}\left(\hat{A}^\dagger(\vec{k})\hat{A}(\vec{k}) + \frac{1}{2}\right) = \sum_{\vec{k}} \hbar\vec{k}\left(N(\vec{k}) + \frac{1}{2}\right) \tag{7.42}$$

and the *four-momentum operator* $p^\mu \mapsto P^\mu = (\hat{H}/c, \hat{P})$. Note, that these are just the equations we obtain for the quantum harmonic oscillator [78, 231].

We are now interested in computing probabilities analogous to the non-relativistic case, where the dynamics of a system is described by the Schrödinger equation [36]. The quantum state of the system is described by the wave function $\psi(\vec{r}, t)$ and obeys the normalization condition

$$\forall t \in \mathbb{R}\colon \quad 1 = \int_V \psi(\vec{r}, t)\psi^\dagger(\vec{r}, t)\ d^3r = \int_V \varrho(\vec{r}, t)\ d^3r,$$

where $\varrho(\vec{t}, t) = |\psi(\vec{r}, t)|^2$ is the probability density. As $\psi(\vec{r}, t)$ is a solution of the Schrödinger equation for a Hamiltonian $\hat{H}$, the probability density $\varrho(\vec{r}, t)$ obeys a continuity equation

$$\begin{aligned}\frac{\partial}{\partial t}\varrho(\vec{r}, t) &= \frac{\partial}{\partial t}\psi(\vec{r}, t)\psi^\dagger(\vec{r}, t) = \psi^\dagger(\vec{r}, t)\frac{\partial}{\partial t}\psi(\vec{t}, t) + \psi(\vec{r}, t)\frac{\partial}{\partial t}\psi^\dagger(\vec{r}, t)\\ &= \frac{i}{\hbar}\left[\psi^\dagger(\vec{r}, t)\hat{H}\psi(\vec{r}, t) - \psi(\vec{r}, t)\hat{H}\psi^\dagger(\vec{r}, t)\right].\end{aligned}$$

The Hamiltonian of a free particle with mass m is given by $\hat{H} = -\frac{-\hbar^2}{2m}\nabla^2$; using

$$\left(\nabla^2\psi(\vec{r}, t)\right)\psi^\dagger(\vec{r}, t) = \nabla\left(\nabla\psi(\vec{r}, t)\right)\psi^\dagger(\vec{r}, t) + \left(\nabla\psi(\vec{r}, t)\right)\left(\nabla\psi^\dagger(\vec{r})\right)$$

we simplify the continuity equation and introduce the *probability flux density* $\vec{j}(\vec{r}, t)$

$$\partial_t\varrho(\vec{r}, t) = -\frac{i\hbar}{2m}\nabla\left(\psi^\dagger(\vec{r}, t)\nabla\psi(\vec{r}, t) - \psi(\vec{r}, t)\nabla\psi^\dagger(\vec{r}, t)\right) = -\nabla\vec{j}(\vec{r}, t) \tag{7.43}$$

Since the probability density satisfies a continuity equation, it must be a conserved quantity and is strictly positive. We will show in the following paragraph, that the Klein-Gordon equation violates this condition: while a conserved quantity exists, the probability density also be negative [231, 243].

Let $\hat{\Phi}(r^\mu)$ be a field which satisfies the Klein-Gordon equation: multiplying Eq. [7.25] from the left with $\hat{\Phi}^\dagger(r^\mu)$ yields

$$\hat{\Phi}^\dagger(r^\mu)\left(\Box + \frac{m^2c^2}{\hbar^2}\right)\hat{\Phi}(r^\mu) = 0,$$

which is equal to its hermitian conjugate. We obtain the continuity equation

$$\begin{aligned}
\hat{\Phi}^\dagger(r^\mu)\left(\Box + \frac{m^2c^2}{\hbar^2}\right)\hat{\Phi}(r^\mu) &= \hat{\Phi}(r^\mu)\left(\Box + \frac{m^2c^2}{\hbar^2}\right)\hat{\Phi}^\dagger(r^\mu) \\
\hat{\Phi}^\dagger(r^\mu)\Box\hat{\Phi}(r^\mu) &= \hat{\Phi}(r^\mu)\Box\hat{\Phi}^\dagger(r^\mu) \\
\hat{\Phi}^\dagger(r^\mu)\frac{\partial^2}{\partial t^2}\hat{\Phi}(r^\mu) - \hat{\Phi}(r^\mu)\frac{\partial^2}{\partial t^2}\hat{\Phi}^\dagger(r^\mu) &= \hat{\Phi}^\dagger(r^\mu)\nabla^2\hat{\Phi}(r^\mu) - \hat{\Phi}(r^\mu)\nabla^2\hat{\Phi}^\dagger(r^\mu) \\
i\frac{\partial}{\partial t}\left(\hat{\Phi}^\dagger(r^\mu)\frac{\partial}{\partial t}\hat{\Phi}(r^\mu) - \hat{\Phi}(r^\mu)\frac{\partial}{\partial t}\hat{\Phi}^\dagger(r^\mu)\right) &= -i\nabla\left(\hat{\Phi}(r^\mu)\nabla\hat{\Phi}^\dagger(r^\mu) - \hat{\Phi}^\dagger(r^\mu)\nabla\hat{\Phi}(r^\mu)\right) \\
\partial_t\varrho(\hat{\Phi}, \partial_t\hat{\Phi}) &= -\nabla\vec{j}(\hat{\Phi})
\end{aligned} \tag{7.44}$$

where $\varrho(\hat{\Phi}, \partial_t\hat{\Phi})$ and $\vec{j}(\hat{\Phi})$ are the probability density and flux, respectively. Note that we have multiplied both sides with the complex number i to obtain real-valued densities[8].

In contrast to the non-relativistic case, a solution $\hat{\Phi}(r^\mu)$ of the Klein-Gordon equation can yield negative probabilities. We obtain an additional degree of freedom, since the density is defined by both $\hat{\Phi}(r^\mu)$ and its derivative with respect to time $\partial_t\hat{\Phi}(r^\mu)$, respectively its conjugates. Hence, a perfectly valid solution $\hat{\Phi}(r^\mu)$ can produce non-physical outcomes [243]. Moreover, while the Klein-Gordon equation includes the mass of particles, it neglects their charge and spin. These issues are resolved by the *Dirac equation*, which we will introduce in the next section.

7.3.2 *The Dirac field*

Two fundamental problems of the Klein-Gordon equation were pointed out in 1928 by Dirac [229]. First, the negative probability density $\varrho(\hat{\Phi}, \partial_t\hat{\Phi})$ lacks a clear physical interpretation. Our argument in the previous section attributes the cause to an additional degree of freedom introduced by the derivative $\partial_t\hat{\Phi}$. Ultimately, the issue arises from the Klein-Gordon equation, which is second order in both space and time – in contrast to the non-relativistic Schrödinger equation, which is only first order in time. Second, solutions in the non-relativistic limit should reflect the classical dynamics of a massive particle. However, if one introduces charges, two oppositely charged particles with net charges $\pm e$ would behave identically regardless of the sign, which evidently contradicts experimental observations. Moreover, transitions between positive and negative energies are generally not forbidden but violate the conservation of charge. Consequently, a relativistic wave equation [229]

> *"[...] should thus be such that its solutions split up into two non-combining sets, referring respectively to the charge $-e$ and the charge $+e$."*

8 Since the product of $\hat{\Phi}(r^\mu)\partial_t\hat{\Phi}^\dagger(r^\mu)$ is complex and $\hat{\Phi}^\dagger(r^\mu)\partial_t\hat{\Phi}(r^\mu)$ is its hermitian conjugate, the difference must be purely imaginary.

In this context the charges $\pm e$ are associated with positive and negative energies. We therefore introduce two fields $\phi^{\pm}(r^\mu)$, which describe free particles of mass m and momentum $\vec{p}$ and satisfy the relativistic energy-momentum relation with respective $\pm E$. Following the seminal work by Dirac we introduce four coefficients $\alpha_{i=0,\dots 3}$ and factorize [36, 229]

$$E^2 = \vec{p}^2c^2 + m^2c^4 = c^2\left(\alpha_0 mc + \vec{\alpha}\vec{p}\right)^2, \qquad [7.45]$$

where $\vec{\alpha} = (\alpha_1, \alpha_2, \alpha_3)$; consequently, the α_i must satisfy

$$\begin{aligned} E^2 &= c^2\left(\alpha_0^2 m^2c^2 + mc\sum_{i=1}^{3}\alpha_0\alpha_i p_i + mc\sum_{i=1}^{3}\alpha_i\alpha_0 p_i + \sum_{i=1}^{3}\sum_{j=1}^{3}\alpha_i\alpha_j p_i p_j\right) \\ &= \alpha_0^2 m^2c^4 + mc^3\sum_{i=1}^{3} p_i\left(\alpha_0\alpha_i + \alpha_i\alpha_0\right) + c^2\sum_{i=1}^{3}\sum_{j=1}^{3}\alpha_i\alpha_j p_i p_j \end{aligned}$$

$$\Rightarrow \alpha_0^2 = 1 \quad \Rightarrow \forall i = 1,2,3\colon\ \alpha_0\alpha_i + \alpha_i\alpha_0 = 0 \quad \Rightarrow \forall i = 1,2,3\colon\ \alpha_i\alpha_j = \delta_{i,j}. \qquad [7.46]$$

If $\phi^{\pm}(r^\mu)$ were scalar functions, the *anti-commutator* would yield $\{\alpha_0, \alpha_i\} = \alpha_0\alpha_i + \alpha_i\alpha_0 = 2\alpha_i\alpha_0$, implying that either $\alpha_0 = 0$ or $\alpha_i = 0\ \forall i$. As both cases violate the energy-momentum relation, the α_i must be anti-commuting matrices. This is a reflection of the particle's spin, which arises naturally through the factorization of Eq. [7.45]. Consequently, each solution $\phi^{\pm}(r^\mu)$ has two components corresponding to the spin configurations $(\uparrow, \downarrow)$, which are represented by the fields $\phi^{\pm}(r^\mu) = (\phi^{\pm}_{\uparrow}(r^\mu), \phi^{\pm}_{\downarrow}(r^\mu))$.

Together with the identity matrix $\alpha_0 = \mathbb{1}$, the Pauli matrices[9] σ_i evidently satisfy the conditions in Eq. [7.46]. However, we must still distinguish two solutions corresponding to different energies $\pm E$. Therefore, we combine both fields $\phi^{\pm}(r^\mu)$ into a four-component *Dirac-field* $\Phi(r^\mu) = (\phi^{+}(r^\mu), \phi^{-}(r^\mu))$ and expand the matrices α_i such that

$$\alpha_0 = \begin{pmatrix} \mathbb{1} & 0 \\ 0 & -\mathbb{1} \end{pmatrix} \quad \text{and} \quad \forall i = 1,2,3\colon\ \alpha_i = \begin{pmatrix} 0 & \sigma_i \\ \sigma_i & 0 \end{pmatrix}.$$

Upon substitution of energy and momentum with their respective operators[10] $E = i\hbar\partial_t$ and $\vec{p} = -i\hbar\nabla$ in Eq. [7.45] we obtain the *Dirac equation* [229, 244]

$$\begin{aligned} \mathbb{1}\cdot\frac{E}{c}\Phi(r^\mu) &= \left(\alpha_0 mc + \sum_{i=1}^{3}\alpha_i p_i\right)\Phi(r^\mu) \\ \alpha_0\frac{E}{c}\Phi(r^\mu) &= \left(\mathbb{1}\cdot mc + \sum_{i=1}^{3}\alpha_0\alpha_i p_i\right)\Phi(r^\mu) \ \Rightarrow \text{let } \gamma_0 = \alpha_0 \text{ and } \gamma_i = \alpha_0\alpha_i = \begin{pmatrix} 0 & \sigma_i \\ -\sigma_i & 0 \end{pmatrix} \\ \Rightarrow i\hbar\gamma_0\frac{1}{c}\partial_t\Phi(r^\mu) &= \left(\mathbb{1}\cdot mc - i\hbar\sum_{i=1}^{3}\gamma_i\partial_i\right)\Phi(r^\mu) \\ 0 &= \left(i\hbar\gamma_0\frac{1}{c}\partial_t + i\hbar\sum_{i=1}^{3}\gamma_i\partial_i - \mathbb{1}\cdot mc\right)\Phi(r^\mu) \\ 0 &= \left(i\hbar\gamma^\mu\partial_\mu - mc\right)\Phi(r^\mu), \end{aligned} \qquad [7.47]$$

9 To be consistent with the definition of the Pauli matrices in Eq. [1.13] we map the integers $i = 1,2,3$ to the coordinate axes, such that $1 = x$, $2 = y$ and $3 = z$.

10 Note that this is already a first step towards the quantization of the Dirac field.

with *Dirac matrices* γ^μ and covariant derivative ∂_μ, cf. Eq. [7.8]. In this form, the equation is a relativistic treatment of free spin-1/2 particles with mass m, accounting for both charges $\pm e$ and spin states $(\uparrow, \downarrow)$.

Suppose that the field $\Phi(r^\mu)$ is a solution of the Dirac equation. Consequently, each $\phi^\pm(r^\mu)$ and the fields associated with the respective spin states $\phi^\pm_{\uparrow,\downarrow}(r^\mu)$ must also independently satisfy the equation. We obtain the orthogonality relations [78]

$$\begin{aligned} \phi_j^{\pm\,\dagger}(r^\mu)\gamma_0\left(i\hbar\gamma^\mu\partial_\mu \mp mc\right)\phi_k^\pm(r^\mu) = 0 &\Longrightarrow \phi_j^{\pm\,\dagger}(r^\mu)\phi_k^\pm(r^\mu) = \frac{E}{mc^2}\delta_{j,k} \\ \phi_j^{\pm\,\dagger}(r^\mu)\gamma_0\left(i\hbar\gamma^\mu\partial_\mu \mp mc\right)\phi_k^\mp(r^\mu) = 0 &\Longrightarrow \phi_j^{\pm\,\dagger}(r^\mu)\phi_k^\mp(r^\mu) = 0 \end{aligned} \tag{7.48}$$

where the subscripts j, k label the particle's spin $\uparrow, \downarrow$. Note that these relations imply the conservation of charge: fields associated with different energies are orthogonal. Moreover, all commutators involving $\phi_j^\pm(r^\mu)$ and $\phi_k^\pm(r^\mu)$ vanish naturally, which reflects Pauli's exclusion principle, whereby fermionic wave functions are anti-symmetric; therefore, we are left with computing the anti-commutator $\{\Phi(r^\mu), \Phi^\dagger(r^\mu)\}$.

We decompose the general field into a superposition of solutions for opposite charges $\Phi(r^\mu) = C\Phi^+(r^\mu) + D\Phi^-(r^\mu)$ with amplitudes C, D and use the orthogonality relations in Eq. [7.48] to simplify the anti-commutator[11]

$$\begin{aligned} \{\Phi(r^\mu), \Phi^\dagger(r^\mu)\} &= C^2\{\Phi^+(r^\mu), \Phi^{+\,\dagger}(r^\mu)\} + \cancel{CD\{\Phi^+(r^\mu), \Phi^{-\,\dagger}(r^\mu)\}} \\ &\quad + \cancel{CD\{\Phi^-(r^\mu), \Phi^{+\,\dagger}(r^\mu)\}} + D^2\{\Phi^-(r^\mu), \Phi^{-\,\dagger}(r^\mu)\} \\ &= C^2\{\phi_\uparrow^+(r^\mu), \phi_\uparrow^{+\,\dagger}(r^\mu)\} + C^2\{\phi_\downarrow^+(r^\mu), \phi_\downarrow^{+\,\dagger}(r^\mu)\} \\ &\quad + D^2\{\phi_\uparrow^-(r^\mu), \phi_\uparrow^{-\,\dagger}(r^\mu)\} + D^2\{\phi_\downarrow^-(r^\mu), \phi_\downarrow^{-\,\dagger}(r^\mu)\}. \end{aligned} \tag{7.49}$$

The independent solutions $\phi^\pm_{\uparrow,\downarrow}$ of the Dirac equation can be expressed as a superposition of plane waves [78]

$$\phi^+_{\uparrow,\downarrow}(r^\mu) = \sum_{k_\mu} \alpha_{\uparrow,\downarrow}(\vec{k}) u_{\uparrow,\downarrow}(\vec{k}) e^{-ik_\mu r^\mu} \quad \text{and} \quad \phi^-_{\uparrow,\downarrow}(r^\mu) = \sum_{k_\mu} \beta_{\uparrow,\downarrow}(\vec{k}) v_{\uparrow,\downarrow}(\vec{k}) e^{-ik_\mu r^\mu} \tag{7.50}$$

where $u_{\uparrow,\downarrow}(\vec{k})$ and $v_{\uparrow,\downarrow}(\vec{k})$ are disjoint sets of *bi-spinors*[12] associated with the positive and negative energies, respectively [78, 244]. Analogous to the quantization of the Klein-Gordon field, we normalize the amplitudes $\alpha_{\uparrow,\downarrow}(\vec{k})$ and $\beta_{\uparrow,\downarrow}(\vec{k})$ following Eq. [7.48] and obtain [232]

$$\begin{aligned} \phi^+_{\uparrow,\downarrow}(r^\mu) &= \sum_{k_\mu} \sqrt{\tfrac{mc^2}{2E(\vec{k})}}\alpha_{\uparrow,\downarrow}(\vec{k}) u_{\uparrow,\downarrow}(\vec{k}) e^{-ik_\mu r^\mu} \\ &= \sum_{k_\mu} a_{\uparrow,\downarrow}(\vec{k}) u_{\uparrow,\downarrow}(\vec{k}) e^{-ik_\mu r^\mu} \end{aligned} \qquad \begin{aligned} \phi^-_{\uparrow,\downarrow}(r^\mu) &= \sum_{k_\mu} \sqrt{\tfrac{mc^2}{2E(\vec{k})}}\beta_{\uparrow,\downarrow}(\vec{k}) v_{\uparrow,\downarrow}(\vec{k}) e^{ik_\mu r^\mu} \\ &= \sum_{k_\mu} b_{\uparrow,\downarrow}(\vec{k}) v_{\uparrow,\downarrow}(\vec{k}) e^{ik_\mu r^\mu} \end{aligned} \tag{7.51}$$

The amplitudes are now promoted to operators $a_{\uparrow,\downarrow}(\vec{k}) \mapsto A_{\uparrow,\downarrow}(\vec{k})$ and $b_{\uparrow,\downarrow}(\vec{k}) \mapsto B_{\uparrow,\downarrow}(\vec{k})$ with their conjugates denoted by $A^\dagger_{\uparrow,\downarrow}(\vec{k})$ and $B^\dagger_{\uparrow,\downarrow}(\vec{k})$, respectively. These operators cor-

11 Note that $\{\Phi^\pm(r^\mu), \Phi^{\mp\,\dagger}(r^\mu)\} = 0$ since any product of fields $\phi^\pm_{\uparrow,\downarrow}(r^\mu)$ with opposite charge vanishes, see the second line in Eq. [7.48].

12 For a thorough introduction to spinors the reader is referred to the comprehensive summary by Steane [245].

respond to the creation and annihilation operators for fermions, which satisfy the anti-commutation relations [232]

$$\{A_i(\vec{k}), A_j^\dagger(\vec{k}')\} = \delta_{i,j}\delta(\vec{k}-\vec{k}') \quad \text{and} \quad \{B_i(\vec{k}), B_j^\dagger(\vec{k}')\} = \delta_{i,j}\delta(\vec{k}-\vec{k}') \quad \forall i,j \in \{\uparrow,\downarrow\}. \tag{7.52}$$

All combinations of the operators which are not explicitly mentioned in Eq. [7.52] vanish as a consequence of Eq. [7.48]. Using these relations, the anti-commutators in Eq. [7.49] become [78, 232]

$$\{\phi_j^+(x^\mu), {\phi_k^+}^\dagger(y^\mu)\} = \delta_{j,k}\delta(x^\mu - y^\mu) \quad \text{and} \quad \{\phi_j^-(x^\mu), {\phi_k^-}^\dagger(y^\mu)\} = \delta_{j,k}\delta(x^\mu - y^\mu) \tag{7.53}$$

for $i,j \in \{\uparrow,\downarrow\}$ and two spacetime coordinates x^μ, y^μ.

We now derive the Hamiltonian H from the Lagrangian density of the free Dirac field, which is defined by [78]

$$\mathcal{L}(\Phi, \partial_\mu\Phi) = \Phi^\dagger(r^\mu)\gamma_0\left(i\hbar c\gamma^\mu\partial_\mu - mc^2\right)\Phi(r^\mu). \tag{7.54}$$

Following Eq. [7.30] we compute the momentum conjugate

$$\Pi(r^\mu) = \frac{\partial}{\partial(\partial_0\Phi)}\mathcal{L}(\Phi,\partial_\mu\Phi) = i\hbar c\Phi^\dagger(r^\mu)\gamma_0^2 = i\hbar c\Phi^\dagger(r^\mu) \tag{7.55}$$

which is simply the hermitian conjugate of $\Phi(r^\mu)$. With the introduction of the fermionic number operators $N_{\uparrow,\downarrow}^+(\vec{k}) = A_{\uparrow,\downarrow}^\dagger(\vec{k})A_{\uparrow,\downarrow}(\vec{k})$ and $N_{\uparrow,\downarrow}^-(\vec{k}) = B_{\uparrow,\downarrow}^\dagger(\vec{k})B_{\uparrow,\downarrow}(\vec{k})$ we obtain [78]

$$\begin{aligned}
\hat{H} &= \int_V \left(\Pi(r^\mu)\partial_t\Phi(r^\mu) - \mathcal{L}(\Phi,\partial_\mu\Phi)\right)\, d^3r \\
&= \int_V \left(i\hbar c\Phi^\dagger(r^\mu)\partial_t\Phi(r^\mu) - \Phi^\dagger(r^\mu)\left[i\hbar c\partial_t + i\hbar c\sum_{j=1}^3\gamma_0\gamma^j\partial_j - \gamma_0 mc^2\right]\Phi(r^\mu)\right)\, d^3r \\
&= \int_V \Phi^\dagger(r^\mu)\gamma_0\left(-i\hbar c\sum_{j=1}^3\gamma^j\partial_j + mc^2\right)\Phi(r^\mu)\, d^3r = \int_V E(\vec{k})\Phi^\dagger(r^\mu)\gamma_0\Phi(r^\mu)\, d^3r \\
&= \sum_{k^\mu}\sum_{j=\uparrow,\downarrow} E(\vec{k})\left(N_j^+(\vec{k}) - N_j^-(\vec{k})\right).
\end{aligned} \tag{7.56}$$

Here we have used the orthogonality of the fields $\phi^\pm(r^\mu)_{\uparrow,\downarrow}$ which satisfy the Dirac equation and the anti-commutation relations in Eq. [7.53].

The simultaneous eigenstates of $\hat{H}$, $N_{\uparrow,\downarrow}^\pm$ are again the number states $|n\rangle_k$ in Eq. [7.39] for $n \in \mathbb{N}$ with the unique vacuum state $|0\rangle$. Excitations of the fields $\phi^\pm(r^\mu)_{\uparrow,\downarrow}$ are *fermions*, i.e. spin-1/2 particles of mass m satisfying the relativistic energy-momentum relation in Eq. [7.29]. We attribute the two solutions with energies $\pm E$ to opposing charges $\pm e$, respectively. Therefore, we have to distinguish between particles and their *antiparticles*, which have equal mass but opposite charge.

7.3.3 *Symmetry transformations and gauge fields*

The identification and classification of the symmetries of a target problem lie at the heart of many theories in physics. Once discovered, symmetries can greatly simplify abstract theoretical frameworks. However, their importance extends far beyond mathematical convenience. In her seminal work *Invariante Variationsprobleme* published in 1918, the German mathematician Emmy Noether formulated one of the most profound theorems in physics [246, 247]:

> *"If (the integral) I is invariant with respect to a (symmetry group) $\mathfrak{S}_\rho$, then ρ linear-independent combinations of the Lagrange expressions become divergences – and from this, conversely, the invariance of I with respect to a $\mathfrak{S}_\rho$ will follow. [...]"*

Noether's theorem states that symmetries are fundamentally linked to conserved quantities. More precisely, any symmetry under an infinitesimal transformation – a so-called *continuous symmetry*[13] – is accompanied by a *conservation law*[14] [78].

We now investigate the symmetries in the Lagrangian density $\mathcal{L}(\Phi, \partial_\mu \Phi)$ of the Dirac field introduced in Eq. [7.54] and consider a small perturbation $\delta\Phi \ll \Phi$ of the field, which transforms the field according to $\Phi \mapsto \Phi + \delta\Phi$. Under such a transformation the Lagrangian density reads [232]

$$\begin{aligned}
\mathcal{L}(\Phi + \delta\Phi, \partial_\mu\Phi + \partial_\mu\delta\Phi) &= \mathcal{L}(\Phi, \partial_\mu\Phi) + \delta\Phi \frac{\partial\mathcal{L}(\Phi, \partial_\mu\Phi)}{\partial\Phi} + \frac{\partial\mathcal{L}(\Phi, \partial_\mu\Phi)}{\partial(\partial_\mu\Phi)}\partial_\mu\delta\Phi \\
&= \mathcal{L}(\Phi, \partial_\mu\Phi) + \delta\Phi\left[\frac{\partial\mathcal{L}(\Phi, \partial_\mu\Phi)}{\partial\Phi} - \partial_\mu\frac{\partial\mathcal{L}(\Phi, \partial_\mu\Phi)}{\partial(\partial_\mu\Phi)}\right] \\
&\qquad + \partial_\mu\left(\frac{\partial\mathcal{L}(\Phi, \partial_\mu\Phi)}{\partial(\partial_\mu\Phi)}\delta\Phi\right) \\
&= \mathcal{L}(\Phi, \partial_\mu\Phi) + \delta\mathcal{L}(\Phi, \partial_\mu\Phi)
\end{aligned}$$

with

$$\delta\mathcal{L}(\Phi, \partial_\mu\Phi) = \delta\Phi\left[\frac{\partial\mathcal{L}(\Phi, \partial_\mu\Phi)}{\partial\Phi} - \partial_\mu\frac{\partial\mathcal{L}(\Phi, \partial_\mu\Phi)}{\partial(\partial_\mu\Phi)}\right] + \partial_\mu\left(\frac{\partial\mathcal{L}(\Phi, \partial_\mu\Phi)}{\partial(\partial_\mu\Phi)}\delta\Phi\right). \qquad [7.57]$$

This result is precisely what we have obtained in Eq. [7.16], and the terms in the square brackets are the already familiar Euler-Lagrange equations, see Eq. [7.22]. We demand that our transformation preserves Lorentz invariance and consequently

$$\delta\mathcal{L}(\Phi, \partial_\mu\Phi) \stackrel{!}{=} 0.$$

For a field $\Phi(r^\mu)$ which satisfies the equations of motion we are then left with the term

$$\delta\mathcal{L}(\Phi, \partial_\mu\Phi) = \partial_\mu\left(\frac{\partial\mathcal{L}(\Phi, \partial_\mu\Phi)}{\partial(\partial_\mu\Phi)}\delta\Phi\right) \stackrel{!}{=} 0. \qquad [7.58]$$

13 A formulation with respect to continuous symmetries $\mathfrak{S}_{\infty,\rho}$ is given in Noether's second argument, which is essentially an extension to the claim presented in the main text. Furthermore, Noether explicitly mentions conservation laws in the context of special relativity, referencing Klein's "second note" [248].

14 We briefly mention two symmetries and their conserved quantities. Translation symmetry *in space* implies conservation of momentum: naively, a spatial displacement does not change the velocity v of e.g. a free particle with mass m, and thus its momentum $p = mv$ remains invariant. In contrast, translation symmetry *in time* leads to the conservation of energy.

We will discover in the next paragraphs how this equation leads to a conservation law. Eq. [7.58] is analogous to the term we have obtained in our discussion of the principle of least action, see Sec. 7.2.1. Given a Lagrangian $L(q, \dot{q})$ for a trajectory $q(t)$, the action [78]

$$S[q] = \int_{t_0}^{t_1} L(q, \dot{q})\, dt$$

must remain stationary if we introduce a perturbation $\delta q(t)$. We then demanded that the variation vanishes at the boundary $\delta q(t_0) = \delta q(t_1) = 0$, such that

$$\int_{t_0}^{t_1} \frac{d}{dt}\left(\delta q(t) \frac{\partial}{\partial \dot{q}} L(q, \dot{q})\right)\, dt = \delta q(t)\, \frac{\partial}{\partial \dot{q}} L(q, \dot{q})\Big|_{t_0}^{t_1} = 0$$

when evaluated at t_0 and t_1. However, such a boundary condition is unnecessarily restrictive. We are interested in more general variations, especially those corresponding to *symmetry transformations*, i.e. transformations that leave the Lagrangian invariant.

Since the $\Phi(r^\mu)$ is complex and the Lagrangian density $\mathcal{L}(\Phi, \partial_\mu \Phi)$ contains both $\Phi(r^\mu)$ and its Dirac adjoint $\Phi^\dagger(r^\mu)\gamma_0$, it must be invariant under global phase transformations of the form [249]

$$\forall \theta \in \mathbb{R}\colon\ \hat{U}(\theta) = e^{-i\theta} \in U(1)\colon\ \Phi(r^\mu) \mapsto \hat{U}(\theta)\Phi(r^\mu) = e^{-i\theta}\Phi(r^\mu),$$

where $U(1)$ is the *circle group*, the unitary group in one dimension [42]. For an infinitesimal angle θ, we approximate the exponential to first order, such that

$$\Phi(r^\mu) \mapsto \Phi'(r^\mu) = e^{-i\theta}\Phi(r^\mu) \approx \Phi(r^\mu) - i\theta\Phi(r^\mu)$$

and we identify the perturbation $\delta\Phi = -i\theta\Phi(r^\mu)$; an infinitesimal rotation introduces a linear displacement of the field. We then compute Eq. [7.58] and obtain [78]

$$\partial_\mu \left(\frac{\partial \mathcal{L}(\Phi, \partial_\mu \Phi)}{\partial(\partial_\mu \Phi)} \Delta\Phi\right) = \theta\hbar c \cdot \partial_\mu \left(\Phi^\dagger(r^\mu)\gamma_0\gamma^\mu\Phi(r^\mu)\right) \stackrel{!}{=} 0$$

$$\partial_\mu \left(\Phi^\dagger(r^\mu)\gamma_0\gamma^\mu\Phi(r^\mu)\right) = \partial_\mu J^\mu(r^\mu) = 0,$$

where $J^\mu(r^\mu) = (c\varrho, \vec{j})$ denotes the *probability current*[15] with probability density ϱ and flux density $\vec{j}$, respectively. This *continuity equation* follows directly from the global $U(1)$ symmetry and implies the conservation of probability

$$\partial_\mu J^\mu(r^\mu) = \partial_0 J^0(r^\mu) + \sum_{i=1}^{3} \partial_i J^i(r^\mu) = \partial_0 \Phi^\dagger(r^\mu)\Phi(r^\mu) + \nabla\vec{j}(r^\mu) = \partial_t \varrho(r^\mu) + \nabla\vec{j}(r^\mu) = 0 \qquad [7.59]$$

within a volume V in spacetime. The probability density $\varrho(r^\mu)$ can only change over time if a current $\vec{j}(r^\mu)$ flows in- or outward through the boundary of V. Later in this chapter we will associate this equation with the conservation of the electric charge.

15 We have already encountered this quantity as the four-current associated with charge and current density in the covariant formulation of Maxwell's equations in Sec. 7.1.3.

It is quite intuitive that a global phase transformation is accompanied by the conservation of physical quantities, since the spatial rotation of a closed system S does not change the laws of physics within S. A more interesting case are *local* phase transformations [232]: let $\theta \mapsto \theta(r^\mu)$ be a differentiable function varying in spacetime, which decays as the distance in space goes to infinity. We compute how the transformation $\Phi(r^\mu) \mapsto \Phi'(r^\mu) = e^{-i\theta(r^\mu)}\Phi(r^\mu)$ impacts the Lagrangian density of the free Dirac field [78]:

$$\begin{aligned}
\mathcal{L}(\Phi', \partial_\mu \Phi') &= e^{i\theta(r^\mu)}\Phi^\dagger(r^\mu)\gamma_0 \left(i\hbar c\gamma^\mu \partial_\mu - mc^2\right) e^{-i\theta(r^\mu)}\Phi(r^\mu) \\
&= e^{i\theta(r^\mu)}\Phi^\dagger(r^\mu)\gamma_0 i\hbar c\gamma^\mu \partial_\mu \left(e^{-i\theta(r^\mu)}\Phi(r^\mu)\right) - mc^2 \underbrace{e^{i\theta(r^\mu)}e^{-i\theta(r^\mu)}}_{=1}\Phi^\dagger(r^\mu)\gamma_0\Phi(r^\mu) \\
&= i\hbar c e^{i\theta(r^\mu)} J^\mu(r^\mu)\partial_\mu e^{-i\theta(r^\mu)} \\
&\qquad + \underbrace{e^{i\theta(r^\mu)}e^{-i\theta(r^\mu)}}_{=1}\Phi^\dagger(r^\mu)\gamma_0 i\hbar c\gamma^\mu \partial_\mu \Phi(r^\mu) - mc^2\Phi^\dagger(r^\mu)\gamma_0\Phi(r^\mu) \\
&= -i^2\hbar c \underbrace{e^{i\theta(r^\mu)}e^{-i\theta(r^\mu)}}_{=1} J^\mu(r^\mu)\partial_\mu\theta(r^\mu) + \Phi^\dagger(r^\mu)\gamma_0\left(i\hbar c\gamma^\mu\partial_\mu - mc^2\right)\Phi(r^\mu) \\
&= \hbar c J^\mu(r^\mu)\partial_\mu\theta(r^\mu) + \mathcal{L}(\Phi, \partial_\mu\Phi),
\end{aligned} \tag{7.60}$$

where the expression $\partial_\mu\theta(r^\mu)$ for a general $\theta(r^\mu)$ breaks the invariance of $\mathcal{L}(\Phi, \partial_\mu\Phi)$.

The Lagrangian density seems to violate local $U(1)$ symmetry, however, we can always enforce Lorentz invariance by introducing an appropriate four-vector field $\Theta_\mu(r^\mu)$ to the covariant derivative, such that [232, 249]

$$\partial_\mu \mapsto \partial_\mu + i\Theta_\mu(r^\mu) = \mathcal{D}_\mu. \tag{7.61}$$

Substituting ∂_μ by $\mathcal{D}_\mu$ in Eq. [7.60] we obtain

$$\begin{aligned}
\mathcal{L}(\Phi', \partial_\mu\Phi') &= e^{i\theta(r^\mu)}\Phi^\dagger(r^\mu)\gamma_0\left(i\hbar c\gamma^\mu\mathcal{D}_\mu - mc^2\right)e^{-i\theta(r^\mu)}\Phi(r^\mu) \\
&= \mathcal{L}(\Phi, \partial_\mu\Phi) - \hbar c \cdot J^\mu(r^\mu)\underbrace{\left(\Theta_\mu(r^\mu) - \partial_\mu\theta(r^\mu)\right)}_{\overset{!}{=}}
\end{aligned} \tag{7.62}$$

and by $\Theta_\mu(r^\mu) = \partial_\mu\theta(r^\mu)$ the Lagrangian density retains its invariance. Our field $\Theta_\mu(r^\mu)$ is equal in magnitude, but opposite in sign to the gradient of the angle $\theta(r^\mu)$. Therefore, $\Theta_\mu(r^\mu)$ is intimately coupled with the transformation itself, since

$$\theta(r^\mu) = \int \Theta_\mu(r^\mu)\, d^3r \Longrightarrow e^{-i\theta(r^\mu)} = e^{-i\int\Theta_\mu(r^\mu)\, d^3r}. \tag{7.63}$$

We call $\Theta_\mu(r^\mu)$ a *gauge field* associated with the *gauge transformation* [230, 232]. Including our gauge field in the Lagrangian density, we obtain

$$\begin{aligned}
\mathcal{L}(\Phi, \partial_\mu\Phi) &= \Phi^\dagger(r^\mu)\gamma_0\left(i\hbar c\gamma^\mu\partial_\mu - \hbar c\gamma^\mu\Theta_\mu(r^\mu) - mc^2\right)\Phi(r^\mu) \\
&= \Phi^\dagger(r^\mu)\gamma_0\left(i\hbar c\gamma^\mu\partial_\mu - mc^2\right)\Phi(r^\mu) - \hbar c \cdot J^\mu(r^\mu)\Theta_\mu(r^\mu)
\end{aligned} \tag{7.64}$$

Thus far, the introduction of $\Theta_\mu(r^\mu)$ merely seems like a convenient mathematical trick to recover the local $U(1)$ symmetry. However, since the Lagrangian density is a sum of energy densities, the gauge field must be associated with physical observables[16].

16 The term $\hbar c \cdot J^\mu(r^\mu)\Theta_\mu(r^\mu)$ must itself be an energy density and since $J^\mu(r^\mu)$ is a probability current, the field $\Theta_\mu(r^\mu)$ must somehow have physical significance.

Consequently, $\Theta_\mu(r^\mu)$ must exist independently, regardless if we apply a local phase transformation or not. This implies that our Lagrangian density in Eq. [7.64] must be incomplete. Therefore, we introduce another term $\mathcal{L}(\Theta_\mu)$, such that

$$\mathcal{L}(\Phi, \partial_\mu \Phi) = \Phi^\dagger(r^\mu)\gamma_0 \left(i\hbar c\gamma^\mu \partial_\mu - mc^2\right) \Phi(r^\mu) - \hbar c \cdot J^\mu(r^\mu)\Theta_\mu(r^\mu) + \mathcal{L}(\Theta_\mu). \quad [7.65]$$

The Lagrangian density must still remain invariant under Lorentz transformations. Since the four-vector field $\Theta_\mu(r^\mu)$ couples to the gauge transformation according to [249]

$$\Phi(r^\mu) \mapsto e^{-i\theta'(r^\mu)}\Phi(r^\mu) \Longrightarrow \Theta_\mu(r^\mu) \mapsto \Theta_\mu(r^\mu) + \partial_\mu \theta'(r^\mu),$$

the term $\mathcal{L}(\Theta_\mu)$ cannot contain an expression proportional to $\Theta^\mu(r^\mu)\Theta_\mu(r^\mu)$, because

$$\Theta^\mu(r^\mu)\Theta_\mu(r^\mu) \mapsto (\Theta^\mu(r^\mu) + \partial^\mu\theta'(r^\mu), \Theta_\mu(r^\mu) + \partial_\mu\theta'(r^\mu)) \neq \Theta^\mu(r^\mu)\Theta_\mu(r^\mu).$$

This term corresponds to the *self-energy* of the gauge field and consequently, $\Theta_\mu(r^\mu)$ is *mass-less*[17] [230]. Note that we can also arrive at the same conclusion from a physical argument: rotations in spacetime cannot change the energy density. Following a similar argument, $\mathcal{L}(\Theta_\mu)$ cannot depend on the gradient $\partial_\nu\Theta_\mu(r^\mu)$, since this term would also break Lorentz-invariance. Consequently, we are tempted to believe that $\Theta_\mu(r^\mu)$ is stationary. However, $\Theta_\mu(r^\mu)$ can still exhibit dynamics if we introduce two gradients [249]

$$\mathcal{L}(\Theta_\mu) \propto \partial_\nu\Theta_\mu - \partial_\mu\Theta_\nu \quad [7.66]$$

which cancel each other. We have encountered this term already in the covariant formulation of electrodynamics discussed in Sec. 7.1.3, where $\Theta_\mu(r^\mu)$ appears as the four-potential $A_\mu(r^\mu)$ and Eq. [7.66] defines the electromagnetic tensor $F_{\mu,\nu}(r^\mu)$, see Eq. [7.11] [234].

Indeed, the gauge field $\Theta_\mu(r^\mu)$ is the four-potential $A_\mu(r^\mu)$, which couples the Dirac fermions with the electromagnetic field. $A_\mu(r^\mu)$ emerges naturally from the local $U(1)$ symmetry and since it is mass-less, its excitations are associated with the *photon*, the *exchange particle* of electromagnetism, cf. Ref. [78] and Ref. [230]. We ultimately arrive at the Lagrangian density

$$\mathcal{L}(\Phi, \partial_\mu\Phi, A_\mu) = \Phi^\dagger(r^\mu)\gamma_0 \left(i\hbar c\gamma^\mu\partial_\mu - mc^2\right)\Phi(r^\mu) - e\cdot J^\mu(r^\mu)A_\mu(r^\mu) - \frac{1}{16\pi}F^{\mu,\nu}(r^\mu)F_{\mu,\nu}(r^\mu),$$

where we have introduced the charge e and the free radiation field[18] [230, 233]

$$\mathcal{L}(\Theta_\mu) \longrightarrow \mathcal{L}_{rad.}(A_\mu) = -\frac{1}{16\pi}F^{\mu,\nu}(r^\mu)F_{\mu,\nu}(r^\mu). \quad [7.67]$$

Using Eq. [7.61] we substitute

$$\mathcal{D}_\mu = \partial_\mu + i\frac{e}{\hbar c}A_\mu(r^\mu)$$

and obtain a more compact notation [232, 233]

$$\mathcal{L}(\Phi, \partial_\mu\Phi, A_\mu) = \Phi^\dagger(r^\mu)\gamma_0 \left(i\hbar c\gamma^\mu\mathcal{D}_\mu - mc^2\right)\Phi(r^\mu) - \frac{1}{16\pi}F^{\mu,\nu}(r^\mu)F_{\mu,\nu}(r^\mu). \quad [7.68]$$

This is the Lagrangian density of *quantum electrodynamics* (QED), describing the dynamics of relativistic charged fermions coupling with electromagnetic fields. In the upcoming chapter, we will discuss QED extensively and quantize the radiation field.

17 Here we use the equivalence of mass and energy: if the gauge field has a non-vanishing self-energy, it must have mass, and vice versa.

18 A clean way to introduce the radiation field is shown in Ref. [230] via the *Proca equation*, which describes the dynamics of Spin-1 bosons. If we then require the Lagrangian density of the field to be mass-less, we obtain the term $-F^{\mu,\nu}F_{\mu,\nu}/16\pi$.

7.4 QUANTUM ELECTRODYNAMICS

We have developed a framework to adequately describe the dynamics of relativistic charged fermions with mass m, which emerge as excitations of a *matter field* $\Phi(r^\mu)$. Demanding that the global $U(1)$ symmetry becomes local naturally lead to the introduction of a *gauge field* $A_\mu(r^\mu)$, which is intimately coupled with the physical electromagnetic field. *Quantum electrodynamics* (QED) first formulated by Dirac in 1927 is a prime example of a so-called *gauge theory* [228]. Despite its age, it is still an extensively studied subject, both experimentally and theoretically. In this section we will first quantize the free field and derive the *Feynman propagator*, an essential tool in the study of interactions between the fundamental particles. We then investigate *vacuum polarizations*, a phenomenon by which the true charge of e.g. an electron is masked by virtual particle pair creation; this effect will be studied experimentally in Ch. 8.

7.4.1 *Gauge fixing*

There are an infinite number of four-potentials $A_\mu(r^\mu) = (\phi(r^\mu), \vec{A}(r^\mu))$, which satisfy the equation $F_{\mu,\nu} = \partial_\mu A_\nu - \partial_\nu A_\mu$, however, the electromagnetic tensor $F_{\mu,\nu}$ is unique. Indeed, $F_{\mu,\nu}$ remains invariant under any gauge transformation of the form [232]

$$A_\mu(r^\mu) \mapsto A_\mu(r^\mu) + \partial_\mu \alpha(r^\mu),$$

see Sec. 7.1.3 for comparison. We can thus choose from an infinite number of gauge fields, all leading to the same physical quantities. Although this *gauge freedom* by itself does not pose an issue, it is still convenient to *fix* a suitable gauge to describe a target problem.

A prominent choice is the *Coulomb gauge* with the condition [235]

$$\nabla \vec{A}(\vec{r}, t) = 0, \tag{7.69}$$

where $\vec{A}(\vec{r}, t) = \vec{A}(r^\mu)$ is the vector potential. Note that we have already encountered this gauge in our discussion of the interactions between trapped ions and coherent light fields, cf. Sec. 2.2. The Coulomb gauge enables a straightforward computation of the geometric properties of electromagnetic waves. To see this, we apply the Fourier transformation

$$\vec{A}(\vec{r}, t) = \frac{1}{\sqrt{(2\pi)^3}} \int \vec{A}(\vec{k}, t) e^{-i\vec{k}\vec{r}}\, d^3k \tag{7.70}$$

with wave vectors $\vec{k}$ and decompose $\vec{A}(\vec{k}, t)$ into two components which are parallel respectively perpendicular to $\vec{k}$, such that

$$\vec{A}(\vec{k}, t) = \vec{A}_\parallel(\vec{k}, t) + \vec{A}_\perp(\vec{k}, t).$$

From the gauge condition we then obtain

$$\begin{aligned} \nabla \vec{A}(\vec{r}, t) &= -\frac{i}{\sqrt{(2\pi)^3}} \int \vec{k} \vec{A}(\vec{k}, t) e^{-i\vec{k}\vec{r}}\, d^3k \\ &= -\frac{i}{\sqrt{(2\pi)^3}} \int \left[\vec{k} \vec{A}_\parallel(\vec{k}, t) + \cancel{\vec{k} \vec{A}_\perp(\vec{k}, t)} \right] e^{-i\vec{k}\vec{r}}\, d^3k \stackrel{!}{=} 0, \end{aligned}$$

where the scalar product $\vec{k}\vec{A}_\perp(\vec{k}, t)$ vanishes regardless of the magnitude of $\vec{A}_\perp(\vec{k}, t)$, since both vectors are by definition orthogonal. Consequently, a vector potential satisfying Eq. [7.69] must obey

$$\vec{A}_\parallel(\vec{k}, t) = 0,$$

which implies that $\vec{A}(\vec{r},t)$ is *transversal*: its non-zero components are defined in a plane perpendicular to its direction of propagation governed by $\vec{k}$.

While the Coulomb gauge allows us to deduce the geometric properties of $\vec{A}(\vec{r},t)$, the *Lorenz gauge* [232]

$$\partial^\mu A_\mu(r^\mu) = 0 \Longrightarrow \frac{1}{c}\partial_t\phi(\vec{r},t) = \nabla\vec{A}(\vec{r},t)$$

directly leads to the dynamics of $A_\mu(r^\mu)$. From the electromagnetic tensor $F_{\mu,\nu}$ it follows

$$\partial^\mu F_{\mu,\nu} = \partial^\mu\partial_\mu A_\nu - \partial^\mu\partial_\nu A_\mu = \Box A_\mu - \partial_\nu\cancel{\left[\partial^\mu A_\mu\right]} = \Box A_\mu,$$

where $\partial^\mu\partial_\mu = \Box = \partial_t^2/c^2 - \nabla^2$ denotes the wave operator acting on the four-potential and $\partial_\nu(\partial^\mu A_\mu) = 0$. In the absence of charges and currents $\partial^\mu F_{\mu,\nu} = 0$ and we obtain the homogeneous wave equation[19]

$$\frac{1}{c^2}\frac{\partial^2}{\partial t^2}\vec{A}(\vec{r},t) = \nabla^2\vec{A}(\vec{r},t).$$

7.4.2 *Quantization of the radiation field*

For simplicity we consider the free radiation field in the absence of charges and currents and introduce the *normal variable* [250]

$$\begin{aligned}\vec{\alpha}(\vec{k},t) &= \lambda(\vec{k})\left(\vec{E}(\vec{k},t) - c\frac{\vec{k}}{|\vec{k}|}\times\vec{B}(\vec{k},t)\right)\\ &= \lambda(\vec{k})\left(-\partial_t\vec{A}(\vec{k},t) + ic|\vec{k}|\vec{A}(\vec{k},t)\right)\end{aligned} \qquad [7.71]$$

where $\lambda(\vec{k}) \in \mathbb{R}$ is a normalization constant and $\vec{A}(\vec{k},t)$ denotes the amplitude of the vector potential associated with the wave vector $\vec{k}$ in momentum space, see Eq. [7.70]. We then take the derivative with respect to time and use Maxwell's equations, in particular Ampere's law Eq. [7.9](iv), such that[20]

$$\begin{aligned}\partial_t\vec{\alpha}(\vec{k},t) &= \lambda(\vec{k})\left(ic|\vec{k}|\partial_t\vec{A}(\vec{k},t) - \partial_t^2\vec{A}(\vec{k},t)\right)\\ &= \lambda(\vec{k})\left(ic|\vec{k}|\partial_t\vec{A}(\vec{k},t) - i^2c^2|\vec{k}|^2\vec{A}(\vec{k},t)\right)\\ &= ic|\vec{k}|\cdot\lambda(\vec{k})\left(\partial_t\vec{A}(\vec{k},t) - ic|\vec{k}|\vec{A}(\vec{k},t)\right)\\ &= -ic|\vec{k}|\cdot\vec{\alpha}(\vec{k},t)\end{aligned}$$

$$\longrightarrow \partial_t\vec{\alpha}(\vec{k},t) + i\omega(\vec{k})\cdot\vec{\alpha}(\vec{k},t) = 0$$

with frequency $\omega(\vec{k}) = c|\vec{k}|$. A general solution to this differential equation is given by

$$\vec{\alpha}(\vec{k},t) = \vec{\alpha}(\vec{k},0)e^{-i\omega(\vec{k})t} = a(\vec{k})\cdot\vec{\epsilon}\cdot e^{-i\omega(\vec{k})t}, \qquad [7.72]$$

19 Note that if we include charges with a charge density ϱ and currents $\vec{j}$ we recover the inhomogeneous Maxwell equations, cf. Eq. [7.4.1].

20 Note that $\partial_t\vec{E}(\vec{k},t) = -c\vec{E}(\vec{k},t)$ and since $\frac{1}{c}\partial_t\vec{E}(\vec{r},t) = \nabla\times\vec{B}(\vec{r},t) = \nabla\times\left(\nabla\times\vec{A}(\vec{r},t)\right) = -\nabla^2\vec{A}(\vec{r},t)$ we identify in momentum space $\nabla\times\vec{B}(\vec{r},t) \Longrightarrow |\vec{k}|^2\vec{A}(\vec{k},t)$ and thus $\partial_t^2\vec{A}(\vec{k},t) = -c^2|\vec{k}|^2\vec{A}(\vec{k},t) = i^2c^2|\vec{k}|^2\vec{A}(\vec{k},t)$.

where we have introduced the *polarization* vector $\vec{\epsilon}$ describing the orientation of $\vec{A}(\vec{k},t)$ in the plane perpendicular to $\vec{k}$ and the amplitude $a(\vec{k})$ [250].

Using the Fourier transformation of the vector potential in Eq. [7.70] we identify that the complex conjugate in momentum space must satisfy

$$\vec{A}^*(\vec{k},t) = \vec{A}(-\vec{k},t)$$

and with the definition of the normal variable in Eq. [7.71] we obtain [250]

$$\begin{aligned}\vec{\alpha}^*(\vec{k},t) &= \lambda(\vec{k})\left(-ic|\vec{k}|\vec{A}^*(\vec{k},t) - \partial_t\vec{A}^*(\vec{k},t)\right)\\ &= -\lambda(\vec{k})\left(ic|\vec{k}|\vec{A}(-\vec{k},t) + \partial_t\vec{A}(-\vec{k},t)\right)\\ \longrightarrow \vec{\alpha}^*(-\vec{k},t) &= -\lambda(\vec{k})\left(i\omega(\vec{k})\vec{A}(\vec{k},t) + \partial_t\vec{A}(\vec{k},t)\right)\end{aligned} \tag{7.73}$$

Note that the frequency $\omega(\vec{k}) = c|\vec{k}|$ only depends on the absolute value of $\vec{k}$ and consequently $\omega(\vec{k}) = \omega(-\vec{k})$. We can now express $\vec{A}(\vec{k},t)$ in terms of the normal variables $\vec{\alpha}(\vec{k},t)$ and $\vec{\alpha}^*(-\vec{k},t)$, such that

$$\vec{\alpha}(\vec{k},t) + \vec{\alpha}^*(-\vec{k},t) = 2\lambda(\vec{k})i\omega(\vec{k})\vec{A}(\vec{k},t) \longrightarrow \vec{A}(\vec{k},t) = \frac{\vec{\alpha}(\vec{k},t) + \vec{\alpha}^*(-\vec{k},t)}{2i\lambda(\vec{k})\omega(\vec{k})}$$

To be consistent with common literature we choose $\lambda(\vec{k})$ accordingly and obtain [235]

$$\begin{aligned}\vec{A}(\vec{k},t) &= \frac{\hbar c}{\sqrt{2E(\vec{k})}}\left(\vec{\alpha}(\vec{k},t) + \vec{\alpha}^*(-\vec{k},t)\right)\\ &= \frac{\hbar c}{\sqrt{2E(\vec{k})}}\left(a(\vec{k})\vec{\epsilon}e^{-i\omega(\vec{k})t} + a^*(-\vec{k})\vec{\epsilon}^*e^{i\omega(\vec{k})t}\right)\end{aligned}$$

where $E(\vec{k}) = \hbar\omega(\vec{k})$ denotes the energy of a wave associated with the wave vector $\vec{k}$.

In the quantization we promote the amplitudes $a(\vec{k})$ and $a^*(\vec{-k})$ to the bosonic ladder operators $\hat{a}(\vec{k})$ and $\hat{a}^\dagger(-\vec{k})$, respectively, which satisfy the commutation relations introduced in Eq. [7.38]. From the Fourier transformation of $\vec{A}(\vec{r},t)$ in Eq. [7.70]

$$\begin{aligned}\hat{A}(\vec{r},t) &= \frac{1}{(2\pi)^3}\int_V \frac{\hbar c}{\sqrt{2E(\vec{k})}}\left(\hat{a}(\vec{k})\vec{\epsilon}e^{-i\omega(\vec{k})t} + \hat{a}^\dagger(-\vec{k})\vec{\epsilon}^*e^{i\omega(\vec{k})t}\right)e^{-i\vec{k}\vec{r}}\,d^3k\\ &= \frac{1}{(2\pi)^3}\int_V \frac{\hbar c\cdot\vec{\epsilon}}{\sqrt{2E(\vec{k})}}\left(\hat{a}(\vec{k})e^{-ik_\mu r^\mu} + \hat{a}^\dagger(\vec{k})e^{ik_\mu r^\mu}\right)\,d^3k\end{aligned}$$

where we have assumed the polarization $\vec{\epsilon}$ to be real. Since each wave can exist in multiple polarizations we have to include a sum to finally obtain [250]

$$\hat{A}(\vec{r},t) = \frac{\hbar c}{\sqrt{2}(2\pi)^3}\int_V \sum_{\vec{\epsilon}} \frac{\vec{\epsilon}}{\sqrt{E(\vec{k})}}\left(\hat{a}(\vec{k})e^{-ik_\mu r^\mu} + \hat{a}^\dagger(\vec{k})e^{ik_\mu r^\mu}\right)\,d^3k. \tag{7.74}$$

We will return to this definition later in this chapter and conclude this section by computing the Hamiltonian $H_{rad.}$ for the free radiation field using the Lagrangian density $\mathcal{L}_{rad.}(A_\mu)$ defined in Eq. [7.67]. Following Eq. [7.30] we compute the field conjugate

$$\begin{aligned}
\Pi^\mu &= \frac{\partial \mathcal{L}_{rad.}(A_\mu)}{\partial(\partial_0 A_\mu)} = -\frac{1}{16\pi}\frac{\partial}{\partial(\partial_0 A_\mu)} F_{\mu,\nu}F^{\mu,\nu} = -\frac{1}{16\pi}\frac{\partial}{\partial(\partial_0 A_\mu)} F_{\mu,\nu}F_{\alpha,\beta}g^{\alpha,\mu}g^{\beta,\nu} \\
&= -\frac{1}{16\pi}\frac{\partial}{\partial(\partial_0 A_\mu)} \left(\partial_\mu A_\nu - \partial_\nu A_\mu\right)\left(\partial_\alpha A_\beta - \partial_\beta A_\alpha\right) g^{\alpha,\mu}g^{\beta,\nu} \\
&= -\frac{1}{16\pi}\frac{\partial}{\partial(\partial_0 A_\mu)} (\partial_\mu A_\nu \partial_\alpha A_\beta - \partial_\mu A_\nu \partial_\beta A_\alpha - \underbrace{\partial_\nu A_\mu \partial_\alpha A_\beta}_{(i)} + \underbrace{\partial_\nu A_\mu \partial_\beta A_\alpha}_{(ii)}) g^{\alpha,\mu}g^{\beta,\nu} \\
&\quad \longrightarrow (i) \text{ swap indices } \mu \leftrightarrow \alpha \text{ and } \nu \leftrightarrow \beta\text{:} \\
&\qquad \partial_\nu A_\mu \partial_\alpha A_\beta g^{\alpha,\mu}g^{\beta,\nu} = \partial_\beta A_\alpha \partial_\mu A_\nu g^{\mu,\alpha}g^{\nu,\beta} = \partial_\mu A_\nu \partial_\beta A_\alpha g^{\mu,\alpha}g^{\nu,\beta} \\
&\qquad g^{i,j} = g^{j,i} \rightarrow \partial_\mu A_\nu \partial_\beta A_\alpha g^{\mu,\alpha}g^{\nu,\beta} = \partial_\mu A_\nu \partial_\beta A_\alpha g^{\alpha,\mu}g^{\beta,\nu} \\
&\quad \longrightarrow (ii) \text{ analogous: } \partial_\nu A_\mu \partial_\beta A_\alpha g^{\alpha,\mu}g^{\beta,\nu} = \partial_\mu A_\nu \partial_\alpha A_\beta g^{\alpha,\mu}g^{\beta,\nu} \\
&= -\frac{1}{8\pi}\frac{\partial}{\partial(\partial_0 A_\mu)} (\underbrace{\partial_\mu A_\nu \partial_\alpha A_\beta}_{(i)} - \underbrace{\partial_\mu A_\nu \partial_\beta A_\alpha}_{(ii)}) g^{\alpha,\mu}g^{\beta,\nu} \\
&\quad \longrightarrow (i) \text{ use } \frac{\partial}{\partial(\partial_i A_j)}\partial_k A_l = \delta^i_k \delta^j_l \text{ with } \delta^j_k = 1 \text{ if and only if } i = j\text{:} \\
&\qquad \frac{\partial}{\partial(\partial_i A_j)}\partial_\mu A_\nu \partial_\alpha A_\beta g^{\alpha,\mu}g^{\beta,\nu} = \delta^i_\mu \delta^j_\nu \partial_\alpha A_\beta g^{\alpha,\mu}g^{\beta,\nu} + \delta^i_\alpha \delta^j_\beta \partial_\mu A_\nu g^{\alpha,\mu}g^{\beta,\nu} \\
&\qquad\qquad = \delta^i_\mu \delta^j_\nu \partial^\mu A^\nu + \delta^i_\alpha \delta^j_\beta \partial^\alpha A^\beta = 2\partial^i A^j \\
&\quad \longrightarrow (ii)\text{: } [\dots] = 2\partial^j A^i \\
&\quad \longrightarrow (i) - (ii) \text{ and } i = 0, j = \mu\text{: } 2\partial^0 A^\mu - 2\partial^\mu A^0 \\
&= -\frac{1}{4\pi}\left(\partial^0 A^\mu - \partial^\mu A^0\right) \\
&= -\frac{1}{4\pi}F^{0,\mu} = \frac{1}{4\pi c}(0, E_x, E_y, E_z) = \frac{1}{4\pi c}(0, \vec{E}),
\end{aligned}$$

where we have used the definition of the electromagnetic tensor $F^{\mu,\nu}$ in Eq. [7.11] to identify the electric field $\vec{E}$. Since $\mathcal{L}_{rad.}(A_\mu)$ does not include physical charges, the scalar potential $\phi(r^\mu) = A_0(r^\mu)$ must be zero. Therefore, $\partial_0 A_\mu(r^\mu) = \frac{1}{c}(0, \vec{E}) = F_{0,\mu}$ and we obtain the Hamiltonian [250]

$$\begin{aligned}
\hat{H}_{rad.} &= \int d^3r \left(\Pi^\mu(r^\mu)\frac{1}{c}\partial_t A_\mu(r^\mu) - \mathcal{L}_{rad.}(A_\mu)\right) = \int d^3r \left(\frac{\hat{\vec{E}}(\vec{r})^2}{4\pi c^2} + \frac{1}{16\pi}F_{\mu,\nu}F^{\mu,\nu}\right) \\
&= \frac{1}{4\pi}\int d^3r \left(\frac{\hat{\vec{E}}(r^\mu)^2}{c^2} + \frac{1}{2}\left(\hat{\vec{B}}(r^\mu)^2 - \frac{\hat{\vec{E}}(r^\mu)^2}{c^2}\right)\right) \\
&= \frac{1}{8\pi}\int d^3r \left(\frac{1}{c^2}\hat{\vec{E}}(r^\mu)^2 + \hat{\vec{B}}(r^\mu)^2\right).
\end{aligned} \tag{7.75}$$

Note that $\hat{\vec{E}}(r^\mu)^2$ and $\hat{\vec{B}}(r^\mu)^2$ are operators, since both are defined in terms of the creation and annihilation operators $\hat{a}^\dagger(\vec{k})$ and $\hat{a}(\vec{k})$, respectively. We will return to $\hat{H}_{rad.}$ later in this chapter, when we discuss gauge fields on a spacetime lattice.

7.4.3 *Propagators*

Investigating the dynamics of a system relies on the observation of its properties and their evolution in spacetime. However, in an experimental setting we do not have an infinite number of measurement outcomes at our disposal, but rather observe a phenomenon at discrete coordinates $x_i^\mu = (\vec{x}_i, t_i)$. Recall for example a quantum state $|\psi(t)\rangle$ at a time t evolving under a Hamiltonian $\hat{H}$ and according to Schrödinger's equation we may observe

$$|\psi(t')\rangle = e^{-\frac{i}{\hbar}\hat{H}(t'-t)}\,|\psi(t)\rangle = \hat{U}(t'-t)\,|\psi(t)\rangle\,. \tag{7.76}$$

at a later time $t' > t$. Moreover, if we assume $|\psi(0)\rangle$ to be the state before $\hat{H}$ takes any effect, we obtain

$$\hat{U}(t'-t)\,|\psi(t)\rangle = \hat{U}(t'-t)\hat{U}(t)\,|\psi(0)\rangle\,. \tag{7.77}$$

Evidently, the time dynamics must be contained in products of the operators $\hat{U}(t_i)$ at different time coordinates t_i. Provided we have sufficient knowledge about the Hamiltonian and the system's initial state, we can compute the state at any time t.

However, we will also be interested in the dynamics of the wave function

$$\psi(x^\mu) = \psi(\vec{x}, t) = \langle\vec{x}|\psi(t)\rangle$$

at some coordinate $x^\mu = (\vec{x}, t)$ in spacetime. Since this is the information we can experimentally access we thus ask whether we can compute $\psi(y^\mu)$ at any point $y^\mu = (\vec{y}, t')$ different from x^μ. For instance, we may be unable to directly observe the scattering of two moving electrons and rather record their impact on a set of detectors after the event has already taken place; the collision is then studied from the collected data [251, 252].

Essentially, we seek to solve the inhomogeneous differential equation [36, 43]

$$\left(i\hbar\frac{d}{dt} - \hat{H}\right)\psi(y^\mu) = S(y^\mu)\psi(y^\mu), \tag{7.78}$$

where the inhomogeneity $S(y^\mu)$ contains the relevant information about the process of interest. An elegant approach to solving such equations is Green's formalism, where we introduce a function $G(y^\mu, x^\mu)$ satisfying

$$\left(i\hbar\frac{d}{dt} - \hat{H}\right)G(y^\mu, x^\mu) = i\hbar\delta(\vec{y}-\vec{x})\delta(t'-t),$$

and thus

$$\psi(y^\mu) = \psi_h(y^\mu) - \frac{i}{\hbar}\int d^4x\; G(y^\mu, x^\mu)S(x^\mu)\psi(x^\mu)$$

where $\psi_h(x^\mu)$ is the homogeneous solution to Eq. [7.78]. We call $G(y^\mu, x^\mu)$ the *Green's function*[21] or *propagator* associated with the differential operator $\left(i\hbar\partial_t - \hat{H}\right)$.

Using the initial time evolution in Eq. [7.76] and the fact that $\int d^3x'\;|\vec{y}\rangle\langle\vec{y}| = \mathbb{1}$ is complete, we obtain

$$\begin{aligned}\psi(\vec{x}, t') &= \langle\vec{x}|\psi(t')\rangle = \langle\vec{x}|\hat{U}(t'-t)|\psi(t)\rangle \\ &= \int d^3y\;\langle\vec{x}|\hat{U}(t'-t)|\vec{y}\rangle\langle\vec{y}|\psi(t)\rangle = -\frac{i}{\hbar}\int d^4y\; G(x^\mu, y^\mu)\psi(y^\mu)\end{aligned}$$

21 A thorough introduction to Green's formalism is found in Ref. [43].

and thus by comparison $G(x^\mu, y^\mu) = i\hbar \langle \vec{x}|\hat{U}(t'-t)|\vec{y}\rangle \, \delta(t'-t)$ for this specific problem.

Since we are dealing with quantum fields, we are interested in a similar formalism describing the dynamics of field operators. As an example we consider the operator $\hat{A}(r^\mu)$ given by Eq. [7.74] at two coordinates x^μ and y^μ in spacetime. Akin to Eq. [7.77] we are interested in products of operators of the form $\hat{A}(x^\mu)\hat{A}(y^\mu)$, which we compute in the following paragraph [78, 230, 253].

For compactness we evaluate the commutator $\left[\hat{A}(x^\mu), \hat{A}(y^\mu)\right]$; using the bosonic commutation relations defined in Eq. [7.38], we obtain [78]

$$\begin{aligned}\left[\hat{A}(x^\mu), \hat{A}(y^\mu)\right] &= \hat{A}(x^\mu)\hat{A}(y^\mu) - \hat{A}(y^\mu)\hat{A}(x^\mu) \\ &= \frac{\hbar^2 c^2}{2(2\pi)^4} \sum_{\vec{\epsilon},\vec{\epsilon}'} \vec{\epsilon}\cdot\vec{\epsilon}' \int d^4k \int d^4k' \, \frac{1}{\sqrt{E(\vec{k})E(\vec{k}')}} \Big(\cancel{\left[\hat{a}(\vec{k}), \hat{a}(\vec{k}')\right]} e^{-ik_\mu x^\mu - ik'_\mu y^\mu} \\ &\quad + \left[\hat{a}(\vec{k}), \hat{a}^\dagger(\vec{k}')\right] e^{-ik_\mu x^\mu + ik'_\mu y^\mu} + \left[\hat{a}^\dagger(\vec{k}), \hat{a}(\vec{k}')\right] e^{ik_\mu x^\mu - ik'_\mu y^\mu} \\ &\quad + \cancel{\left[\hat{a}^\dagger(\vec{k}), \hat{a}^\dagger(\vec{k}')\right]} e^{ik_\mu x^\mu + ik'_\mu y^\mu} \Big)\end{aligned} \tag{7.79}$$

where $E(\vec{k}) = \hbar\omega(\vec{k})$ denotes the energy. We emphasize that due to $\left[\hat{a}(\vec{k}), \hat{a}^\dagger(\vec{k}')\right] = \delta(\vec{k}-\vec{k}')$ we only consider $\vec{k} = \vec{k}'$ in the remainder of our discussion. Applying Eq. [7.79] to the vacuum state $|0\rangle$ yields

$$\begin{aligned}\left[\hat{A}(x^\mu), \hat{A}(y^\mu)\right]|0\rangle &= \frac{\hbar^2 c^2}{2(2\pi)^4} \sum_{\vec{\epsilon},\vec{\epsilon}'} \vec{\epsilon}\cdot\vec{\epsilon}' \int d^4k \, \frac{1}{E(\vec{k})} \Big(\left[\hat{a}(\vec{k}), \hat{a}^\dagger(\vec{k})\right]|0\rangle \, e^{-ik_\mu(x^\mu - y^\mu)} \\ &\qquad + \left[\hat{a}^\dagger(\vec{k}), \hat{a}(\vec{k})\right]|0\rangle \, e^{ik_\mu(x^\mu - y^\mu)} \Big) \\ &= \frac{\hbar^2 c^2}{2(2\pi)^4} \sum_{\vec{\epsilon},\vec{\epsilon}'} \vec{\epsilon}\cdot\vec{\epsilon}' \int d^4k \, \frac{1}{E(\vec{k})} \left(e^{-ik_\mu(x^\mu - y^\mu)} - e^{ik_\mu(x^\mu - y^\mu)} \right)|0\rangle\end{aligned}$$

where the first term is attributed to $\hat{A}(x^\mu)\hat{A}(y^\mu)$ and the second term to $\hat{A}(y^\mu)\hat{A}(x^\mu)$ in Eq. [7.79] respectively. Therefore

$$\hat{A}(x^\mu)\hat{A}(y^\mu)|0\rangle = \frac{\hbar^2 c^2}{2(2\pi)^4} \sum_{\vec{\epsilon},\vec{\epsilon}'} \vec{\epsilon}\cdot\vec{\epsilon}' \int d^4k \, \frac{e^{-ik_\mu(x^\mu - y^\mu)}}{E(\vec{k})}|0\rangle = i\hbar\Delta^+(x^\mu - y^\mu)|0\rangle, \tag{7.80}$$

which describes the creation of a particle from the vacuum at $y^\mu = (\vec{y}, t')$, its propagation towards $x^\mu = (\vec{x}, t)$ [78, 232]. Since $\hat{A}(r^\mu)$ gives rise to electric and magnetic fields, we associate the particle with a *photon*, the so-called *exchange particle* of the electromagnetic interaction. We emphasize that a photon cannot arrive at $x^\mu = (\vec{x}, t)$ before it has been created at $y^\mu = (\vec{y}, t')$. Thus, the time coordinates must obey $t > t'$, which is denoted by the plus-sign in the superscript of $\Delta^+(x^\mu - y^\mu)$. The converse process – a photon traveling from x^μ to y^μ – is captured by

$$\hat{A}(y^\mu)\hat{A}(x^\mu)|0\rangle = -\frac{\hbar^2 c^2}{2(2\pi)^4} \sum_{\vec{\epsilon},\vec{\epsilon}'} \vec{\epsilon}\cdot\vec{\epsilon}' \int d^4k \, \frac{e^{ik_\mu(x^\mu - y^\mu)}}{E(\vec{k})}|0\rangle = i\hbar\Delta^-(x^\mu - y^\mu)|0\rangle \tag{7.81}$$

for $t < t'$. Since a complete description of the dynamics must encompass both processes, we introduce the *time-ordering* T-product [78]

$$T\left\{A_\mu(x^\mu)A_\mu(y^\mu)\right\} = \begin{cases} t > t': & A_\mu(x^\mu)A_\mu(y^\mu) = i\hbar\Delta^+(x^\mu - y^\mu) \\ t < t': & A_\mu(y^\mu)A_\mu(x^\mu) = i\hbar\Delta^-(x^\mu - y^\mu) \end{cases} \tag{7.82}$$

and ultimately define the *Feynman propagator* [78, 254]

$$i\hbar\Delta_F(x^\mu - y^\mu) = \langle 0|T\left\{A_\mu(x^\mu)A_\mu(y^\mu)\right\}|0\rangle\,. \tag{7.83}$$

Once we have computed the energy $E(\vec{k})$ for a given process, we can find an analytic expression for $\Delta_F(x^\mu - y^\mu)$ using the residue theorem [43] to solve the Fourier integrals in Eq. [7.80] and Eq. [7.81], respectively [78]. In essence, the propagator mediates interactions which arise during the process we seek to investigate. We will present its application using the elastic scattering of two fermions in the next section.

7.4.4 *Feynman diagrams*

We now seek to compute interactions between fields. Two field configurations $\hat{\Phi}(t = -\infty, \vec{x})$ and $\hat{\Phi}(t = \infty, \vec{y})$ describing the system long before and after the interaction, respectively, are formally connected by [78, 255]

$$\hat{\Phi}(\infty, \vec{y}) = S\hat{\Phi}(-\infty, \vec{x}),$$

where S is a matrix characteristic of the process. S can be expanded to order N in a Dyson series

$$S = \sum_{n=1}^{N} \frac{(-i)^n}{n!} \int d^4x_1 \int d^4x_2 \ldots \int d^4x_n T\{\mathcal{H}_I(x_1^\mu)\mathcal{H}_I(x_2^\mu)\ldots\mathcal{H}_I(x_n^\mu)\}, \tag{7.84}$$

with Hamiltonian density $\mathcal{H}_I(x_i^\mu)$ of the interaction for each point in spacetime x_i^μ, cf. Eq. [7.44]. Note that $T\{\ldots\}$ denotes the time-ordered T-product introduced in Eq. [7.82].

The S-matrix enables the computation of physical observables, such as *cross-sections* and *scattering amplitudes*, which fully encompass the relevant information about the interacting fields [230]. As an example we compute the scattering amplitude $\mathcal{M}$ for the elastic collision of an electron e^- and a *muon* μ^-. We employ a diagrammatic formalism introduced by Feynman [256], which does not only provide a graphical representation of the process, but also serves as an efficient computational tool.

We explain the formalism using the diagram shown in Fig. 7.3(a) [78, 230]. Time progresses from left to right: e^- and μ^- carry the (external) momenta p_1 and p_2, respectively, and are represented by arrows[22] pointing towards a vertex (black dots). An interaction is indicated by vertical (internal) connections between the vertices. These correspond to the propagators Δ_F introduced in the previous section: a vertex indicates an "event" associated with an exchange in momentum q. Note that solid lines represent particles, while the *"squiggles"* correspond to photons labeled γ.

22 Note that if the process would involve antiparticles, the arrowheads would be inverted; time and momentum remain unaffected, see [230].

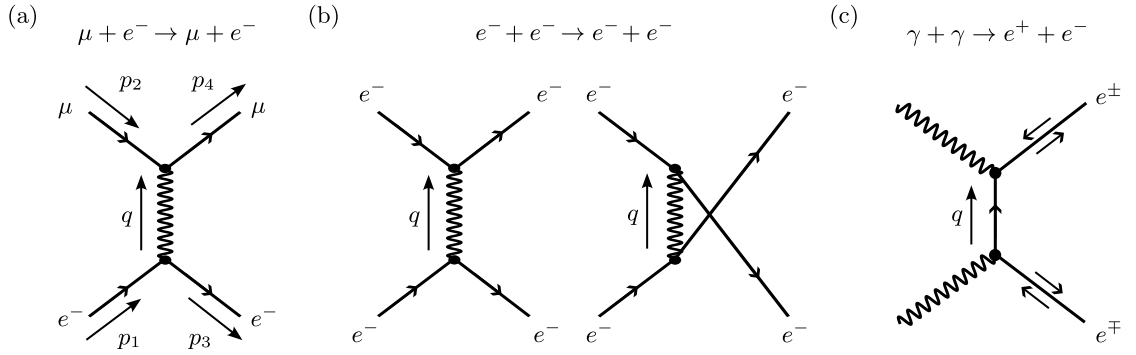


Figure 7.3: Illustrative examples for Feynman diagrams corresponding to common scattering processes in QED: (a) scattering of an electron and a muon with momenta p_i under the exchange of a virtual photon with momentum q. (b) the *Møller scattering* of an electron pair is accompanied by two diagrams, which are subtracted to obtain an antisymmetric (fermionic) field. While both (a) and (b) are elastic processes, the *pair creation* of an electron and a positron shown in (c) is inelastic. The diagrams provide a graphical method to calculate the particle's dynamics, e.g. in terms of the scattering amplitude $\mathcal{M}$ presented in the main text.

Each symbol in the graph contributes to the calculation of the scattering amplitude $\mathcal{M}$ as follows:

- *Incoming* lines are Dirac spinors $\phi^{\pm}_{\uparrow,\downarrow}(r^\mu)$ introduced in Eq. [7.51], representing a particle $\phi^{+}_{\uparrow,\downarrow}(r^\mu)$ ($\to$) or antiparticle $\phi^{-}_{\uparrow,\downarrow}$ ($\leftarrow$); the *outgoing* spinors are the respective adjoints $\phi^{\dagger\pm}_{\uparrow,\downarrow}(r^\mu)\gamma_0$. An incoming photon with polarization $\vec{\epsilon} = \epsilon_\mu$ is given by [230]

$$A_\mu(r^\mu) = \hat{a}(k_\mu)(e^{-ik_\mu r^\mu})\vec{\epsilon}$$

  with $A^\dagger_\mu(r^\mu)$ for the outgoing path.

- *Internal* lines are the propagators Δ_F, which are essentially excitations of the vacuum, see Eq. [7.83]. We think of these excitations as exchange particles mediating the interaction between vertices, which contribute to the process by a factor [230]

$$\begin{aligned} &\frac{i\gamma^\mu q_\mu + imc}{q^2 - m^2c^2} && \dots \text{ for fermions} \\ \text{or} \quad &-\frac{ig_{\mu,\nu}}{q^2} && \dots \text{ for photons,} \end{aligned} \qquad [7.85]$$

  where $g_{\mu,\nu}$ denotes the metric tensor introduced in Eq. [7.5].

- Each vertex is described by

$$\bullet: \quad ig_e\gamma^\mu \cdot (2\pi)^4\delta(\sum p_i \pm q),$$

  where the coupling constant g_e is given by $g_e = \sqrt{4\pi\alpha}$ with the fine structure constant $\alpha = e^2/\hbar c$; the Delta-distribution represents the conservation of energy and momentum [230].

- The *internal* momenta q_i correspond to the integrals $\frac{1}{(2\pi)^4}\int d^4q_i$.

The scattering amplitude $\mathcal{M}$ is then computed for each particle by taking the ordered products of the factors along a line from *right to left*. We label the respective spin states of the particles with s_i in the subscript and compute the "electron line" $e^- \to \bullet \to e^-$

$$e^- \to \bullet \to e^- : \; i\phi^\dagger_{s_3}(r^\mu)\gamma_0 g_e \gamma^\mu \phi_{s_1}(r^\mu)(2\pi)^4 \delta(p_1 - p_3 - q), \tag{7.86}$$

where p_1 and p_3 denote the momenta, see Fig. 7.3(a). Similarly, the "muon line" $\mu \to \bullet \to \mu$ yields

$$\mu \to \bullet \to \mu : \; i\phi^\dagger_{s_4}(r^\nu)\gamma_0 g_e \gamma^\nu \phi_{s_2}(r^\nu)(2\pi)^4 \delta(p_2 - p_4 + q), \tag{7.87}$$

and together with the propagator and an integral for the momentum q associated with the virtual photon γ we obtain [230]

$$\begin{aligned} e^- + \mu \to e^- + \mu : \; (2\pi)^4 g_e^2 \int d^4q \; \phi^\dagger_{s_3}(r^\mu)\gamma_0\gamma^\mu \phi_{s_1}(r^\mu)\delta(p_1 - p_3 - q) \cdot \frac{-ig_{\mu,\nu}}{q^2} \\ \times \phi^\dagger_{s_4}(r^\nu)\gamma_0\gamma^\nu \phi_{s_2}(r^\nu)\delta(p_2 - p_4 + q) \\ = -i\frac{(2\pi)^4 g_e^2}{(p_1 - p_3)^2}\phi^\dagger_{s_3}(r^\mu)\gamma_0\gamma^\mu \phi_{s_1}(r^\mu)\phi^\dagger_{s_4}(r^\mu)\gamma_0\gamma_\mu \phi_{s_2}(r^\mu)\delta(p_1 + p_2 - p_3 - p_4). \end{aligned}$$

The scattering amplitude $\mathcal{M}$ is then obtained by dropping the distribution $(2\pi)^4\delta(\sum_i p_i)$, which is a consequence of the conservation of energy, *and* multiplying the overall equation by $(-i)$ [230, 256]; ultimately, we obtain

$$\mathcal{M} = -\frac{g_e^2}{(p_1 - p_3)^2}\phi^\dagger_{s_3}(r^\mu)\gamma_0\gamma^\mu \phi_{s_1}(r^\mu) g_{\mu,\nu} \phi^\dagger_{s_4}(r^\mu)\gamma_0\gamma^\nu \phi_{s_2}(r^\mu). \tag{7.88}$$

Since fermionic fields anti-commute, we have to subtract Feynman diagrams where the incoming and outgoing particles are identical or only differ by the exchange of a particle with its anti-particle. An example is given by the elastic *Møller scattering* of two electrons as illustrated in Fig. 7.3(b). There, both incoming electrons are either scattered in opposite directions or cross paths. This also applies to inelastic scattering processes, such as the particle pair creation shown in (c), where an electron-positron pair is created by the scattering of two photons. A rare exception is the process illustrated in Fig. 7.3(a) due to the significantly larger mass m_μ of the muon compared to the electron's with mass $m_e \approx 10^{-2} m_\mu$ [78, 230].

7.4.5 *Renormalization and running coupling*

The Feynman diagram shown in Fig. 7.3(a) describes the electron-muon scattering up to second order in the S-matrix expansion, see Eq. [7.84]. In fourth order, we have to include the *polarization of the vacuum* illustrated in Fig. 7.4 [78, 230]., where a virtual electron-positron pair emerges from the photon, which is then immediately absorbed by another (virtual) photon.

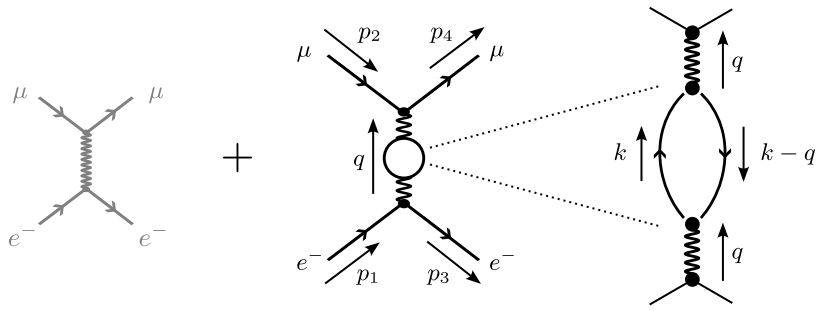


Figure 7.4: Feynman diagram for the electron-muon scattering including the vacuum polarization, a fourth-order correction to the scattering matrix. This effect is a prime example justifying the *renormalization* of the coupling constant g_e, i.e. a *renormalization of the charge*.

We compute the scattering amplitude for this correction using the previous results for the electron and muon in Sec. 7.4.4. The interaction $\gamma \to \bullet \left(\begin{smallmatrix}\to e^{\pm} \to \\ \leftarrow e^{\mp} \leftarrow\end{smallmatrix}\right) \bullet \to \gamma$ is described by [230]

$$\begin{aligned}\longrightarrow \frac{ig_{\mu,\nu}}{q^2} ig_e \gamma^\nu (2\pi)^4 \delta(q+k-q-k) \cdot \mathrm{Tr}\left[\frac{i\gamma^\alpha k_\alpha + imc}{k^2 - m^2c^2} \cdot \frac{i\gamma^\beta (k_\beta - q_\beta) + imc}{(k-q)^2 - m^2c^2}\right] \\ \times ig_e \gamma^\xi (2\pi)^4 \underbrace{\delta(k-q-(k-q))}_{=\delta(0)=1} \frac{ig_{\xi,\chi}}{q^2} \\ = i\frac{g_e^2}{q^4} \gamma_\mu \frac{\gamma^\alpha k_\alpha + mc}{k^2 - m^2c^2} \times \frac{\gamma^\beta (k_\beta - q_\beta) + mc}{(k-q)^2 - m^2c^2} \gamma_\chi\end{aligned}$$

where q and k are the momenta, $g_{\mu,\nu}$ is the metric tensor, the γ^μ label the Dirac matrices and g_e is the coupling constant. The virtual particle pair is accounted for by the product of their fermion factors defined in Eq. [7.85] and taking the trace. Combining these results with Eq. [7.86] and Eq. [7.87] we obtain the amplitude [230]

$$\begin{aligned}\mathcal{M}_{vac.} = -\frac{ig_e^4}{q^4} \phi^\dagger_{s_3}(r^\mu) \gamma_0 \gamma^\mu \phi_{s_1}(r^\mu) \\ \times \left(\int \frac{d^4k}{(2\pi)^4} \frac{\mathrm{Tr}[\gamma_\mu (\gamma^\alpha k_\alpha + mc) \gamma_\nu (\gamma^\beta (k_\beta - q_\beta) + mc)]}{(k^2 - m^2c^2)((k-q)^2 - m^2c^2)} \right) \\ \times \phi^\dagger_{s_4}(r^\mu) \gamma_0 \gamma^\nu \phi_{s_2}(r^\mu),\end{aligned}$$

where the subscripts s_i denote the spin configuration of the respective spinors $\phi^\pm_{s_i}(r^\mu)$. The vacuum polarization yields a complex correction to the scattering amplitude $\mathcal{M}$ of the lowest-order process in Eq. [7.88]. Substituting $p_1 - p_3 = q$ we take the sum and obtain

$$\begin{aligned}\mathcal{M}' &= \mathcal{M} + \mathcal{M}_{vac.} \\ &= -\frac{g_e^2}{q^2} \phi^\dagger_{s_3}(r^\mu) \gamma_0 \gamma^\mu \phi_{s_1}(r^\mu) \left(g_{\mu,\nu} + \frac{ig_e^2}{q^2} \int \frac{d^4k}{(2\pi)^4} [\dots] \right) \phi^\dagger_{s_4}(r^\mu) \gamma_0 \gamma^\nu \phi_{s_2}(r^\mu),\end{aligned} \tag{7.89}$$

which is a more complete description of the scattering process. However, the integrand grows quadratically with k and consequently with q, causing the scattering amplitude $\mathcal{M}'$ to diverge. This puts us in a predicament, since this divergence seems to contradict all experimental observations. It appears that including higher order terms in the expansion of S leads to our theoretical model becoming *less* exact, even unphysical.

This contradiction between theory and experimental outcomes motivates *renormalization*, which we briefly discuss in the upcoming paragraphs. Following Ref. [230] we use the identities in Appendix E of Ref. [257] to approximate the integral

$$\int \frac{d^4k}{(2\pi)^4}[\dots] \approx \frac{ig_{\mu,\nu}q^2}{12\pi^2}\left[\int_{m^2}^{\infty}\frac{dz}{z} - f\left(\frac{-q^2}{m^2c^2}\right)\right]$$

where $f(x)$ is a smooth function, which is linear for $x \ll 1$ and follows the natural logarithm for $x \gg 1$. Since the integral $\int dz/z = ln(z)$ is still unbounded, we introduce a large *regulator* or *cut-off mass* M, such that

$$\int \frac{d^4k}{(2\pi)^4}[\dots] \approx \frac{ig_{\mu,\nu}q^2}{12\pi^2}\left[\int_{m^2}^{M^2}\frac{dz}{z} - f\left(\frac{-q^2}{m^2c^2}\right)\right] = \frac{ig_{\mu,\nu}q^2}{12\pi^2}\left[\ln\left(\frac{M^2}{m^2}\right) - f\left(\frac{-q^2}{m^2c^2}\right)\right]$$

and consequently

$$\begin{aligned}\mathcal{M}'_R &= -\frac{g_e^2}{q^2}\phi^\dagger_{s_3}(r^\mu)\gamma_0\gamma^\mu\phi_{s_1}(r^\mu)g_{\mu,\nu} \\ &\qquad \times\left(1 - \frac{g_e^2}{12\pi^2}\left[\ln\left(\frac{M^2}{m^2}\right) - f\left(\frac{-q^2}{m^2c^2}\right)\right]\right)\phi^\dagger_{s_4}(r^\mu)\gamma_0\gamma^\nu\phi_{s_2}(r^\mu) \qquad [7.90]\\ &= -\frac{g_R^2(q^2)}{q^2}\phi^\dagger_{s_3}(r^\mu)\gamma_0\gamma^\mu\phi_{s_1}(r^\mu)\phi^\dagger_{s_4}(r^\mu)\gamma_0\gamma_\mu\phi_{s_2}(r^\mu)\end{aligned}$$

with renormalized coupling constant [230]

$$g_R(q^2) = g_e\sqrt{1 - \frac{g_e^2}{12\pi^2}\left[\ln\left(\frac{M^2}{m^2}\right) - f\left(\frac{-q^2}{m^2c^2}\right)\right]}. \qquad [7.91]$$

This result contains one of the most profound observations in the field of particle physics. Since the *bare coupling constant* is given by $g_e^2 = 4\pi\alpha$, we obtain a renormalized fine structure constant $\alpha_R(q^2) = g_R^2(q^2)/4\pi$, which depends on the energy q^2 of the scattered particles. Consequently, α is only constant at low energies, where q is negligible. Indeed, this phenomenon has been experimentally observed: precision measurements of the recoil frequency of ^{133}Cs atoms yield $\alpha = 1/137.036$ [258], while the results at high impact energies of 91 GeV yield $\alpha \approx 1/127.5$ [259]. Therefore, the electron's charge $e \propto \alpha$ we measure is different from the true, *bare charge* e_b of the electron, which is *screened* by virtual particle pairs created in the limit of high energy scattering processes [260]. We will present a crucial step towards the investigation of this so-called *"running coupling"* with our experimental quantum simulation of QED later in Ch. 8 [78].

7.5 HAMILTONIAN FORMULATION OF GAUGE THEORIES ON A LATTICE

Systematic studies of field theories have proven to be challenging due to the essentially infinite degrees of freedom. Therefore, we rely on established methods in perturbation theory to investigate quantum fields. While perturbative treatments yield remarkable results, we have already seen first hand that the description of a process in lowest order does not fully capture the underlying physics [261]. However, as more higher order terms are included, the theory may again yield non-physical outcomes. For instance, in our discussion of the electron-muon scattering, the amplitude $\mathcal{M}'$ describing the process diverges if we include the correction accounting for the polarization of the vacuum, see Eq. [7.89] [230].

In such cases we resort to the – somewhat unsatisfactory – renormalization of the coupling constant to recover a finite, well-behaved theory. Although this strategy is in agreement with experimental evidence, Feynman stated that [262]

> *"[...] Having to resort to such hocus-pocus has prevented us from proving that the theory of quantum electrodynamics is mathematically self-consistent. [...] I suspect that renormalization is not mathematically legitimate."*

Moreover, perturbative treatments cannot capture fundamental phenomena, most notably the *confinement of quarks* [263, 264]. Therefore, Wilson proposed a non-perturbative method: a *regularization* of the theory by discretization of spacetime [265]. We introduce a *lattice*, discretizing the continuous variables $r^\mu = (ct, \vec{r})$ onto a – in our discussion uniform – grid illustrated in Fig. 7.5(a). Two points in spacetime x^μ and y^μ are then related by

$$y^\mu = x^\mu + n^\mu a,$$

where $n^\mu = (n_t, n_x, n_y, n_z)$ for $n_i \in \mathbb{Z}$ represent the number of steps of size a we must *"walk"* along the lattice in each direction to cover the distance between x^μ and y^μ.

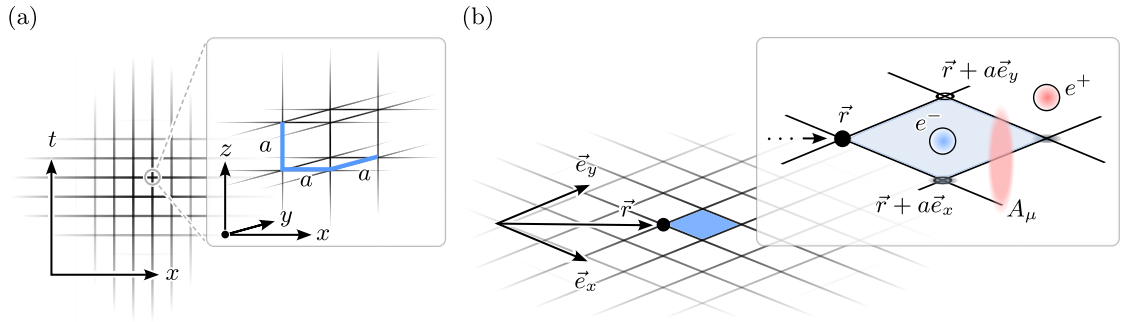


Figure 7.5: Discretization of spacetime by a regular lattice (a): we imagine a four-dimensional grid of equally spaced lines in an Euclidean coordinate system. The lines are separated by a distance a, which we call the *lattice constant*. Particles and antiparticles populate the lattice on the vertices called *sites*, while gauge fields occupy the *links* connecting two neighboring sites. For simplicity, we discuss a two-dimensional plane and focus on a single *plaquette* (blue square) (b): the origin (black) is given by the vector $\vec{r}$ and the neighboring sites are given with respect to $\vec{r}$ by parallel displacement by a along the unit vectors $\vec{e}_{x,y}$. Particles and anti-particles are shown by the circles hovering over the lattice sites, while the gauge field is represented by a shaded oval on the link between the populated sites.

We call a the *lattice constant*, which imposes a cutoff akin to the regulator M in the renormalization of the scattering amplitude in Eq. [7.90]. The theory in the continuum is then always recovered if we let a go to zero. Therefore, we can perform our analysis on the lattice for suitable a before taking the limit $a \to 0$ [233].

Wilson's lattice regularization is the foundation of *lattice gauge theorys* (LGTs), allowing us to investigate phenomena in quantum fields theories on classical computers and, most notably, digital quantum simulators. Here we discuss the Hamiltonian formulation of LGTs, where the time coordinate is treated as continuous and space is discretized. Notably, we investigate QED on a regular lattice with constant a and restrict the problem to two dimensions for simplicity. We consider a single *plaquette* (blue) illustrated in Fig. 7.5(b), which is constructed by the four lattice sites labeled with respect to the plaquette's origin $\vec{r}$.

7.5.1 *Wilson lines and loops*

We first discuss how gauge fields manifest on the lattice and consider a point charge traveling along a contiguous (and continuous) path $\mathcal{P}$ connecting two points x^μ and y^μ in spacetime. The configurations of the matter fields $\Phi(x^\mu)$ and $\Phi(y^\mu)$ are related by [233]

$$\Phi(y^\mu) = \hat{U}(y^\mu, x^\mu)\Phi(x^\mu) = \exp\left(-i \int_{\mathcal{P}} A_\mu(r^\mu) d^4 r\right) \Phi(x^\mu),$$

where $\hat{U}(y^\mu, x^\mu)$ denotes the *transport operator*, which depends on $\mathcal{P}$ and the gauge field $A_\mu(r^\mu)$. When bound to a lattice, $\hat{U}(y^\mu, x^\mu)$ becomes discrete and is called an oriented *Wilson line* from x^μ to y^μ [253, 265].

We consider the plaquette on the lattice illustrated in Fig. 7.5(b). A connection between a pair of lattice sites $(\vec{r}, \vec{r} + a\vec{e}_j)$ is called a *link*

$$\vec{r} \to \vec{r} + a\vec{e}_j,$$

with $\vec{e}_j$ denoting the unit vector along the j axis, in our case x or y. The Wilson line associated with the link is then given by [233, 265]

$$\hat{U}_{\vec{r}, a\vec{e}_j} = e^{-ia\vec{A}_j(\vec{r})}, \tag{7.92}$$

where the first index denotes the start of the link and the second index labeling the displacement along the j axis. Moreover, we introduce its Hermitian conjugate $\hat{U}^\dagger_{\vec{r}, a\vec{e}_j}$ which corresponds to the trajectory on the same link in the opposite direction, i.e. from $\vec{r} + a\vec{e}_j$ to $\vec{r}$.

Another Wilson line acting on the link $\vec{r} + a\vec{e}_j \to \vec{r} + a(\vec{e}_j + \vec{e}_k)$ perpendicular to $\vec{r} \to \vec{r} + a\vec{e}_j$ displaced from the origin by $a\vec{e}_j$ reads

$$\hat{U}_{\vec{r} + a\vec{e}_j, a\vec{e}_k} = e^{-iaA_k(\vec{r} + a\vec{e}_j)} \approx e^{-iaA_k(\vec{r}) - ia^2 \partial_j A_k(\vec{r})}, \tag{7.93}$$

where the gauge field is approximated to first order by the Taylor series [253]

$$A_k(\vec{r} + a\vec{e}_j) \approx A_k(\vec{r}) + a\partial_j A_k(\vec{r}).$$

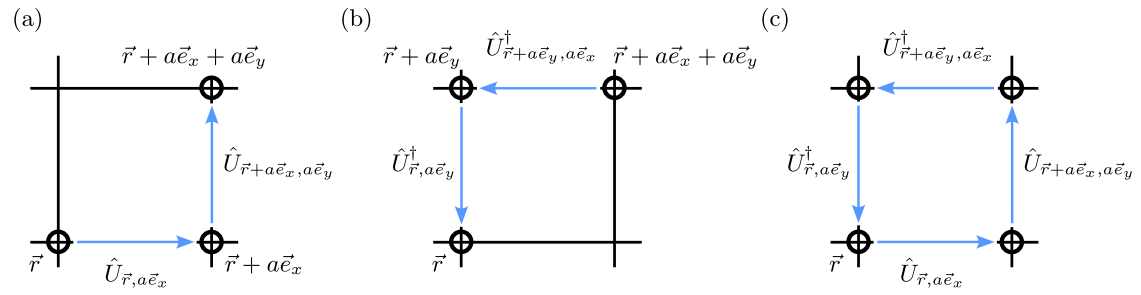


Figure 7.6: Wilson lines and loops (a): the two *Wilson lines* $\hat{U}_{\vec{r},a\vec{e}_x}$ and $\hat{U}_{\vec{r}+a\vec{e}_x,a\vec{e}_y}$ (blue) describe the trajectory from the origin $\vec{r}$ to top right corner $\vec{r}+a(\vec{e}_x+\vec{e}_y)$ of the plaquette via the site $\vec{r}+a\vec{e}_x$. (b) the path from $\vec{r}+a(\vec{e}_x+\vec{e}_y)$ back to the origin passing the top left corner is described by the Hermitian conjugate of the Wilson lines pointing from $\vec{r}$ to $\vec{r}+a(\vec{e}_x+\vec{e}_y)$. (c) the concatenation of all four Wilson lines forms a closed *Wilson loop* $\hat{P}$, which is related to the magnetic field in lattice QED.

We now consider the path shown by the blue lines in Fig. 7.6(a) and compute its associated Wilson line by taking the product of Eq. [7.92] and Eq. [7.93] [233, 253]

$$\hat{U}_{\vec{r}+a\vec{e}_x,a\vec{e}_y}\hat{U}_{\vec{r},a\vec{e}_x} = e^{-iaA_y(\vec{r})-ia^2\partial_x\vec{A}_y(\vec{r})}e^{-iaA_x(\vec{r})}. \tag{7.94}$$

Since the Wilson lines are operators which do not necessarily commute, both factors must be ordered appropriately. Applying the *Baker-Campbell-Hausdorff* (BCH) formula[23] up to the first order in the commutator, Eq. [7.94] is well approximated by [233]

$$\begin{aligned}\hat{U}_{\vec{r}+a\vec{e}_x,a\vec{e}_y}\hat{U}_{\vec{r},a\vec{e}_x} &\approx e^{-iaA_x(\vec{r})-iaA_y(\vec{r})-ia^2\partial_xA_y(\vec{r})-\frac{a^2}{2}\left[A_y(\vec{r})+a\partial_xA_y(\vec{r}),A_x(\vec{r})\right]}\\ &\approx e^{-iaA_x(\vec{r})-iaA_y(\vec{r})-ia^2\partial_xA_y(\vec{r})-\frac{a^2}{2}\left[A_y(\vec{r}),A_x(\vec{r})\right]-\cancel{\frac{a^3}{2}\left[a\partial_xA_y(\vec{r}),A_x(\vec{r})\right]}}\end{aligned}$$

Note that we neglect the last commutator scaling with a^3, which is insignificant in the limit of small lattice constants $a\to 0$ [233].

We continue with another path pointing from the top right corner to the origin of the plaquette as shown in Fig. 7.6(b), with its Wilson line given by

$$\hat{U}^\dagger_{\vec{r},a\vec{e}_y}\hat{U}^\dagger_{\vec{r}+a\vec{e}_y,a\vec{e}_x} \approx e^{iaA_x(\vec{r})+iaA_y(\vec{r})+ia^2\partial_yA_x(\vec{r})+\frac{a^2}{2}\left[A_y(\vec{r}),A_x(\vec{r})+\cancel{a\partial_yA_x(\vec{r})}\right]}.$$

Taking the product of all four lines we obtain the oriented *Wilson loop* $\hat{W}$ shown in Fig. 7.6(c). Using the BCH formula and dropping terms of $\mathcal{O}(a^3)$ we obtain

$$\hat{W} = \hat{U}^\dagger_{\vec{r},a\vec{e}_y}\hat{U}^\dagger_{\vec{r}+a\vec{e}_y,a\vec{e}_x}\hat{U}_{\vec{r}+a\vec{e}_x,a\vec{e}_y}\hat{U}_{\vec{r},a\vec{e}_x} \approx e^{-ia^2\left(\partial_xA_y(\vec{r})-\partial_yA_x(\vec{r})\right)} = e^{-ia^2F_{x,y}}, \tag{7.95}$$

where we have identified the argument in the exponential as the entry $F_{x,y}$ of the electromagnetic tensor $F_{\mu,\nu}$, see Eq. [7.11]. Note that the physical orientation of the lattice is reflected by the indices of $F_{\mu,\nu}$.

23 Consider two non-commuting operators $\hat{A}$ and $\hat{B}$. The product $e^{i\hat{A}}e^{i\hat{B}}$ can be approximated to arbitrary precision by $e^{\hat{A}}e^{\hat{B}} = e^{f(\hat{A},\hat{B})}$ with $f(\hat{A},\hat{B}) = \hat{A}+\hat{B}+\frac{1}{2}\left[\hat{A},\hat{B}\right]+\frac{1}{12}\left(\left[\hat{A},\left[\hat{A},\hat{B}\right]\right]-\left[\hat{B},\left[\hat{A},\hat{B}\right]\right]\right)-\frac{1}{24}[\ldots]$, where $\left[\hat{A},\hat{B}\right] = \hat{A}\hat{B}-\hat{B}\hat{A}$ denotes the commutator.

Wilson lines are used to construct lattice observables [265, 266]. In particular, the loop $\hat{W}$ is associated with the magnetic field permeating the plaquette perpendicular to the lattice plane. We define the *plaquette operator*

$$\hat{\square} = \frac{1}{2}\left(\hat{W} + \hat{W}^\dagger\right) \tag{7.96}$$

and compute its expectation value $\langle\hat{\square}\rangle$ by taking the trace [266, 267]. The exponential in Eq. [7.95] is approximated by the Taylor series

$$e^{-ia^2 F_{x,y}} \approx 1 - ia^2 F_{x,y} - \frac{a^4}{2} F_{x,y} F_{x,y} + \mathcal{O}(a^6)$$

and therefore

$$\mathrm{Tr}[\hat{W}] = \mathrm{Tr}[e^{-ia^2 F_{x,y}}] \approx \mathrm{Tr}[1 - ia^2 F_{x,y} - \frac{a^4}{2} F_{x,y} F_{x,y} + [\dots]].$$

Since $F_{\mu,\nu}$ is trace-less, the most significant contribution to the series is given by the product $F_{x,y}F_{x,y}$. Using the definition of the electromagnetic tensor in Eq. [7.11] we identify $F_{x,y} = B_z$ and therefore [233]

$$\mathrm{Tr}[\hat{W}] \approx -\frac{a^4}{2} B_z^2,$$

where B_z is the magnetic field along the z-axis perpendicular to the lattice plane;. Using the definition Eq. [7.96] we obtain

$$\langle\hat{\square}\rangle = \frac{1}{2}\left(\mathrm{Tr}[\hat{W}] + \mathrm{Tr}[\hat{W}^\dagger]\right) = -\frac{a^4}{2} B_z^2. \tag{7.97}$$

Therefore, by comparison with Eq. [7.75] we argue that the plaquette operator must reflect the contribution of the magnetic field to the Hamiltonian $H_{rad.}$ of the radiation field [267].

7.5.2 *Fermions on the lattice*

At first glance, the lattice formulation of fermions appears analogous to the treatment of periodic potentials in solids. However, it was soon recognized by Wilson that their description on the lattice is unfortunately not straightforward [265]. To illustrate the problem we follow the arguments by Susskind and consider a mass-less fermion in one spatial dimension as it moves on the lattice along the x direction [268]. Suppose the field $\Psi(x,t)$ satisfies the 1D Dirac equation

$$i\hbar\partial_t\gamma_0\Psi(x,t) + i\hbar c\gamma_1\partial_x\Psi(x,t) = 0$$

with $\gamma_0 = \mathbb{1} \otimes \sigma_z$ and $\gamma_1 = i\sigma_y \otimes \sigma_x$, see Eq. [7.47]. The dynamics are described by

$$i\hbar\partial_t\Psi(x,t) = -i\hbar c\gamma_0\gamma_1\partial_x\Psi(x,t) \tag{7.98}$$

where we have multiplied the equation by γ_0 from the left. We then discretize space $x \to x + n \cdot a$ to the lattice with constant a and replace the derivative $\partial_x\Psi(x,t)$ by the difference

$$\partial_x\Psi(x,t) \approx \frac{\Psi(x+a,t) - \Psi(x,t)}{a} = \frac{\Psi(x+a,t) - \Psi(x-a,t)}{2a}.$$

The lattice version of Eq. [7.98] then reads

$$i\hbar\partial_t\Psi(x,t) = -i\hbar c\gamma_0\gamma_1\left(\frac{\Psi(x+a,t) - \Psi(x-a,t)}{2a}\right) \tag{7.99}$$

We describe the field $\Psi(x,t)$ by the components $\psi_\pm(x,t)$ of a Dirac bi-spinor by the integral

$$\psi_\pm(x,t) = \frac{1}{\sqrt{2\pi}} \int dk\, e^{\mp ikx} c_{\pm,k}(t)$$

and compute the corresponding energies $E_\pm(k)$ as a function of the momentum k.

In the continuous case, the Hamiltonian capturing the dynamics in Eq. [7.98] is given by

$$\begin{aligned} H &= -i\hbar c \int dx\, \psi_\pm^\dagger(x,t) \partial_x \psi_\pm(x,t) \\ &= \pm \frac{\hbar c}{\sqrt{2\pi}} \int dk \int dx\, \psi_\pm^\dagger(x) k \cdot e^{\mp ikx} c_{\pm,k}(t) = \pm \frac{\hbar c}{2\pi} \int dk\, k \int dk'\, c_{\pm,k'}^\dagger(t) c_{\pm,k}(t) \underbrace{\int dx\, e^{\pm i(k'-k)x}}_{2\pi\delta(k-k')} \\ &= \pm \hbar c \int dk\, k \cdot c_{\pm,k}^\dagger(t) c_{\pm,k}(t) \end{aligned}$$

and the dispersion relation is thus [233, 268]

$$E_\pm(k) = \pm \hbar c k. \qquad [7.100]$$

In contrast, on the lattice the momenta are confined to the Brillouin zone, i.e. we consider the interval $k = \left[-\frac{\pi}{a}, \frac{\pi}{a}\right]$ and since the lattice Hamiltonian is given by [233]

$$\hat{H} = -i\hbar c \sum_{x=na} \psi_\pm^\dagger(x,t) \frac{\psi_\pm(x+a,t) - \psi_\pm(x-a,t)}{2a}$$

we obtain

$$E_\pm(k) = \pm \frac{\hbar c}{a} \cdot \sin(ka). \qquad [7.101]$$

If space is treated as a continuous variable, the energy $E_\pm(k)$ grows linearly with the momentum k as illustrated in Fig. 7.7(a). Such a dispersion relation cannot exist when space is discretized, since $E_\pm(k)$ must reflect the periodicity of the lattice in both real and momentum space [233]. Consequently, the dispersion Eq. [7.101] is periodic and has additional nodes at the boundaries of the Brillouin zone as shown in Fig. 7.7(b), where $k = \pm\frac{\pi}{a}$. However, these introduce a fundamental problem in our formulation, since an excitation at $k = 0$ is energetically equivalent to those at $k = \pm\frac{\pi}{a}$. It is thus equally likely that a low-energy excitation of ψ_+ creates a right-moving particle[24] with momentum $|k| \ll \frac{\pi}{2a}$ near the origin of the Brillouin zone, as it is to create left-moving particle at either of the boundaries – this phenomenon is known as *fermion doubling* [233, 268].

There are two simple strategies to resolve the doubling problem[25]. In the formulation of Ginsparg and Wilson [272], the lattice Hamiltonian is modified by an additional term, which introduces an energy gap at the boundaries of the Brillouin zone. Since the theory has to reflect the properties of the system in the continuum limit, this term must vanish as the lattice constant a goes to zero. A more elegant solution are *staggered fermions* by Kogut and Susskind [266, 268], which we discuss in the following paragraph.

24 The direction of travel is given by the slope of the dispersion relation: a positive slope correspond to a right-moving fermion.

25 A third, more elaborate approach involves a generalization of the derivative operator, which yields to the so-called SLAC fermions [269–271], owing their name to the SLAC (Stanford Linear Accelerator Center) "bag" model proposed to describe the structure of hadrons.

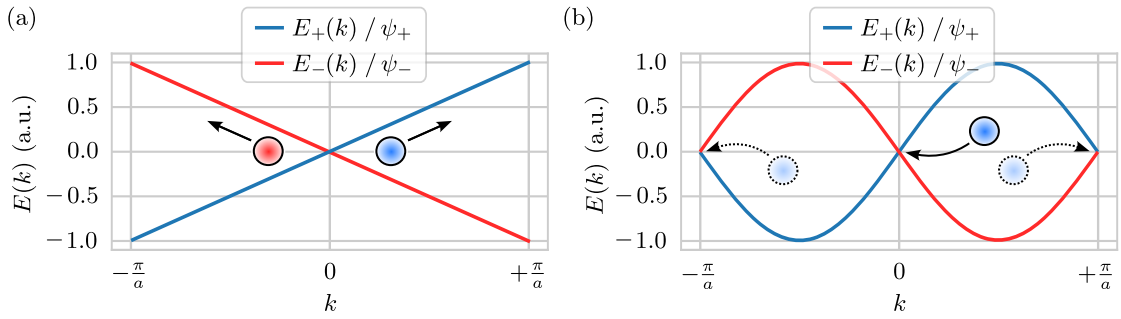


Figure 7.7: Fermions on the lattice: (a) in continuous space a right-moving particle (blue) described by the spinor $\psi_+(x,t)$ has an energy $E_+(k)$, while $\psi_-(k)$ corresponds to the left-moving antiparticle (red) with energy $E_-(k)$. (b) on the lattice $E_\pm$ is periodic with additional nodes on the boundaries, where $k = \pm\frac{\pi}{a}$. In the limit of low energies, excitations of the field $\psi_+(x,t)$ – i.e. particles – with momentum $k = 0$ and $k = \pm\frac{\pi}{a}$ are equivalent; these excitations are called *doublers*.

We consider a regular lattice with lattice constant a and enumerate the sites by $n \in \mathbb{N}$. To each site we assign a single component $\psi_\pm(x,t)$ of the Dirac spinor $\Psi(x,t)$: $\psi_+(x,t)$ is hosted on sites with even n, while $\psi_-(x,t)$ is assigned to sites with odd n. Since x is restricted to the lattice sites, we replace x by n, implying $x = na$ and recall that $\Psi(n)$ must satisfy the anti-commutation relations for fermions

$$\{\Psi(n), \Psi(m)\} = 0 \qquad \text{and} \qquad \{\Psi^\dagger(n), \Psi(m)\} = \delta_{m,n}, \tag{7.102}$$

where m and n label the respective sites; c.f. Eq. [7.52]. The Hamiltonian of the mass-less fermion field is then given by [268]

$$\hat{H} = -\frac{i\hbar c}{2a}\gamma_0\gamma_1 \sum_n \left(\Psi^\dagger(n)\Psi(n+1) - \Psi^\dagger(n+1)\Psi(n)\right) \tag{7.103}$$

capturing the dynamics

$$i\hbar\partial_t\Psi(m) = -[H, \Psi(m)] = \frac{i\hbar c}{2a}\gamma_0\gamma_1 \sum_n \left([\Psi^\dagger(n)\Psi(n+1), \Psi(m)] - [\Psi^\dagger(n+1)\Psi(n), \Psi(m)]\right)$$

in agreement with Eq. [7.99]. Using the anti-commutators in Eq. [7.102] for the staggered fermions we compute

$$\begin{aligned}
\implies [\Psi^\dagger(n)\Psi(n+1), \Psi(m)] &= \Psi^\dagger(n)\Psi(n+1)\Psi(m) - \Psi(m)\Psi^\dagger(n)\Psi(n+1) \\
&= \Psi^\dagger(n)\Psi(n+1)\Psi(m) \\
&\qquad - \left(\{\Psi^\dagger(n), \Psi(m)\} - \Psi^\dagger(n)\Psi(m)\right)\Psi(n+1) \\
&= \Psi^\dagger(n)\left(\Psi(n+1)\Psi(m) + \Psi(m)\Psi(n+1)\right) - \delta_{m,n}\Psi(n+1) \\
&= \Psi^\dagger(n)\cancel{\{\Psi(n+1), \Psi(m)\}} - \delta_{m,n}\Psi(n+1) = -\Psi(m+1) \\
\implies [\Psi^\dagger(n+1)\Psi(n), \Psi(m))] &= [\dots] = -\Psi(m-1)
\end{aligned}$$

and obtain [268]

$$i\hbar\partial_t\Psi(m) = -[H, \Psi(m)] = -\frac{i\hbar c}{2a}\gamma_0\gamma_1\left(\Psi(m+1) - \Psi(m-1)\right).$$

We conclude our discussion by introducing the term [266, 268]

$$\hat{H}_{mass} = mc^2\gamma_0 \sum_n \Psi^\dagger(n)\Psi(n)$$

accounting for the fermion's rest mass m. As $\Psi(n)$ describes both particles and antiparticles alike, the staggerization *by design* factors $\Psi(n)$ into its components $\psi_\pm(n)$. Thus the particle's nature is encoded in the lattice sites, allowing for the substitution [268]

$$\Psi(n) \mapsto \phi(n) \qquad \text{with} \qquad \phi(n) = \begin{cases} \psi_+(n) \text{ for } n \text{ even} \\ \psi_-(n) \text{ for } n \text{ odd} \end{cases}$$

and we account for the opposite signs introduced by γ_0 by the factor $(-1)^n$ in $\hat{H}_{mass}$, which is then given by [266]

$$\hat{H}_{mass} = mc^2 \sum_n (-1)^n \phi^\dagger(n)\phi(n) = m\hat{H}_m.$$

Since the $\psi_\pm(n)$ are essentially two-component spinors, so must be $\phi(n)$ and we can replace the product of Dirac matrices $\gamma_0\gamma_1$ with the Pauli matrix σ_x.

After the appropriate substitutions the Hamiltonian $\hat{H}_{mat.}$ describing a field of massive fermions reads [266]

$$\hat{H}_{mat.} = -\frac{i\hbar c}{2a} \sum_n \sigma_x \left(\phi^\dagger(n)\phi(n+1) - \phi^\dagger(n+1)\phi(n) \right) + m\hat{H}_m. \qquad [7.104]$$

However, we emphasize that $\hat{H}_{mat.}$ is not invariant under local gauge transformations. For a transformation $G(n)$ acting on $\phi(n)$, such that [253]

$$\phi(n) \longrightarrow G(n)\phi(n)$$

the products of the field operators on neighboring lattice sites transform according to

$$\phi^\dagger(n)\phi(n+1) \longrightarrow (G(n)\phi(n))^\dagger G(n+1)\phi(n+1) = \phi^\dagger(n)G^\dagger(n)G(n+1)\phi(n+1).$$

which is generally not invariant, i.e. $G^\dagger(n)G(n+1) \neq \mathbb{1}$. However, we can restore gauge invariance by introducing a Wilson operator on the link between neighboring sites, see Sec. 7.5.1. The operator satisfies

$$\hat{U}_{n,a\vec{e}_x} = \hat{U}_{n,n+1} = G(n)\hat{U}_{n,n+1}G^\dagger(n+1)$$

and thus [253, 266]

$$\phi^\dagger(n)\hat{U}_{n,n+1}\phi(n+1) = \phi^\dagger(n)G^\dagger(n)G(n)\hat{U}_{n,n+1}G^\dagger(n+1)G(n+1)\phi(n+1).$$

is invariant. We thus adapt Eq. [7.104] and arrive at the gauge invariant Hamiltonian

$$\hat{H}_{mat.} = -\frac{i\hbar c}{2a} \sum_n \sigma_x \left(\phi^\dagger(n)\hat{U}_{n,n+1}\phi(n+1) - \phi^\dagger(n+1)\hat{U}^\dagger_{n,n+1}\phi(n) \right) + m\hat{H}_m, \qquad [7.105]$$

where we have used the property $\hat{U}_{n+1,n} = \hat{U}^\dagger_{n,n+1}$.

While at first glance it might appear unjustified to introduce a Wilson operator to enforce gauge invariance, our approach is essentially identical to the discussion in Sec. 7.3.3, where we have first introduced a gauge field from a symmetry argument. There, the gauge field $A_\mu(r^\mu)$ was essentially "absorbed" by the substitution of the differential operator $D_\mu = \partial_\mu + \frac{ie}{\hbar c}A_\mu(r^\mu)$. However, in this section we have used the regular derivative ∂_μ and in doing so, we had to reintroduce $\hat{U}_{n,n+1}$ to establish gauge invariance; if we had used D_μ in our discussion, we would arrive at a solution analogous to Eq. [7.105] [253].

7.5.3 *Kogut-Susskind Hamiltonian*

Using the framework developed in the preceding sections, we now construct a Hamiltonian formulation of QED on the lattice by combining $\hat{H}_{mat.}$ with the radiation field. Since magnetic fields do not manifest in one spatial dimension, we consider the 2D lattice shown in Fig. 7.5(b) as the next simplest case in the upcoming discussion.

We initially follow the approach presented by Kogut and Susskind in Ref. [266] and first consider the Hamiltonian of the matter field. Since $\hat{H}_{mat.}$ in Eq. [7.105] reflects a staggered lattice in one dimension, we introduce the unit vector $\vec{n}$ associated with each link $n \to n + a\vec{e}_{x,y}$. The product $\vec{\sigma}\vec{n}$ with $\vec{\sigma} = (\sigma_x, \sigma_y)$ then assigns the appropriate matrix σ_x or σ_y to each link connecting a pair of lattice sites. Adapting Eq. [7.105] accordingly yields

$$\begin{aligned}\hat{H}_{mat.} &= -\frac{i\hbar c}{2a}\sum_n \vec{\sigma}\vec{n}\left(\phi^\dagger(n)\hat{U}_{n,n+1}\phi(n+1) - \phi^\dagger(n+1)\hat{U}^\dagger_{n,n+1}\phi(n)\right) + m\hat{H}_m \\ &= \Omega\hat{H}_K + m\hat{H}_m,\end{aligned} \tag{7.106}$$

where we have introduced the coupling constant Ω for a compact notation in agreement with literature, e.g. Ref. [267]. Due to $\Omega\hat{H}_K$ capturing the dynamics of the particles as they move along the lattice, we call $\hat{H}_K$ the *kinetic* term of the Hamiltonian, while $\hat{H}_m$ is called the *mass* term.

We now add the radiation field given by the Hamiltonian $\hat{H}_{rad.}$ in Eq. [7.75]. Our strategy will depart from the original work by Kogut and Susskind[26] and rather follow a more argumentative approach, which is conceptually more appealing and leads to the same result. We therefore express $\hat{H}_{rad.}$ as the sum of $\hat{H}_{el.}$ and $\hat{H}_{mag.}$

$$\hat{H}_{rad.} = \frac{1}{8\pi c^2}\int d^3r\ \hat{\vec{E}}(r^\mu)^2 + \frac{1}{8\pi}\int d^3r\ \hat{\vec{B}}(r^\mu)^2 = \hat{H}_{el.} + \hat{H}_{mag.}, \tag{7.107}$$

each representing the contributions of the electric and magnetic fields, respectively, and first examine $\hat{H}_{mag.}$ using the Wilson operators introduced in Sec. 7.5.1. Specifically, we recall that the expectation value of the operator $\hat{\square}$ is proportional to the square of the magnetic field permeating the plaquette in the z direction, see Eq. [7.97]. By comparison with $\hat{H}_{mag.}$ we argue that

$$\langle\hat{H}_{mag.}\rangle = \frac{1}{8\pi}\int d^3r\ \langle\hat{\vec{B}}(r^\mu)\rangle^2 \propto B^2 = -\frac{2}{a^4}\sum_{\vec{r}}\langle\hat{\square}_{\vec{r}}\rangle$$

for a magnetic field pointing along an axis perpendicular to the lattice plane with strength $B = \langle\hat{\vec{B}}(r^\mu)\rangle$. Note that the expectation values $\langle\hat{\square}_{\vec{r}}\rangle$ are identified by the subscript $\vec{r}$, which denotes the origin of each plaquette as shown in Fig. 7.5(b). By summing over the whole lattice we obtain

$$\hat{H}_{mag.} = g^{-2}\hat{H}_B = -g^{-2}\sum_{\vec{r}}\hat{\square}_{\vec{r}} \tag{7.108}$$

where we have introduced the coupling constant g following Zohar et al. [267]; note that $g \propto a^2$ with lattice constant a.

26 Kogut and Susskind introduce the gauge field by establishing an analogy with the physics of a rigid rotor, which, in author's opinion, is not particularly illustrative. Since we have already introduced the concept of Wilson lines in Sec. 7.5.1, the inclusion of $\hat{H}_{rad.}$ and its connection with the link variables can be made more naturally.

For the electric term $\hat{H}_{el.}$ we consider two charged particles on a single plaquette of the lattice as shown in Fig. 7.8(a). We assign an integer $i = 1$ to the site at the origin $\vec{r}$ and enumerate the remaining sites $i = 2 \ldots 4$ in a clockwise orientation. Recall that in the staggered-fermion formulation of the matter fields, sites with an even index i can only be populated by particles; conversely, odd indices indicate sites that can host antiparticles.

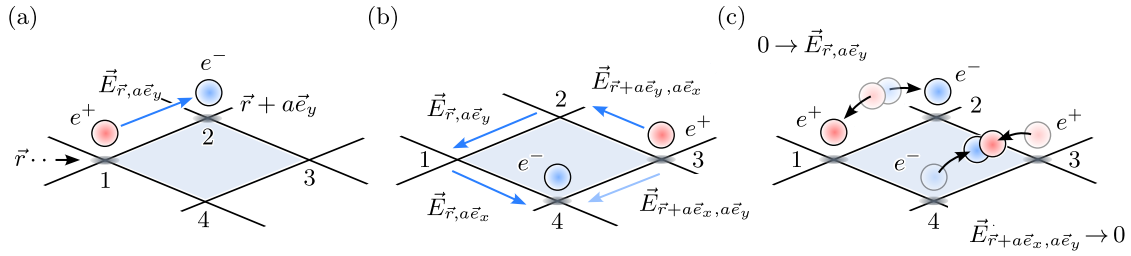


Figure 7.8: Electric fields on a regular 2D lattice: (a) the lattice is populated by electrons (blue, charge $-e$) and positrons (red, charge $+e$) occupying sites with even and odd indices, respectively. The electric field is represented by a vector on the link, pointing from the positive to the negative charge. (b) the field vector $\vec{E}_{\vec{r}+a\vec{e}_x,a\vec{e}_y}$ is equivalent to the sum of vectors on the links around the plaquette. (c) due to the staggerization of the lattice particles hopping between neighboring sites will annihilate each other and the electric field on the link vanishes. Conversely, a particle pair that is being created from the vacuum gives rise to an electric field.

Let the particles be electrons (blue) with charge $-e$ and their antiparticles positrons (red) with charge $+e$, respectively. With the charges distributed as shown in Fig. 7.8(a) the electric field described by the vector $\vec{E}_{\vec{r},a\vec{e}_i}$ must point along the link $\vec{r} \to \vec{r} + a\vec{e}_y$, e.g. from odd towards even site indices if both sites are populated.

An alternative configuration is shown in Fig. 7.8(b), where the electric field $\vec{E}_{\vec{r}+a\vec{e}_x,a\vec{e}_y}$ again points from the odd towards the even site index. However, the same vector can be represented by the sum of field vectors *around* the plaquette including the two unpopulated sites with indices $(1,2)$. This redundancy is a consequence of *Gauss' law* [17, 18]

$$\sum_{\pm a\vec{e}_j} \vec{E}_{\vec{r},\pm a\vec{e}_j} = Q_{\vec{r}} \qquad [7.109]$$

where $Q_{\vec{r}}$ denotes the net charge and $\vec{E}_{\vec{r},\pm a\vec{e}_j}$ the electric fields associated with links connecting the site with its immediate neighbors $\vec{r} \pm a\vec{e}_j$. Note that to each field vector *entering* an unpopulated site there must be at least one vector associated with a field of equal magnitude *leaving* the site, thereby satisfying

$$\sum_{\pm a\vec{e}_j} \vec{E}_{\vec{r},\pm a\vec{e}_j} = 0.$$

Evidently, the configuration of the fermions is intimately coupled to the electric field, and vice versa. Moreover, the staggerization of the lattice imposes additional boundary conditions which manifest in redundant fields: a single plaquette is completely described by the population of the four matter sites and – following Gauss' law – one of the electric field vectors in Fig. 7.8(b).

We conclude that the energy of the electric field $\langle \hat{H}_{el.} \rangle \propto \langle \hat{\vec{E}}^2 \rangle$ must be equal to the sum of all the small contributions coming from each link. Attributing the field operators $\hat{E}_{\vec{r},\pm a\vec{e}_j}$ to the respective links we therefore introduce the Hamiltonian

$$\hat{H}_{el.} = \frac{1}{g^{-2}} \sum_{\vec{r},\pm a\vec{e}_j} \hat{E}^2_{\vec{r},\pm a\vec{e}_j} = \frac{1}{g^{-2}} \hat{H}_{el.} \tag{7.110}$$

with coupling constant g according to Refs. [266, 267].

We are left to identify a suitable representation of the operators $\hat{E}_{\vec{r},a\vec{e}_j}$ and $\hat{U}_{n,n+1}$, which we deduce from Fig. 7.8. Let $|E\rangle_{\vec{r},a\vec{e}_y}$ be the eigenstate of the electric field operator $\hat{E}_{\vec{r},a\vec{e}_y}$ on the link $\vec{r} \to \vec{r} + a\vec{e}_y$ in Fig. 7.8(a), which satisfies

$$\hat{E}_{\vec{r},a\vec{e}_y} |E\rangle_{\vec{r},a\vec{e}_y} = E |E\rangle_{\vec{r},a\vec{e}_y} .$$

The eigenvalue must encode both the direction of the field vector as well as its strength, which is proportional to the product of the charges $Q_{\vec{r}} Q_{\vec{r}+a\vec{e}_y}$ present at each end of the link. Employing a staggered formulation of the matter field and allowing at most one fermion per lattice site, the electric field operator on a single plaquette must take the form

$$\hat{E}_{\vec{r},a\vec{e}_y} = \begin{pmatrix} 1 & 0 & 0 \\ 0 & 0 & 0 \\ 0 & 0 & -1 \end{pmatrix} . \tag{7.111}$$

with eigenstates $|+1\rangle$, $|-1\rangle$ and $|0\rangle$, of which the latter represents the vacuum state.

For the Wilson operator $\hat{U}_{\vec{r},a\vec{e}_y}$ we consider the action of the kinetic term of the Hamiltonian $\hat{H}_{mat.}$ on the link $\vec{r} \to \vec{r} + a\vec{e}_y$, which is given by [18]

$$\hat{H}_K = \Omega \left(\phi^\dagger(\vec{r}) \hat{U}_{\vec{r},a\vec{e}_y} \phi(\vec{r} + a\vec{e}_y) + \text{h.c.} \right) ,$$

where the abbreviation "h.c." denotes the hermitian conjugate. A positron hopping along the link will recombine with the electron on the neighboring site, and the electric field will return to the vacuum state as shown in Fig. 7.8(c). Conversely, the process of *pair creation* will create an electron and a position at the respective end of the link and simultaneously excite the electric field. Therefore $\hat{U}_{\vec{r},a\vec{e}_y}$ must act as the lowering operator of the electric field and consequently

$$\hat{U}_{\vec{r},a\vec{e}_y} = \begin{pmatrix} 0 & 0 & 0 \\ 1 & 0 & 0 \\ 0 & 1 & 0 \end{pmatrix} . \tag{7.112}$$

The lattice Hamiltonian is now constructed by taking the sum of $\hat{H}_{mat.}$ given by Eq. [7.106] and $\hat{H}_{rad.}$ in Eq. [7.107] to obtain the expression [17, 18]

$$\begin{aligned} \hat{H} &= \hat{H}_{mat.} + \hat{H}_{rad.} \\ &= \Omega \hat{H}_K + m \hat{H}_M + \frac{1}{g^{-2}} \hat{H}_E + g^{-2} \hat{H}_B \end{aligned} \tag{7.113}$$

which is known as the *effective Kogut-Susskind Hamiltonian* describing QED on a lattice. We will investigate the ground state properties of this Hamiltonian in the upcoming chapter, where we present the implementation of a single plaquette involving dynamic gauge fields and matter on a trapped-ion qudit processor.

8

SIMULATION OF A (2 + 1)D LATTICE GAUGE THEORY ON A QUDIT QUANTUM SIMULATOR

In this chapter we present the quantum simulation of a lattice gauge theory in $(2+1)D$ [17–19]. We investigate the minimal instance of lattice QED: a single plaquette defined by a two-dimensional grid of four sites labeled i, which are populated by electrons (positrons) on even (odd) lattice sites and coupled by gauge fields residing on the links. Our target Hamiltonian developed by Kogut and Susskind has been introduced in the previous chapter. Here we discuss its implementation on a trapped-ion quantum processor and prepare approximations of the true ground states of the Hamiltonian using a VQE protocol for various coupling strengths.

In Sec. 8.1 we present an experiment simulating the fundamental building block of a larger lattice in 2D including gauge fields and dynamical matter. Here we observe the emergence of a magnetic field, a phenomenon that cannot not be observed in 1D [273]. We then show the process of particle pair creation and annihilation by simulating the time evolution of the system under the Hamiltonian. Moreover, an alternative lattice model studied in condensed matter physics is introduced, which exhibits different kinetics of the particles on the lattice. In Sec. 8.2 we then realize a pure-gauge theory and study interacting gauge fields and truncation effects. By allowing more discrete states to represent the gauge fields, our results show an improvement in the description of lattice QED, as it is predicted in theory when moving closer towards the continuum limit. Since the plaquette operator is related to the renormalized coupling constant g_R discussed in Sec. 7.4.5 [263, 274], our experiment is a crucial first step towards an investigation of the *running coupling*, an extensively studied subject in the field of particle physics.

8.1 A GAUGE FIELD INTERACTING WITH DYNAMICAL MATTER

We investigate QED on the 2D lattice illustrated in Fig. 8.1(a) including particles and gauge fields. The fundamental building block of the lattice is a *plaquette* of four sites labeled by $i = 1 \ldots 4$. Each site is populated either by an electron (e^-, even i) or a positron (e^+, odd i), which interact via gauge fields on the links; the absence of particles and fields is called the *vacuum state*. We experimentally realize a single plaquette with *open boundary condtions* (OBCs) for the parameters $m = 0.1$ and $\Omega = 5$ in the Hamiltonian given by Eq. [7.113]. This choice is motivated by the underlying physics: in this non-perturbative regime, particle pair creation has a significant effect, allowing us to investigate both the dynamics of particles and their coupling to the electromagnetic field [17, 19].

Electrons and positrons are represented by qubits in the states $|\downarrow\rangle$ and $|\uparrow\rangle$, which are encoded in the electronic levels of trapped $^{40}Ca^{+}$ ions. Electrons populating sites with an even index are represented by the state $|\downarrow\rangle$, while $|\uparrow\rangle$ indicates an empty site; the opposite applies for positrons on odd sites. The gauge field describes the electric field vectors $\vec{E}_{i,j}$ on the link $(i \leftrightarrow j)$ between two sites (i, j).

Due to the conservation of charge a given configuration of the matter field must define the orientation of the $\vec{E}_{i,j}$ on each link and vice versa. For example, if the sites $(1, 2)$ are populated by a particle pair as illustrated in Fig. 8.1(a), the electric field vector $\vec{E}_{1,2}$ will point from $1 \to 2$, which is represented by the state $\vec{E}_{1,2} = |+1\rangle$. Moreover, a pair on the sites $(3', 4')$ and its accompanying a field $\vec{E}_{3',4'}$ pointing from $3' \to 4'$ can be equivalently described by the field vectors pointing *around* the plaquette along the path $3' \to 2' \to 1' \to 4'$; the field $\vec{E}_{1',2'}$ on the link $(1' \to 2')$ points from $2' \to 1'$, which we associate with the state $\vec{E}_{1',2'} = |-1\rangle$, see Fig. 7.8 in Sec. 7.5.2 for comparison. This is a manifestation of Gauss' law: the intimate coupling of matter and field allows us to reduce our formulation of a single plaquette to one gauge field on the link $(1 \leftrightarrow 2)$, while the other fields are implicitly encoded in the configuration of the particles populating the lattice sites [18, 275]. Furthermore, the absence of a field on the link $(i \leftrightarrow j)$ is given by the vacuum state $\vec{E}_{i,j} = |0\rangle$. Since three states are required to adequately describe the configuration of the gauge field, it can be efficiently encoded in a qudit with local dimension $d = 3$.

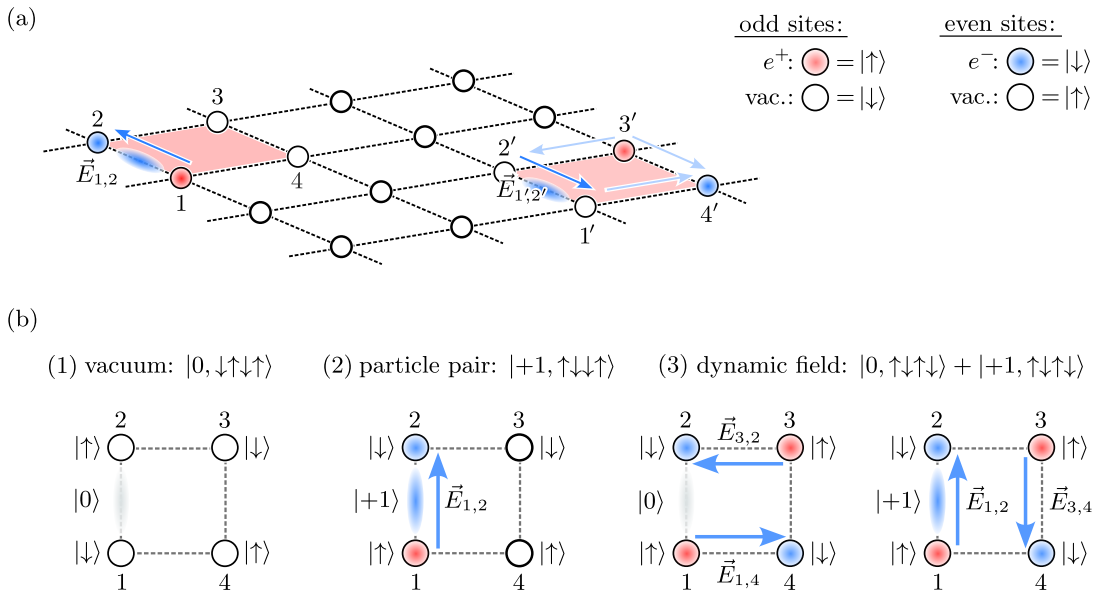


Figure 8.1: QED on a 2D square lattice: (a) the lattice is populated by electrons (e^-, blue) and positrons (e^+, red), which reside on the vertices. Neighboring sites labeled i and j are coupled by a gauge field (ovals), which are associated with the electric field $\vec{E}_{i,j}$ pointing from the e^+ to e^-. Matter is encoded the states $|\downarrow\rangle$ and $|\uparrow\rangle$, which indicate the presence or absence (vacuum, vac.) of an electron at the site i; the encoding of positrons is opposite. We consider a single *plaquette* of four sites and observe the characteristic states in (b): (1) a bare vacuum state $|0, \downarrow\uparrow\downarrow\uparrow\rangle$, (2) the particle-pair state $|+1, \uparrow\downarrow\downarrow\uparrow\rangle$ and (3) a fully populated plaquette with the gauge field in the superposition $(|+1\rangle + |0\rangle) \otimes |\uparrow\downarrow\uparrow\downarrow\rangle$; the significance of these states is discussed in the main text.

We choose the encoding in Tab. 8.1 and refer to Fig. 3.1 for a description of the respective states. Note that the $4^2S_{1/2}(m = -1/2)$ ground state on the qudit acts as the auxiliary state $|g\rangle$ required for the implementation of the controlled rotation gates $C\hat{R}(\theta, \phi)$ introduced in Sec. 4.3.2. Prior to every simulation, the system is prepared in the vacuum state $|0, \downarrow\uparrow\downarrow\uparrow\rangle$, before the ground state of the Hamiltonian is approximated by the variational circuit presented in Sec. 8.1.1 [17].

	$4S^2_{1/2}(m = -1/2)$	$3D^2_{5/2}(m = -3/2)$	$3DS^2_{5/2}(m = -1/2)$	$3D^2_{5/2}(m = +1/2)$
positron	$\|\downarrow\rangle$ (vac.)	-	$\|\uparrow\rangle$	-
electron	$\|\downarrow\rangle$	-	$\|\uparrow\rangle$ (vac.)	-
field	$\|g\rangle$	$\|-1\rangle$	$\|0\rangle$	$\|+1\rangle$

Table 8.1: Encoding of particles and gauge fields in the electronic states of $^{40}Ca^+$ for the simulation of 2D-QED with *open boundary condtions* (OBCs). The particles on the matter sites are encoded in the $4^2S_{1/2}(m = -1/2)$ ground state and the $3^2D_{5/2}(m = -1/2)$ excited state. In contrast, the gauge field occupies the states with $m = (-3/2, -1/2, +1/2)$ in the $3^2D_{5/2}$ manifold, using $|g\rangle$ in $4^2S_{1/2}(m = -1/2)$ only as an auxiliary state to realize the controlled rotation gates $C\hat{R}(\theta, \phi)$, cf. Sec. 4.3.2.

Fig. 8.1(b) shows the physically relevant states we observe in our simulation. In the bare vacuum state $|\downarrow\uparrow\downarrow\uparrow\rangle$, the ions are in the staggered Neél state, which is characterized by the absence of particles and fields. The ions encoding the matter are always in a staggered state with magnetization $\hat{M} = 0$, which further allows us to distinguish physical from non-physical states. For example, the state $|0, \uparrow\uparrow\uparrow\uparrow\rangle$ representing two positrons on the sites $(1, 3)$ with $\langle M \rangle = +4$ violates the conservation of charge and is therefore not realized in nature. In the strong coupling regime $g^{-2} \ll 1$, a pair of particle is created on the sites $(1, 2)$ and we obtain the state $|+1, \uparrow\downarrow\downarrow\uparrow\rangle$. As the coupling strength g^{-2} in Eq. [7.113] increases, another pair emerges on the sites $(3, 4)$, leading to the superposition $(|0\rangle + |1\rangle) \otimes |\uparrow\downarrow\uparrow\downarrow\rangle$ [17].

Experimentally, we seek to measure the expectation value of the *plaquette operator* $\hat{\square}$ which we have introduced in Sec. 7.5.1. Following the labeling in Fig. 8.1(b) to identify the links, we define

$$\hat{\square} = \frac{1}{2}\left(\hat{W} + \hat{W}^\dagger\right) = \frac{1}{2}\left(\hat{U}_{1,2}\hat{U}_{3,2}\hat{U}_{3,4}\hat{U}_{1,4} + \hat{U}^\dagger_{1,4}\hat{U}^\dagger_{3,4}\hat{U}^\dagger_{3,2}\hat{U}^\dagger_{1,2}\right), \tag{8.1}$$

where $\hat{U}_{i,j} = |-1\rangle\langle 0| + |0\rangle\langle 1|$ are the lowering operators acting on the electric fields at the respective link $(i \leftrightarrow j)$. Since our plaquette can be fully described by a single gauge field on the link $(1 \leftrightarrow 2)$, the plaquette operator simplifies to [17, 18]

$$\hat{\square} = \frac{1}{2}\left(\hat{U} + \hat{U}^\dagger\right) = -\hat{H}_B, \tag{8.2}$$

where $\hat{H}_B$ is the magnetic component of the effective Hamiltonian given by Eq. [7.113], see Sec. 7.5.1 [253].

8.1.1 *Variational circuit and ground state approximation*

We employ the variational quantum circuit illustrated in Fig. 8.2(a), which is adapted from the proposal by Paulson et al. [17]. Its structure is motivated by the ground state of the Hamiltonian in Eq. [7.113]. As the physically meaningful configurations of the gauge field and matter sites are known, one can construct a circuit that creates weighted superpositions of these physical states [17, 184, 276, 277]. The weights are adjusted by a set of nine rotation angles $\boldsymbol{\theta} = \{\theta_i\}_{i=1\ldots9}$ controlling two types of quantum gate operations. Interactions between the gauge field and the matter sites are realized by the controlled rotation gates $C\hat{R}^{(i,j)}(\theta)$ (red boxes) introduced in Sec. 4.3.2. Since the sum of the charges carried by the particles populating the plaquette must be vanish, quantum gates coupling any pair of matter sites must preserve parity. We therefore employ the *partial swap gates* $\hat{A}^{(i,j)}(\theta)$ thoroughly studied by Gard et al. [278]. On a subset of two qubits labeled by the tuple (i,j), the gate is defined as

$$\hat{A}^{(i,j)}(\theta) = \begin{pmatrix} 1 & 0 & 0 & 0 \\ 0 & \cos(\theta) & \sin(\theta) & 0 \\ 0 & \sin(\theta) & -\cos(\theta) & 0 \\ 0 & 0 & 0 & 1 \end{pmatrix}, \tag{8.3}$$

acting non-trivially only on input states with odd parity. Depending on the input state we distinguish between *reduced* and *general partial swap gates*, which differ in their physical implementation.

We first discuss the reduced partial swap gate $\hat{A}_{red.}(\theta)$, which is applicable whenever the initial state of one of the participating qudits is known. The gate is realized by the sequence shown in Fig. 8.2(b) using the blue sideband gates introduced in Sec. 4.3. Consider two qubits labeled i and j in the motional ground state $|n=0\rangle$. The quantum state of i is given by the superposition $|i\rangle = \alpha\,|\downarrow\rangle + \beta\,|\uparrow\rangle$ with $\alpha, \beta \in \mathbb{C}$, while j is in either of the computational basis states $|j\rangle = |\downarrow\rangle$ or $|j\rangle = |\uparrow\rangle$. In the case $|j\rangle = |\downarrow\rangle$ we use an additional local rotation $\hat{R}^{(j)}(\pi, 0)$ to prepare $|j\rangle = |\uparrow\rangle$. The system is then in the state

$$|i\rangle \otimes \left[\hat{R}^{(j)}(\pi,0)\right] |j\rangle = \alpha\,|\downarrow,\uparrow\rangle + \beta\,|\uparrow,\uparrow\rangle \tag{8.4}$$

and transforms under $\hat{A}^{(i,j)}_{red.}(\theta)$ as

$$\hat{A}^{(i,j)}_{red.}(\theta)\,[\alpha\,|\downarrow,\uparrow\rangle + \beta\,|\uparrow,\uparrow\rangle] = \alpha\,[\cos(\theta)\,|\downarrow,\uparrow\rangle + \sin(\theta)\,|\uparrow,\downarrow\rangle] + \beta\,|\uparrow,\uparrow\rangle\,.$$

This operation is efficiently realized by the two blue sideband gates shown in Fig. 8.2(b)

$$\begin{aligned} &\hat{B}^{(j)}(\pi,\pi)\hat{B}^{(i)}(\theta,0)\,[\alpha\,|\downarrow,\uparrow\rangle + \beta\,|\uparrow,\uparrow\rangle] \otimes |n=0\rangle = \\ &= \hat{B}^{(j)}(\pi,\pi)\,[\alpha\cos(\theta)\,|\downarrow,\uparrow\rangle + \beta\,|\uparrow,\uparrow\rangle] \otimes |n=0\rangle + \alpha\sin(\theta)\hat{B}^{(j)}(\pi,\pi)\,|\uparrow,\uparrow\rangle\,|n=1\rangle \\ &= \alpha\,[\cos(\theta)\,|\downarrow,\uparrow\rangle + \sin(\theta)\,|\uparrow,\downarrow\rangle] \otimes |n=0\rangle + \beta\,|\uparrow,\uparrow\rangle \otimes |n=0\rangle\,. \end{aligned}$$

Note that the optional local gate in Eq. [8.4] applied in the case of j being initially in the state $|\downarrow\rangle$ must be inverted by the gate $\hat{R}^{(j)}(\pi,\pi)$ to obtain the correct final state.

This strategy is applied to realize the partial swap gates associated with the angles θ_1, θ_2 and θ_7 in the circuit illustrated in Fig. 8.2(a), where the input state of at least one of the

participating qubits is precisely known[1]. The implementation of the blue sideband gates is thoroughly discussed in Sec. 4.3. Since we work in the qubit regime, it is sufficient to employ the far off-resonant beam technique introduced in Sec. 4.3.1 to compensate for AC Stark shifts. For blue sideband gates implementing constant rotations with angle $\theta = \pi$ we aim for Rabi frequencies of $\Omega_\pi = 2\pi \cdot 10$ kHz, while gates with arbitrary angles are significantly slower with $\Omega \approx 2\pi \cdot 2.5$ kHz to faithfully resolve small θ. We follow the same strategy on the qudit to realize the controlled rotation gates.

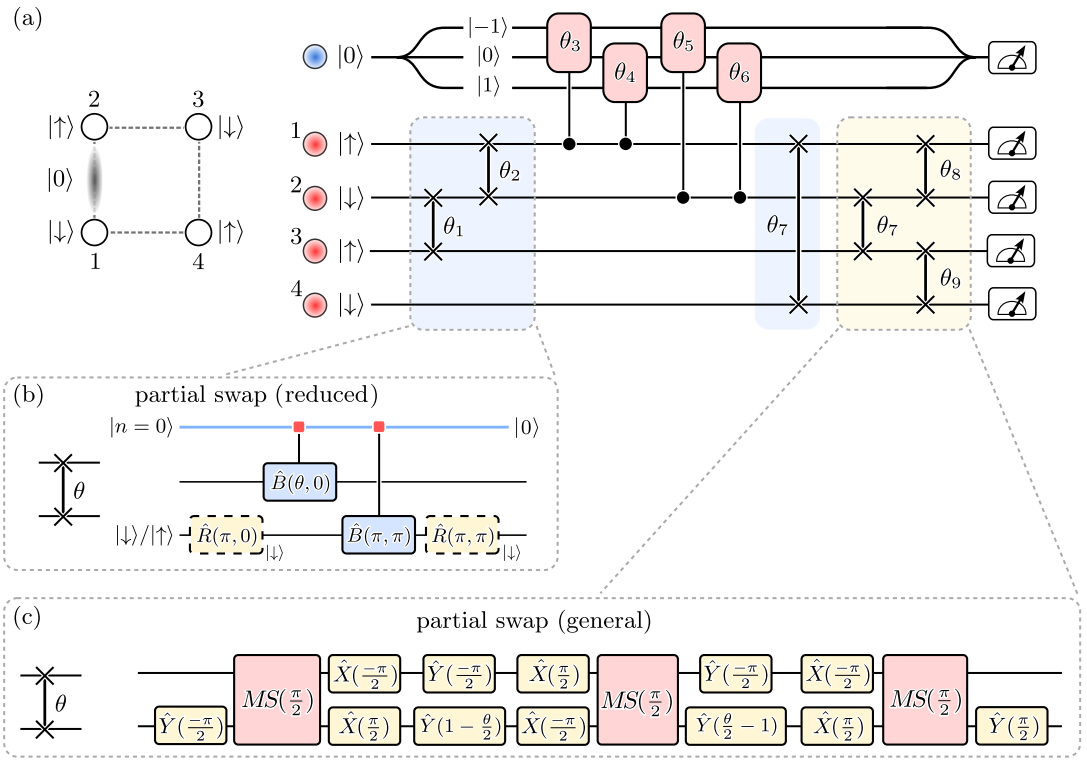


Figure 8.2: Variational quantum circuit preparing the ground state of a gauge field with four matter sites: (a) the field is described by a qudit with $d = 3$ (blue circle) with states $|-1\rangle$, $|0\rangle$ and $|+1\rangle$ representing the configuration of the electric field. The field is defined on a link between two matter sites, which are populated by particles and antiparticles encoded in the states $|\uparrow\rangle$ and $|\downarrow\rangle$ of qubits (red circles). The circuit is parameterized by a set of nine angles labeled $\theta_{i=1\ldots9}$, each corresponding to controlled rotations (red boxes) on the qudit and partial swaps acting on the qubits, respectively. Partial swap gates are realized using two different strategies: (b) if the state of one of the qubits is known, the swap operation can be implemented using two blue sideband gates $\hat{B}$ and local operations $\hat{R}$ to create the desired input state. In the general case, where the state of both qubits is arbitrary, we employ the more complex sequence in (c), which requires three maximally entangling MS gates and local operations.

For an input state $|\downarrow,\uparrow\rangle$ the operation $\hat{A}^{(i,j)}_{red.}(\pi/2)$ realizes the maximally entangled state $(|\downarrow,\uparrow\rangle + |\uparrow,\downarrow\rangle)/\sqrt{2}$, which we use as an estimate of the gate fidelity $\mathcal{F}$. By averaging the outcomes from parity oscillation and state population measurements we compute a fidelity of $\mathcal{F} = 98.7(4)\%$. This result is consistent with our estimate given in Sec. 6.2.2, where we claim $\mathcal{F} = 99.23\%$ for a single blue sideband pulse.

1 For example, consider the fourth qubit initialized in the state $|\downarrow\rangle$ and follow the circuit in Fig. 8.2(a). Since this qubit does not participate in the circuit until the partial swap gate with angle θ_7 is applied, its state up until this point is deterministic.

The implementation of a *general partial swap gate* is notably more complex, requiring local operations and three maximally entangling MS gates with characteristic duration $\tau = 200\ \mu$s as illustrated in Fig. 8.2(c). This sequence is applied for the gates corresponding to the angles θ_7, θ_8 and θ_9 highlighted by the yellow box in Fig. 8.2(a), where the input state of both participating qubits is unknown. Assuming a fidelity of $\mathcal{F} = 99.0\%$ for the MS gates, we estimate the fidelity of the general $\hat{A}^{(i,j)}(\theta)$ to $\mathcal{F} \approx 97\%$.

We approximate the ground state of the Hamiltonian in Eq. [7.113] using a Bayesian optimization protocol [184, 279], which proposes sets of parameters $\boldsymbol{\theta} = \{\theta_i\}_{i=1..9}$ as inputs to our quantum circuit. Each set corresponds to a trial state $|\psi(\boldsymbol{\theta})\rangle$ with energy

$$\langle \hat{H}(\boldsymbol{\theta}) \rangle = \frac{1}{g^{-2}} \langle \hat{H}_E(\boldsymbol{\theta}) \rangle + g^{-2} \langle \hat{H}_B(\boldsymbol{\theta}) \rangle + m \langle \hat{H}_m(\boldsymbol{\theta}) \rangle + \Omega \langle \hat{H}_K(\boldsymbol{\theta}) \rangle \qquad [8.5]$$

that the optimizer seeks to minimize. We use the strategy described in Sec. 4.1.3 to decompose the Hamiltonian and construct a measurement protocol consisting of 18 different basis measurements [139]. After all bases have been measured, the energy is computed and registered by the optimizer, which uses the result as a quantifier to gauge its progress after each iteration.

Since the measurement outcomes themselves do not explicitly depend on the coupling strength g^{-2} we can compute the energy for any value of g^{-2}. Therefore, our algorithm can be coupled to a database holding all previous outcomes. The algorithm initializes this database by taking 130 randomly distributed measurements, before sampling the energy landscape at a specific $g_i^{-2} \in [10^{-2}, 10^2]$ to further improve its best guess. Convergence is achieved if five consecutive iterations labeled by $k \in \mathbb{N}$ do not exceed the threshold

$$|\boldsymbol{\theta}_{k-1} - \boldsymbol{\theta}_k| = \sqrt{\sum_i (\theta_{k-1,i} - \theta_{k,i})^2} < 0.01,$$

which has been chosen after numerical simulations including realistic noise have shown to reliably approximate the ground state over multiple runs. For each g_i^{-2} the algorithm takes up to 300 samples or until it converges, before proceeding with g_{i+1}^{-2}. With the assumption, that the optimal solutions change smoothly for small variations in the coupling strength, the already found minimum for g_i^{-2} is a good candidate for an initial guess for g_{i+1}^{-2}. Taking all previous outcomes held by the database into account, this strategy promises faster convergence.

We prepare the vacuum state $|0, \uparrow\downarrow\uparrow\downarrow\rangle$ using the encoding in Tab. 8.1 and run the variational optimizer for $m = 0.1$ and $\Omega = 5$. Fig. 8.3 shows the first 500 iterations of the algorithm, where each data point corresponds to an evaluation of the quantum circuit for a trial parameter set $\boldsymbol{\theta}_i$. After an initial exploration phase covering the aforementioned 130 data point, the algorithm has acquired sufficient knowledge to perform the first proper optimization in the weak coupling regime $g^{-2} = 10^2$, where the magnetic field term dominates. Here, the absolute value of the energy associated with the ground state is large compared to the noise introduced by imperfections in the experiment, making the approximation of the true ground state more resilient. At $g^{-2} = 10^2$ the optimizer then refines its current "best guess" until it has found an optimum at $\langle H \rangle_{opt.} = -73(6)$, which is close to the true ground state energy of $\langle H \rangle_{exact} = -83.9$. The algorithm then continues until it has probed all the coupling strengths we wish to evaluate.

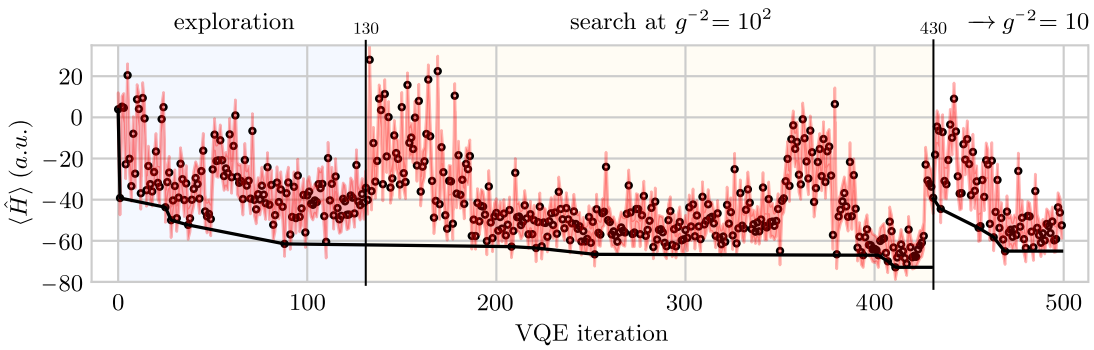


Figure 8.3: Ground state approximation using a Bayesian optimization algorithm coupled with a database: in each iteration the optimizer proposes a new set of trial parameters $\boldsymbol{\theta}$, which implement the quantum state $|\psi(\boldsymbol{\theta})\rangle$. Circles represent the energy $\langle \hat{H}(\boldsymbol{\theta}) \rangle$ in arbitrary units (a.u.) computed from the outcomes of 18 measurements of $|\psi(\boldsymbol{\theta})\rangle$, while the red area indicates one standard deviation of statistical uncertainty obtained from resampling on the raw datasets. An exploration phase of 130 data points initializes the database, before the algorithm samples up to 300 times at a specific coupling strength $g^{-2} = 10^2$; the progress is shown by the black solid line. We achieve a minimum of $\langle \hat{H}(\boldsymbol{\theta}) \rangle = -73(6)$ compared to the theoretical minimum $\langle H \rangle_{exact} = -83.9$, before proceeding with $g^{-2} = 10$.

The algorithm approximates the ground state for seven different values of the coupling strength g^{-2}; the results are presented in the upcoming sections. Since $\langle \hat{H} \rangle$ is computed from the outcomes of 18 basis measurements, one evaluation of the energy takes ≈ 1.5 minutes and consequently, an optimization run covering 300 data points is completed after ≈ 7.5 hours of continuous operation. Accounting for automatic re-calibration of the apparatus[2], which occur every 30 minutes, the optimizer has found its best guess after ≈ 8 hours. Consequently, sweeping over the seven g^{-2} requires ≈ 2.5 days of uninterrupted, mostly unsupervised operation. Note that this estimate assumes the worst case, where the algorithm must exhaust its full budget of 300 points for each g^{-2}. However, since our optimizer is coupled to a database, convergence at later stages can be achieved faster, bringing the runtime closer towards ≈ 2 days.

8.1.2 *Experimental imperfections and noise modeling*

Before we discuss our results in the next sections, we analyze experimental imperfections introduced by the apparatus and develop a noise model, allowing for a quantitative comparison of our data with numerical simulations of the quantum circuit. Intensity fluctuations of the laser exciting the $4^2S_{1/2} \leftrightarrow 3^2D_{5/2}$ quadrupole transitions results in errors $\delta\theta$ of the rotation angles $\theta \mapsto \theta + \delta\theta$ for each applied quantum gate. We model $\delta\theta$ as a Gaussian $\mathcal{N}(\mu, \sigma^2)$ centered around the mean $\mu = 0$ with variance σ^2. Since local rotations can be realized with a higher fidelity compared to the MS gates in the partial swap gates, we employ different variances in our simulations, namely $\sigma^2_{\text{int.},1}$ for single-qubit (-qudit) and $\sigma^2_{\text{int.},2}$ for entangling gates, and empirically estimate $\sigma^2_{\text{int.},2} = 10 \cdot \sigma^2_{\text{int.},1}$.

2 Calibration routines: π-time calibration of local rotations and blue sideband gates via robust phase estimation, rotation angles of the amplitude-scaled MS gates (includes π-time measurements) and AC Stark shift compensation (active / passive) for blue sideband gates.

Controlled rotation gates $C\hat{R}(\theta,\phi)$ and the reduced partial swap gates $\hat{A}_{red.}(\theta)$ are implemented as sequences of single-qudit blue sideband gates $\hat{B}(\theta,\phi)$. Since these gates are accompanied by large AC Stark shifts, we must consider imperfections in the phase by $\phi \mapsto \phi + \delta\phi$. We employ the techniques discussed in Sec. 4.3.1: on the qubits, we only use the active shift compensation scheme, while the qudit calls for both active and passive methods. Consider a qudit populating the $4^2S_{1/2}(m=-1/2)$ ground state labeled $|g\rangle$ with probability amplitude c_i and a set of (populated) spectator states $\{|j\rangle\}_j$ in the $3^2D_{5/2}$ manifold with amplitudes c_j, respectively. A noisy blue sideband operation on the transition $|g\rangle \to |i\rangle$ is well approximated by

$$\hat{B}(\pi,\phi=0)\left(c_i|g\rangle + \sum_{j\neq i} c_j|j\rangle\right)\otimes|n=0\rangle = \left(c_i e^{i\delta\phi_i}|i\rangle + \sum_{j\neq i} c_j e^{i\delta\Phi_j}|j\rangle\right)\otimes|n=1\rangle\,, \quad [8.6]$$

where $\delta\phi_i$ and $\delta\Phi_j$ are residual phase errors introduced by the active and passive compensation scheme, respectively. Following the sequence in Fig. 4.11(b), each $C\hat{R}^{(m,n)}(\theta,\phi)$ coupling two states $|i\rangle, |j\rangle$ on the target qudit n is effectively modeled by

$$c_i^{(n)}|i\rangle + c_j^{(n)}|j\rangle + \sum_{k\neq i,j} c_k^{(n)}|k\rangle \mapsto c_i'^{(n)} e^{2\delta\phi_i + i\delta\Phi_i}|i\rangle + c_j'^{(n)} e^{i\delta\phi_j + 2i\delta\Phi_j}|j\rangle + \sum_{k\neq i,j} c_k^{(n)} e^{3i\delta\Phi_k}|k\rangle\,, \quad [8.7]$$

while the control qudit m is mapped to

$$c_i^{(m)}|i\rangle \sum_{j\neq i} c_j^{(m)}|j\rangle \mapsto c_i^{(m)} e^{2i\delta\phi_i}|i\rangle + \sum_{j\neq i} c_j^{(m)} e^{2i\delta\Phi_j}|j\rangle\,. \quad [8.8]$$

Noise models for compositions and contractions of controlled rotations are constructed by counting the number of blue sideband gates, each accumulating an error according to Eq. [8.6]. From experimental data we determine that the error $\delta\phi_i$ is small compared to the $\delta\Phi_j$ on the spectator states; we thus neglect $\delta\phi_i$ and further assume that all $\delta\Phi_j$ are equal. Eq. [8.7] simplifies to

$$c_i^{(n)}|i\rangle + c_j^{(n)}|j\rangle + \sum_{k\neq i,j} c_k^{(n)}|k\rangle \mapsto c_i'^{(n)} e^{i\delta\Phi}|i\rangle + c_j'^{(n)} e^{2i\delta\Phi}|j\rangle + e^{3i\delta\Phi}\sum_{k\neq i,j} c_k^{(n)}|k\rangle\,, \quad [8.9]$$

which is the model we apply in our numerical simulations of the quantum circuit. Similar to the intensity noise, we model the $\delta\Phi$ using a Gaussian distribution $\mathcal{N}(\mu,\sigma_\Phi^2)$ with mean $\mu = 0$ and variance σ_Φ^2.

8.1.3 *Observation of the dynamics between gauge field and matter*

The optimal parameters $\boldsymbol{\theta}_{opt.}$ found by the optimization algorithm discussed in the previous section are used to prepare approximations of the ground states. Seven values of the coupling strength in the interval $g^{-2} \in [10^{-2}, 10^2]$ are chosen to resolve both the strong ($g^{-2} \ll 1$) and the weak coupling regime ($g^{-2} \gg 1$). For each data point we simulate the quantum circuit using the $\boldsymbol{\theta}_{opt.}$ and apply the noise model for the parameters $\sigma_{I,1}^2 = 4.7\cdot10^{-3}$ and $\sigma_\Phi^2 = 7.3\cdot10^{-2}$, cf. Sec. 8.1.2. Uncertainties on the experimental outcomes represent one standard deviation computed via resampling of the raw data.

We present our results for the energy $\langle\hat{H}\rangle$ in Fig. 8.4(a) and the plaquette operator $\langle\hat{\square}\rangle$ in (b), respectively. The experimental data is accompanied by the noise model, which agrees well with both our measurements and the exact solution. In the strong coupling regime

$g^{-2} \ll 1$, the electric field term in Eq. [7.113] dominates and the system remains in the (initial) vacuum state $|0, \downarrow\uparrow\downarrow\uparrow\rangle$. As g^{-2} increases, the coupling becomes weaker, allowing for the creation of particle pairs in the states illustrated in Fig. 8.2(b). The kinetic energy $\langle \hat{H} \rangle_K$ of the particles induces a magnetic field, which in turn leads to increasing values in the plaquette operator. This effect is clearly observed in the interval $g^{-2} \in [0.1, 1]$, where the slope of $\langle \hat{\square} \rangle$ deviates significantly from the case of the pure gauge theory, where the matter is absent.

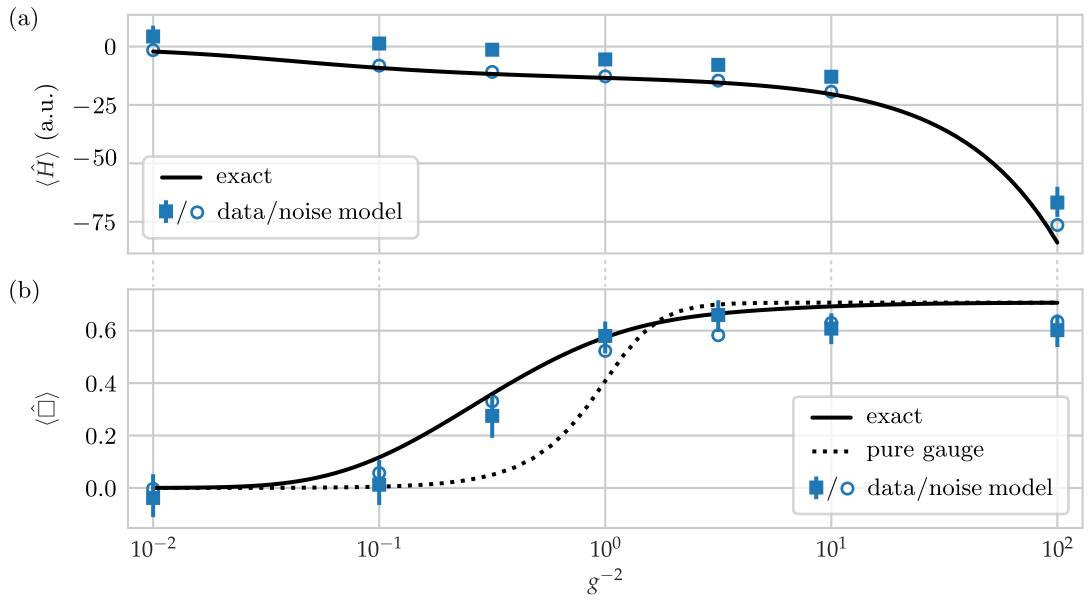


Figure 8.4: Quantum simulation of QED in two spatial dimensions including a gauge field and dynamical matter: (a) the energy $\langle \hat{H} \rangle$ in arbitrary units (a.u.) is computed from the quantum state prepared by the circuit in Fig. 8.2(a) using the optimal parameters obtained by variational optimization. The experimental data (squares) is accompanied by the energy of the exact ground state (black) predicted by the theory. Numerical simulations (circles) incorporate the noise model described in Sec. 8.1.2. Error bars indicate one standard deviation of statistical uncertainty; at intermediate coupling strengths the error bares are hidden by the data markers. The positive offset in the data is explained by the population of unphysical states, see the discussion in the main text. (b) Expectation value of the operator $\langle \hat{\square} \rangle$, reflecting the magnetic field enclosed by the plaquette. Particle pair creation is indicated by the change in the slope, which is significantly steeper in the absence of matter (pure gauge, dashed).

Our results for the plaquette operator are in good agreement with the theoretical values. Since $\langle \hat{\square} \rangle = -\langle H \rangle_B$, we conclude that the quantum state of the qudit adequately reflects the predicted state of the gauge field. However, the measured energies $\langle \hat{H} \rangle$ are shifted by a positive offset that can be explained by the population of states corresponding to unphysical configurations of the matter sites. For example, the state $|\downarrow\uparrow\downarrow\downarrow\rangle$ on the qubits would encode two electrons and one positron, which clearly violates charge conservation. In our experimental data, unphysical matter states make up as much as 20% of the measurement outcomes, which cause a positive shift in $\langle \hat{H} \rangle$.

Since the contributions of the kinetic energy $\Omega \langle \hat{H}_K \rangle$ and the rest mass $m \langle \hat{H}_M \rangle$ to $\langle \hat{H} \rangle$ in Eq. [8.5] are independent of the coupling strength g^{-2}, this shift is observed for all outcomes regardless of g^{-2}. Especially in the regime of intermediate coupling strengths, where electric and magnetic fields compete, the energy of the gauge field is negligible

and thus the shift appears more pronounced. In future experiments we may employ post-selection to enhance the quality of our data, which may also assist the VQE to converge within fewer iterations. Here we deliberately decided to present the data "as is", further highlighting the capabilities of variational quantum algorithms and robust measurement protocols in noisy environments.

8.1.4 *Real-time evolution*

We simulate the evolution of the initial state $|0,\downarrow\uparrow\downarrow\uparrow\rangle$ under the Hamiltonian in Eq. [7.113] using a Trotter-Suzuki protocol [4, 280]. The quantum state $|\Psi(t)\rangle$ of the system at a time t can be approximated by

$$|\Psi(t)\rangle = \exp\left(-\frac{i}{\hbar}\hat{H}t\right)|0,\downarrow\uparrow\downarrow\uparrow\rangle \approx \prod_{n=1}^{N}\prod_{j}\exp\left(-\frac{i}{\hbar}\hat{h}_j\tau\right)|0,\downarrow\uparrow\downarrow\uparrow\rangle\,, \tag{8.10}$$

where the Hamiltonian is decomposed into a sum $\hat{H} = \sum_j \hat{h}_j$, which is applied for a duration $\tau = t/N$ and repeated for N *Trotter steps*. We introduce the electric field operator $\hat{E} = |1\rangle\langle 1| - |-1\rangle\langle -1|$ and choose the decomposition [19]

$$\begin{aligned}
\hat{h}_1 &= \Omega\left(\hat{\sigma}_+^{(1)}\hat{U}^\dagger\hat{\sigma}_-^{(2)} + \hat{\sigma}_-^{(1)}\hat{U}\hat{\sigma}_+^{(2)} - \hat{\sigma}_+^{(3)}\hat{\sigma}_-^{(4)} - \hat{\sigma}_-^{(3)}\hat{\sigma}_+^{(4)}\right)\\
\hat{h}_2 &= \Omega\left(\hat{\sigma}_+^{(2)}\hat{\sigma}_-^{(3)} + \hat{\sigma}_-^{(2)}\hat{\sigma}_+^{(3)} - \hat{\sigma}_+^{(1)}\hat{\sigma}_-^{(4)} - \hat{\sigma}_-^{(1)}\hat{\sigma}_+^{(4)}\right)\\
\hat{h}_3 &= \frac{1}{4g^{-2}}\left(\hat{\sigma}_z^{(1)}\hat{\sigma}_z^{(4)} - 4\hat{E}\hat{\sigma}_z^{(1)} + 2\hat{E}\hat{\sigma}_z^{(2)} - 2\hat{E}\hat{\sigma}_z^{(4)}\right)\\
\hat{h}_4 &= \frac{m}{2}\left(\hat{\sigma}_z^{(1)} + \hat{\sigma}_z^{(3)} - \hat{\sigma}_z^{(2)} - \hat{\sigma}_z^{(4)}\right) + \frac{1}{4g^{-2}}\left(8\hat{E}^2 - 4\hat{E} + \hat{\sigma}_z^{(1)} - \hat{\sigma}_z^{(2)} + 3\cdot\mathbb{1}\right)\\
\hat{h}_5 &= -\frac{g^{-2}}{2}\left(\hat{U} + \hat{U}^\dagger\right) = g^{-2}\hat{H}_B,
\end{aligned}$$

where $\hat{\sigma}_+^{(i)} = |\uparrow\rangle\langle\downarrow|$ and $\hat{\sigma}_-^{(i)} = |\downarrow\rangle\langle\uparrow|$ create and annihilate particles at site i, respectively.

Experimentally, the terms $\exp\left(-i\hat{h}_i t/\hbar\right)$ in Eq. [8.10] are applied in ascending order to realize a single Trotter step. Couplings between matter sites are realized using local rotations and the tunable MS gates discussed in Sec. 4.2.1. Since $\hat{\sigma}_\pm^{(j)} = \hat{\sigma}_x^{(j)} \pm i\hat{\sigma}_y^{(j)}$, the odd-parity gates coupling two matter sites j and k are equivalent to

$$\hat{h}_i \propto \hat{\sigma}_+^{(j)}\hat{\sigma}_-^{(k)} + \hat{\sigma}_-^{(j)}\hat{\sigma}_+^{(k)} = 2\left(\hat{\sigma}_x^{(j)}\hat{\sigma}_x^{(k)} + \hat{\sigma}_y^{(j)}\hat{\sigma}_y^{(k)}\right) \Longrightarrow e^{-i\hat{h}_i t/\hbar} = \hat{MS}(\theta,0) + \hat{MS}(\theta,\pi/2) \tag{8.11}$$

with $\theta = \Omega t/\hbar$. A similar decomposition exists for the interactions between the gauge field and a site j of the form $\hat{h}_i \propto \hat{E}\hat{\sigma}_z^{(j)}$, which are implemented by a single $\hat{MS}(\theta,0)$ and local rotations [12, 14]. The term $\hat{\sigma}_+^{(1)}\hat{U}\hat{\sigma}_-^{(2)} + h.c.$ in $\hat{h}_1$ is significantly more complex, requiring up to 24 MS gates [19]. However, as our initial state is the vacuum state $|0,\downarrow\uparrow\downarrow\uparrow\rangle$, the implementation simplifies to four $\hat{MS}^{(i,j)}(\pi/2,0)$ gates coupling the qudit i with the matter qubits $j \in \{1,2\}$; the angle θ is realized by a local $\hat{Z}(\theta)$ on the qudit.

We measure the expectation value of the plaquette operator $\langle\hat{\square}\rangle = -\langle\hat{H}_B\rangle$ and define the particle number density [19]

$$\nu = \frac{1}{4}\langle\hat{H}_M\rangle + \frac{1}{2}, \tag{8.12}$$

which enables the observation of pair creation processes on the matter sites. Using the aforementioned decomposition we simulate the real-time evolution of the system for a single Trotter step $N = 1$ with varying step size τ. Our choice of the coupling strength $g^{-2} = 10^{-1.4} \approx 0.04$ is motivated by the dynamics in the strong field regime, where the vacuum state evolves towards the pair state $|{+1}, \uparrow\downarrow\downarrow\uparrow\rangle$ illustrated in Fig. 8.1(b), allowing the observation of particle creation and annihilation processes.

Fig. 8.5(a) shows the experimental data for $\langle\hat{\square}\rangle$ as a function of the interaction time $\theta \propto t$, accompanied by numerical simulations for $N = 1$ and $N = 10$) and the exact solution. The evolution of ν is presented in Fig. 8.5(b), describing the creation of a electron-positron pair at $\theta = \pi/4$ and its subsequent annihilation as $\theta \to \pi/2$.

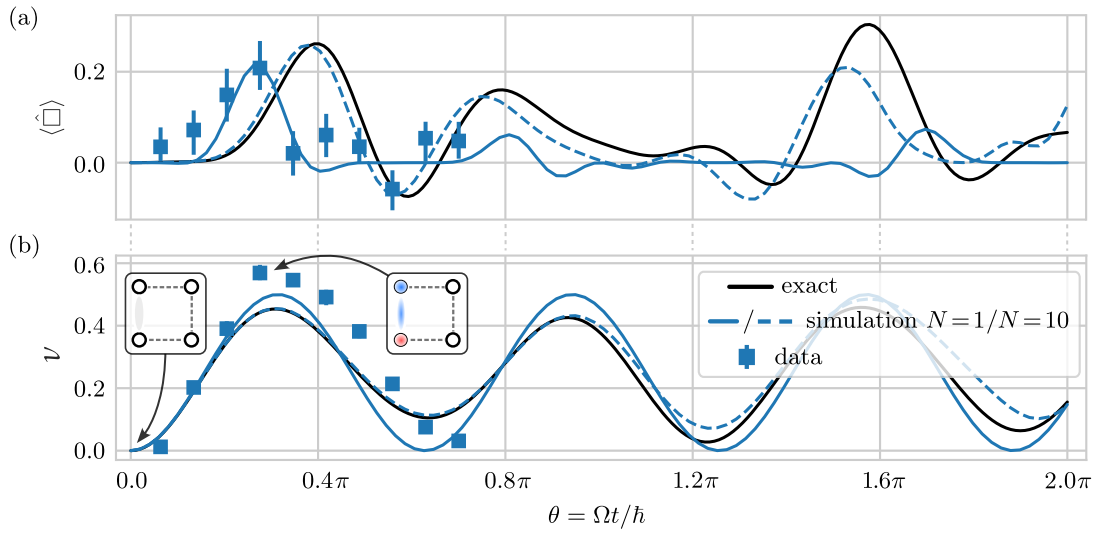


Figure 8.5: Real-time evolution of the system under the Kogut-Susskind Hamiltonian for a single Trotter step. We show the evolution of the plaquette operator $\langle\hat{\square}\rangle$ in Eq. [8.2] in (a) and the particle number density ν in (b). The solid black line corresponds to the exact evolution, while the blue lines are numerical simulations of $N = 1$ and $N = 10$ Trotter steps. The system evolves from the initial vacuum state $|0, \downarrow\uparrow\downarrow\uparrow\rangle$ towards $|{+1}, \uparrow\downarrow\downarrow\uparrow\rangle$ at $\theta = \pi/4$. An electron-positron pair is created populating the sites $(1, 2)$, which is reflected by the particle number density $\nu = 0.57(2)$ and the electric field in the state $|{+1}\rangle$ pointing along the link $1 \leftrightarrow 2$. The magnetic field causes an increase in $\langle\hat{\square}\rangle = 0.21(6)$ right before the pair is created. As we approach $\theta \approx \pi/2$, the particles are annihilated and the magnetic field dampens, before reviving at a later time $\theta \approx 3\pi/2$ in the exact result.

8.1.5 *Alternative lattice model*

We investigate a second lattice model, which has been extensively studied in the context of condensed matter physics [17, 281, 282], with applications in the description of high-temperature superconductors [283, 284]. It is characterized by an opposite phase in the kinetic term of the Hamiltonian Eq. [7.113], which leads to a different behavior in the continuum limit. This phase change is reflected in the experiment by placing the gauge field on a different link as shown in Fig. 8.6(a), see Fig. 8.1 for comparison. After applying

the Jordan Wigner transformation and eliminating the redundant gauge fields we obtain for the kinetic term [17]

$$\hat{H}_K = \sigma_+^{(1)}\sigma_-^{(2)} + \sigma_+^{(2)}\hat{U}^\dagger\sigma_-^{(3)} + \sigma_+^{(4)}\sigma_-^{(3)} - \sigma_+^{(1)}\sigma_-^{(4)} + h.c.,$$

while the other terms are identical to Eq. [7.113]. Its implementation requires a minor modification of the quantum circuit presented in Fig. 8.2(a). Since the coupling of the matter sites with the gauge field is controlled by the presence (absence) of a particle (antiparticle) on each end of the link, we must implement the controlled-rotation gates acting on the qudit with respect to the second and third qubit as illustrated in Fig. 8.6(b).

Moreover, we exchange the order of the partial-swap operations corresponding to the angles θ_1 and θ_2. Note that our set of resource operations and the overall depth of the circuit remains unchanged.

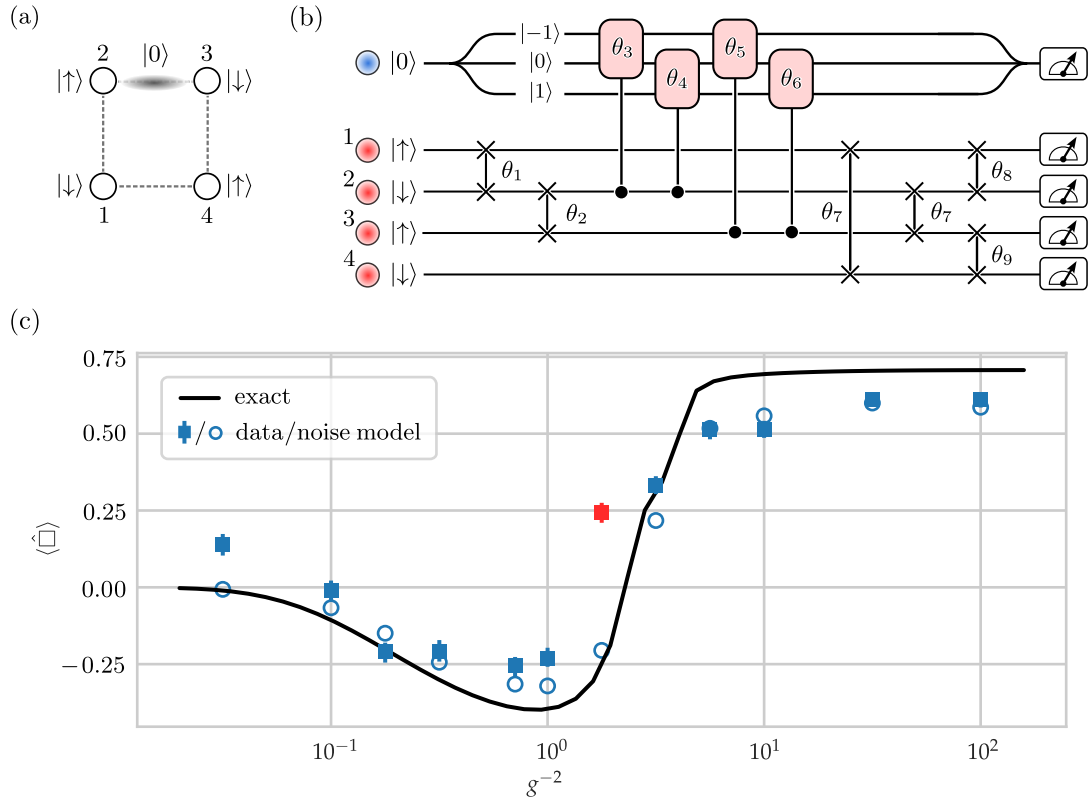


Figure 8.6: Quantum simulation of an alternative lattice model: (a) the gauge field is moved to the link $2 \leftrightarrow 3$, inducing a phase in the kinetic term of the Hamiltonian. (b) minor modifications of the original circuit must be implemented, notably the coupling to those qubits encoding the particles neighboring the gauge field. (c) expectation value $\langle\hat{\square}\rangle$ of the plaquette operator: while the alternative model exhibits the same dynamics in both the strong and weak coupling limits, the kinetic term induces a flux opposite to the magnetic field, leading to negative values of $\langle\hat{\square}\rangle$. This effect is captured by our experimental data (squares). The origin of the outlier at $g^{-2} = 10^{1/4}$ is discussed in the main text. Error bars are computed by resampling of the data and indicate one standard deviation of statistical uncertainty. Our data is in good agreement with numerical simulations (circles) employing the noise model introduced in Sec. 8.1.2; the solid line represents the exact solution.

We follow the strategy presented in Sec. 8.1.1 and employ same the variational optimizer to approximate the ground states of the model with parameters $\Omega = 5$ in $\hat{H}_K$ and $m = 0.1$ in $\hat{H}_M$, respectively. Utilizing the database coupled to the optimization algorithm, the interval $g^{-2} \in \left[10^{-3/2}, 10^2\right]$ is scanned three times before the final result is accepted after the last run.

We first describe the behavior of the model in the respective regimes using the theoretical predictions shown in Fig. 8.6(c) before discussing our experimental data. The alternative model reproduces the behavior of the original model in the strong (weak) coupling limit, where the electric (magnetic) field is most pronounced. However, in the intermediate regime the kinetic term $\hat{H}_K$ – now having the opposite phase – competes with the terms $\hat{H}_E$ and $\hat{H}_B$. While $\hat{H}_K$ amplifies the magnetic field in the previous model, here the pair creation process induces an opposing magnetic flux through the plaquette, thereby lowering the expectation value to a theoretical minimum of $\langle \hat{\square} \rangle \approx -0.398$.

Our data is in good agreement with the theoretical predictions. We employ the same noise model introduced in Sec. 8.1.2, which manages to capture our experimental results. The outlier highlighted in Fig. 8.6(c) can be explained upon closer inspection of the database. At $g^{-2} = 10^{1/4}$ the algorithm has accepted its initial best guess previously obtained at $g^{-2} = 10^{1/2}$ as a potential candidate solution, since no further improvement has been made after the measurement budget had been exhausted. It would thus be more appropriate to accept only those solutions, which have been obtained after the optimization at each g^{-2} and use the database only to prime the optimizer when initializing the search. However, our strategy captures the behavior of the model introduced by the opposite phase in $\hat{H}_K$ in the regime $g^{-2} \approx 10^0$, where we obtain a minimum $\langle \hat{\square} \rangle = -0.255(3)$.

8.2 INTERACTIONS BETWEEN PURE GAUGE FIELDS ON A SQUARE LATTICE

We now investigate the effects of the gauge field discretization by simulating 2D-QED as a pure gauge theory without dynamical matter, encoding the gauge fields in *qutrits* and *ququints* with dimensions $d = 3$ and $d = 5$, respectively. In the absence of particles, the configuration of a single plaquette is defined with respect to the surrounding lattice. Therefore, we employ *periodic boundary conditions* (PBCs) and realize the geometry shown in Fig. 8.7(a): the vertices $i = 1, \ldots, 4$ are connected by four links $(i \leftrightarrow i \pm 1)$, with eight more links $(i \leftrightarrow j)$ coupling to the sites j on the neighboring (eight) plaquettes [18]. Under PBCs the lattice deforms into a torus and using Gauss' law $\sum_i \vec{E}_i = 0$ on each vertex we reduce the description to five links harboring independent gauge fields illustrated in Fig. 8.7(b). The effective Hamiltonian in Eq. [7.113] simplifies to

$$\hat{H} = \frac{1}{g^2} \hat{H}_E + g^{-2} \hat{H}_B, \qquad [8.13]$$

which is expressed in terms of the five independent gauge fields. In this description, the implementation on the quantum hardware requires many three-body interactions, which are notoriously difficult to engineer[3] [18, 19]. However, the model can be simplified significantly if the fields are described by the set of four *rotators* $\mathcal{R}_i$ [18], which are defined on different plaquettes $i = 1, \ldots, 4$ as shown in Fig. 8.7(b). Moreover, we define *strings* $\mathcal{S}_{x,y}$ connecting the origins of plaquettes obtained by translation of the entire lattice by two

3 Recall the term $\hat{\sigma}_+^{(1)} \hat{U} \hat{\sigma}_-^{(2)} + h.c.$ in Sec. 8.1.4, which requires 24 two-body interactions (MS gates).

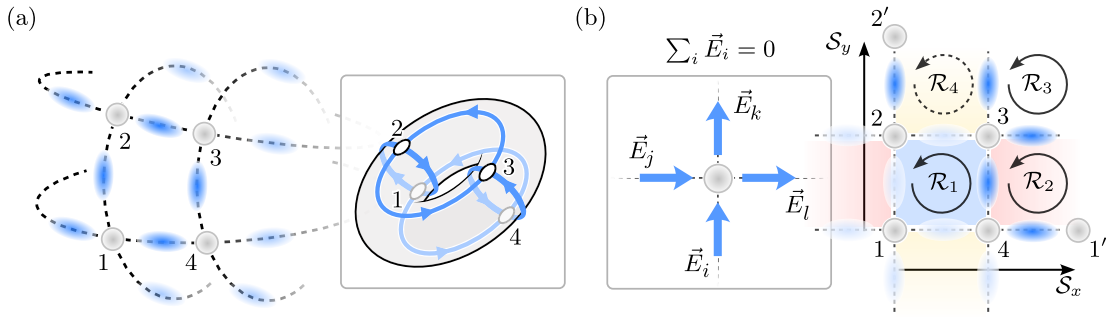


Figure 8.7: Quantum simulation of pure gauge theory: (a) we consider a lattice of four sites with 12 gauge fields (ovals) on the links. Employing periodic boundary conditions, the system can be imagined as a torus, which is described by eight gauge fields (arrows) $\vec{E}$. (b) Using Gauss' law $\sum_i \vec{E}_i = 0$, the configuration is completely determined by five independent gauge fields, which can be further reduced to the *rotators* $\mathcal{R}_i$ looping around different plaquettes (colored). The *strings* $\mathcal{S}_{x,y}$ are defined along the x and y axis with respect to translation of the lattice by two sites.

sites along the x or y axis, e.g. $1 \to 1'$ for $\mathcal{S}_x$. Since we employ PBCs, the lattice is invariant under such transformations and we can identify the electric fields by sums of $\mathcal{S}_{x,y}$ and $\mathcal{R}_i$ satisfying Gauss' law [17, 18].

The state of any given rotator $\mathcal{R}_i$ with $i \in \{1, \ldots, 4\}$ can always be defined by the set $\{\mathcal{R}_j\}_{j \neq i}$. We therefore eliminate $\mathcal{R}_4$ and describe $\hat{H}$ in Eq. [8.13] with respect to $\mathcal{R}_{i=1,2,3}$ and $\mathcal{S}_{x,y}$. The observables value $\langle \hat{H} \rangle$ and $\langle \hat{\square} \rangle$ defined in Eq. [8.2] are reconstructed from the three loops on the torus' surface illustrated in Fig. 8.8 [18]. Each loop represents one of the d-dimensional rotators $\mathcal{R}_i$, which are encoded in the quantum states of trapped ion qudits [19].

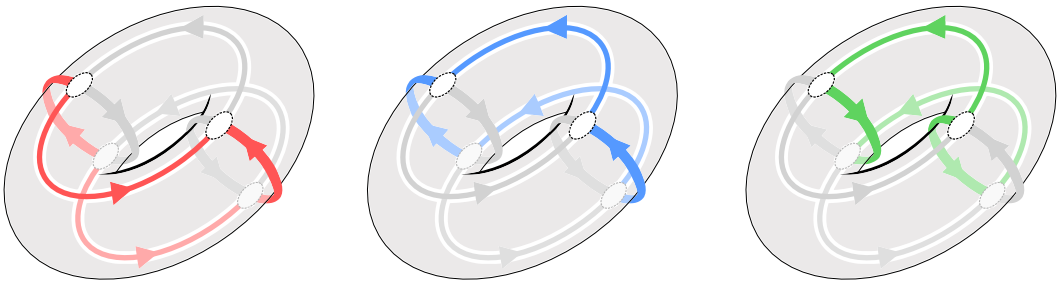


Figure 8.8: Loops on the torus: although the system is represented by four vertices, the torus resembles multiple plaquettes bordering on each link between a pair of vertices. The observables $\langle \hat{H} \rangle$ and $\langle \hat{\square} \rangle = -\langle \hat{H}_B \rangle$ are computed from the three loops (colored) on the surface of the torus, which represent the d-dimensional rotators $\mathcal{R}_i$ [18].

8.2.1 *Variational circuits in two representations*

Lattice gauge theories are usually formulated in the eigenbasis of the gauge field, in which the operator $\hat{H}_E$ in Eq. [8.13] is diagonal. This *electric representation* of the Hamiltonian is convenient in the strong coupling regime $g^{-2} \ll 1$, where contributions of the magnetic field are negligible. In the limit of weak coupling strengths $\hat{H}_B$ dominates, which leads to errors arising from the truncation of the gauge fields and consequently of the $\mathcal{R}_i$ to a finite

number of states [18]. These errors warrant the introduction of a *magnetic representation*, which diagonalizes $\hat{H}_B$ in the regime $g^{-2} \gg 1$.

In the electric basis (el.), the Hamiltonian is given by [18]

$$\begin{aligned}\hat{H}^{(el.)} &= \frac{1}{g^{-2}}\hat{H}_E^{(el.)} + g^{-2}\hat{H}_B^{(el.)} \\ &= \frac{2}{g^{-2}}\left(\mathcal{R}_1^2 + \mathcal{R}_2^2 + \mathcal{R}_3^2 - \mathcal{R}_2(\mathcal{R}_1 + \mathcal{R}_3)\right) \\ &\qquad - \frac{g^{-2}}{2}\left(\hat{P}_1 + \hat{P}_2 + \hat{P}_3 + \hat{P}_1\hat{P}_2\hat{P}_3 + h.c.\right)\end{aligned} \tag{8.14}$$

where the operators $\hat{P}_i$ are products of link operators $\hat{U}_{\alpha,\beta}$ analogous to Eq. [8.1] acting on the respective plaquette $i = 1, 2, 3$. Using the discrete Fourier transformation of the rotators

$$\mathcal{R}_i \mapsto \sum_{j=1}^{d+1} f_j^s \sin\left(\frac{2\pi j}{d+2}\mathcal{R}_i\right) \qquad \mathcal{R}_i^2 \mapsto \sum_{j=1}^{d+1} f_j^c \cos\left(\frac{2\pi j}{d+2}\mathcal{R}_i\right) + \frac{(d+1)(d+3)}{12}\cdot\mathbb{1}$$

with coefficients f_j^s and f_j^c defined in Ref. [18], we change the basis and obtain the Hamiltonian in the magnetic representation (mag.)

$$\begin{aligned}\hat{H}^{(mag.)} &= \frac{1}{g^{-2}}\hat{H}_E^{(mag.)} + g^{-2}\hat{H}_B^{(mag.)} \\ &= \frac{1}{g^{-2}}\left\{\sum_j^{d+1}\left[f_j^c\sum_{i=1}^{3}\hat{P}_i^i + \frac{f_j^s}{2}\left(\hat{P}_2^j - (\hat{P}_2^\dagger)^j\right)\cdot\sum_{j=1}^{d+1} f_j^s\left(\hat{P}_1^j + \hat{P}_3^j\right)\right] + h.c.\right\} \\ &\qquad - g^{-2}\left[\sum_{i=1}^{3}\cos\left(\frac{2\pi}{d+2}\mathcal{R}_i\right) + \cos\left(\frac{2\pi}{d+2}\sum_{i=1}^{3}\mathcal{R}_i\right)\right].\end{aligned} \tag{8.15}$$

We implement the variational circuits illustrated in Fig. 8.9 to approximate the ground state of the pure-gauge Hamiltonian in the electric and magnetic basis $\hat{H}^{(el.)}$ and $\hat{H}^{(mag.)}$, respectively. Each circuit captures the properties in the respective limits: (a) prepares states in the limit $g^{-2} \ll 1$, while (b) is applied in the weak coupling regime $g^{-2} \gg 1$. The rotators $\mathcal{R}_{i=1,2,3}$ are encoded in the quantum states of trapped-ion qudits with local dimension $d = 3$ and $d = 5$, which are manipulated using the single-qudit operations $\hat{R}(\theta, \phi)$ and controlled-rotation gates $C\hat{R}(\theta, \phi)$ introduced in Sec. 4.1.1 and Sec. 4.3.2.

8.2.2 *Encoding rotators in trapped-ion qudits*

The capabilities of our trapped-ion qudit hardware enables the observation of truncation effects by increasing the local dimension of the qudits from $d = 3$ to $d = 5$. Each of the circuits shown in Fig. 8.9 requires only minor modifications: the gates highlighted in blue are applied for $d = 5$, while those in red represent the case $d = 3$. Both circuits are inspired by the Hamiltonians in their respective bases [17], see App. A.2 for a more detailed discussion . We employ the encoding of the states $\{|\pm 2\rangle, |\pm 1\rangle, |0\rangle\}$ in the $3^2D_{5/2}$ manifold according to Tab. 8.2 and use $|g\rangle$ in the $4^2S_{1/2}$ ground state to realize the $C\hat{R}(\theta, \phi)$.

Furthermore, we apply the *qudit-enhanced encoding* scheme presented in Sec. 6.2.1 to mitigate errors introduced by optical cross-talk between neighboring ions. However, this strategy is only applicable for dimension $d = 3$, where the Zeeman states factorize into

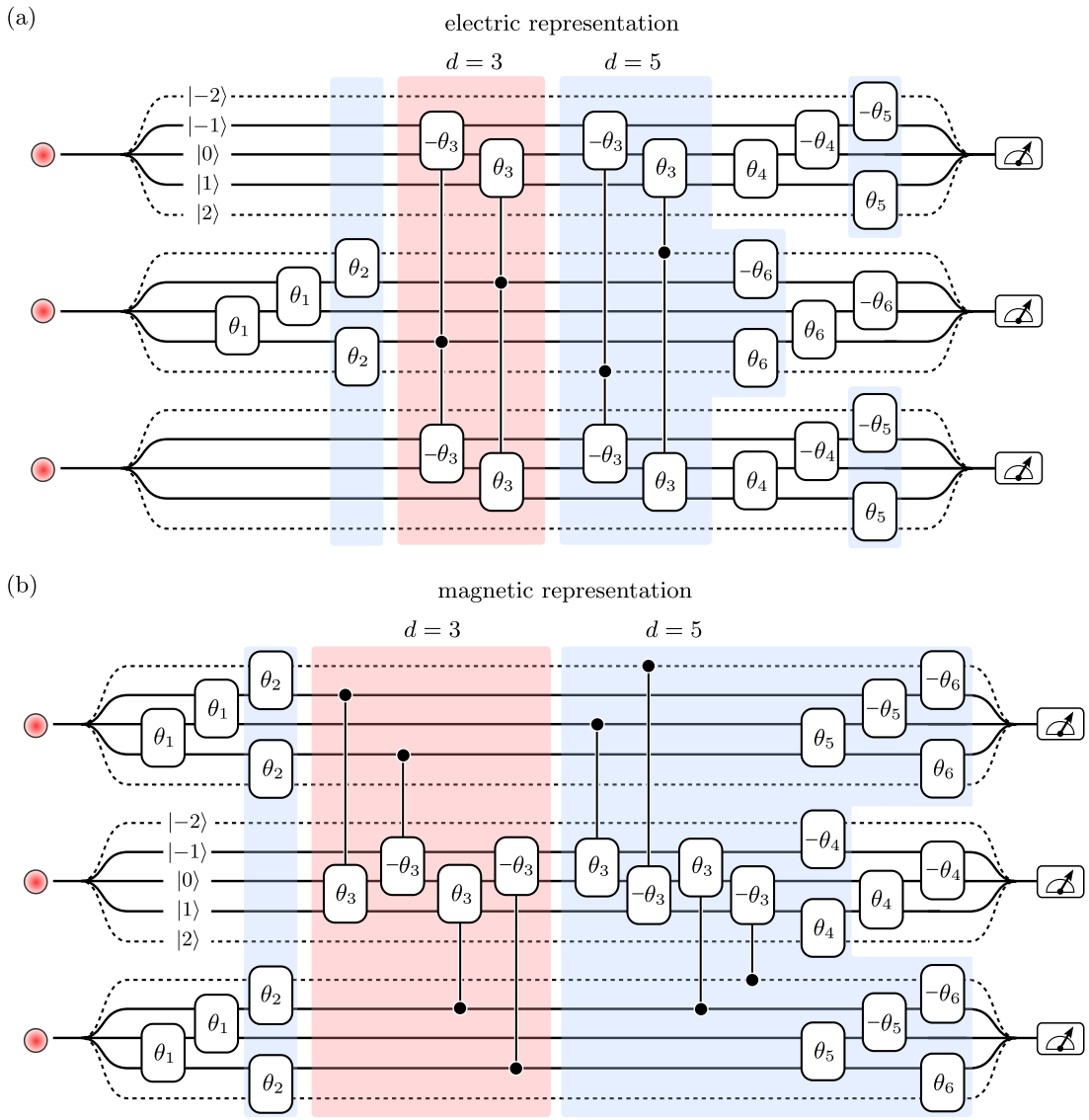


Figure 8.9: Quantum circuits employed in variational optimization to approximate the ground state of the pure-gauge theory in 2D. Each circuit is constructed to capture the properties of the Hamiltonian in different coupling regimes, see App. A.2 for details. The electric representation (a) yields good results in the strong coupling regime $g^{-2} \ll 1$, however, for $g^{-2} > 1$ errors introduced by the finite dimension d of the rotors increase. Vice versa, the magnetic representation (b) is suitable in the limit of weak couplings $g^{-2} \gg 1$ with errors at larger coupling strengths. We realize both circuits for the rotors encoded in the states of qudits with local dimensions $d = 3$ and $d = 5$. The circuits require only minor modifications highlighted by the shaded regions (red / blue) without increasing the number of entangling operations, which are realized by controlled rotation gates.

two disjoint subsets with positive and negative magnetic quantum number m, respectively. For $d = 5$ we place two additional ions between each qudit, thereby artificially increasing the separation between the qudits encoding the rotators without sacrificing axial confinement. The additional ions do not participate in the computation, but are excited to the $3^2D_{5/2}(m = +5/2)$ state prior to every computation to suppress parasitic coupling to the motional states introduced by the blue-sideband interactions.

electric representation

	$4^2\mathbf{S}_{1/2}(\mathbf{m}=...)$		$3^2\mathbf{D}_{5/2}(\mathbf{m}=...)$					
$\mathbf{d=3}$	$...-1/2$	$...+1/2$	$...-5/2$	$...-3/2$	$...-1/2$	$...+1/2$	$...+3/2$	$...+5/2$
$\mathcal{R}_1$, $\mathcal{R}_3$	-	$\|g\rangle$	-	-	-	$\|-1\rangle$	$\|0\rangle$	$\|1\rangle$
$\mathcal{R}_2$	$\|g\rangle$	-	$\|0\rangle$	$\|-1\rangle$	$\|1\rangle$	-	-	-
$\mathbf{d=5}$	$...-1/2$	$...+1/2$	$...-5/2$	$...-3/2$	$...-1/2$	$...+1/2$	$...+3/2$	$...+5/2$
$\mathcal{R}_1$, $\mathcal{R}_3$	$\|g\rangle$	-	$\|-2\rangle$	$\|-1\rangle$	$\|0\rangle$	$\|+1\rangle$	$\|+2\rangle$	-
$\mathcal{R}_2$	$\|g\rangle$	-	$\|-1\rangle$	$\|-2\rangle$	$\|0\rangle$	$\|+2\rangle$	$\|+1\rangle$	-

magnetic representation

	$4^2\mathbf{S}_{1/2}(\mathbf{m}=...)$		$3^2\mathbf{D}_{5/2}(\mathbf{m}=...)$					
$\mathbf{d=3}$	$...-1/2$	$...+1/2$	$...-5/2$	$...-3/2$	$...-1/2$	$...+1/2$	$...+3/2$	$...+5/2$
$\mathcal{R}_1$, $\mathcal{R}_3$	$\|g\rangle$	-	$\|-1\rangle$	$\|0\rangle$	$\|1\rangle$	-	-	-
$\mathcal{R}_2$	-	$\|g\rangle$	-	-	-	$\|-1\rangle$	$\|0\rangle$	$\|1\rangle$
$\mathbf{d=5}$	$...-1/2$	$...+1/2$	$...-5/2$	$...-3/2$	$...-1/2$	$...+1/2$	$...+3/2$	$...+5/2$
$\mathcal{R}_1$, $\mathcal{R}_3$	$\|g\rangle$	-	$\|-1\rangle$	$\|-2\rangle$	$\|0\rangle$	$\|+1\rangle$	$\|+2\rangle$	-
$\mathcal{R}_2$	$\|g\rangle$	-	$\|-2\rangle$	$\|-1\rangle$	$\|0\rangle$	$\|+1\rangle$	$\|+2\rangle$	-

Table 8.2: Mapping of the rotators $\mathcal{R}_i$ onto the electronic states of trapped-ion qudits: the states $|\pm2\rangle$, $|\pm1\rangle$ and $|0\rangle$ are encoded in the $3^2D_{5/2}$ manifold of $^{40}Ca^+$ ions; an auxiliary ground state $|g\rangle$ is used to realize the controlled rotation gates. The encoding varies between the rotators $\mathcal{R}_i$, the respective representation and the local dimension d of the qudits. The states are then assigned to optimize the performance of the blue sideband gates by selecting the transitions with favorable couplings to $|g\rangle$ while simultaneously reducing the AC Stark shifts on the spectator states.

Moreover, our encoding schemes are tailored to the quantum circuits for each representation by careful choice of the transitions $|g\rangle \leftrightarrow |i\rangle_{i=\pm2,\pm1,0}$ involved in the implementation of the blue sideband operations. Those transitions which change the magnetic quantum number m by at most $\Delta m = \pm1$ couple well with the respective ground state $|g\rangle$. Consequently, the intensity of the laser required to realize a quantum gate can be reduced while still achieving Rabi frequencies of $\Omega \approx 2\pi \cdot 10$ kHz (constant angle π) and $\Omega \approx 2\pi \cdot 2.5$ kHz (variational parameters θ_i), respectively.

8.2.3 *Approximating the ground state of the pure-gauge Hamiltonian*

The ground states of the Hamiltonians $\hat{H}^{(el-)}$ and $\mathcal{H}^{(mag.)}$ defined in Eq. [8.14] and Eq. [8.15] are approximated using a VQE analogous to the algorithm discussed in Sec. 8.1.1 [184, 279]. We prepare the state $|000\rangle$ and implement the quantum circuits in both representations for coupling strengths in the interval $g^{-2} \in [10^{-2}, 10^2]$. Although the validity of each representation is restricted to its respective regime, we implement both quantum circuits illustrated

in Fig. 8.9 across the full range of g^{-2}. At each iteration of the algorithm we calculate the energy $\langle \hat{H}^{(el.)/(mag.)} \rangle$ from the outcomes of consecutive measurements in a set of bases computed following the protocol outlined in Sec. 4.1.2 [139]. Both Hamiltonians $\hat{H}^{(el.)}$ and $\hat{H}^{(mag.)}$ are divided into sets of Pauli strings, which are then converted into sequences of the local spin operators $\hat{S}_\alpha^{(i)}$ defined in Eq. [4.8]. These are then further decomposed into a set of native quantum gates by QR decomposition, cf. Sec. 4.1.3.

We first discuss the results shown in Fig. 8.10(a) for rotators with local dimension $d = 3$. In the electric representation, the total energy is obtained from five measurement outcomes, while we require eight measurements to compute $\langle \hat{H} \rangle$ in the magnetic representation. Our data shows the final result after the optimizer has either exhausted its sampling budget or has converged to a solution. We reduce the maximum number of samples to 130, since the space of variational parameters $\boldsymbol{\theta} = \{\theta_1, \theta_3, \theta_4, \theta_6\}$ is significantly smaller compared to the circuit in Fig. 8.2(a) involving dynamical matter. Typically, the algorithm converges in the range of 70 to 90 iterations. The best guess $\boldsymbol{\theta}_{opt.}$ for each g^{-2} is used in numerical simulations of the respective circuit, including experimental noise according to the model introduced in Sec. 8.1.2. Uncertainties are computed by resampling of the raw measurement data and indicate one standard deviation from the mean.

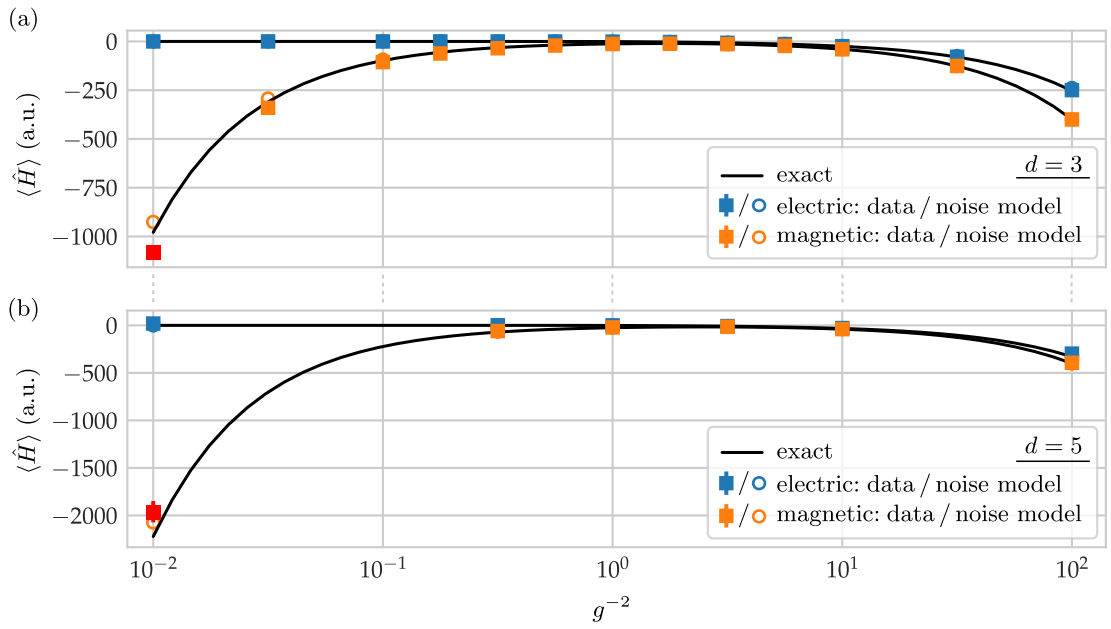


Figure 8.10: Energy $\langle \hat{H} \rangle$ in arbitrary units (a.u.) for the quantum states approximating the true ground state of the Hamiltonian in both the electric (blue) and the magnetic basis (orange) for $d = 3$ in (a) and $d = 5$ in (b), respectively. The error bars are computed by resampling of the measurement data and represent one standard deviation of statistical uncertainty. Since the uncertainties are small compared to the measured outcomes the bars cannot be resolved on this scale. The outliers in the magnetic representation are discussed in App. A.3. Numerical simulations (circles) of the quantum circuits employing the noise model introduced in Sec. 8.1.2 and theoretical predictions (black) are shown for direct comparison.

Our results corresponding to the electric representation are in agreement with the theoretical predictions in the strong coupling limit $g^{-2} \ll 1$; the magnetic representation performs complementarily for $g^{-2} \gg 1$. At intermediate coupling strengths $g^{-2} \approx 1$ both representations perform equally well, while deviations are observed as we move towards the opposite

regime, where the respective representation proves to be a less effective description of the quantum state. These deviations appear more prominent in the expectation values of the plaquette operator, which is discussed later in Sec. 8.2.4 [19]. The experimentally measured energies are below the energy of the first excited state of the theory in a noisy environment, which confirms that the optimization algorithm generates good approximations of the true ground state, see Ref. [18] and App. A.3. A discussion of the outlier in the magnetic representation highlighted in Fig. 8.10(a) is included in the appendix.

We repeat the variational optimization for $d = 5$ and obtain the data presented in Fig. 8.10(b). As the number of variational parameters has increased from four to six, we allow the algorithm to acquire up to 200 samples at each g^{-2}; convergence is achieved on average after 160 iterations. The measurement budget increases significantly to 25 basis evaluations in each representation. Consequently, the runtime of the total experiment is comparable to the estimate given in Sec. 8.1.3 with two days of continuous operation of the apparatus. Our results agree well with the theoretical predictions, however we obtain an outlier in the magnetic representation at $g^{-2} = 10^{-2}$, which is close to the energy of the first excited state. Here, the energy is dominated by the electric field term $\hat{H}_E$, which is not well captured in the magnetic representation. This further highlights the benefits of our strategy to employ two representation, each being tailored its respective regime.

8.2.4 *Refining the gauge field discretization*

We reconstruct the expectation value of the plaquette operator $\langle \hat{\square} \rangle = -\langle \hat{H}_B \rangle$ from the measurement outcomes corresponding to the optimal solutions obtained by the variational algorithm. For each representation the gauge field is truncated to $d = 3$, respectively $d = 5$ discrete states, see Fig. 8.11. The local dimensions of the qudits encoding the rotators – and thereby the gauge fields – is increased from $d = 3$ in (a) to $d = 5$ in (b). For each outcome of the experiment the corresponding quantum circuit is simulated numerically, employing the aforementioned noise model, see Sec. 8.1.2.

A fundamental consequence of the gauge field truncation is the finite gap separating the curves in the intermediate coupling regime $g^{-2} \approx 10^0$, where both representations perform equally. This gap vanishes in the continuum $d \to \infty$, which is already well approximated for $d = 21$ as shown in Fig. 8.11. Notably, we already see a significant improvement as we increase the qudit dimension in the experiment from $d = 3$ to $d = 5$.

The strategy of using two representations allows us to obtain good results over all coupling regimes. Since the number of gauge field states we can encode in a $^{40}Ca^+$ is limited to $d = 7$ we can always obtain a continuous curve by choosing the appropriate basis as we enter the intermediate coupling regime. The gap is minimal for $g^{-2} \approx 10^{1/4}$, which indicates the point where we must switch to the complementary representation. If we continue to work in the less efficient basis, the number of states describing the gauge fields must increase substantially to adequately capture the physics. Since the qudit dimension is kept constant, the plaquette operator plateaus at a value that is characteristic for the chosen truncation.

This so-called *"freezing"* is best observed in the strong coupling regime $g^{-2} > 1$ in the electric representation: as we increase the qudit dimension from $d = 3$ in Fig. 8.11(a) to $d = 5$ in Fig. 8.11(b), the expectation value of the plaquette operator also increases substantially from $\langle \hat{\square} \rangle \approx 0.62(1)$ to $\langle \hat{\square} \rangle \approx 0.74(4)$ at $g^{-2} = 10^2$. Consequently, the plateau

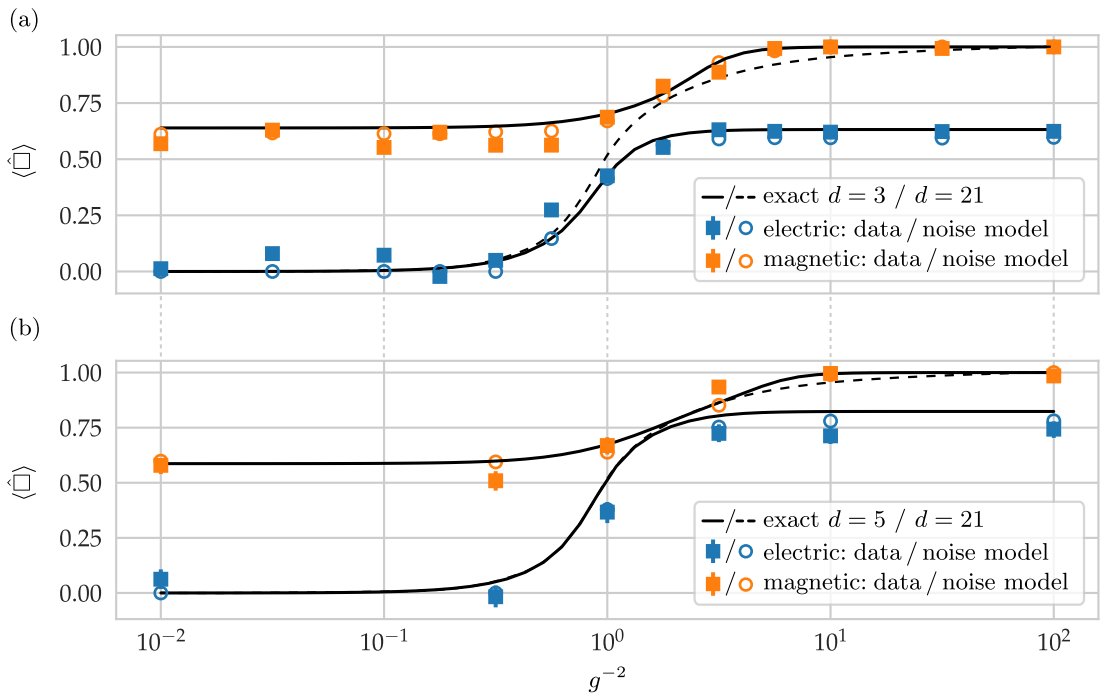


Figure 8.11: Plaquette operator of the pure gauge theory for two gauge field truncations. We compute the expectation value $\langle \hat{\square} \rangle$ from the results obtained by variational optimization. The curves corresponding to the data in the electric (blue) and magnetic (orange) representation are separated by a finite gap in the intermediate coupling regime $g^{-2} \approx 10^0$. This gap is a consequence of the truncation of the gauge fields to $d = 3$ states in (a) and $d = 5$ states in (b), respectively. Our data is in good agreement with the numerical simulations of the noisy circuits (circles) and follows the theoretical predictions (black, solid) for each d. As we increase the local dimension, the gap between the curves becomes smaller, until both representations ultimately agree in the continuum; simulations show a good approximation for $d = 21$ (dashed).

is an indicator for how well our model approximates the theory in the continuum limit. Since freezing is an effect associated with the truncation of the gauge fields, we investigate how the qudit states are populated in different coupling regimes. The validity of each representation is restricted to the regime where the number of basis states needed to describe the (approximated) ground state is smaller than the chosen truncation. Consequently, a narrow distribution of the populations indicates an appropriate representation.

As shown in Fig. 8.12(a), the electric representation is valid in the strong coupling regime, where the distribution is narrow and centered around $|0\rangle$. Moreover, it continues to be appropriate up to $g^{-2} = 1$, where the distribution in the magnetic representation in Fig. 8.12(b) is broadened. This broadening causes the plateau in the plaquette operator, as the number of states needed to fully capture the spread of the wave function exceeds the dimension of the qudit. Therefore one must switch to the complementary representation, which is supposed to adequately describe the theory in the opposite regime.

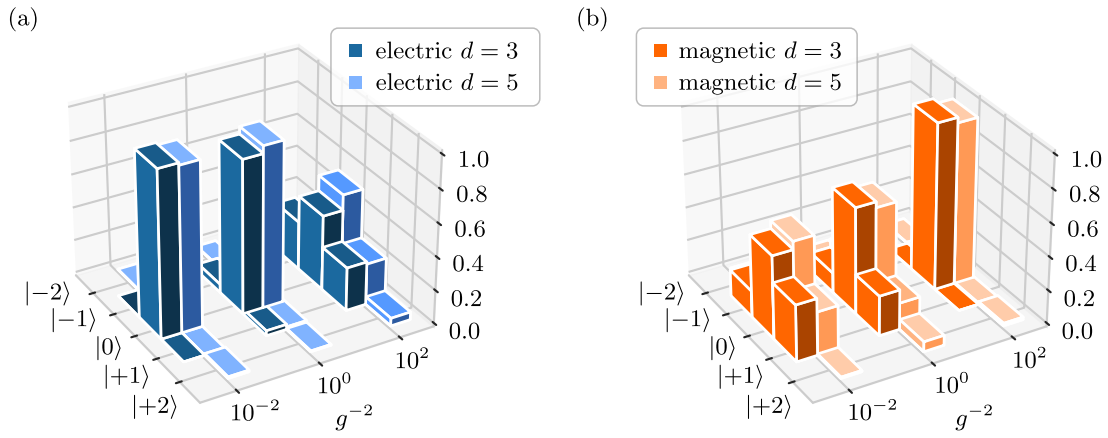


Figure 8.12: Population of the qudit states in the pure gauge theory. A narrow distribution indicates that the chosen representation provides a good approximation of the theory in the respective regime. In the electric representation (a), the distribution broadens as we approach the weak coupling limit $g^{-2} \gg 1$. The number of states is insufficient to capture the spread of the wave function. However, the magnetic representation (b) is well suited to describe the weak coupling regime as indicated by the narrow distribution. Note that both representations are complementary and we can always choose an appropriate representation to probe the respective regimes.

We emphasize that our experiment is a crucial step towards the simulation of the running coupling described in Sec. 7.4.5 [285]. Since the expectation value of the plaquette operator is associated with the renormalized coupling strength by

$$g_R^{-2} = g^{-2} \cdot \langle \hat{\square} \rangle^{1/4},$$

our strategy has the potential to enable the systematic study of phenomena in high energy physics [17, 274]. With the ability to control the gauge field truncation and lattice geometry, future qudit-based quantum processors could be used to compute mass spectra and bound states in *quantum chromodynamics* (QCD) [286].

9

SUMMARY AND OUTLOOK

This thesis introduced the concept of qudits, their implementation on a trapped-ion quantum processor, and presented two applications in the context of quantum simulation.

In Chapter 1, we discussed methods of expressing numbers in different positional numeral systems. Modern computer architectures operate almost exclusively in the binary numeral system, where information is represented by sequences of bits. By comparing binary with other numeral systems, we argued that a ternary system may, in some applications, be better suited for encoding and manipulating data. Nevertheless, the binary system has prevailed, primarily due to its technical simplicity. With the advent of quantum computing, this binary paradigm was naturally carried over to the quantum domain, where information is typically represented by qubits, i.e. two-level quantum systems. However, since many physical quantum systems are inherently high-dimensional, we motivated the use of qudits – d-dimensional quantum systems – as a more natural and efficient representation for certain target problems.

Chapter 2 addressed the physical principles underlying the realization of a trapped-ion based quantum processor. We introduced the linear Paul trap, the heart of the system confining a chain of ions in space, and discussed the interaction between laser light and matter, which is the fundamental mechanism enabling laser cooling, qudit encoding and manipulation, and readout via electron shelving. In Chapter 3, we looked at our experimental apparatus in more detail. We began with the simplified level structure of $^{40}Ca^{+}$, the ion species used in our system, and continued with a brief description of the vacuum chamber, the ion trap, the relevant parameters and resulting geometries. We then introduced the optical setup, placing greater emphasis on the interplay between *acousto-optic modulators* (AOMs) and real-time capable electronic hardware, which together enable precise control over the light focused onto the ions. We then introduced the native set of quantum gates and their implementation at the hardware level in Chapter 4. Our focus was put on two-qudit interactions, which mediate entanglement by coupling the electronic states of individual ions with the *center-of-mass* (COM) motion of the ion chain. Notably, we developed a scheme to realize a controlled-rotation gate – a natural extension of the original controlled-NOT scheme proposed by Cirac and Zoller, which is native to qudit platforms. The versatility of this gate was demonstrated by implementing the quantum Toffoli gate – an interaction notoriously difficult to realize in purely qubit-based platforms.

In Chapter 5, we introduced the concept of *matrix product state* (MPS) a formalism enabling an efficient description of quantum states of many-body systems. The systematic study of such systems is fundamental in physics, chemistry and material science. Of particular interest are exotic states of quantum matter, which do not have a classical counterpart

e.g. in ordinary solid state systems. A prime example are topological quantum states, where long-range correlations emerge, rendering the otherwise fragile quantum state more resilient to noise. We illustrated the concept of topological order first hand using the *extended Su-Schrieffer-Heeger* (ESSH) model – a one-dimensional spin chain with tunable nearest-neighbor interactions – and experimentally studied its properties in Chapter 6. Employing a *variational quantum eigensolver* (VQE), a hybrid optimization protocol which couples our quantum processor with a classical co-processor, we approximated the ground states of the ESSH model in different coupling regimes. For a short chain of eight ions we measured *many-body topological invariants* (MBTIs) in the bulk, i.e. the four ions in the center of the register. Via these MBTIs we were able to observe a quantum phase transition from a *trivial* towards a symmetry-protected topological state and vice versa. Although this experiment was carried out on qubits, we implicitly used qudits employing spectroscopic decoupling to improve the quality of our results by efficiently suppressing optical cross-talk between neighboring ions. The capability to encode qudits greatly enhanced the performance of our apparatus.

In Chapter 7, we gave an overview of quantum field theories, outlining their fundamental concepts and methods. Starting with the quantization of the classical Klein-Gordon field, we then proceeded to the Dirac field, which governs the dynamics of fermions. Based on symmetry arguments, we motivated the inclusion of a gauge field, which ensures local gauge invariance of Dirac's theory. Notably, it is the gauge field which mediates the interaction between fields and gives rise to physical particles. By combining the Dirac field with the electromagnetic field, we arrived at the description of *quantum electrodynamics* (QED) – the quantum theory of electromagnetism. We introduced the concept of propagators and Feynman diagrams, illustrated their application and encountered the problem of infinities: as our description became more precise from a physical point of view, the mathematical framework led to non-physical outcomes. This dilemma was resolved by renormalization and regularization, which naturally led us to *lattice gauge theories* (LGTs). We introduced the concept of Wilson lines and studied the fermion doubling problem, ultimately arriving at a lattice formulation of QED. Having established the theoretical foundations, we turned to the realization of lattice QED on our trapped-ion quantum processor in Chapter 8. We simulated a single plaquette – the fundamental building block of a 2D lattice – and studied the interplay of gauge fields and fermionic matter. Due to the high dimensional nature of the gauge fields, we discretized and truncated them down to a small set of states, which we then encoded in trapped-ion qudits. A VQE was employed to prepare approximate ground states of the theory over a continuous range of interaction strengths, thereby enabling the exploration of both the weak and strong coupling regime. We investigated pair creation processes: excitations of the gauge fields manifest in physical particles populating the lattice. Notably, we observed a dynamic magnetic flux permeating the plaquette – a genuine 2D phenomenon that cannot manifest in 1D lattice geometries. Using a Trotter-Suzuki protocol we simulated the time evolution of the system in a proof of concept experiment as a step towards the systematic study of LGTs beyond the equilibrium. Moreover, we investigated the impact of truncation effects on the quality of the simulation: truncating the field to a small number of states does not faithfully capture the physics in the continuum limit. With the ability to encode qudits up to dimension $d = 7$, our quantum processor enabled us to seamlessly increase the local dimension from $d = 3$ to $d = 5$. Here we could already see a clear improvement in the quality of our simulation as our data converges closer to the true outcome predicted by the theory.

Our work addressed key challenges in many-body, condensed matter, and high-energy physics, highlighting the versatility of our trapped-ion qudit quantum processor. With recent progress in qudit-based algorithms and a renewed interest in digital quantum simulations, we expect that our apparatus – despite some of its core components now having surpassed the ripe age of 20 years – will continue to make valuable contributions to cutting-edge research in quantum physics.

Tremendous progress over the recent years in the field of quantum computing has led to the commercialization of the first hardware platforms. Since these systems mostly follow the binary paradigm of computing, significant efforts have been made to increase the number of qubits. Neutral atom processors and superconducting devices have surpassed the hallmark of 1000 qubits [58, 287], a number that is only expected to grow in the near future. In contrast, the register sizes in trapped-ion quantum processors cannot compete with these impressive numbers, rarely exceeding a few 100 qubits [288, 289]. Trapped-ion platforms excel in other areas, offering exceptionally long coherence times, high-fidelity quantum gate operations and efficient readout schemes – challenges which are notoriously difficult to address in superconducting platforms. Notably, the capability of selectively addressing small subsets of ions enables the efficient implementation of algorithms, resulting in significantly shallower quantum circuits.

The rich level structure of ions naturally allows for the encoding and manipulation of qubits with already well established methods [14]. Although the number of states in $^{40}Ca^{+}$ is limited, using isotopes with non-zero nuclear spin I will significantly increase the local dimension. For example, $^{43}Ca^{+}$ with $I = 7/2$ offers $(2S+1)(2I+1) = 48$ states in the metastable $3^2D_{5/2}$ level [290]; including the ground states, which are indistinguishable upon readout, it may be fundamentally possible to encode and control a 49-dimensional hyperfine qudit. Despite being low in abundance [291], our platform is already capable of trapping $^{43}Ca^{+}$ without any changes to the existing experimental setup as demonstrated by Lancaster and colleagues [292–294], and high-fidelity quantum gates have already been implemented by Ballance et al. as early as 2016 [295]. In a recent publication, Low et al. used $^{137}Ba^{+}$ to control 13 out of the 25 hyperfine states [63], thereby having realized a 13-dimensional qudit.

Qudits may also be exploited to realize efficient *quantum error correction* (QEC) schemes [296]. Although stabilizer codes have been extensively studied qubit-based platforms [297–299] and can, in principle, be extended to qudits [300–302], another class of codes may be better suited to implement fault-tolerant qudits. Gottesman, Kitaev and Preskill proposed to encode a robust qubit in a harmonic oscillator [9], i.e. a qudit. These GKP codes are naturally tailored to qudits and have already been implemented in trapped-ion systems [303, 304] and superconducting cavities [305], with further ideas applicable to ultracold atomic mixtures [306, 307]. In a recent publication, Brock et al. [308] reported the encoding of logical qutrits and ququarts using the GKP scheme and demonstrated – for the first time – beyond break-even error correction in logical qudits.

More fundamental are strategies to enhance the performance of already existing qubit-based algorithms with the aid of qudits. Stricker et al. demonstrated the reconstruction of qubit quantum states from a single measurement [309], which significantly outperforms conventional state tomography protocols in terms of computation time. Other proposals are concerned with the verification of quantum states, which can be efficiently imple-

mented using interactions natively available on our trapped-ion qudit platform [310–313]. Moreover, many physical phenomena intrinsically require larger local Hilbert spaces, such as symmetry-protected topological order in integer-spin systems. Recently, Edmunds et al. studied the Haldane phase – a phenomenon absent in spin-$1/2$ systems – using a linear chain of qutrits encoding spin-1 particles [314]. With the ability to induce Rabi oscillations between two robust edge states, their work offers a pathway towards the realization of robust topological qubits [315].

Since digital quantum simulators have proven to be successful in addressing problems in high-energy and condensed matter physics, a plethora of ideas and concrete proposals have been put forward, waiting to be experimentally realized. From the experimental realizations of lattice QED in $(1+1)D$ [273, 316], the field has now evolved towards $(2+1)D$ [19, 317]. Proposals include the study of electrons in $\mathbb{Z}_2$ gauge theories [318–320] and the $\mathbb{Z}_3$ symmetry group relevant in QCD [321]. Ultimately, we seek to study LGT in 3D: while moving from 1D to 2D lattices required significant efforts, the protocols – such as the one presented in this thesis – can be readily extended to 3D [322, 323]. With the ability to investigate non-abelian gauge groups we may simulate Yang-Mills theories [324, 325], enabling the systematic study of the interactions that govern our universe.

The relatively young field of qudits holds great potential for applications ranging from the enhancement of existing algorithms to robust computing, error correction, and the quantum simulation of nature. Given the growing number of proposals, we suspect that quantum computation with qudits will gain in popularity, with the possibility to outperform qubit-based platforms in problems where high-dimensional systems offer a more natural description.

A

APPENDIX

A.1 FORCED SYMMETRY BREAKING IN THE SSH MODEL BY INTRODUCTION OF A MAGNETIC BIAS FIELD

The symmetry-broken phase in the ESSH model for $\delta = 4$ is significantly more pronounced than what we would expect from exact numerical simulations for finite systems of identical size. Our results indicate that the VQE cannot adequately resolve the non-degenerate ground states in the presence of experimental imperfections and noise, see Fig. 6.6. The algorithm converges to solutions corresponding to less entangled states with smaller finite-size effects, which yield values for the MBTIs Z_R and Z_T that are closer to the thermodynamic limit.

Since the MBTIs are computed from density matrices reconstructed from quantum state tomography on the bulk spins, we can directly compare the bulk state with numerical simulations. We can force the symmetry to be broken by introducing a magnetic bias term with strength B to the Hamiltonian, which acts on the two spins on either edge of the spin chain, see Eq. [6.5].

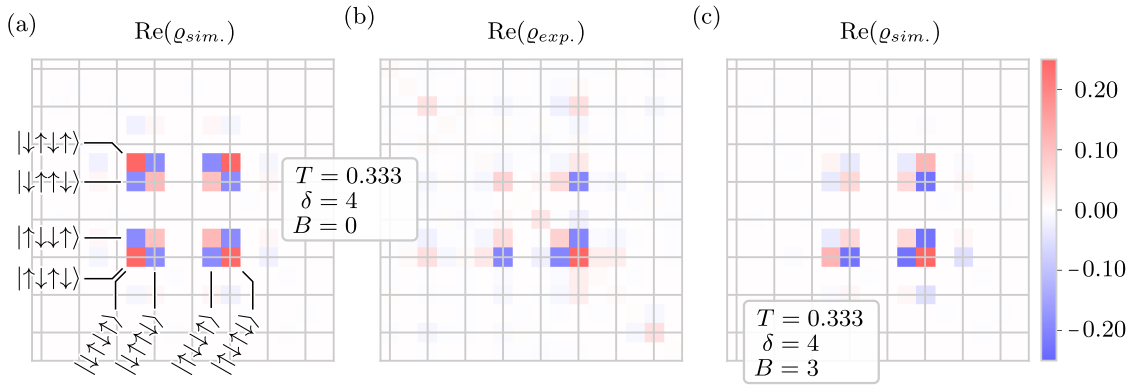


Figure A.1: Forced symmetry breaking by magnetic bias fields: we numerically compute the exact ground state of the ESSH model with an additional magnetic bias field acting on the edge qubits. (a) shows the density matrix of the bulk spins for the exact ground state in the absence of a bias field $B = 0$ for $T = 0.333$ and $\delta = 4$; the experimental data for the same parameters is shown in (b). Simulations including a bias field with strength $B = 3$ yield the density matrix in (c), which is in good agreement with our measurements.

Using this model we investigate the state at $T = 0.333$ in the regime $\delta = 4$. For $B = 0$ numerical simulations yield the density matrix $\varrho_{sim.}$ in Fig. A.1(a) with our experimental outcome $\varrho_{exp.}$ shown in Fig. A.1(b); we compute a state fidelity of $\mathcal{F}(\varrho_{exp.}, \varrho_{sim.}) = 73.7\%$.

In contrast, for $B = 3$ we obtain $\varrho_{sim.}$ in Fig. A.1(c), which is in good agreement with the experimental data with a fidelity $\mathcal{F}(\varrho_{exp.}, \varrho_{sim.}) = 89.3\%$.

Heating of the COM motion and dephasing of the motional states negatively impact the gate operations entangling the electronic state of the ion with the QDB. It is expected that the fidelities of the gates deteriorate as the circuit is executed. Since the spin on the right edge of the chain participates only at the very end of the circuit, see Fig. 6.1, these accumulated errors might manifest as polarization effects akin to a magnetic field acting on the edge spins.

A.2 DESIGN OF THE VARIATIONAL CIRCUITS IN THE PURE-GAUGE CASE

Both circuits illustrated in Fig. 8.9 are designed by inspection of the Hamiltonians given in Eq. 8.14 and Eq. 8.15, respectively. Ref. [17] provides a formulation for qubits employing the *one-hot encoding* described in Sec. 1.3.2, which substantially simplifies when using qudits. The qubit Hamiltonian for $d = 3$ in the electric basis is given by [17]

$$\hat{H}_E^{(el.)} = -\frac{1}{2g^{-2}}\left[\hat{\sigma}_4^z(\hat{\sigma}_5^z+1)(\hat{\sigma}_1^z+\hat{\sigma}_7^z+\hat{\sigma}_7^z\hat{\sigma}_8^z)\right] - \frac{1}{2g^{-2}}\hat{\sigma}_2^z\left[\hat{\sigma}_1^z\hat{\sigma}_4^z(\hat{\sigma}_5^z+1) - 2\hat{\sigma}_5^z + 2\hat{\sigma}_8^z + 6\right]$$

$$\begin{aligned}\hat{H}_B^{(el.)} = &-\frac{g^{-2}}{2}\left(\hat{\sigma}_1^-\hat{\sigma}_2^+ + \hat{\sigma}_2^-\hat{\sigma}_3^+ + \hat{\sigma}_4^-\hat{\sigma}_5^+ + \hat{\sigma}_5^-\hat{\sigma}_6^+ + \hat{\sigma}_7^-\hat{\sigma}_8^+ + \hat{\sigma}_8^-\hat{\sigma}_9^+\right)\\ &-\frac{g^{-2}}{2}\left(\hat{\sigma}_1^-\hat{\sigma}_2^+ + \hat{\sigma}_2^-\hat{\sigma}_3^+\right)\left(\hat{\sigma}_4^-\hat{\sigma}_5^+ + \hat{\sigma}_5^-\hat{\sigma}_6^+\right)\left(\hat{\sigma}_7^-\hat{\sigma}_8^+ + \hat{\sigma}_8^-\hat{\sigma}_9^+\right)\end{aligned} \qquad [A.1]$$

where $\sigma_i^{\pm}$ are the raising and lowering operators acting on the basis states of the i-th qubit and σ_i^- is the Pauli-z matrix. The three qubits labeled 1, 2 and 3 correspond to the rotator $\mathcal{R}_1$ in Eq. [8.14] and encoding the states of the first gauge field; $\mathcal{R}_2$ and $\mathcal{R}_3$ are encoded in the qubits $(4,5,6)$ and $(7,8,9)$, respectively, see Fig. 6 in Ref. [17].

We then translate Eq. [A.1] into the qudit framework and note that the products $\hat{\sigma}_i^-\hat{\sigma}_j^+$ in the first term of $\hat{H}_B^{(el.)}$ become local operations acting on the subspace (i,j) of the respective qudit. Let $|-1\rangle$, $|0\rangle$ and $|+1\rangle$ label the basis states of each qudit; the magnetic term then simplifies to

$$\begin{aligned}\hat{H}_B^{(el.)} = &\underbrace{-\frac{g^{-2}}{2}\left(\hat{\sigma}^x_{1,(-1,0)} + \hat{\sigma}^x_{1,(0,+1)} + \hat{\sigma}^x_{2,(-1,0)} + \hat{\sigma}^x_{2,(0,+1)} + \hat{\sigma}^x_{3,(-1,0)} + \hat{\sigma}^x_{3,(-1,0)}\right)}_{\hat{H}_{loc.}}\\ &\underbrace{-\frac{g^{-2}}{2}\left(\hat{\sigma}^x_{1,(-1,0)} + \hat{\sigma}^x_{1,(0,+1)}\right)\left(\hat{\sigma}^x_{2,(-1,0)} + \hat{\sigma}^x_{2,(0,+1)}\right)\left(\hat{\sigma}^x_{3,(-1,0)} + \hat{\sigma}^x_{3,(0,+1)}\right)}_{\hat{H}_{int.}}\end{aligned} \qquad [A.2]$$

and we call $\hat{H}_{loc.}$ the local term and $\hat{H}_{int.}$ the interaction term of the Hamiltonian.

Now we seek to construct a quantum circuit that approximates the ground state labeled $|\Psi_0\rangle$ of the $\hat{H}^{(el.)}$ by adjusting a set of variational parameters, see Ref. [184] and Sec. 5.2.2 for a brief introduction on VQEs. Consider a state $|\Phi\rangle$ that has a finite overlap with $|\Psi_0\rangle$, i.e. it satisfies

$$\langle\Phi|\Psi_0\rangle \neq 0. \tag{A.3}$$

We then employ a strategy called *Imaginary Time Evolution* (ITE) [326, 327], which we briefly discuss in this paragraph; for a more thorough introduction the reader is referred to Ref. [327]. The time evolution of a system in the state $|\Phi\rangle$ under a target Hamiltonian $\hat{H}$ is given by

$$|\Phi(t)\rangle = \frac{e^{-it\hat{H}/\hbar}|\Phi\rangle}{\sqrt{\langle\Phi|e^{-2it\hat{H}/\hbar}|\Phi\rangle}}$$

and by trivially substituting $it = \beta$ one introduces the *imaginary time* β [327]. In this formulation we obtain

$$|\Phi(\beta)\rangle = \frac{e^{-\beta\hat{H}/\hbar}|\Phi\rangle}{\sqrt{\langle\Phi|e^{-2\beta\hat{H}/\hbar}|\Phi\rangle}}, \tag{A.4}$$

which in the limit $\beta \to \infty$ approximates the ground state

$$\lim_{\beta\to\infty} |\Phi(\beta)\rangle \approx |\Psi_0\rangle$$

if $|\Phi\rangle$ satisfies the condition in Eq. [A.3] [327]. A naive analogy is the lemma discussed in Sec. 5.1.6: since Eq. [A.4] is an approximation of the ground state projector, each time it is applied to $|\Phi\rangle$ the overlap

$$\langle\Phi(\beta)|\Psi_0\rangle > \langle\Phi|\Psi_0\rangle,$$

increases, eventually approaching unity for large β. By breaking down β into N small imaginary time steps $\Delta\beta$, one can then employ the Suzuki-Trotter formula in Eq. [8.10] to construct a quantum circuit that promises to approximate $|\Psi_0\rangle$ [280, 326, 327].

We return to the Hamiltonian in Eq. [A.2] and construct the circuit that brings us from an initial state $|\Phi\rangle$ to the ground state using ITE. Recall the condition in Eq. [A.3], which is trivially satisfied if $|\Phi\rangle$ is the ground state of $\hat{H}_E^{(el.)}$ in the regime $g^{-2} \ll 1$, since $\hat{H}^{(el.)} \approx \hat{H}_E^{(el.)}$. In this regime, the variational circuit should essentially "do nothing", since we are already in – or very close to – the exact ground state. However, as we move to $g^{-2} \gg 1$, the Hamiltonian is governed by $\hat{H}_B^{(el.)}$, the circuit must act non-trivially on $|\Phi\rangle$ and transform it into $|\Psi_0\rangle$. Therefore, the structure of the circuit is essentially determined by $\hat{H}_B^{(el.)}$ and we neglect $\hat{H}_E^{(el.)}$ in the construction.

Now consider

$$e^{-\beta\hat{H}_B^{(el.)}/\hbar}|\Phi\rangle \approx \prod_j \prod_i \mathcal{U}_j(\theta_i)|\Phi\rangle$$

with $\hat{H}_B^{(el.)}$ given in the qudit formulation, cf. Eq. [A.2]. Each $\mathcal{U}_j(\theta_i)$ is unitary operation parametrized by θ_i that can be implemented on our hardware, i.e. one of the quantum gates discussed in Ch. 4.

For the sake of brevity we define

$$\hat{P}_i = \hat{\sigma}^x_{i,(-1,0)} \qquad \text{and} \qquad \hat{Q}_i = \hat{\sigma}^x_{i,(0,+1)} \tag{A.5}$$

and note that $\hat{P}_i$ and $\hat{Q}_i$ satisfy

$$[\hat{P}_k, \hat{P}_l] = [\hat{Q}_k, \hat{Q}_l] = 0 \text{ and } [\hat{P}_k, \hat{Q}_l] = i\hat{\sigma}^y_{k,(-1,+1)}\delta_{k,l} = (|-1\rangle\langle+1| - |+1\rangle\langle-1|)_k\,\delta_{k,l} \tag{A.6}$$

with $\delta_{k,l}$ denoting the Kronecker-Delta. The local term $\hat{H}_{loc.}$ in Eq. [A.2] is then given by

$$\hat{H}_{loc.} - \frac{g^{-2}}{2}\sum_{j=1}^{3}(\hat{P}_j + Q_j)$$

and the interaction term $\hat{H}_{int.}$ yields

$$\hat{H}_{int.} = -\frac{g^{-2}}{2}\prod_{j=1}^{3}(\hat{P}_j + Q_j) \tag{A.7}$$

Using the approximate *Baker-Campbell-Hausdorff* (BCH) formula

$$e^{\hat{A}+\hat{B}} \approx e^{\hat{A}}e^{\hat{B}}e^{-[\hat{A},\hat{B}]/2}$$

for two operators $\hat{A}$ and $\hat{B}$, we decompose

$$e^{-\beta\hat{H}_B^{(el.)}} = e^{-\beta\left(\hat{H}_{loc.}+\hat{H}_{int.}\right)} \tag{A.8}$$

by first factoring out the local terms. Since the sum $\hat{P}_i + \hat{Q}_i$ acting on the qudit i satisfies

$$[\hat{P}_i + \hat{Q}_i, \hat{P}_j + \hat{Q}_j] = 0$$

for any $j \neq i$, the local term $\hat{H}_{loc.}$ is equivalent to the product

$$e^{-\beta\hat{H}_{loc.}} = \prod_{i=1}^{3} e^{\beta\frac{g^{-2}}{2}(\hat{P}_i+\hat{Q}_i)}. \tag{A.9}$$

Moreover, due to

$$\begin{aligned}[\hat{P}_i + \hat{Q}_i, \hat{H}_{int.}] &= \prod_{j\neq i}(\hat{P}_j + \hat{Q}_j)[\hat{P}_i + \hat{Q}_i, \hat{P}_i + \hat{Q}_i] \\ &= \prod_{j\neq i}(\hat{P}_j + \hat{Q}_j)\left(\cancel{[\hat{P}_i, \hat{P}_i]} + [\hat{P}_i, \hat{Q}_i] + [\hat{Q}_i, \hat{P}_i] + \cancel{[\hat{Q}_i, \hat{Q}_i]}\right)\end{aligned} \tag{A.10}$$

$$[\hat{P}_i, \hat{Q}_i] = -[\hat{Q}_i, \hat{P}_i] \longrightarrow = 0$$

the interaction term $\hat{H}_{int.}$ commutes with $\hat{H}_{loc.}$ and therefore

$$e^{-\beta\hat{H}_B^{(el.)}} = e^{-\beta\hat{H}_{loc.}}e^{-\beta\hat{H}_{int.}}. \tag{A.11}$$

Each of the factors in Eq. [A.9] can be decomposed further into

$$e^{\beta\frac{g^{-2}}{2}(\hat{P}_j+\hat{Q}_j)} = e^{\beta\frac{g^{-2}}{2}\hat{P}_j}e^{\beta\frac{g^{-2}}{2}\hat{Q}_j}e^{-i\frac{1}{2}\left(\frac{\beta g^{-2}}{2}\right)^2\hat{\sigma}^y_{j,(-1,1)}} = e^{i\theta\hat{P}_j}e^{i\theta\hat{Q}_j}e^{-i\phi\hat{\sigma}^y_{j,(-1,1)}}$$

with $i\theta = \frac{\beta g^{-2}}{2}$ and $\phi = \frac{1}{2}\left(\frac{\beta g^{-2}}{2}\right)^2$, which is equivalent to the circuit illustrated in Fig. A.2.

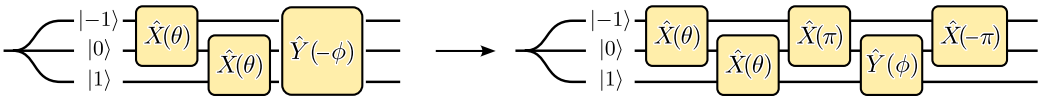


Figure A.2: Decomposition of $\hat{H}_{loc.}$ into quantum gates to be employed in the variational quantum algorithm. The operators $e^{i\theta\hat{P}_i}$, $e^{i\theta\hat{P}_i}$ and $e^{-i\phi\hat{\sigma}^y_{j,(-1,1)}}$ correspond to single-qudit gates that can be implemented on the quantum hardware, see Sec. 4.1.

Note that the circuits in Fig. A.2 have the same structure as the leading and trailing gates in the circuits shown in Fig. 8.9, see Sec. 8.2.1 in the main text.

The decomposition of the interaction term $\hat{H}_{int.}$ is notably more difficult. Next to local terms that can be implemented by sequences of single-qudit gates, the decomposition yields to operations of the form

$$\exp\left(i\psi\sigma^y_{j,(-1,1)}\sigma^x_{k,(a,b)}\right)$$

which can be realized by the controlled rotation gates $C\hat{R}(\theta,\phi)$ discussed in Sec. 4.3.2. A similar decomposition using controlled-controlled-rotation gates $C^2\hat{R}(\theta,\phi)$ in Sec. 4.3.3 exist for the three-body terms [328]

$$\exp\left(i\psi\sigma^y_{j,(-1,1)}\sigma^x_{k,(a,b)}\sigma^x_{l,(a,b)}\right).$$

Once both terms have been fully decomposed, the resulting circuit is inspected to find sequences of local gates that can be contracted into a single rotation and identify redundancies. Moreover, classical simulations of the circuit can reveal that some gates do not contribute in the variational algorithm, and can thus be neglected [17, 18].

A.3 APPROXIMATING THE GROUND STATES OF THE PURE-GAUGE THEORY

We use a VQE protocol to approximate the ground state of lattice QED. Employing periodic boundary conditions we simulate a pure-gauge theory, i.e. the interaction of gauge fields in the absence of matter. The dynamics of four plaquettes are encoded in rotators $\mathcal{R}_{i=1,2,3}$, each representing a gauge field, see Sec. 8.2 and Ref. [18]. In this section we investigate how well the VQE algorithm can resolve the exact ground state of the theory.

Using $\hat{H}_E$ and $\hat{H}_B$ in both representations, we compute the exact spectrum of the pure-gauge Hamiltonian

$$\hat{H} = \hat{H}_E / g^{-2} + g^{-2} \hat{H}_B \qquad \text{[A.12]}$$

across the interval $g^{-2} = [10^{-2}, 10^2]$. For each eigenstate $\varrho_i(g^{-2})$ we introduce a depolarization channel

$$\varrho_i'(g^{-2}) = (1-p) \cdot \varrho_i(g^{-2}) + \frac{1}{d^3} \cdot \mathbb{1}$$

to model a noisy state $\varrho_i'(g^{-2})$ with a fraction $p \ll 1$ in the maximally mixed state. We then compute the energies

$$E_i = \mathrm{Tr}[\hat{H} \varrho_i'(g^2 - 2)]$$

as an approximation to the spectrum for a noisy theory.

We compute the probability p using the noise model introduced in Sec. 8.1.2 and attribute the imperfections to the controlled rotation gates $C\hat{R}(\theta, \phi)$ as the dominant source of error. For 100 trials of the gate we obtain an average fidelity of $\mathcal{F}_{d=3} = 97.6(3)\%$ for $d = 3$ and $\mathcal{F}_{d=5} = 97.0(4)\%$. Since each circuit is constructed by four $C\hat{R}(\theta, \phi)$ we estimate

$$p = 1 - \mathcal{F}_d^4$$

and use the statistical uncertainties to compute a confidence interval for the E_i.

Fig. A.3 shows the energy of the exact (noiseless) ground state for $d = 3$, the confidence interval for the noisy ground state energy E_0, and the energies for the first and second excited state E_1 and E_2, respectively. Our experimental data is presented next to the numerical simulation of the VQE employing the noise model in Sec. 8.1.2. Since our data is consistently below the noisy gorund state, we claim that the variational algorithm indeed approximates the true ground state rather than any of the other low-energy eigenstates of the theory. A similar analysis is presented for $d = 5$ in Fig. A.4.

We observe that the measured energies in the magnetic representation in Fig. A.3(a) at small coupling strengths $g^{-2} < 1$ are below the exact ground state. Notably, at $g^{-2} = 10^{-2}$, the experimental outcome $\langle \hat{H} \rangle_{\text{exp.}} = -1083(7)$ is significantly below the theoretical minimum $\langle \hat{H} \rangle_{\text{exact}} = -978.4$. In this coupling regime the performance of the magnetic representation is expected to be poor. Moreover, the variational circuit is – compared to the circuit in the electric representation – notably more complex, see Fig. 8.9(b). Since the state of the second qudit is conditioned on *both* other qudits, it is twice as sensitive to entangling gate errors. These errors introduce asymmetries in the population of the gauge field states in Fig. 8.12(b), increasing the weight of the state $|+1\rangle$. At small g^{-2}, where the contribution of the electric term to the pure-gauge Hamiltonian in Eq. [A.12] dominates, these asymmetries artificially lower the measured energies. However, we emphasize that the structure of the circuit prevents the asymmetries from becoming too pronounced, cf. Fig. 8.9(b).

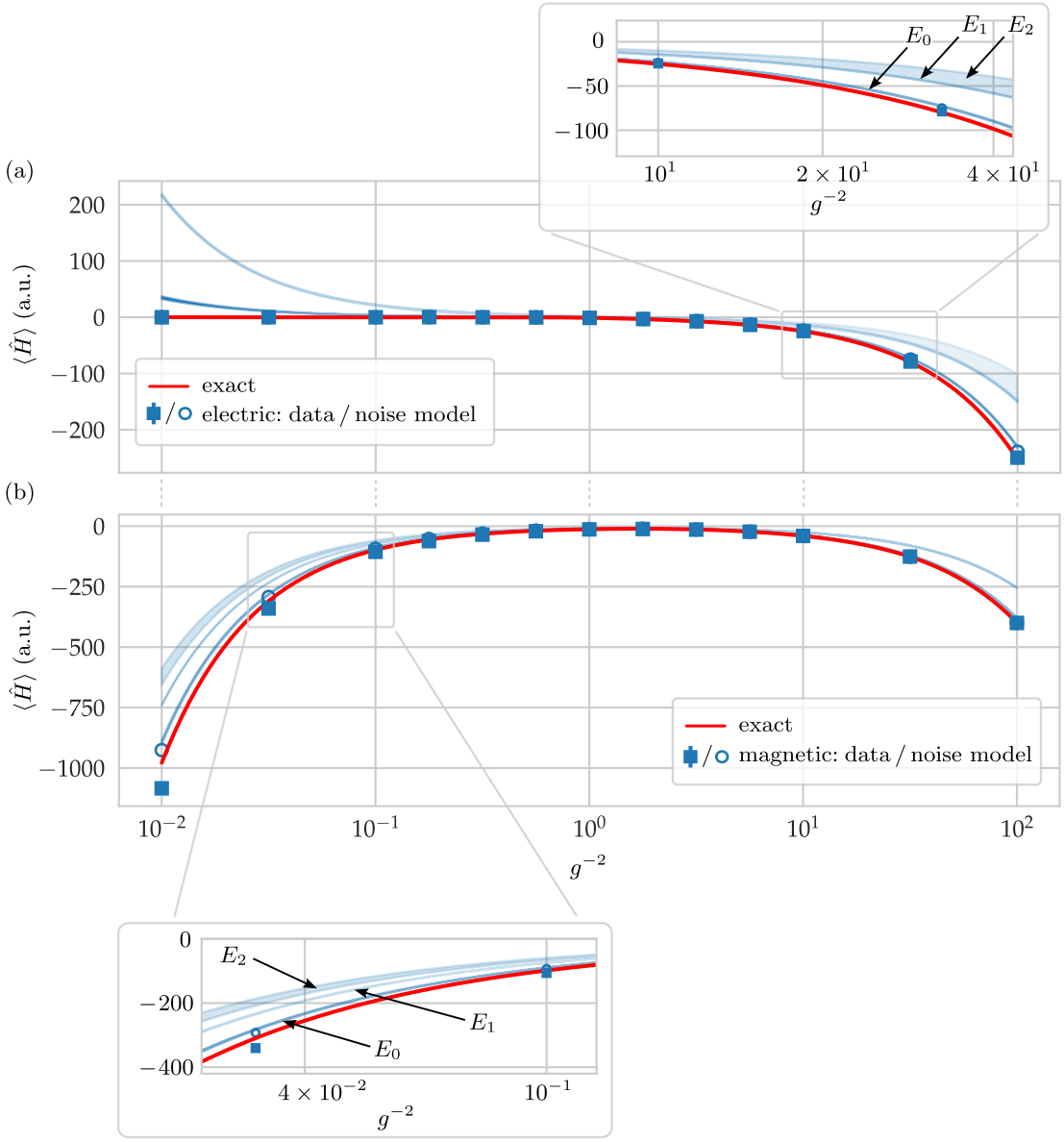


Figure A.3: Energies of the lowest eigenstates in the pure-gauge theory for $d = 3$; electric representation in (a) and magnetic representation in (b). Experimental noise is modeled using a depolarizing channel applied to the eigenstates $\varrho_i(g^{-2})$ with probability $p = 1 - \mathcal{F}_{d=3}^4$, where $\mathcal{F}_{d=3} = 97.6(3)\%$ is the fidelity of a single controlled rotation gate $C\hat{R}(\theta, \phi)$ computed from 100 evaluations of the gate using the noise model in Sec. 8.1.2. The energy of the exact (noiseless) ground state of the theory is shown in red with noisy energies E_i of the three lowest eigenstates in blue. Our data (squares) is accompanied by numerical simulations (circles) of the noisy circuit for comparison; error bars are hidden by the data markers.

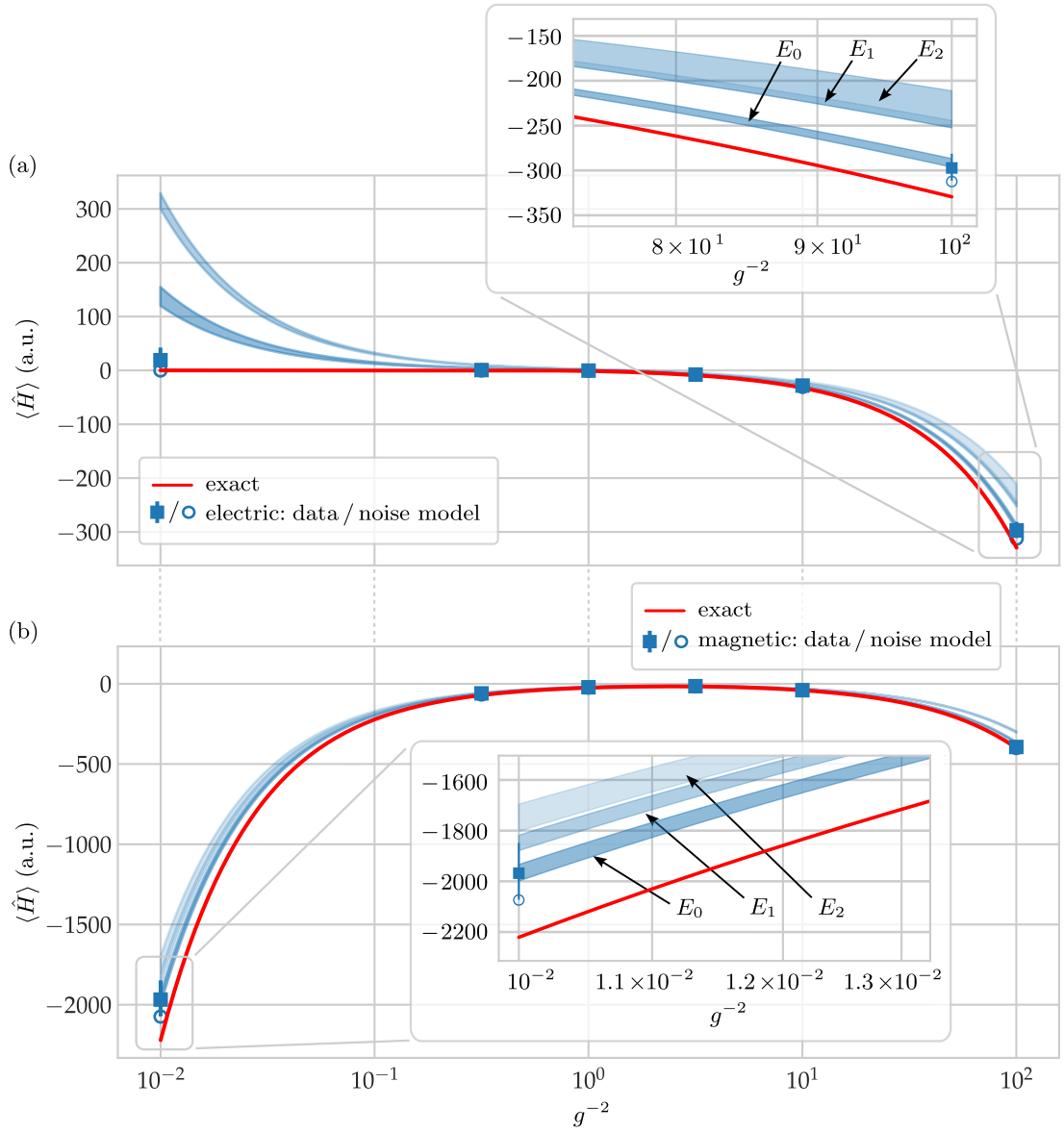


Figure A.4: Energies of the lowest eigenstates in the pure-gauge theory for $d = 5$. For an average gate fidelity $\mathcal{F}_{d=5} = 97.0(4)\%$ of the $C\hat{R}(\theta, \phi)$ we obtain the confidence intervals (blue, shaded) for the noisy energies E_i. In the electric representation (a) the exact ground state (red) lies consistently below our measurement outcomes (squares); error bars are partially hidden by the data markers. Our data agrees well with the energy of the noisy ground state E_0. Numerical simulations of the noisy circuit (circles) capture the measurement outcomes, slightly underestimating the experimental errors. This is best observed at large coupling strength as illustrated in the inset for $g^{-2} = 10^2$. Here, the simultated outcome is $\Delta E \approx 20$ below E_0, however still agrees within one standard deviation of statistical uncertainty with our experimental data. Analogous results are obtained in the magnetic representation (b).

B

LIST OF PUBLICATIONS

The work presented in this thesis led to the publication of the following journal articles:

1. [16] M. Meth *et al.* - Probing phases of quantum matter with an ion-trap tensor-network quantum eigensolver, *Phys. Rev. X* 12, 041035 (2022)
2. [19] M. Meth *et al.* - Simulating 2D lattice gauge theories on a qudit quantum computer, *Nature Physics* 21, 570–576 (2025)

Over the course of my graduate studies I had the honor to contribute to the following journal publications and pre-print articles:

1. [329] A. Erhard *et al.* - Characterizing large-scale quantum computers via cycle benchmarking, *Nature Communications* 10, 5347 (2019)
2. [37] R. Stricker *et al.* - Experimental deterministic correction of qubit loss, *Nature* 585, 207-210 (2020)
3. [330] A. Erhard *et al.* - Entangling logical qubits with lattice surgery, *Nature* 589, 220-224 (2021)
4. [120] I. Pogorelov *et al.* - A compact ion-trap quantum computing demonstrator, *PRX Quantum* 2, 020343 (2021)
5. [14] M. Ringbauer *et al.* - A universal qudit quantum processor with trapped ions, *Nature Physics* 18, 1053 (2022)
6. [331] R. Stricker *et al.* - Characterizing quantum instruments: from non-demolition measurements to quantum error correction, *PRX Quantum* 3, 030318 (2022)
7. [297] L. Postler *et al.* - Demonstration of fault-tolerant universal quantum gate operations, *Nature* 605, 675-680 (2022)
8. [309] R. Stricker *et al.* - Experimental single-setting quantum state tomography, *PRX Quantum* 3, 040310 (2022)
9. [332] P. Popov *et al.* - Variational quantum simulation of $U(1)$ lattice gauge theories with qudit systems, *Phys. Rev. Research* 6, 013202 (2024)
10. [333] R. Stricker *et al.* - Towards experimental classical verification of quantum computation, *Quantum Sci. Technol.* 9 02LT01 (2024)
11. [334] G. Camacho *et al.* - Observing dynamical localization on a trapped-ion qudit quantum processor, *arXiv:2412.13141* (2024)

12. [335] M. Ringbauer *et al.* - Verifiable measurement-based quantum random sampling with trapped ions, *Nature Communications* 16, 106 (2025)

13. [314] C. Edmunds *et al.* - Symmetry-Protected Topological Haldane Phase on a Qudit Quantum Processor, *PRX Quantum* 6, 020349 (2025)

14. [336] R. Joshi *et al.* - Probing Hadron Scattering in Lattice Gauge Theories on Qudit Quantum Computers, *arXiv:2507.12614* (2025)

15. [337] R. Joshi *et al.* - Efficient Qudit Circuit for Quench Dynamics of D Quantum Link Electrodynamics, *arXiv:2507.12589* (2025)

16. [338] R. Starek *et al.* - Experimental verification of multi-copy activation of genuine multipartite entanglement, *arXiv:2510.12457* (2025)

17. [339] L. S. V. Santos *et al.* - Device-independent quantum memory certification in two-point measurement experiments, *arXiv:2601.14191* (2026)

BIBLIOGRAPHY

[1] Richard P. Feynman. "Simulating physics with computers." In: *International Journal of Theoretical Physics* 21.6–7 (June 1982), pp. 467–488. ISSN: 1572-9575. DOI: 10.1007/bf02650179.

[2] Paul Benioff. "The computer as a physical system: A microscopic quantum mechanical Hamiltonian model of computers as represented by Turing machines." In: *Journal of Statistical Physics* 22.5 (May 1980), pp. 563–591. ISSN: 1572-9613. DOI: 10.1007/bf01011339.

[3] Iulia Buluta and Franco Nori. "Quantum Simulators." In: *Science* 326.5949 (Oct. 2009), pp. 108–111. ISSN: 1095-9203. DOI: 10.1126/science.1177838.

[4] Seth Lloyd. "Universal Quantum Simulators." In: *Science* 273.5278 (Aug. 1996), pp. 1073–1078. ISSN: 1095-9203. DOI: 10.1126/science.273.5278.1073.

[5] Tomi H Johnson, Stephen R Clark, and Dieter Jaksch. "What is a quantum simulator?" In: *EPJ Quantum Technology* 1.1 (July 2014). ISSN: 2196-0763. DOI: 10.1140/epjqt10.

[6] V. W. Scarola and S. Das Sarma. "Cold-atom optical lattices as quantum analog simulators for aperiodic one-dimensional localization without disorder." In: *Physical Review A* 73.4 (Apr. 2006), p. 041609. ISSN: 1094-1622. DOI: 10.1103/physreva.73.041609.

[7] Jochen Braumüller, Michael Marthaler, Andre Schneider, Alexander Stehli, Hannes Rotzinger, Martin Weides, and Alexey V. Ustinov. "Analog quantum simulation of the Rabi model in the ultra-strong coupling regime." In: *Nature Communications* 8.1 (Oct. 2017). ISSN: 2041-1723. DOI: 10.1038/s41467-017-00894-w.

[8] Dominik Hangleiter, Jacques Carolan, and Karim P. Y. Thébault. *Analogue Quantum Simulation: A New Instrument for Scientific Understanding*. Springer International Publishing, 2022. ISBN: 9783030872168. DOI: 10.1007/978-3-030-87216-8.

[9] Daniel Gottesman, Alexei Kitaev, and John Preskill. "Encoding a qubit in an oscillator." In: *Physical Review A* 64.1 (June 2001), p. 012310. ISSN: 1094-1622. DOI: 10.1103/physreva.64.012310.

[10] R. T. Thew, K. Nemoto, A. G. White, and W. J. Munro. "Qudit quantum-state tomography." In: *Physical Review A* 66.1 (July 2002), p. 012303. ISSN: 1094-1622. DOI: 10.1103/physreva.66.012303.

[11] Markus Grasls, Martin Rötteler, and Thomas Beth. "Efficient Quantum Circuits for Non-Qubit Quantum Error-Correcting Codes." In: *International Journal of Foundations of Computer Science* 14.05 (Oct. 2003), pp. 757–775. ISSN: 1793-6373. DOI: 10.1142/s0129054103002011.

[12] Yuchen Wang, Zixuan Hu, Barry C. Sanders, and Sabre Kais. "Qudits and High-Dimensional Quantum Computing." In: *Frontiers in Physics* 8 (Nov. 2020). ISSN: 2296-424X. DOI: 10.3389/fphy.2020.589504.

[13] Yulin Chi et al. "A programmable qudit-based quantum processor." In: *Nature Communications* 13.1 (Mar. 2022). ISSN: 2041-1723. DOI: 10.1038/s41467-022-28767-x.

[14] Martin Ringbauer, Michael Meth, Lukas Postler, Roman Stricker, Rainer Blatt, Philipp Schindler, and Thomas Monz. "A universal qudit quantum processor with trapped ions." In: *Nature Physics* 18.9 (July 2022), 1053–1057. ISSN: 1745-2481. DOI: 10.1038/s41567-022-01658-0. URL: http://dx.doi.org/10.1038/s41567-022-01658-0.

[15] Viacheslav V. Kuzmin and Pietro Silvi. "Variational quantum state preparation via quantum data buses." In: *Quantum* 4 (July 2020), p. 290. ISSN: 2521-327X. DOI: 10.22331/q-2020-07-06-290. URL: https://doi.org/10.22331/q-2020-07-06-290.

[16] Michael Meth, Viacheslav Kuzmin, Rick van Bijnen, Lukas Postler, Roman Stricker, Rainer Blatt, Martin Ringbauer, Thomas Monz, Pietro Silvi, and Philipp Schindler. "Probing Phases of Quantum Matter with an Ion-Trap Tensor-Network Quantum Eigensolver." In: *Phys. Rev. X* 12 (4 2022), p. 041035. DOI: 10.1103/PhysRevX.12.041035. URL: https://link.aps.org/doi/10.1103/PhysRevX.12.041035.

[17] Danny Paulson et al. "Simulating 2D Effects in Lattice Gauge Theories on a Quantum Computer." In: *PRX Quantum* 2.3 (Aug. 2021), p. 030334. ISSN: 2691-3399. DOI: 10.1103/prxquantum.2.030334.

[18] Jan F. Haase, Luca Dellantonio, Alessio Celi, Danny Paulson, Angus Kan, Karl Jansen, and Christine A. Muschik. "A resource efficient approach for quantum and classical simulations of gauge theories in particle physics." In: *Quantum* 5 (Feb. 2021), p. 393. ISSN: 2521-327X. DOI: 10.22331/q-2021-02-04-393. URL: http://dx.doi.org/10.22331/q-2021-02-04-393.

[19] Michael Meth et al. "Simulating two-dimensional lattice gauge theories on a qudit quantum computer." In: *Nature Physics* (Mar. 2025). ISSN: 1745-2481. DOI: 10.1038/s41567-025-02797-w.

[20] J. I. Cirac and P. Zoller. "Quantum Computations with Cold Trapped Ions." In: *Phys. Rev. Lett.* 74 (20 1995), pp. 4091–4094. DOI: 10.1103/PhysRevLett.74.4091. URL: https://link.aps.org/doi/10.1103/PhysRevLett.74.4091.

[21] Carola Metzner-Nebelsick. "Central Europe." In: *The Oxford Handbook of the European Iron Age*. Oxford University Press, Oct. 2019, pp. 217–274. ISBN: 9780191756931. DOI: 10.1093/oxfordhb/9780199696826.013.33.

[22] Carola Metzner-Nebelsick, E. Pernicka, S. Kutscher, and H. Krause. "82 kg gebündeltes Kupfer." In: *Die Welt der Himmelsscheibe von Nebra - Neue Horizonte. Begleitband zur Sonderausstellung im Landesmuseum für Vorgeschichte Halle (Saale), 4. Juni 2021 bis 9. Januar 2022*. Ed. by Harald Meller and Michael Schefzik. Halle (Saale) ; Darmstadt: Landesamt für Denkmalpflege und Archäologie Sachsen-Anhalt, Landesmuseum für Vorgeschichte ; wbg Theiss, 2020, pp. 152–155.

[23] Otto Neugebauer. *The exact sciences in antiquity*. Unabridged, slightly corrected reprint of the 2. ed., Brown Univ. Press, 1957. Dover classics of science and mathematics. New York: Dover Publ, 2004. 240 pp. ISBN: 0-486-22332-9.

[24] David Fowler and Eleanor Robson. "Square Root Approximations in Old Babylonian Mathematics: YBC 7289 in Context." In: *Historia Mathematica* 25.4 (Nov. 1998), pp. 366–378. ISSN: 0315-0860. DOI: 10.1006/hmat.1998.2209.

[25] Brian Hayes. "Third Base." In: *American Scientist* 89.6 (2001), p. 490. ISSN: 1545-2786. DOI: 10.1511/2001.40.3268.

[26] Lloyd Strickland. "Why Did Thomas Harriot Invent Binary?" In: *The Mathematical Intelligencer* 46.1 (Apr. 2023), pp. 57–62. ISSN: 1866-7414. DOI: 10.1007/s00283-023-10271-9.

[27] C. E. Shannon. "A Symmetrical Notation for Numbers." In: *The American Mathematical Monthly* 57.2 (Feb. 1950), pp. 90–93. ISSN: 1930-0972. DOI: 10.1080/00029890.1950.11999490.

[28] Nikolay Petrovich Brusentsov and José Ramil Alvarez. "Ternary Computers: The Setun and the Setun 70." In: *Perspectives on Soviet and Russian Computing*. Springer Berlin Heidelberg, 2011, pp. 74–80. ISBN: 9783642228162. DOI: 10.1007/978-3-642-22816-2_10.

[29] Don D. Roberts. *The Existential Graphs of Charles S. Peirce*. Approaches to Semiotics [AS] 27. Description based upon print version of record. Berlin: De Gruyter, 1973. 168 pp. ISBN: 978-3-11022622-5.

[30] Charles Sanders Peirce. *A Boolean Algebra With One Constant*. Copy by Michele Balat, last accessed 2025/04/06. 1880. URL: https://michelbalat.fr/wp-content/uploads/2025/01/A_BOOLIAN_ALGEBRA_WITH_ON.doc.

[31] J. Bardeen and W. H. Brattain. "The Transistor, A Semi-Conductor Triode." In: *Physical Review* 74.2 (July 1948), pp. 230–231. ISSN: 0031-899X. DOI: 10.1103/physrev.74.230.

[32] Ang Fei. "A review of the development of transistor technology and its application in electronic devices." In: *Applied and Computational Engineering* 56.1 (Apr. 2024), pp. 141–145. ISSN: 2755-273X. DOI: 10.54254/2755-2721/56/20240642.

[33] Robert Lockhart. "Low-rank separable states are a set of measure zero within the set of low-rank states." In: *Physical Review A* 65.6 (June 2002), p. 064304. ISSN: 1094-1622. DOI: 10.1103/physreva.65.064304.

[34] Menas Kafatos, ed. *Bell's Theorem, Quantum Theory and Conceptions of the Universe*. Springer Netherlands, 1989. ISBN: 9789401708494. DOI: 10.1007/978-94-017-0849-4.

[35] Daniel M. Greenberger, Michael A. Horne, and Anton Zeilinger. *Going Beyond Bell's Theorem*. 2007. arXiv: 0712.0921 [quant-ph]. URL: https://arxiv.org/abs/0712.0921.

[36] Claude Cohen-Tannoudji. *Quantum Mechanics. Volume I: Basic Concepts, Tools, and Applications*. Ed. by Bernard Diu, Frank Laloe, Nicole Ostrowsky, and Daniel Ostrowsky. 2nd. Weinheim: Wiley-VCH GmbH Co. KGaA, 2020. 1944 pp. ISBN: 978-3-527-82271-3.

[37] Roman Stricker, Davide Vodola, Alexander Erhard, Lukas Postler, Michael Meth, Martin Ringbauer, Philipp Schindler, Thomas Monz, Markus Müller, and Rainer Blatt. "Experimental deterministic correction of qubit loss." In: *Nature* 585.7824 (Sept. 2020), 207–210. ISSN: 1476-4687. DOI: 10.1038/s41586-020-2667-0. URL: http://dx.doi.org/10.1038/s41586-020-2667-0.

[38] Omar Gamel and Daniel F. V. James. "Measures of quantum state purity and classical degree of polarization." In: *Physical Review A* 86.3 (Sept. 2012), p. 033830. ISSN: 1094-1622. DOI: 10.1103/physreva.86.033830.

[39] Michael A. Nielsen and Isaac L. Chuang. *Quantum Computation and Quantum Information: 10th Anniversary Edition*. Cambridge University Press, June 2012. ISBN: 9780511976667. DOI: 10.1017/cbo9780511976667.

[40] D. Cavalcanti, F. G. S. L. Brandão, and M. O. Terra Cunha. "Are all maximally entangled states pure?" In: *Physical Review A* 72.4 (Oct. 2005), p. 040303. ISSN: 1094-1622. DOI: 10.1103/physreva.72.040303.

[41] A. Uhlmann. "The transition probability in the state space of a star-algebra." In: *Reports on Mathematical Physics* 9.2 (1976), pp. 273–279. ISSN: 0034-4877. DOI: https://doi.org/10.1016/0034-4877(76)90060-4. URL: https://www.sciencedirect.com/science/article/pii/0034487776900604.

[42] Roy McWeeny. *Symmetry. An introduction to group theory and its applications*. unabrdiged republ. of the 1963 original. Originally published: Oxford ; New York : Pergamon Press, 1963 - Includes bibliographical references and index. Mineola, NY: Dover Publications, 2002. 248 pp. ISBN: 978-0486421827.

[43] Sadri Hassani. *Mathematical Physics: A Modern Introduction to Its Foundations*. Springer International Publishing, 2013. ISBN: 9783319011950. DOI: 10.1007/978-3-319-01195-0.

[44] Gabriel Lugo. *Differential geometry in physics*. Wilmington: UNCW, University of North Carolina Wilmington, William Madison Randall Library, 2021. 361 pp. ISBN: 978-1469669243.

[45] David Deutsch and Roger Penrose. "Quantum theory, the Church–Turing principle and the universal quantum computer." In: *Proceedings of the Royal Society of London. A. Mathematical and Physical Sciences* 400.1818 (1985), pp. 97–117. DOI: 10.1098/rspa.1985.0070. eprint: https://royalsocietypublishing.org/doi/pdf/10.1098/rspa.1985.0070. URL: https://royalsocietypublishing.org/doi/abs/10.1098/rspa.1985.0070.

[46] David Deutsch and Richard Jozsa. "Rapid solution of problems by quantum computation." In: *Proceedings of the Royal Society of London. Series A: Mathematical and Physical Sciences* 439.1907 (1992), pp. 553–558. DOI: 10.1098/rspa.1992.0167. eprint: https://royalsocietypublishing.org/doi/pdf/10.1098/rspa.1992.0167. URL: https://royalsocietypublishing.org/doi/abs/10.1098/rspa.1992.0167.

[47] J. A. Jones and M. Mosca. "Implementation of a quantum algorithm on a nuclear magnetic resonance quantum computer." In: *The Journal of Chemical Physics* 109.5 (Aug. 1998), pp. 1648–1653. ISSN: 1089-7690. DOI: 10.1063/1.476739.

[48] Stephan Gulde, Mark Riebe, Gavin P. T. Lancaster, Christoph Becher, Jürgen Eschner, Hartmut Häffner, Ferdinand Schmidt-Kaler, Isaac L. Chuang, and Rainer Blatt. "Implementation of the Deutsch–Jozsa algorithm on an ion-trap quantum computer." In: *Nature* 421.6918 (Jan. 2003), pp. 48–50. ISSN: 1476-4687. DOI: 10.1038/nature01336.

[49] P.W. Shor. "Algorithms for quantum computation: discrete logarithms and factoring." In: *Proceedings 35th Annual Symposium on Foundations of Computer Science*. 1994, pp. 124–134. DOI: 10.1109/SFCS.1994.365700.

[50] Peter W. Shor. "Polynomial-Time Algorithms for Prime Factorization and Discrete Logarithms on a Quantum Computer." In: *SIAM Journal on Computing* 26.5 (Oct. 1997), 1484–1509. ISSN: 1095-7111. DOI: 10.1137/s0097539795293172. URL: http://dx.doi.org/10.1137/S0097539795293172.

[51] Lov K. Grover. "A fast quantum mechanical algorithm for database search." In: *Proceedings of the twenty-eighth annual ACM symposium on Theory of computing - STOC '96*. STOC '96. ACM Press, 1996, pp. 212–219. DOI: 10.1145/237814.237866.

[52] Tommaso Toffoli. "Reversible computing." In: *Automata, Languages and Programming*. Springer Berlin Heidelberg, 1980, pp. 632–644. ISBN: 9783540393467. DOI: 10.1007/3-540-10003-2_104.

[53] Ville Bergholm et al. *PennyLane: Automatic differentiation of hybrid quantum-classical computations*. 2022. arXiv: 1811.04968 [quant-ph]. URL: https://arxiv.org/abs/1811.04968.

[54] Ali Javadi-Abhari et al. *Quantum computing with Qiskit*. 2024. arXiv: 2405.08810 [quant-ph]. URL: https://arxiv.org/abs/2405.08810.

[55] Steven T. Flammia, Andrew Silberfarb, and Carlton M. Caves. "Minimal Informationally Complete Measurements for Pure States." In: *Foundations of Physics* 35.12 (Dec. 2005), 1985–2006. ISSN: 1572-9516. DOI: 10.1007/s10701-005-8658-z. URL: http://dx.doi.org/10.1007/s10701-005-8658-z.

[56] S. A. Moses et al. "A Race-Track Trapped-Ion Quantum Processor." In: *Phys. Rev. X* 13 (4 2023), p. 041052. DOI: 10.1103/PhysRevX.13.041052. URL: https://link.aps.org/doi/10.1103/PhysRevX.13.041052.

[57] Minzhao Liu et al. "Certified randomness using a trapped-ion quantum processor." In: *Nature* (Mar. 2025). ISSN: 1476-4687. DOI: 10.1038/s41586-025-08737-1.

[58] Davide Castelvecchi. "IBM releases first-ever 1,000-qubit quantum chip." In: *Nature* 624.7991 (Dec. 2023), pp. 238–238. ISSN: 1476-4687. DOI: 10.1038/d41586-023-03854-1.

[59] T. C. Ralph, K. J. Resch, and A. Gilchrist. "Efficient Toffoli gates using qudits." In: *Phys. Rev. A* 75 (2 2007), p. 022313. DOI: 10.1103/PhysRevA.75.022313. URL: https://link.aps.org/doi/10.1103/PhysRevA.75.022313.

[60] Benjamin P. Lanyon, Marco Barbieri, Marcelo P. Almeida, Thomas Jennewein, Timothy C. Ralph, Kevin J. Resch, Geoff J. Pryde, Jeremy L. O'Brien, Alexei Gilchrist, and Andrew G. White. "Simplifying quantum logic using higher-dimensional Hilbert spaces." In: *Nature Physics* 5.2 (Dec. 2008), pp. 134–140. ISSN: 1745-2481. DOI: 10.1038/nphys1150.

[61] Ming-Xin Dong, Wei-Hang Zhang, Lei Zeng, Ying-Hao Ye, Da-Chuang Li, Guang-Can Guo, Dong-Sheng Ding, and Bao-Sen Shi. "Highly Efficient Storage of 25-Dimensional Photonic Qudit in a Cold-Atom-Based Quantum Memory." In: *Physical Review Letters* 131.24 (Dec. 2023), p. 240801. ISSN: 1079-7114. DOI: 10.1103/physrevlett.131.240801.

[62] Noah Goss et al. "High-fidelity qutrit entangling gates for superconducting circuits." In: *Nature Communications* 13.1 (Dec. 2022). ISSN: 2041-1723. DOI: 10.1038/s41467-022-34851-z.

[63] Pei Jiang Low, Brendan White, and Crystal Senko. "Control and readout of a 13-level trapped ion qudit." In: *npj Quantum Information* 11.1 (May 2025). ISSN: 2056-6387. DOI: 10.1038/s41534-025-01031-y.

[64] Murray Gell-Mann. "Symmetries of Baryons and Mesons." In: *Physical Review* 125.3 (Feb. 1962), pp. 1067–1084. ISSN: 0031-899X. DOI: 10.1103/physrev.125.1067.

[65] Reinhold A Bertlmann and Philipp Krammer. "Bloch vectors for qudits." In: *Journal of Physics A: Mathematical and Theoretical* 41.23 (May 2008), p. 235303. ISSN: 1751-8121. DOI: 10.1088/1751-8113/41/23/235303.

[66] David P. DiVincenzo. "Quantum Computation." In: *Science* 270.5234 (1995), pp. 255–261. DOI: 10.1126/science.270.5234.255. URL: https://www.science.org/doi/abs/10.1126/science.270.5234.255.

[67] D. P. DiVincenzo. "Topics in Quantum Computers." In: *Mesoscopic Electron Transport*. Ed. by Lydia L. Sohn, Leo P. Kouwenhoven, and Gerd Schön. Dordrecht: Springer Netherlands, 1997, pp. 657–677. ISBN: 978-94-015-8839-3. DOI: 10.1007/978-94-015-8839-3_18. URL: https://doi.org/10.1007/978-94-015-8839-3_18.

[68] David P. DiVincenzo. "The Physical Implementation of Quantum Computation." In: *Fortschritte der Physik* 48.9-11 (2000), pp. 771–783. DOI: https://doi.org/10.1002/1521-3978(200009)48:9/11<771::AID-PROP771>3.0.CO;2-E. URL: https://onlinelibrary.wiley.com/doi/abs/10.1002/1521-3978%28200009%2948%3A9/11%3C771%3A%3AAID-PROP771%3E3.0.CO%3B2-E.

[69] Wolfgang Paul. "Electromagnetic traps for charged and neutral particles." In: *Rev. Mod. Phys.* 62 (3 1990), pp. 531–540. DOI: 10.1103/RevModPhys.62.531. URL: https://link.aps.org/doi/10.1103/RevModPhys.62.531.

[70] Wolfgang Paul and Helmut Steinwedel. "Verfahren zur Trennung bzw. zum getrennten Nachweis von Ionen verschiedener spezifischer Ladung." Pat. DE944900C. Dec. 1953. URL: https://worldwide.espacenet.com/patent/search/family/025948048/publication/DE944900C?q=pn%3DDE944900C.

[71] Wolfgang Paul and Helmut Steinwedel. "Notizen: Ein neues Massenspektrometer ohne Magnetfeld." In: *Zeitschrift für Naturforschung A* 8.7 (1953), pp. 448–450. DOI: doi:10.1515/zna-1953-0710. URL: https://doi.org/10.1515/zna-1953-0710.

[72] Wolfgang Paul, Otto Osberghaus, and Erhardt Fischer. *Ein Ionenkäfig*. Forschungsberichte des Wirtschafts- und Verkehrsministeriums Nordrhein-Westfalen 415. Bonn [a.o.]: Springer Fachmedien Wiesbaden, 1958.

[73] Fouad G. Major, Viorica N. Gheorghe, and Günther Werth. *Charged Particle Traps*. 1st ed. Vol. 37. Springer Series on Atomic, Optical, and Plasma Physics. Springer-Verlag, 2005. ISBN: 3540220437. DOI: 10.1007/b137836.

[74] Ivana Kovacic, Richard Rand, and Si Mohamed Sah. "Mathieu's Equation and Its Generalizations: Overview of Stability Charts and Their Features." In: *Applied Mechanics Reviews* 70.2 (Feb. 2018). ISSN: 2379-0407. DOI: 10.1115/1.4039144.

[75] D. Leibfried, R. Blatt, C. Monroe, and D. Wineland. "Quantum dynamics of single trapped ions." In: *Rev. Mod. Phys.* 75 (1 2003), pp. 281–324. DOI: 10.1103/RevModPhys.75.281. URL: https://link.aps.org/doi/10.1103/RevModPhys.75.281.

[76] Chris Brimacombe, Robert M. Corless, and Mair Zamir. *Computation and applications of Mathieu functions: A historical perspective*. 2020. DOI: 10.48550/ARXIV.2008.01812.

[77] D.F.V. James. "Quantum dynamics of cold trapped ions with application to quantum computation." In: *Applied Physics B: Lasers and Optics* 66.2 (Feb. 1998), 181–190. ISSN: 1432-0649. DOI: 10.1007/s003400050373. URL: http://dx.doi.org/10.1007/s003400050373.

[78] Franz Mandl and Graham Shaw. *Quantum field theory*. 2. ed., repr. with corr. Chichester: Wiley, 2011. 478 pp. ISBN: 978-0-471-49683-0.

[79] James Clerk Maxwell. "A dynamical theory of the electromagnetic field." In: *Philosophical Transactions of the Royal Society of London* 155 (Dec. 1865), pp. 459–512. ISSN: 2053-9223. DOI: 10.1098/rstl.1865.0008.

[80] Christopher J. Foot. *Atomic physics*. Repr. (twice with corr.) Oxford master series in physics 7. Oxford [u.a.]: Oxford Univ. Press, 2011. 331 pp. ISBN: 978-0-19-850696-6.

[81] Robert M. Eisberg and Robert Resnick. *Quantum physics of atoms, molecules, solids, nuclei, and particles*. Ed. by Wiley. 2nd. Previous ed.: 1974. New York [u.a.]: John Wiley and Sons, Inc., 1985. ISBN: 978-0-471-87373-0.

[82] Christian Felix Roos. "Controlling the quantum state of trapped ions." PhD thesis. Universität Innsbruck, 2000.

[83] Claude Cohen-Tannoudji and David Guéry-Odelin. *Advances in Atomic Physics*. World Scientific, 2011. DOI: 10.1142/6631. URL: https://www.worldscientific.com/doi/abs/10.1142/6631.

[84] Stig Stenholm. "The semiclassical theory of laser cooling." In: *Rev. Mod. Phys.* 58 (3 1986), pp. 699–739. DOI: 10.1103/RevModPhys.58.699. URL: https://link.aps.org/doi/10.1103/RevModPhys.58.699.

[85] D. J. Wineland and Wayne M. Itano. "Laser cooling of atoms." In: *Phys. Rev. A* 20 (4 1979), pp. 1521–1540. DOI: 10.1103/PhysRevA.20.1521. URL: https://link.aps.org/doi/10.1103/PhysRevA.20.1521.

[86] J. Dalibard and C. Cohen-Tannoudji. "Laser cooling below the Doppler limit by polarization gradients: simple theoretical models." In: *J. Opt. Soc. Am. B* 6.11 (1989), pp. 2023–2045. DOI: 10.1364/JOSAB.6.002023. URL: https://opg.optica.org/josab/abstract.cfm?URI=josab-6-11-2023.

[87] G. S. Agarwal. "Master-Equation Approach to Spontaneous Emission." In: *Phys. Rev. A* 2 (5 1970), pp. 2038–2046. DOI: 10.1103/PhysRevA.2.2038. URL: https://link.aps.org/doi/10.1103/PhysRevA.2.2038.

[88] Jürgen Eschner, Giovanna Morigi, Ferdinand Schmidt-Kaler, and Rainer Blatt. "Laser cooling of trapped ions." In: *Journal of the Optical Society of America B* 20.5 (May 2003), p. 1003. ISSN: 1520-8540. DOI: 10.1364/josab.20.001003.

[89] J. Javanainen and S. Stenholm. "Broad band resonant light pressure: I. Basic equations." In: *Applied Physics* 21.1 (Jan. 1980), pp. 35–45. ISSN: 1432-0649. DOI: 10.1007/bf00886481.

[90] D. J. Wineland, R. E. Drullinger, and F. L. Walls. "Radiation-Pressure Cooling of Bound Resonant Absorbers." In: *Phys. Rev. Lett.* 40 (25 1978), pp. 1639–1642. DOI: 10.1103/PhysRevLett.40.1639. URL: https://link.aps.org/doi/10.1103/PhysRevLett.40.1639.

[91] W. Neuhauser, M. Hohenstatt, P. Toschek, and H. Dehmelt. "Optical-Sideband Cooling of Visible Atom Cloud Confined in Parabolic Well." In: *Physical Review Letters* 41.4 (July 1978), pp. 233–236. ISSN: 0031-9007. DOI: 10.1103/physrevlett.41.233.

[92] Paul D. Lett, Richard N. Watts, Christoph I. Westbrook, William D. Phillips, Phillip L. Gould, and Harold J. Metcalf. "Observation of Atoms Laser Cooled below the Doppler Limit." In: *Phys. Rev. Lett.* 61 (2 1988), pp. 169–172. DOI: 10.1103/PhysRevLett.61.169. URL: https://link.aps.org/doi/10.1103/PhysRevLett.61.169.

[93] Y. Shevy, D. S. Weiss, P. J. Ungar, and Steven Chu. "Bimodal speed distributions in laser-cooled atoms." In: *Phys. Rev. Lett.* 62 (10 1989), pp. 1118–1121. DOI: 10.1103/PhysRevLett.62.1118. URL: https://link.aps.org/doi/10.1103/PhysRevLett.62.1118.

[94] D. J. Wineland, J. Dalibard, and C. Cohen-Tannoudji. "Sisyphus cooling of a bound atom." In: *J. Opt. Soc. Am. B* 9.1 (1992), pp. 32–42. DOI: 10.1364/JOSAB.9.000032. URL: https://opg.optica.org/josab/abstract.cfm?URI=josab-9-1-32.

[95] J. I. Cirac, R. Blatt, P. Zoller, and W. D. Phillips. "Laser cooling of trapped ions in a standing wave." In: *Physical Review A* 46.5 (Sept. 1992), pp. 2668–2681. ISSN: 1094-1622. DOI: 10.1103/physreva.46.2668.

[96] M K Joshi, A Fabre, C Maier, T Brydges, D Kiesenhofer, H Hainzer, R Blatt, and C F Roos. "Polarization-gradient cooling of 1D and 2D ion Coulomb crystals." In: *New Journal of Physics* 22.10 (Oct. 2020), p. 103013. ISSN: 1367-2630. DOI: 10.1088/1367-2630/abb912. URL: http://dx.doi.org/10.1088/1367-2630/abb912.

[97] I. Marzoli, J. I. Cirac, R. Blatt, and P. Zoller. "Laser cooling of trapped three-level ions: Designing two-level systems for sideband cooling." In: *Physical Review A* 49.4 (Apr. 1994), pp. 2771–2779. ISSN: 1094-1622. DOI: 10.1103/physreva.49.2771.

[98] K. Wright et al. "Benchmarking an 11-qubit quantum computer." In: *Nature Communications* 10.1 (2019). ISSN: 2041-1723. DOI: 10.1038/s41467-019-13534-2. URL: http://dx.doi.org/10.1038/s41467-019-13534-2.

[99] J. M. Pino et al. "Demonstration of the trapped-ion quantum CCD computer architecture." In: *Nature* 592.7853 (Apr. 2021), pp. 209–213. ISSN: 1476-4687. DOI: 10.1038/s41586-021-03318-4.

[100] A. G. Wright. *The Photomultiplier Handbook*. Description based on publisher supplied metadata and other sources. Oxford: Oxford University Press USA - OSO, 2017. 1639 pp. ISBN: 9780199565092.

[101] Paul Jerram, Peter J. Pool, Ray Bell, David J. Burt, Steve Bowring, Simon Spencer, Mike Hazelwood, Ian Moody, Neil Catlett, and Philip S. Heyes. "The LLCCD: low-light imaging without the need for an intensifier." In: *Sensors and Camera Systems for Scientific, Industrial, and Digital Photography Applications II*. Ed. by Morley M. Blouke, John Canosa, and Nitin Sampat. Vol. 4306. SPIE, May 2001, p. 178. DOI: 10.1117/12.426953.

[102] J. Hynecek. "Impactron-a new solid state image intensifier." In: *IEEE Transactions on Electron Devices* 48.10 (2001), pp. 2238–2241. ISSN: 0018-9383. DOI: 10.1109/16.954460.

[103] Werner Geafer. *Optical fundamentals for system design and lab. An introduction into technical optics*. Printsystem-Medienverlag, 2014. 205 pp. ISBN: 978-3938295793.

[104] Jian Jin and D. A. Church. "Precision lifetimes for the Ca^+ $4p^2P$ levels: Experiment challenges theory at the 1% level." In: *Physical Review Letters* 70.21 (May 1993), pp. 3213–3216. ISSN: 0031-9007. DOI: 10.1103/physrevlett.70.3213.

[105] P. A. Barton, C. J. S. Donald, D. M. Lucas, D. A. Stevens, A. M. Steane, and D. N. Stacey. "Measurement of the lifetime of the $3d^2D_{5/2}$ state in $^{40}Ca^+$." In: *Physical Review A* 62.3 (Aug. 2000), p. 032503. ISSN: 1094-1622. DOI: 10.1103/physreva.62.032503.

[106] Stephan Timo Gulde. "Experimental realization of quantum gates and the Deutsch-Josza algorithm with trapped $^{40}Ca^+$ ions." PhD thesis. Universität Innsbruck, 2003.

[107] Alexander Erhard. "Towards scalable quantum computation with trapped ions." PhD thesis. Universität Innsbruck, 2021.

[108] Hanns-Christoph Nägerl. "Ion Strings for Quantum Computation." PhD thesis. Universität Innsbruck, 1998.

[109] Philipp Schindler et al. "A quantum information processor with trapped ions." In: *New Journal of Physics* 15.12 (Dec. 2013), p. 123012. ISSN: 1367-2630. DOI: 10.1088/1367-2630/15/12/123012.

[110] F. Schmidt-Kaler et al. "How to realize a universal quantum gate with trapped ions." In: *Applied Physics B* 77.8 (Dec. 2003), pp. 789–796. ISSN: 1432-0649. DOI: 10.1007/s00340-003-1346-9.

[111] Andor Technology. *Andor Technology iXon3*. en. Data sheet 1.5. Belfast, BT12 7AL, UK: Oxford Instruments / Andor Technology, 2011. URL: https://andor.oxinst.com/downloads/uploads/iXon3_Hardware_Guide.pdf.

[112] Adrian Korpel. *Acousto-Optics*. CRC Press LLC, 1997. ISBN: 9780585400044.

[113] Alexander Franzen. *ComponentLibrary*. vector graphics library for illustration of optics experiments (adapted). 2006. URL: https://www.gwoptics.org/ComponentLibrary/.

[114] IEEE Terminology Working Group. "IEEE Standard Letter Designations for Radar-Frequency Bands." In: *IEEE Std 521-2019 (Revision of IEEE Std 521-2002)* (2020), pp. 1–15. DOI: 10.1109/IEEESTD.2020.8999849.

[115] E. A. Donley, T. P. Heavner, F. Levi, M. O. Tataw, and S. R. Jefferts. "Double-pass acousto-optic modulator system." In: *Review of Scientific Instruments* 76.6 (June 2005). ISSN: 1089-7623. DOI: 10.1063/1.1930095.

[116] Julian Rickert. "Simultaneous and individual ion addressing for quantum information processing." MA thesis. Universität Innsbruck, 2018.

[117] Joonhyuk Kwon, William J. Setzer, Michael Gehl, Nicholas Karl, Jay Van Der Wall, Ryan Law, Matthew G. Blain, Daniel Stick, and Hayden J. McGuinness. "Multi-site integrated optical addressing of trapped ions." In: *Nature Communications* 15.1 (May 2024). ISSN: 2041-1723. DOI: 10.1038/s41467-024-47882-5.

[118] Lukas Postler. "Universal operations on protected qubits." PhD thesis. Universität Innsbruck, 2025.

[119] Sangtaek Kim, Robert R. Mcleod, M. Saffman, and Kelvin H. Wagner. "Doppler-free, multiwavelength acousto-optic deflector for two-photon addressing arrays of Rb atoms in a quantum information processor." In: *Applied Optics* 47.11 (Apr. 2008), p. 1816. ISSN: 1539-4522. DOI: 10.1364/ao.47.001816.

[120] I. Pogorelov et al. "Compact Ion-Trap Quantum Computing Demonstrator." In: *PRX Quantum* 2.2 (2 2021), p. 020343. ISSN: 2691-3399. DOI: 10.1103/PRXQuantum.2.020343. URL: https://link.aps.org/doi/10.1103/PRXQuantum.2.020343.

[121] Alex Steiner. "Design, implementation, and characterization of a rack-mountable laser system for the optical control of trapped Calcium 40 ions." MA thesis. Universität Innsbruck, 2023.

[122] Tetsu Takekoshi and Alpine Quantum Technologies GmbH. "Methods and apparatuses for laser stabilization." Pat. EP3940898. Jan. 2022. URL: https://worldwide.espacenet.com/publicationDetails/biblio?FT=D&date=20220119&DB=&locale=de_EP&CC=EP&NR=3940898A1&KC=A1&ND=5.

[123] Roman Stricker. "Gatteroperationen hoher Güte in einem optischen Quantenbit." MA thesis. Universität Innsbruck, 2017.

[124] Alexander Erhard. "Frequenzstabilisierung eines Diodenlasersystems mit 729 nm Wellenlänge." MA thesis. Universität Innsbruck, 2015.

[125] R. Freund, Ch. D. Marciniak, and T. Monz. "A self-referenced optical phase noise analyzer for quantum technologies." In: *Review of Scientific Instruments* 95.6 (June 2024), p. 063005. ISSN: 0034-6748. DOI: 10.1063/5.0183502. URL: https://doi.org/10.1063/5.0183502.

[126] Vlad Negnevitsky. "Feedback-stabilised quantum states in a mixed-species ion system." PhD thesis. Eidgenössische Technische Hochschule (ETH) Zürich, 2018.

[127] Martin Stadler. "Classical control for trapped ion quantum physics." PhD thesis. Eidgenössische Technische Hochschule (ETH) Zürich, 2024.

[128] Michael Meth. "Dynamische Kontrolle von Laserimpulsen zur Quanteninformationsverarbeitung." MA thesis. Universität Innsbruck, 2017.

[129] Marc Georg Bußjäger. "Automated frequency locking via spectroscopy on trapped $^{40}Ca^{+}$ ions." MA thesis. Universität Innsbruck, 2020.

[130] Xilinx Inc. *Zynq-7000 SoC First Generation Architecture*. en. Product specification DS190 V.1.11.1. San Jose, CA: Xilinx Inc., 2012-2018.

[131] Inc. Analog Devices. *AD9910 1GSPS, 14 bit, 3.3 V CMOS Direct Digital Synthesizer*. en. Data sheet Rev. E. Norwood, MA: Analog Devices Inc., 2016. URL: https://www.analog.com/static/imported-files/Data_Sheets/AD9910.pdf.

[132] JEDEC Solid State Technology Association. *Interface standard for nominal 3.0V/3.3V supply digital integrated circuits*. en. Standard JESD 8. Arlington, VA: JEDEC, 2007.

[133] Bahaa E. A. Saleh. *Fundamentals of Photonics*. Ed. by Malvin Carl Teich. 2nd edition. Wiley Series in Pure and Applied Optics. Description based upon print version of record. Chicester: John Wiley and Sons, 2013. 1202 pp. ISBN: 978-0471358329.

[134] Daniel Nigg. "Towards fault tolerant quantum computation." PhD thesis. Universität Innsbruck, 2016.

[135] H. Häffner, S. Gulde, M. Riebe, G. Lancaster, C. Becher, J. Eschner, F. Schmidt-Kaler, and R. Blatt. "Precision Measurement and Compensation of Optical Stark Shifts for an Ion-Trap Quantum Processor." In: *Phys. Rev. Lett.* 90 (14 2003), p. 143602. DOI: 10.1103/PhysRevLett.90.143602. URL: https://link.aps.org/doi/10.1103/PhysRevLett.90.143602.

[136] E. Knill, D. Leibfried, R. Reichle, J. Britton, R. B. Blakestad, J. D. Jost, C. Langer, R. Ozeri, S. Seidelin, and D. J. Wineland. "Randomized benchmarking of quantum gates." In: *Physical Review A* 77.1 (Jan. 2008). ISSN: 1094-1622. DOI: 10.1103/physreva.77.012307. URL: http://dx.doi.org/10.1103/PhysRevA.77.012307.

[137] Robin Blume-Kohout, John King Gamble, Erik Nielsen, Kenneth Rudinger, Jonathan Mizrahi, Kevin Fortier, and Peter Maunz. "Demonstration of qubit operations below a rigorous fault tolerance threshold with gate set tomography." In: *Nature Communications* 8.1 (Feb. 2017). ISSN: 2041-1723. DOI: 10.1038/ncomms14485. URL: http://dx.doi.org/10.1038/ncomms14485.

[138] Ariel Shlosberg, Andrew J. Jena, Priyanka Mukhopadhyay, Jan F. Haase, Felix Leditzky, and Luca Dellantonio. "Adaptive estimation of quantum observables." In: *Quantum* 7 (2023), p. 906. ISSN: 2521-327X. DOI: 10.22331/q-2023-01-26-906. URL: http://dx.doi.org/10.22331/q-2023-01-26-906.

[139] Rick P. A. Simon, Andrew J. Jena, and Luca Dellantonio. *Qudit measurements using bayesian estimation*. to be published. 2026.

[140] Mark Howard and Jiri Vala. "Qudit versions of the qubit $\pi/8$ gate." In: *Phys. Rev. A* 86 (2 2012), p. 022316. DOI: 10.1103/PhysRevA.86.022316. URL: https://link.aps.org/doi/10.1103/PhysRevA.86.022316.

[141] G. Cybenko. "Reducing quantum computations to elementary unitary operations." In: *Computing in Science and Engineering* 3.2 (2001), pp. 27–32. ISSN: 1521-9615. DOI: 10.1109/5992.908999.

[142] Faisal Shah Khan and Marek Perkowski. "Synthesis of multi-qudit hybrid and d-valued quantum logic circuits by decomposition." In: *Theoretical Computer Science* 367.3 (Dec. 2006), 336–346. ISSN: 0304-3975. DOI: 10.1016/j.tcs.2006.09.006. URL: http://dx.doi.org/10.1016/j.tcs.2006.09.006.

[143] Gene H. Golub and Charles F. Van Loan. *Matrix computations*. 3rd ed. Johns Hopkins studies in the mathematical sciences. Literaturverz. S. 637 - 686. Baltimore [u.a.]: Johns Hopkins Univ. Press, 1996. 694 pp. ISBN: 9780801854149.

[144] Kevin Mato, Stefan Hillmich, and Robert Wille. "Mixed-Dimensional Qudit State Preparation Using Edge-Weighted Decision Diagrams." In: *Proceedings of the 61st ACM/IEEE Design Automation Conference*. DAC '24. ACM, June 2024, 1–6. DOI: 10.1145/3649329.3656260. URL: http://dx.doi.org/10.1145/3649329.3656260.

[145] Kevin Mato, Martin Ringbauer, Lukas Burgholzer, and Robert Wille. *MQT Qudits: A Software Framework for Mixed-Dimensional Quantum Computing*. 2024. arXiv: 2410.02854 [quant-ph]. URL: https://arxiv.org/abs/2410.02854.

[146] G. J. Milburn. *Simulating nonlinear spin models in an ion trap*. 1999. arXiv: quant-ph/9908037 [quant-ph]. URL: https://arxiv.org/abs/quant-ph/9908037.

[147] Anders Sørensen and Klaus Mølmer. "Quantum Computation with Ions in Thermal Motion." In: *Phys. Rev. Lett.* 82 (9 1999), pp. 1971–1974. DOI: 10.1103/PhysRevLett.82.1971. URL: https://link.aps.org/doi/10.1103/PhysRevLett.82.1971.

[148] Anders Sørensen and Klaus Mølmer. "Entanglement and quantum computation with ions in thermal motion." In: *Physical Review A* 62.2 (July 2000). ISSN: 1094-1622. DOI: 10.1103/physreva.62.022311. URL: http://dx.doi.org/10.1103/PhysRevA.62.022311.

[149] Christian F Roos. "Ion trap quantum gates with amplitude-modulated laser beams." In: *New Journal of Physics* 10.1 (Jan. 2008), p. 013002. ISSN: 1367-2630. DOI: 10.1088/1367-2630/10/1/013002.

[150] A. Nuttall. "Some windows with very good sidelobe behavior." In: *IEEE Transactions on Acoustics, Speech, and Signal Processing* 29.1 (1981), pp. 84–91. DOI: 10.1109/TASSP.1981.1163506.

[151] Ferdinand Schmidt-Kaler, Hartmut Häffner, Mark Riebe, Stephan Gulde, Gavin P. T. Lancaster, Thomas Deuschle, Christoph Becher, Christian F. Roos, Jürgen Eschner, and Rainer Blatt. "Realization of the Cirac–Zoller controlled-NOT quantum gate." In: *Nature* 422.6930 (Mar. 2003), pp. 408–411. ISSN: 1476-4687. DOI: 10.1038/nature01494.

[152] D. G. Cory, M. D. Price, W. Maas, E. Knill, R. Laflamme, W. H. Zurek, T. F. Havel, and S. S. Somaroo. "Experimental Quantum Error Correction." In: *Physical Review Letters* 81.10 (Sept. 1998), 2152–2155. ISSN: 1079-7114. DOI: 10.1103/physrevlett.81.2152. URL: http://dx.doi.org/10.1103/PhysRevLett.81.2152.

[153] T. Monz, K. Kim, W. Hänsel, M. Riebe, A. S. Villar, P. Schindler, M. Chwalla, M. Hennrich, and R. Blatt. "Realization of the Quantum Toffoli Gate with Trapped Ions." In: *Phys. Rev. Lett.* 102 (4 2009), p. 040501. DOI: 10.1103/PhysRevLett.102.040501. URL: https://link.aps.org/doi/10.1103/PhysRevLett.102.040501.

[154] M. D. Reed, L. DiCarlo, S. E. Nigg, L. Sun, L. Frunzio, S. M. Girvin, and R. J. Schoelkopf. "Realization of three-qubit quantum error correction with superconducting circuits." In: *Nature* 482.7385 (Feb. 2012), 382–385. ISSN: 1476-4687. DOI: 10.1038/nature10786. URL: http://dx.doi.org/10.1038/nature10786.

[155] Chao Fang, Ye Wang, Ke Sun, and Jungsang Kim. *Realization of Scalable Cirac-Zoller Multi-Qubit Gates*. 2023. arXiv: 2301.07564 [quant-ph]. URL: https://arxiv.org/abs/2301.07564.

[156] Isaac L. Chuang and M. A. Nielsen. "Prescription for experimental determination of the dynamics of a quantum black box." In: *Journal of Modern Optics* 44.11–12 (Nov. 1997), 2455–2467. ISSN: 1362-3044. DOI: 10.1080/09500349708231894. URL: http://dx.doi.org/10.1080/09500349708231894.

[157] Seth T. Merkel, Jay M. Gambetta, John A. Smolin, Stefano Poletto, Antonio D. Córcoles, Blake R. Johnson, Colm A. Ryan, and Matthias Steffen. "Self-consistent quantum process tomography." In: *Physical Review A* 87.6 (June 2013). ISSN: 1094-1622. DOI: 10.1103/physreva.87.062119. URL: http://dx.doi.org/10.1103/PhysRevA.87.062119.

[158] W. P. Su, J. R. Schrieffer, and A. J. Heeger. "Solitons in Polyacetylene." In: *Phys. Rev. Lett.* 42 (25 1979), pp. 1698–1701. DOI: 10.1103/PhysRevLett.42.1698. URL: https://link.aps.org/doi/10.1103/PhysRevLett.42.1698.

[159] Bram Vancraeynest-De Cuiper, Weronika Wiesiolek, and Frank Verstraete. *Les Houches Lectures Notes on Tensor Networks*. 2025. arXiv: 2512.24390 [cond-mat.str-el]. URL: https://arxiv.org/abs/2512.24390.

[160] J. Ignacio Cirac, David Pérez-García, Norbert Schuch, and Frank Verstraete. "Matrix product states and projected entangled pair states: Concepts, symmetries, theorems." In: *Reviews of Modern Physics* 93.4 (Dec. 2021). ISSN: 1539-0756. DOI: 10.1103/revmodphys.93.045003. URL: http://dx.doi.org/10.1103/RevModPhys.93.045003.

[161] F. Verstraete, V. Murg, and J.I. Cirac. "Matrix product states, projected entangled pair states, and variational renormalization group methods for quantum spin systems." In: *Advances in Physics* 57.2 (Mar. 2008), pp. 143–224. ISSN: 1460-6976. DOI: 10.1080/14789940801912366.

[162] Guifré Vidal. "Efficient Classical Simulation of Slightly Entangled Quantum Computations." In: *Physical Review Letters* 91.14 (Oct. 2003), p. 147902. ISSN: 1079-7114. DOI: 10.1103/physrevlett.91.147902.

[163] Raffael Gawatz. "Matrix Product State based algorithms for ground states and dynamics." MA thesis. University of Copenhagen, 2017.

[164] Barbara M. Terhal and Paweł Horodecki. "Schmidt number for density matrices." In: *Physical Review A* 61.4 (Mar. 2000), p. 040301. ISSN: 1094-1622. DOI: 10.1103/physreva.61.040301.

[165] Jacob C Bridgeman and Christopher T Chubb. "Hand-waving and interpretive dance: an introductory course on tensor networks." In: *Journal of Physics A: Mathematical and Theoretical* 50.22 (May 2017), p. 223001. ISSN: 1751-8121. DOI: 10.1088/1751-8121/aa6dc3.

[166] Peter Pippan, Steven R. White, and Hans Gerd Evertz. "Efficient matrix-product state method for periodic boundary conditions." In: *Physical Review B* 81.8 (Feb. 2010), p. 081103. ISSN: 1550-235X. DOI: 10.1103/physrevb.81.081103.

[167] Damian Draxler, Jutho Haegeman, Frank Verstraete, and Matteo Rizzi. "Continuous matrix product states with periodic boundary conditions and an application to atomtronics." In: *Physical Review B* 95.4 (Jan. 2017), p. 045145. ISSN: 2469-9969. DOI: 10.1103/physrevb.95.045145.

[168] D. Perez-Garcia, F. Verstraete, M. M. Wolf, and J. I. Cirac. "Matrix product state representations." In: *Quantum Info. Comput.* 7.5 (July 2007), 401–430. ISSN: 1533-7146.

[169] F. Verstraete, J. J. García-Ripoll, and J. I. Cirac. "Matrix Product Density Operators: Simulation of Finite-Temperature and Dissipative Systems." In: *Physical Review Letters* 93.20 (Nov. 2004), p. 207204. ISSN: 1079-7114. DOI: 10.1103/physrevlett.93.207204.

[170] Matheus Schossler, Li Chen, and Alexander Seidel. "Linking infinite bond-dimension matrix product states with frustration-free Hamiltonians." In: *Physical Review B* 109.8 (Feb. 2024), p. 085106. ISSN: 2469-9969. DOI: 10.1103/physrevb.109.085106.

[171] Gemma De las Cuevas, Norbert Schuch, David Pérez-García, and J Ignacio Cirac. "Purifications of multipartite states: limitations and constructive methods." In: *New Journal of Physics* 15.12 (Dec. 2013), p. 123021. ISSN: 1367-2630. DOI: 10.1088/1367-2630/15/12/123021.

[172] V Zauner, D Draxler, L Vanderstraeten, M Degroote, J Haegeman, M M Rams, V Stojevic, N Schuch, and F Verstraete. "Transfer matrices and excitations with matrix product states." In: *New Journal of Physics* 17.5 (2015), p. 053002. DOI: 10.1088/1367-2630/17/5/053002. URL: https://dx.doi.org/10.1088/1367-2630/17/5/053002.

[173] Jutho Haegeman and Frank Verstraete. "Diagonalizing Transfer Matrices and Matrix Product Operators: A Medley of Exact and Computational Methods." In: *Annual Review of Condensed Matter Physics* 8.1 (Mar. 2017), pp. 355–406. ISSN: 1947-5462. DOI: 10.1146/annurev-conmatphys-031016-025507.

[174] M. B. Hastings. *Locality in Quantum Systems*. 2010. URL: https://arxiv.org/abs/1008.5137.

[175] W. Heisenberg. "Zur Theorie des Ferromagnetismus." In: *Zeitschrift für Physik* 49.9–10 (Sept. 1928), pp. 619–636. ISSN: 1434-601X. DOI: 10.1007/bf01328601.

[176] H. Bethe. "Zur Theorie der Metalle: I. Eigenwerte und Eigenfunktionen der linearen Atomkette." In: *Zeitschrift für Physik* 71.3–4 (Mar. 1931), pp. 205–226. ISSN: 1434-601X. DOI: 10.1007/bf01341708.

[177] Dorit Aharonov, Itai Arad, Zeph Landau, and Umesh Vazirani. *The Detectability Lemma and Quantum Gap Amplification*. 2008. URL: https://arxiv.org/abs/0811.3412.

[178] Dorit Aharonov, Itai Arad, Zeph Landau, and Umesh Vazirani. "The detectability lemma and its applications to quantum Hamiltonian complexity." In: *New Journal of Physics* 13.11, 113043 (Nov. 2011), p. 113043. DOI: 10.1088/1367-2630/13/11/113043.

[179] Matthew B. Hastings and Tohru Koma. "Spectral Gap and Exponential Decay of Correlations." In: *Communications in Mathematical Physics* 265.3 (Apr. 2006), 781–804. ISSN: 1432-0916. DOI: 10.1007/s00220-006-0030-4. URL: http://dx.doi.org/10.1007/s00220-006-0030-4.

[180] Bruno Nachtergaele and Robert Sims. "Lieb-Robinson Bounds and the Exponential Clustering Theorem." In: *Communications in Mathematical Physics* 265.1 (Mar. 2006), 119–130. ISSN: 1432-0916. DOI: 10.1007/s00220-006-1556-1. URL: http://dx.doi.org/10.1007/s00220-006-1556-1.

[181] Yuval Baum, Thore Posske, Ion Cosma Fulga, Björn Trauzettel, and Ady Stern. "Gapless topological superconductors: Model Hamiltonian and realization." In: *Physical Review B* 92.4 (July 2015), p. 045128. ISSN: 1550-235X. DOI: 10.1103/physrevb.92.045128.

[182] R. Shankar. *Topological Insulators – A review*. 2018. URL: https://arxiv.org/abs/1804.06471.

[183] Itai Arad, Alexei Kitaev, Zeph Landau, and Umesh Vazirani. *An area law and sub-exponential algorithm for 1D systems*. 2013. URL: https://arxiv.org/abs/1301.1162.

[184] M. Cerezo et al. "Variational quantum algorithms." In: *Nature Reviews Physics* 3.9 (Aug. 2021), 625–644. ISSN: 2522-5820. DOI: 10.1038/s42254-021-00348-9. URL: http://dx.doi.org/10.1038/s42254-021-00348-9.

[185] J. Eisert. "Computational Difficulty of Global Variations in the Density Matrix Renormalization Group." In: *Phys. Rev. Lett.* 97 (26 2006), p. 260501. DOI: 10.1103/PhysRevLett.97.260501. URL: https://link.aps.org/doi/10.1103/PhysRevLett.97.260501.

[186] Norbert Schuch, Ignacio Cirac, and Frank Verstraete. "Computational Difficulty of Finding Matrix Product Ground States." In: *Physical Review Letters* 100.25 (June 2008). ISSN: 1079-7114. DOI: 10.1103/physrevlett.100.250501. URL: http://dx.doi.org/10.1103/PhysRevLett.100.250501.

[187] Steven R. White. "Density-matrix algorithms for quantum renormalization groups." In: *Phys. Rev. B* 48 (14 1993), pp. 10345–10356. DOI: 10.1103/PhysRevB.48.10345. URL: https://link.aps.org/doi/10.1103/PhysRevB.48.10345.

[188] F. Verstraete, D. Porras, and J. I. Cirac. "Density Matrix Renormalization Group and Periodic Boundary Conditions: A Quantum Information Perspective." In: *Phys. Rev. Lett.* 93 (22 2004), p. 227205. DOI: 10.1103/PhysRevLett.93.227205. URL: https://link.aps.org/doi/10.1103/PhysRevLett.93.227205.

[189] Jorge Nocedal and Stephen J Wright. *Numerical Optimization*. 2nd ed. Springer New York, July 2006. ISBN: 978-0-387-30303-1. DOI: 10.1007/978-0-387-40065-5. URL: https://doi.org/10.1007/978-0-387-40065-5.

[190] M. Sanz, M. M. Wolf, D. Pérez-García, and J. I. Cirac. "Matrix product states: Symmetries and two-body Hamiltonians." In: *Physical Review A* 79.4 (Apr. 2009). ISSN: 1094-1622. DOI: 10.1103/physreva.79.042308. URL: http://dx.doi.org/10.1103/PhysRevA.79.042308.

[191] R.E. Peierls. *Quantum Theory of Solids*. International series of monographs on physics. Clarendon Press, 1955. ISBN: 9780198507819.

[192] D. Kartoon, U. Argaman, and G. Makov. "Driving forces behind the distortion of one-dimensional monatomic chains: Peierls theorem revisited." In: *Physical Review B* 98.16 (Oct. 2018), p. 165429. ISSN: 2469-9969. DOI: 10.1103/physrevb.98.165429.

[193] W. P. Su, J. R. Schrieffer, and A. J. Heeger. "Erratum: Soliton excitations in polyacetylene." In: *Phys. Rev. B* 28 (2 1983), pp. 1138–1138. DOI: 10.1103/PhysRevB.28.1138. URL: https://link.aps.org/doi/10.1103/PhysRevB.28.1138.

[194] Hideki Shirakawa, Edwin J. Louis, Alan G. MacDiarmid, Chwan K. Chiang, and Alan J. Heeger. "Synthesis of electrically conducting organic polymers: halogen derivatives of polyacetylene, (CH) x." In: *Journal of the Chemical Society, Chemical Communications* 16 (1977), p. 578. ISSN: 0022-4936. DOI: 10.1039/c39770000578.

[195] C. K. Chiang, C. R. Fincher, Y. W. Park, A. J. Heeger, H. Shirakawa, E. J. Louis, S. C. Gau, and Alan G. MacDiarmid. "Electrical Conductivity in Doped Polyacetylene." In: *Phys. Rev. Lett.* 39 (17 1977), pp. 1098–1101. DOI: 10.1103/PhysRevLett.39.1098. URL: https://link.aps.org/doi/10.1103/PhysRevLett.39.1098.

[196] Navketan Batra and Goutam Sheet. "Physics with Coffee and Doughnuts: Understanding the Physics Behind Topological Insulators Through Su-Schrieffer-Heeger Model." In: *Resonance* 25.6 (June 2020), 765–786. ISSN: 0973-712X. DOI: 10.1007/s12045-020-0995-x. URL: http://dx.doi.org/10.1007/s12045-020-0995-x.

[197] Rudolf Gross and Achim Marx. *Festkörperphysik*. Berlin, Boston: De Gruyter, 2018. ISBN: 9783110559187. DOI: doi:10.1515/9783110559187. URL: https://doi.org/10.1515/9783110559187.

[198] Bo-Hung Chen and Dah-Wei Chiou. "An elementary rigorous proof of bulk-boundary correspondence in the generalized Su-Schrieffer-Heeger model." In: *Physics Letters A* 384.7 (Mar. 2020), p. 126168. ISSN: 0375-9601. DOI: 10.1016/j.physleta.2019.126168. URL: http://dx.doi.org/10.1016/j.physleta.2019.126168.

[199] Tristan Needham. *Visual complex analysis*. Ed. by Roger Penrose. 25th anniversary edition. First edition published in 1997. Oxford, United Kingdom: Oxford University Press, 2023. 675 pp. ISBN: 9780192868923.

[200] Scott J. Carter and Masahico Saito. *Knotted Surfaces and their Diagrams*. Ed. by Masahico Saito. Online-Ausg. Mathematical Surveys and Monographs 0076-5376 (print) 2331-7159 (online) v. 55. Includes bibliographical references (p. 243-255) and index. - Electronic reproduction; Providence, Rhode Island; American Mathematical Society; 2012. - Description based on print version record. Providence, R.I: American Mathematical Society, Dec. 1997. 1258 pp. ISBN: 0821805932.

[201] T. Senthil. "Symmetry-Protected Topological Phases of Quantum Matter." In: *Annual Review of Condensed Matter Physics* 6.1 (Mar. 2015), 299–324. ISSN: 1947-5462. DOI: 10.1146/annurev-conmatphys-031214-014740. URL: http://dx.doi.org/10.1146/annurev-conmatphys-031214-014740.

[202] Subir Sachdev. *Quantum Phase Transitions*. Cambridge University Press, Apr. 2011. ISBN: 9780511973765. DOI: 10.1017/cbo9780511973765. URL: http://doi.org/10.1017/CBO9780511973765.

[203] Jutho Haegeman, David Pérez-García, Ignacio Cirac, and Norbert Schuch. "Order Parameter for Symmetry-Protected Phases in One Dimension." In: *Physical Review Letters* 109.5 (July 2012). ISSN: 1079-7114. DOI: 10.1103/physrevlett.109.050402. URL: http://dx.doi.org/10.1103/PhysRevLett.109.050402.

[204] Andreas Elben, Jinlong Yu, Guanyu Zhu, Mohammad Hafezi, Frank Pollmann, Peter Zoller, and Benoît Vermersch. "Many-body topological invariants from randomized measurements in synthetic quantum matter." In: *Science Advances* 6.15 (Apr. 2020). ISSN: 2375-2548. DOI: 10.1126/sciadv.aaz3666. URL: http://dx.doi.org/10.1126/sciadv.aaz3666.

[205] Frank Pollmann and Ari M. Turner. "Detection of symmetry-protected topological phases in one dimension." In: *Physical Review B* 86.12 (Sept. 2012). ISSN: 1550-235X. DOI: 10.1103/physrevb.86.125441. URL: http://dx.doi.org/10.1103/PhysRevB.86.125441.

[206] G. Mauro D'Ariano, Matteo G.A. Paris, and Massimiliano F. Sacchi. "Quantum Tomography." In: *Advances in Imaging and Electron Physics*. Elsevier, 2003, pp. 205–308. ISBN: 9780120147700. DOI: 10.1016/s1076-5670(03)80065-4.

[207] J. A. Nelder and R. Mead. "A Simplex Method for Function Minimization." In: *The Computer Journal* 7.4 (Jan. 1965), pp. 308–313. ISSN: 0010-4620. DOI: 10.1093/comjnl/7.4.308. eprint: https://academic.oup.com/comjnl/article-pdf/7/4/308/1013182/7-4-308.pdf. URL: https://doi.org/10.1093/comjnl/7.4.308.

[208] Z. Hradil. "Quantum-state estimation." In: *Phys. Rev. A* 55 (3 1997), R1561–R1564. DOI: 10.1103/PhysRevA.55.R1561. URL: https://link.aps.org/doi/10.1103/PhysRevA.55.R1561.

[209] K. Banaszek, G. M. D'Ariano, M. G. A. Paris, and M. F. Sacchi. "Maximum-likelihood estimation of the density matrix." In: *Phys. Rev. A* 61 (1 1999), p. 010304. DOI: 10.1103/PhysRevA.61.010304. URL: https://link.aps.org/doi/10.1103/PhysRevA.61.010304.

[210] Robert Hooke and T. A. Jeeves. "" Direct Search" Solution of Numerical and Statistical Problems." In: *J. ACM* 8.2 (Apr. 1961), 212–229. ISSN: 0004-5411. DOI: 10.1145/321062.321069. URL: https://doi.org/10.1145/321062.321069.

[211] Virginia Torczon. "On the Convergence of Pattern Search Algorithms." In: *SIAM Journal on Optimization* 7.1 (1997), pp. 1–25. DOI: 10.1137/S1052623493250780. URL: https://doi.org/10.1137/S1052623493250780.

[212] William C. Davidon. "Variable Metric Method for Minimization." In: *SIAM Journal on Optimization* 1.1 (1991), pp. 1–17. DOI: 10.1137/0801001. URL: https://doi.org/10.1137/0801001.

[213] Thomas Beckers. *An Introduction to Gaussian Process Models*. 2021. URL: https://arxiv.org/abs/2102.05497.

[214] Carl Edward Rasmussen and Christopher K. I. Williams. *Gaussian Processes for Machine Learning*. The MIT Press, Nov. 2005. ISBN: 9780262256834. DOI: 10.7551/mitpress/3206.001.0001. URL: https://doi.org/10.7551/mitpress/3206.001.0001.

[215] Michael C. Fu, Chun-Hung Chen, and Leyuan Shi. "Some topics for simulation optimization." In: *2008 Winter Simulation Conference*. 2008, pp. 27–38. DOI: 10.1109/WSC.2008.4736053.

[216] Norman Richard Draper and Harry Smith, eds. *Applied regression analysis*. Third edition. Wiley series in probability and statistics. New York: Wiley, 2011. 1706 pp. ISBN: 0-471-17082-8.

[217] Steven T. Flammia and Joel J. Wallman. "Efficient Estimation of Pauli Channels." In: *ACM Transactions on Quantum Computing* 1.1 (Dec. 2020), 1–32. ISSN: 2643-6817. DOI: 10.1145/3408039. URL: http://dx.doi.org/10.1145/3408039.

[218] Michael Faraday. "On the physical character of the lines of magnetic force." In: *The London, Edinburgh, and Dublin Philosophical Magazine and Journal of Science* 3.20 (June 1852), pp. 401–428. ISSN: 1941-5990. DOI: 10.1080/14786445208647033.

[219] J.C. Maxwell. "On physical lines of force." In: *Philosophical Magazine* 90.sup1 (1861), pp. 11–23. ISSN: 1478-6443. DOI: 10.1080/14786431003659180.

[220] A. Einstein. "Zur Elektrodynamik bewegter Körper." In: *Annalen der Physik* 322.10 (Jan. 1905), pp. 891–921. ISSN: 1521-3889. DOI: 10.1002/andp.19053221004.

[221] Albert Einstein and Marcel Grossmann. "Entwurf einer verallgemeinerten Relativitätstheorie und einer Theorie der Gravitation." In: *Zeitschrift für Mathematik und Physik* 62 (1913), A38–A38. ISSN: 1436-5081. DOI: 10.1007/bf01999515.

[222] A. Einstein. "Die Grundlage der allgemeinen Relativitätstheorie." In: *Annalen der Physik* 354.7 (Jan. 1916), pp. 769–822. ISSN: 1521-3889. DOI: 10.1002/andp.19163540702.

[223] Albert Einstein. "Ether and the Theory of Relativity." In: *The Genesis of General Relativity*. Originally published as Äther und Relativitätstheory in 1920 by Springer, Berlin. English translation 1922 by Methuen publishing, London. Springer Netherlands, 2007, pp. 1537–1542. ISBN: 9781402040009. DOI: 10.1007/978-1-4020-4000-9_34.

[224] Louis De Broglie. "Recherches sur la théorie des Quanta." In: *Annales de Physique* 10.3 (1925). Translation by A. Kracklauer (2004), pp. 22–128. ISSN: 1286-4838. DOI: 10.1051/anphys/192510030022.

[225] E. Schrödinger. "An Undulatory Theory of the Mechanics of Atoms and Molecules." In: *Physical Review* 28.6 (Dec. 1926), pp. 1049–1070. ISSN: 0031-899X. DOI: 10.1103/physrev.28.1049.

[226] M. Born and P. Jordan. "Zur Quantenmechanik." In: *Zeitschrift für Physik* 34.1 (Dec. 1925), pp. 858–888. ISSN: 1434-601X. DOI: 10.1007/bf01328531.

[227] M. Born, W. Heisenberg, and P. Jordan. "Zur Quantenmechanik. II." In: *Zeitschrift für Physik* 35.8–9 (Aug. 1926), pp. 557–615. ISSN: 1434-601X. DOI: 10.1007/bf01379806.

[228] Paul Adrien Maurice Dirac. "The quantum theory of the emission and absorption of radiation." In: *Proceedings of the Royal Society of London. Series A, Containing Papers of a Mathematical and Physical Character* 114.767 (Mar. 1927), pp. 243–265. ISSN: 2053-9150. DOI: 10.1098/rspa.1927.0039.

[229] Paul Adrien Maurice Dirac and Ralph Howard Fowler. "The quantum theory of the electron." In: *Proceedings of the Royal Society of London. Series A, Containing Papers of a Mathematical and Physical Character* 117.778 (1928), pp. 610–624. DOI: 10.1098/rspa.1928.0023. URL: https://royalsocietypublishing.org/doi/abs/10.1098/rspa.1928.0023.

[230] David J. Griffiths. *Introduction to elementary particles*. 2., rev. ed., 5. reprint. Weinheim: Wiley-VCH, 2011. 454 pp. ISBN: 978-3527406012.

[231] Steven Weinberg. *The quantum theory of fields. Volume I: Foundations*. 10th ed. Vol. 1. Cambridge Univ. Press, 2014. 609 pp. ISBN: 9780521670562.

[232] David Tong. *Lectures on Quantum Field Theory*. Course Material (online). Cambridge University, 2006. URL: https://www.damtp.cam.ac.uk/user/tong/qft.html.

[233] David Tong. *Lectures on Gauge Theory*. Course Material (online). Cambridge University, 2018. URL: https://www.damtp.cam.ac.uk/user/tong/gaugetheory/gt.pdf.

[234] Hans Briegl. *Relativitätstheorie*. Lecture Notes, 705715. Universität Innsbruck, 2014.

[235] David J. Griffiths. *Introduction to electrodynamics*. 4. ed., international ed. Always learning. Boston [u.a.]: Pearson, 2013. 599 pp. ISBN: 9780321847812.

[236] J.-M. Lévy. "A simple derivation of the Lorentz transformation and of the accompanying velocity and acceleration changes." In: *American Journal of Physics* 75.7 (July 2007), pp. 615–618. ISSN: 1943-2909. DOI: 10.1119/1.2719700.

[237] Lev Davidovič Landau and Evgenij M. Lifšic. *Landau. Lev Davidovič*. 3. ed., repr. Vol. 1. Mechanics. Amsterdam: Elsevier, Butterworth-Heinemann, 2011. 170 pp. ISBN: 978-0750628969.

[238] R. Rosenfelder. *Path Integrals in Quantum Physics*. 2017. arXiv: 1209.1315 [nucl-th]. URL: https://arxiv.org/abs/1209.1315.

[239] Walter Gordon. "Der Comptoneffekt nach der Schrödingerschen Theorie." In: *Zeitschrift für Physik* 40.1–2 (Jan. 1926), pp. 117–133. ISSN: 1434-601X. DOI: 10.1007/bf01390840.

[240] Oskar Klein. "Quantentheorie und fünfdimensionale Relativitätstheorie." In: *Zeitschrift für Physik* 37.12 (Dec. 1926), pp. 895–906. ISSN: 1434-601X. DOI: 10.1007/bf01397481.

[241] H.J. Groenewold. "On the principles of elementary quantum mechanics." In: *Physica* 12.7 (Oct. 1946), pp. 405–460. ISSN: 0031-8914. DOI: 10.1016/s0031-8914(46)80059-4.

[242] H. Lehmann, K. Symanzik, and W. Zimmermann. "Zur Formulierung quantisierter Feldtheorien." In: *Il Nuovo Cimento* 1.1 (Jan. 1955), pp. 205–225. ISSN: 1827-6121. DOI: 10.1007/bf02731765.

[243] Roderick Sutherland. "Interpretation of the Klein-Gordon Probability Density." In: (2015). DOI: 10.48550/ARXIV.1509.07380.

[244] W. Pauli. "Relativistic Field Theories of Elementary Particles." In: *Reviews of Modern Physics* 13.3 (July 1941), pp. 203–232. ISSN: 0034-6861. DOI: 10.1103/revmodphys.13.203.

[245] Andrew M. Steane. *An introduction to spinors*. 2013. DOI: 10.48550/ARXIV.1312.3824.

[246] E. Noether. "Invariante Variationsprobleme." ger. In: *Nachrichten von der Gesellschaft der Wissenschaften zu Göttingen, Mathematisch-Physikalische Klasse* 1918 (1918), pp. 235–257. URL: http://eudml.org/doc/59024.

[247] Emmy Noether and M. A. Tavel. "Invariant Variation Problems." In: (2005). DOI: 10.48550/ARXIV.PHYSICS/0503066.

[248] F. Klein. "Über die Differentialgesetze für Erhaltung von Impuls und Energie in der Einsteinschen Gravitationstheorie." In: *Nachrichten von der Gesellschaft der Wissenschaften zu Göttingen, Mathematisch-Physikalische Klasse* 1918 (1918), pp. 171–189. URL: http://eudml.org/doc/59022.

[249] Robert Mills. "Gauge fields." In: *American Journal of Physics* 57.6 (June 1989), pp. 493–507. ISSN: 1943-2909. DOI: 10.1119/1.15984.

[250] Romero Isart Josep Oriol. *Quantum Mechanics II*. Lecture Notes, 705851. Universität Innsbruck, 2016.

[251] Chris D White. "The SAGEX review on scattering amplitudes Chapter 12: Amplitudes and collider physics." In: *Journal of Physics A: Mathematical and Theoretical* 55.44 (Nov. 2022), p. 443013. ISSN: 1751-8121. DOI: 10.1088/1751-8121/ac8649.

[252] Gösta Gustafson, Stefan Prestel, Michael Spannowsky, and Simon Williams. "Collider events on a quantum computer." In: *Journal of High Energy Physics* 2022.11 (Nov. 2022). ISSN: 1029-8479. DOI: 10.1007/jhep11(2022)035.

[253] Heinz J. Rothe. *Lattice Gauge Theories: An Introduction. An Introduction (4th Edition)*. Singapore: World Scientific Publishing Co, 2012. 1628 pp. ISBN: 978-9814365864.

[254] Richard Phillips Feynman, Albert R. Hibbs, and Daniel F. Styer. *Quantum Mechanics and Path Integrals Emended Edition. Emended Edition*. Dover Publications, Incorporated, 2012. ISBN: 0-486-13463-6.

[255] John A. Wheeler. "On the Mathematical Description of Light Nuclei by the Method of Resonating Group Structure." In: *Physical Review* 52.11 (Dec. 1937), pp. 1107–1122. ISSN: 0031-899X. DOI: 10.1103/physrev.52.1107.

[256] R. P. Feynman. "Space-Time Approach to Quantum Electrodynamics." In: *Physical Review* 76.6 (Sept. 1949), pp. 769–789. ISSN: 0031-899X. DOI: 10.1103/physrev.76.769.

[257] Jun J. Sakurai. *Advanced quantum mechanics*. Always learning. Includes index. - Hier auch später erschienene, unveränderte Nachdrucke. New Delhi: Pearson, 1967. 344 pp. ISBN: 8177589164.

[258] Richard H. Parker, Chenghui Yu, Weicheng Zhong, Brian Estey, and Holger Müller. "Measurement of the fine-structure constant as a test of the Standard Model." In: *Science* 360.6385 (Apr. 2018), pp. 191–195. ISSN: 1095-9203. DOI: 10.1126/science.aap7706.

[259] H. Fritzsch. "Fundamental Constants at High Energy." In: (2002). DOI: 10.48550/ARXIV.HEP-PH/0201198.

[260] M. Gell-Mann and F. E. Low. "Quantum Electrodynamics at Small Distances." In: *Physical Review* 95.5 (Sept. 1954), pp. 1300–1312. ISSN: 0031-899X. DOI: 10.1103/physrev.95.1300.

[261] Othmar Steinmann. *Perturbative Quantum Electrodynamics and Axiomatic Field Theory*. Springer Berlin Heidelberg, 2000. ISBN: 9783662042977. DOI: 10.1007/978-3-662-04297-7.

[262] Richard P. Feynman. *QED - The strange theory of light and matter. The strange theory of light and matter; Alix G. Mautner memorial lectures*. 7. print, with corr. Princeton, NJ: Princeton Univ. Pr., 1988. 158 pp. ISBN: 0691024170.

[263] Michael Creutz. "Gauge fixing, the transfer matrix, and confinement on a lattice." In: *Physical Review D* 15.4 (Feb. 1977), pp. 1128–1136. ISSN: 0556-2821. DOI: 10.1103/physrevd.15.1128.

[264] Thomas Appelquist, J. Carazzone, H. Kluberg-Stern, and M. Roth. "Infrared Finiteness in Yang-Mills Theories." In: *Physical Review Letters* 36.14 (Apr. 1976), pp. 768–772. ISSN: 0031-9007. DOI: 10.1103/physrevlett.36.768.

[265] Kenneth G. Wilson. "Confinement of quarks." In: *Physical Review D* 10.8 (Oct. 1974), pp. 2445–2459. ISSN: 0556-2821. DOI: 10.1103/physrevd.10.2445.

[266] John Kogut and Leonard Susskind. "Hamiltonian formulation of Wilson's lattice gauge theories." In: *Physical Review D* 11.2 (Jan. 1975), pp. 395–408. ISSN: 0556-2821. DOI: 10.1103/physrevd.11.395.

[267] Erez Zohar and Michele Burrello. "Formulation of lattice gauge theories for quantum simulations." In: *Physical Review D* 91.5 (Mar. 2015), p. 054506. ISSN: 1550-2368. DOI: 10.1103/physrevd.91.054506.

[268] Leonard Susskind. "Lattice fermions." In: *Physical Review D* 16.10 (Nov. 1977), pp. 3031–3039. ISSN: 0556-2821. DOI: 10.1103/physrevd.16.3031.

[269] Sidney D. Drell, Marvin Weinstein, and Shimon Yankielowicz. "Strong-coupling field theory. I: Variational approach to ϕ^4 theory." In: *Physical Review D* 14.2 (July 1976), pp. 487–516. ISSN: 0556-2821. DOI: 10.1103/physrevd.14.487.

[270] Luuk H. Karsten and Jan Smit. "Axial symmetry in lattice theories." In: *Nuclear Physics B* 144.2–3 (Nov. 1978), pp. 536–546. ISSN: 0550-3213. DOI: 10.1016/0550-3213(78)90385-1.

[271] Luuk H. Karsten and Jan Smit. "The vacuum polarization with SLAC lattice fermions." In: *Physics Letters B* 85.1 (July 1979), pp. 100–102. ISSN: 0370-2693. DOI: 10.1016/0370-2693(79)90786-x.

[272] Paul H. Ginsparg and Kenneth G. Wilson. "A remnant of chiral symmetry on the lattice." In: *Physical Review D* 25.10 (May 1982), pp. 2649–2657. ISSN: 0556-2821. DOI: 10.1103/physrevd.25.2649.

[273] Esteban A. Martinez et al. "Real-time dynamics of lattice gauge theories with a few-qubit quantum computer." In: *Nature* 534.7608 (June 2016), pp. 516–519. ISSN: 1476-4687. DOI: 10.1038/nature18318.

[274] S Booth et al. "The strong coupling constant from lattice QCD with Nf = 2 dynamical quarks." In: *Nuclear Physics B - Proceedings Supplements* 106–107 (Mar. 2002), pp. 308–310. ISSN: 0920-5632. DOI: 10.1016/s0920-5632(01)01697-8.

[275] Arianna Crippa, Karl Jansen, and Enrico Rinaldi. "Analysis of the confinement string in (2+1)-dimensional Quantum Electrodynamics with a trapped-ion quantum computer." In: *Communications Physics* 9.1 (Jan. 2026). ISSN: 2399-3650. DOI: 10.1038/s42005-025-02465-8.

[276] Ying Li and Simon C. Benjamin. "Efficient Variational Quantum Simulator Incorporating Active Error Minimization." In: *Physical Review X* 7.2 (June 2017), p. 021050. ISSN: 2160-3308. DOI: 10.1103/physrevx.7.021050.

[277] Xiao Yuan, Suguru Endo, Qi Zhao, Ying Li, and Simon C. Benjamin. "Theory of variational quantum simulation." In: *Quantum* 3 (Oct. 2019), p. 191. ISSN: 2521-327X. DOI: 10.22331/q-2019-10-07-191.

[278] Bryan T. Gard, Linghua Zhu, George S. Barron, Nicholas J. Mayhall, Sophia E. Economou, and Edwin Barnes. "Efficient symmetry-preserving state preparation circuits for the variational quantum eigensolver algorithm." In: *npj Quantum Information* 6.1 (Jan. 2020). ISSN: 2056-6387. DOI: 10.1038/s41534-019-0240-1.

[279] Peter I. Frazier. *A Tutorial on Bayesian Optimization*. 2018. DOI: 10.48550/ARXIV.1807.02811.

[280] H. F. Trotter. "On the product of semi-groups of operators." In: *Proceedings of the American Mathematical Society* 10.4 (Aug. 1959), pp. 545–551. ISSN: 1088-6826. DOI: 10.1090/s0002-9939-1959-0108732-6.

[281] Erez Zohar, Alessandro Farace, Benni Reznik, and J. Ignacio Cirac. "Digital lattice gauge theories." In: *Physical Review A* 95.2 (Feb. 2017), p. 023604. ISSN: 2469-9934. DOI: 10.1103/physreva.95.023604.

[282] Giuseppe Clemente, Arianna Crippa, and Karl Jansen. "Strategies for the determination of the running coupling of (2+1)-dimensional QED with quantum computing." In: *Physical Review D* 106.11 (Dec. 2022), p. 114511. ISSN: 2470-0029. DOI: 10.1103/physrevd.106.114511.

[283] Walter Rantner and Xiao-Gang Wen. "Electron Spectral Function and Algebraic Spin Liquid for the Normal State of Underdoped High-T_c Superconductors." In: *Physical Review Letters* 86.17 (Apr. 2001), pp. 3871–3874. ISSN: 1079-7114. DOI: 10.1103/physrevlett.86.3871.

[284] Ian Affleck and J. Brad Marston. "Large-n limit of the Heisenberg-Hubbard model: Implications for high-T_c superconductors." In: *Physical Review B* 37.7 (Mar. 1988), pp. 3774–3777. ISSN: 0163-1829. DOI: 10.1103/physrevb.37.3774.

[285] Arianna Crippa, Simone Romiti, Lena Funcke, Karl Jansen, Stefan Kühn, Paolo Stornati, and Carsten Urbach. "Towards determining the (2+1)-dimensional quantum electrodynamics running coupling with Monte Carlo and quantum computing methods." In: *Communications Physics* 8.1 (Sept. 2025). ISSN: 2399-3650. DOI: 10.1038/s42005-025-02243-6.

[286] Christof Gattringer and Christian B. Lang. *Quantum Chromodynamics on the Lattice: An Introductory Presentation*. Springer Berlin Heidelberg, 2010. ISBN: 9783642018503. DOI: 10.1007/978-3-642-01850-3.

[287] Grégoire Pichard et al. "Rearrangement of individual atoms in a 2000-site optical-tweezer array at cryogenic temperatures." In: *Physical Review Applied* 22.2 (Aug. 2024), p. 024073. ISSN: 2331-7019. DOI: 10.1103/physrevapplied.22.024073.

[288] M. DeCross et al. "Computational Power of Random Quantum Circuits in Arbitrary Geometries." In: *Physical Review X* 15.2 (May 2025), p. 021052. ISSN: 2160-3308. DOI: 10.1103/physrevx.15.021052.

[289] Shi-An Guo et al. "Hamiltonian learning for 300 trapped ion qubits with long-range couplings." In: *Science Advances* 11.5 (Jan. 2025). ISSN: 2375-2548. DOI: 10.1126/sciadv.adt4713.

[290] C. D. Jeffries. "The Spin and Magnetic Moment of ^{43}Ca." In: *Physical Review* 90.6 (June 1953), pp. 1130–1130. ISSN: 0031-899X. DOI: 10.1103/physrev.90.1130.

[291] R. Dupree, A.P. Howes, and S.C. Kohn. "Natural abundance solid state 43Ca NMR." In: *Chemical Physics Letters* 276.5–6 (Sept. 1997), pp. 399–404. ISSN: 0009-2614. DOI: 10.1016/s0009-2614(97)00863-4.

[292] G.P.T. Lancaster, H. Häffner, M.A. Wilson, C. Becher, J. Eschner, F. Schmidt-Kaler, and R. Blatt. "Doppler cooling a single Ca^+ ion with a violet extended-cavity diode laser." In: *Applied Physics B* 76.8 (July 2003), pp. 805–808. ISSN: 1432-0649. DOI: 10.1007/s00340-003-1223-6.

[293] A. Kreuter et al. "Experimental and theoretical study of the $3d^2D$–level lifetimes of $^{40}Ca^+$." In: *Physical Review A* 71.3 (Mar. 2005), p. 032504. ISSN: 1094-1622. DOI: 10.1103/physreva.71.032504.

[294] J. Benhelm, G. Kirchmair, U. Rapol, T. Körber, C. F. Roos, and R. Blatt. "Measurement of the hyperfine structure of the $S_{1/2}$ - $D_{5/2}$ transition in Ca+43." In: *Physical Review A* 75.3 (Mar. 2007), p. 032506. ISSN: 1094-1622. DOI: 10.1103/physreva.75.032506.

[295] C. J. Ballance, T. P. Harty, N. M. Linke, M. A. Sepiol, and D. M. Lucas. "High-fidelity Quantum Logic Gates Using Trapped-Ion Hyperfine Qubits." In: *Physical Review Letters* 117.6 (Aug. 2016), p. 060504. ISSN: 1079-7114. DOI: 10.1103/physrevlett.117.060504.

[296] Daniel Gottesman. *Stabilizer Codes and Quantum Error Correction*. 1997. DOI: 10.48550/ARXIV.QUANT-PH/9705052.

[297] Lukas Postler et al. "Demonstration of fault-tolerant universal quantum gate operations." In: *Nature* 605.7911 (May 2022), 675–680. ISSN: 1476-4687. DOI: 10.1038/s41586-022-04721-1. URL: http://dx.doi.org/10.1038/s41586-022-04721-1.

[298] Dolev Bluvstein et al. "Logical quantum processor based on reconfigurable atom arrays." In: *Nature* 626.7997 (Dec. 2023), 58–65. ISSN: 1476-4687. DOI: 10.1038/s41586-023-06927-3. URL: http://dx.doi.org/10.1038/s41586-023-06927-3.

[299] Sergey Bravyi, Andrew W. Cross, Jay M. Gambetta, Dmitri Maslov, Patrick Rall, and Theodore J. Yoder. "High-threshold and low-overhead fault-tolerant quantum memory." In: *Nature* 627.8005 (Mar. 2024), pp. 778–782. ISSN: 1476-4687. DOI: 10.1038/s41586-024-07107-7.

[300] Carlo Cafaro, Federico Maiolini, and Stefano Mancini. "Quantum stabilizer codes embedding qubits into qudits." In: *Physical Review A* 86.2 (Aug. 2012), p. 022308. ISSN: 1094-1622. DOI: 10.1103/physreva.86.022308.

[301] Vlad Gheorghiu. "Standard form of qudit stabilizer groups." In: *Physics Letters A* 378.5–6 (Jan. 2014), pp. 505–509. ISSN: 0375-9601. DOI: 10.1016/j.physleta.2013.12.009.

[302] Fern H. E. Watson, Hussain Anwar, and Dan E. Browne. "Fast fault-tolerant decoder for qubit and qudit surface codes." In: *Physical Review A* 92.3 (Sept. 2015), p. 032309. ISSN: 1094-1622. DOI: 10.1103/physreva.92.032309.

[303] C. Flühmann, T. L. Nguyen, M. Marinelli, V. Negnevitsky, K. Mehta, and J. P. Home. "Encoding a qubit in a trapped-ion mechanical oscillator." In: *Nature* 566.7745 (Feb. 2019), pp. 513–517. ISSN: 1476-4687. DOI: 10.1038/s41586-019-0960-6.

[304] Brennan de Neeve, Thanh-Long Nguyen, Tanja Behrle, and Jonathan P. Home. "Error correction of a logical grid state qubit by dissipative pumping." In: *Nature Physics* 18.3 (Feb. 2022), pp. 296–300. ISSN: 1745-2481. DOI: 10.1038/s41567-021-01487-7.

[305] P. Campagne-Ibarcq et al. "Quantum error correction of a qubit encoded in grid states of an oscillator." In: *Nature* 584.7821 (Aug. 2020), pp. 368–372. ISSN: 1476-4687. DOI: 10.1038/s41586-020-2603-3.

[306] Valentin Kasper, Daniel González-Cuadra, Apoorva Hegde, Andy Xia, Alexandre Dauphin, Felix Huber, Eberhard Tiemann, Maciej Lewenstein, Fred Jendrzejewski, and Philipp Hauke. "Universal quantum computation and quantum error correction with ultracold atomic mixtures." In: *Quantum Science and Technology* 7.1 (Nov. 2021), p. 015008. ISSN: 2058-9565. DOI: 10.1088/2058-9565/ac2d39.

[307] Harry C. P. Kendell, Giacomo Ferranti, and Carrie A. Weidner. *Error Correcting States in Ultracold Atoms*. 2023. DOI: 10.48550/ARXIV.2312.07746.

[308] Benjamin L. Brock, Shraddha Singh, Alec Eickbusch, Volodymyr V. Sivak, Andy Z. Ding, Luigi Frunzio, Steven M. Girvin, and Michel H. Devoret. "Quantum error correction of qudits beyond break-even." In: *Nature* 641.8063 (May 2025), pp. 612–618. ISSN: 1476-4687. DOI: 10.1038/s41586-025-08899-y.

[309] Roman Stricker, Michael Meth, Lukas Postler, Claire Edmunds, Chris Ferrie, Rainer Blatt, Philipp Schindler, Thomas Monz, Richard Kueng, and Martin Ringbauer. "Experimental Single-Setting Quantum State Tomography." In: *PRX Quantum* 3.4 (Oct. 2022), p. 040310. ISSN: 2691-3399. DOI: 10.1103/prxquantum.3.040310.

[310] F. Riera-Sàbat, P. Sekatski, A. Pirker, and W. Dür. "Entanglement-Assisted Entanglement Purification." In: *Physical Review Letters* 127.4 (July 2021), p. 040502. ISSN: 1079-7114. DOI: 10.1103/physrevlett.127.040502.

[311] Jorge Miguel-Ramiro, Ferran Riera-Sàbat, and Wolfgang Dür. "Collective Operations Can Exponentially Enhance Quantum State Verification." In: *Physical Review Letters* 129.19 (Oct. 2022), p. 190504. ISSN: 1079-7114. DOI: 10.1103/physrevlett.129.190504.

[312] Ferran Riera-Sàbat, Jorge Miguel-Ramiro, and Wolfgang Dür. "Nondestructive verification of entangled states via fidelity witnessing." In: *Physical Review A* 107.2 (Feb. 2023), p. 022414. ISSN: 2469-9934. DOI: 10.1103/physreva.107.022414.

[313] Pavel P. Popov, Kevin T. Geier, Valentin Kasper, Maciej Lewenstein, and Philipp Hauke. "Qudit-native measurement protocol for dynamical correlations using Hadamard tests." In: *Physical Review A* 111.4 (Apr. 2025), p. 042604. ISSN: 2469-9934. DOI: 10.1103/physreva.111.042604.

[314] C.L. Edmunds, E. Rico, I. Arrazola, G.K. Brennen, M. Meth, R. Blatt, and M. Ringbauer. "Symmetry-Protected Topological Haldane Phase on a Qudit Quantum Processor." In: *PRX Quantum* 6.2 (June 2025), p. 020349. ISSN: 2691-3399. DOI: 10.1103/prxquantum.6.020349.

[315] A. Yu. Kitaev. "Fault-tolerant quantum computation by anyons." In: *Annals of Physics* 303.1 (Jan. 2003), pp. 2–30. ISSN: 0003-4916. DOI: 10.1016/s0003-4916(02)00018-0.

[316] N. Klco, E. F. Dumitrescu, A. J. McCaskey, T. D. Morris, R. C. Pooser, M. Sanz, E. Solano, P. Lougovski, and M. J. Savage. "Quantum-classical computation of Schwinger model dynamics using quantum computers." In: *Physical Review A* 98.3 (Sept. 2018), p. 032331. ISSN: 2469-9934. DOI: 10.1103/physreva.98.032331.

[317] T. A. Cochran et al. "Visualizing dynamics of charges and strings in (2 + 1)D lattice gauge theories." In: *Nature* 642.8067 (June 2025), 315â€"320. ISSN: 1476-4687. DOI: 10.1038/s41586-025-08999-9.

[318] T. Senthil and Matthew P. A. Fisher. "$\mathbb{Z}_2$ gauge theory of electron fractionalization in strongly correlated systems." In: *Physical Review B* 62.12 (Sept. 2000), pp. 7850–7881. ISSN: 1095-3795. DOI: 10.1103/physrevb.62.7850.

[319] Umberto Borla, Jesse J. Osborne, Sergej Moroz, and Jad C. Halimeh. *String Breaking in a* $2+1D$ $\mathbb{Z}_2$ *Lattice Gauge Theory*. 2025. DOI: 10.48550/ARXIV.2501.17929.

[320] Reinis Irmejs, Mari-Carmen Bañuls, and J. Ignacio Cirac. "Quantum simulation of $\mathbb{Z}_2$ lattice gauge theory with minimal resources." In: *Physical Review D* 108.7 (Oct. 2023), p. 074503. ISSN: 2470-0029. DOI: 10.1103/physrevd.108.074503.

[321] Daniel Robaina, Mari Carmen Banuls, and J. Ignacio Cirac. "Simulating 2+1D $\mathbb{Z}_3$ Lattice Gauge Theory with an Infinite Projected Entangled-Pair State." In: *Physical Review Letters* 126.5 (Feb. 2021), p. 050401. ISSN: 1079-7114. DOI: 10.1103/physrevlett.126.050401.

[322] Angus Kan, Lena Funcke, Stefan Kühn, Luca Dellantonio, Jinglei Zhang, Jan F. Haase, Christine A. Muschik, and Karl Jansen. "Investigating a (3+1)D topological θ-term in the Hamiltonian formulation of lattice gauge theories for quantum and classical simulations." In: *Physical Review D* 104.3 (Aug. 2021), p. 034504. ISSN: 2470-0029. DOI: 10.1103/physrevd.104.034504.

[323] Erez Zohar. "Quantum simulation of lattice gauge theories in more than one space dimension - requirements, challenges and methods." In: *Philosophical Transactions of the Royal Society A: Mathematical, Physical and Engineering Sciences* 380.2216 (Dec. 2021). ISSN: 1471-2962. DOI: 10.1098/rsta.2021.0069.

[324] Anthony Ciavarella, Natalie Klco, and Martin J. Savage. "Trailhead for quantum simulation of SU(3) Yang-Mills lattice gauge theory in the local multiplet basis." In: *Physical Review D* 103.9 (May 2021), p. 094501. ISSN: 2470-0029. DOI: 10.1103/physrevd.103.094501.

[325] Jad C. Halimeh, Masanori Hanada, Shunji Matsuura, Franco Nori, Enrico Rinaldi, and Andreas Schäfer. *A universal framework for the quantum simulation of Yang-Mills theory*. 2024. DOI: 10.48550/ARXIV.2411.13161.

[326] Mario Motta, Chong Sun, Adrian T. K. Tan, Matthew J. O'Rourke, Erika Ye, Austin J. Minnich, Fernando G. S. L. Brandão, and Garnet Kin-Lic Chan. "Determining eigenstates and thermal states on a quantum computer using quantum imaginary time evolution." In: *Nature Physics* 16.2 (Nov. 2019), pp. 205–210. ISSN: 1745-2481. DOI: 10.1038/s41567-019-0704-4.

[327] Andreu Anglés-Castillo, Luca Ion, Tanmoy Pandit, Rafael Gomez-Lurbe, Rodrigo Martínez, and Miguel Angel Garcia-March. *Understanding Quantum Imaginary Time Evolution and its Variational form*. 2025. DOI: 10.48550/ARXIV.2510.02015.

[328] Farrokh Vatan and Colin P. Williams. *Realization of a General Three-Qubit Quantum Gate*. 2004. DOI: 10.48550/ARXIV.QUANT-PH/0401178.

[329] Alexander Erhard, Joel J. Wallman, Lukas Postler, Michael Meth, Roman Stricker, Esteban A. Martinez, Philipp Schindler, Thomas Monz, Joseph Emerson, and Rainer Blatt. "Characterizing large-scale quantum computers via cycle benchmarking." In: *Nature Communications* 10.1 (Nov. 2019). ISSN: 2041-1723. DOI: 10.1038/s41467-019-13068-7.

[330] Alexander Erhard et al. "Entangling logical qubits with lattice surgery." In: *Nature* 589.7841 (Jan. 2021), pp. 220–224. ISSN: 1476-4687. DOI: 10.1038/s41586-020-03079-6.

[331] Roman Stricker, Davide Vodola, Alexander Erhard, Lukas Postler, Michael Meth, Martin Ringbauer, Philipp Schindler, Rainer Blatt, Markus Müller, and Thomas Monz. "Characterizing Quantum Instruments: From Nondemolition Measurements to Quantum Error Correction." In: *PRX Quantum* 3.3 (Aug. 2022), p. 030318. ISSN: 2691-3399. DOI: 10.1103/prxquantum.3.030318.

[332] Pavel P. Popov, Michael Meth, Maciej Lewestein, Philipp Hauke, Martin Ringbauer, Erez Zohar, and Valentin Kasper. "Variational quantum simulation of U(1) lattice gauge theories with qudit systems." In: *Physical Review Research* 6.1 (Feb. 2024), p. 013202. ISSN: 2643-1564. DOI: 10.1103/physrevresearch.6.013202.

[333] Roman Stricker et al. "Towards experimental classical verification of quantum computation." In: *Quantum Science and Technology* 9.2 (Feb. 2024), 02LT01. ISSN: 2058-9565. DOI: 10.1088/2058-9565/ad2986.

[334] Gonzalo Camacho, Claire L. Edmunds, Michael Meth, Martin Ringbauer, and Benedikt Fauseweh. *Observing dynamical localization on a trapped-ion qudit quantum processor*. 2024. DOI: 10.48550/ARXIV.2412.13141.

[335] Martin Ringbauer et al. "Verifiable measurement-based quantum random sampling with trapped ions." In: *Nature Communications* 16.1 (Jan. 2025). ISSN: 2041-1723. DOI: 10.1038/s41467-024-55342-3.

[336] Rohan Joshi, Jan C. Louw, Michael Meth, Jesse J. Osborne, Kevin Mato, Guo-Xian Su, Martin Ringbauer, and Jad C. Halimeh. *Probing Hadron Scattering in Lattice Gauge Theories on Qudit Quantum Computers*. 2025. DOI: 10.48550/ARXIV.2507.12614.

[337] Rohan Joshi, Michael Meth, Jan C. Louw, Jesse J. Osborne, Kevin Mato, Martin Ringbauer, and Jad C. Halimeh. *Efficient Qudit Circuit for Quench Dynamics of* $2+1D$ *Quantum Link Electrodynamics*. 2025. DOI: 10.48550/ARXIV.2507.12589.

[338] Robert Stárek, Tim Gollerthan, Olga Leskovjanová, Michael Meth, Peter Tirler, Nicolai Friis, Martin Ringbauer, and Ladislav Mišta. *Experimental verification of multi-copy activation of genuine multipartite entanglement*. 2025. DOI: 10.48550/ARXIV.2510.12457.

[339] Leonardo S. V. Santos, Peter Tirler, Michael Meth, Lukas Gerster, Manuel John, Keshav Pareek, Tim Gollerthan, Martin Ringbauer, and Otfried Gühne. *Device-independent quantum memory certification in two-point measurement experiments*. 2026. DOI: 10.48550/ARXIV.2601.14191.